frontiers | Research Topics

Advances in observations and modeling of physical processes in the marine environment

Edited by
Guihua Wang, Darko Koracin and Dujuan Kang

Published in
Frontiers in Earth Science

ISSN 1664-8714
ISBN 978-2-83251-284-5
DOI 10.3389/978-2-83251-284-5

About Frontiers

Frontiers is more than just an open access publisher of scholarly articles: it is a pioneering approach to the world of academia, radically improving the way scholarly research is managed. The grand vision of Frontiers is a world where all people have an equal opportunity to seek, share and generate knowledge. Frontiers provides immediate and permanent online open access to all its publications, but this alone is not enough to realize our grand goals.

Frontiers journal series

The Frontiers journal series is a multi-tier and interdisciplinary set of open-access, online journals, promising a paradigm shift from the current review, selection and dissemination processes in academic publishing. All Frontiers journals are driven by researchers for researchers; therefore, they constitute a service to the scholarly community. At the same time, the *Frontiers journal series* operates on a revolutionary invention, the tiered publishing system, initially addressing specific communities of scholars, and gradually climbing up to broader public understanding, thus serving the interests of the lay society, too.

Dedication to quality

Each Frontiers article is a landmark of the highest quality, thanks to genuinely collaborative interactions between authors and review editors, who include some of the world's best academicians. Research must be certified by peers before entering a stream of knowledge that may eventually reach the public - and shape society; therefore, Frontiers only applies the most rigorous and unbiased reviews. Frontiers revolutionizes research publishing by freely delivering the most outstanding research, evaluated with no bias from both the academic and social point of view. By applying the most advanced information technologies, Frontiers is catapulting scholarly publishing into a new generation.

What are Frontiers Research Topics?

Frontiers Research Topics are very popular trademarks of the *Frontiers journals series*: they are collections of at least ten articles, all centered on a particular subject. With their unique mix of varied contributions from Original Research to Review Articles, Frontiers Research Topics unify the most influential researchers, the latest key findings and historical advances in a hot research area.

Find out more on how to host your own Frontiers Research Topic or contribute to one as an author by contacting the Frontiers editorial office: frontiersin.org/about/contact

Advances in observations and modeling of physical processes in the marine environment

Topic editors

Guihua Wang — Fudan University, China

Darko Koracin — University of Split, Croatia

Dujuan Kang — The State University of New Jersey, United States

Citation

Wang, G., Koracin, D., Kang, D., eds. (2023). *Advances in observations and modeling of physical processes in the marine environment*. Lausanne: Frontiers Media SA. doi: 10.3389/978-2-83251-284-5

Table of contents

frontiers | Frontiers in Earth Science

TYPE Editorial
PUBLISHED 22 December 2022
DOI 10.3389/feart.2022.1116287

OPEN ACCESS

EDITED AND REVIEWED BY
Yuqing Wang,
University of Hawaii at Manoa,
United States

*CORRESPONDENCE
Guihua Wang,
wanggh@fudan.edu.cn

SPECIALTY SECTION
This article was submitted to Atmospheric Science, a section of the journal Frontiers in Earth Science

RECEIVED 05 December 2022
ACCEPTED 12 December 2022
PUBLISHED 22 December 2022

CITATION
Wang G, Koračin D and Kang D (2022), Editorial: Advances in observations and modeling of physical processes in the marine environment.
Front. Earth Sci. 10:1116287.
doi: 10.3389/feart.2022.1116287

Editorial: Advances in observations and modeling of physical processes in the marine environment

Guihua Wang[1]*, Darko Koračin[2,3] and Dujuan Kang[4]

[1]Department of Atmospheric and Oceanic Sciences and CMA-FDU Joint Laboratory of Marine Meteorology, Fudan University, Shanghai, China, [2]Desert Research Institute, Reno, NV, United States, [3]University of Split, Split, Croatia, [4]Department of Environmental Sciences, Rutgers, The State University of New Jersey, New Brunswick, NJ, United States

KEYWORDS

marine meteorology, physical processes, fog, tropical cyclone, extropical cyclone

Editorial on the Research Topic
Advances in observations and modeling of physical processes in the marine environment

Marine meteorology is a subfield of meteorology, which deals with the weather and climate and the associated processes in the ocean environment. It is always challenging to understand the atmospheric variability over the ocean and complex interplay of the dynamic and thermodynamic processes in the marine environment (North et al., 2014). Analyses and modeling of high winds, wind surges, tropical cyclones, hurricanes, typhoons, fog, lightning, and thunderstorm over the ocean are relevant to scientific interests and practical applications. This Research Topic highlights various methods of using observations and modeling to investigate physical processes in the marine environment.

The contributions of the 14 articles in this Research Topic can be divided into four main areas: A) Fog observations and modeling; B) Analysis and modeling of tropical cyclones and typhoons; C) Observations and mechanisms of explosive cyclones and high winds; and D) Analytical and modeling techniques to investigate ocean and atmospheric processes.

Understanding the spatial and temporal variability of marine fog is important, and how to improve the forecast skill is also a concern (Koračin and Dorman, 2017). Li et al. investigate the atmospheric circulation and marine atmospheric boundary layer structure associated with marine fog over the northeast Pacific (NEP) in winter, and suggest the eastern flank of the Aleutian low and the northwestern flank of the Pacific subtropical high jointly contribute to a northward air flow over the NEP favoring warm and moist air flows through a cooler sea surface and facilitates the formation of advection-cooling fog. Based on hourly observations from buoys and automatic weather stations distributed in Qingdao and its adjacent islands, Song et al. analyze composite sea fog penetration

(SFP) events to reveal their spatio-temporal features and further show that the daytime anomalous moistening, together with the following diurnal cooling at night facilitates SFP. Zhou et al. examine the differences in sea fog properties at Xuwen and Zhanjiang harbors, and develop new different monitoring and early warning schemes of sea fog prediction for the harbors. Based on the operational version of the China Meteorological Administration Typhoon Model, Huang et al. demonstrate that the equitable threat score for the hindcasting sea fog increases by 61% through several improvements such as a more accurate sea surface temperature dataset, an optimum boundary layer turbulence parameterization scheme, and higher vertical resolution. Gao et al. also propose another data assimilation method to increase the equitable threat score of simulated fog area by including temperature constraint into the satellite-derived humidity.

The tropical cyclone (TC) intensity accompanied with precipitation and thunderstorm are main components of TC research (Emanuel, 2005). Zhang et al. study the rapid intensification process of Super Typhoon Rammasun (1409) in the South China Sea, and show vertical wind shear influenced by diurnal radiation cycle is a key factor in the TC rapid intensification. Zhou and Cao use a hybrid integral method to partition the horizontal wind fields in a limited domain with high accuracy to investigate development and evolution of a typhoon, and emphasize the relative importance of the divergent and non-divergent winds in the kinetic energy budget during the TC pre-development, re-intensification and dissipation stages. Xiang et al. examine the detailed characteristics of the inner rainbands distribution of both RI (rapid-intensification) and non-RI landfall TCs (LTCs) in the South China Sea during 2015–2020 with a multi-source merged precipitation dataset, and find that RI LTCs exhibit a relatively higher averaged rain rate in the inner core region than that of non-RI LTCs. Zhang et al. examine the radial and asymmetry distributions of thunderstorm as a function of TC intensity, landing location, and vertical wind shear with lightning data from the World Wide Lightning Location Network, indicating the effects of dry continental air intrusion and the enhanced surface frictional convergence.

The explosive cyclones are key phenomena in the middle and high latitudes, and important for understanding the atmosphere-ocean interactions there (Marco et al., 2019). Gao et al. compare explosive cyclones (ECs) and non-explosive cyclones (or ordinary cyclones) using 10 years of ERA5 reanalysis data, and find potential vorticity is important for ECs development. Wang et al. analyze vorticity and kinetic energy budgets for typical explosive extratropical cyclones, and show that the lower-level convergence-related vertical stretching and the vertical transport of vorticity are important for increasing the cyclone's cyclonic vorticity. Because observations of marine wind are rare, the estimation and forecasting of gusts over sea are difficult. Hu et al. establish a gust estimation equation applicable to the Bohai Sea based on reanalysis data and observations on the coast and offshore stations.

In addition, some special analytical and modeling techniques to investigate physical processes in the marine environment are also included. Lu et al. analyze transient luminous events from space-borne platform to reveal properties of continental and oceanic thunderstorms, and verify that negative cloud-to-ground strokes spawned by oceanic thunderstorms are more readily to produce sprites based on the existing ground-based observations in both Caribbean Sea and near the coast of South China. They further argue that the production of negative sprites heavily depends on the size of parent thunderstorms. With assimilation experiments, Sun et al. show that the sea surface temperature assimilation into a coupled Earth system model can significantly improve the strength of the Pacific Equatorial Undercurrent, the North Equatorial Countercurrent and the South Equatorial Current through reducing biases in the air–sea turbulence flux.

All these results can contribute to broadening a global vision of marine meteorology and guiding best decisions for human activities relevant to the marine environment. The proposed observational techniques as well as modeling and forecasting methodologies can be applied to the open sea and coastal regions worldwide.

Author contributions

GHW, DK and DJK co-wrote this editorial.

Funding

GHW was supported by the National Key R&D Program of China (Grant Number: 2019YFC1510100). DK was partially funded by STIM - REI (University of Split)—European Regional Development Fund—Operational Programme Competitiveness and Cohesion 2014-2020, Grant/Award Numbers: KK.01.1.1.01.0003, KK.01.1.1.01. DK was also partially funded by the University of Notre Dame, USA (ONR Grant Number: N00014-21-1- 2296).

Acknowledgments

We thank all authors of the papers included in this Research Topic for their excellent contributions.

Conflict of interest

The authors declare that the research was conducted in the absence of any commercial or financial relationships that could be construed as a potential conflict of interest.

Publisher's note

References

Emanuel, K. (2005). *Divine wind: The history and science of hurricanes*. London & New York: Oxford University Press. ISBN: 978-0195149418 296P.

Koračin, D., and Dorman, C. E. (2017). "Marine fog: Challenges and advancements in observations and forecasting," in *Springer atmospheric sciences series* (Cham, Switzerland: Springer International Publishing), 537. doi:10.1007/978-3-319-45229-6

Marco, R., Liberato, M. L. R., Lionello, P., Joaquim, G., Pinto, J. G., Salon, S., et al. (2019). A global climatology of explosive cyclones using a multi-tracking approach. *Tellus A Dyn. Meteorology Oceanogr.* 71, 1611340. doi:10.1080/16000870.2019.1611340

North, G. R., Zhang, F., and Pyle, J. (2014). *Encyclopedia of atmospheric sciences*. Second Edition. Elsevier. 2902P.

frontiers in Earth Science

ORIGINAL RESEARCH
published: 09 March 2022
doi: 10.3389/feart.2022.854438

Improvements of Sea Fog Forecasting Based on CMA-TYM

Bin Huang[1], *Jin Zhang*[2,3]*, *Yuenan Cao*[1], *Xiaoyu Gao*[3], *Suhong Ma*[2,3] *and Chenghu Sun*[4,5]

[1]National Meteorological Center, China Meteorological Administration, Beijing, China, [2]CMA Earth System Modeling and Prediction Centre (CEMC), Beijing, China, [3]State Key Laboratory of Severe Weather, Chinese Academy of Meteorological Sciences, Beijing, China, [4]State Key Laboratory of Severe Weather and Institute of Climate System, Chinese Academy of Meteorological Sciences, Beijing, China, [5]Collaborative Innovation Center on Forecast and Evaluation of Meteorological Disasters, Nanjing University of Information Science and Technology, Nanjing, China

Based on the operational version of the China Meteorological Administration Typhoon Model (CMA-TYM, formerly known as GRAPES_TYM), a series of numerical tests are conducted by optimizing the boundary layer parameterization scheme, vertical resolution, and boundary conditions. Instead of the sea surface temperature (SST) from the Global Forecast System (GFS) model, more accurate daily SST data reflecting the daily SST variation are used as the boundary condition. The new SST dataset is capable of representing the key points in the area, including the low coastal SST related to upwelling, the intrusion of the Yellow Sea (YS) Warm Current, and the ocean front between the YS and the East China Sea. An analysis of the performances of two boundary layer parameterization schemes (the Yonsei University scheme and the Medium-Range Forecast scheme) in characterizing turbulent heat exchange reveals that the former can more accurately reflect offshore turbulence and forecast the fog area. By increasing the number of vertical layers of the model to 68 and reducing the height of the bottom layer to approximately 10 m, the model presents a better performance in simulating the rapid formation and dissipation of sea fog. With the above improvements, the equitable threat score (ETS) for the hindcasting of eleven sea fog cases in the spring of 2018 increases by 61%, mainly due to the increase in the correctly forecasted fog area.

Keywords: sea fog, numerical forecast, boundary layer parameterization scheme, vertical resolution, bottom boundary conditions

OPEN ACCESS

Edited by:
Guihua Wang,
Fudan University, China

Reviewed by:
Runling Yu,
China Meteorological Administration, China
Yanzhen Qian,
Ningbo Meteorological Bureau, China

***Correspondence:**
Jin Zhang
zhangjin@cma.cn

Specialty section:
This article was submitted to Atmospheric Science, a section of the journal Frontiers in Earth Science

Received: *14 January 2022*
Accepted: *21 February 2022*
Published: *09 March 2022*

Citation:
Huang B, Zhang J, Cao Y, Gao X, Ma S and Sun C (2022) Improvements of Sea Fog Forecasting Based on CMA-TYM. Front. Earth Sci. 10:854438. doi: 10.3389/feart.2022.854438

INTRODUCTION

Sea fog is a phenomenon in which water vapour condenses in the lower atmosphere over the sea (including shores and islands) under the influence of the ocean (Wang, 1983). In recent years, the casualties and property losses caused by sea fog have gradually approached those caused by extreme weather events, such as typhoons and tornadoes (Gultepe et al., 2007). The offshore waters of China are characterized by one of the highest frequencies of sea fog occurrence worldwide; here, this phenomenon arises due to the strong sea temperature gradient and poses serious hazards to the economic development and social security of coastal China. If the occurrence, duration, extent of influence and concentration of sea fog could be accurately predicted by an operational department, early warnings could be provided, and thus, corresponding emergency measures could be taken to reduce and avoid losses.

However, as a weather phenomenon influenced by a weak pressure field, sea fog is difficult to be numerically predicted. The formation and development of sea fog are affected by a series of dynamic

and thermodynamic processes, such as synoptic circulations, air-sea heat and water vapour exchanges, boundary layer turbulence and entrainment, and long-wave and shortwave radiation. In particular, one of the most important mechanisms responsible for the formation of sea fog is the condensation caused by the cooling of warm and humid air advecting to the cold sea surface. In some early attempts to numerically simulate sea fog, many scholars employed mesoscale forecasting models (Ballard et al., 1991; Golding, 1993; Nakanishi, 2000; Pagowski et al., 2004; Koračin et al., 2005). Mesoscale models have been used to simulate the formation of sea fog in China since the turn of the century, and the corresponding mechanisms have been investigated (Fu et al., 2004; Fu et al., 2006; Fu et al., 2008; Wang et al., 2012; Cheng et al., 2013; Huang et al., 2015; Huang et al., 2019). Focusing on ten cases of sea fog over the Yellow Sea (YS) in spring, Lu et al. (2014) carried out a sensitivity study on the parameterization schemes of the Weather Research and Forecasting (WRF) model and found that the best combination of the boundary layer scheme and the microphysical scheme comprises the Yonsei University (YSU) scheme and the Purdue Lin scheme, respectively. Based on the simulation of fog over the YS through the WRF model, Yang and Gao (2016) reported that increasing the vertical resolution could significantly improve the ability to forecast the horizontal fog area. In addition, the quality of the initial field is essential for sea fog forecasts and can be improved by assimilating multi-source observation data, which also helps improve the forecasting skill (Gao et al., 2010a; Gao et al., 2010b; Wang and Gao, 2016; Gao and Gao, 2019).

Compared with the rapid development in other research aspects of atmospheric science, the operational application of a numerical prediction technique for sea fog in China is still in its infancy. National Meteorological Center of China and meteorological services in coastal provinces and cities have gradually established a numerical prediction system for sea fog in recent years based on imported regional models such as the WRF and the Regional Atmospheric Modeling System (RAMS) to develop related forecast products, which can provide certain support for operational forecasts (Huang et al., 2014). In the operations of national marine meteorological forecasts, the continuously improving the China Meteorological Administration Typhoon Model (CMA-TYM, formerly known as GRAPES_TYM) has become an important reference for meteorological departments to forecast marine weather (Ma and Chen, 2018, Ma et al., 2018, Zhang et al., 2017). However, CMA-TYM was originally developed for the numerical prediction of tropical cyclones. Sea fog prediction is only its by-product and has not been carefully evaluated. In order to improve its sea fog forecast skill, the description of the marine boundary layer closely related to the formation and evolution of sea fog in CMA-TYM needs to be further refined. Therefore, this study intends to improve the simulation and prediction of sea fog by CMA-TYM to support controllable operational forecasts in China.

DATA, METHOD AND MODEL DESCRIPTION

Data

The background field uses 3-hourly data with a resolution of 0.5°×0.5° and 26 vertical layers from the Global Forecast System (GFS) produced by the National Centers for Environmental Prediction (NCEP), and multi-source observation data are assimilated for the initial field. Another sea surface temperature (SST) dataset used in the forecast is composed of daily SST data with a resolution of 0.25°×0.25° produced by the North-East Asian Regional Global Ocean Observing System (NEAR-GOOS).

Due to the lack of the routine observations over the sea, satellite images with high spatial and temporal resolution have already been used as an important approach to monitor the process of sea fog evolution (e.g., Wu et al., 2015; Wang et al., 2018). The satellite cloud images employed for the retrieval of sea fog are based on high-resolution infrared brightness temperature and visible albedo data obtained by the Japanese Himawari-8 geostationary satellite, and the SST data used for the retrieval originate from the NCEP reanalysis product. In the paper, we adopt the retrieval method proposed by Wang et al. (2015), which was proved feasible by comparison with observation data in the offshore areas of China, to provide sea fog retrievals to verify model forecasts. For convenience, we refer to such retrieval data as observations below.

CMA-TYM

The model domain utilized in current operational forecasts is shown in **Figure 1**, which uses an equal-latitude and equal-longitude grid system with a horizontal resolution of 0.09°×0.09° and 50 vertical layers with a height-based terrain-following coordinate. The purpose of this study is to improve the framework of operational forecasts by CMA-TYM. Therefore, although such a large area is not required to forecast sea fog in the offshore waters of China, this domain is used to conduct the numerical experiment in this study. Other specifications of the model parameters are shown in **Table 1**.

Model Diagnostic Methods of Sea Fog

When visible light travels through the air, it is scattered and blocked by suspended liquid and solid particles. The extinction coefficient can be used to comprehensively reflect the weakening effect of air on light. Assuming that the air near the observation point is homogeneous, the extinction coefficient is constant. According to Koschmieder's law, the calculation formula for horizontal visibility is as follows:

$$V_H = \frac{-\ln(0.02)}{\beta}$$

where V_H is the horizontal visibility (unit: km) and β is the extinction coefficient (unit: km^{-1}) determined by air impurities. For fog over the YS, the influencing factor on horizontal visibility is the content of liquid water particles. Therefore, the Kunkel (1984) method is used to measure the relationship between β and the liquid water content:

$$\beta = 144.7C^{0.88}$$

where C is the mass concentration of liquid water (unit: gm^{-3}). Since the fog area is defined as the region where $V_H \leq 1$ km, the cloud-water mixing ratio of $q_c \geq 0.016\ g\ kg^{-1}$ in the fog area can be obtained according to the above formula.

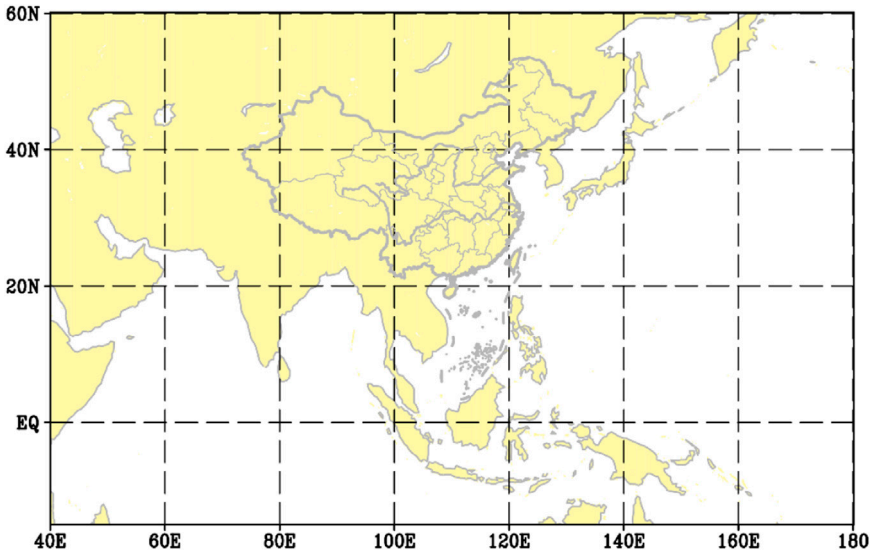

FIGURE 1 | Simulation domain of CMA-TYM.

TABLE 1 | Parameter settings of CMA-TYM.

Model parameter		Parameter setting
Region	Central point	22.53°N, 110.02°E
	Number of grids (west-east× south-north)	1557 × 835
	Horizontal resolution	0.09°
	Number of vertical layers	55
Time step		60 s
Boundary layer option		MRF scheme
Cumulus option		Kain–Fritsch scheme
Microphysics option		WSM6 scheme
Long-wave and shortwave radiation scheme		RRTMG scheme
Land surface option		Noah model

Nevertheless, we cannot determine whether the bottom of sea fog is decoupled from the sea surface (thereby becoming a low-level stratus cloud) since satellite monitoring is employed to determine the fog area at sea regardless of whether a subjective or objective method is used. If the structure of stratus clouds (condensation is present at low altitudes but not at the bottom of the model) can be accurately predicted by the model but stratus clouds are treated as sea fog in satellite observations, the forecasted fog area is seriously underestimated when the liquid water content at the bottom of the model domain is compared with that observed within the fog area. To avoid this error, forecasted low-level stratus clouds are regarded as sea fog, and the height of 500 m is taken as the threshold for the fog-top height since the thickness of advecting fog over the YS generally does not exceed 400 m (Zhou and Du, 2010). Therefore, the forecasted fog area should meet the following criteria simultaneously: first, in model layers where the height ≤500 m, at least one layer is characterized by $q_c \geq 0.016\ \mathrm{g\ kg^{-1}}$; second, the fog-top height ≤500 m.

Figure 2 shows several typical cases regarding the diagnosis of sea fog in the model. In the case shown in **Figure 2A**, condensed water particles stretch from the first layer z_1 to layer z_2 of the model, indicating that the fog is coupled to the sea surface. The fog-top height is diagnosed as the height of the bottom of layer z_2, which is obviously much lower than 500 m. In the case shown in **Figure 2B**, condensed water vapour appears in both z_2 and z_3, the liquid water contents of which are both greater than $0.016\ \mathrm{g\ kg^{-1}}$. Although there is no liquid water in z_1, for a convenient comparison with the retrieved fog area, the bottom of z_3 is taken as the fog-top height. In the case shown in **Figure 2C**, condensation occurs in both z_3 and z_4, but a large amount of cloud water is also present in z_5 (above 500 m), indicating that clouds have a higher top than this threshold and are therefore not considered sea fog.

Evaluation Methods

To quantitatively assess the forecast results, a point-to-point comparison is made based on the gridded sea fog forecasts and the observed fog areas. The numbers of grid points in the observation area and forecasted fog area are set as O and F, respectively, and the correctly forecasted fog area (where sea fog is found in both the observation and the forecast) is set as H. Four metrics, including the probability of detection (POD), false alarm rate (FAR), bias ($BIAS$) and equitable threat score (ETS), are calculated as follows:

$$\mathrm{POD} = \frac{\mathrm{H}}{\mathrm{O}}$$

$$\mathrm{FAR} = \frac{\mathrm{F} - \mathrm{H}}{\mathrm{F}}$$

$$\mathrm{bias} = \frac{\mathrm{F}}{\mathrm{O}}$$

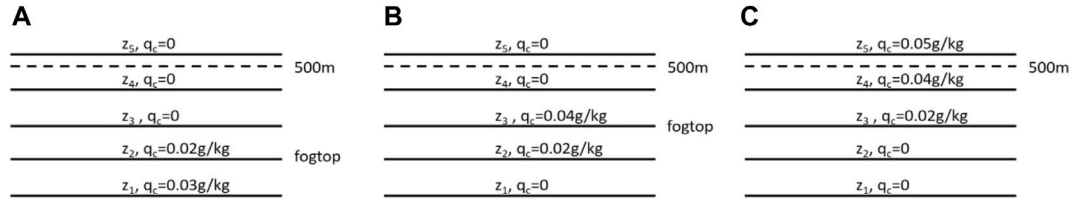

FIGURE 2 | Diagnosis of the fog-top heights corresponding to three kinds of cloud water distributions. **(A-C)** See text for details.

$$\mathrm{ETS} = \frac{\mathrm{H} - \mathrm{R}}{\mathrm{F} + \mathrm{O} - \mathrm{H} - \mathrm{R}}$$

where $R = F(O/N)$ is the random hit item and N is the sum of the numbers of grids in the verification areas. According to the formula, the *POD* is a measure of the proportion of the correctly forecasted fog area: the larger the correctly forecasted fog area, the higher the *POD* is. The *FAR* is a measure of the proportion of the falsely forecasted fog area (where fog is found in the observation but not in the forecast): the larger the falsely forecasted fog area, the higher the *FAR* is. Bias is the ratio of the forecasted fog area to the observed fog area. Finally, as a comprehensive score that considers the forecasts, observations and correctly forecasted fog area simultaneously, the *ETS* is the most important criterion for comparing the forecast results.

MODEL IMPROVEMENT SCHEME

Improved Bottom Boundary Condition

Studies have shown that the bottom boundary conditions, especially the SST distribution, are important factors affecting the formation and development of sea fog (Fu et al., 2016). When warm and humid air advects to the cold sea surface, the initial heat exchange originates at the air-sea interface: heat is transferred to the ocean from the air near the sea surface (below a height of 1 m), and the region in which the temperature decreases extends upward under the influence of atmospheric turbulence, which affects the offshore layer (below a height of 10 m) and the boundary layer. Therefore, sea fog is triggered by warm, humid air and a cold sea surface. According to a sensitivity test of large-scale sea fog (figure omitted), when the offshore SST increases by 1 K, the forecasted fog area shrinks by tens of thousands of square kilometres. Furthermore, the SST near the shore may be lower than that of the open sea under the action of coastal upwelling, which creates favourable conditions for the formation of coastal sea fog.

At present, the SST field used in operational forecasts by CMA-TYM is entirely derived from global GFS data, which are updated every 3 h. However, the coarse grid of the GFS product is insufficient for sea fog forecasts. Therefore, daily SST data with a resolution of 0.25°×0.25° from NEAR-GOOS are used in this study; these data have been assimilated with multi-source observation data and are updated daily and thus are suitable for operational forecasts. However, the SST field from NEAR-GOOS is a daily average; hence, the daily variation trend is excluded. Therefore, the NEAR-GOOS SST is considered as the background field. The result of superimposing the NEAR-GOOS SST onto the daily variation trend of the GFS SST is taken as the SST boundary conditions for driving CMA-TYM. Both types of data are interpolated to the grids of CMA-TYM with 0.09°×0.09° horizontal resolution before superimposing. The new SST boundary condition of CMA-TYM is expressed as:

$$T(i,j,t) = \bar{T}_N(i,j) + \left(T_G(i,j,t) - \bar{T}_G(i,j)\right)$$

where $T(i,j,t)$ is the SST value at point (i,j) in the model at time t; $\bar{T}_N(i,j)$ and $\bar{T}_G(i,j)$ are the daily SST averages from NEAR-GOOS and GFS, respectively; and $T_G(i,j,t)$ is the GFS SST at time t. The above formula means that the daily variation trend obtained by removing the daily average from the GFS data is superimposed onto the NEAR-GOOS SST.

Figure 3 plots the SST distributions at 1200 UTC on April 18, 2018, before and after the inclusion of the NEAR-GOOS SST. The bottom boundary conditions before and after the addition of NEAR-GOOS SST data are roughly the same in the subtropical western Pacific. Specifically, in the Bohai Sea, the improved SST is approximately 0.5°C higher. In the central YS, the improved SST appears as a strong warm ridge. The low temperatures of the coastal waters on both sides of this warm ridge strengthen the temperature gradients, whereas the distribution of the GFS SST alone is smoother. The improved SST better reflects the tributaries of the Kuroshio Extension in the offshore waters of China, making it easier for the model to predict the occurrence of sea fog near the Shandong Peninsula, the coast of Jiangsu, and the Korean Peninsula, while sea fog is more difficult to forecast over the central YS due to the higher SST there. This result is basically consistent with the real situation; that is, sea fog in this area often appears over the eastern and western YS, while the central YS exhibits clear or cloudy skies. Moreover, a large number of ship observations have reported a strong sea temperature gradient (called an ocean front) at the junction between the YS and East China Sea (near 124°E, 30°N) in spring, which is accurately depicted by the improved SST.

Improved Boundary Layer Scheme

The Medium-Range Forecast (MRF) boundary layer scheme, which has been thoroughly verified in forecasting the intensity and paths of typhoons, is used in operational forecasts by CMA-TYM. However, the MRF scheme may underestimate the turbulent mixing process when considering the entrainment process and the internal processes of the boundary layer together. Although this underestimation has little effect on

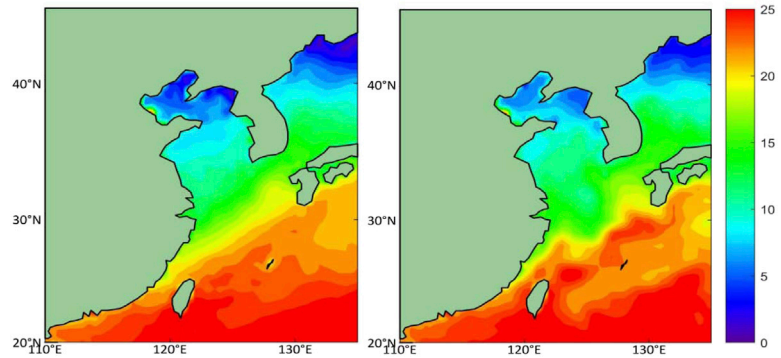

FIGURE 3 | SST distributions (°C) at 1200 UTC on April 18, 2018. The left panel shows the GFS data, while the right panel shows the weighted average of the GFS and NEAR-GOOS data.

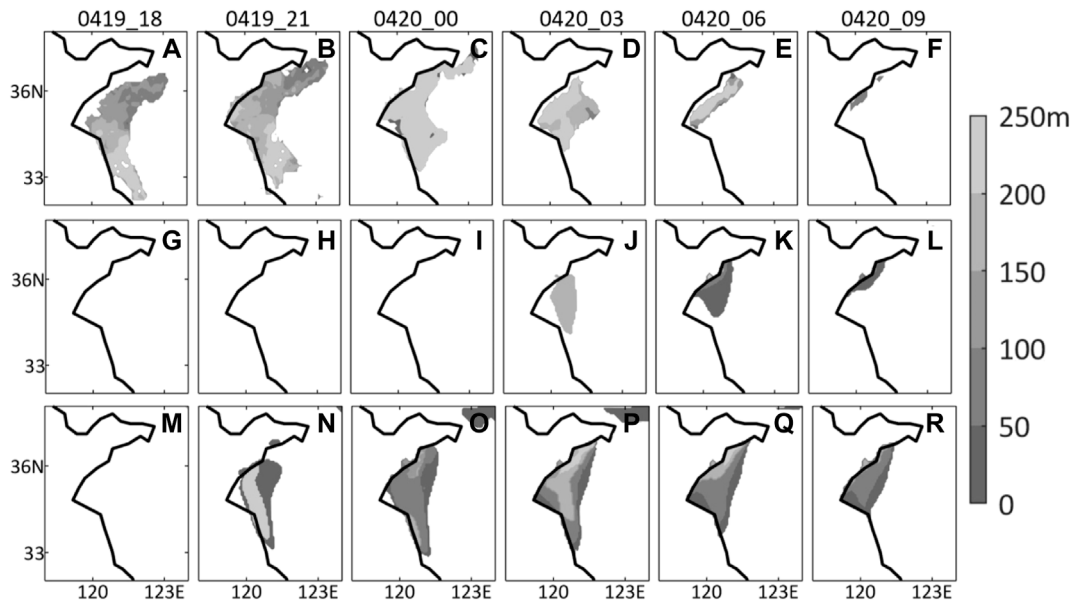

FIGURE 4 | Comparison between the forecasted fog-top height and retrieved fog-top height from 1800 UTC on April 19 to 0600 UTC on April 20, 2018, from the **(A–F)** retrieval, **(G–L)** Exp-MRF and **(M–R)** Exp-YSU.

TABLE 2 | Scores of the fog area (the number in brackets is the percentage by which the forecast results using the YSU scheme are improved compared with those using the MRF scheme).

Experiment	POD	FAR	Bias	ETS
Exp-MRF	0.160	0.247	0.116	0.116
Exp-YSU	0.583 (**264**)	0.311 (-**26**)	0.969 (**96**)	0.338 (**191**)

severe weather processes such as typhoons and extratropical cyclones, the effect is unfavourable for sea fog forecasts. Numerical experiments on sea fog cases in the spring seasons of 2005–2011 show that the forecast results of the YSU scheme are better than those of the quasi-normal scale elimination, Mellor–Yamada and Mellor–Yamada–Nakanishi–Niino-2.5/3 models. However, no studies have compared the advantages and disadvantages of the YSU scheme with those of the MRF scheme. Therefore, comparative experiments for these two schemes are carried out in this study.

Taking an offshore sea fog case from April 19 to April 20, 2018, as an example, the MRF scheme and the YSU scheme are separately set as the boundary scheme, and the experiments are correspondingly denoted Exp-MRF and Exp-YSU, respectively. The forecast initial time is set to 1200 UTC on April 19. **Figure 4** presents a comparison between the forecast results and observations. This sea fog was produced by southerly wind behind a high-pressure system; the fog began to form over the offshore sea surface and gradually developed upward due to the low SST of the coastal waters. During the day on

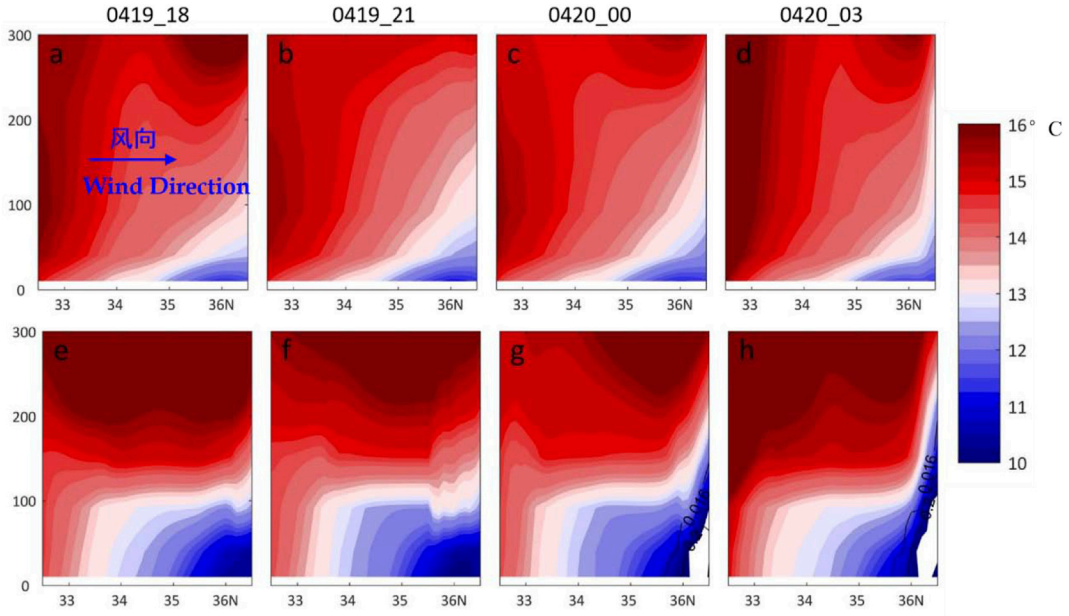

FIGURE 5 | Temporal variation in the forecast results of **(A–D)** Exp-MRF and **(E–H)** Exp-YSU on the meridional vertical section along 121.5°E. The shading represents the temperature (unit: °C), and the contours represent the cloud-water mixing ratio (unit: g kg^{-1}).

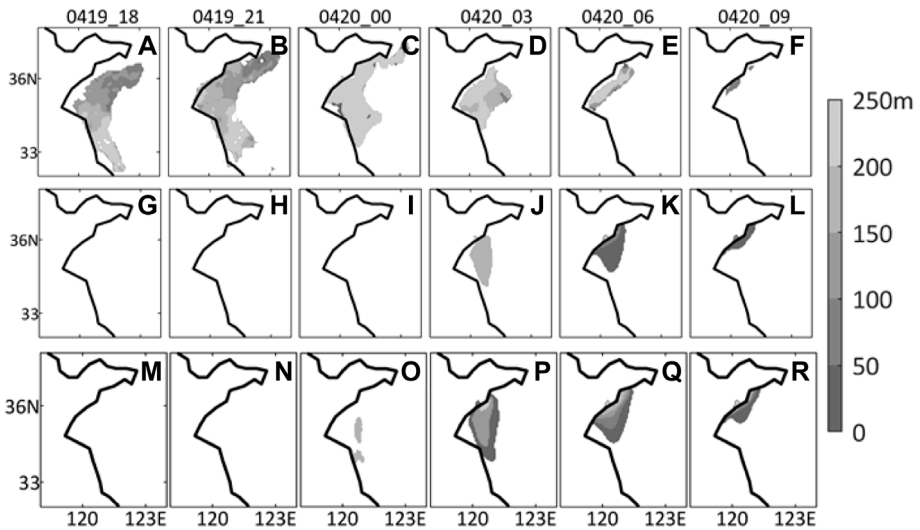

FIGURE 6 | Comparison between the forecasted fog-top height and retrieved fog-top height from 1800 UTC on April 19 to 0600 UTC on April 20, 2018, from the **(A–F)** retrieval, **(G–L)** Exp-50 and **(M–R)** Exp-68.

April 20, the land cyclone system moved eastward, and the southwesterly wind strengthened; the sea fog stretched to the northeast and then weakened and disappeared due to solar radiation. Sea fog did not appear within 12 h in the Exp-MRF forecasts until a small area of sea fog appeared at 0300 UTC on April 20, which then quickly dissipated. In the Exp-YSU forecasts, a large area of fog formed on the night of April 19, and the forecast results were relatively close to the observations until 0300 UTC on April 20. Although Exp-YSU does not capture the dissipation well in the later stage of the forecasts, its forecast results are significantly better than those of Exp-MRF in general.

Table 2 shows the comprehensive scores of the two tests. For the MRF scheme, the *POD*, *BIAS* and *ETS* are all less than 0.2, and the correctly forecasted fog area is less than 20% of the

TABLE 3 | Scores of the fog area (the number in brackets is the percentage by which the results of EXP-68 are improved compared to those of EXP-50).

Experiment	POD	FAR	Bias	ETS
Exp-50	0.160	0.247	0.116	0.116
Exp-68	0.257 (**61**)	0.112 (**18**)	0.382 (**30**)	0.180 (**55**)

observed fog area because a considerable amount of the actual fog area is missing. In contrast, for the YSU scheme, the *POD* is improved by 264%, and the *BIAS* is improved by 96%. Although the *FAR* also increases, the overall *ETS* reaches 0.338, which is almost thrice that for the Exp-MRF scheme.

Figure 5 shows that due to the weak turbulent mixing in the MRF scheme, the low-temperature air mass below 13°C always accumulates near the offshore surface (below a height of 50 m). However, in the YSU scheme, higher air masses are affected by the cooling of the offshore surface, and the region with a temperature below 13°C extends up to a height of 100 m. This intense cooling process in Exp-YSU facilitates the condensation of water vapour, and thus, the simulated fog area is larger than that in Exp-MRF.

Improved Vertical Resolution

The vertical resolution determines the model accuracy in depicting vertical motions within the atmosphere and energy exchange and material exchange processes. For sea fog forecasting, a finer vertical resolution means more model layers in the boundary layer, which is conducive to the turbulent transfer of heat between layers. However, increasing the number of layers also means reducing the height of the bottom layer (z_1) in the model. The previous version of CMA-TYM uses 50 vertical layers, and the height of z_1 is approximately 20 m. Increasing the number of layers to 68, the height of z_1 is reduced to approximately 10 m. Layer z_1 is a bridge that connects the ocean and the atmospheric boundary layer. When the bottom boundary of the model has a different temperature than the external atmosphere, it changes the temperature in z_1 through the sensible heat flux and further affects the overlying atmosphere. The variation trend of the temperature in z_1 can be expressed as follows:

$$F = \frac{HFX}{\rho C_p \cdot 2z_1}$$

where HFX is the sensible heat flux. The lower the height of z_1, the smaller the specific heat capacity of z_1 is and the more sensitive the layer is to temperature changes at the bottom boundary. Therefore, lowering the height of z_1 accelerates the formation of sea fog.

To compare the forecasts of the two schemes for the sea fog case during April 19–20, the experiments adopt two vertical resolutions of 50 layers and 68 layers, and the experiments are correspondingly denoted Exp-50 and Exp-68, respectively. The forecast initial time is set to 1200 UTC on April 19.

Figure 6 presents a comparison between the forecasts and observations. The increasing vertical resolution increases the fog area around the 12-h forecast. The improved trend is similar to that in the YSU scheme but weaker (**Figure 4**). It is worth noting that in the late forecast period, the fog dissipates faster in Exp-68 than in Exp-50. At 0600 UTC on April 20, the fog area forecasted in Exp-68 is much larger than that in Exp-50. After only 3 h, the fog area in Exp-68 is almost as large as that in Exp-50 since the

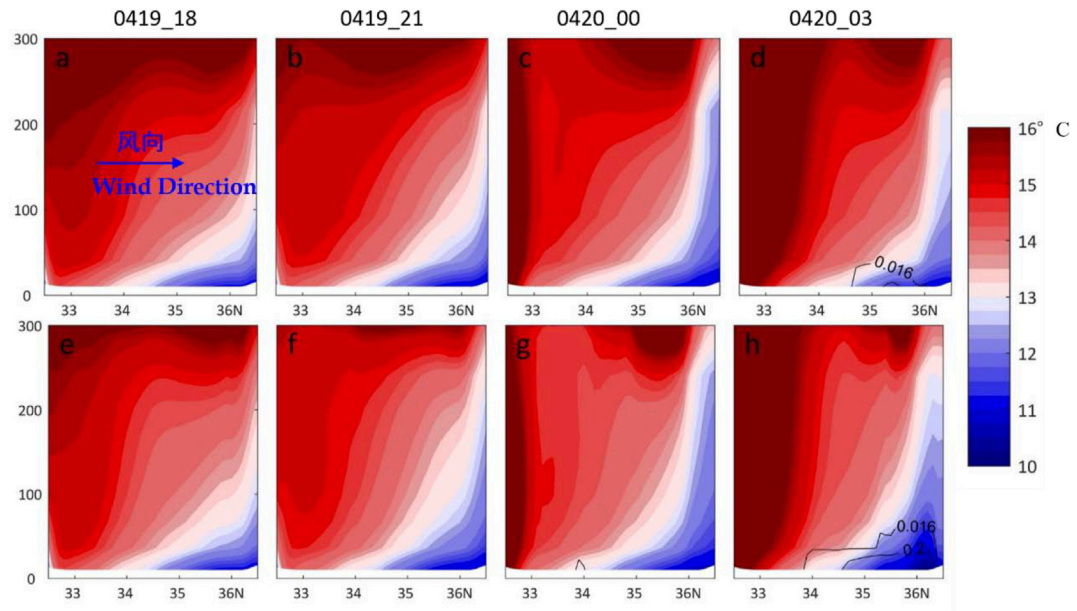

FIGURE 7 | Temporal variation in the forecast results of **(A–D)** Exp-50 and **(E–H)** Exp-68 on the meridional vertical section along 121°E. The shading represents the temperature (unit: °C), and the contours represent the cloud-water mixing ratio (unit: g kg^{-1}).

TABLE 4 | Sea fog cases in the spring of 2018.

Date	Initial time	End time
March 3rd	1200 UTC March 2nd	1200 UTC March 3rd
March 12th	1200 UTC March 11th	1200 UTC March 12th
March 13th	1200 UTC March 12th	1200 UTC March 13th
March 27th	1200 UTC March 26th	1200 UTC March 27th
March 28th	1200 UTC March 27th	1200 UTC March 28th
March 29th	1200 UTC March 28th	1200 UTC March 29th
March 30th	1200 UTC March 29th	1200 UTC March 30th
March 31st	1200 UTC March 30th	1200 UTC March 31st
April 1st	1200 UTC March 31st	1200 UTC April 1st
April 2nd	1200 UTC April 1st	1200 UTC April 2nd
May 10th	1200 UTC May 9th	1200 UTC May 10th

lower height of z_1 is more sensitive to the changes in the upper-level air temperature. When shortwave radiation raises the temperature of the fog top, turbulence transmits the temperature change downward, and the lower z_1 responds quickly to this temperature change, causing the fog area to dissipate. In short, the increased vertical resolution causes fog to both form and dissipate more quickly, which is consistent with observations.

Table 3 further shows the comprehensive scores of the two experiments. Compared with those of Exp-50, the *POD*, *FAR* and *BIAS* of Exp-68 are improved by 61%, 18% and 30%, respectively. The overall *ETS* reaches 0.180, with an improvement of 55%.

The meridional cross-section along 121°E is plotted in **Figure 7**. In Exp-68, the temperature drops significantly below a height of 300 m, while the upper bound of the region with a temperature below 13°C increases in height. After the fog area (cloud water content greater than 0.016 g kg^{-1}) is formed, the long-wave radiation of liquid water particles causes rapid cooling inside the fog area. At 0300 UTC on April 20, the surface air temperature in Exp-68 at 36°N is approximately 2°C lower than that in Exp-50.

Assessment of the Overall Improvement

With the above results, an improved scheme for the forecasting of sea fog by CMA-TYM is established. The first step is to use the daily NEAR-GOOS SST as the bottom boundary of the model; the second step is to adopt the YSU scheme as the boundary layer scheme; and the third step is to increase the vertical resolution from 50 to 68 layers. To assess the overall improvement effect, simulation-based forecasts are carried out for eleven sea fog cases in the spring of 2018 (**Table 4**). The forecast initial time is set to 1200 UTC on the day before, and the lead time is 24 h. To compare the difference in the forecast effect before and after the improvement, two groups of experiments are designed. Group-A is a control test that adopts the settings of the operational forecast before the improvement; Group-B applies the abovementioned improved schemes, while the remaining settings are exactly the same as those of Group A. **Table 5** shows the specifications.

Table 6 lists the forecast scores of the eleven sea fog cases in the two groups. The forecasted fog area in Group-A is generally small. The *POD* s of four cases on March 12, 27 and 29 and May 10 are all less than 0.15, resulting in *ETS* values below 0.1. In particular, the *ETS* on March 27 is zero, indicating that the forecast is completely unsuccessful. The average *ETS* values for the eleven cases in Group-A is 0.162, and the *BIAS* is 0.582.

The forecasted fog area in Group-B is higher than that in Group-A due to the improved scheme, and the forecast scores of

TABLE 5 | Specifications of the control test and improvement test.

Experiment	Bottom boundary condition	Boundary layer scheme	Vertical layers
Group-A	GFS SST data	MRF scheme	50
Group-B	NEAR-GOOS + GFS SST data	YSU scheme	68

TABLE 6 | Forecast scores (the number in brackets is the percentage of the improvement of Group-B over Group-A).

DATE mm-dd	Group-A				Group-B			
	POD	FAR	Bias	ETS	POD	FAR	Bias	ETS
03-03	0.608	0.294	0.861	0.255	0.773	0.340	1.170	0.284
03-12	0.111	0.752	0.446	0.061	0.416	0.810	2.194	0.100
03-13	0.263	0.721	0.942	0.098	0.464	0.730	1.720	0.129
03-27	0.000	1.000	0.008	0.000	0.407	0.663	1.207	0.148
03-28	0.291	0.402	0.487	0.189	0.388	0.651	1.113	0.133
03-29	0.099	0.086	0.108	0.066	0.639	0.251	0.854	0.389
03-30	0.298	0.295	0.423	0.215	0.575	0.425	0.999	0.322
03-31	0.373	0.225	0.482	0.265	0.668	0.350	1.027	0.387
04-01	0.641	0.392	1.054	0.331	0.845	0.428	1.478	0.380
04-02	0.683	0.566	1.573	0.289	0.952	0.613	2.462	0.295
05-10	0.011	0.381	0.017	0.008	0.340	0.024	0.349	0.304
Average value	0.307	0.465	0.582	0.162	0.588 (**92**)	0.480 (–**3**)	1.325 (**22**)	0.261 (**61**)

the former are better (except for the case on March 28). In particular, on May 10, the *ETS* of Group-B is 0.304, which is 30 times that of Group-A. On average, the *POD*, *BIAS* and *FAR* of Group-B are improved by 92%, 22% and 3%, respectively, indicating that both correctly and incorrectly forecasted areas have increased. However, the rate of improvement in *ETS* exceeds 60%, implying that the improved scheme can overall improve the forecast effects of CMA-TYM for sea fog.

CONCLUSION AND DISCUSSION

Based on the operational version of CMA-TYM, numerical experiments and improvement studies are carried out on sea fog forecasts regarding three aspects: the boundary layer scheme, the vertical resolution and the bottom boundary conditions. The main conclusions are as follows.

Highly precise and dynamic SST data are adopted as the bottom layer boundary conditions. The use of SST data can better reflect the low offshore SST caused by coastal upwelling, the temperature ridge in the middle of the YS, and the ocean front between the YS and the East China Sea. As the new boundary condition, these SST data are more conducive to improving the forecasting skills for sea fog.

Comparing the accuracies of the YSU scheme and MRF scheme in describing the turbulent heat exchange reveals that the former can more accurately reflect offshore turbulence and forecast the fog area.

A finer vertical resolution facilitates heat transfer simulation. Specifically, the lower bottom layer of the model is highly sensitive to changes in the SST and temperature of the overlying atmosphere, and this sensitivity is conducive to the rapid formation and dissipation of sea fog, thus correcting the current forecast error.

Through the improved scheme, the overall *ETS* of eleven cases in the spring of 2018 is increased by 61% due to the increase in the correctly forecasted fog area.

After implementing these improvements, CMA-TYM is significantly improved in forecasting the extent of sea fog over the offshore water of China and thus can provide an important reference for operational forecasts. However, the current numerical forecast level for sea fog cannot fully satisfy the required accuracy of operational services due to the complexity of the structure and evolution of sea fog. Future models should be further improved by assimilating observational data from additional sources and developing regional air-ocean coupled models. In addition, the development of ensemble forecasts using multiple initial fields will be an important direction to reduce the uncertainties in sea fog forecasts.

DATA AVAILABILITY STATEMENT

The raw data supporting the conclusion of this article will be made available by the authors, without undue reservation.

AUTHOR CONTRIBUTIONS

BH: Formal analysis; Methodology and software; Writing–original draft. JZ: Supervision; Numerical Modeling. YC: Data curation. XG: Numerical Modeling. SM: Supervision. CS: Writing–review and editing.

FUNDING

This work was supported by the National Key Research and Development Program of China (2019YFC1510102, 2019YFC1510104).

ACKNOWLEDGMENTS

We thank the management and publishing organizations responsible for the NCEP GFS data, NCEP reanalysis data, NEAR-GOOS SST data, and Himawari-8 satellite data.

REFERENCES

Ballard, S. P., Golding, B. W., and Smith, R. N. B. (1991). Mesoscale Model Experimental Forecasts of the Haar of Northeast Scotland. *Mon. Wea. Rev.* 119, 2107–2123. doi:10.1175/1520-0493(1991)119<2107:mmefot>2.0.co;2

Cheng, X. K., Cheng, H., Xu, J., and Ma, Y. J. (2013). Forming Reason of a Sea Fog Event and its Numerical Simulation over the Yellow Sea. *J. Meteorology Environ.* 29 (6), 15–23. (in Chinese). doi:10.3969/j.issn.1673-503X.2013.06.003

Fu, G., Li, P., Zhang, S., and Gao, S. H. (2016). A Brief Overview of the Sea Fog Study in China. *Adv. Meteorol. Sci. Technol.* 6 (2), 20–28. (in Chinese). doi:10.1016/0011-2275(95)95350-N

Fu, G., Wang, J. Q., Zhang, M. G., Guo, M. K., Guo, K. C., et al. (2004). An Observational and Numerical Study of a Sea Fog Event over the Yellow Sea on 11 April, 2004. *Periodical Ocean Univ. China* 34 (5), 720–726. (in Chinese). doi:10.1007/BF02873095

Fu, G., Guo, J., Pendergrass, A., and Li, P. (2008). An Analysis and Modeling Study of a Sea Fog Event over the Yellow and Bohai Seas. *J. Ocean Univ. China* 7 (1), 27–34. doi:10.1007/s11802-008-0027-z

Fu, G., Guo, J., Xie, S.-P., Duan, Y., and Zhang, M. (2006). Analysis and High-Resolution Modeling of a Dense Sea Fog Event over the Yellow Sea. *Atmos. Res.* 81, 293–303. doi:10.1016/j.atmosres.2006.01.005

Gao, S. H., Qi, Y. L., Zhang, S. B., et al. (2010a). Initial Conditions Improvement of Sea Fog Numerical Modeling over the Yellow Sea by Using Cycling 3DVAR Part I:WRF Numerical Experiments. *Periodical Ocean Univ. China* 40 (10), 001–009. (in Chinese).

Gao, S. H., Zhang, S. B., Qi, Y. L., and Gang, F. (2010b). Initial Conditions Improvement of Sea Fog Numerical Modeling over the Yellow Sea by Using Cycling 3DVAR Part II:RAMS Numerical Experiments. *Periodical Ocean Univ. China* 40 (11), 001–010. (in Chinese). doi:10.3969/j.issn.1672-5174.2010.11.001

Gao, X. Y., and Gao, S. H. (2019). EnKF Assimilation of Cloud Water Path in Nowcasting Sea Fog over the Yellow Sea. *Oceanologia Et Limnologia Sinica* 50 (2), 248–260. (in Chinese). doi:10.11693/hyhz20181000243

Golding, B. W. (1993). A Study of the Influence of Terrain on Fog Development. *Mon. Wea. Rev.* 121, 2529–2541. doi:10.1175/1520-0493(1993)121<2529:asotio>2.0.co;2

Gultepe, I., Tardif, R., Michaelides, S. C., Cermak, J., Bott, A., Bendix, J., et al. (2007). Fog Research: A Review of Past Achievements and Future Perspectives. *Pure Appl. Geophys.* 164, 1121–1159. doi:10.1007/s00024-007-0211-x

Huang, B., Yan, L. F., Yang, C., and Xu, J. (2014). Development and marine Meteorological Numerical Prediction in China. *Adv. Meteorol. Sci. Technol.* 4 (3), 57–61. (in Chinese). doi:10.3969/j.issn.2095-1973.2014.03.010

Huang, H. J., Zhan, G. W., Liu, C. X., Tu, J., and Mao, W. K. (2015). A Case of Numerical Simulation of Sea Fog on the Southern China Coast. *J. Trop. Meteorology* 31 (5), 643–654. (in Chinese). doi:10.16032/j.issn.1004-4965.2015.05.007

Huang, S., Zhang, S. P., and Yi, L. (2019). The Analysis of the Formation of Coastal Fog under Surface Offshore Airflow in the Western Yellow Sea in spring. *Periodical Ocean Univ. China* 49 (6), 20–29. (in Chinese). doi:10.16441/j.cnki.hdxb.20180154

Koračin, D., Businger, J. A., Dorman, C. E., and Lewis, J. M. (2005). Formation, Evolution, and Dissipation of Coastal Sea Fog. *Boundary-Layer Meteorology* 117, 447–478. doi:10.1007/s10546-005-2772-5

Kunkel, B. A. (1984). Parameterization of Droplet Terminal Velocity and Extinction Coefficient in Fog Models. *J. Clim. Appl. Meteorol.* 23, 34–41. doi:10.1175/1520-0450(1984)023<0034:podtva>2.0.co;2

Lu, X., Gao, S. H., Rao, L. J., and Wang, Y. (2014). Sensitivity Study of WRF Parameterization Schemes for the spring Sea Fog in the Yellow Sea. *J. Appl. Meteorol. Sci.* 25 (3), 312–320. (in Chinese). doi:10.3969/j.issn.1001-7313.2014.03.008

Ma, S. H., and Chen, D. H. (2018). Performance of Regional Typhoon Model of National Meteorological Center. *J. Trop. Meteorology* 34 (4), 451–459. (in Chinese). doi:10.16032/j.issn.1004-4965.2018.04.002

Ma, S. H., Zhang, J., Shen, X., et al. (2018). The Upgrade of GRAPE_TYM in 2016 and its Impacts on Tropical Cyclone Prediction. *J. Appl. Meterological Sci.* 35 (3), 257–269. (in Chinese).

Nakanishi, M. (2000). Large-Eddy Simulation of Radiation Fog. *Boundary-Layer Meteorology* 94, 461–493. doi:10.1023/a:1002490423389

Pagowski, M., Gultepe, I., and King, P. (2004). Analysis and Modeling of an Extremely Dense Fog Event in Southern Ontario. *J. Appl. Meteorol.* 43, 3–16. doi:10.1175/1520-0450(2004)043<0003:aamoae>2.0.co;2

Wang, B. H. (1983). *Sea Fog*. Beijing: Marine Press. (in Chinese).

Wang, H., Zhang, Z., Liu, D., Yuan, C., Zhou, L., and Qian, W. (2018). Detection of Fog at Night by Using the New Geostationary Satellite Himawari-8[J]. *Plateau Meteorology* 37 (6), 17491764. (in Chinese). doi:10.7522/j.issn.1000-0534.2018.00037

Wang, S., Fu, D., Chen, D. L., Li, L. Y., and Fu, G. (2012). An Observation and Numerical Simulation of a Sea Fog Event over the Yellow Sea in the spring of 2009. *Trans. Atmos. Sci.* 35 (3), 282–294. (in Chinese). doi:10.1007/s11783-011-0280-z

Wang, Y. M., Gao, S. H., and Fu, G. (2015). Assimilating MTSAT-Derived Humidity in Nowcasting Sea Fog over the Yellow Sea. *Weather Forecast.* 29, 205–225. doi:10.1175/WAF-D-12-00123.1

Wang, Y. M., and Gao, S. H. (2016). Assimilation of Doppler Radar Radial Velocity in Yellow Sea Fog Numerical Modeling. *Periodical Ocean Univ. China* 46 (8), 1–12. (in Chinese). doi:10.16441/j.cnki.hdxb.20150361

Wu, X. J., Li, S. M., Liao, M., Cao, Z. Q., Wang, L., and Zhu, J. (2015). Analyses of Seasonal Feature of Sea Fog over the Yellow Sea and Bohai Sea Based on the Recent 20 Years of Satellite Remote Sensing Data[J]. *Haiyang Xuebao* 37 (1), 63–72. (in Chinese). doi:10.3969/j.issn.0253-4193.2015.01.007

Yang, Y., and Gao, S. H. (2016). Sensitivity Study of Vertical Resolution in WRF Numerical Simulation for Sea Fog over the Yellow Sea. *Acta Meteorologica Sinica* 74 (6), 974–988. (in Chinese).

Zhang, J., Ma, S. H., Chen, D., and Huang, L. P. (2017). The Improvements of CMA-TYM and its Performance in Northwest Pacific Ocean and South China Sea in 2013. *J. Trop. Meteorology* 33 (1), 64–73. (in Chinese).

Zhou, B., and Du, J. (2010). Fog Prediction from a Multimodel Mesoscale Ensemble Prediction System. *Weather Forecast.* 25 (1), 303–322. doi:10.1175/2009waf2222289.1

Conflict of Interest: The authors declare that the research was conducted in the absence of any commercial or financial relationships that could be construed as a potential conflict of interest.

frontiers in Earth Science

ORIGINAL RESEARCH
published: 18 March 2022
doi: 10.3389/feart.2022.828253

The Improvements of the Upper Zonal Currents by SST Assimilation Over the Tropical Pacific in a Coupled Climate Model

Zhikuo Sun[1], Xin Gao[2], Jiangbo Jin[2,3], Juanxiong He[2], Fei Zheng[2]*, He Zhang[2], Xiao Dong[2] and Qingcun Zeng[2]*

[1]Southern Marine Science and Engineering Guangdong Laboratory (Zhuhai), Zhuhai, China, [2]ICCES, Institute of Atmospheric Physics, Chinese Academy of Sciences, Beijing, China, [3]State Key Laboratory of Satellite Ocean Environment Dynamics, Second Institute of Oceanography, Ministry of Natural Resources, Hangzhou, China

The upper zonal oceanic circulations in the tropical Pacific play a crucial role in modulating weather and climate in the tropical Pacific Ocean. However, they are poorly simulated in state-of-the-art climate models. We apply a simple bias correction scheme by only assimilating observed sea surface temperature (SST) data into a coupled earth system model, named the Chinese Academy of Sciences Earth System Model version 2 (CAS-ESM 2.0), to better reproduce the upper zonal currents in tropical oceans. There are mainly two reasons for this usage of SST assimilating method: 1) SST has dominant effects on the air–sea interactions over the tropical region; 2) The lack of effective and long-term ocean-current observation data currently. Our results show that the SST assimilation can significantly improve the strength of the Pacific Equatorial Undercurrent (EUC), the North Equatorial Countercurrent (NECC) and the South Equatorial Current (SEC) through reducing biases in the air–sea turbulence flux. Nevertheless, the SST assimilation has limited effects on improving the simulation of the spatial structure of these zonal currents in the tropical Pacific. The improvement of the wind stress curl over the tropical Pacific region mainly contributes to the improved simulated strength of the Pacific EUC, the NECC and the SEC. It also connects to the reduced biases in atmospheric convective precipitation and sea-level pressure induced by the reduction of the SST bias.

Keywords: SST bias correction, air-sea interaction, the upper zonal currents, CAS-ESM, tropical pacific

OPEN ACCESS

Edited by:
Guihua Wang,
Fudan University, China

Reviewed by:
Shang-Min Long,
Hohai University, China
Jingzhi Su,
Chinese Academy of Meteorological Sciences, China
Shijian Hu,
Institute of Oceanology (CAS), China

****Correspondence:***
Jiangbo Jin
jinjiangbo@mail.iap.ac.cn
Fei Zheng
zhengfei@mail.iap.ac.cn

Specialty section:
This article was submitted to Atmospheric Science, a section of the journal Frontiers in Earth Science

Received: *03 December 2021*
Accepted: *21 February 2022*
Published: *18 March 2022*

Citation:
Sun Z, Gao X, Jin J, He J, Zheng F, Zhang H, Dong X and Zeng Q (2022) The Improvements of the Upper Zonal Currents by SST Assimilation Over the Tropical Pacific in a Coupled Climate Model. Front. Earth Sci. 10:828253. doi: 10.3389/feart.2022.828253

HIGHLIGHTS

1. We mainly show the effects of the sea surface temperature assimilation on the upper zonal currents over the tropical Pacific in a coupled model.
2. The strength of the Pacific Equatorial Undercurrent, the North Equatorial Countercurrent and the South Equatorial Current significantly increases through the reduction of the SST bias.
3. The improvements in the simulated wind stress curl over the tropical Pacific are mainly due to the improved air–sea interaction simulation with the SST assimilation.

INTRODUCTION

The upper zonal oceanic circulations in the tropical Pacific (10°S–10°N) are mainly characterized by three zonal ocean currents: the eastward Equatorial Under Current (EUC) and North Equatorial Countercurrent (NECC) and the westward South Equatorial Current (SEC). The Pacific EUC is an intense subsurface eastward jet located at the Pacific equator with a maximum velocity of greater than 1.0 m/s (Philander, 1973). The Pacific NECC is an eastward upper-ocean zonal flow between 2 and 10°N, with a maximum value of approximately 0.4 m/s near 140°W (Johnson et al., 2002). The Pacific SEC controls a wide range of ocean between 15°S and 4°N and splits into a northern and a southern branch (Wyrtki, 1974), herein referred to as SEC(N) and SEC(S), due to a near-equatorial minimum in the westward surface flow or sometimes the eastward surface flow (McPhaden and Taft, 1988; Johnson et al., 2002). These Pacific upper zonal currents play crucial roles in transporting heat, salt, carbon and oxygen nutrients and modulate atmospheric precipitation, winds and tropical cyclone intensities in the tropical Pacific Ocean (Picaut et al., 1996; Delcroix and Picaut 1998; Bonjean 2001; Kim and Jin, 2011; Bellenger et al., 2014; Hu et al., 2015; Hu et al., 2021). The above currents are also thought to be important factors in the representation of ENSO in coupled models (Jin et al., 2006).

The upper zonal oceanic circulations in the tropical Pacific are poorly simulated in state-of-the-art climate models currently. Zhu et al. (2020) evaluate 50 models from the Coupled Model Inter-Comparison Project phase 6 (CMIP6) and find that simulations of the Pacific EUC and the NECC tend to be weak. Compared to the observed value of ~0.3 m/s, the annual mean zonal speed of the NECC given by the model is only approximately 0.1 m/s, while the EUC is also underestimated by approximately 3.7 Sv in the CMIP6 multi-model ensemble. The weak upper zonal oceanic currents are mainly caused by the model's deficiency in simulating the surface wind stress curl (WSC) (Sun et al., 2019; Zhu et al., 2020), which is attributed to the significant double intertropical convergence zone (ITCZ) bias in the tropical North Pacific and the coarse resolution of ocean models. Currently, few studies have focused on evaluating the Pacific SEC simulation in CMIP6 and we take the Pacific SEC into consideration in this study. As there are no effective and long-term ocean-current observation datasets, it's difficult to directly assimilate ocean currents. Therefore, one motivation of the present study is to provide some additional and possibly useful information that could help us to improve the simulation of upper zonal oceanic circulations in the tropical Pacific region.

Here, we aim to reproduce the Pacific upper zonal currents through assimilating the tropical Pacific sea surface temperature (SST) to reduce the common tropical SST biases—for instance, the cold SST biases in the western tropical Pacific and the excessive westward extension of the cold-tongue bias in the eastern equatorial Pacific (Zhou et al., 2020). We also aim to investigate the impacts of SST on the upper zonal currents in the tropical Pacific Ocean. One reason is that the effective and long-term SST observation data are easier to obtain. Another is that the SST plays an important role in air–sea interactions (Richter and Tokinaga, 2020), including the atmospheric 10 m wind and the corresponding surface wind stress (Wallace et al., 1989; Chelton et al., 2001). Compared with mid-to-high latitudes, the Coriolis force in the tropical region is small and the wind field has a strong influence on the upper ocean currents. The air–sea momentum flux, also known as surface wind stress, is crucial for the proper simulation of the upper zonal oceanic circulations in the tropical Pacific (Sverdrup 1947; Kessler et al., 2003; Zheng and Zhu, 2010; Thomas et al., 2014; Sun et al., 2019). The reduction of SST bias can effectively improve the 10 m wind and surface wind stress through air-sea interaction, including the large-scale, non-adiabatic heating and changes in atmospheric circulation. Our research provides the possibility to further improve the simulation of upper ocean currents in ocean models.

This paper proceeds as follows. The model, data and simulation scheme are described in *Introduction*. The results of numerical experiments are introduced in *Model, Numerical Experimental Design, Methodology and Data*, which is followed by a discussion and summary in *Improvements of the Upper Zonal Currents With SST Simulation*.

MODEL, NUMERICAL EXPERIMENTAL DESIGN, METHODOLOGY AND DATA

Model

The coupled model used in the present study is the second version of the Chinese Academy of Sciences Earth System Model (CAS-ESM2.0)—which consists of IAP-AGCM5.0 (Zhang et al., 2020) for atmosphere, revised LICOM2.0 for ocean (Liu et al., 2012; Dong et al., 2021), CoLM (Dai et al., 2004; Ji et al., 2014) for land surface, CICE4.0 (Hunke and Lipscomb, 2008) for sea ice and the Weather Research and Forecasting (WRF) model. The horizontal resolution of IAP AGCM5.0 is approximately 1.4° latitude × 1.4° longitude and has 35 vertical levels with a model top at 2.2 hPa. The domain of revised LICOM2.0 is located between 78.5°S and 87.5°N with a 1° zonal resolution. The meridional resolution is refined to 0.5° between 10°S and 10°N and increases gradually from 0.5 to 1° between 10 and 20°. There are 30 levels in the vertical direction with 10 m per layer in the upper 150 m. The horizontal resolution of CoLM and CICE 4.0 is the same with the atmosphere model and ocean model, respectively. The infrastructure of the Community Earth System Model (CESM) Coupler seven is adopted to ensure these components coupled together. Additional components in CAS-ESM2.0 include the IAP Vegetation Dynamics Model, the IAP fire model, the IAP ocean biogeochemistry model, the atmospheric aerosol, the chemistry model and various emission models. The details of CAS-ESM2.0 can be found in Zhang et al. (2020). Here, four climate components are the focus in this study, including atmosphere, ocean, land and sea ice.

Numerical Experimental Design

CAS-ESM2.0 is a newcomer in the community and it is the first time to participate in the historical CMIP6 experiment. Corresponding datasets have been uploaded onto the Earth

System Grid Federation (ESGF) data server for CMIP6 users to download. Here, we estimate the impact of realistic SST on the simulation of upper zonal currents in the tropical Pacific Ocean by running two historical experiments: one without applying the assimilated method is denoted as "SST-noAssim" and the other with applying the assimilated method is denoted as "SST-Assim". The SST assimilated scheme applied in this study is the SST nudging method proposed by Keenlyside et al. (2005) and this method is widely used for generating the initial conditions and correcting the subsurface temperature field in climate model (Chen et al., 2020). The SST nudging method is that the simulated SSTs are nudged towards the observed SST through damping constant with latitude. The damping constant equals to 0.25 days [about 3.8 × 103 W/(m K)] between 30°S and 30°N in the global area, which means that the simulated SSTs are nudged towards the daily observed SST four times 1 days. Poleward of 30°S and 30°N, the damping constant linearly decreases to zero at 60°S and 60°N. The observed daily mean SSTs used in our research are from the NOAA High-Resolution Blended Analysis of Sea Surface Temperature dataset (Reynolds et al., 2007). These two experiments are all integrated for 33 years from 1982 to 2014 and the SST-Assim experiment starts from the 1982 state of SST-noAssim experiment. Through comparing the results between SST-noAssim and SST-Assim experiments, we can further estimate the effects of SST bias reduction on zonal currents in the tropical Pacific. In this study, we mainly focus on the EUC, the NECC and the SEC.

Methodology and Data

To better understand the dynamic of the EUC, NECC and SEC in these two experiments, the zonal volume transport in the tropical Pacific is diagnosed following Sverdrup (1947) and Kessler et al. (2003). The equation for the zonal transport is derived from momentum equations as follows:

$$U = \frac{1}{\beta}\int_{x}^{EB} curl\left(\vec{\tau}\right)_{y} dx + U_{EB} \quad (1)$$

Here, $\vec{\tau}$ represents the surface wind stress and U_{EB} is the transport at the eastern boundary (EB). It can be found that the wind-driven zonal transport (U) is mainly determined by the zonal integration of the meridional gradient of the WSC ($curl\,(\vec{\tau})_y$). Namely, the zonal integration of positive (negative) $curl\,(\vec{\tau})_y$ contributes to the formation of eastward (westward) zonal transport.

The following observational datasets are used in this study:

1) Daily mean SSTs from NOAA's High-Resolution Blended Analysis of Sea Surface Temperature dataset from 1982 to 2014, version 2.1, with a horizontal resolution of 0.25° * 0.25° (Reynolds et al., 2007).
2) Wind stress from the Scatterometer Climatology of Ocean Winds (SCOW) dataset, with a horizontal resolution of 0.25° *0.25°, based on 8 years (September 1999-August 2007) of QuikSCAT scatterometer data (Risien and Chelton, 2008).
3) *In situ* observation of ocean currents, also known as Johnson climatology, which is primarily constructed during the 1990s and contains ten meridional sections: 143°, 156°, 165°, and 180°E, 170°, 155°, 140°, 125°, 110,° and 95°W. Missing values exist at certain depths and latitudes, particularly in the westernmost section (143°E). Meridional sections of contemporaneous conductivity—temperature—depth (CTD) and acoustic Doppler current profiler (ADCP) data across the Pacific are used to construct the climatology of the upper 400 m zonal current in the Equatorial Pacific (Johnson et al., 2002).
4) NCAR's monthly ocean temperature dataset from the Simple Ocean Data Assimilation version (SODAsi.3) from 1982 to 2013, with a horizontal resolution of 0.5° *0.5° (Giese et al., 2016).

IMPROVEMENTS OF THE UPPER ZONAL CURRENTS WITH SST SIMULATION

Assimilation of the Tropical Pacific SST

Figure 1 shows the spatial distribution of climatological SST in the tropical Pacific (25°S–25°N, 120°E–90°W). Observationally, an SST maximum above 28°C locates in the tropical western Pacific (20°S–20°N, 120°E–160°W), hereafter referred to as the "warm pool" (Wyrtki, 1989). The spatial pattern of the whole warm pool is distributed from northwest to southeast. Two zonal high-SST strips do not follow a north–south symmetrical structure between the two hemispheres: One locates in the north Pacific and spans the entire Pacific, the formation of which is related to the Pacific ITCZ. The other locates in the south Pacific and the boundary only extends eastward to approximately 140°W, which also has a larger east-west temperature gradient compared to the north zonal high-SST strip.

The SST simulated in the SST-noAssim experiment exhibits significant biases compared with the observations (**Figure 1B**). Especially in the western tropical Pacific region, the warm pool is separated into north and south parts by a low-temperature strip, which extends westward from the East Pacific at the equator. This low-temperature strip is related to the persistent cold equatorial SST bias in the tropical Pacific and is a common bias in coupled climate models (Adam et al., 2018; Samanta et al., 2019). The spatial pattern of the warm pool in the SST-noAssim experiment is more biased towards a west-east distribution, instead of a northwest-southeast distribution in the observation. Moreover, the high-SST strip in the south zone extending further eastward attributes to the longstanding double-ITCZ bias in the tropical Pacific (Tian and Dong, 2020).

The simulated tropical Pacific SST in the SST-Assim experiment is largely improved compared to the SST-noAssim experiment (**Figure 1C**). The cold bias in the subtropical Pacific and western Pacific and the warm bias in the extra-equatorial eastern Pacific improve significantly in the SST-Assim experiment (**Figure 1D**). The warm pool west of 160°E is still connected in the northern and southern hemispheres and distributes in northwest-southeast direction. The high-SST zonal strip becomes more similar to the observations especially in the southern hemisphere. Need to mention, although the bias

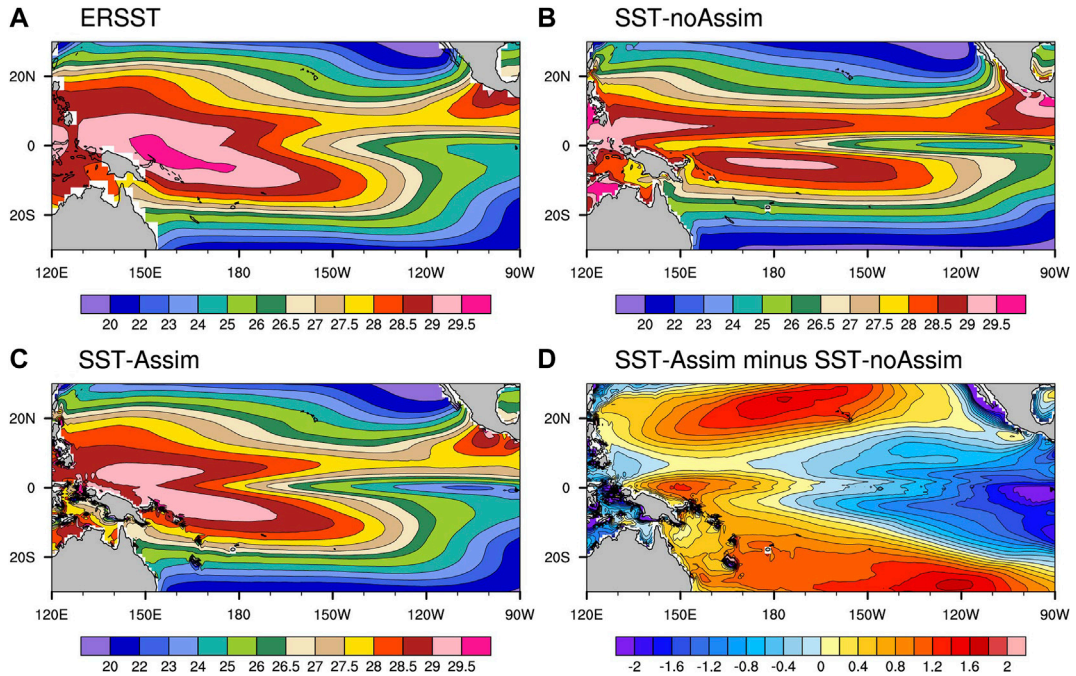

FIGURE 1 | Annual mean SST from **(A)** ERSST, **(B)** SST-noAssim experiment and **(C)** SST-Assim experiment; **(D)** The difference between SST-Assim experiment and SST-noAssim experiment (SST-Assim minus SST-noAssim). The average period of observations and model results is from 1982 to 2014, the unit is °C.

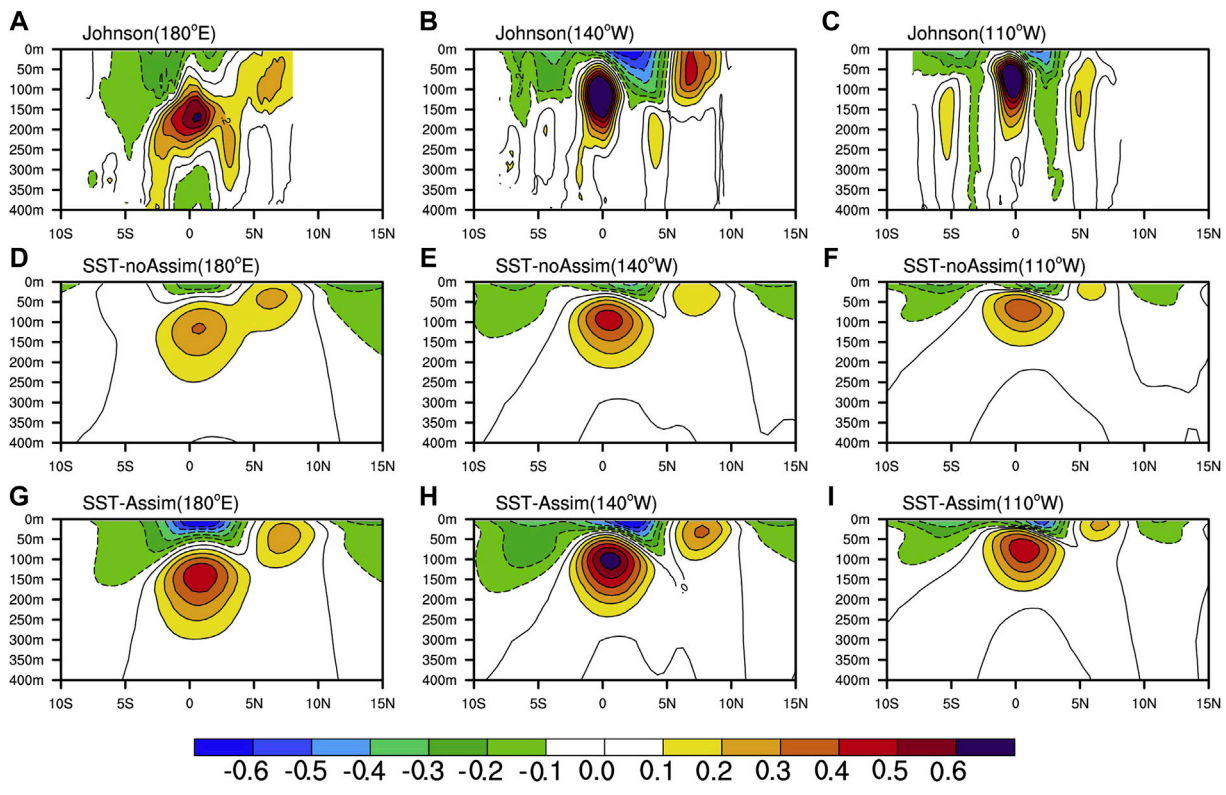

FIGURE 2 | Meridional–vertical sections of annual mean zonal currents (m/s) at **(A)** 180°E, **(B)** 140°W, and **(C)** 110°W for Johnson et al. (2002) climatology **(D–F)** and **(G–I)** are the same as **(A–C)** but for the SST-noAssim experiment and the SST-Assim experiment, respectively. The contour interval for all the panels is 0.1 m/s. The eastward (westward) velocities are shown as solid (dashed) lines. The average period of the model data is from 1985 to 2000, and the positive values indicate an eastward direction.

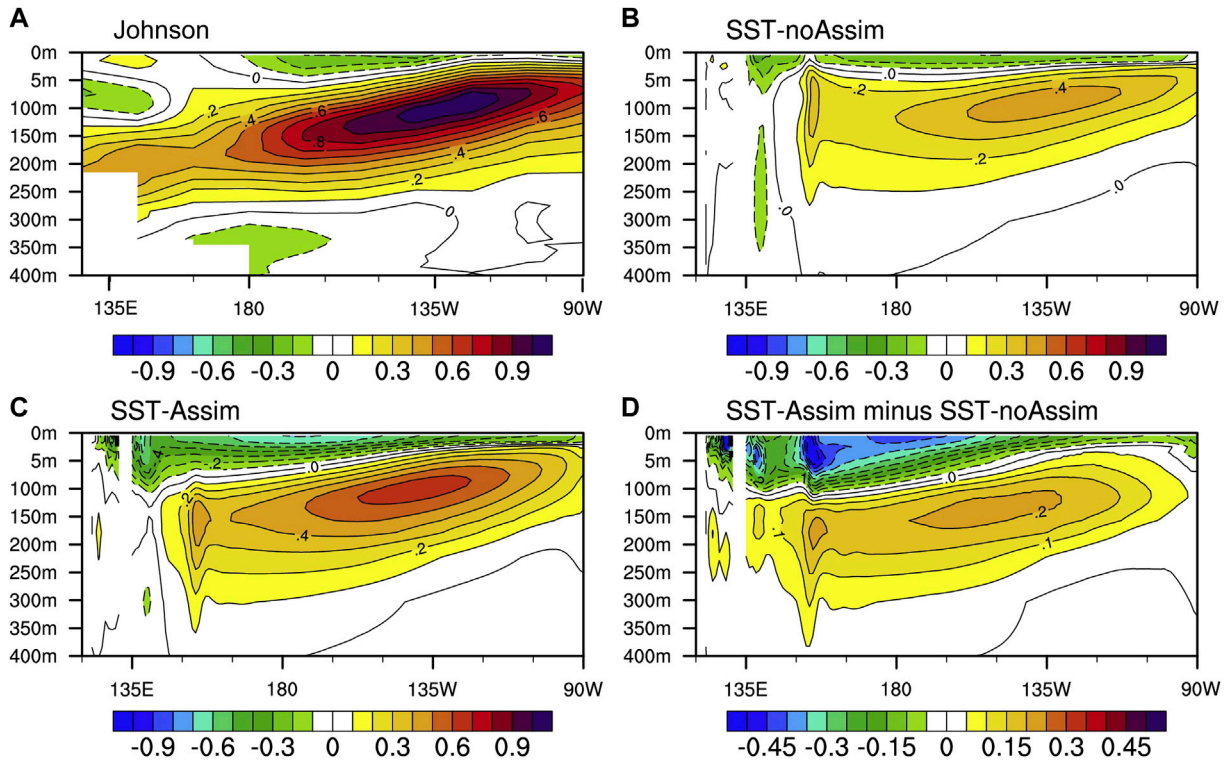

FIGURE 3 | Longitude–depth diagram of annual mean zonal current (shaded and contour; in m/s; eastward in solid, and westward in dashed lines) at the equator (0°N) for **(A)** Johnson data, **(B)** SST-noAssim experiment and **(C)** SST-Assim experiment, respectively; **(D)** The difference between SST-Assim experiment and SST-noAssim experiment (SST-Assim minus SST-noAssim). The average period for the model data is from 1985 to 2000, and the positive values indicate an eastward direction.

in the excessive westward extension of the equatorial Pacific cold tongue is alleviated, the cold bias in the eastern equatorial Pacific increases in the SST-Assim experiment (**Figure 1D**). It indicates that the SST-Assim experiment exhibits a larger east-west temperature gradient in the equatorial tropical Pacific compared with the SST-noAssim experiment. The possible reason is that although the intensity of SST nudging is the strongest in the tropics, the evolution of the coupled model is also important and needs to be fully considered here. Therefore, the assimilated SST still deviates to some extent from the observation.

Reduced Biases of Tropical Pacific Upper Zonal Ocean Currents

To investigate the impacts of SST bias reduction in the simulation of upper zonal ocean currents in the tropical Pacific, **Figure 2** shows the observed and simulated vertical-meridional sections of the mean zonal current at three longitudes, 180°E, 140°W, and 110°W, representing the western, central and eastern equatorial Pacific, respectively. The observation is from the Johnson climatology dataset (Johnson et al., 2002) and allows the direct estimation of the properties of near-equatorial currents, including the measurement of the velocity of the tropical upper Pacific Ocean current. Both experiments capture the eastward NECC, the westward SEC and the eastward EUC well in the tropical Pacific. There were two subsurface eastward jets on two sides of the EUC in the observations (**Figures 2A,B**), representing the North Subsurface Countercurrent (NSCC) and the South Subsurface Countercurrent (SSCC) (Wyrtki and Kilonsky, 1984), respectively. However, the NSCC and the SSCC cannot be portrayed separately in both simulations probably relating to the coarse resolution of ocean model.

Regarding the simulation of the Pacific EUC, both experiments exhibit very weak current strength at all longitudes relative to the observations (**Figure 2**). Compared with the SST-noAssim experiment, the Pacific EUC has significant improvements in strength in the SST-Assim experiment. The maximum values of the observed EUC are approximately 0.6, 1.0, 1.0 m/s at 180°E, 140°W and 110°W, respectively. The corresponding values are approximately 0.3 (0.4) m/s, 0.4 (0.6) m/s and 0.3 (0.4) m/s in the SST-noAssim (SST-Assim) experiment, respectively. The weak simulation of the Pacific EUC further shows in the vertical zonal sections of the EUC in the equatorial Pacific shown in **Figure 3**, in which the eastward subsurface ocean current represents the EUC and accompanies by the westward South Equatorial Current (SEC) above it (**Figure 3**). The maximum of the equatorial EUC locates at ~ 135°W, with values of 1.0, 0.4 and 0.6 m/s for the observation, the SST-noAssim experiment and the SST-Assim experiment,

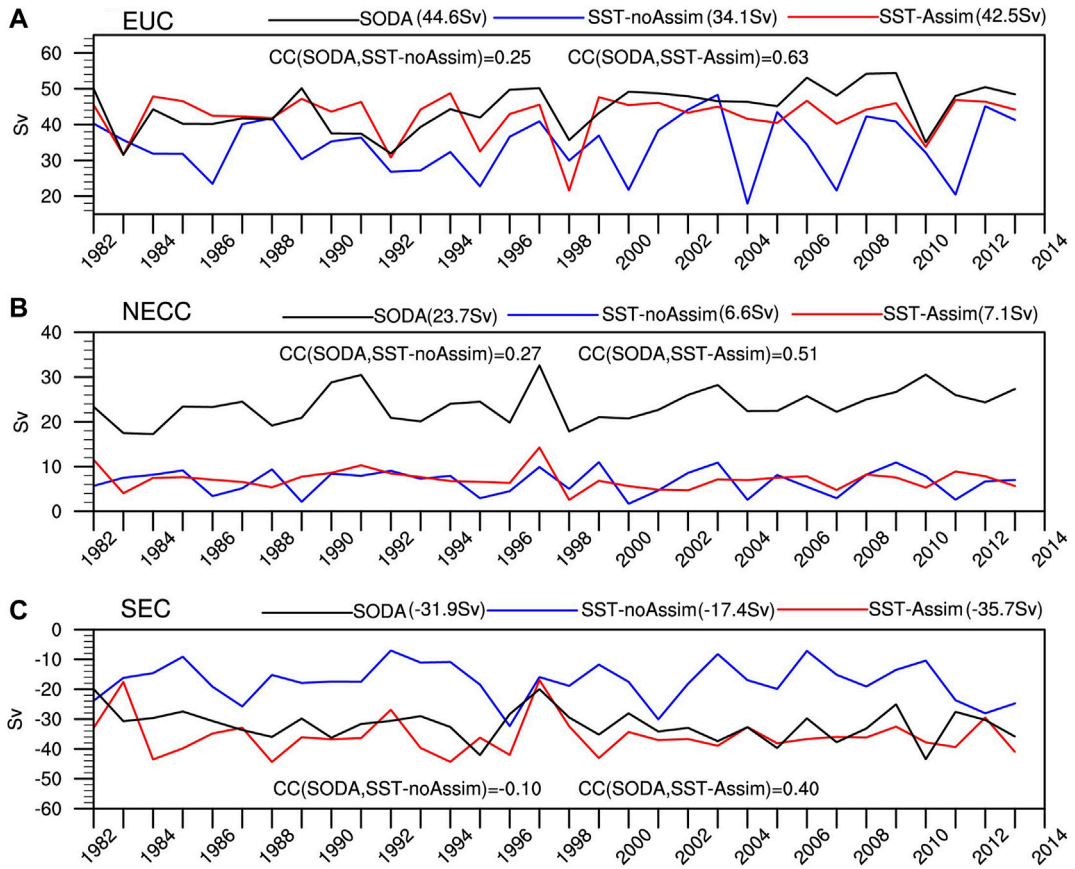

FIGURE 4 | The interannual variability of the zonal volume transport at 140°W of the Pacific **(A)** EUC, **(B)** NECC and **(C)** SEC of the SODA (black line), SST-noAssim experiment (blue line) and SST-Assim experiment (red line), respectively (units: Sv; 1Sv = 106 m3/s). Values in the parentheses mean the annual average values from 1982 to 2013 at 140°W. The abbreviation "CC" represents the correlation coefficient value.

respectively. The maximum difference of Pacific EUC between SST-Assim and SST-noAssim experiment can reach 0.2 m/s, clearly shown in **Figure 3D**.

As for the center depth of the Pacific EUC, the observed EUC centers locate at approximately 180, 130 and 80 m at 180°E, 140°W and 110°W, respectively (**Figure 2**), exhibiting a tilting-up structure from west to east. Both experiments can reasonably simulate this tilting-up structure but the simulated center depth is relatively shallow, especially at 180°E and 140°W. The corresponding values are 120 m at 180°E and 100 m at 140°W for both two experiments. Furthermore, we also find that both experiments have deeper bottom boundary depth of the EUC, greater than 400 m in the equatorial western and central Pacific, whereas the corresponding value is only less than 350 m in the observations (**Figure 3**).

The strength of the Pacific NECC also has significant improvements under more realistic SST, especially in the central and eastern Pacific (**Figure 2**). The observational maximum speeds of the NECC are approximately 0.2, 0.4 and 0.2 m/s at 180°E, 140°W and 110°W, respectively. The corresponding values are 0.2 (0.2), 0.1 (0.3), and 0.1 (0.2) m/s in the SST-noAssim (SST-Assim) experiment, respectively. As for the center depth of the Pacific NECC, small improvements are found and both experiments have shallower center depth compared with the observation data. The observational center depths of the Pacific NECC are approximately 75, 50 and 150 m at 180°E, 140°W and 110°W, respectively. But the corresponding values are only approximately 40 m (50 m), 30 m (30 m) and 20 m (20 m) for the SST-noAssim (SST-Assim) experiment. Both two experiments have deeper bottom boundary depth, greater than 400 m, which is only ~200 m in the observations.

As for the SEC, the SST-Assim experiment has more accurate strength compared to the SST-noAssim experiment. The maximum speeds are 0.2 (0.6), 0.4 (0.6), and 0.3 (0.5) m/s for the SST-noAssim (SST-Assim) experiment at 180°E, 140°W and 110°W, respectively. And the corresponding observed values are 0.2, 0.6 and 0.5 m/s, respectively. We find that the SEC strength in the SST-Assim experiment is almost equivalent to the observations in the central and eastern Pacific. But the SST-Assim experiment gets stronger SEC in the western Pacific compared with the observations (**Figure 2G**). The downward extending depth of the Pacific SEC is shallower for both experiments, which has been slightly alleviated in the SST-Assim experiment.

The SST-nudging also improves the simulation of year-to-year variations of these three zonal ocean currents. **Figure 4** shows the

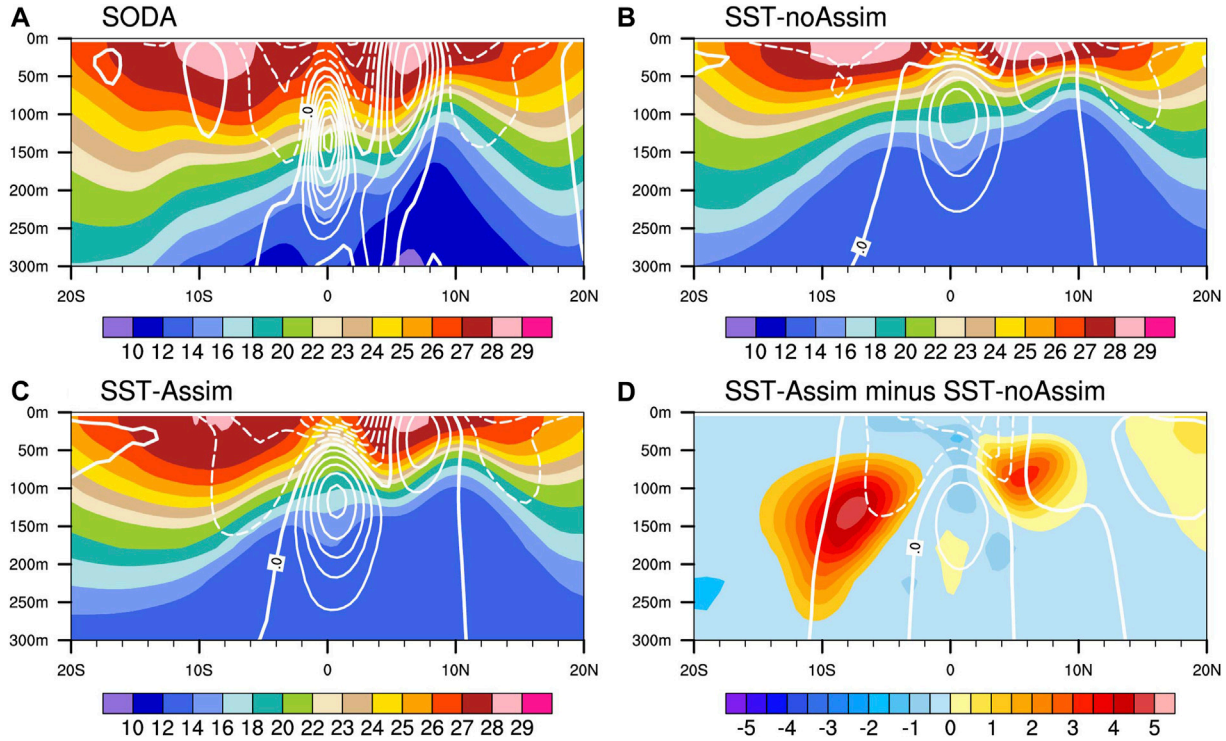

FIGURE 5 | Latitude–depth diagram of annual mean oceanic temperature (shaded, in °C) and zonal current (white contours, eastward in solid and westward in dashed lines), averaged over 160°E—110°W for **(A)** the reanalysis data SODA, **(B)** SST-noAssim experiment and **(C)** SST-Assim experiment, respectively; **(D)** The difference between SST-Assim experiment and SST-noAssim experiment (SST-Assim minus SST-noAssim). The average period of SODA (temp and U) is from 1982 to 2013. The average period of the model data is from 1982 to 2014.

interannual variability of the zonal volume transport at 140°W of the Pacific EUC, NECC and SEC, respectively. We choose SODA reanalysis data as the "real" data to evaluate the experiments due to lack of continuously long-time observed equatorial zonal current data. SST-Assim experiment has stronger Pacific EUC, NECC and SEC compared with SST-noAssim experiment, closer to the SODA reanalysis data and consistents with our previous results shown from **Figures 2**, **3**. The correlation coefficients of the interannual variability of these three zonal currents between the SST-Assim experiment and SODA reanalysis are all higher than the SST-noAssim experiment, from 0.25 to 0.63 for EUC, 0.27 to 0.51 for NECC and −0.1 to 0.4 for SEC, respectively. The lower correlation between SST-noAssim and SODA reanalysis relative to SST-Assim experiment may be resulted from the inconsistent the model year and the actual year.

Key Processes for Improving the Zonal Currents in the Tropical Pacific

To further investigate the effects of sea-temperature bias reduction on zonal currents in the tropical Pacific, **Figure 5** shows the latitude-depth diagram of annual mean oceanic temperature and zonal current, averaged from 160°E to 110°W for the reanalysis data (SODA) and model results. Compared with the SST-noAssim experiment, the averaged Pacific EUC, NECC and SEC are stronger in the SST-Assim experiment. Here, the strength of these zonal currents can be linked to temperature distribution. For instance, the formation of the NECC and the SEC is related to the north-south meridional temperature gradient: the negative meridional temperature gradient between 5 and 10°N and the positive meridional temperature gradient between 0 and 5°N in the northern hemisphere, connected to the strength of the NECC and SEC(N), respectively. Similarly, the formation of the Pacific SEC(S) in the southern hemisphere is related to the negative meridional temperature gradient between 5°S and 0°N. The difference between two experiments is further shown in **Figure 5D**: the north-south meridional temperature gradient increases due to the warmer subsurface temperatures at 8°S and 6°N in the SST-Assim experiment. The stronger absolute values of these north–south meridional temperature gradients, along with the corresponding stronger zonal ocean current, can partly explain the improved simulation of the Pacific NECC and the SEC in the SST-Assim experiment.

To further investigate the relationship between the change in SST, surface wind stress and zonal ocean currents, the annual mean surface wind stress and WSC of the observations and both experiments are shown in **Figure 6**. Compared to the SST-noAssim experiment, the improvements in wind stress field in the SST-Assim experiment mainly include the following two points: 1) the easterly wind stress in the equatorial Pacific is strengthened; 2) the subtropical easterly trade wind stress between 5 and 10° in both hemispheres becomes weaker. The strengthening of the easterly wind stress at the equator,

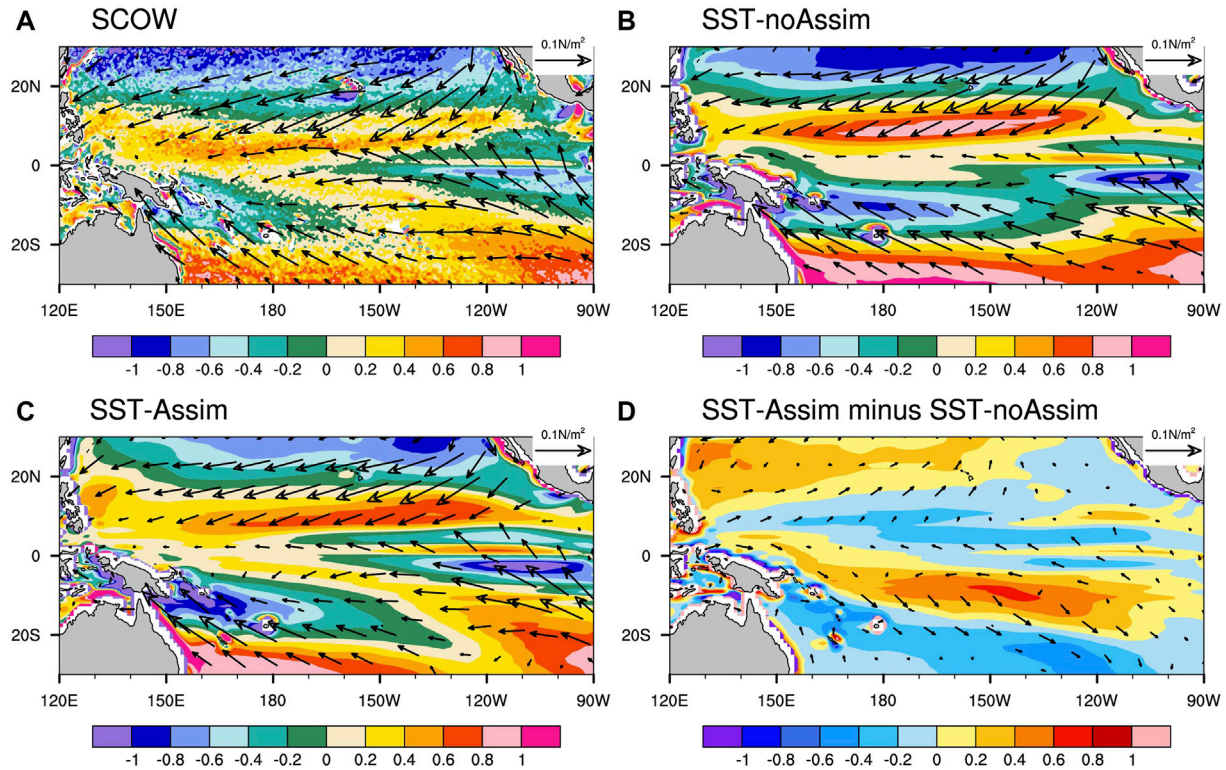

FIGURE 6 | Annual mean wind stress curl (WSC, shaded, in $*10^{-7}$ N/m^3) and wind stress vector (arrows, in N/m^2) from **(A)** SCOW, **(B)** SST-noAssim experiment, **(C)** SST-Assim experiment and **(D)** the difference between SST-Assim experiment and SST-noAssim experiment (SST-Assim minus SST-noAssim). The average period of the model data is from 1982 to 2014.

combined with the weaker northeasterly trade wind stress between 5 and 10°N in the northern hemisphere, leads to a weaker positive WSC in the ITCZ region in the SST-Assim experiment and becomes more consistent with the observations (**Figures 6A–C**). Similarly, the strengthening of the easterly wind at the equator, accompanied by the weaker southeasterly wind stress between 5 and 10°S in the southern hemisphere in the SST-Assim experiment, leads to a positive center in the WSC difference in the south of 5°S between two experiments (SST-Assim minus SST-noAssim, **Figure 6D**). This positive center in the WSC difference corresponds to the more realistic simulation of the "sandwich-like" WSC structure (negative–positive–negative) between 0°N and 20°S in the northeast–southwest direction in the SST-Assim experiment, which is consistent with the observations and cannot be seen in the SST-noAssim experiment (**Figure 6**).

The zonal Sverdrup transport contributed by the linear wind term is shown in **Figure 7B** to illustrate the relationship between the surface wind stress and the zonal Sverdrup transport in more detail. According to the wind-driven zonal transport formula (**Eq. 1**), the wind-driven zonal transport (U) is mainly determined by the zonal integration of the meridional gradient of the WSC ($curl\,(\vec{\tau})_y$) from the eastern to the western Pacific. The positive (negative) $curl\,(\vec{\tau})_y$, especially the values in the eastern Pacific, contributes to the formation of eastward (westward) zonal transport (Sverdrup, 1947; Kessler et al., 2003; Sun et al., 2019). There are mainly five extreme centers of WSC difference between SST-Assim experiment and SST-noAssim experiment occurred in the east of 150°W (**Figure 7A**): Three positive regions with the central latitudes locate at 10°N, 2°N and 10°S, respectively. Two negative regions with the central latitudes locate at 5°N and 2°S, respectively. The difference of $curl\,(\vec{\tau})_y$ between SST-Assim experiment and SST-noAssim experiment due to these five extreme centers of WSC can partly explain the stronger simulation of Pacific EUC, NECC, SEC(N) and SEC(S) in the SST-Assim experiment. For instance, the positive difference of $curl\,(\vec{\tau})_y$ at equator, corresponding to the stronger simulation of Pacific EUC in SST-Assim, is contributed by two extreme centers of WSC difference locating at 2°S and 2°N, respectively (**Figure 7A**). Similarly, the eastward zonal ocean currents with the center position locating at around 0 and 8°N represent the stronger Pacific EUC and NECC in SST-Assim experiment, respectively (**Figure 7B**). And the westward zonal ocean currents between 2 and 7°N and between 2 and 7°S represent the stronger Pacific SEC(N) and SEC(S) in SST-Assim experiment, respectively. The relationship between the WSC and the zonal ocean current used in this research is consistent with Kessler et al. (2003).

SUMMARY AND DISCUSSION

In our present study, we apply a simple assimilated scheme using only SST data to a coupled earth system model named CAS-

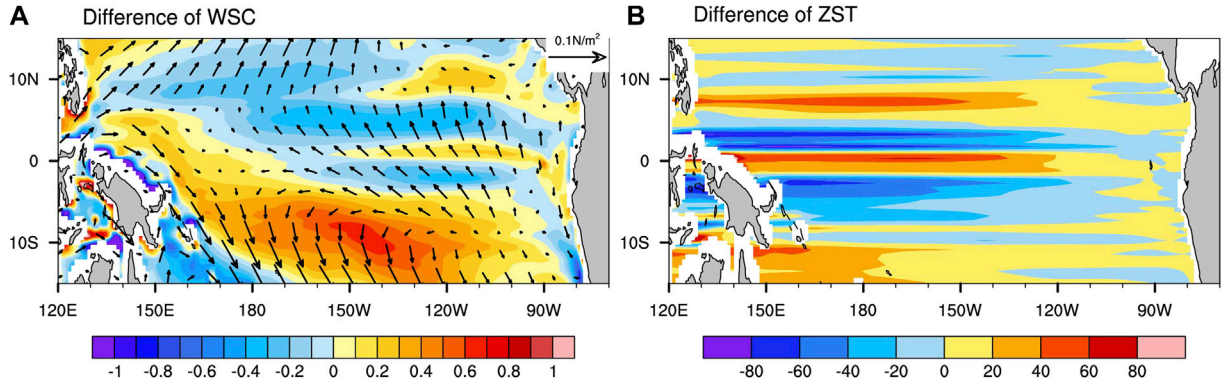

FIGURE 7 | (A) The difference in annual mean WSC (shaded, in $*10^{-7}$ N/m^3) and wind stress vector (arrows, in N/m^2) between SST-Assim experiment and SST-noAssim experiment (SST-Assim minus SST-noAssim); **(B)** the difference in annual mean zonal Sverdrup transport (shaded, in m^2/s) between SST-Assim experiment and SST-noAssim experiment (SST-Assim minus SST-noAssim) and the positive values indicate an eastward direction. The average period of the model data is from 1982 to 2014.

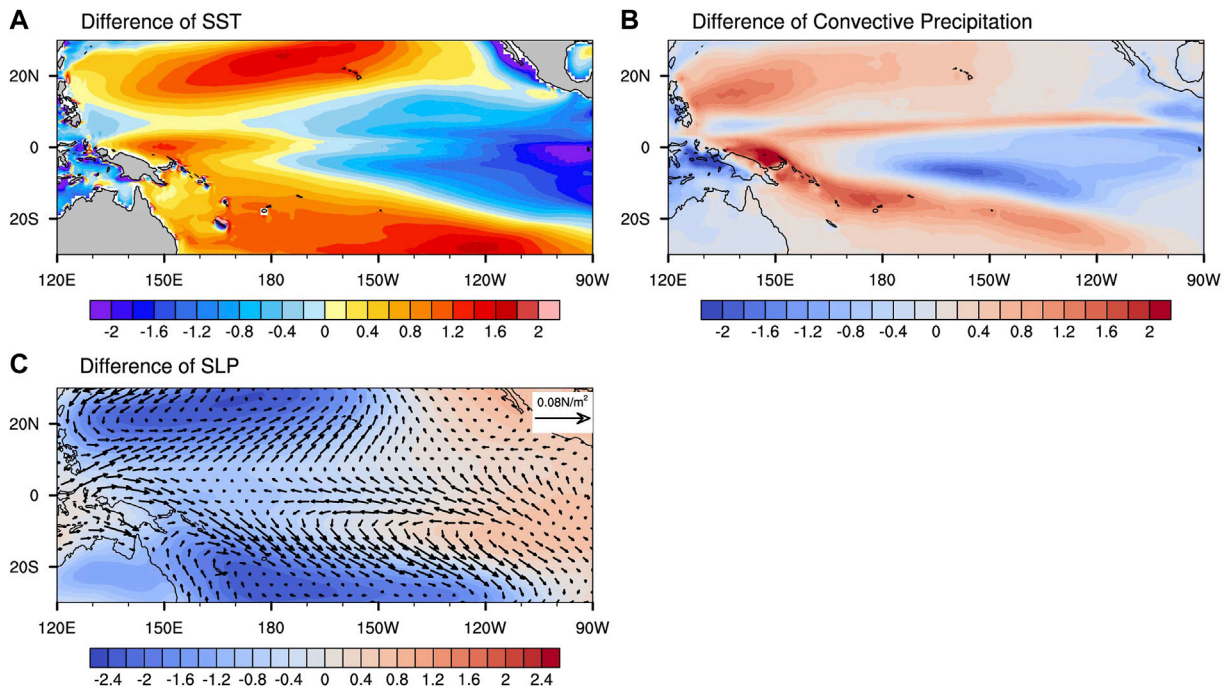

FIGURE 8 | (A) The difference in annual mean SST (°C) between SST-Assim experiment and SST-noAssim experiment (SST-Assim minus SST-noAssim); **(B)** the difference in annual mean convective precipitation (mm/d) between SST-Assim experiment and SST-noAssim experiment (SST-Assim minus SST-noAssim); **(C)** the difference in annual mean sea surface pressure (shaded, in hPa) and wind stress vector (arrows, in N/m^2) between SST-Assim experiment and SST-noAssim experiment (SST-Assim minus SST-noAssim); the average period of the model data is from 1982 to 2014.

ESM2.0 and try to better reproduce the upper zonal currents in the tropical Pacific Ocean. It is achieved by reducing air-sea turbulence flux (especially for wind stress flux) biases and providing useful guides for model improvement and development. Through comparing the results of the SST-noAssim experiment with no-assimilated scheme and the SST-Assim experiment with SST-assimilation, we find that the simulated SST in the SST-Assim experiment becomes more reasonable in the tropical Pacific. In the SST-Assim experiment, the equatorial low-SST strip, which extends excessively westward from the East Pacific and relates to the persistent cold equatorial SST bias in the tropical Pacific in many coupled climate models, is improved to the west of 170°W. Moreover, the spatial pattern of the warm pool (which was

above 28°C) becomes closer to the observations and distributes from the biased west-east distribution converting to the observational northwest-southeast distribution. Need to mention, although the intensity of SST nudging is the strongest in the tropics, the temperature evolution in coupled models especially for vertical diffusion process is also important. The assimilated SST still deviates to some extent from the observation and the impacts of different SST assimilation methods are relatively small for this problem. Maybe assimilating the sea temperature from sea surface to the depth of 2000 m is a choice and will make the SST simulation better.

The SST has significant effects on the strength of the Pacific EUC, the NECC and the SEC across the tropical Pacific. The maximum of the equatorial Pacific EUC locating at ~135°W increases from 0.4 m/s in the SST-noAssim experiment to 0.6 m/s in the SST-Assim experiment and the corresponding value in the observations is 1.0 m/s. The maximum speed of the Pacific NECC at 140°W rises from approximately 0.1 m/s in the SST-noAssim experiment to 0.3 m/s in the SST-Assim experiment and the corresponding value in the observations is 0.4 m/s. The speed of the Pacific SEC increases to almost the same as the observations in the Central and Eastern Pacific, but becomes too strong in the western Pacific in the SST-Assim experiment.

The improvements in the strength of the Pacific EUC, the NECC and the SEC in the SST-Assim experiment are mainly related to the improvements in the surface wind stress and its curl. As shown in **Figure 7A**, there are five centers of WSC difference between the SST-Assim and the SST-noAssim experiment locating between 10°S and 10°N to the east of 150°W. As for the biased spatial structure of the upper Pacific equatorial zonal currents, including the shallower center depth and deeper bottom boundary of the Pacific EUC and the NECC, limited improvements are found. Here, we only pay attention to the downward extending depth of Pacific SEC, which is still shallower and slightly alleviated in the SST-Assim experiment.

Zheng et al. (2014) shows that the SST impacts the surface wind stress predominantly through the changes in total diabatic heating and sea-level pressure (SLP). Diabatic heating is often represented by only the latent heating related to precipitation (convective precipitation), due to the lack of cloud data and the small contribution from the cloud radiative heating (Lin, 2007). Therefore, we show the differences in annual mean SST, atmospheric convective precipitation, surface wind stress and SLP between two experiments (SST-Assim minus SST-noAssim) in **Figure 8** to further illustrate the influence of SST assimilation on the simulation of tropical equatorial zonal ocean currents. The SST difference distributes in the west-warm-east-cold pattern, accompanied by the zonal precipitation difference in west-strong-east-weak pattern and the SLP difference in west-low-east-high distribution between two experiment. Therefore, a stronger easterly wind forms in the tropical Pacific in the SST-Assim experiment compared to the SST-noAssim experiment (**Figure 8**). Similarly, the meridional difference in SST between two experiments contributes to the differences of southwestly wind stress locating between 0 and 20°N and northwestly wind stress locating between 0°N and 20°S, with the warmer SST and the lower SLP center being in the subtropical Pacific in the SST-Assim experiment (**Figure 8**). Further analyses of the specific relationship between the SST, surface wind and the surface wind stress will be performed in our future work. The present study highlights the importance of improved tropical SST in reproducing tropical upper zonal ocean currents in coupled models. The reduction in SST bias can be achieved to some extent by increasing the spatial resolution (Balaguru et al., 2021) and oceanic parameterization scheme (Noh et al., 2016).

DATA AVAILABILITY STATEMENT

The original contributions presented in the study are included in the article/Supplementary Material, further inquiries can be directed to the corresponding authors.

AUTHOR CONTRIBUTIONS

JJ and FZ designed experiments and provided research guidance for this article; ZS, JJ, and FZ analyzed experimental results and write the manuscript; XG, JH, HZ, XD, and QZ further give the suggestions and corrections for this manuscript.

FUNDING

This work is jointly supported by the Key Research Program of Frontier Sciences, the Chinese Academy of Sciences (Grant No. ZDBS-LY-DQC010), the National Natural Science Foundation of China (Grant No's 42005123, 41991282; 41876012, and 42175045), the Strategic Priority Research Program of the Chinese Academy of Sciences (Grant No. XDB42000000), and the open fund of State Key Laboratory of Satellite Ocean Environment Dynamics, Second Institute of Oceanography (Grant No. QNHX 2017). The simulations were performed on supercomputers provided by the Earth System Science Numerical Simulator Facility (EarthLab).

REFERENCES

Adam, O., Schneider, T., and Brient, F. (2018). Regional and Seasonal Variations of the Double-ITCZ Bias in CMIP5 Models. *Clim. Dyn.* 51 (1), 101–117. doi:10.1007/s00382-017-3909-1

Balaguru, K., Van Roekel, L. P., Leung, L. R., and Veneziani, M. (2021). Subtropical Eastern North Pacific SST bias in earth system models. *J. Geophys. Res. Oceans* 126 (8), e2021JC017359.

Bellenger, H., Guilyardi, É., Leloup, J., Lengaigne, M., and Vialard, J. (2014). ENSO Representation in Climate Models: From CMIP3 to CMIP5. *Clim. Dyn.* 42 (7), 1999–2018. doi:10.1007/s00382-013-1783-z

Bonjean, F. (2001). Influence of Surface Currents on the Sea Surface Temperature in the Tropical Pacific Ocean. *J. Phys. Oceanogr.* 31 (4), 943–961. doi:10.1175/1520-0485(2001)031<0943:ioscot>2.0.co;2

Chelton, D. B., Esbensen, S. K., Schlax, M. G., Thum, N., Freilich, M. H., Wentz, F. J., et al. (2001). Observations of Coupling between Surface Wind Stress and Sea Surface Temperature in the Eastern Tropical Pacific. *J. Clim.* 14 (7), 1479–1498. doi:10.1175/1520-0442(2001)014<1479:oocbsw>2.0.co;2

Chen, X., Wang, H., Zheng, F., and Cai, Q. (2020). An Ensemble-Based SST Nudging Method Proposed for Correcting the Subsurface Temperature Field in Climate Model. *Acta Oceanol. Sin.* 39 (3), 73–80. doi:10.1007/s13131-020-1568-2

Dai, Y., Dickinson, R. E., and Wang, Y.-P. (2004). A Two-Big-Leaf Model for Canopy Temperature, Photosynthesis, and Stomatal Conductance. *J. Clim.* 17, 2281–2299. doi:10.1175/1520-0442(2004)017<2281:atmfct>2.0.co;2

Delcroix, T., and Picaut, J. (1998). Zonal Displacement of the Western Equatorial Pacific "Fresh Pool". *J. Geophys. Res.* 103 (C1), 1087–1098. doi:10.1029/97jc01912

Dong, X., Jin, J., Liu, H., Zhang, H., Zhang, M., Lin, P., et al. (2021). CAS-ESM2.0 Model Datasets for the CMIP6 Ocean Model Intercomparison Project Phase 1 (OMIP1). *Adv. Atmos. Sci.* 38 (2), 307–316. doi:10.1007/s00376-020-0150-3

Giese, B. S., Seidel, H. F., Compo, G. P., and Sardeshmukh, P. D. (2016). An Ensemble of Ocean Reanalyses for 1815-2013 with Sparse Observational Input. *J. Geophys. Res. Oceans* 121 (9), 6891–6910. doi:10.1002/2016jc012079

Hu, D., Wu, L., Cai, W., Gupta, A. S., Ganachaud, A., Qiu, B., et al. (2015). Pacific Western Boundary Currents and Their Roles in Climate. *Nature* 522 (7556), 299–308. doi:10.1038/nature14504

Hu, S., Lu, X., Li, S., Wang, F., Guan, C., Hu, D., et al. (2021). Multi-decadal Trends in the Tropical Pacific Western Boundary Currents Retrieved from Historical Hydrological Observations. *Sci. China Earth Sci.* 64 (4), 600–610. doi:10.1007/s11430-020-9703-4

Hunke, E. C., and Lipscomb, W. H. (2008). *CICE: The Los Alamos Sea Ice Model User's Manual, Version 4*. Los Alamos: Los Alamos National Laboratory Tech. Rep. LA-CC-06-012, 76.

Ji, D., Wang, L., Feng, J., Wu, Q., Cheng, H., Zhang, Q., et al. (2014). Description and Basic Evaluation of Beijing Normal University Earth System Model (BNU-ESM) Version 1. *Geosci. Model. Dev.* 7, 2039–2064. doi:10.5194/gmd-7-2039-2014

Jin, F. F., Kim, S. T., and Bejarano, L. (2006). A Coupled-stability index for ENSO. *Geophys. Res. Lett.* 33 (23), 1. doi:10.1029/2006gl027221

Johnson, G. C., Sloyan, B. M., Kessler, W. S., and McTaggart, K. E. (2002). Direct Measurements of Upper Ocean Currents and Water Properties across the Tropical Pacific during the 1990s. *Prog. Oceanography* 52 (1), 31–61. doi:10.1016/s0079-6611(02)00021-6

Keenlyside, N., Latif, M., Botzet, M., Jungclaus, J., and Schulzweida, U. (2005). A Coupled Method for Initializing El Niño Southern Oscillation Forecasts Using Sea Surface Temperature. *Tellus A: Dynamic meteorology and oceanography* 57 (3), 340–356. doi:10.3402/tellusa.v57i3.14661

Kessler, W. S., Johnson, G. C., and Moore, D. W. (2003). Sverdrup and Nonlinear Dynamics of the Pacific Equatorial Currents*. *J. Phys. Oceanogr.* 33 (5), 994–1008. doi:10.1175/1520-0485(2003)033<0994:sandot>2.0.co;2

Kim, S. T., and Jin, F. F. (2011). An ENSO Stability Analysis. Part I: Results from a Hybrid Coupled Model. *Clim. Dyn.* 36 (7-8), 1593–1607. doi:10.1007/s00382-010-0796-0

Lin, J.-L. (2007). The Double-ITCZ Problem in IPCC AR4 Coupled GCMs: Ocean-Atmosphere Feedback Analysis. *J. Clim.* 20, 4497–4525. doi:10.1175/jcli4272.1

Liu, H., Lin, P., Yu, Y., and Zhang, X. (2012). The Baseline Evaluation of LASG/IAP Climate System Ocean Model (LICOM) Version 2. *Acta Meteorol. Sin* 26 (3), 318–329. doi:10.1007/s13351-012-0305-y

McPhaden, M. J., and Taft, B. A. (1988). Dynamics of Seasonal and Intraseasonal Variability in the Eastern Equatorial Pacific. *J. Phys. Oceanography* 18 (1713), 1520–0485. doi:10.1175/1520-0485(1988)018<1713:dosaiv>2.0.co;2

Noh, Y., Ok, H., Lee, E., Toyoda, T., and Hirose, N. (2016). Parameterization of Langmuir Circulation in the Ocean Mixed Layer Model Using LES and its Application to the OGCM. *J. Phys. Oceanography* 46 (1), 57–78. doi:10.1175/jpo-d-14-0137.1

Philander, S. G. H. (1973). Equatorial Undercurrent: Measurements and Theories. *Rev. Geophys.* 11 (3), 513–570. doi:10.1029/rg011i003p00513

Picaut, J., Ioualalen, M., Menkes, C., Delcroix, T., and Mcphaden, M. J. (1996). Mechanism of the Zonal Displacements of the Pacific Warm Pool: Implications for ENSO. *Science* 274 (5292), 1486–1489. doi:10.1126/science.274.5292.1486

Reynolds, R. W., Smith, T. M., Liu, C., Chelton, D. B., Casey, K. S., and Schlax, M. G. (2007). Daily High-Resolution-Blended Analyses for Sea Surface Temperature. *J. Clim.* 20 (22), 5473–5496. doi:10.1175/2007jcli1824.1

Richter, I., and Tokinaga, H. (2020). An Overview of the Performance of CMIP6 Models in the Tropical Atlantic: Mean State, Variability, and Remote Impacts. *Clim. Dyn.* 55, 2579–2601. doi:10.1007/s00382-020-05409-w

Risien, C. M., and Chelton, D. B. (2008). A Global Climatology of Surface Wind and Wind Stress fields from Eight Years of QuikSCAT Scatterometer Data. *J. Phys. Oceanography* 38 (11), 2379–2413. doi:10.1175/2008jpo3881.1

Samanta, D., Karnauskas, K. B., and Goodkin, N. F. (2019). Tropical Pacific SST and ITCZ Biases in Climate Models: Double Trouble for Future Rainfall Projections? *Geophys. Res. Lett.* 46 (4), 2242–2252. doi:10.1029/2018gl081363

Sun, Z., Liu, H., Lin, P., Tseng, Y. H., Small, J., and Bryan, F. (2019). The Modeling of the North Equatorial Countercurrent in the Community Earth System Model and its Oceanic Component. *J. Adv. Model. Earth Syst.* 11 (2), 531–544. doi:10.1029/2018ms001521

Sverdrup, H. U. (1947). Wind-driven Currents in a Baroclinic Ocean; with Application to the Equatorial Currents of the Eastern Pacific. *Proc. Natl. Acad. Sci.* 33 (11), 318–326. doi:10.1073/pnas.33.11.318

Thomas, M. D., De Boer, A. M., Johnson, H. L., and Stevens, D. P. (2014). Spatial and Temporal Scales of Sverdrup Balance*. *J. Phys. Oceanography* 44 (10), 2644–2660. doi:10.1175/jpo-d-13-0192.1

Tian, B., and Dong, X. (2020). The Double-ITCZ Bias in CMIP3, CMIP5, and CMIP6 Models Based on Annual Mean Precipitation. *Geophys. Res. Lett.* 47, 8. doi:10.1029/2020gl087232

Wallace, J. M., Mitchell, T. P., and Deser, C. (1989). The Influence of Sea-Surface Temperature on Surface Wind in the Eastern Equatorial Pacific: Seasonal and Interannual Variability. *J. Clim.* 2 (12), 1492–1499. doi:10.1175/1520-0442(1989)002<1492:tiosst>2.0.co;2

Wyrtki, K. (1974). Equatorial Currents in the Pacific 1950 to 1970 and Their Relations to the Trade Winds. *J. Phys. Oceanogr.* 4 (3), 372–380. doi:10.1175/1520-0485(1974)004<0372:ecitpt>2.0.co;2

Wyrtki, K., and Kilonsky, B. (1984). Mean Water and Current Structure during the Hawaii-to-Tahiti Shuttle experiment. *J. Phys. Oceanogr.* 14 (2), 242–254. doi:10.1175/1520-0485(1984)014<0242:mwacsd>2.0.co;2

Wyrtki, K. (1989). "Some Thoughts about the West Pacific Warm Pool," in *Proceedings of the Western pacific International Meeting and Workshop on TOGA COARE* (New Caledonia: ORSTOM/Nouméa), 99–109.

Zhang, H., Zhang, M., Jin, J., Fei, K., Ji, D., Wu, C., et al. (2020). Description and Climate Simulation Performance of CAS-ESM Version 2. *J. Adv. Model. Earth Syst.* 12 (12), e2020MS002210. doi:10.1029/2020ms002210

Zheng, F., Fang, X.-H., Yu, J.-Y., and Zhu, J. (2014). Asymmetry of the Bjerknes Positive Feedback between the Two Types of El Niño. *Geophys. Res. Lett.* 41, 7651–7657. doi:10.1002/2014GL062125

Zheng, F., and Zhu, J. (2010). Coupled Assimilation for an Intermediated Coupled ENSO Prediction Model. *Ocean Dyn.* 60 (5), 1061–1073. doi:10.1007/s10236-010-0307-1

Zhou, S., Huang, G., and Huang, P. (2020). Excessive ITCZ but Negative SST Biases in the Tropical Pacific Simulated by CMIP5/6 Models: The Role of the Meridional Pattern of SST Bias. *J. Clim.* 33 (12), 5305–5316. doi:10.1175/jcli-d-19-0922.1

Zhu, Y., Zhang, R. H., Li, D., and Chen, D. (2020). The Thermocline Biases in the Tropical North Pacific and Their Attributions. *J. Clim.* 34 (5), 1635–1648.

Conflict of Interest: The authors declare that the research was conducted in the absence of any commercial or financial relationships that could be construed as a potential conflict of interest.

frontiers in Earth Science

ORIGINAL RESEARCH
published: 30 March 2022
doi: 10.3389/feart.2022.841948

Kinetic Energy and Vorticity Perspectives of the Rapid Development of an Explosive Extratropical Cyclone Over the Northwest Pacific Ocean in February 2018

Hui Wang[1]*, *Mengjiao Du*[2], *Chenghu Sun*[3] and *Bo Zhang*[1]

[1]National Meteorological Center, Beijing, China, [2]Institute of Science and Technology, China Three Gorges Corporation, Beijing, China, [3]Chinese Academy of Meteorological Sciences, Beijing, China

OPEN ACCESS

Edited by:
Guihua Wang,
Fudan University, China

Reviewed by:
Jai Sukhatme,
Indian Institute of Science (IISc), India
Chenghai Wang,
Lanzhou University, China
Gang Fu,
Ocean University of China, China
Zhiqiang Gong,
Beijing Climate Center (BCC), China

***Correspondence:**
Hui Wang
wangh1@cma.gov.cn

Specialty section:
This article was submitted to Atmospheric Science, a section of the journal Frontiers in Earth Science

Received: 23 December 2021
Accepted: 21 February 2022
Published: 30 March 2022

Citation:
Wang H, Du M, Sun C and Zhang B (2022) Kinetic Energy and Vorticity Perspectives of the Rapid Development of an Explosive Extratropical Cyclone Over the Northwest Pacific Ocean in February 2018. Front. Earth Sci. 10:841948. doi: 10.3389/feart.2022.841948

Explosive extratropical cyclones (EECs) have long been a research focus for the meteorological society as they often cause serious economic losses and casualties. However, after a long period of research, there still remain some knowledge gaps about their rapid development. In this article, we conducted the first study by using both vorticity and kinetic energy (KE) budgets simultaneously on a typical EEC, which was the strongest EEC that affected the coastal areas of China in the last 3 years, to further the understanding of the mechanisms governing its rapid enhancement in rotation and wind speed. The vorticity budget shows that the lower-level convergence-related vertical stretching and the vertical transport of vorticity acted as the most and second most favorable factors for the increase in the cyclone's cyclonic vorticity, respectively, which were different from those findings based on the Zwack–Okossi vorticity budget. In contrast, the horizontal transport of vorticity and tilting mainly decelerated the EEC's development. Energetics features governing the rapid wind enhancement of the EEC were shown for the first time. It is found that the work on the rotational wind by the pressure gradient force and the net import transport of KE by the rotational wind contributed the largest and second largest to the cyclone's increase in wind speed. In contrast, the upward transport of KE and the cyclone's displacement mainly acted in an opposite way. Analysis based on the Green's theorem and rotational wind shows that the enhancement of the EEC's rotation and wind speed were linked to each other solidly.

Keywords: EEC, vorticity budget, KE budget, rotation, wind speed

INTRODUCTION

Extratropical cyclones are one of the most important systems in the mid-latitude regions, as they often cause severe weather such as torrential rainfall, strong winds, cold waves, and so on (Fu et al., 2014; Schultz et al., 2018). Of the extratropical cyclones, there are a special type, called the explosive extratropical cyclone (EEC), which deepens sharply with its central pressure decreased by at least 24 hPa (relative to 60°N) in 24 h (Sanders and Gyakum, 1980). The most severe disastrous weather tends to appear during

EECs' rapid development (Yoshida and Asuma, 2004); therefore, many previous studies conducted investigations on dynamical and thermodynamical processes governing EECs' rapid development. It is found that favorable dynamical factors for EECs' rapid development mainly contain a cyclonic vorticity advection aloft (Sanders, 1986; Macdonald and Reiter, 1988), a strong jet streak at upper level (Uccellini et al., 1984; Uccellini and Kocin, 1987), a strong baroclinic instability in the middle and lower troposphere (Bosart, 1981; Jia and Zhao, 1994; Iwao et al., 2012), and a notable tropopause folding process in the upper and middle troposphere (Rossa et al., 2000; Fu et al., 2014, 2018; Wang et al., 2017). Favorable thermodynamical factors mainly contain a warm temperature advection aloft (Hirschberg and Fritsch, 1991a, b; Lupo et al., 1992), strong latent heat release in the middle and lower troposphere (Bosart, 1981; Reed and Albright, 1986; Chen and Dell'Osso, 1987), reduced static stability in the lower troposphere (Smith and Tsou, 1988), and upward energy fluxes from the surface (Kuo et al., 1991).

As mentioned above, previous studies have deepened the understanding of EECs' evolution; however, as EECs' development can be affected by numerous factors, governing mechanisms may be quite different. Therefore, more case studies should be conducted. There are three indicators that can effectively measure an EEC: its central pressure, rotation, and wind speed (Sanders and Gyakum, 1980; Yoshida and Asuma, 2004; Fu et al., 2018). During EECs' developing stages, although their pressure and rotation (which can be reflected by the area-averaged vorticity within its central region) both enhance notably (Zwack and Okossi, 1986; Lupo et al., 1992; Parsons and Smith, 2004; Fu et al., 2018), their associated winds do not always strengthen simultaneously (Jiang et al., 2021a). For those EECs which showed rapid intensification in their rotation and wind (these cyclones usually have larger destructive force), what are the key mechanisms that govern these two processes? Is there a solid link between these two features? These two scientific questions remain unanswered.

At the end of February 2018, an EEC appeared over the Northwest Pacific Ocean. It was the strongest EEC that affected the coastal areas of China in the last 3 years. During its life span, strong winds (above 24 m/s) appeared, which caused severe cold waves and huge waves and resulted in great economic losses. In this study, we applied vorticity and kinetic energy (KE) budgets to this cyclone, so as to partly address the two scientific questions raised above. The remainder of this article is structured as follows: In **Section 2**, data and methods used in this study are provided; in **Section 3**, an overview of the event is shown; in **Section 4**, the results of vorticity and KE budgets were analyzed; and finally, a conclusion and discussion is presented in **Section 5**.

DATA AND METHOD

This study used hourly, 0.25° × 0.25°ERA5 reanalysis data (Hersbach et al., 2020) provided by the European Centre for Medium-Range Weather Forecasts (ECMWF) for analyses and calculations. This dataset has a total of 37 vertical levels. In this study, the definition from Yoshida and Asuma (2004) was used to calculate the deepening rate (DR) of the EEC:

$$\mathrm{DR} = \left[\frac{p(t-6)-p(t+6)}{12}\right]\left[\frac{\sin 60^{\circ}}{\sin\left(\phi(t-6)+\phi(t+6)/2\right)}\right] \quad (1)$$

where t is time (units: h), p is the cyclone's central sea level pressure [SLP (units: hPa)], and ϕ is the latitude of the cyclone center.

In order to clarify the mechanisms governing the EEC's rapid development, two methods were used: one is the vorticity budget (Kirk, 2003; Fu et al., 2016; Jiang et al., 2021b) and the other is the KE budget (Chen et al., 1978; Fu et al., 2011). The former was used to analyze the rotation enhancement associated with the cyclone, and the latter was utilized to investigate its wind intensification. Although EECs have long been a research focus, their energetics features still remain vague. Investigation on EECs' wind enhancement in terms of energy is helpful to reach a more comprehensive understanding of their rapid development. The vorticity budget equation is as follows:

$$\frac{\partial\zeta}{\partial t} = \boldsymbol{k}\cdot\left(\frac{\partial \boldsymbol{V}_h}{\partial p}\times\nabla_h\omega\right) - \boldsymbol{V}_h\cdot\nabla_h\zeta - \omega\frac{\partial\zeta}{\partial p} - (\zeta+f)\nabla_h\cdot\boldsymbol{V}_h - \beta v + \mathrm{RES} \quad (2)$$

where ζ is the vertical component of the relative vorticity (vorticity for short); (i, j, k) are unit vectors pointing to the east, north, and zenith, respectively; $\boldsymbol{V}_h = u\mathbf{i} + v\mathbf{j}$ denotes the horizontal velocity vector; subscript "h" stands for the horizontal component; p is pressure; $\nabla_h = \partial\mathbf{i}/\partial x + \partial\mathbf{j}/\partial y$ is horizontal gradient operator; ω is vertical velocity in pressure coordinate; f is Coriolis parameter; and $\beta = \partial f/\partial y$. The first term on the right-hand side of **Eq. 2** was defined as TIL, as it shows the tilting effect; the second and third terms were defined as HAV (representing the horizontal advection of vorticity) and VAV (denoting the vertical advection of vorticity), respectively; the fourth term was defined as STR, which stands for stretching effect associated with divergence; the fifth term was defined as APV, which represents the advection of planetary vorticity; and the last term is RES, which denotes the residual effect (mainly due to friction, subgrid processes, and calculation errors.). The sum of TIL, HAV, VAV, STR, and APV was defined as TOT, which shows the total effect of all terms on the right-hand side of **Eq. 2**.

The kinetic budget equation (Chen et al., 1978) is as follows:

$$\frac{1}{Sg}\int_{p_t}^{p_b}\iint\frac{\delta k}{\delta t}dsdp = \frac{1}{Sg}\int_{p_t}^{p_b}\iint M_h\cdot\nabla_h k dsdp - \frac{1}{Sg}\int_{p_t}^{p_b}\iint\nabla_h\cdot\left(\boldsymbol{V}_\psi k\right)dsdp - \frac{1}{Sg}\int_{p_t}^{p_b}\iint\nabla_h\cdot\left(\boldsymbol{V}_\chi k\right)dsdp - \frac{1}{Sg}\int_{p_t}^{p_b}\iint\frac{\partial(\omega k)}{\partial p}dsdp - \frac{1}{Sg}\int_{p_t}^{p_b}\iint\boldsymbol{V}_\psi\cdot\nabla_h\Phi\, dsdp - \frac{1}{Sg}\int_{p_t}^{p_b}\iint\boldsymbol{V}_\chi\cdot\nabla_h\Phi\, dsdp + \mathrm{RES} \quad (3)$$

where S is the area of the cyclone's central region; P_b and P_t are the pressure at the bottom and top level of an air column; k is the horizontal KE; $\mathbf{M}_h$ is the horizontal moving speed vector of the cyclone; $\mathbf{V}_\psi$ and $\mathbf{V}_\chi$ are the rotational and divergent wind vectors, respectively; and Φ is geopotential. The first to the sixth terms on

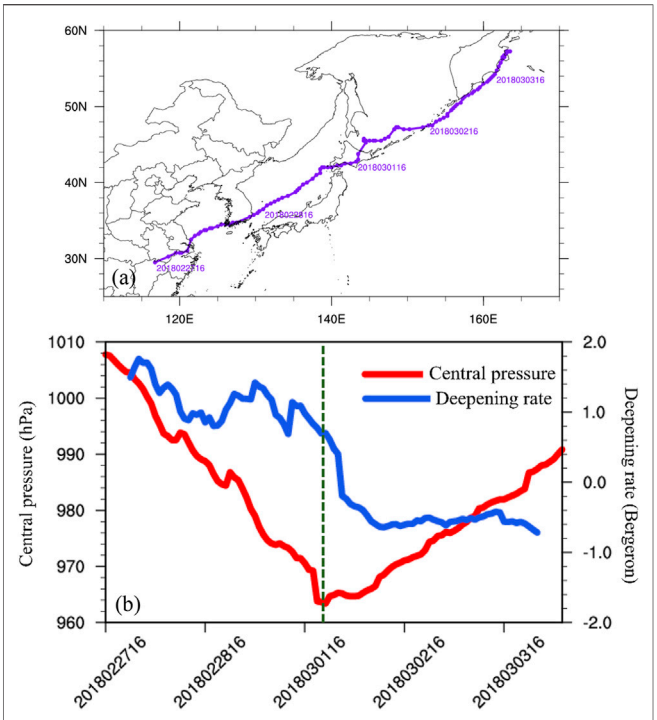

FIGURE 1 | (A) The track of the explosive cyclone (purple line with dots), where the dots show the location of the cyclone's center. **(B)** The central pressure of the cyclone (thick red solid line; hPa) and its deepening rate (thick blue solid line; Bergeron), where the green dashed line shows the time when the cyclone reached minimum central pressure.

the right-hand side of **Eq. 3** denote the KE variations due to the cyclone's displacement (Term 1), the rotational wind's transport (Term 2), the divergent wind's transport (Term 3), the vertical transport (Term 4), the work on rotational wind by pressure gradient force (Term 5), and the work on divergent wind by pressure gradient force (Term 6), respectively. The term RES denotes the residual effects that were mainly due to friction, subgrid processes, and calculation errors.

In this study, the rotational/divergent wind was calculated by using the method developed by Cao and Xu (2011), which had been proven to be accurate and effective in generating rotational/divergent wind within a limited domain.

OVERVIEW OF THE EVENT

During the period from February 27 to March 4, 2018, an extratropical cyclone appeared over the northwest Pacific Ocean (**Figure 1A**), which caused strong winds in its surrounding regions. This cyclone formed at 1600 UTC on February 27, around the junction of Anhui and Jiangxi provinces, moved in the northeast direction in its whole life span, and dissipated at 0600 UTC on March 4 (it lasted for ~110 h), around Kamchatka Peninsula. During this period, an upper-level jet was mainly located in the zonal band of 22–46°N (not shown), with a large-value zone exceeding 100 m s^{-1} stretching from East China to the central section of Japan. In the same period, a middle-tropospheric shortwave trough moved from East China to the central and southern sections of Japan along with the EEC (not shown), west of which a strong cold advection appeared. Along with the upper-level jet and the shortwave trough, a notable tropopause folding process appeared (not shown), which resulted in positive potential vorticity anomalies in the middle troposphere. These were favorable for the developing of the EEC (Fu et al., 2018). In this study, the evolutionary processes of this cyclone may be roughly divided into two stages: the first is from 1600 UTC on February 27 to 1800 UTC on March 1, during which the cyclone's central pressure lowered rapidly (**Figure 1B**); the second is from 1800 UTC on March 1 to 0600 UTC on March 4, during which the cyclone increased gradually in its central pressure. Therefore, the first stage is named the developing stage of the cyclone. In this stage, the mean DR and maximum DR of the cyclone were 1.25 and 1.81 Bergeron, respectively, both of which indicated that the cyclone was an EEC (Sanders and Gyakum, 1980).

During the cyclone's developing stage, corresponding to its decreasing central pressure (**Figure 1A**), the cyclonic vorticity and wind speed both enhanced notably (**Figure 2**). According to the cyclone's mean size during its developing stage, a 10° (latitude) × 12° (longitude) box (purple dashed boxes in **Figure 2**) was determined to focus on the central region of the cyclone. This box was defined as the central region of the cyclone. The calculations based on this central region were insensitive to relatively small changes (±0.5°) to its each boundary line, which means that the selection of the central region was representative. Overall, the selection of the EEC's central region was consistent with the principles documented in Fu (2001): "It should be large enough to cover the cyclone thoroughly but small enough to exclude other undesirable disturbances from the area." The correlations between the central region averaged KE/vorticity and the cyclone's central pressure were −0.75/−0.83, implying that both KE and vorticity were effective indicators for the cyclone's rapid development.

KINETIC ENERGY AND VORTICITY BUDGETS

Kinetic Energy Budget

During the developing stage, the cyclone showed rapid enhancement of KE (i.e., wind speed) in the layer of 950–850 hPa (not shown); therefore, this layer was used to calculate **Eq. 3**: P_b = 950 hPa and P_t = 850 hPa. As the gray line in **Figure 3A** shows, the sum of Terms 1–6 was positive in the developing stage. This means that there was an overall favorable condition for enhancing the cyclone's wind speed. Of all the six terms in **Eq. 3**, Term 5 (i.e., the work on the rotational wind by pressure gradient force) made the largest contribution to the cyclone's increasing wind speed (**Figure 3E**). This was because: 1) centripetal pressure gradient force grew quickly as the central pressure of the cyclone lowered (**Figure 2**); 2) rotational wind was much larger than divergent wind (not shown); and (iii), the angle

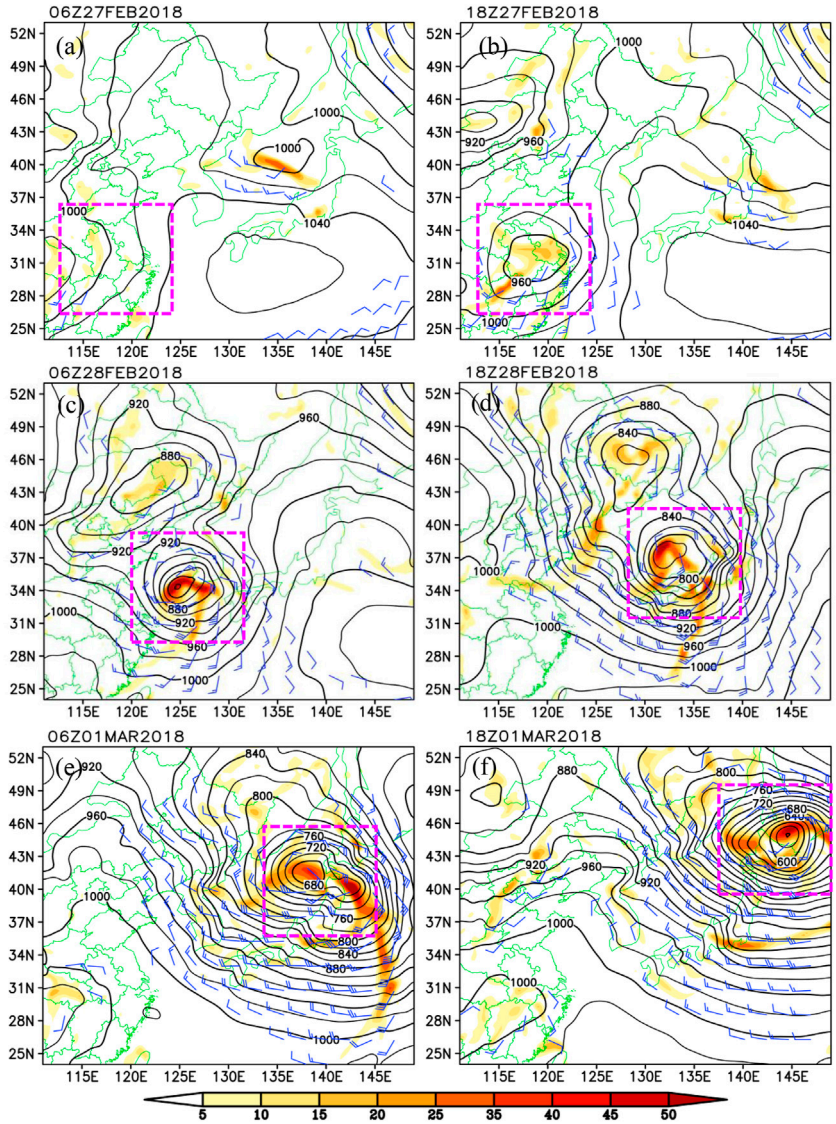

FIGURE 2 | Geopotential height (black solid lines; gpm), wind above 10 m s^{-1} (blue wind bar; a full bar is 10 m s^{-1}), and cyclonic vorticity (shading; 10^{-5} s^{-1}) at 900 hPa at **(A)** 06 Z on Feburary 27, 2018, **(B)** 18 Z on Feburary 27, 2018, **(C)** 06 Z on Feburary 28, 2018, **(D)** 18 Z on Feburary 28, 2018, **(E)** 06 Z on March 1, 2018, **(F)** 18 Z on March 1, 2018, where the purple dashed boxes mark the central region of the explosive cyclone.

between rotational wind and the centripetal pressure gradient force was overall smaller than 90° (not shown). Term 2 (i.e., rotational wind's transport of KE) acted as the second dominant factor for the wind enhancement (**Figure 3B**). As **Figure 2** shows, the regions surrounding the cyclone's central region featured strong wind (i.e., KE was large). Overall, the rotational wind transported large KE centripetally (not shown). This resulted in net import of KE into the central region that enhanced the cyclone's wind speed. Term 6 (i.e., the work on the divergent wind by pressure gradient force) was also favorable, whereas its relative contribution was small (**Figure 3F**). Term 4 (vertical transport of KE) exerted the largest effect in decelerating the KE associated with the cyclone (**Figure 3D**). This was because the ascending motions (not shown) transported lower-level strong KE upward, which resulted in a net export of KE from the lower troposphere. Term 1, which denoted the effect due to the cyclone's displacement, mainly decelerated the cyclone's development in wind speed (**Figure 3A**). This was because the cyclone mainly moved from regions with stronger KE to those with weaker KE (Fu and Sun, 2012). The KE features within the background environment affected the variation of EECs through this effect. Term 3 (divergent wind's transport of KE) showed a nearly neutral effect, as divergent wind was generally weak (not shown).

Vorticity Budget

Corresponding to the rapid enhancement in KE, the cyclone's cyclonic vorticity also intensified quickly in the layer of

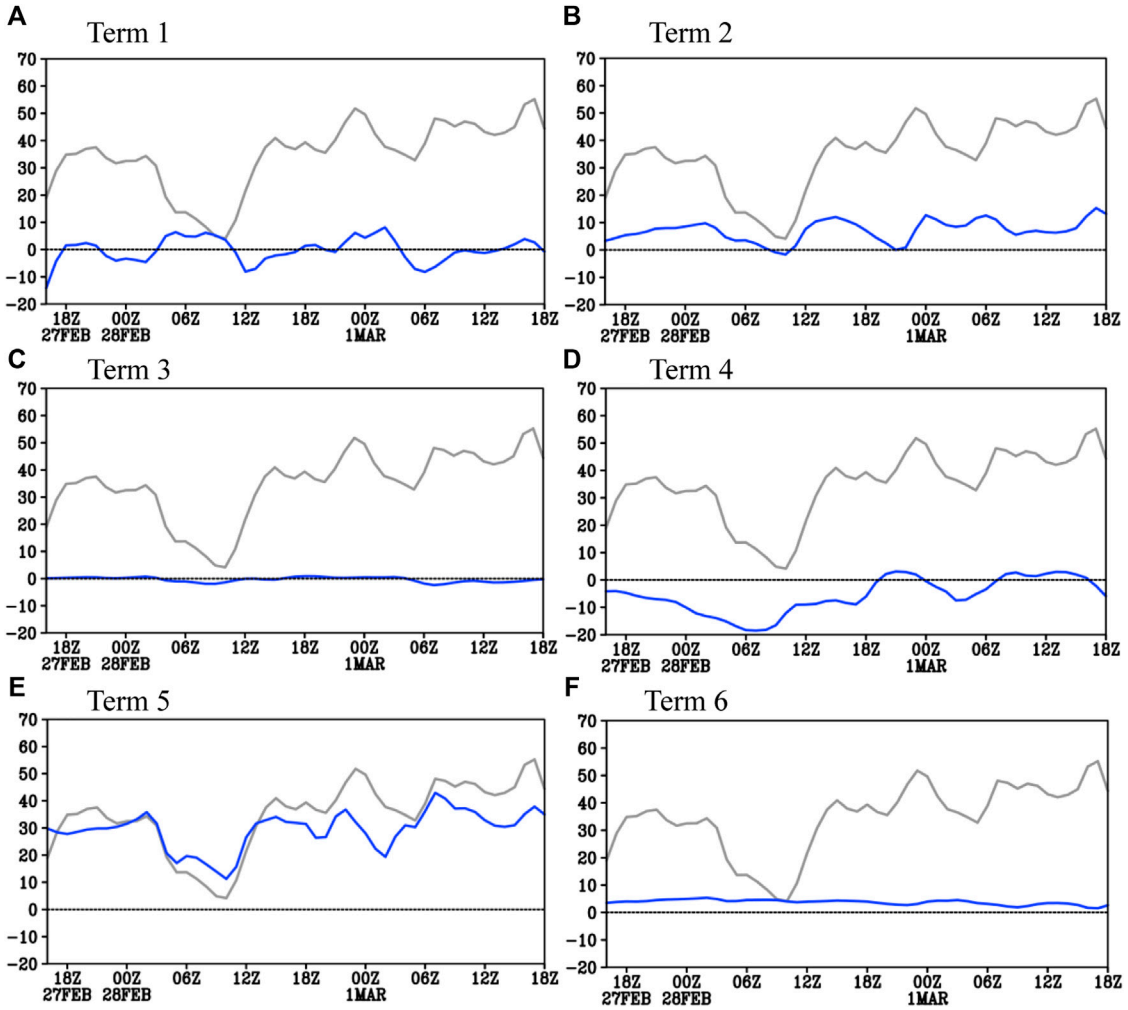

FIGURE 3 | Vertical integral (from 950 hPa to 850 hPa) of the kinetic budget terms (units: J $s^{-1}m^{-2}$), where the grey solid lines show the sum of Terms 1-6, black dashed lines mark the value of 0, and blue solid lines represent each budget term. **(A)** Term1: The cyclone's displacement, **(B)** Term2: The rotational wind's transport, **(C)** Term3: The divergent wind's transport, **(D)** Term4: The vertical transport, **(E)** Term5: The rotational wind by pressure gradient force, **(F)** Term6: The divergent wind by pressure gradient force.

850–950 hPa, as term TOT (black lines in **Figure 4**) kept a large positive value in this layer. Among the four budget terms of **Eq. 2**, the convergence-associated STR (red lines in **Figure 4**) was the most favorable factor for the increase of the cyclone's cyclonic vorticity (strong lower-level convergence within the central region produced cyclonic vorticity through vertical stretching) during its developing stage. The second most favorable factor was the vertical transport of vorticity (blue lines in **Figure 4**) before 2000 UTC on February 28 (not shown), after that, the tilting effect (green line in **Figure 4D**) became the second most favorable factor for the cyclone's enhancement in cyclonic vorticity. The horizontal transport of vorticity (i.e., HAV) was the most detrimental factor for the cyclone's development (orange lines in **Figure 4**), as it kept transporting cyclonic vorticity out from the cyclone's central region. Overall, the temporal mean effect of STR and VAV were positive, whereas those of HAV and TIL were negative. Therefore, the former two terms favored the cyclone's increase in cyclonic vorticity, whereas the latter two terms acted conversely. From **Figure 4**, it can also be found that, in the layer of 850–450 hPa, the dominant factor for enhancing the cyclonic vorticity within the central region was VAV, i.e., the vertical transport of cyclonic vorticity from lower levels (this cyclonic vorticity was produced in the level below 850 hPa through the convergence-related STR). In contrast, term STR showed an overall negative effect. This means that this cyclone showed a vertical stretching from the bottom up; divergence governed the layer of 850–450 hPa during the cyclone's developing stage.

It should be noted that the Zwack–Okossi vorticity budget developed by Zwack and Okossi (1986) was used in previous studies to understand the evolutionary mechanisms of the EECs (e.g., Yoshida and Asuma, 2004; Fu et al., 2018). Some of these studies found that a strong upper tropospheric positive absolute vorticity advection and a warm advection associated with an upper-level jet usually acted as the key factors for the EECs'

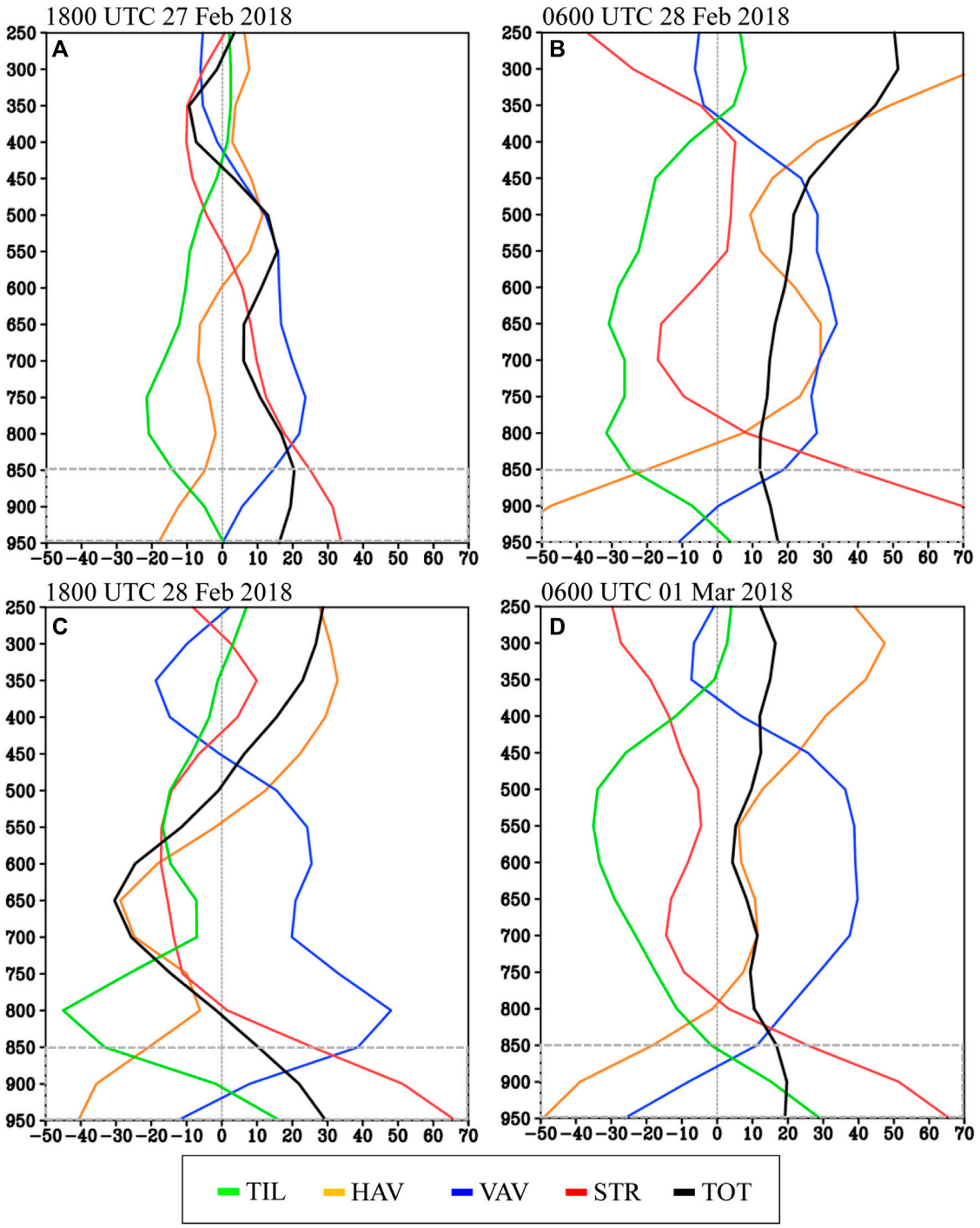

FIGURE 4 | Central-region averaged vorticity budget terms ($10^{-10}s^{-2}$) at typical stages, where the grey dashed lines mark the value of 0, and the grey dashed boxes outline the layer of 950-850 hPa. The green lines indicate the tilting effect, the orange lines indicate the horizontal advection of vorticity, the blue lines indicate the vertical advection of vorticity, the red lines indicate the stretching effect associated with divergence, and the blace lines indicate the sum of TIL, HAV, VAV, STR, and APV.

development. The differences between the findings of these studies and the vorticity budget results in this study were mainly due to the following: 1) the Zwack–Okossi vorticity budget used the geostrophic vorticity instead of vorticity to describe the variation of an EEC; and 2) the previous studies focused on the effects from the whole troposphere instead of only the lower troposphere (in this study we only focused on the lower layer).

CONCLUSION AND DISCUSSION

In order to further the understanding of the mechanisms governing the rapid enhancement of EECs' rotation and wind speed during their developing stage, the vorticity and KE budgets were conducted on a typical EEC that appeared at the end of February 2018 over the Northwest Pacific Ocean. This cyclone lasted for ~110 h, and it was the strongest EEC that affected the coastal areas of China in the last 3 years. During its rapid development, its rotation and wind speed both strengthened quickly. The vorticity budget shows that the lower-level convergence-related vertical stretching (i.e., STR) was the most favorable factor for the increase of the cyclone's cyclonic vorticity; the second most favorable factor was the vertical transport of vorticity (i.e., VAV), which transported cyclonic vorticity upward (contributing to the upward extending of the cyclone). In contrast, the horizontal transport (i.e., HAV) caused a net export of cyclonic vorticity from the cyclone's central region, which made it the most detrimental factor for the cyclone's development. The KE budget indicates that the work on the rotational wind by the pressure gradient force made the largest contribution to the cyclone's increasing wind speed, and the net import transport of KE by the rotational wind acted as the second dominant factor. In contrast, the upward transport of KE exerted the largest effect in decelerating the KE associated with the EEC, and the effect due to the cyclone's displacement was the second most detrimental factor.

Overall, the enhancement of the EEC's rotation and wind speed was consistent with the deepening in its central pressure. A link between the rotation and the wind speed of an EEC is shown as follows: according to Green's theorem, the area-averaged vorticity within the EEC's central region equals the velocity circulation along the boundary line of the central region (Fu et al., 2017). Therefore, the enhancement in the cyclone's rotation (reflected by the central region averaged vorticity) means increase in velocity circulation; increase in velocity circulation means that wind along the boundary line of an EEC's central region strengthens. In this event, as the rotational wind was the dominant component of the horizontal wind associated with the EEC, and the rotational wind was mainly along the central region's boundary line, the enhancement of the EEC's rotation was consistent with the intensification in its wind speed. It should be noted that, although this study shows some useful results for understanding the mechanisms dominating the rapid development of the rotation and wind speed associated with the EEC over the Northwest Pacific Ocean, it surely has limitations in representing the universal features of this type of cyclone. To analyze more EECs in the future, is an effective way to fully address the two scientific questions raised in the Introduction.

DATA AVAILABILITY STATEMENT

Publicly available datasets were analyzed in this study. These data can be found here: https://cds.climate.copernicus.eu/cdsapp#!/dataset/reanalysis-era5-single-levels?tab=overview.

AUTHOR CONTRIBUTIONS

HW and MD contributed to conception and design of the research. CS organized the database. BZ performed the statistical analysis. MD drew the figures. HW wrote the manuscript. All authors contributed to manuscript revision and read and approved the submitted version.

FUNDING

This work was supported by the national key R&D Program of China (Grant Nos.2019YFC1510104).

REFERENCES

Bosart, L. F. (1981). The Presidents' Day Snowstorm of 18-19 February 1979: A Subsynoptic-Scale Event. *Mon. Wea. Rev.* 109, 1542–1566. doi:10.1175/1520-0493(1981)109<1542:tpdsof>2.0.co;2

Cao, J., and Xu, Q. (2011). Computing Streamfunction and Velocity Potential in a Limited Domain of Arbitrary Shape. Part II: Numerical Methods and Test Experiments. *Adv. Atmos. Sci.* 28, 1445–1458. doi:10.1007/s00376-011-0186-5

Chen, S.-J., and Dell'Osso, L. (1987). A Numerical Case Study of East Asian Coastal Cyclogenesis. *Mon. Wea. Rev.* 115, 477–487. doi:10.1175/1520-0493(1987)115<0477:ancsoe>2.0.co;2

Chen, T.-C., Alpert, J. C., and Schlatter, T. W. (1978). The Effects of Divergent and Nondivergent Winds on the Kinetic Energy Budget of a Mid-latitude Cyclone: A Case Study. *Mon. Wea. Rev.* 106, 458–468. doi:10.1175/1520-0493(1978)106<0458:teodan>2.0.co;2

Fu, G. (2001). *Polar Lows: Intense Cyclone in Winter*. Beijing, China: China Meteorological Press, 206.

Fu, S.-M., Sun, J.-H., Li, W.-L., and Zhang, Y.-C. (2018). Investigating the Mechanisms Associated with the Evolutions of Twin Extratropical Cyclones over the Northwest Pacific Ocean in Mid-january 2011. *J. Geophys. Res. Atmos.* 123, 4088–4109. doi:10.1002/2017jd027852

Fu, S.-M., Sun, J.-H., Luo, Y.-L., and Zhang, Y.-C. (2017). Formation of Long-Lived Summertime Mesoscale Vortices over Central East China:Semi-Idealized Simulations Based on a 14-Year Vortex Statistic. *J. Atmos. Sci.* 74, 3955–3979. doi:10.1175/jas-d-16-0328.1

Fu, S.-M., Zhang, J.-P., Sun, J.-H., and Zhao, T.-B. (2016). Composite Analysis of Long-Lived Mesoscale Vortices over the Middle Reaches of the Yangtze River valley: Octant Features and Evolution Mechanisms. *J. Clim.* 29, 761–781. doi:10.1175/jcli-d-15-0175.1

Fu, S., and Sun, J. (2012). Circulation and Eddy Kinetic Energy Budget Analyses on the Evolution of a Northeast China Cold Vortex (NCCV) in May 2010. *J. Meteorol. Soc. Jpn.* 90, 553–573. doi:10.2151/jmsj.2012-408

Fu, S., Sun, J., and Sun, J. (2014). Accelerating Two-Stage Explosive Development of an Extratropical Cyclone over the Northwestern Pacific Ocean: a Piecewise Potential Vorticity Diagnosis. *Tellus* 66, 1–22. doi:10.3402/tellusa.v66.23210

Fu, S., Sun, J., Zhao, S., and Li, W. (2011). The Energy Budget of a Southwest Vortex with Heavy Rainfall over South China. *Adv. Atmos. Sci.* 28, 709–724. doi:10.1007/s00376-010-0026-z

Hersbach, H., Bell, B., Berrisford, P., Hirahara, S., Horányi, A., Muñoz-Sabater, J., et al. (2020). The ERA5 Global Reanalysis. *Q.J.R. Meteorol. Soc.* 146, 1999–2049. doi:10.1002/qj.3803

Hirschberg, P. A., and Fritsch, J. M. (1991b). Tropopause Undulations and the Development of Extratropical Cyclones. Part II: Diagnostic Analysis and

Conceptual Model. *Mon. Wea. Rev.* 119, 518–550. doi:10.1175/1520-0493(1991)119<0518:tuatdo>2.0.co;2

Hirschberg, P. A., and Fritsch, J. M. (1991a). Tropopause Undulations and the Development of Extratropical Cyclones. Part I. Overview and Observations from a Cyclone Event. *Mon. Wea. Rev.* 119, 496–517. doi:10.1175/1520-0493(1991)119<0496:tuatdo>2.0.co;2

Iwao, K., Inatsu, M., and Kimoto, M. (2012). Recent Changes in Explosively Developing Extratropical Cyclones over the winter Northwestern Pacific. *J. Clim.* 25, 7282–7296. doi:10.1175/jcli-d-11-00373.1

Jia, Y., and Zhao, S. (1994). A Diagnostic Study of Explosive Development of Extratropical Cyclone over East Asia and West Pacific Ocean. *Adv. Atmos. Sci.* 11, 251–270.

Jiang, L. Z., Fu, S. M., Sun, J. H., Fu, R., Li, W. L., Zhao, S. X., et al. (2021a). Surface Wind and Vertical Extent Features of the Explosive Cyclones in the Northern Hemisphere Based on the ERA-I Reanalysis Data. *Int. J. Climatol.* 42, 993–1014. doi:10.1002/joc.7284

Jiang, L. Z., Yu, H., Dong, L., Fu, S. M., Sun, J. H., Zheng, F., et al. (2021b). On the Vertical Extending of the Explosive Extratropical Cyclone: A Case Study. *Atmos. Sci. Lett.* 2021, e1028. doi:10.1002/asl.1028

Kirk, J. R. (2003). Comparing the Dynamical Development of Two Mesoscale Convective Vortices. *Mon. Wea. Rev.* 131, 862–890. doi:10.1175/1520-0493(2003)131<0862:ctddot>2.0.co;2

Kuo, Y.-H., Low-Nam, S., and Reed, R. J. (1991). Effects of Surface Energy Fluxes during the Early Development and Rapid Intensification Stages of Seven Explosive Cyclones in the Western Atlantic. *Mon. Wea. Rev.* 119, 457–476. doi:10.1175/1520-0493(1991)119<0457:eosefd>2.0.co;2

Lupo, A. R., Smith, P. J., and Zwack, P. (1992). A Diagnosis of the Explosive Development of Two Extratropical Cyclones. *Mon. Wea. Rev.* 120, 1490–1523. doi:10.1175/1520-0493(1992)120<1490:adoted>2.0.co;2

Macdonald, B. C., and Reiter, E. R. (1988). Explosive Cyclogenesis over the Eastern United States. *Mon. Wea. Rev.* 116, 1568–1586. doi:10.1175/1520-0493(1988)116<1568:ecoteu>2.0.co;2

Parsons, K. E., and Smith, P. J. (2004). An Investigation of Extratropical Cyclone Development Using a Scale-Separation Technique. *Mon. Wea. Rev.* 132, 956–974. doi:10.1175/1520-0493(2004)132<0956:aioecd>2.0.co;2

Reed, R. J., and Albright, M. D. (1986). A Case Study of Explosive Cyclogenesis in the Eastern Pacific. *Mon. Wea. Rev.* 114, 2297–2319. doi:10.1175/1520-0493(1986)114<2297:acsoec>2.0.co;2

Rossa, A. M., Wernli, H., and Davies, H. C. (2000). Growth and Decay of an Extra-tropical Cyclone's PV-Tower. *Meteorology Atmos. Phys.* 73, 139–156. doi:10.1007/s007030050070

Sanders, F. (1986). Explosive Cyclogenesis in the West-Central North Atlantic Ocean, 1981-84. Part I: Composite Structure and Mean Behavior. *Mon. Wea. Rev.* 114, 1781–1794. doi:10.1175/1520-0493(1986)114<1781:ecitwc>2.0.co;2

Sanders, F., and Gyakum, J. R. (1980). Synoptic-Dynamic Climatology of the "Bomb". *Mon. Wea. Rev.* 108, 1589–1606. doi:10.1175/1520-0493(1980)108<1589:sdcot>2.0.co;2

Schultz, D. M., Winters, A. C., Colle, B. A., Davies, H. C., and Volkert, H. (2018). Extratropical Cyclones: A century of Research on Meteorology's Centerpiece. *Meteorol. Monogr.* 59, 1610–1656. doi:10.1175/AMSMONOGRAPHS-D-18-0015.1

Smith, P. J., and Tsou, C.-H. (1988). Static Stability Variations during the Development of an Intense Extratropical Cyclone. *Mon. Wea. Rev.* 116, 1245–1250. doi:10.1175/1520-0493(1988)116<1245:ssvdtd>2.0.co;2

Uccellini, L. W., Kocin, P. J., Petersen, R. A., Wash, C. H., and Brill, K. F. (1984). The Presidents' Day Cyclone of 18-19 February 1979: Synoptic Overview and Analysis of the Subtropical Jet Streak Influencing the Pre-cyclogenetic Period. *Mon. Wea. Rev.* 112, 31–55. doi:10.1175/1520-0493(1984)112<0031:tpdcof>2.0.co;2

Uccellini, L. W., and Kocin, P. J. (1987). The Interaction of Jet Streak Circulations during Heavy Snow Events along the East Coast of the United States. *Wea. Forecast.* 2, 289–308. doi:10.1175/1520-0434(1987)002<0289:tiojsc>2.0.co;2

Wang, S., Fu, G., and Pang, H. (2017). Structure Analyses of the Explosive Extratropical Cyclone: A Case Study over the Northwestern Pacific in March 2007. *J. Ocean Univ. China* 16, 933–944. doi:10.1007/s11802-017-3287-7

Yoshida, A., and Asuma, Y. (2004). Structures and Environment of Explosively Developing Extratropical Cyclones in the Northwestern Pacific Region. *Mon. Wea. Rev.* 132, 1121–1142. doi:10.1175/1520-0493(2004)132<1121:saeoed>2.0.co;2

Zwack, P., and Okossi, B. (1986). A New Method for Solving the Quasi-Geostrophic omega Equation by Incorporating Surface Pressure Tendency Data. *Mon. Wea. Rev.* 114, 655–666. doi:10.1175/1520-0493(1986)114<0655:anmfst>2.0.co;2

Conflict of Interest: The authors declare that the research was conducted in the absence of any commercial or financial relationships that could be construed as a potential conflict of interest.

frontiers | Frontiers in Earth Science

METHODS
published: 22 July 2022
doi: 10.3389/feart.2022.920048

Establishment of Wind Gust Estimation Equation in Bohai Sea

Haichuan Hu, Bin Huang, Kan Dai* and Hongyu Qu*

National Meteorological Center, China Meteorological Administration, Beijing, China

Wind gusts over the ocean can have a great influence on maritime transport and production operations. However, owing to the scarcity of marine observation data and the complex causes of wind gusts, the estimation and forecasting of gusts at sea are even more difficult. In this study, a gust estimation equation applicable to the Bohai Sea is established based on observation and reanalysis data, with representative observation stations on the coast and offshore in the Bohai Sea. During the process, partial correlation analysis and a significance test of correlation coefficient differences were used to further clarify the influence of average wind speed and vertical wind shear at different heights on wind gusts. The final gust estimation equation includes a mean wind speed term, a turbulence term, and a convection term, which are statistically significant contributors; in addition, there are clear physical meanings. Comparing two gust factor methods in this study, the average errors and fitting errors of the least squares gust estimation equation are the smallest. For wind gusts between 10 and 26 m/s, the fitting error in the gust estimation equation is 7.68–12.25% and 21.10–30.08% lower than those of the two gust factor methods in this study. The gust estimation equation better reflects the difference of wind gusts typical under different average wind speeds and vertical wind shear conditions, so a better prediction for wind gusts can be achieved.

Keywords: wind gust, estimation equation, partial correlation analysis, multiple regression, marine weather forecast

OPEN ACCESS

Edited by:
Guihua Wang,
Fudan University, China

Reviewed by:
Zhengkun Qin,
Nanjing University of Information Science and Technology, China
Delei Li,
Institute of Oceanology (CAS), China

****Correspondence:***
Bin Huang
hbzbj199928@163.com
Kan Dai
daikan1998@163.com

Specialty section:
This article was submitted to Atmospheric Science, a section of the journal Frontiers in Earth Science

Received: *14 April 2022*
Accepted: *16 June 2022*
Published: *22 July 2022*

Citation:
Hu H, Huang B, Dai K and Qu H (2022) Establishment of Wind Gust Estimation Equation in Bohai Sea. Front. Earth Sci. 10:920048. doi: 10.3389/feart.2022.920048

INTRODUCTION

Wind gusts are strong, short-duration wind events that are measured by the average wind speed over several seconds. Wind gusts exceeding a certain threshold have a significant impact on housing, transportation, and/or maritime production (Sheridan, 2018; Teoh et al., 2019; Su et al., 2021). Accurate and timely wind gust forecast information can effectively reduce the loss of life and property. The formation mechanism of wind gusts is complex and is not only related to average wind speed and boundary layer turbulence but also affected by surface roughness and atmospheric stability (Harris and Kahl, 2017). For this reason, the prediction of wind gusts is a difficult problem in operational weather forecasting (Kahl, 2020). The wind gust factor was an early wind gust forecasting metric that was calculated as the ratio of the maximum wind speed to the average wind speed within a set time period. From this metric, the strength of wind speed pulsation was obtained, and the expected maximum wind gust value was estimated (Sherlock, 1952). The wind gust factor methodology is still widely used in practical operational forecasting owing to its simplicity and convenience (Cook et al., 2008; Blaes et al., 2014). However, because of the influence of different underlying surface conditions, altitude, and weather systems, the wind gust factor varies significantly. Therefore, in order to obtain more accurate wind gust forecasts, there has been considerable research on the factors driving wind gusts (Davis and Newstein, 1968; Krayer and Marshall, 1992; Ágústsson

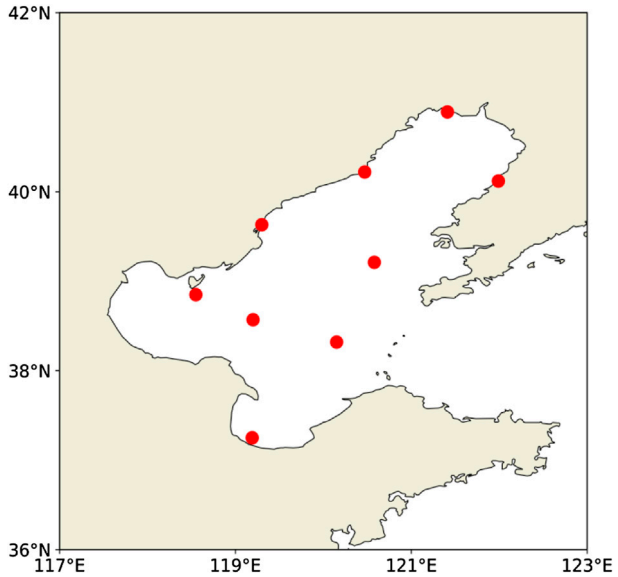

FIGURE 1 | The distribution of representative stations in coastal and offshore areas.

and Ólafsson, 2004; Yu and Chowdhury, 2009; Kahl et al., 2021). The wind gust factor methodology considers only the general relationship between the average wind speed and wind gusts and ignores the effects of the vertical distribution of upper-level wind speeds on surface wind gusts. When the vertical wind shear near the surface is large, strong turbulent momentum flux will occur, and this strong turbulent momentum flux will increase the surface wind gusts. Strong vertical wind shear in the troposphere is conducive to the development of convective weather, and when convective weather occurs, downdrafts in the troposphere reach the surface, thereby increasing the surface wind gusts (Brasseur, 2001; ECMWF, 2016; Minola et al., 2020). Therefore, by considering the effects of turbulence and convection on the average surface wind speed, which the wind gust factor method ignores, more accurate wind gust predictions can be obtained.

Compared with the average wind speed, strong wind gusts offshore have a greater impact on the safety of both maritime shipping and offshore production operations. However, the lack of observational data at sea, either high-altitude observations or ground-level observations, limits the accurate representation of the initial marine meteorological conditions in numerical models. This restricts the development of objective forecasting methods over the oceans. However, the underlying conditions at the sea surface are relatively uniform, which provides favorable conditions for the development of wind gust forecasting at sea (Leston et al., 2018).

The Bohai Sea is a relatively small inland sea in northern China, which has a substantial network of *in situ* observing sites, such as coastal observation sites, buoys, and oil platforms. Therefore, this study will use the gusts and mean wind observation data of these stations and the upper-air wind field data from reanalysis data to establish a gust estimation model that can be applied to the Bohai Sea. Through this model, the wind gusts can be more accurately estimated for varying average wind speeds and vertical wind shear conditions to provide a new method for wind gust forecasting in the Bohai Sea.

DATA

In this article, we use hourly wind speed data from surface observations taken by the China Meteorological Administration during 2017–2019 and wind field data on 1,000, 925, and 850 hPa from the ERA5 reanalysis data to establish an hourly wind gust forecast model for the Bohai Sea. The spatial resolution of the ERA5 reanalysis data is 0.25 × 0.25. A bilinear interpolation method is used to interpolate the upper-air data to the locations of the selected coastal and representative offshore stations shown in **Figure 1**. There are nine representative stations selected from the coastal and offshore areas in this study. The average elevation of the selected stations is 10 m, so the wind speed observation data do not need to be corrected in height. When using wind speed data to calculate wind gusts, the wind speed should be averaged over a 10-min interval (Harper et al., 2010; WMO, 2012). However, the numerical prediction model used in weather forecasting mainly outputs the wind speed at the forecast time. Therefore, in order to apply the established wind gust estimation equation in operational forecasting in the future, the average wind speed at the observation time is used instead of the 10-min average wind speed. In this study, it is a 2-min average and is recorded as integer values.

FACTOR ANALYSIS

In general, the speed of wind gusts rises with the increase of the average wind speed. The observational data from 2017 to 2019 show that when the average wind speed is between 14 and 16 m/s, the corresponding average value of observed wind gusts is approximately 19 m/s, and when the average wind increases to 22–24 m/s, average wind gusts can reach 28 m/s. Since there is only one parameter, there is a direct relationship between the average wind speed and the gust prediction. However, in practice, different gusts can occur at any specific average wind speed (**Figure 2**). Therefore, as the average wind speed is an important factor in gust estimation, it alone is not an accurate predictor for the wind gust speed.

Turbulence is the main characteristic of the atmospheric boundary layer and plays an important role in the transfer of heat, momentum, and water vapor between the surface and the upper atmosphere (Gousseau et al., 2012). Strong vertical wind shear is conducive to the enhancement of turbulence (Kim et al., 2003). The height of 1,000 hPa is close to the ground, so this study attempts to use the difference between the wind speed of 1,000 hPa (F_{1000}) and that at 10 m (F_{10}) to estimate the vertical wind shear in the near-ground layer. **Figure 3** is an array boxplot of different average wind speeds from 2017 to 2019 under the conditions of F_{1000}-$F_{10} > 0$ and F_{1000}-$F_{10} \leq 0$. As is

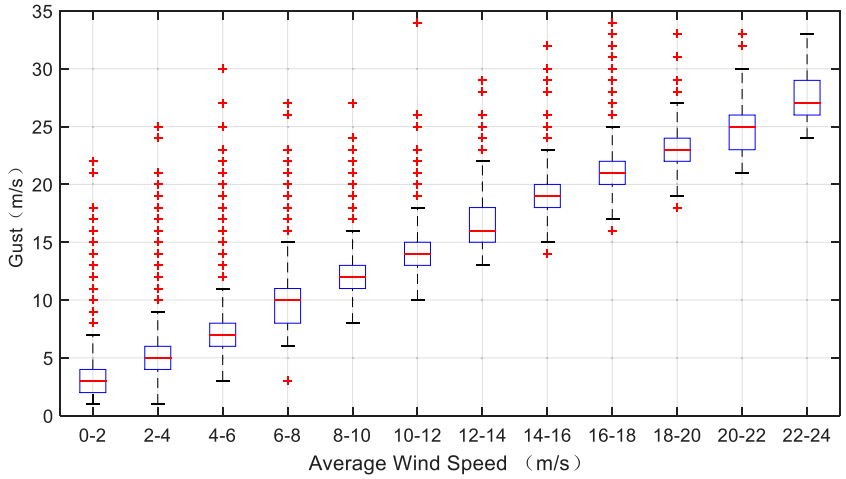

FIGURE 2 | Boxplots of average wind speed and wind gust from 2017 to 2019. The boxplot corresponds to the minimum, 25th percentile, 50th percentile (red lines), 75th percentile, and maximum values from bottom to top, respectively. Red crosses in the figure represent outliers that are more than 1.5 quartiles away from the 75th percentile or 25th percentile of the box.

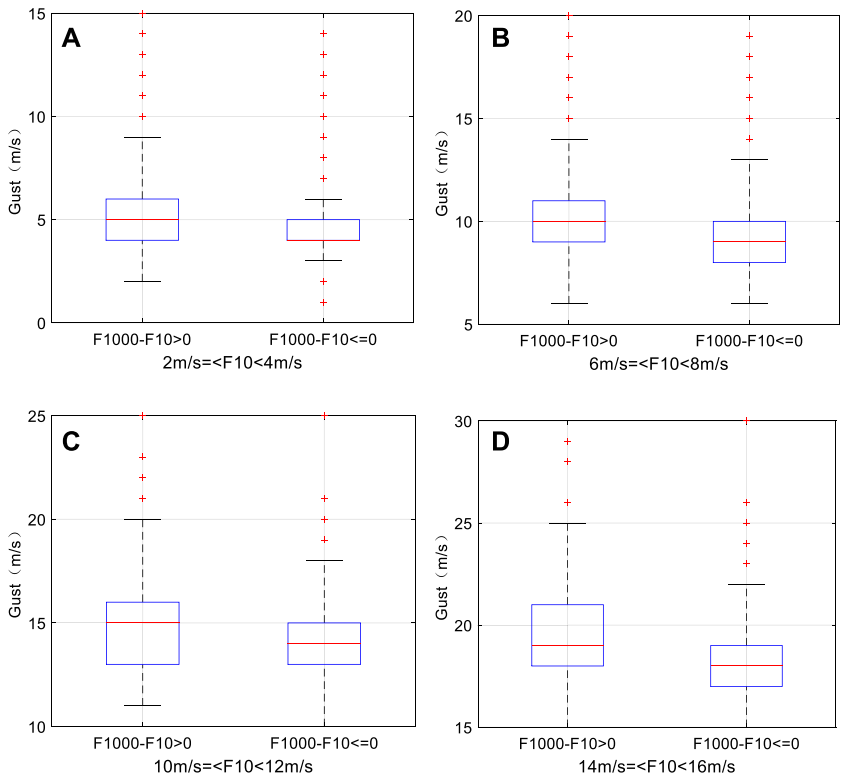

FIGURE 3 | Boxplots of gusts under different average wind speeds when F1000-F10 > 0 and F1000-F10 ≤ 0 from 2017 to 2019: **(A)** 2 m/s ≤ F10 < 4 m/s; **(B)** 2 m/s ≤ F10 <4 m/s; **(C)** 2 m/s ≤ F10 < 4 m/s; and **(D)** 2 m/s ≤ F10 < 4 m/s.

shown in **Figure 3**, by comparing the gust distribution in the two cases, it can be seen that under the same average wind speed, the larger gust is more likely to appear in the case of F_{1000}-$F_{10} > 0$. The case of F_{1000}-$F_{10} > 0$ may correspond to a stronger turbulence, which would be associated with larger surface wind gusts.

When a severe convective weather system occurs, downdrafts in the troposphere will transport momentum downward and

affect surface wind gusts. However, severe convective weather has the characteristics of small spatial scale, short life, and strong suddenness. The prediction of severe convective weather is still a difficult problem (Grabowski et al., 2019), and it is even more difficult to quantitatively calculate the surface gusts caused by severe convective weather. In the gust forecast product of the European Center for Medium-Range Weather Forecasts (ECMWF) model, the maximum positive wind speed difference between 850 and 950 hPa is used to represent the gust caused by convective weather, so as to realize the quantitative calculation of convective gust (ECMWF, 2016). In this study, the vertical wind shears between the 850- and 1,000-hPa surfaces (F_{850}-F_{1000}) and between the 850 and 925-hPa surfaces (F_{850}-F_{925}) are used to characterize the effects of convection.

CORRELATION ANALYSIS

Since the average surface wind speed and vertical wind shear both can affect the intensity of surface wind gusts, the relationship between them needs to be further clarified. The simple correlation coefficient only shows the degree of linear relation between two variables and does not fully clarify the relationship between those independent variables and the dependent variables in multiple regression analysis. Therefore, a partial correlation analysis needs to be performed, which considers other impact factors and temporarily ignores their influence, to study the relationship between the two remaining factors (Baka et al., 2004). When the partial correlation coefficient is first order, there are only two influence factors. The influence of one independent variable is being controlled, and the relationship between the other independent variable and the dependent variable is calculated according to the following (Hu and Wu, 2020):

$$r_{ab\_c} = \frac{r_{ab} - r_{ac}r_{bc}}{\sqrt{\left(1 - r_{ac}^2\right)\left(1 - r_{bc}^2\right)}} \tag{1}$$

where r_{ab_c} is the partial correlation coefficient between dependent variable a and independent variable b when controlling the effect of the independent variable $\boldsymbol{c}$, and r_{ab}, r_{ac}, and r_{bc} are the simple correlation coefficients between $\boldsymbol{a}$ and $\boldsymbol{b}$, $\boldsymbol{a}$ and $\boldsymbol{c}$, and $\boldsymbol{b}$ and $\boldsymbol{c}$, respectively. When there are three impact factors, it is necessary to control the influence of two of them to calculate the relationship between the remaining one and the dependent variable. Therefore, it is necessary to calculate the second-order partial correlation coefficient according to the following (Ashok et al., 2007):

$$r_{ab\_cd} = \frac{r_{ab\_c} - r_{ad\_c}r_{bd\_c}}{\sqrt{\left(1 - r_{ad\_c}^2\right)\left(1 - r_{bd\_c}^2\right)}} \tag{2}$$

where r_{ab_cd} is the correlation between dependent variable $\boldsymbol{a}$ and independent variable $\boldsymbol{b}$ when controlling the effects of the independent variable $\boldsymbol{c}$ and $\boldsymbol{d}$.

The vertical wind shear is divided into four cases, and the partial correlation coefficients of the wind shear variables under the four different vertical wind shear conditions from 2017 to 2019 are calculated. By using partial correlation analysis to compare the effects of F_{850}-F_{925} and F_{850}-F_{1000} on surface gusts, it is found that the effects of F_{850}-F_{925} is smaller than that of F_{850}-F_{1000} (not show), so F_{850}-F_{1000} is finally selected to represent the gust caused by convective weather (**Table 1**). The partial correlation coefficients in **Table 1** are all significant at the 95% level. These results show that the partial correlation coefficient of the average wind speed is the largest regardless of the vertical wind shear conditions, indicating that the average wind speed is the most important factor affecting the surface wind gusts. When F_{1000}-$F_{10} > 0$, the partial correlation coefficients are 0.314 and 0.346 (Case 1 and Case 2), which are much larger than 0.072 and 0.135 when F_{1000}-$F_{10} \leq 0$ (Case 3 and Case 4). When F_{850}-$F_{1000} > 0$ (Case 1 and Case 3), the partial correlation coefficients are 0.07 and 0.103, which are also greater than 0.016 and 0.02 when F_{850}-$F_{1000} \leq 0$ (Case 2 and Case 4).

TABLE 1 | Partial correlation coefficients of forecast factors under different vertical wind shear conditions from 2017 to 2019.

Predictor	Partial correlation coefficient			
	Case 1	Case 2	Case 3	Case 4
	F_{1000}-$F_{10} > 0$	F_{1000}-$F_{10} > 0$	F_{1000}-$F_{10} \leq 0$	F_{1000}-$F_{10} \leq 0$
	F_{850}-$F_{1000} > 0$	F_{850}-$F_{1000} \leq 0$	F_{850}-$F_{1000} > 0$	F_{850}-$F_{1000} \leq 0$
F_{10}	0.886	0.878	0.934	0.936
F_{1000}-F_{10}	0.314	0.346	0.072	0.135
F_{850}-F_{1000}	0.070	0.016	0.103	0.020

The partial correlation coefficients are calculated from the corresponding sample data. However, before comparing different correlation coefficients, a statistical test should be performed to make sure whether the difference between different correlation coefficients is statistically significant or possibly caused by sampling differences or random chance. In 1915, Fisher proposed the Fisher Z transform, which can convert correlation coefficients that do not conform to normal distribution into variables that conform to normal distribution (Needham, 1978). The formula is calculated as follows:

$$z_r = \frac{1}{2}\ln\left(\frac{1 + r_r}{1 - r_r}\right) \tag{3}$$

where r_r is the correlation coefficient of a sample data and z_r is the transformed correlation coefficient. Using this transformed correlation coefficient, Snedecor (1980) proposed a method to test the differences between two correlation coefficients. The procedure is as follows: Define

$$z = \frac{z_{r1} - z_{r2}}{VAR\left(z_{r1} - z_{r2}\right)} \tag{4}$$

where Z_{r1} and Z_{r2} are the transformed correlation coefficients and $VAR(Z_{r1}–Z_{r2})$ is calculated by the following:

$$VAR\left(z_{r1} - z_{r2}\right) = \sqrt{\frac{1}{n_1 - 3} + \frac{1}{n_2 - 3}} \tag{5}$$

where n_1 and n_2 represent the sample sizes of variables z_1 and z_2 in the data, respectively. The numbers of samples under

TABLE 2 | Model overview.

Case no.	Model factors	Regression coefficients	R2	Standard error	VIF
1	F_{10}	1.385	0.951	1.729	1.858
	F_{1000}-F_{10}	0.403	—	—	1.956
	F_{850}-F_{1000}	0.137	—	—	2.021
2	F_{10}	1.336	0.963	1.776	1.644
	F_{1000}-F_{10}	0.439	—	—	1.644
3	F_{10}	1.307	0.974	1.490	1.744
	F_{850}-F_{1000}	0.168	—	—	1.744
4	F_{10}	1.292	0.987	1.437	1.000

four different vertical wind shear conditions in this study are 85,453, 49,929, 24,365, and 10,333 (Case 1–Case 4, respectively). When the absolute value of Z exceeds 1.96, the differences in the correlation coefficients of the two variables are statistically significant at the 95% confidence level. When the absolute value of Z is less than 1.96, the correlation coefficients are not significantly different.

The above procedure is used to test the difference of correlation coefficients for the different vertical wind shear conditions. The results show that only two of the correlation coefficient differences are not statistically significant. The first is F_{10} for the two cases where F_{1000}-F_{10} is nonpositive and the partial correlation coefficients are 0.934 and 0.936, and the second is F_{850}-F_{1000} for the two cases where F_{1000}-F_{10} is positive and the partial correlation coefficients are 0.016 and 0.020. The significance test shows that the correlation coefficient between different samples can be compared, and the larger the correlation coefficient is, the greater the influence on the gusts will be. When F_{1000}-$F_{10} > 0$, the impact of F_{1000}-F_{10} on gusts is greater than that of F_{1000}-$F_{10} \le 0$. The corresponding physical meaning of this correlation is likely related to the fact that the positive vertical wind shear in the near-ground layer can stimulate strong turbulence, thereby enhancing gusts. When F_{850}-F_{1000} is greater than 0, it also has a greater impact on gusts, and its corresponding physical meaning is that the positive vertical wind shear is more likely to cause downdrafts in the troposphere to affect the surface gusts.

Therefore, the influence of F_{1000}-$F_{10} \le 0$ and F_{850}-$F_{1000} \le 0$ will be ignored when establishing the gust estimation equation, and the equation established in this way has a clearer physical meaning. The influence of different factors on surface wind gusts is more clearly revealed using partial correlation analysis and the significance test of correlation coefficient differences, which provide a basis for the establishment of a wind gust estimation equation.

ESTIMATION EQUATION

The multiple linear gust estimation equation established from a multiple regression analysis can be written in the form of a piecewise function, as follows:

$$F_{gust} = \begin{cases} a_1F_{10} + b_1(F_{1000} - F_{10}) + c_1(F_{850} - F_{1000}) & F_{1000} - F_{10} > 0;\ F_{850} - F_{1000} > 0 \\ a_2F_{10} + b_2(F_{1000} - F_{10}) & F_{1000} - F_{10} > 0;\ F_{850} - F_{1000} \le 0 \\ a_3F_{10} + c_3(F_{850} - F_{1000}) & F_{1000} - F_{10} \le 0;\ F_{850} - F_{1000} > 0 \\ a_4F_{10} & F_{1000} - F_{10} \le 0;\ F_{850} - F_{1000} \le 0 \end{cases} \quad (6)$$

where a_i, b_i, and c_i are the coefficients of the three different influencing factors under the ith vertical wind shear condition. Using the least squares method to solve the regression coefficients, we obtain the results presented in **Table 2**. The problem of collinearity among predictors in multiple linear regressions is an unavoidable problem. Severe collinearity can affect the fitting and may even lead to erroneous conclusions. The variance inflation factor (VIF) is an important metric to test for collinearity among the predictors. It is generally considered that if VIF > 10, there is a serious collinearity problem among the predictors (Al-Ashkar et al., 2021). The formula for calculating VIF is as follows:

$$VIF_i = \frac{1}{1 - R_i^2} \quad (7)$$

where R_i^2 is the square of R of independent variable i and the remaining independent variables in the linear regression. It can be seen in **Table 2** that the range of VIFs in the different forecasting models ranges from 1.0 to 2.021 $\ll$ 10, indicating that there are no serious collinearity problems for any of the forecasting factors. Therefore, the estimation equation can be fitted by using the least squares method, and there is no need to use either a partial least squares or ridge regression method to eliminate collinearity (Delsole, 2007; Smoliak et al., 2015; Lala et al., 2020).

As shown in **Table 2**, in the case when F_{1000}-$F_{10} \le 0$ and F_{850}-$F_{1000} \le 0$ (Case 4), the only significant influencing factor in the wind gust estimation equation is F_{10}. In this case, the R^2 of the estimation equation is 0.987, which is the largest of all estimation equations. R^2 is the goodness of fit, and the closer the value is to 1, the better the fitting effect is. In this case, only using F_{10} as a predictor achieves a better forecast of the wind gusts, and the standard error of the estimated value is the smallest of all cases (1.437 m/s). When F_{1000}-$F_{10} > 0$ and F_{850}-$F_{1000} > 0$ (Case 1), there are three factors in the estimation equation. In this case, the R^2 of the gust estimation equation is the smallest (0.951). Among the four gust estimation equations, the average wind speed has influence with a regression coefficient ranging from 1.292 to 1.385. The regression coefficients of F_{1000}-F_{10} are 0.403 and 0.439, and the regression coefficients of F_{850}-F_{1000} are 0.168 and 0.137. The regression coefficient of any particular factor is not very sensitive to the specific wind shear case, so we integrated the piecewise functions to make the gust estimation equation more concise and easy to use for operational forecasts. The procedure adopted in this study is to replace all the data for F_{1000}-$F_{10} \le 0$ and F_{850}-$F_{1000} \le 0$ with 0, merge all the sample data together, and use the least squares method to re-solve the regression coefficients for the different influencing factors. The VIF values between the influencing factors in the combined data are 1.446, 1.408, and 1.344, so there is no serious collinearity problem between the factors. The R^2 of the integrated gust estimation equation is 0.963, and the standard error of the estimated value is 1.703 m/s. The

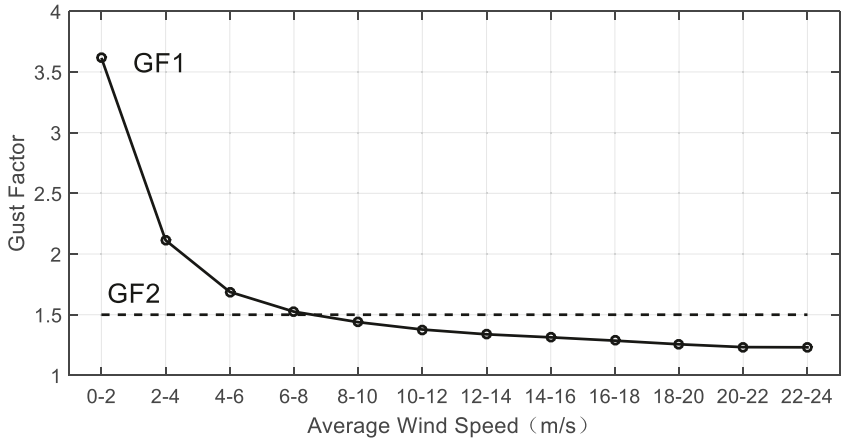

FIGURE 4 | The gust factors as a function of average wind speed (GF1) and overall sample (GF2) calculated from the data from 2017 to 2019.

coefficients in the integrated gust estimation equation are 1.332, 0.437, and 0.153, which are basically equivalent to the average values of the coefficients of different influence factors in **formula 6**(1.33, 0.421, and 0.153, respectively). The final form of the wind gust estimation equation is as follows:

$$F_{gust} = 1.332F_{10} + 0.437\max(0, F_{1000} - F_{10}) + 0.153\max(0, F_{850} - F_{1000}) \tag{8}$$

where $\max(0, F_{1000} - F_{10})$ and $\max(0, F_{850} - F_{1000})$ includes only positive values of F_{1000}-F_{10} and F_{850}-F_{1000}, respectively.

The wind gust estimation equation involves the wind speed on the 1,000-hPa surface. However, when the height of the 1,000-hPa surface is less than 10 m, F_{1000}-F_{10} and F_{850}-F_{1000} have no real physical meaning. Therefore, in this study, when the height of the 1,000-hPa surface is less than 10 m, the 1,000-hPa surface height data from the ERA5 reanalysis data is used to calculate the relationship between the 1,000- and 850-hPa wind speeds and the 10-m wind speed. However, the situation when the height of the 1,000-hPa surface is below 10 m and F_{1000}-F_{10} is positive accounts for only ~1.7% of all samples during 2017–2019, and the average value of F_{1000}-F_{10} is ~1.95 m/s. This situation primarily occurs when F_{10} is relatively small (1–3 m/s), with a frequency of roughly 51.6% of the time. The proportion of cases when the height of the 1,000-hPa surface is below 10 m and F_{850}-F_{1000} is positive is approximately 2.2%, of which roughly 64.7% of the magnitudes of F_{850}-F_{1000} are less than 5 m/s. In general, when the height of the 1000-hPa surface is below 10 m, F_{1000}-F_{10} and F_{850}-F_{1000} have relatively little meaning and have little effect on the wind gust estimates.

PERFORM VALIDATIONS

In this study, according to the definition of the gust factor method, two wind gust factors are calculated using the hourly wind speed observation data from 2017 to 2019. The first is the gust factor calculated based on different average wind speeds (GF1), and the second is the gust factor calculated based on the overall sample (GF2). As shown in **Figure 4**, GF1 monotonically decreases with the increase of average wind speed. When the average wind speed is 0–2 m/s, GF1 is 3.6155. When the average wind speed increases to 22–24 m/s, GF1 is 1.2314. At each average wind speed, GF2 is 1.5.

The gust estimation equation arising from the multiple regressions (MR) and the gust factors GF1 and GF2 are used to hind cast the data from 2017 to 2020 and compare their mean errors and fitting errors. The fitting error is estimated by the following:

$$RMSE = \sqrt{\frac{1}{n}\sum_{i=1}^{n}(y_i - \hat{y}_i)^2} \tag{9}$$

where y_i is the observational wind gust data and $\hat{y}_i$ is the hindcasted wind gusts from MR, GH1, or GF2. As is shown in **Figure 5A**, the amplitude of the mean error from MR is lower than that from GF1 at all wind gust speeds except 6–10 m/s. In some cases, the mean error from the MR is less than half that of GF1. When the wind gusts are above 10 m/s, the estimated value of the wind gusts estimated from GF1 are obviously smaller than the observed gusts, and the difference enlarges with the increase of wind gusts. When the observed gusts are 22–24, 24–26, and 26–28 m/s, the estimated gusts from GF1 are 32.9, 52.4, and 63% smaller, respectively, than the observed value by more than 2 m/s. The reduction in mean error in the MR model translates into a reduction in both the underestimation of strong wind gusts and the overestimation of low wind gusts. In comparison, the gust hindcasts from the GF2 model show a negative mean error for wind gusts below 14 m/s and a positive mean error when they are above 14 m/s. The estimations from the GF2 model are independent of the average wind speed, so the hindcasts are overestimates for weak wind gusts and underestimates for strong ones. Except in a few cases, the magnitude of the mean error of the MR model is smaller than that of the GF2 model (**Figure 5B**).

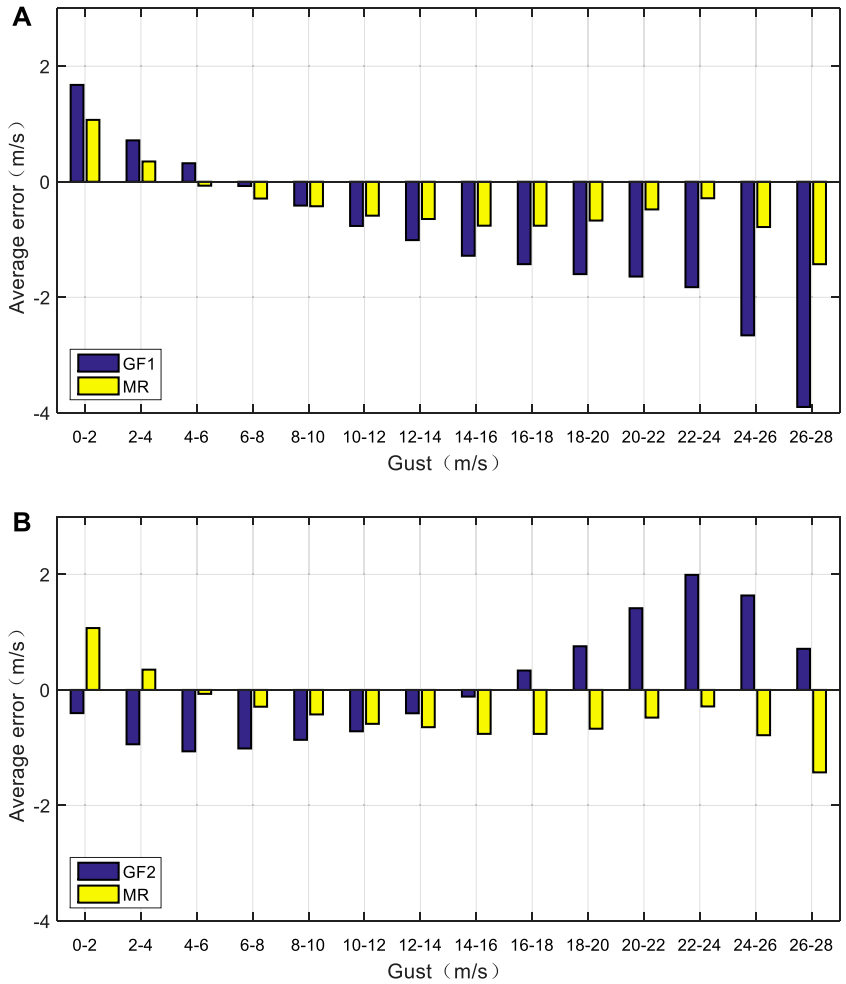

FIGURE 5 | Comparison of mean error in the multiple regression model to that in the **(A)** gust factor and **(B)** gust factor 2 models from 2017 to 2019.

TABLE 3 | Reduction rate of the multiple regression model relative to the gust factor 1 and gust factor 2 fitting error in 2017–2019.

Wind speed (m/s)	Reduction rate (100%)	
	GF1	GF2
2–4	-7.36	12.66
4–6	0.09	27.73
6–8	1.48	28.12
8–10	2.47	26.99
10–12	7.68	26.74
12–14	10.99	26.26
14–16	12.25	24.80
16–18	11.67	24.23
18–20	11.66	25.47
20–22	11.18	28.98
22–24	8.98	30.08
24–26	8.89	21.10
26–28	11.67	13.67

However, the mean error comparison does not prove that the estimation capability of the MR model is better than that of the GH1 or GF2 model. **Table 3** shows the reduction of percentage in the fitting error of the MR model related to the fitting error in the GF1 and GF2 models. In **Table 3**, except when the observed wind gusts are between 2 and 4 m/s, the fitting error reduction rate of MR relative to that of the GF1 model is negative, and all others are positive. For wind gusts between 12 m/s and 22 m/s, the fitting error in the MR model is 10.99–12.25% lower than that of the GF1 model. For wind gusts between 4 and 26 m/s, the fitting error reduction of the MR model is more than 20% relative to that of the GF2 model.

Figure 6 shows the scatter diagrams of absolute errors of the MR and GF1 models. As can be seen, when the absolute error of GF1 is small, the absolute error of MR is also small, so that the scattered points near the origin are densely packed. As the absolute error of GF1 increases, the scattered points begin shifting to the left of the diagonal, indicating that the MR error is less than that in GF1. **Figure 7** shows the scatter diagrams comparing the absolute error of the MR and GF2 models. The results in **Figure 7** are basically the same as those in **Figure 6**; the absolute error in the MR model has fewer large deviations in the gust than the GF2 model does.

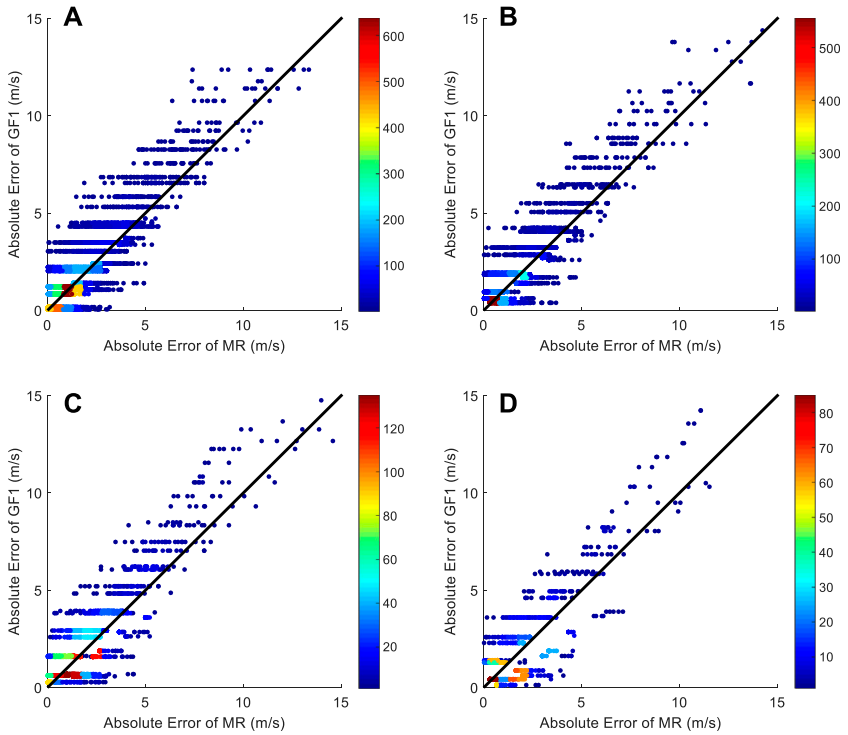

FIGURE 6 | The scatter diagrams of absolute errors of the multiple regression method (MR) and the wind gust factor method (GF1) for four different observed gust magnitudes: **(A)** 14–16 m/s, **(B)** 16–18 m/s, **(C)** 18–20 m/s, **(D)** 20–22 m/s. The color in the scatter in the figure indicates the number of repeated scatter points.

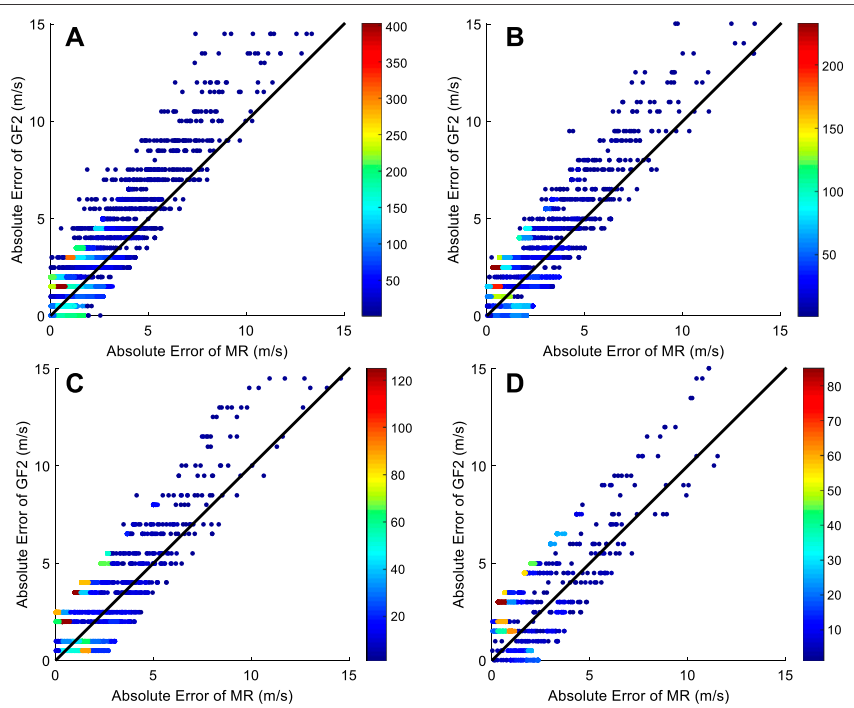

FIGURE 7 | The scatter diagrams of absolute errors of the multiple regression method (MR) and the wind gust factor method (GF2) for four different observed gust magnitudes: **(A)** 14–16 m/s, **(B)** 16–18 m/s, **(C)** 18–20 m/s, **(D)** 20–22 m/s. The color in the scatter in the figure indicates the number of repeated scatter points.

By comparing the mean error, fitting error, and the scatter diagrams of the absolute error between the gust estimation equations method and the two gust factor methods, it is clear that the regression estimation equation is considerably better than the other two gust factor methods. This is because the regression considers both average wind speed and wind shear at different heights.

SUMMARY AND DISCUSSION

In this study, based on both observational and ERA5 reanalysis data, the relationship among average wind speed, vertical wind shear at different levels in the lower atmosphere, and surface wind gusts is determined by the analysis of partial correlation and the development of wind gust estimation equation suitable for Bohai Sea using the least squares method. By comparing the gust estimation equation and the two gust coefficients, the results are as follows:

1. The average wind speed term F_{10} and the wind shear terms F_{1000}-F_{10} and F_{850}-F_{1000} are selected to establish an estimation equation for wind gusts in the Bohai Sea. While average wind speed is the dominant factor in the surface wind gust estimation, the near-surface wind shear is also an important term. Owing to the low frequency and intermittency of convective weather systems, the effects of convection as estimated using the wind shear across 850–1,000 hPa are relatively small.
2. Based on the significance test of the correlation coefficient difference, it is clear that the positive vertical wind shear has a greater impact on the ground gust than the negative vertical wind shear. The gust estimation equation ultimately includes the importance of vertical wind shear, which is more physically meaningful.
3. Compared with the two gust factor methods presented in this study (GF1 and GF2), the mean error and fitting error of the least squares regression gust estimation equation (MR) are the smallest. For wind gusts between 10 and 26 m/s, the fitting error in the gust estimation equation is 7.68–12.25% and 21.10–30.08% lower than those of the two gust factor methods in this study. The least squares regression gust estimation equation includes the effects of the average wind speed and different vertical wind shear conditions, so a better prediction for the wind gusts can be achieved.

The surface 10-m wind speed and 1,000- and 850-hPa wind speed data predicted using the numerical model can be applied in the gust estimation equation to realize the gust forecast. In this study, the gust estimation equation was established based on the Bohai Sea. If the gust estimation equation is applied to other sea areas, it is necessary to reselect representative stations to calculate the regression coefficients of different influencing factors. The regression coefficients of different sea areas will be slightly different. The gust estimation equation in this study considers only the average surface wind speed and vertical wind shear and does not consider the influence of temperature at different heights on gust. At the same time, the method is a linear regression method, which does not take the nonlinear relationship among different influencing factors and gusts into consideration. In future work, the influence of thermal factors will be considered, and the forecasting model of gust will be constructed using a nonlinear method, so as to further improve the forecasting ability of gust.

DATA AVAILABILITY STATEMENT

Publicly available datasets were analyzed in this study. The data can be found here: http://data.cma.cn/data/detail/dataCode/A.0012.0001.html https://www.ecmwf.int/en/forecasts/datasets/reanalysis-datasets/era5.

AUTHOR CONTRIBUTIONS

HH: data analysis, method establishment, and article writing. BH: method guide. KD: method improvement. HQ: data collection and analysis.

FUNDING

The study received funding from the National Key Research and Development Plan of China (2021YFC3000905).

REFERENCES

Ágústsson, H., and Ólafsson, H. (2004). Mean Gust Factors in Complex Terrain. *Meteor. Z.* 13, 149–155.

Al-Ashkar, I., Ibrahim, A., Ghazy, A., Attia, K., Al-Ghamdi, A. A., and Al-Dosary, M. A. (2021). Assessing the Correlations and Selection Criteria between Different Traits in Wheat Salt-Tolerant Genotypes. *Saudi J. Biol. Sci.* 28, 5414–5427. doi:10.1016/j.sjbs.2021.05.076

Ashok, K., Nakamura, H., and Yamagata, T. (2007). Impacts of ENSO and Indian Ocean Dipole Events on the Southern Hemisphere Storm-Track Activity during Austral Winter. *J. Clim.* 20, 3147–3163. doi:10.1175/jcli4155.1

Baka, K., Shibata, R., and Sibuya, M. (2004). "Partial Correlation and Conditional Correlation as Measures of Conditional Independence,", 657–664.*Aust. N. Z. J. Statistics*46

Blaes, J. L., Glenn, D., Hawkins, D., Oliva, V., et al. (2014). "Developing a Dataset of Wind Gust Factors to Improve Forecasts of Wind Gusts in Tropical Cyclones," in 39th National Weather Association Annual Meeting (Salt Lake City, UT: National Weather Association), P1.43.

Brasseur, O. (2001). Development and Application of a Physical Approach to Estimating Wind Gusts. *Mon. Wea. Rev.* 129, 5–25. doi:10.1175/1520-0493(2001)129<0005:daaoap>2.0.co;2

Cook, K. R., Gruenbacher, B., and Williams, L. D. (2008). Wichita,KS: National Weather Service, 21.Assessment of Science and Methodologies to Forecast Wind and Wind Gust Speed12th Annual High Plains Conf.

Davis, F. K., and Newstein, H. (1968). The Variation of Gust Factors with Mean Wind Speed and with Height. *J. Appl. Meteor.* 7, 372–378. doi:10.1175/1520-0450(1968)007<0372:tvogfw>2.0.co;2

Delsole, T. (2007). A Bayesian Framework for Multimodel Regression. *J. Clim.* 20, 2810–2826. doi:10.1175/jcli4179.1

European Center for Medium-Range Weather Forecasts (ECMWF) (2016). *IFS Documentation CY45R2—Part IV: Physical Processes*. IFS doc. Reading, UK: ECMWF.

Gousseau, P., Blocken, B., and Van Heijst, G. J. F. (2012). Large-eddy Simulation of Pollutant Dispersion Around a Cubical Building: Analysis of the Turbulent Mass Transport Mechanism by Unsteady Concentration and Velocity Statistics. *Environ. Pollut.* 167, 47–57. doi:10.1016/j.envpol.2012.03.021

Grabowski, W. W., Morrison, H., Shima, S.-I., Abade, G. C., Dziekan, P., and Pawlowska, H. (2019). Modeling of Cloud Microphysics: Can We Do Better? *Bull. Amer. Meteor. Soc.* 100, 655–672. doi:10.1175/bams-d-18-0005.1

Harper, B. A., Kepert, J. D., and Ginger, J. D. (2010). *Guidelines for Converting between Various Wind Averaging Periods in Tropical Cyclone Conditions*. Geneva: World Meteorological Organization Tech.Doc. WMO/TD-1555, 64.

Harris, A. R., and Kahl, J. D. W. (2017). Gust Factors: Meteorologically Stratified Climatology, Data Artifacts, and Utility in Forecasting Peak Gusts. *Appl. Meteor. Climatol.* 56, 3151–3166. doi:10.1175/jamc-d-17-0133.1

Hu, C. C., and Wu, C. C. (2020). Ensemble Sensitivity Analysis of Tropical Cyclone Intensification Rate during the Development Stage. *J. Atmos. Sci.* 77, 3387–3405. doi:10.1175/jas-d-19-0196.1

Kahl, J. D. W. (2020). Forecasting Peak Wind Gusts Using Meteorologically Stratified Gust Factors and MOS Guidance. *Weather Forecast.* 35, 1129–1143. doi:10.1175/waf-d-20-0045.1

Kahl, J. D. W., Selbig, B. R., and Harris, A. R. (2021). Meteorologically Stratified Gust Factors for Forecasting Peak Wind Gusts across the United States. *Am. Meteorological Soc.* 102, 1665–1671. doi:10.1175/bams-d-21-0013.1

Kim, S. W., Park, S. U., and Moeng, C. H. (2003). Entrainment Processes in the Convective Boundary Layer with Varying Wind Shear. *Boundary-Layer Meteorol.* 108, 221–245. doi:10.1023/a:1024170229293

Krayer, W. R., and Marshall, R. D. (1992). Gust Factors Applied to Hurricane Winds. *Bull. Amer. Meteor. Soc.* 73, 613–618. doi:10.1175/1520-0477(1992)073<0613:gfathw>2.0.co;2

Lala, J., Tilahun, S., and Block, P. (2020). Predicting Rainy Season Onset in the Ethiopian Highland for Agricultural Planning. *J. Hydrometeorol.* 21, 1675–1688. doi:10.1175/jhm-d-20-0058.1

Letson, F., Pryor, S. C., Barthelmie, R. C., and Hu, W. (2018). Observed Gust Wind Speeds in the Coterminous United States,and Their Relationship to Local and Regional Drivers. *Wind Eng.Ind.Aerodyn.* 173, 199–209. doi:10.1016/j.jweia.2017.12.008

Minola, L., Zhang, F., and Azorin-Molina, C. (2020). Near-surface Mean and Gust Wind Speeds in ERA5 across Sweden:towards an Improved Gust Parametrization. *Clim. Dyn.* 55, 887–907. doi:10.1007/s00382-020-05302-6

Needham, R. M., and Schroeder, M. (1978). Using Encryption for Authentication in Large Networks of Computers. *Commun. ACM* 21, 993–999. doi:10.1145/359657.359659

Sheridan, P. (2018). Current Gust Forecasting Techniques, Developments and Challenges. *Adv. Sci. Res.* 15, 159–172. doi:10.5194/asr-15-159-2018

Sherlock, R. H. (1952). Variation of Wind Velocity and Gust with Height. *Proc. Amer. Soc. Civ. Eng.* 78, 26. (Separate No.126; Paper 2553).

Smoliak, B. V., Wallace, J. M., and Lin, P. (2015). Dynamical Adjustment of the Northern Hemisphere Surface Air Temperature Field: Methodology and Application to Observations. *J. Clim.* 28, 1613–1629. doi:10.1175/jcli-d-14-00111.1

Snedecor, C. (1980). *Statistical Methods*. Ames, Iowa: Iowa State University Press, 185–188.

Su, N., Peng, S., and Hong, N. (2021). Stochastic Dynamic Transient Gusty Wind Effect on the Sliding and Overturning of Quayside Container Cranes. *Struct. Infrastruct. Eng.* 17, 1271–1283. doi:10.1080/15732479.2020.1809465

Teoh, Y. E., Alipour, A., and Cancelli, A. (2019). Probabilistic Performance Assess¬ment of Power Distribution Infrastructure under Wind Events. *Eng. Struct.* 197, 109199.1–109199.16. doi:10.1016/j.engstruct.2019.05.041

WMO (2012). *Measurement of Surface Wind. Guide to Meteorological Instruments and Methods of Observation*. Geneva: World Meteorological Organization. WMO-No. 8, 2008 edition Updated in 2010.

Yu, B., and Chowdhury, A. G. (2009). Gust Factors and Turbulence Intensities for the Tropical Cyclone Environment. *Appl. Meteorology Climatol.* 48, 534–552. doi:10.1175/2008jamc1906.1

Conflict of Interest: The authors declare that the research was conducted in the absence of any commercial or financial relationships that could be construed as a potential conflict of interest.

frontiers | Frontiers in Earth Science

ORIGINAL RESEARCH
published: 09 August 2022
doi: 10.3389/feart.2022.940205

Lightning Distribution in Tropical Cyclones Making Landfall in China

Wenjuan Zhang[1], *Yijun Zhang*[2,3,4]*, *Shoujuan Shu*[5], *Dong Zheng*[1] and *Liangtao Xu*[1]

[1]State Key Laboratory of Severe Weather, Chinese Academy of Meteorological Sciences, Beijing, China, [2]Department of Atmospheric and Oceanic Sciences and Institute of Atmospheric Sciences, Fudan University, Shanghai, China, [3]CMA-FDU Joint Laboratory of Marine Meteorology and Shanghai Frontiers Science Center of Atmosphere-Ocean Interaction, Shanghai, China, [4]Shanghai Qi Zhi Institute, Shanghai, China, [5]Department of Atmospheric Sciences, School of Earth Sciences, Zhejiang University, Hangzhou, China

Lightning data from the World Wide Lightning Location Network (WWLLN) are used to document the lightning characteristics in tropical cyclones (TCs) making landfall in China. The landfall period is confined to 48 h prior to and after landfall (t_{-24}~t_{+24}). Data from a total of 74 TCs are collected from 2010 to 2020, providing 3,293 individual time periods (1-h periods). To examine the radial and asymmetry distributions as a function of TC intensity, landing location, and vertical wind shear, the dataset is classified into two intensity categories, three shear groups, and four landing locations. WWLLN detected lightning activity in all TCs during the 48-h landfall, with lightning rates most frequently appearing between 250 and 600 str h^{-1}. Extreme hourly lightning rates of 3,154 str h^{-1} and 4,426 str h^{-1} are observed in the inner core in Tropical Storm Cimaron (2013) and the outer rainbands in Severe Typhoon Matmo (2014), respectively, comparable to lightning activity in mesoscale convection systems on land. TCs landing in Guangdong and Hainan have the largest peak lightning rates, while those landing in Zhejiang and Shanghai show the lowest lightning rates. The maximum lightning density is found in the inner-core region of weak TCs (<32.7 m s^{-1}) that are located approximately 100–200 km away from the coastline. The radial distribution of lightning density at landing stages is consistent with that at mature stages when TCs are over the ocean. However, there is a shift in the lightning maximum from the inner core prior to landfall (t_{-24}~t_0) to the outer rainbands after landfall (t_0~t_{+24}), indicating the effects of dry continental air intrusion and the enhanced surface frictional convergence. Vertical wind shear is the dominant factor in producing lightning and convective asymmetry for TCs landing in all locations. Lightning asymmetries are enhanced with the increase in shear magnitude from low (<5 m s^{-1}) to moderate (5–10 m s^{-1}) and high (>10 m s^{-1}) shear environments, both in weak and strong TCs (≥32.7 m s^{-1}).

Keywords: lightning, convection, tropical cyclone, landfall, China

OPEN ACCESS

Edited by:
Dujuan Kang,
Rutgers, The State University of New Jersey, United States

Reviewed by:
Jilong Chen,
The Chinese University of Hong Kong, China
Qiaoyan Wu,
Ministry of Natural Resources, China

***Correspondence:**
Yijun Zhang
zhangyijun@fudan.edu.cn

Specialty section:
This article was submitted to Atmospheric Science, a section of the journal Frontiers in Earth Science

Received: *10 May 2022*
Accepted: *09 June 2022*
Published: *09 August 2022*

Citation:
Zhang W, Zhang Y, Shu S, Zheng D and Xu L (2022) Lightning Distribution in Tropical Cyclones Making Landfall in China. Front. Earth Sci. 10:940205. doi: 10.3389/feart.2022.940205

1 INTRODUCTION

The northwest Pacific is the most active tropical cyclone (TC) basin (Gray, 1968) in terms of genesis, intensity and landfall events. The frequent disasters caused by landing TCs pose a significant threat to human life and property in China. One of the most serious disasters is heavy rainfall, which causes widespread flooding over coastal areas. For example, Typhoon Morakot affected much of China's

southeast coast during August 2009. Extreme rainfall of 1623.5 mm was recorded in 24 h at stations located in Fujian and Taiwan, causing an estimated 789 deaths and economic losses of 6.2 billion dollars (Chien and Kuo, 2011; Chen and Xu, 2017). Therefore, knowing the specific location of heavy rainfall during TC landfall is crucial for disaster reduction.

The heavy rainfall in TCs is related not only to the large-scale environments but also to the vortex structure and its cloud microphysical process (Houze, 2010). Intense convective cells are usually responsible for the maxima of TC rainfall near the coastline (Chan et al., 2004). A numerical study on Typhoon Morakot (2009) indicates that ice-phase processes and the large number of ice particles and graupels generated in deep convection in the rainbands are responsible for the extreme rainfall during Morakot's landfall (Chen and Xu, 2017). The ice particles transported outward by the radial wind increase the number of condensation nuclei in the stratiform region, where they melt and fall out in the form of large raindrops (Houze, 2010). Cloud electrification is closely related to microphysics, especially ice-phase processes (Williams, 1988). Therefore, the study of lightning characteristics in landing TCs can improve our understanding of TC convective distribution and its potential signals for cloud microphysical processes associated with heavy rainfall during landfall.

Over the previous few decades, a number of studies have examined the temporal and spatial distributions of lightning in TCs. Earlier studies have used lightning data from regional and national ground-based lightning detection networks, such as the National Lightning Detection Network (NLDN; Samsury and Orville, 1994; Molinari et al., 1994; Molinari et al., 1999; Molinari et al., 2004), Long-range Lightning Detection Network (LLDN; Squires and Businger, 2008; Leary and Ritchie, 2009), Los Alamos Sferics Array (LASA, Shao et al., 2005; Fierro et al., 2011), and Guangdong Lightning Location System in China (GDLLS; Zhang et al., 2012). Thanks to the remote detection of very-low-frequency electromagnetic waves over the open oceans, recent studies have used the global ground-based lightning location network, e.g., the World Wide Lightning Location Network (WWLLN; Pan et al., 2010; Thomas et al., 2010; Abarca et al., 2011; Bovalo et al., 2014; Zhang et al., 2015; Solorzano et al., 2018; Lin and Chou, 2020), Vaisala's Global Lightning Dataset (GLD360; Vagasky, 2017; Fierro et al., 2018), and Earth Networks Total Lightning Network (ENTLN; Ringhausen and Bitzer, 2021), to monitor lightning activity during the entire life cycle of TCs in different basins.

Satellite instruments, such as the Optical Transient Detector (OTD) on the Microlab-1 satellite and the Lightning Imaging Sensor (LIS) on the Tropical Rainfall Measuring Mission (TRMM) satellite, provide the first observations of total (intracloud and cloud-to-ground; IC and CG) lightning in TCs around the world (Cecil and Zipser, 1999; Cecil et al., 2002; Xu et al., 2017). Different from the orbiting satellites that view a fixed area over a short time, lightning imagers on board geostationary satellites launched in recent years have provided continuous sampling of total lightning with a higher detection efficiency (Goodman et al., 2013). These instruments include the Geostationary Lightning Mapper (GLM; Fierro et al., 2018; Duran et al., 2021; Ringhausen and Bitzer, 2021) onboard Geostationary Operational Environmental Satellite-16 (GOES-16) and Lightning Mapping Imagery (LMI; Hui et al., 2020; Zhang et al., 2020a) onboard Fengyun-4A (FY-4A), which will provide more useful information on total lightning in TCs and reestablish the relationship between lightning activity and TC intensification.

WWLLN data have been widely utilized in recent studies to observe lightning activity and deep convection in TCs (Pan et al., 2010; DeMaria et al., 2012; Pan et al., 2014; Zhang et al., 2015; Stevenson et al., 2016; Stevenson et al., 2018). The global lightning detection system is the most suitable system for detecting TC lightning, particularly for the landfall period during which storms move from the open sea to coastal regions and then to land. Ground-based lightning location networks, such as the Chinese National Lightning Detection Network, detect lightning over land at a higher detection efficiency (80%–90%; Xia et al., 2015). However, the detection range is limited to several hundred kilometers off the coast, and the detection efficiency decreases with increasing distance from lightning to the network. Since the WWLLN provides continuous lightning detection (in both longitude and latitude) in coastal areas, this study employs WWLLN data to study lightning distribution in TCs making landfall (including pre-landfall, landfall and post-landfall) in China. Comparisons between lightning observations from the WWLLN and FY-4A LMI in Super Typhoon Mangkhut (2018) indicated that the temporal and spatial evolution of lightning observed in these two systems are consistent (Zhang et al., 2020a).

Previous studies have found that the radial distribution of TC lightning shows an obvious pattern with two maxima in the inner core and outer rainbands and one minimum in the inner rainbands (Cecil et al., 2002; DeMaria et al., 2012; Stevenson et al., 2016). A positive correlation has been shown between lightning frequency and the maximum sustained wind speed of TCs (Price et al., 2009; Whittaker et al., 2015; Kong et al., 2021). The increase in lightning frequency may indicate the enhancement of TC intensity (Abarca et al., 2011; Pan et al., 2014; Wang et al., 2016). Stevenson et al. (2018) proposed that TCs are more likely to intensify 24 h after a burst of inner-core lightning if 1) the storm is stable or intensifying prior to the burst and 2) the burst has initiated downshear inside the radius of maximum wind. Additionally, the azimuthal distribution of lightning in mature hurricanes is consistent with TC convective and precipitation structures (Molinari et al., 1994; Molinari et al., 1999). Samsury and Orville (1994) found that during the pre-landfall and post-landfall periods of Hurricanes Hugo and Jerry (1989), the majority of lightning is located in the right quadrants in the outer convective rainbands. This maximum coincides with the highest reflectivity region observed by land-based radar. Xu et al. (2017) investigated the characteristics of TC lightning using 16-year global data from TRMM LIS. This relationship is found in the variation in lightning density and radar quantities (volume of 30 dBZ echoes in the mixed phase) in the outer rainbands. For landing TCs in China, lightning activities vary largely from

storm to storm (Zhang et al., 2012), suggesting that many factors, from large-scale environments to vortex dynamics, can influence the lightning distribution during TC landfall.

Other studies have examined the connection between lightning and environmental factors (i.e., storm motion and vertical wind shear) and investigated their influence on lightning asymmetry. Lightning maximum and strong convection are generally found in the front quadrant of TC motion, particularly the right-front quadrant, indicating the importance of frictional convergence in the boundary layer (Corbosiero and Molinari, 2003). However, vertical wind shear is a more dominant factor than storm motion in producing TC lightning asymmetry, similar to the asymmetry in TC convection (Corbosiero and Molinari, 2002) and precipitation (Cecil, 2007; Pei and Jiang, 2018). Lightning tends to occur primarily downshear left in the inner core and downshear right in the outer rainbands both in the Atlantic (Corbosiero and Molinari, 2002) and Pacific storms (Stevenson et al., 2016; Wang et al., 2018). Chan et al. (2004) examined the convective asymmetry for 4 TCs making landfall in South China and found that convection was strengthened a few hours prior to landfall. Enhanced convection first occurred on the western side in the mid-to lower troposphere and then rotated to the southward side in the upper troposphere by cyclonic flow and upward motion. TC vortex tilts downshear in response to environmental wind shear, resulting in the enhancement of deep convection in this quadrant (Houze, 2010).

While most of the abovementioned studies focused on TC lightning over the oceans, few studies have been performed on landing TCs. A quantitative description of some of the fundamental questions concerning lightning variability in landing TCs is needed. These fundamental questions include, but are not limited to, 1) Does every storm produce lightning during its landfall? Are lightning distributions in landing TCs different from those in TCs over water? 2) How do the lightning densities evolve prior to, during, and after landfall? 3) How do environmental and TC-specific factors affect the lightning distribution? The current study aims to document the characteristics of TC lightning during landfall in China and to examine the radial and asymmetry distributions as a function of TC intensity, landing location, and vertical wind shear. Answers to these questions can help to improve our basic understanding of lightning activity in TCs during landfall and possibly be utilized as guidance for the prediction of deep convection in TCs when they are approaching the coastline and finally making landfall.

2 DATA AND METHODS

2.1 Lightning Data

Lightning data used in this study are from WWLLN (http://wwlln.net). The WWLLN is a global ground-based lightning detection network operated by the University of Washington (Virts et al., 2013). WWLLN sensors receive very-low-frequency radio waves emitted by lightning, and the network locates lightning *via* a time-of-arrival technique with at least five sensors (Rodger et al., 2006). WWLLN primarily detects CG lightning, although it is also capable of detecting some IC lightning. Studies have suggested that the detection efficiency of WWLLN ranges from 10% over the continental United States (Abarca et al., 2010) to greater than 20% over the oceans (Rudlosky and Shea, 2013). Furthermore, for strokes with peak currents larger than 50 kA, the detection efficiency of the network is above 50% (Holzworth et al., 2019). Despite the low detection efficiency, WWLLN is capable of detecting almost all lightning-producing storms (Jacobson et al., 2006) and has expanded the detection range away from land to the open ocean.

The number of WWLLN stations has continued to grow since the network was set up in 2004. Currently, the network consists of over 80 stations worldwide (Holzworth et al., 2019). In addition, WWLLN began to save the integration of the electromagnetic field and accomplished algorithm improvement in April 2009 (Holzworth et al., 2019). All these factors have led to a higher and more stable detection efficiency since 2010 than it was before (Wang et al., 2018; Holzworth et al., 2021). Thus, we use WWLLN data from 2010 to 2020 to analyze the characteristics of lightning in landfalling TCs in China.

In this study, TC lightning is defined as lightning occurring within a radius of 500 km from the TC center. Lightning is segregated into three radial regions: the inner core (0–100 km), the inner rainbands (100–200 km), and the outer rainbands (200–500 km). The radial extents are close to the mean radii of the 3 TC regions revealed by Jiang et al. (2013) and are commonly used in studies analyzing TC lightning over the northwest Pacific (Zhang et al., 2015; Wang et al., 2018). Our large TC samples from 2010–2020 result in robust data of 1,302,625 WWLLN lightning strokes to investigate in this study. Lightning data are grouped into sets of 1-h periods called individual time periods (ITPs). Only ITPs with at least one lightning stroke are analyzed, which resulted in a total of 3293 ITP samples to study.

2.2 TC Best-Track Data

TC best-track data are obtained from the China Meteorological Administration best-track dataset. The dataset gives the location and intensity of TCs every 6 h (sometimes 3 h) at synoptic times (0000, 0600, 1200, and 1800 UTC). The best-track data are linearly interpolated to hourly data to estimate the distance of lightning to the storm center. In this study, TC intensities are classified into two categories based on the maximum wind speed at the time when lightning occurs: 1) weak TC (WTC) with sustained maximum wind speed <32.7 m s^{-1}, including tropical depression (TD, 10.8–17.1 m s^{-1}), tropical storm (TS, 17.2–24.4 m s^{-1}), and severe tropical storm (STS, 24.5–32.6 m s^{-1}); 2) strong TC (STC) with sustained maximum wind speed ≥32.7 m s^{-1}, including typhoon (TY, 32.7–41.4 m s^{-1}), severe typhoon (STY, 41.5–50.9 m s^{-1}) and super typhoon (SuperTY, ≥ 51 m s^{-1}).

2.3 Environmental Variables

The vertical wind shear is quantified by using pressure level data, i.e., the U-component and V-component of wind form the European Centre for Medium-Range Weather Forecasts (ECMWF) reanalysis (ERA5, https://cds.climate.copernicus.eu/)

TABLE 1 | Samples of TCs at different intensity levels by the time of landfall in mainland China from 2010 to 2020.

Year	TS (17.2–24.4 m s^{-1})	STS (24.5–32.6 m s^{-1})	TY (32.7–41.4 m s^{-1})	STY (41.5–50.9 m s^{-1})	SuperTY (≥51 m s^{-1})	Total
2010	2	0	5	0	0	7
2011	4	2	2	0	0	8
2012	1	1	1	2	0	5
2013	2	3	1	3	0	9
2014	2	2	0	1	1	6
2015	0	3	1	0	1	5
2016	2	1	4	0	1	8
2017	3	3	1	1	0	8
2018	7	2	1	1	0	11
2019	5	0	1	1	0	7
2020	1	1	2	1	0	5
Total	29 (37%)	18 (23%)	19 (24%)	10 (12%)	3 (4%)	79 (100%)

TD, tropical depression; TS, tropical storm; STS, severe tropical storm; TY, typhoon; STY, severe typhoon; SuperTY, super typhoon.

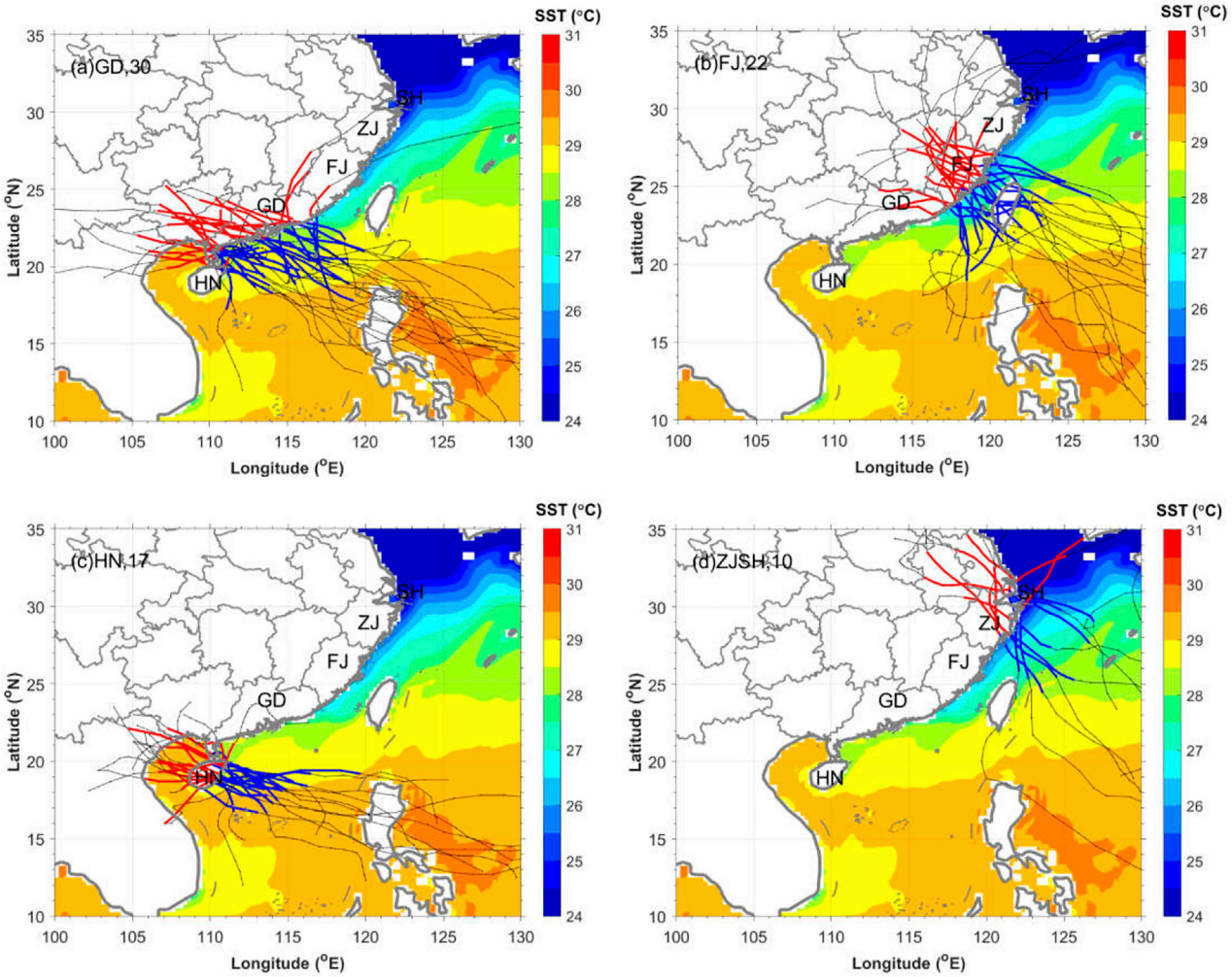

FIGURE 1 | Best tracks and samples of tropical cyclones that made landfall in different regions over China from 2010 to 2020 overlaid with SST. **(A)** Guangdong (GD), **(B)** Fujian (FJ), **(C)** Hainan (HN), and **(D)** Zhejiang and Shanghai (ZJSH). The blue lines indicate the tracks 24 h prior to landfall, the red lines indicate the tracks 24 h after landfall, and the black lines indicate the tracks beyond the 48-h landfall period. The numbers in the figure indicate the landfall samples in that region. SST data are the mean value for the TC season (June to October) in 1989–2019 from the ERA5 database.

dataset. The dataset is available hourly at 0.25° resolution in latitude and longitude. Deep-layer vertical wind shear is calculated between 850 and 200 hPa by averaging horizontal winds over a radius of 500 km from the storm center. This method was also adopted by Corbosiero and Molinari (2002) and DeMaria et al. (2012).

2.4 Methodology

2.4.1 Sample Selection and Definitions

The cases analyzed in this study are confined to TCs at the strength of tropical storms or greater by the time of landfall. TCs that landed north of 35°N are excluded to avoid the extratropical cyclone. The landfall period is confined to 48 h from 24 h prior to landfall to 24 h after landfall. TCs that dissipated within 24 h of landfall are also included.

TC landing locations are determined based on the following standards. ① According to the provinces on mainland China where TCs made landfall, the landfall locations are grouped into four categories: Guangdong (GD), Hainan (HN), Fujian (FJ), and Zhejiang and Shanghai (ZJSH). ② If a storm first made landfall over Taiwan and arrived at mainland China (e.g., FJ) for its second landfall, the landfall location is recorded as the mainland location (FJ). ③ For a TC that made landfall more than one time, if the time interval between the second landing and the first landing is <6 h, the first landfall is considered. If the landfall interval is ≥6 h, the second landfall is taken as a new landfall sample. Since the landfall time is not exactly synoptic time given by the best-track dataset, the nearest synoptic time (0000, 0600, 1200, and 1800 UTC) is used as the landfall time (Yu et al., 2017). Based on the above criteria, a total of 79 landfalls from 74 TCs are selected in 2010–2020 over mainland China, including 29 TSs, 18 STSs, 19 TYs, 10 STYs, and 3 SuperTYs (**Table 1**). The 79 landfalls are distributed over the provinces of GD with 30 landfalls, FJ with 22 landfalls, HN with 17 landfalls, and ZJSH with 10 landfalls (**Figure 1**).

2.4.2 Asymmetry Analysis

In analyzing the asymmetry distributions, lightning data are rotated to the shear vector and put into shear-relative coordinates. Each lightning is represented by the distance from its location to the storm center and its rotation angle with respect to the shear vector. Lightning densities are grouped into four quadrants: downshear-right (DR), downshear-left (DL), upshear-right (UR) and upshear-left (UL). The magnitude of the asymmetry in lightning density is calculated following Cecil (2007) and Xu et al. (2014). First, with a radius step of 100 km, the lightning density of five annular regions in each quadrant is calculated. Then, the average value of the five annular regions is the average lightning density for that quadrant. Last, the asymmetry magnitude is defined as the ratio of the averaged lightning density in the favored quadrants to that in the unflavored quadrants relative to shear. To investigate the impact of shear on lightning asymmetry, shear magnitudes are grouped into three categories: low shear (<5 m s^{-1}), moderate shear (5–10 m s^{-1}), and high shear (>10 m s^{-1}).

3 CHARACTERISTICS OF TC LIGHTNING RATE

3.1 Overall and The Extreme

Each storm in our cases produces lightning during its 48-h landfall period. The WWLLN detected lightning activity in all TCs that made landfall in 2010–2020, with the average and median lightning rates of 364 and 174 stroke h^{-1}, respectively. Tropical Storm Haitang (2017) produced the highest amount of lightning, with 71,055 strokes in 48 h landing in Fujian. In contrast, Severe Tropical Storm Ampil (2018) has the lowest lightning count, with only 6 strokes during its 48-h landfall in Shanghai. Among all the detected lightning, 56% of lightning occurred before landfall and 44% after landfall (**Table 2**); 6.2% occurred in the inner core, 9.6% in the inner rainbands, and 84.2% in the outer rainbands; 27.9% occurred during the intensification stages (ΔVmax>0), 49.9% in the weakening stages (ΔVmax<0), and 22.2% in the stable stages. **Table 3** shows the top ten storms with the highest lightning count during landfall. All these active-lightning storms made landfall between June and September. Five of the storms (Fanapi, Matmo, Nepartak, Nida, and Kalmaegi) made landfall at intensity levels ≥TY, and the others (Haitang, Bailu, Bebinca, Kujira, and Doksuri) made landfall at intensity levels of TS and STS.

The extreme hourly lightning rate in the inner core is 3,154 str h^{-1} generated by Tropical Storm Cimaron (2013). It occurred at 0100 UTC on 18 July 2013, 10 h before Typhoon Cimaron made landfall in Fujian (**Figure 2A**). The center of Cimaron was located in the north of the South China Sea and off the coast of southeastern Fujian, at approximately 21.9°N and 118.1°E. The maximum sustained winds were approximately 23 m s^{-1}, making the storm a TS. Cimaron was moving almost due north. TC lightning was mainly concentrated in the inner-core region at this hour on the right and front right of the storm motion. The majority of the extreme inner-core cases occur south of 23°N prior to landfall, indicating that a large inner-core lightning rate tends to occur in low-latitude oceanic regions with high sea surface temperatures (SSTs).

The extreme hourly lightning rate in the outer rainbands is 4,426 str h^{-1}, produced by Severe Typhoon Matmo (2014). It occurred 7 h after Matmo's landfall in Fujian at 1200 UTC on 23 July 2014 (**Figure 2B**). The maximum wind speed was 25 m s^{-1}, and the minimum sea level pressure was 988 hPa (STS intensity level). The eyewall structure was not clear, and TC lightning displayed strong asymmetry. The strong convections were mainly located in a long and narrow rainband to the south of the storm center. The convective elements in the outer rainbands developed arc-shaped lines observed by coastal radars, indicating that the storm was reacting to land surfaces. Previous studies revealed that the electrification mechanism in the outer rainbands is markedly different from that in the eyewall but more likely similar to that of ordinary cumulonimbus (Williams, 1988; Houze, 2010). The high lightning rate in the rainband region is comparable to lightning activity in mesoscale convection systems on land (Liu et al., 2021).

TABLE 2 | The statistics of lightning strokes at different periods, regions and stages during TC landfall.

Period		Region			Stage			Lightning count (48 h)	
Prior to landfall	**After landfall**	**Inner rainbands**	**Inner core**	**Outer rainbands**	**Intensifying**	**Stable**	**Weakening**	**Maximum**	**Minimum**
$t_{-24\sim0}$	$t_{0\sim+24}$	100–200 km	0–100 km	200–500 km	ΔVmax>0	ΔVmax=0	ΔVmax<0	strokes	strokes
56%	44%	9.6%	6.2%	84.2%	27.9%	22.2%	49.9%	71,055	6

TABLE 3 | The top ten storms in 2010–2020 with the largest lightning count during the 48-h landfall period. V_{max} and intensity are the maximum wind speed (m s^{-1}) and its intensity level during the 48-h landfall period. Lightning count is the number of lightning strokes in the whole TC region (0–500 km).

Rant	TC	Year	Month	Landfall	V_{max} (m s^{-1})	Intensity	Landfall hours	Lightning count	Mean TC lightning rate (str h^{-1})
1	Haitang	2017	Jul	FJ	24	TS	48	71,055	1480
2	Fanapi	2010	Sep	FJ	45	STY	48	67,763	1412
3	Bailu	2019	Aug	FJ	30	STS	48	53,928	1124
4	Matmo	2014	Jul	FJ	42	STY	48	52,132	1086
5	Nepartak	2016	Jul	FJ	38	TY	42	47,200	1124
6	Nida	2016	Aug	GD	36	TY	48	43,609	909
7	Bebinca	2018	Aug	GD	28	STS	48	43,094	898
8	Kalmaegi	2014	Sep	HN	42	STY	48	42,506	886
9	Kujira	2015	Jun	HN	25	STS	48	37,970	791
10	Doksuri	2012	Jun	GD	24	TS	36	31,848	885

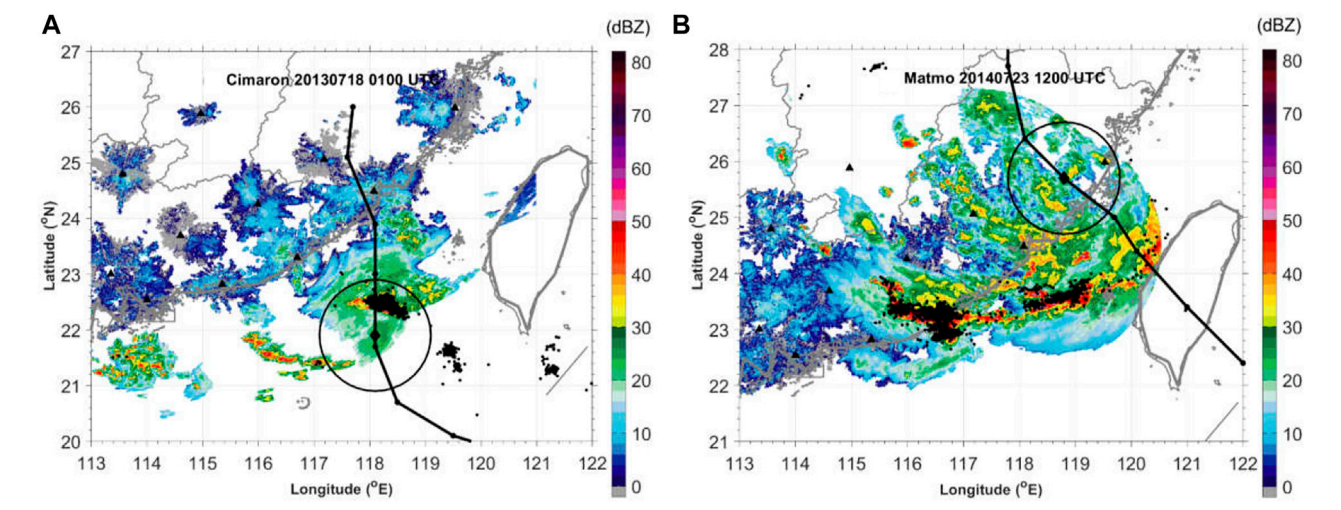

FIGURE 2 | Overlay of lightning activity and radar composite reflectivity at the hours producing the maximum lightning rates in **(A)** the inner core for Tropical Storm Cimaron (2013) and **(B)** the outer rainbands for Severe Typhoon Matmo (2014). The black dots denote WWLLN strokes. The black triangles represent the costal radar stations. The black circle indicates the 100-km radius from the storm center.

3.2 PDF of Lightning Rates

The probability density function (PDF) of lightning rates represents the basic characteristics of lightning activity. **Figure 3** shows the PDF distributions of lightning rates for all ITPs calculated within 500 km of the storm center. Lightning rates are shown on a dB scale or $10\times\log_{10}$ (lightning rates). The lightning rates of landing TCs are between 1 and 4,447 str h^{-1}. The mode is approximately 400 str h^{-1} for all the samples, and lightning rates most frequently appear between 250 and 600 str h^{-1} (**Figure 3A**). The occurrence frequency for lightning rates higher than 100 str h^{-1} is relatively higher in pre-landfall samples than post-landfall samples, indicating that lightning is more active when the storm center is over water.

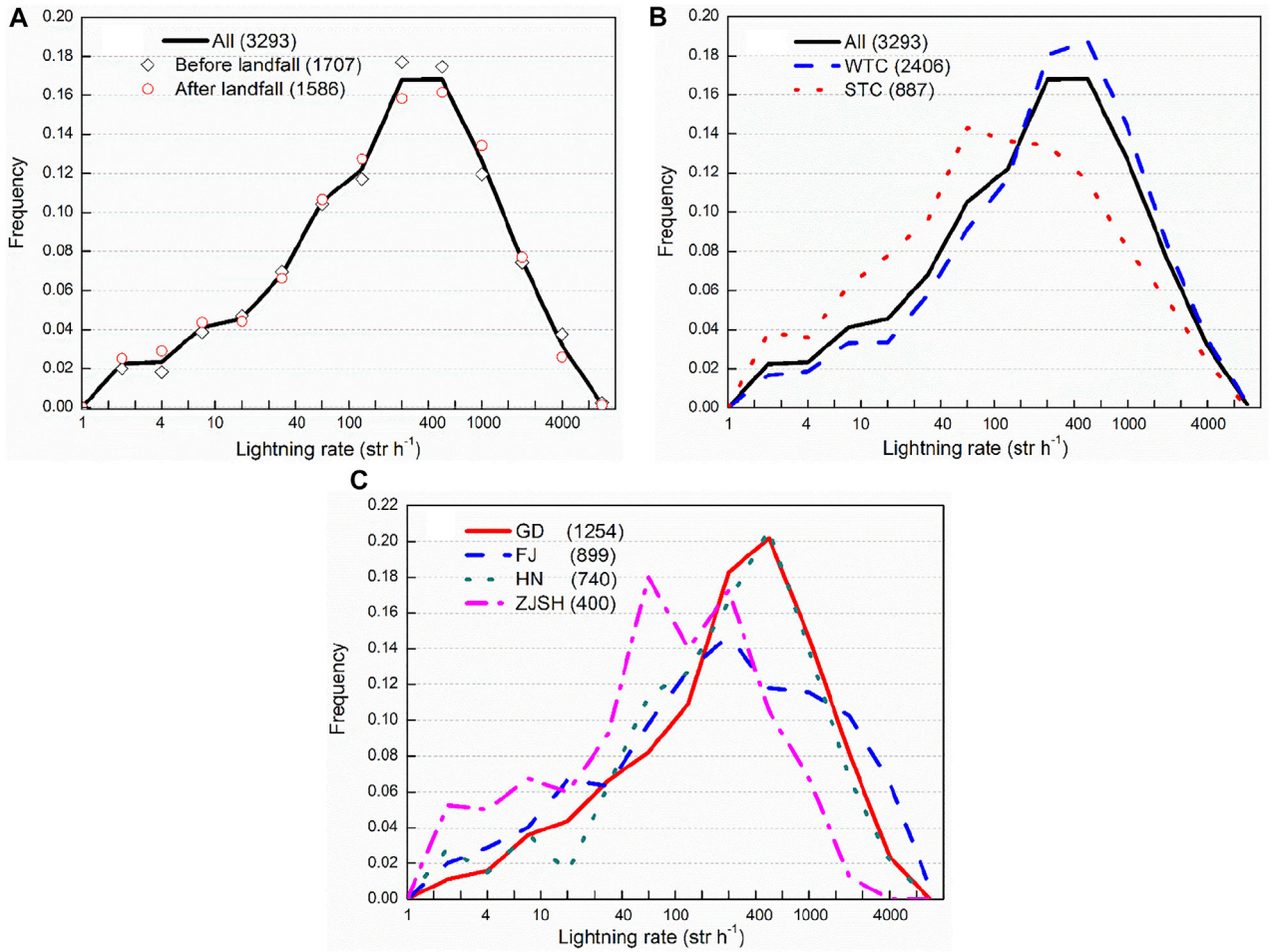

FIGURE 3 | Probability density functions of lightning rates within 500 km of the storm center for **(A)** before and after landfall groups, **(B)** weak and strong groups, and **(C)** landing location groups. The number in parentheses indicates the samples.

For the PDF distribution of different intensity categories (**Figure 3B**), the lightning rates shift toward lower values as the storm intensities increase. For WTC, the highest probability is approximately 18% for a lightning rate of 400 str h^{-1}, while for STC, the highest probability drops to approximately 14% for 63 str h^{-1}. When the lightning rate exceeds 158 str h^{-1}, the PDF probability in WTC is higher than that in STC, indicating that weaker TCs would have higher probabilities of larger lightning rates during landfall. The 75% (50%) percentiles of the lightning rate are 530 (211) str h^{-1} for WTC and 288 (83) str h^{-1} for STC. Previous studies based on WWLLN data have found that lightning tends to occur in weak storms and that samples of lightning occurrence in WTCs are larger than those in STCs when TCs are over water (Abarca et al., 2011; Zhang et al., 2015; Wang et al., 2018; Lin and Chou, 2020). Our study confirms that this relationship also exists during TC landfall. Based on infrared satellite observations, Zhang et al. (2020b) revealed that the large contribution of lightning in WTCs is due to the high occurrence of deep convection (IR<220 K) in these weak storms during their landfall.

In the distribution of PDFs for different landing locations, the frequency and amplitude of the PDF show some differences (**Figure 3C**). TCs landing in Guangdong and Hainan have the largest peak lightning rates and the narrowest distributions, and the PDF distribution is similar to the overall PDFs. However, TCs that made landfall in Fujian show a reduced peak lightning rate but with a wider distribution. In **Table 3**, we find that TCs landing in Fujian could also produce high lightning rates at certain hours, which leads to the wide PDF distribution skewed toward higher rates. The PDF distribution of the lightning rate in Zhejiang and Shanghai is bimodal, with one peak at approximately 250 str h^{-1} and a second peak near 60 str h^{-1}. Note that when the lightning rate is greater than 400 str h^{-1}, the distribution frequency decreases rapidly for ZJSH. One possible reason is the lower SST in coastal regions that are north in latitude (>23.5°N). Previous studies (e.g., Stevenson et al., 2016; Xu et al., 2017) found that TC lightning tends to occur in areas with warmer SSTs. Lower SSTs inhibit environments that support strong convection and active lightning activity. **Figure 3** indicates that both TC intensity and landfall

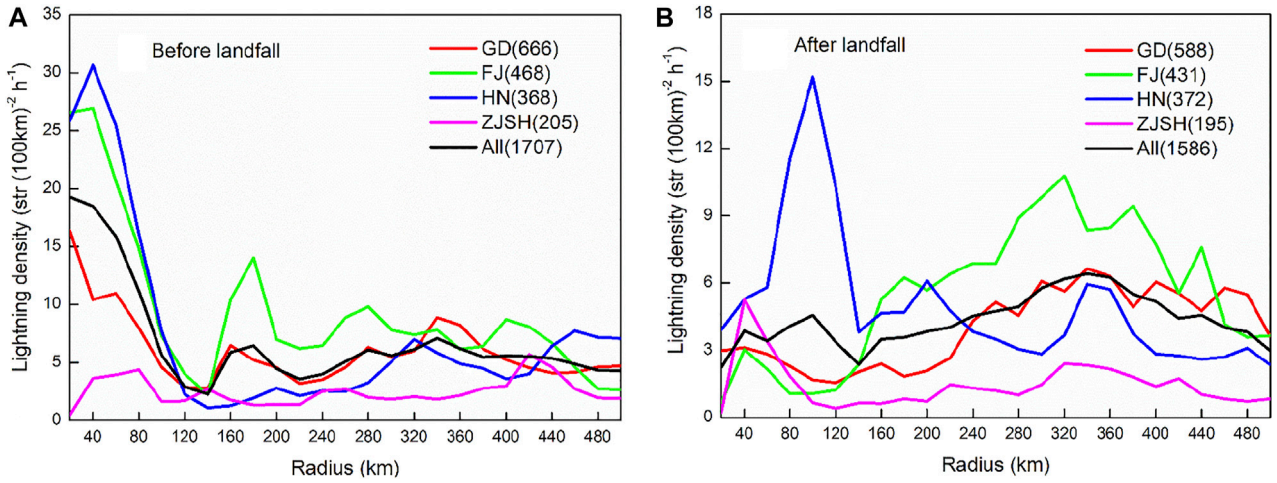

FIGURE 4 | Radial distribution of lightning density (str (100 km)$^{-2}$ h^{-1}) in TCs at different landing locations **(A)** 24 h before and **(B)** 24 h after landfall.

locations are important factors that affect lightning rates in landing TCs.

4 CHARACTERISTICS OF TC LIGHTNING DISTRIBUTION

4.1 Radial Distribution

It is important to show how the radial distributions of lightning vary according to landing stages, locations and TC intensities. The mean lightning density is computed using 20-km bins from the storm center to a radius of 500 km and then averaged in each azimuthal bin. **Figure 4** shows the radial distribution of lightning density in TCs landing at different locations 24 h before (t_{-24}~t_0) and after (t_0~t_{+24}) landfall. In general, for all samples, the peak lightning density is located within 40 km from the storm center and is approximately 22 str (100 km)$^{-2}$ h^{-1} prior to landfall (**Figure 4A**). The variability in the radial distribution is large from geographic location to location. The mean lightning densities vary between 5 and 30 str (100 km)$^{-2}$ h^{-1} within the inner core before landfall, possibly because of the different environments in which the eyewall was embedded. The lightning density reaches the minimum at a radius of 120 km (inner rainbands) and then increases again in the outer rainbands. The radial structure of TC lightning before landfall corresponds well to the lightning distribution in mature hurricanes (DeMaria et al., 2012).

After TC made landfall, the averaged lightning density drops to approximately 6 str (100 km)$^{-2}$ h$^{-1,}$ and the maximum shifts to the outer rainbands approximately 350 km from the center (**Figure 4B**). Therefore, the peak lightning density decreases significantly during landfall and shifts outward from the eyewall to the outer rainbands, which is consistent with Zhang

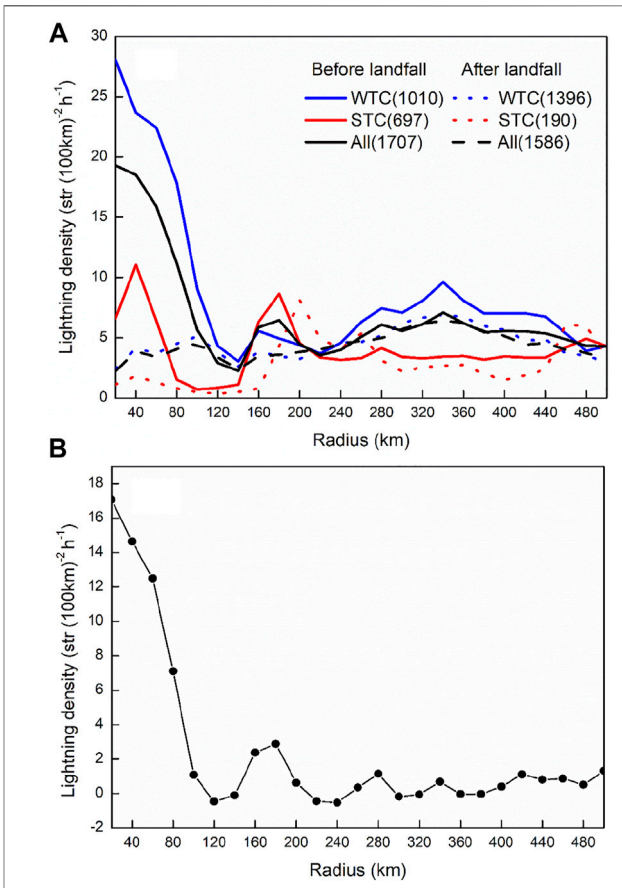

FIGURE 5 | Radial distribution of **(A)** lightning density (str (100 km)$^{-2}$ h^{-1}) for weak (TD\TS\STS) and strong (TY/STY/SuperTY) TCs 24 h before and after landfall, and **(B)** lightning density before landfall minus after landfall.

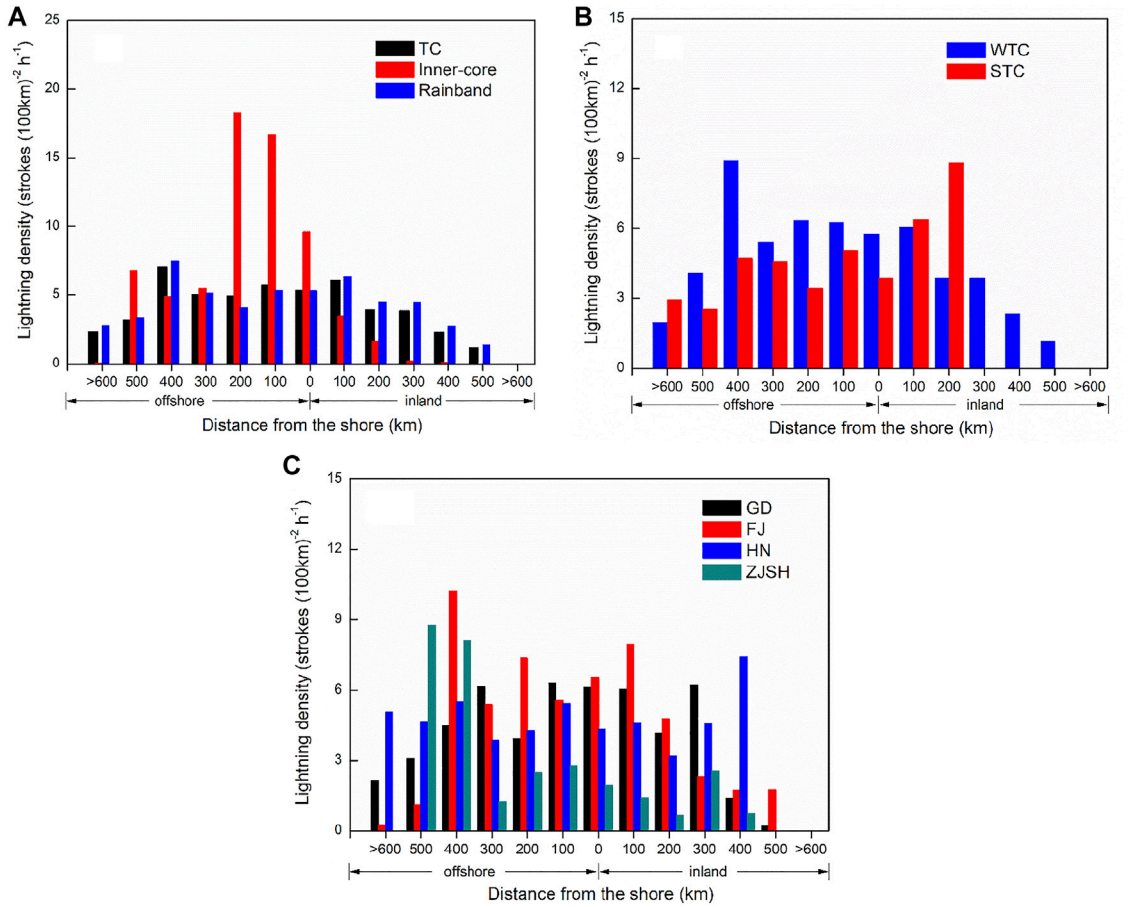

FIGURE 6 | Mean TC lightning density (strokes (100 km)$^{-2}$ h^{-1}) as a function of distance from the shoreline for categories of **(A)** TC regions, **(B)** TC intensities (weak TC and strong TC), and **(C)** landing locations.

et al. (2012). This is due to eyewall collapse and the enhanced surface frictional convergence in the outer rainbands during the landfall period. Note that there is an exception in the outward movement of lightning density. For TCs making landfall in HN, there is still a peak of lightning density in the inner-core region after landfall. This distribution is consistent with the radial structure of precipitation of TCs landing in HN (Yu et al., 2017). The comparison between **Figures 4A,B** obviously reflects the impact of landfall on lightning activity for TCs in different regions over China.

Figure 5 shows the radial distribution of lightning density for different TC intensity categories before and after landfall. For weak storms (i.e., TS category), the averaged lightning density within the inner core prior to landfall is much higher than that after landfall. Lightning densities larger than 25 str (100 km)$^{-2}$ h^{-1} are found within 40 km of the storm center and decrease to 5–10 str (100 km)$^{-2}$ h^{-1} at 200–440 km in weak TCs before landfall (**Figure 5A**). For strong storms (i.e., TY category), lightning densities in both the inner core and the outer rainbands are lower than those of weak storms. Overall, the averaged lightning densities in all radii decreased after landfall, with the largest reduction in the inner-core region (**Figure 5B**). In addition, after landfall, the difference in lightning density between STC and WTC decreases sharply. Lightning density in weak storms decreases more sharply with radius compared to strong storms during the 48-h landfall. Total lightning observations from LIS and GLM revealed that the dominant type of lightning (IC or CG) and rain regime (oceanic or continental) may change from the outer rainbands to the inner core (Cecil et al., 2002; Yokoyama and Takayabu, 2008; Fierro et al., 2018). The high lightning rate within the inner core may be related to the increased ratio of IC to CG lightning in that region.

4.2 Lightning Density With Distance From the Shore

Due to the weakening of TC intensity and the collapse of its structure, it is believed that lightning activity tends to weaken as landfall approaches as well as after making landfall. However, interactions between TC remnants and outer rainbands with land may also produce strong lightning much farther inland from the coast (Samsury and Orville, 1994; Zhang et al., 2012). Here, we investigate the mean TC lightning density as a function of distance from the shore (**Figure 6**). The distance is defined as

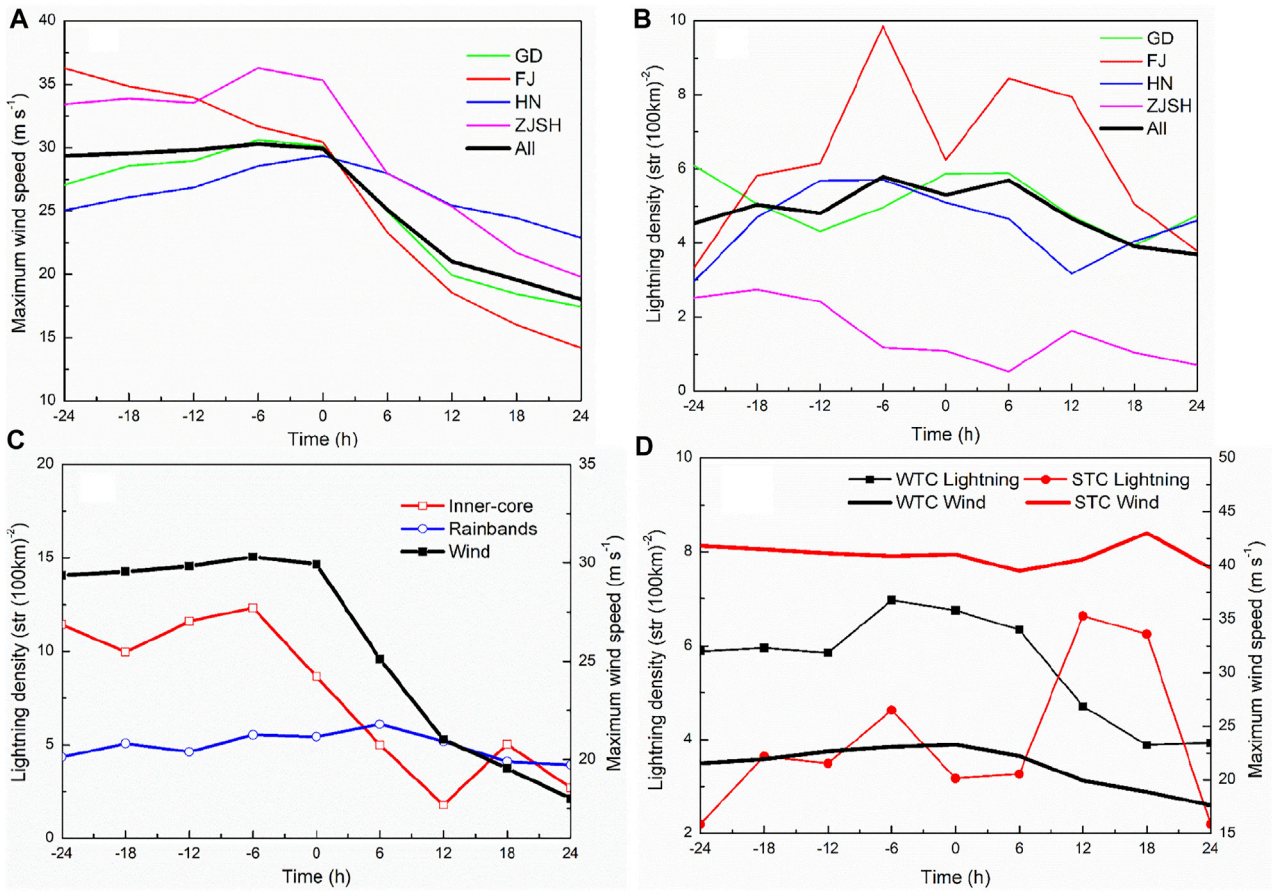

FIGURE 7 | Evolution of the mean maximum wind speed and lightning density (str (100 km)$^{-2}$) as a function of **(A,B)** landing locations, **(C)** TC regions, and **(D)** TC intensities at 6-h intervals from 24 h prior to and 24 h after landfall.

the closest distance from the TC center to the coastline. For lightning in TC and the outer rainband, the maximum density can be found when the TC center is located approximately 400 km offshore from the shoreline (**Figure 6A**). Lightning density gradually decreases as the storm moves inland and then remains constant at lower values in coastal areas 0–300 km from the shoreline. It is worth noting that the largest inner-core lightning density occurs before landfall when the TC center is located 100–200 km away from the coastline. This implies that when TCs are about to make landfall, strong lightning and convection could occur in the inner core, which may cause TCs to strengthen again in coastal areas. The possible reason is the re-strengthen of some typhoons when locate about 100–200 km away from the coastline, causing intense lightning activity within the inner-core region. Typhoon Hato (2017) is an example. The inner-core lightning tends to weaken faster than the outer rainbands with inland distance due to the collapse of the eyewall structure.

Weak storms produce the largest lightning density when the centers are located approximately 400 km onshore during pre-landfall. The lightning densities of the WTC gradually decrease after landfall. On the other hand, the lightning density of strong storms increases after landfall, and the largest value is found when the TC center moves 200 km inland (**Figure 6B**). For TCs landing in Guangdong and Fujian, lightning is mainly confined within 300 km from the shoreline in both inland and coastal areas (**Figure 6C**). TCs landing in Zhejiang and Shanghai produce the most lightning when their centers are 400–500 km onshore. The subsequent rapid decrease is likely related to the farther north landing locations and the lower SST in that coastal area. For TCs landing on Hainan Island, there is a weaker dependence of TC lightning on the distance from the shoreline.

Figure 7 shows the evolution of the hourly lightning density and maximum wind speed during the 48-h landfall period. From 24 to 6 h (t_{-24}~t_{-6}) prior to landfall, the mean maximum wind speeds increase for TCs making landfall in GD, HN, and ZJSH. However, the wind speeds decrease for TCs making landfall in FJ, which is probably due to the weakening effect of Taiwan Island on TC intensity. After the storm makes landfall (t_0~t_{24}), all the maximum wind speeds decrease rapidly (**Figure 7A**). **Figures 7B,C** show the evolution of the mean lightning density in the whole TC region (0–500 km), the inner core and the outer rainbands. The variations of lightning density in whole TC (black line in **Figure 7B**) and outer rainbands (blue line in

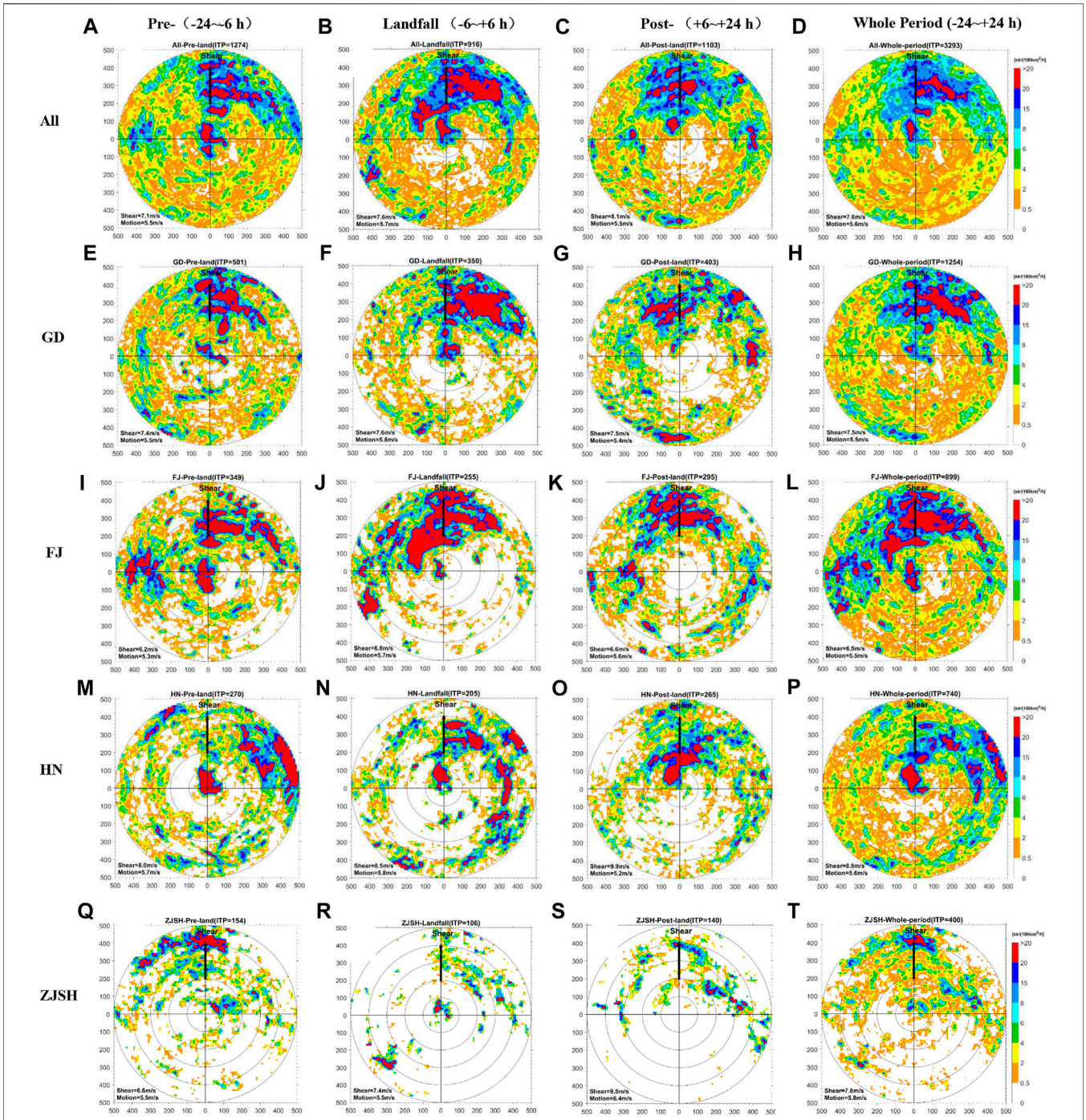

FIGURE 8 | Shear-related lightning density (str (100 km)$^{-2}$ h^{-1}) as a function of landing location for pre-landfall (-24~-6 h), landfall (-6~+6 h), post-landfall (+6~+24 h), and the whole period (-24~+24 h). **(A–D)** all ITPs, **(E–H)** Guangdong, **(I–L)** Fujian, **(M–P)** Hainan, **(Q–T)** Zhejiang and Shanghai.

Figure 7C) is not large, which is not consistent with the trend of wind speeds during the landfall period. In contrast, lightning density in the inner-core region is positively related to TC wind speed (**Figure 7C**). At 6 h prior to landfall, the averaged maximum wind speed and the inner-core lightning density both reach their peak values. In the following 30 h (t_{-6}~t_{24}), the averaged maximum wind speed decreases from 30 m s^{-1} to approximately 18 m s^{-1}, with a decrease rate of 40%. Consequently, the inner-core lightning densities decrease with the weakening of wind speed during this period. Furthermore, the decrease rate of inner-core lightning density is much higher than that of the outer rainbands, indicating that lightning activity within the inner core is more affected by TC intensity. It is interesting to note that during the period of 6–18 h after landfall

(t_6~t_{18}), lightning densities in strong TCs increase with the rise of averaged maximum wind speeds, with the peak of lightning approximately 6 h prior to the peak of wind speed (**Figure 7D**).

5 ASYMMETRY DISTRIBUTION OF TC LIGHTNING

5.1 Asymmetry Distribution as a Function of Landing Location

Figure 8 shows the lightning distribution as a function of landing locations and periods, i.e., pre-landfall (−24~−6 h), landfall (−6~+6 h), post-landfall (+6~+24 h), and whole period (−24~+24 h). In general, all the regions show clear lightning and convection asymmetries, with lightning maxima in the downshear (DL and DR) quadrants prior to, during, and after landfall. This indicates that vertical wind shear plays a major role in the asymmetric distribution of convection during the 48-h landfall period, and the effect of motion is secondary to that of shear. Corbosiero and Molinari (2002) and Stevenson et al. (2016) found that the downshear-favored lightning maximum is obvious even though the storm is moving in the opposite direction of the wind shear. This is also evident in this study for TCs making landfall in ZJSH (**Figures 8Q–T**). Although the averaged angle between the shear and motion vectors is larger than 130°during pre-landfall in ZJSH, the convection is still concentrated in the downshear quadrants. However, it is worth noting that there is a difference in lightning asymmetry between the inner core and outer rainbands. The inner-core lightning tends to distribute in the DL quadrant, while the outer-rainband lightning is distributed in the downshear to DR quadrants (**Figures 8D,H,L,P,T**). These structural changes in different TC regions are consistent with Stevenson et al. (2016) and Corbosiero and Molinari (2002).

In addition to vertical wind shear, the spatial distribution of lightning asymmetry is also related to the landing locations. TCs landing in ZJSH produce the least lightning and a much smaller area of high lightning density than TCs landing in other regions (**Figures 8Q–T**). In contrast to other TCs in which lightning is distributed throughout the whole outer rainbands, lightning in ZJSH TCs is mainly concentrated on the downshear side at 400–500 km. This is due to the higher latitude (~30°N) of the ZJSH regions and the lower SST in their adjacent waters. We also noted that storms landing at ZJSH have higher maximum wind speeds (**Figure 7A**), and this could be another reason for the low lightning occurrence at ZJSH. The climatological distribution of lightning over the northwest Pacific suggests that the TC lightning maximum occurs in the northern part of the South China Sea over warmer SSTs (28–30°C) (see **Figure 5** in Zhang et al., 2020b). In the adjacent sea of ZJSH, the mean SST in the TC season (June-October) is approximately 26°C (**Figure 1D**). This value is much lower than the necessary thermodynamic threshold (SST of 26°C) supporting TC deep convection indicated by Gray (1968). An environment of SST between 28°C and 30°C is favored for stronger convection and higher lightning counts, which is referred to as the "sweet spot" for TC lightning (Stevenson et al., 2016).

Figure 8 also shows the changes in lightning asymmetry in different stages of the landfall period. As TCs move from waters (−24~−6 h; **Figures 8A,E,I,M,Q**) to the coastline (−6~+6 h; **Figures 8B,F,J,N,R**) and finally make landfall (+6~+24 h; **Figures 8C,G,K,O,S**), the distributions of inner-core lightning experience some significant changes. The inner-core lightning is the strongest when TCs are over the open water, with the maximum concentrated in the downshear quadrants. When TCs approach the coast and make landfall, the area of maximum lightning within the inner core is decreased, and its asymmetry distribution is enhanced, which is mainly confined to DL quadrants. Meanwhile, we also noticed that active inner-core lightning is also observed in the upshear quadrant during pre-landfall. Stevenson et al. (2016) found that in some fast-moving TCs in the eastern North Pacific with opposite motion and shear vectors, lightning peaked upshear (i.e., downmotion) instead of downshear sides. Inner-core lightning maximum and convective bursts on the upshear side were also observed during the intensification of Tropical Storm Gabrielle (2001; Molinari et al., 2006) and Hurricane Earl (2010; Stevenson et al., 2014; Susca-Lopata et al., 2015). Deep convection initiated left of shear and then rotated into upshear regions. This convective rotation contributed to TC intensification by making the vortex more aligned and symmetric.

For the outer-rainband lightning, the downshear quadrants dominate its distribution for the whole landfall period. When TC approaches the coast and makes landfall (−6~+6 h), lightning densities in the 200–400 km outer rainbands gradually increase (except for TCs in ZJSH) on the downshear sides (**Figures 8B,F,J,N**). This is due to the strengthening of the frictional convergence between the rainbands and land surface, which plays an important role in the enhancement of convection for landing TCs. During the post-landfall period (+6~+24 h), lightning in the outer rainbands decreases as TCs gradually weaken over land.

5.2 Asymmetry Distribution as a Function of TC Intensity

Lightning asymmetries as a function of TC intensity for different landing periods are shown in **Figure 9**. The ITPs are grouped into WTC cases (<32.7 m/s, ITP=2,406) and STC cases (≥32.7 m/s, ITP=887). In general, the maximum lightning is generally downshear for all cases. As the storms move onshore (**Figures 9A,B**), approach the coast (**Figures 9C,D**), and finally make landfall (**Figures 9E,F**), lightning asymmetries shift slightly cyclonically to the left. Chan et al. (2004) also observed intense convection rotated counterclockwise to the left prior to and during landfall of Typhoons Sam (1999) and York (1999). Furthermore, **Figure 9** indicates that WTCs show stronger lightning densities and larger maximum density areas than STCs. When TCs intensify into typhoons, severe typhoons and super typhoons, the area of high lightning density decreases markedly, especially within the inner-core region (**Figures 9B,D,F,H**). The reason weak storms produce more lightning activity during landfall needs further study.

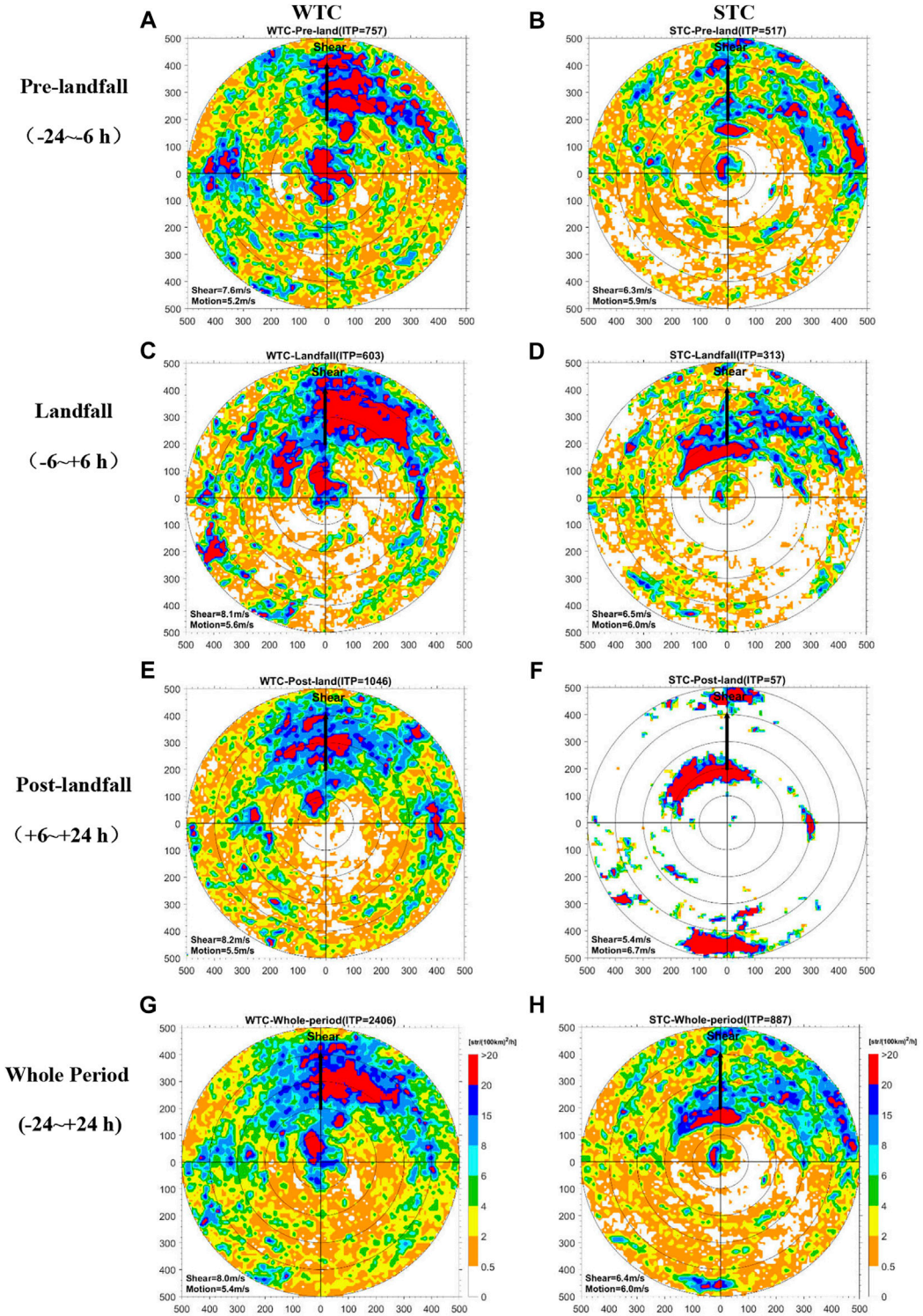

FIGURE 9 | Shear-related lightning density (str (100 km)$^{-2}$ h^{-1}) as a function of storm intensity for **(A,B)** pre-landfall (–24~–6 h), **(C,D)** landfall (-6~+6 h), **(E,F)** post-landfall (+6~+24 h), and **(G,H)** the whole period (–24~+24 h). **(A,C,E,G)** Weak TCs, **(B,D,F,H)** Strong TCs.

It is notable that strong axisymmetric lightning within the inner core in STCs during pre-landfall is observed (**Figure 9B**), which indicates that inner-core deep convections in STCs are more organized than those in WTCs. The difference in deep convection asymmetry in the inner core between the STC and WTC might be due to, on the one hand, the strength of the

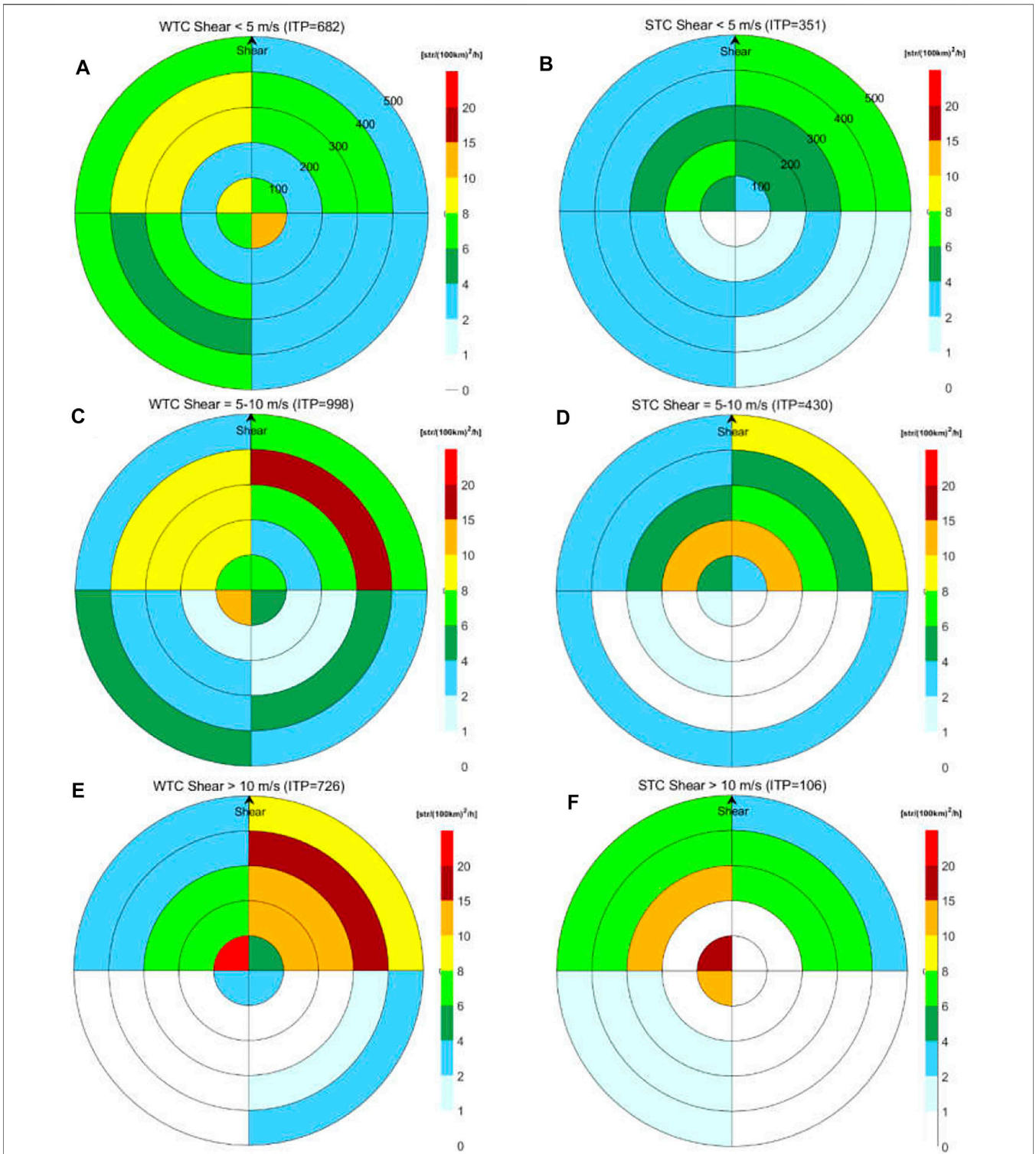

FIGURE 10 | Lightning asymmetry as a function of shear magnitude in WTCs and STCs. **(A,B)**: low shear (<5 m s^{-1}), **(C,D)**: moderate shear (5–10 m s^{-1}), **(E,F)**: high shear (>10 m s^{-1}).

primary circulation of the TC vortex. Strong storms, especially under a low shear environment, have a more organized primary circulation than weak storms. In this case, shear-induced asymmetry is less profound, and deep convections are more symmetrically distributed around the storm center. On the other hand, this might be due to the formation of a secondary

TABLE 4 | The favored quadrant and the magnitude of lightning asymmetry (relative to shear) as a function of landing locations. V_{max}, shear and motion are the mean values during the 48-h landfall period.

Location	ITP	Vmax (m/s)	Motion (m/s)	Shear (m/s)	Favored quadrant	Asymmetry magnitude
FJ	899	27.1	5.5	6.5	DL	4.33
GD	1254	25.9	5.5	7.5	DR	3.57
ZJSH	400	27.2	5.8	7.8	DR	4.92
HN	740	26.6	5.6	8.8	DL	5.48

eyewall during the restrengthening onshore. Using 6-year passive microwave imageries, Hawkins and Helveston (2004) found that approximately 80% of TCs in the western Pacific had double eyes and eyewall replacement cycles. Kuo et al. (2009) also found that 72% of major typhoons (category 5 typhoons) underwent concentric eyewalls (CEs) in the western North Pacific typhoons in 1997–2006. It is suggested that strong typhoons containing CE structure tend to occur farther west in the northwest Pacific. Furthermore, 42% of the samples of CE formation in their study occurred in the sea area west of 130°E (see **Figure 2** in Kuo et al., 2009), which is the domain of this study for landing TCs in China.

Figure 10 demonstrates the shear-relative lightning asymmetry by dividing WTC and STC samples into three subsets: low shear ($<5\ m\ s^{-1}$), moderate shear ($5–10\ m\ s^{-1}$), and high shear ($>10\ m\ s^{-1}$). Lightning asymmetry increases with increasing shear magnitude in both WTCs and STCs. Lightning asymmetry is less pronounced in a low shear environment (**Figures 10A,B**), and the ratio of average lightning density is small between favored and unfavored quadrants. Such asymmetries are more significant in moderate and high shear environments (**Figures 10C,F**). When the shear magnitude is larger than $10\ m\ s^{-1}$, the outer rainband lightning is mainly concentrated in the DR quadrants, and the inner-core lightning is concentrated in the DL quadrant (**Figures 10E,F**). The quadrant-mean lightning densities are much lower for strong TCs than for weak TCs. Furthermore, WTCs tend to have broader deep convection areas in downshear quadrants in high shear environments, with lightning density >15 str $(100\ km)^{-1}$ h^{-1} in the 300–400 km radius (**Figure 10E**). Observational studies (Cecil, 2007; Xu et al., 2014; Yu et al., 2017; Pei and Jiang, 2018) on precipitation have found that TCs in strong vertical wind shear show significant asymmetries, with the maximum rainfall located in the downshear quadrants. Similar patterns are also observed in the lightning asymmetry distribution in this study.

Vertical wind shear dominates lightning asymmetries, particularly in a moderate to high sheared environment. In a low shear environment, the motion vector has a larger contribution than the shear vector, and the down motion left component is more important (Pei and Jiang, 2018). While when the shear becomes strong, intense convection and higher reflectivity will be found on the DL quadrant in TC asymmetry (Rogers et al., 2003). **Table 4** shows the favored quadrant and the magnitude of lightning asymmetry for all landing locations. It is clear that the asymmetry magnitude increases with the value of wind shear. The asymmetry magnitude is 4.33 under smaller shear conditions (6.5 m/s in FJ) and increases to 4.92 and 5.48 in ZJSH and HN, respectively, with larger shear values (7.8 and 8.8 m/s). The convective asymmetry is not significant when the TC is far from land. As it approaches the coastline, stronger convection and asymmetric distributions may develop in the region between the storm core and the land. Just during landfall, storm motion may partly explain the along-coast convective asymmetry, but vertical wind shear is the more dominant factor than storm motion. Such strong convection in downshear quadrants is due to the influences of environmental situations, differential forcing between land and ocean, local topographic effects, and dry air intrusion from the continent (Chan et al., 2004; Shu et al., 2018).

6 CONCLUSION

This study quantified the characteristics of lightning in tropical cyclones making landfall in China using 11 years of lightning data from the WWLLN during 2010–2020. A total of 3,293 individual time periods were collected in 79 landfalls from 74 TCs with intensities ranging from tropical storms to super typhoons. The landfall period is confined to 48 h from 24 h prior to landfall to 24 h after landfall. The statistics of TC lightning rates, including extremes and PDFs, are analyzed, and the radial distribution and evolution of lightning density during landfall are investigated. Lightning asymmetries relative to the vertical wind shear are constructed to examine the impacts of landing location, TC intensity and environmental vertical wind shear on convective asymmetries.

WWLLN detected lightning activity in *all TCs* in 2010–2020 during the 48-h landfall, with the highest lightning count in Tropical Storm Haitang (2017) and the lowest in Severe Tropical Storm Ampil (2018). Extreme inner-core lightning rates (>500 str h^{-1}) prefer to occur in low-latitude oceanic regions (south of 23°N) prior to TC landfall. Extreme lightning rates in the rainband region are comparable to lightning activity in mesoscale convection systems on land. High lightning rates seem more likely to occur in weaker storms at TS and STS intensities, indicating that weak TCs can produce intense lightning and deep convection during their landfall.

The PDF analysis reveals that TC hourly lightning rates are distributed between 1 and 4,447 str h^{-1} and most frequently appear between 250 and 600 str h^{-1}. Weak storms tend to have higher lightning rates during landfall than strong storms. TCs landing in Guangdong and Hainan have the largest peak lightning rates, while those landing in Zhejiang and Shanghai show the lowest lightning rates. The storms landing at Zhejiang

and Shanghai have higher intensity and the lower SST in the waters there inhibits strong convection and active lightning activity in these regions.

During the pre-landfall period, lightning density shows a maximum within 40 km from the storm center. It reaches the minimum at a radius of 120 km and then increases again in the outer rainbands. This radial structure of TC lightning prior to landfall is consistent with the lightning distribution in mature hurricanes (Molinari et al., 1994, 1999; DeMaria et al., 2012). In contrast, starting from landing to 24 h after landfall, lightning densities in all radii are decreased, and the maximum shifts to approximately 350 km from the center. The shift in the lightning maximum from the inner core to the outer rainbands reveals the effect of dry continental air intrusion and the enhanced surface frictional convergence during the landfall period. In addition, lightning density in weak storms decreases more sharply with radius compared to strong storms during the 48-h landfall.

The maximum lightning density is found in the inner core region in weak storms when they are located approximately 100–200 km away from the coastline. Moreover, lightning density within the inner core is positively related to TC wind speed, with a slight increase from 24 to 6 h (t_{-24}~t_{-6}) prior to landfall and a sharp decrease after landfall (t_0~t_{24}). In contrast, lightning density in the outer rainbands remains stable during the 48-h landfall.

This study also investigated the possible influences of vertical wind shear, landing location, and TC intensity on lightning and convective asymmetries. In agreement with Corbosiero and Molinari (2002) and Stevenson et al. (2016), our results suggest that vertical wind shear is a more important factor in producing TC lightning and convective asymmetry during landfall. The lightning maximum is found in the downshear left quadrant in the inner core and the downshear to downshear right quadrants in the outer rainbands. As the storms move onshore, approach the coast, and finally make landfall, intense convections rotate counterclockwise, and lightning asymmetries shift slightly cyclonically to the left.

WTCs (<32.7 m/s) show stronger lightning densities and larger maximum density areas. However, when weak storms intensify into STCs (≥32.7 m/s), the area of high lightning density markedly decreases, especially within the inner-core region. Strong axisymmetric lightning within the inner core in the STCs during pre-landfall is observed, which is possibly due to the more organized primary circulation and the formation of secondary eyewalls during the re-strengthening onshore. Lightning asymmetry increases with increasing shear magnitude in both WTCs and STCs. The asymmetry is less pronounced in low (<5 m s^{-1}) shear environments but more significant in moderate (5–10 m s^{-1}) and high (>10 m s^{-1}) shear environments. The lightning and convective asymmetries for landing TCs are more pronounced than those for TCs over waters, which is possibly due to the combined influences of environmental shear, differential forcing between land and ocean, local topographic effects, and dry air intrusion from the continent.

The results of this study could be used as a basis to improve our current knowledge of lightning and convective structure for TCs making landfall. The next step will be to investigate the favorable large-scale environments for TCs producing high lightning rates during landfall, especially the difference in dominant environmental conditions between the inner core and the outer rainbands to produce extreme high lightning rates in different TC regions.

DATA AVAILABILITY STATEMENT

The original contributions presented in the study are included in the article/Supplementary Material, further inquiries can be directed to the corresponding author.

AUTHOR CONTRIBUTIONS

Conceptualization, WZ and YZ; Formal analysis, WZ and SS; Data curation, WZ and DZ; Figures, WZ and LX; Draft writing, WZ, YZ, and SS.

FUNDING

This work is jointly supported by the National Key Research and Development Program of China (Grant 2019YFC1510103) and the Basic Research Fund of Chinese Academy of Meteorological Sciences (Grant 2020Z009).

REFERENCES

Abarca, S. F., Corbosiero, K. L., and Galarneau, T. J. (2010). An Evaluation of the Worldwide Lightning Location Network (WWLLN) Using the National Lightning Detection Network (NLDN) as Ground Truth. *J. Geophys. Res.* 115, D18206. doi:10.1029/2009JD013411

Abarca, S. F., Corbosiero, K. L., and Vollaro, D. (2011). The World Wide Lightning Location Network and Convective Activity in Tropical Cyclones. *Mon. Weather Rev.* 139, 175–191. doi:10.1175/2010mwr3383.1

Bovalo, C., Barthe, C., Yu, N., and Bègue, N. (2014). Lightning Activity within Tropical Cyclones in the South West Indian Ocean. *J. Geophys. Res. Atmos.* 119, 8231–8244. doi:10.1002/2014JD021651

Cecil, D. J., and Zipser, E. J. (1999). Relationships between Tropical Cyclone Intensity and Satellite-Based Indicators of Inner Core Convection: 85-GHz Ice-Scattering Signature and Lightning. *Mon. Weather Rev.* 127, 103–123. doi:10.1175/1520-0493(1999)127<0103:rbtcia>2.0.co;2

Cecil, D. J., Zipser, E. J., and Nesbitt, S. W. (2002). Reflectivity, Ice Scattering, and Lightning Characteristics of Hurricane Eyewalls and Rainbands. Part I: Quantitative Description. *Mon. Weather Rev.* 130, 769–784. doi:10.1175/1520-0493(2002)130<0769:risalc>2.0.co;2

Cecil, D. J. (2007). Satellite-derived Rain Rates in Vertically Sheared Tropical Cyclones. *Geophys. Res. Lett.* 34, L02811. doi:10.1029/2006GL027942

Chan, J. C. L., Liu, K. S., Ching, S. E., and Lai, E. S. T. (2004). Asymmetric Distribution of Convection Associated with Tropical Cyclones Making Landfall along the South China Coast. *Mon. Weather Rev.* 132, 2410–2420. doi:10.1175/1520-0493(2004)132<2410:adocaw>2.0.co;2

Chen, L., and Xu, Y. (2017). Review of Typhoon Very Heavy Rainfall in China. *Meteorol. Environ. Sci.* 40, 3–10. doi:10.16765/j.cnki.1673-7148.2017.01.001

Chien, F.-C., and Kuo, H.-C. (2011). On the Extreme Rainfall of Typhoon Morakot (2009). *J. Geophys. Res.* 116, D05104. doi:10.1029/2010JD015092

Corbosiero, K. L., and Molinari, J. (2002). The Effects of Vertical Wind Shear on the Distribution of Convection in Tropical Cyclones. *Mon. Weather Rev.* 130, 2110–2123. doi:10.1175/1520-0493(2002)130<2110:teovws>2.0.co;2

Corbosiero, K. L., and Molinari, J. (2003). The Relationship between Storm Motion, Vertical Wind Shear, and Convective Asymmetries in Tropical Cyclones. *J. Atmos. Sci.* 60, 366–376. doi:10.1175/1520-0469(2003)060<0366:trbsmv>2.0.co;2

DeMaria, M., DeMaria, R. T., Knaff, J. A., and Molenar, D. (2012). Tropical Cyclone Lightning and Rapid Intensity Change. *Mon. Weather Rev.* 140, 1828–1842. doi:10.1175/mwr-d-11-00236.1

Duran, P., Schultz, C. J., Bruning, E. C., Stevenson, S. N., PeQueen, D. J., Johnson, N. E., et al. (2021). The Evolution of Lightning Flash Density, Flash Size, and Flash Energy during Hurricane Dorian's (2019) Intensification and Weakening. *Geophys. Res. Lett.* 48, e2020GL092067. doi:10.1029/2020GL092067

Fierro, A. O., Shao, X.-M., Hamlin, T., Reisner, J. M., and Harlin, J. (2011). Evolution of Eyewall Convective Events as Indicated by Intracloud and Cloud-To-Ground Lightning Activity during the Rapid Intensification of Hurricanes Rita and Katrina. *Mon. Weather Rev.* 139, 1492–1504. doi:10.1175/2010mwr3532.1

Fierro, A. O., Stevenson, S. N., and Rabin, R. M. (2018). Evolution of GLM-Observed Total Lightning in Hurricane Maria (2017) during the Period of Maximum Intensity. *Mon. Weather Rev.* 146, 1641–1666. doi:10.1175/mwr-d-18-0066.1

Goodman, S. J., Blakeslee, R. J., Koshak, W. J., Mach, D., Bailey, J., Buechler, D., et al. (2013). The GOES-R Geostationary Lightning Mapper (GLM). *Atmos. Res.* 125-126, 34–49. doi:10.1016/j.atmosres.2013.01.006

Gray, W. M. (1968). Global View of the Origin of Tropical Disturbances and Storms. *Mon. Weather Rev.* 96, 669–700. doi:10.1175/1520-0493(1968)096<0669:gvotoo>2.0.co;2

Hawkins, J. D., and Helveston, M. (2004). "Tropical Cyclone Multiple Eyewall Characteristics," in 26th Conference on Hurricane and Tropical Meteorology. Miami, FL; Date: 3-7 May 2004 (Miami, FL: American Meteorological Society), 1–7.

Holzworth, R. H., McCarthy, M. P., Brundell, J. B., Jacobson, A. R., and Rodger, C. J. (2019). Global Distribution of Superbolts. *JGR Atmos.* 124, 9996–10005. doi:10.1029/2019JD030975

Holzworth, R. H., Brundell, J. B., McCarthy, M. P., Jacobson, A. R., Rodger, C. J., and Anderson, T. S. (2021). Lightning in the Arctic. *Geophys. Res. Lett.* 48, e2020GL091366. doi:10.1029/2020GL091366

Houze, R. A. (2010). Clouds in Tropical Cyclones. *Mon. Weather Rev.* 138, 293–344. doi:10.1175/2009mwr2989.1

Hui, W., Zhang, W., Lyu, W., and Li, P. (2020). Preliminary Observations from the China fengyun-4A Lightning Mapping Imager and its Optical Radiation Characteristics. *Remote Sens.* 12, 2622. doi:10.3390/rs12162622

Jacobson, A. R., Holzworth, R., Harlin, J., Dowden, R., and Lay, E. (2006). Performance Assessment of the World Wide Lightning Location Network (WWLLN), Using the Los Alamos Sferic Array (LASA) as Ground Truth. *J. Atmos. Ocean. Technol.* 23, 1082–1092. doi:10.1175/jtech1902.1

Jiang, H., Ramirez, E. M., and Cecil, D. J. (2013). Convective and Rainfall Properties of Tropical Cyclone Inner Cores and Rainbands from 11 Years of TRMM Data. *Mon. Weather Rev.* 141, 431–450. doi:10.1175/mwr-d-11-00360.1

Kong, X., Zhao, Y., Qiu, Z., Tao, X., and Zhang, W. (2021). A Simple Method for Predicting Intensity Change Using the Peak Time Lag between Lightning and Wind in Tropical Cyclones. *Geophys. Res. Lett.* 48, e2020GL088872. doi:10.1029/2020GL088872

Kuo, H.-C., Chang, C.-P., Yang, Y.-T., and Jiang, H.-J. (2009). Western North Pacific Typhoons with Concentric Eyewalls. *Mon. Weather Rev.* 137, 3758–3770. doi:10.1175/2009mwr2850.1

Leary, L. A., and Ritchie, E. A. (2009). Lightning Flash Rates as an Indicator of Tropical Cyclone Genesis in the Eastern North Pacific. *Mon. Weather Rev.* 137, 3456–3470. doi:10.1175/2009mwr2822.1

Lin, S.-J., and Chou, K.-H. (2020). The Lightning Distribution of Tropical Cyclones over the Western North Pacific. *Mon. Weather Rev.* 148, 4415–4434. doi:10.1175/mwr-d-19-0327.1

Liu, D., Sun, M., Su, D., Xu, W., Yu, H., and Chen, Y. (2021). A Five-Year Climatological Lightning Characteristics of Linear Mesoscale Convective Systems over North China. *Atmos. Res.* 256, 105580. doi:10.1016/j.atmosres.2021.105580

Molinari, J., Moore, P. K., Idone, V. P., Henderson, R. W., and Saljoughy, A. B. (1994). Cloud-to-ground Lightning in Hurricane Andrew. *J. Geophys. Res.* 99, 16665–16676. doi:10.1029/94JD00722

Molinari, J., Moore, P., and Idone, V. (1999). Convective Structure of Hurricanes as Revealed by Lightning Locations. *Mon. Weather Rev.* 127, 520–534. doi:10.1175/1520-0493(1999)127<0520:csohar>2.0.co;2

Molinari, J., Vollaro, D., and Corbosiero, K. L. (2004). Tropical Cyclone Formation in a Sheared Environment: A Case Study. *J. Atmos. Sci.* 61, 2493–2509. doi:10.1175/jas3291.1

Molinari, J., Dodge, P., Vollaro, D., Corbosiero, K. L., and Marks, F. (2006). Mesoscale Aspects of the Downshear Reformation of a Tropical Cyclone. *J. Atmos. Sci.* 63, 341–354. doi:10.1175/jas3591.1

Pan, L., Qie, X., Liu, D., Wang, D., and Yang, J. (2010). The Lightning Activities in Super Typhoons over the Northwest Pacific. *Sci. China Earth Sci.* 53, 1241–1248. doi:10.1007/s11430-010-3034-z

Pan, L., Qie, X., and Wang, D. (2014). Lightning Activity and its Relation to the Intensity of Typhoons over the Northwest Pacific Ocean. *Adv. Atmos. Sci.* 31, 581–592. doi:10.1007/s00376-013-3115-y

Pei, Y., and Jiang, H. (2018). Quantification of Precipitation Asymmetries of Tropical Cyclones Using 16-Year TRMM Observations. *J. Geophys. Res. Atmos.* 123, 8091–8114. doi:10.1029/2018JD028545

Price, C., Asfur, M., and Yair, Y. (2009). Maximum Hurricane Intensity Preceded by Increase in Lightning Frequency. *Nat. Geosci.* 2, 329–332. doi:10.1038/ngeo477

Ringhausen, J. S., and Bitzer, P. M. (2021). An In-Depth Analysis of Lightning Trends in Hurricane Harvey Using Satellite and Ground-Based Measurements. *Geophys Res. Atmos.* 126, e2020JD032859. doi:10.1029/2020JD032859

Rodger, C. J., Werner, S., Brundell, J. B., Lay, E. H., Thomson, N. R., Holzworth, R. H., et al. (2006). Detection Efficiency of the VLF World-wide Lightning Location Network (WWLLN): Initial Case Study. *Ann. Geophys.* 24, 3197–3214. doi:10.5194/angeo-24-3197-2006

Rogers, R., Chen, S., Tenerelli, J., and Willoughby, H. (2003). A Numerical Study of the Impact of Vertical Shear on the Distribution of Rainfall in Hurricane Bonnie (1998). *Mon. Weather Rev.* 131, 1577–1599. doi:10.1175//2546.1

Rudlosky, S. D., and Shea, D. T. (2013). Evaluating WWLLN Performance Relative to TRMM/LIS. *Geophys. Res. Lett.* 40, 2344–2348. doi:10.1002/grl.50428

Samsury, C. E., and Orville, R. E. (1994). Cloud-to-ground Lightning in Tropical Cyclones: A Study of Hurricanes Hugo (1989) and Jerry (1989). *Mon. Weather Rev.* 122, 1887–1896. doi:10.1175/1520-0493(1994)122<1887:ctglit>2.0.co;2

Shao, X.-M., Harlin, J., Stock, M., Stanley, M., Regan, A., Wiens, K., et al. (2005). Katrina and Rita Were Lit up with Lightning. *Eos Trans. AGU* 86, 398. doi:10.1029/2005EO420004

Shu, S., Feng, X., and Wang, Y. (2018). Essential Role of Synoptic Environment on Rainfall Distribution of Landfalling Tropical Cyclones over China. *J. Geophys. Res. Atmos.* 123, 285–311. doi:10.1029/2018JD028842

Solorzano, N., Thomas, J., and Bracy, C. (2018). Monitoring Tropical Cyclones with Lightning and Satellite Data. *EOS* 99. doi:10.1029/2018EO092439

Squires, K., and Businger, S. (2008). The Morphology of Eyewall Lightning Outbreaks in Two Category 5 Hurricanes. *Mon. Weather Rev.* 136, 1706–1726. doi:10.1175/2007mwr2150.1

Stevenson, S. N., Corbosiero, K. L., and Molinari, J. (2014). The Convective Evolution and Rapid Intensification of Hurricane Earl (2010). *Mon. Weather Rev.* 142, 4364–4380. doi:10.1175/mwr-d-14-00078.1

Stevenson, S. N., Corbosiero, K. L., and Abarca, S. F. (2016). Lightning in Eastern North Pacific Tropical Cyclones: A Comparison to the North Atlantic. *Mon. Weather Rev.* 144, 225–239. doi:10.1175/mwr-d-15-0276.1

Stevenson, S. N., Corbosiero, K. L., DeMaria, M., and Vigh, J. L. (2018). A 10-year Survey of Tropical Cyclone Inner-Core Lightning Bursts and Their Relationship to Intensity Change. *Weather Forecast* 33, 23–36. doi:10.1175/waf-d-17-0096.1

Susca-Lopata, G., Zawislak, J., Zipser, E. J., and Rogers, R. F. (2015). The Role of Observed Environmental Conditions and Precipitation Evolution in the Rapid Intensification of Hurricane Earl (2010). *Mon. Weather Rev.* 143, 2207–2223. doi:10.1175/mwr-d-14-00283.1

Thomas, J. N., Solorzano, N. N., Cummer, S. A., and Holzworth, R. H. (2010). Polarity and Energetics of Inner Core Lightning in Three Intense North Atlantic Hurricanes. *J. Geophys. Res.* 115, A00E15. doi:10.1029/2009JA014777

Vagasky, C. (2017). Enveloped Eyewall Lightning: the EEL Signature in Tropical Cyclones. *J. Oper. Meteor.* 05, 171–179. doi:10.15191/nwajom.2017.0514

Virts, K. S., Wallace, J. M., Hutchins, M. L., and Holzworth, R. H. (2013). Highlights of a New Ground-Based, Hourly Global Lightning Climatology. *Bull. Amer. Meteor. Soc.* 94, 1381–1391. doi:10.1175/bams-d-12-00082.1

Wang, F., Qie, X., Liu, D., Shi, H., and Srivastava, A. (2016). Lightning Activity and its Relationship with Typhoon Intensity and Vertical Wind Shear for Super Typhoon Haiyan (1330). *J. Meteorol. Res.* 30, 117–127. doi:10.1007/s13351-016-4228-x

Wang, F., Qie, X., Wang, D., and Srivastava, A. (2018). Lightning Activity in Tropical Cyclones and its Relationship to Dynamic and Thermodynamic Parameters over the Northwest Pacific. *Atmos. Res.* 213, 86–96. doi:10.1016/j.atmosres.2018.05.027

Whittaker, I. C., Douma, E., Rodger, C. J., and Marshall, T. J. C. H. (2015). A Quantitative Examination of Lightning as a Predictor of Peak Winds in Tropical Cyclones. *J. Geophys. Res. Atmos.* 120, 3789–3801. doi:10.1002/2014JD022868

Williams, E. R. (1988). The Electrification of Thunderstorms. *Sci. Am.* 259, 88–99. doi:10.1038/scientificamerican1188-88

Xia, R., Zhang, D.-L., and Wang, B. (2015). A 6-yr Cloud-To-Ground Lightning Climatology and its Relationship to Rainfall over Central and Eastern China. *J. Appl. Meteorol. Climatol.* 54, 2443–2460. doi:10.1175/jamc-d-15-0029.1

Xu, W., Jiang, H., and Kang, X. (2014). Rainfall Asymmetries of Tropical Cyclones Prior to, during, and after Making Landfall in South China and Southeast United States. *Atmos. Res.* 139, 18–26. doi:10.1016/j.atmosres.2013.12.015

Xu, W., Rutledge, S. A., and Zhang, W. (2017). Relationships between Total Lightning, Deep Convection, and Tropical Cyclone Intensity Change. *J. Geophys. Res. Atmos.* 122, 7047–7063. doi:10.1002/2017JD027072

Yokoyama, C., and Takayabu, Y. N. (2008). A Statistical Study on Rain Characteristics of Tropical Cyclones Using TRMM Satellite Data. *Mon. Wea. Rev.* 136, 3848–3862. doi:10.1175/2008mwr2408.1

Yu, Z., Wang, Y., Xu, H., Davidson, N., Chen, Y., Chen, Y., et al. (2017). On the Relationship between Intensity and Rainfall Distribution in Tropical Cyclones Making Landfall over China. *J. Appl. Meteorol. Climatol.* 56, 2883–2901. doi:10.1175/jamc-d-16-0334.1

Zhang, W., Zhang, Y., Zheng, D., and Zhou, X. (2012). Lightning Distribution and Eyewall Outbreaks in Tropical Cyclones during Landfall. *Mon. Weather Rev.* 140, 3573–3586. doi:10.1175/mwr-d-11-00347.1

Zhang, W., Zhang, Y., Zheng, D., Wang, F., and Xu, L. (2015). Relationship between Lightning Activity and Tropical Cyclone Intensity over the Northwest Pacific. *J. Geophys. Res. Atmos.* 120, 4072–4089. doi:10.1002/2014JD022334

Zhang, W., Hui, W., Lyu, W., Cao, D., Li, P., Zheng, D., et al. (2020a). FY-4A LMI Observed Lightning Activity in Super Typhoon Mangkhut (2018) in Comparison with WWLLN Data. *J. Meteorol. Res.* 34, 336–352. doi:10.1007/s13351-020-9500-4

Zhang, W., Zhang, Y., Zheng, D., and Lyu, W. (2020b). Quantifying the Contribution of Tropical Cyclones to Lightning Activity over the Northwest Pacific. *Atmos. Res.* 239, 104906. doi:10.1016/j.atmosres.2020.104906

Conflict of Interest: The authors declare that the research was conducted in the absence of any commercial or financial relationships that could be construed as a potential conflict of interest.

Publisher's Note: All claims expressed in this article are solely those of the authors and do not necessarily represent those of their affiliated organizations, or those of the publisher, the editors and the reviewers. Any product that may be evaluated in this article, or claim that may be made by its manufacturer, is not guaranteed or endorsed by the publisher.

frontiers | Frontiers in Earth Science

TYPE Original Research
PUBLISHED 10 August 2022
DOI 10.3389/feart.2022.940418

OPEN ACCESS

EDITED BY
Guihua Wang,
Fudan University, China

REVIEWED BY
Lin Deng,
Shanghai Typhoon Institute, China Meteorological Administration, China
Yuanlong Li,
Nanjing University, China
Ruifen Zhan,
Fudan University, China

*CORRESPONDENCE
Na Wei,
weina@cma.gov.cn

SPECIALTY SECTION
This article was submitted to Atmospheric Science, a section of the journal Frontiers in Earth Science

RECEIVED 10 May 2022
ACCEPTED 13 July 2022
PUBLISHED 10 August 2022

CITATION
Zhang X, Wei N and Wang Q (2022), Influence of radiation diurnal variation on the rapid intensification process of super Typhoon Rammasun (1409) in the South China Sea.
Front. Earth Sci. 10:940418.
doi: 10.3389/feart.2022.940418

Influence of radiation diurnal variation on the rapid intensification process of super Typhoon Rammasun (1409) in the South China Sea

Xinghai Zhang[1], Na Wei[2,3]* and Qian Wang[4,5]

[1]China Electronic Technology Group Corporation, Glarun Group Co., Ltd., Nanjing, China, [2]Nanjing Joint Institute for Atmospheric Sciences, Nanjing, China, [3]State Key Laboratory of Severe Weather, Chinese Academy of Meteorological Sciences, Beijing, China, [4]Department of Atmospheric and Oceanic Sciences, Fudan University, Shanghai, China, [5]National Meteorological Center, Beijing, China

In this study, a sensitivity experiment based on a numerical model is conducted to study the influence of the diurnal variation of radiation on the rapid intensification process of Super Typhoon Rammasun (1409) in the South China Sea. The result shows that changing the radiation process can change the onset time of the rapid intensification process of the typhoon and its maximum intensity. Vertical wind shear is a key factor in the TC rapid intensification influenced by diurnal radiation cycle, and the diurnal variation of radiation process causes obvious diurnal variation in vertical wind shear by changing the thermal difference between sea and land. The oscillation of vertical wind shear promotes the diurnal variation of the typhoon rainband, with an opposite variation trend in the control and sensitivity experiments, affecting the local convective available potential energy and inward transport of entropy and thus influencing the onset time of deep convective in the typhoon inner core region. By changing the establishment of the typhoon warm core (especially the upper-level warm core), deep convections finally affect the rapid intensification of the typhoon.

KEYWORDS

diurnal variations, South China sea, typhoon, rapid intensification, vertical wind shear

1 Introduction

The diurnal variation of radiation can affect the structure and intensity of tropical cyclones (TCs). It has been found that TC clouds and convection are active in the morning and inactive in the evening when the TC is offshore (Kossin 2002; Dunion et al., 2014). Shu et al. (2013) found that 70% of TC precipitation in the Northwest Pacific exhibits diurnal variability, with the precipitation peak occurring at 06:00 a.m. (local time), which is particularly pronounced during the TC weakening stage. This diurnal variation feature is also influenced by the underlying surface, with the precipitation peak advancing to midnight as the TC moves inland (Bowman et al., 2015). In addition, the diurnal variation

amplitude of the precipitation in the outer region of the typhoon is larger than that of the inner-core precipitation (Hu et al., 2017). Zhang and Xu (2022) revealed that the TC clouds and the diurnal variation of the TC precipitation have outward propagation characteristics, and they are coupled with deep convections.

In addition to typhoon precipitation, the diurnal variation of radiation may affect the TC intensification process. Yaroshevich and Ingel (2013) found that the TC intensification rate in the Northwest Pacific is greater at night than that in the daytime. Sun et al. (2021) counted the number of typhoon convection overshooting in satellite images. They found that the deep convection of strong typhoons and rapidly intensifying typhoons are more active than that of general typhoons, and this deep convection phenomenon is usually stronger in the morning and weaker in the evening. Melhauser and Zhang (2014) investigated the effects of diurnal variations in humidity and radiation on the TC intensity by using numerical simulation, and they suggested that the increased atmospheric static instability due to radiative cooling at night contributed to the TC intensification. Tang and Zhang (2016) proposed that the radiative cooling at night increases ambient relative humidity and atmospheric instability, which promotes active convection at night. On the contrary, the radiative heating near the sea surface during the daytime results in an inversion layer at lower levels and a further reduction in the sea surface heat flux, thereby suppressing convective activity. However, Duran and Molinari (2016) did not find diurnal variations in mean static stability based on an observational study. They also proposed that in terms of mature TCs, the Richardson number at the upper layers is small in the early morning due to radiative cooling and troposphere elevation, which can reduce the upper-level stability and promote convection. Therefore, studies on the influence mechanism of the diurnal variation of radiation on the TC intensity and structure need to be more in-depth.

The above studies prove that TC structure and intensity are obviously influenced by the diurnal variation of radiation. Currently, most studies focused on the impact on typhoons in the thermal perspective, i.e., the effects of environmental factors such as temperature and humidity variations on typhoons caused by the diurnal variation of radiation. Fewer studies were conducted on the influence mechanism of the diurnal variation of radiation on the typhoons in terms of dynamic factors, especially for offshore rapidly intensifying typhoons. The super typhoon Rammasun (1409) underwent rapidly intensification in the northern South China Sea in monsoon season. The monsoon flow not only provided abundant moisture transport but also changed the vertical wind shear which is the important dynamic environment factor for TC intensity change. In this research, we use numerical simulation to study the influence mechanism of the diurnal variation of radiation on the rapid intensification process of Typhoon Rammasun focusing on the dynamical factors. The remainder of this paper is organized as follows. Section 2 briefly introduces the data and methods used in this study. Section 3 presents the result analysis. The main conclusion are shown in Section 4.

2 Data and methods

2.1 Case overview

Super Typhoon Rammasun (1409) in 2014 is selected as a study case. This typhoon was generated in the western North Pacific Ocean and moved westward. At 09:00 UTC on July 15, it landed in the central Philippines as a super typhoon. At 00:00 UTC on July 16, Typhoon Rammasun entered the South China Sea. Typhoon Rammasun strengthened again in the north of the South China Sea, about 500 km far from Hainan Island, with the maximum wind speed increasing from 95 kt to 140 kt within 24 h, meeting the rapidly intensifying standard of typhoons (i.e., 30 kt per 24 h defined by Kaplan and DeMaria, 2003) and reaching the maximum intensity in its lifecycle before landing on Hainan. According to the records of the Joint Typhoon Warning Center (JTWC), the maximum near-surface wind speed of Typhoon Rammasun reached 140 kt (72 m/s), and the central minimum surface pressure was 918 hPa. Hence, Typhoon Rammasun is the strongest typhoon in 2014, and it is also the strongest landing typhoon in China since 1973 (Wang et al., 2019).

2.2 Model and data

The model used in this study is the Typhoon Regional Assimilation and Prediction System developed by the Chinese Academy of Meteorological Sciences. This system adds a dynamic initialization scheme based on the Advanced Research Weather Research and Forecasting (WRF-ARW) model (Liu et al., 2018). In the control experiment, the model adopts a three-nested grid with horizontal resolutions of 18 km × 18 km, 6 km × 6 km, and 2 km × 2 km and grid points of 310 × 250, 270 × 270, and 210 × 210. Among them, the second and third nested grids are mobile nests. The number of vertical layers in the model is 50, and the model top is at 10 hPa. The physical schemes used in this system include the Kain-Fritsch cumulus convective parameterization scheme (Kain, 2004), WRF Single-Moment 6-class cloud microphysics scheme (Hong and Lim, 2006), Bougeault and Lacarrere boundary layer scheme (Bougeault and Lacarrere, 1989) and Dudhia radiation scheme (Dudhia, 1989). Note that the cumulus convective parameterization scheme is only used in the first nest. The simulation period of control experiment is from 00:00 UTC on July 16 to 00:00 UTC on July 19. The initial and boundary conditions used in this system are obtained from the Final analysis

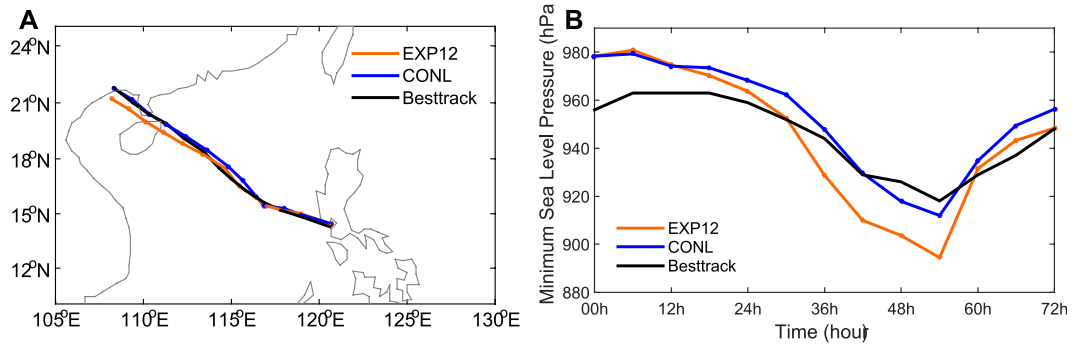

FIGURE 1
The simulated **(A)** track and **(B)** intensity change. "CONL" and "EXP12" denote simulations from the control and sensitivity experiments, respectively, "Besttrack" indicates observations from the joint typhoon warning center tropical cyclone best-track data.

data of the global forecast system released by the National Centers for Environmental Prediction.

2.3 Sensitivity experiment

A sensitivity experiment is performed as a comparison of the control experiment. In the sensitivity experiment, the model initiation file's time is modified from 00:00 UTC on July 16 to 12:00 UTC on July 16, delayed for 12 h, while the initial field, boundary conditions and physical schemes are set the same as in the control experiment. Therefore, the differences between the control and sensitivity experiments are the 12-h difference in the initiation time and the radiation conditions, i.e., the difference between the two experiments only comes from the diurnal variation of radiation. Note that the surface sea temperature is not changed in two sensitivity experiments since the model is initialized and running using the daily-observed surface sea temperature, which eliminates the differences induced by the underlying surface.

3 Result analysis

3.1 Track and intensity of Typhoon Rammasun

The simulations of the TC track and intensity (Figure 1) show that the simulated track is slightly more southward in the sensitivity experiment than in the control experiment. However, both the simulated tracks are highly consistent with the JTWC best-track data, indicating less variation in the steering flow. In terms of the TC intensity, the rapid intensification of the TC occurs earlier in the sensitivity experiment than in the control experiment, and the intensification rate after 30-h integration is markedly larger in the sensitivity experiment than that in the control experiment. The final sea level pressure in the sensitivity experiment is lower than that in the control experiment by about 20 hPa. Therefore, altering the radiation condition alone can change the TC intensification process noticeably.

3.2 Inner-core structure of the typhoon

The difference of the TC intensification process is related to the inner-core structure of the typhoon. The warm-core temperature anomalies are obtained by subtracting the average temperature within a 500-km radius from the average temperature within a 10-km radius near the TC center. Comparing the variation of the warm-core temperature anomalies with height and time, we find a vertical double warm-core structure in both the control and sensitivity experiments (Figures 2A,B). The low-level warm-core height is about 6 km, and the upper-level warm-core height is about 15 km. The warm-core temperature anomalies are higher in the sensitivity experiment than in the control experiment, and this phenomenon is consistent with the difference in TC intensity between the two experiments. Moreover, the upper-level warm core in the sensitivity experiment is established much rapidly than in the control experiment. In sensitivity experiment, the temperature anomaly at 16 km altitude increases rapidly from ~5 K at 30 h to more than 12 K at 36 h while increases to 8 K at 36 h in control simulation. The development of upper-level warm core is conductive to the rapid decrease of the pressure in the TC center.

To study the relationship between the surface pressure and ware-core structure, we introduce the following equation (Eq. 1).

$$\Delta P_s = -\frac{P_s}{T_v(P_s)} \int_{P_s}^{P_t} \Delta T_v \mathrm{d}\ln P \tag{1}$$

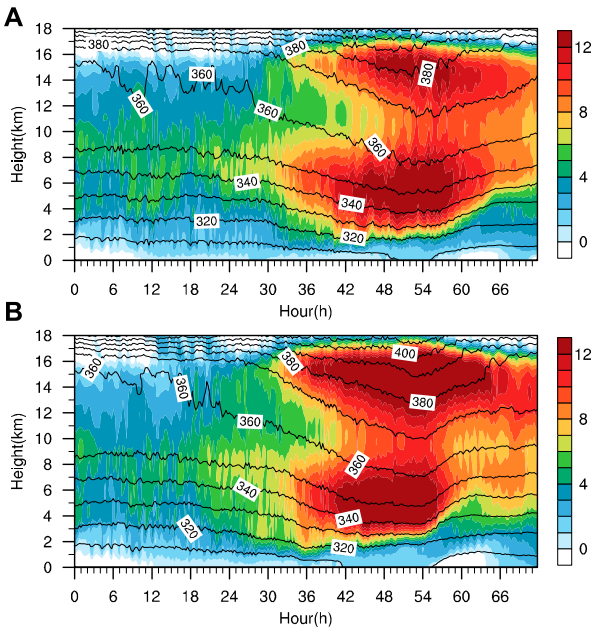

FIGURE 2
Comparison of the warm-core structure in the **(A)** control and **(B)** sensitivity experiments. Colored areas present the warm-core temperature anomalies, and contours denote the average potential temperature in the region within a 10 km radius from the TC center (Unit: K).

where P_s denotes the surface pressure, T_v the virtual temperature, P_t the top pressure, ΔT_v the perturbed virtual temperature and ΔP_s the perturbed surface pressure. Eq. 1 is obtained by the vertical integration of the static and state equations, first proposed by Hirschberg and Fritsch (1993) and independently derived by Holland (1997). This formula has been used several times in studies on TC warm core (Stern and Nolan 2012; Zhang and Chen 2012; Chen and Zhang 2013). Eq. 1 indicates that when the upper-level perturbed temperature increases, the corresponding surface pressure decreases. Moreover, d$\ln P$, as a weighting function, increases continuously with increasing height. Therefore, the influence of upper-level heating on the surface pressure is greater than that of low-level heating (Zhang and Chen 2012; Chen and Zhang 2013).

The diagnosis is performed by using Eq. 1. The temperature and pressure perturbations are defined as the average value in the region within a 10 km radius from the TC center minus the average value in the region within a 500 km radius. For the Hybrid diagnosis, the temperature perturbation below 10 km height from the warm core structure uses the results from the control experiment, and temperature perturbation above 10 km height is the results from the sensitivity experiment.

Figure 3 indicates that the diagnostic equation (Eq. 1) can well reproduce the rapidly intensifying process of the TC compared with the simulations (the control and sensitivity experiments). The diagnostic surface pressure perturbation is higher than the simulations. Overall, the warm-core structure is the main reason for the decrease of surface pressure in the TC center since the diagnostic results are highly consistent with the model simulations in both the control and sensitivity experiments. The Hybrid diagnostic result is almost consistent with the rapid intensification in the sensitivity experiment, demonstrating that the advance establishment of the upper-level warm core is the main reason for the advance occurrence of the TC rapid intensification in the sensitivity experiment.

The formation of upper-level warm core is mainly associated with descending airflow. The overflow from the inner-core convective bursts sinking along the typhoon eyewall plays a key role in establishing the upper-level warm core (Chen and Zhang 2013).

In this study, convective burst is defined as the maximum vertical velocity exceeding 7.5 m s^{-1} at 2–12 km altitude (Wang and Wang 2014). In addition, we count the number of grid points satisfying the definition of the convective burst within the TC core area. Figure 4 shows the number distribution of the convective bursts. The maximum wind speed radii at 2 and 8 km altitudes show decreasing trends during the TC intensification stage (integration of 24–36 h). Convective bursts are mainly near the maximum wind speed radius at 8 km altitude, especially during the rapid intensification stage of the TC. Convective bursts in the control experiment start to increase after about 30-h integration, while in the sensitivity experiment, convective bursts start to be active after 24-h integration, earlier than that in the control experiment. The development of the upper-level warm core lags behind the convective bursts, and the enhancement process of the upper-level warm core in the control experiment also occurs with a lag compared with that in the sensitivity experiment. Therefore, it can be assumed that the earlier occurrence of convective bursts in the sensitivity experiment leads to the establishment of the upper-level warm core in advance, which contributes to the earlier occurrence of the TC intensification process.

From the evolution of the radar reflectivity at 1 km altitude (Figure 5), it is noted that for the 72-h simulation, the rainband simulated in the control experiment shows three active periods, i.e., at 18–30 h and 42–54 h of integration and after 66 h of integration, with a cycle of about 24 h. The rainband simulated in the sensitivity experiment is active at 30–42 h and 54–66 h of integration, with a cycle also approximating 24 h. The time difference in the active rainband between the two experiments is about 12 h, suggesting that the activity of the rainband has an obvious diurnal variation feature, which may be influenced by the radiation process.

The TC rainband activities from both the control experiment and sensitivity experiment (Figure 6, at 6-h intervals) show an

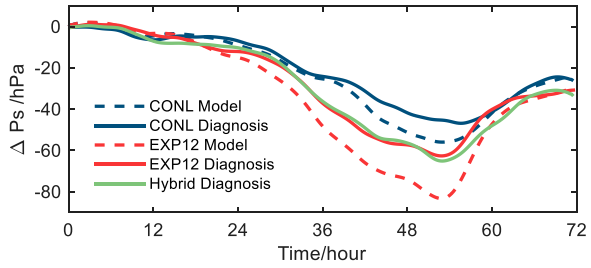

FIGURE 3
The diagnosis of the relationship between the warm core and decrease in the surface pressure. The solid lines indicate the Hybrid diagnostic results (green) and the diagnostic results from the control (CONL; blue) and sensitivity (EXP12; red) experiments, and the dashed lines denote the numerical simulations from the control (CONL; blue) and sensitivity (EXP12; red) experiments.

obvious diurnal variation feature, i.e., they are most active in the early morning (Figures 6A,E,H) and the weakest in the evening (Figures 6C,F,J), which is consistent with the finding of previous studies (Kossin 2002; Dunion et al., 2014; Sun et al., 2021). In the control experiment, the outer rainband is in the weakening stage at 30–36 h of integration when the inner-core convective bursts start to be active near the maximum wind speed radius (Figure 3A).

Wang and Wang (2014) found a close relationship between convective bursts and the low-level slantwise convective available potential energy (SCAPE) through numerical simulations of Typhoon Megi (1013). Since the conventional convective available potential energy (CAPE) is integrated along the vertical direction, and the path of upward motion of air particles is slantwise, the CAPE of the mature TC may be underestimated. The calculation of the SCAPE is similar to that of the CAPE, except that the integration of the SCAPE is performed along the isometric angular momentum line, which is consistent with the outward-inclined feature of the eyewall of the mature TC.

In Figure 7, it can be found that a large amount of energy is accumulated in the TC eyewall region between 6 and 33 h of integration. As the TC intensity increases, the eye region is gradually controlled by descending airflow after 36 h of integration, and the SCAPE decreases, while the subsidence warming leads to the enhancement of the warm core (Figure 2). Note that the SCAPE in the eyewall area at 6–18 h of integration in both the control and sensitivity experiments shows an increasing trend, and the large-value range of the SCAPE expands outward with time. In addition, the SCAPE outside the eyewall area has diurnal variation characteristics. For example, the SCAPE in the control experiment shows a complete trend of decreasing and then increasing at 18–42 h of integration.

Li and Wang (2012) proposed that the CAPE is consumed during rainband active period and recovers in the boundary layer during the rainband inactive period, and the cycle of this CAPE variation process is about 24 h. However, there is no diurnal variation of radiation in Li and Wang (2012), and unlike in the present study, their 24–h cycle is due to the internal dynamics of TCs. That means the diurnal variation of TC may be a combination of external forcing and internal factors.

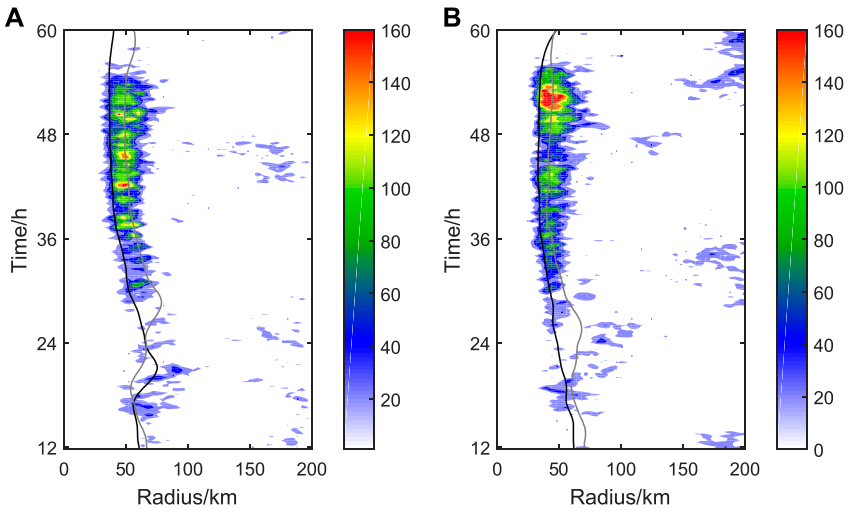

FIGURE 4
Convective burst number (colored area) and maximum wind speed radius (line) in the **(A)** control and **(B)** sensitivity experiments. Black and gray lines indicate the maximum wind speed radius at 2 and 8 km altitudes, respectively.

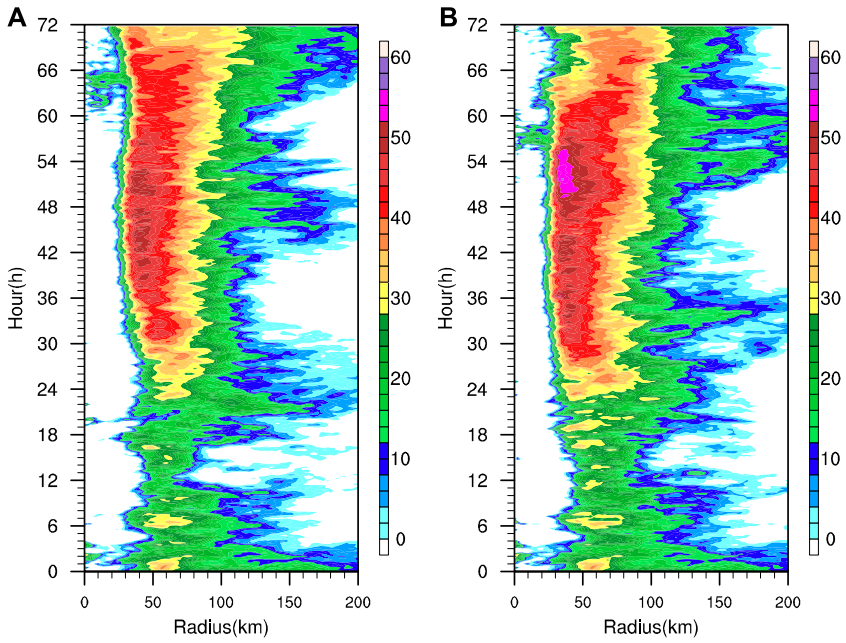

FIGURE 5
Radius-time profiles of the radar echo at 1 km altitude in the **(A)** control and **(B)** sensitivity experiments.

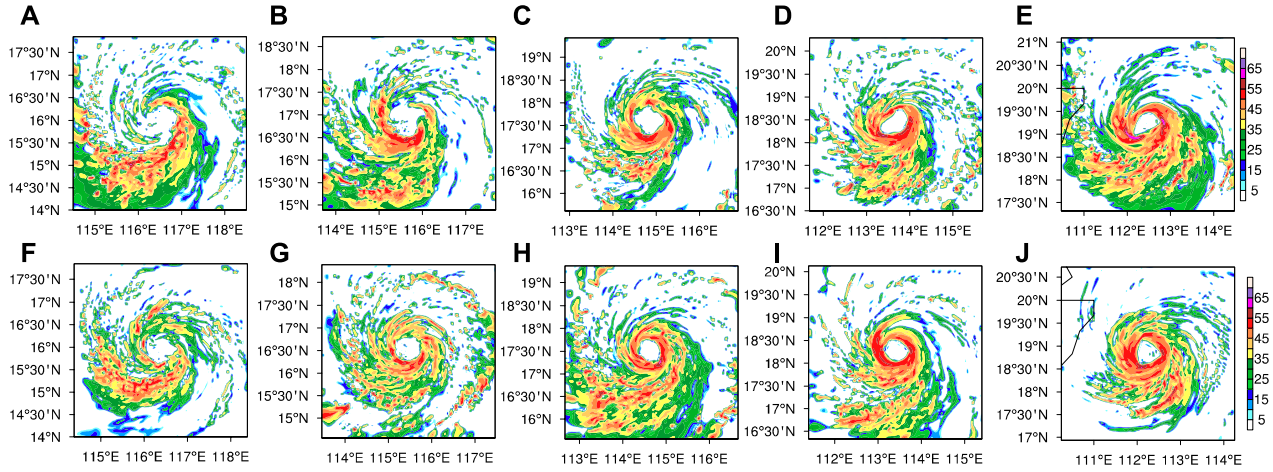

FIGURE 6
Radar reflectivity at 1 km altitude from 24-h integration to 48-h integration in the **(A–E)** control and **(F–J)** sensitivity experiments (Unit: dBZ) with time interval of 6 h.

In the control experiment, the SCAPE decreases rapidly in the area outside the 80 km radius from the TC center at 18–30 h of integration (corresponding to the rainband active period; Figure 5). However, the SCAPE in the sensitivity experiment is in the accumulation phase in the above area and period (Figure 7B), which corresponds to the rainband inactive period in the sensitivity experiment, indicating that the rainband activity can consume local SCAPE. According to Gu et al. (2015), the rainband convections which is induced by strong VWS will lead to downdraft bringing middle-level low-entropy air into boundary layer and may transport low moist enthalpy inward which is negative to deep convections within eyewall.

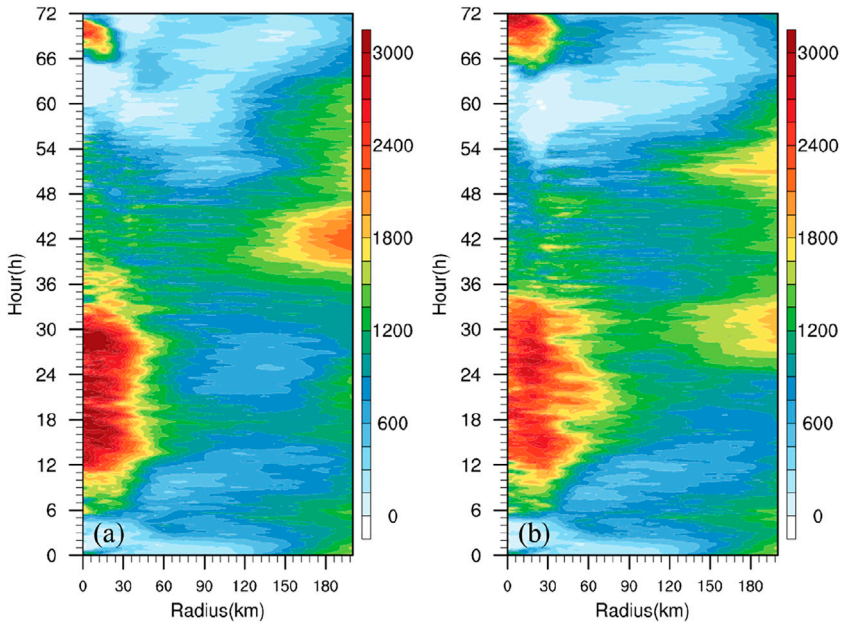

FIGURE 7
Radius-time profiles of the slantwise convective available potential energy (SCAPE) in the **(A)** control and **(B)** sensitivity experiment.

The previous study indicated that the ambient energy transport has an important supporting role for the inner-core convection, considering that the convection in the eyewall and inner-core areas requires energy consumption (Zhang et al., 2017). Due to consuming SCAPE, the outer rainband activity is detrimental to the inner-core convection. On the one hand, the rainband convection activity consumes local energy, and thus it reduces energy transport, which can suppress deep convections within the inner-core area. On the other hand, the dry and cold descending airflow brought by convection enters the boundary layer, further reducing the SCAPE and the energy transport into the inner-core area. Therefore, in the control experiment, the rainband is inactive after 30 h of integration, and the SCAPE recovers before the convective bursts near the maximum wind speed radius. In contrast, in the sensitivity experiment, because the rainband is inactive at 18–30 h of integration, the convective bursts increase after 24 h of integration, earlier than that in the control experiment, prompting the earlier establishment of the warm core.

In summary, the rainband activity cycles in the control and sensitivity experiments are about 24 h, while the rainband active period in the control experiment is about 12 h earlier than that in the sensitivity experiment. During 18–30 h of integration, the rainband is in the active period in the control experiment, leading to energy consumption. However, the rainband in the sensitivity experiment is inactive during this period. The active rainband can consume the local SCAPE, which is not conducive to the energy transport to the inner-core area, thus suppressing the inner-core convective bursts in the control experiment. The deep convective bursts in the sensitivity experiment are earlier than those in the control experiment, eventually leading to an earlier establishment of the upper-level warm core, the occurrence of TC rapid intensification in advance and the stronger maximum TC intensity.

3.3 Environmental field analysis

Previous studies demonstrated that the outer rainband activity is closely associated with environmental factors, among which vertical wind shear is considered to promote rainband activities, especially in the left quadrant of the downshear (Reasor et al., 2013; Gu et al., 2015). Vertical wind shear favors low-level inflow on the downshear side and low-level outflow on the upshear side. In this study, the ambient vertical wind shear is defined as the difference of the average wind velocity between 200 hPa and 850 hPa within the range of 200–800 km radius from the TC center, and its evolution is shown in Figure 8. The TC ambient vertical wind shear in the sensitivity experiment before 12 h of integration is almost identical to that in the control experiment because the initial fields are the same in the two experiments. In the control experiment, the ambient vertical wind shear starts to enhance in the late night under the influence of radiation forcing and reaches the maximum value in the early morning, with an obvious diurnal variation. The variation trend of the ambient vertical wind shear in the sensitivity experiment is opposite to that in the control experiment after 12 h of integration.

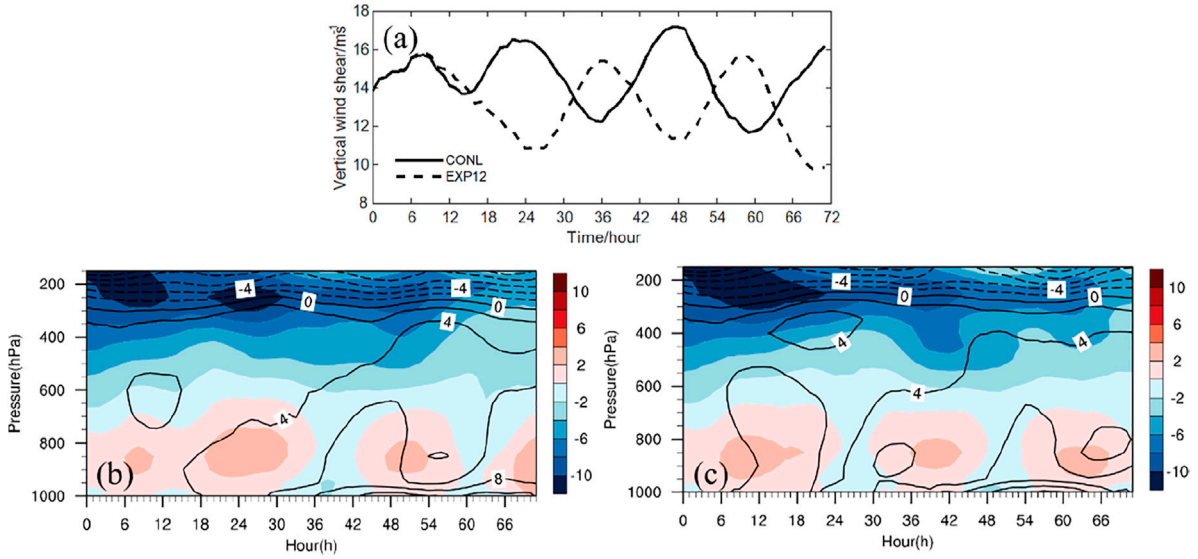

FIGURE 8
(A) Time series and pressure-time profiles of the ambient vertical wind shear in the control **(B)** and sensitivity experiments **(C)**. "CONL" and "EXP12" in Figure 8A denote the results from the control and sensitivity experiments, respectively, and the colored areas and contours in Figures 8B,C indicate the ambient zonal wind and meridional wind, respectively.

When the ambient vertical wind shear enhances (24–36 h of integration in the sensitivity experiment), the rainband is active during the period (Figure 6). Thus, the diurnal variation of the ambient vertical wind shear influences the diurnal variation of the rainband, further affecting the variation of the TC intensity.

Moreover, the average vertical wind shear in the sensitivity experiment is smaller than that in the control experiment, which can partially explain the stronger TC intensity in the sensitivity experiment than that in the control experiment.

To further investigate the variation of vertical wind shear, we analyze the ambient zonal wind and average meridional wind within the radius range of 200–800 km from the TC center. The diurnal variation of vertical wind shear is mainly contributed by the large variations of ambient zonal wind and meridional wind at low level (850 hPa). It is consistent with the observations in numerous studies (Terao et al., 2006; Chen et al., 2009; Chen and Zhang, 2013) which have indicated that the low-level southerly winds exhibit the strongest over southern China from midnight to predrawn. It is often explained by a combine of a clockwise rotation diurnally due to an inertial oscillation (Balckadar, 1957) and a planetary-scale land-sea breeze circulation produced by the couple of a diurnal change in pressure gradient induced by land-sea heating contrast (Holton, 1967) with the global-scale diurnal tide (Huang et al., 2010). Such breezes could cover ~1000 km away from coastline of East Asia and always become the largest in the monsoon season (Chen and Zhang, 2013; Chen, 2020). Note that the typhoon Rammasun occurred in July over South China Sea where experienced the largest breezes accordingly.

4 Conclusion

In this study, two comparison experiments are performed by changing the radiation conditions in numerical models to demonstrate that the diurnal variation of radiation can greatly influence the rapidly intensifying process of TC and its structure. We analyze the diurnal variation of the ambient vertical wind shear, rainband activities and upper-level warm core, and we propose a new explanation for the influence of the diurnal variation of radiation on the structures and intensification processes of TCs in the perspective of a dynamic factor (vertical wind shear).

Overall, the thermal difference between land and sea caused by the diurnal variation of radiation results in variations in the offshore ambient vertical wind shear. During summer, the offshore ambient vertical wind shear reaches the maximum in the early morning and the minimum in the evening. This shear can stimulate variations in rainband activities of TCs, i.e., the rainband is active in the early morning and inactive in the evening. The active rainband consumes the local SCAPE outside the eyewall and reduces the energy transport to the inner core region, thus affecting the inner-core energy accumulation and suppressing the inner-core convective activities, which

is not conducive to the establishment of TC warm core and affect the rapid intensification of TCs.

Unlike previous studies that focused on the influence of radiation on ambient thermal conditions, this study is based on a case in the perspective of dynamic factors. It is worth noting that the diurnal variation of radiation affects TC intensity and structure through the vertical wind shear only in the offshore region. Meanwhile, the diurnal variation process of radiation can also impact TCs by changing the thermal factors such as the ambient temperature and relative humidity. In offshore regions, the diurnal variations of both thermal and dynamical factors can influence TC activities, making TC intensity variations in offshore regions more complex and therefore requiring further investigation.

Data availability statement

The raw data supporting the conclusion of this article will be made available by the authors, without undue reservation.

Author contributions

XZ is the first author to make the main work of our research. NW is the corresponding author who provide the main idea of numerical model experiment and help to finish the manuscript. QW is the third author who help collect data and provide some advice to the paper.

Funding

This study is supported by the National Natural Science Foundation of China (42192554, 42175007), the National Key R&D Program of China (2020YFE0201900) and the program of an integrated platform for the integration of subjective and objective forecast in Meteorological Bureau of Jiangsu.

Conflict of interest

Author XZ was employed by the company China Electronic Technology Group Corporation, Glarun Group Co., Ltd.

The remaining authors declare that the research was conducted in the absence of any commercial or financial relationships that could be construed as a potential conflict of interest.

Publisher's note

All claims expressed in this article are solely those of the authors and do not necessarily represent those of their affiliated organizations, or those of the publisher, the editors and the reviewers. Any product that may be evaluated in this article, or claim that may be made by its manufacturer, is not guaranteed or endorsed by the publisher.

References

Blackadar, A. K. (1957). Boundary-layer wind maxima and their significance for the growth of nocturnal inversions. *Bull. Am. Meteorol. Soc.* 38, 283–290. doi:10.1175/1520-0477-38.5.283

Bougeault, P., and Lacarrere, P. (1989). Parameterization of orography-induced turbulence in a mesobeta-scale model. *Mon. Wea. Rev.* 117, 1872–1890. doi:10.1175/1520-0493(1989)117<1872:pooiti>2.0.co;2

Bowman, K. P., and Fowler, M. D. (2015). The diurnal cycle of precipitation in tropical cyclones. *J. Clim.* 28 (13), 5325. doi:10.1029/2009jd012181

Chen, G. (2020). Diurnal cycle of the asian summer monsoon: Air pump of the second kind. *J. Clim.* 33 (5), 1747–1775. doi:10.1175/jcli-d-19-0210.1

Chen, G., Sha, W., and Iwasaki, T. (2009). Diurnal variation of precipitation over southeastern China: 2. Impact of the diurnal monsoon variability. *J. Geophys. Res.* 114, D21105.

Chen, H., and Zhang, D. L. (2013). On the rapid intensification of Hurricane Wilma (2005). Part II: Convective bursts and the upper-level warm core. *J. Atmos. Sci.* 70 (1), 146–162. doi:10.1175/jas-d-12-062.1

Dudhia, J. (1989). Numerical study of convection observed during the winter monsoon experiment using a mesoscale two-dimensional model. *J. Atmos. Sci.* 46, 3077–3107. doi:10.1175/1520-0469(1989)046<3077:nsocod>2.0.co;2

Dunion, J. P., Thorncroft, C. D., and Velden, C. S. (2014). The tropical cyclone diurnal cycle of mature hurricanes. *Mon. Weather Rev.* 142 (10), 3900–3919. doi:10.1175/mwr-d-13-00191.1

Duran, P., and Molinari, J. (2016). Upper-tropospheric low Richardson number in tropical cyclones: Sensitivity to cyclone Intensity and the diurnal cycle. *J. Atmos. Sci.*, 73, 545–554. doi:10.1175/jas-d-15-0118.1

Gu, J-F., Tan, Z. M., and Qiu, X. (2015). Effects of vertical wind shear on inner-core thermodynamics of an idealized simulated tropical cyclone. *J. Atmos. Sci.* 72 (2), 511–530. doi:10.1175/JAS-D-14-0050.1

Hirschberg, P. A., and Fritsch, J. M. (1993). On understanding height tendency. *Mon. Weather Rev.* 121 (9), 2646–2661. doi:10.1175/1520-0493(1993)121<2646:ouht>2.0.co;2

Holland, G. J. (1997). The maximum potential intensity of tropical cyclones. *J. Atmos. Sci.* 54 (21), 2519–2541. doi:10.1175/1520-0469(1997)054<2519:tmpiot>2.0.co;2

Holton, J. R. (1967). The diurnal boundary layer wind oscillation above sloping terrain. *Tellus* 19, 199–205. doi:10.1111/j.2153-3490.1967.tb01473.x

Hong, S. Y., and Lim, J. O. J. (2006). The WRF single-moment 6-class microphysics scheme (WSM6). *J. Korean Meteorological Soc.* 42, 129–151.

Hu, H., Duan, Y., Wang, Y., and Zhang, X. (2017). Diurnal cycle of rainfall associated with landfalling tropical cyclones in China from rain gauge observations. *J. Appl. Meteorology Climatol.* 56 (9), 2595–2605. doi:10.1175/jamc-d-16-0335.1

Huang, W., Chan, J., and Wang, S. (2010). A planetary-scale land-sea breeze circulation in East Asia and the Western North Pacific. *Q. J. R. Meteorol. Soc.* 136, 1543–1553. doi:10.1002/qj.663

Kain, J. S. (2004). The Kain-Fritsch convective parameterization: An update. *J. Appl. Meteor.* 43, 170–181. doi:10.1175/1520-0450(2004)043<0170:tkcpau>2.0.co;2

Kaplan, J., and DeMaria, M. (2003). Large-scale characteristics of rapidly intensifying tropical cyclones in the north atlantic basin. *Weather Forecast.* 18, 1093–1108. doi:10.1175/1520-0434(2003)018<1093:lcorit>2.0.co;2

Kossin, J. P. (2002). Daily hurricane variability inferred from GOES infrared imagery. *Mon. Weather Rev.* 130 (9), 2260–2270. doi:10.1175/1520-0493(2002)130<2260:dhvifg>2.0.co;2

Li, Q., and Wang, Y. (2012). Formation and quasi-periodic behavior of outer spiral rainbands in a numerically simulated tropical cyclone. *J. Atmos. Sci.* 69, 997–1020. doi:10.1175/2011jas3690.1

Liu, Hao-Yan, Wang, Yuqing, Xu, Jing, and Duan, Yihong (2018). A dynamical initialization scheme for tropical cyclones under the influence of terrain. *Weather Forecast.* 33, 641–659. doi:10.1175/waf-d-17-0139.1

Melhauser, C., and Zhang, F. (2014). Diurnal radiation cycle impact on the pregenesis environment of Hurricane Karl (2010). *J. Atmos. Sci.* 71, 1241–1259. doi:10.1175/jas-d-13-0116.1

Reasor, P. D., Rogers, R., and Lorsolo, S. (2013). Environmental flow impacts on tropical cyclone structure diagnosed from airborne Doppler radar composites. *Mon. Weather Rev.* 141 (9), 2949–2969. doi:10.1175/mwr-d-12-00334.1

Shu, H., Zhang, Q., Xu, B., Steranka, J., Rodgers, E. B., and Gentry, R. C. (2013). Diurnal variation of tropical cyclone rainfall in the Western North Pacific in 2008–2010. *Atmos. Ocean. Sci. Lett.*, 6, 103–108. doi:10.1080/16742834.2013.11447064

Stern, D. P., and Nolan, D. S. (2012). On the height of the warm core in tropical cyclones. *J. Atmos. Sci.* 69 (5), 1657–1680. doi:10.1175/jas-d-11-010.1

Sun, L., Tang, X., Zhuge, X., Tan, Z.-M., and Fang, J. (2021). Diurnal variation of overshooting tops in typhoons detected by Himawari-8 satellite. *Geophys. Res. Lett.* 48 (21). doi:10.1029/2021gl095565

Tang, X., and Zhang, F. (2016). Impacts of the diurnal radiation cycle on the formation, intensity, and structure of Hurricane Edouard (2014). *J. Atmos. Sci.* 73 (7), 2871–2892. doi:10.1175/jas-d-15-0283.1

Terao, T., Islam, M. N., Hayashi, T., and Oka, T. (2006). Nocturnal jet and its effects on early morning rainfall peak over northeastern Bangladesh during the summer monsoon season. *Geophys. Res. Lett.* 33, L18806. doi:10.1029/2006gl026156

Wang, H., and Wang, Y. (2014). A numerical study of Typhoon Megi (2010). Part I: Rapid intensification. *Mon. Weather Rev.* 142 (1), 29–48. doi:10.1175/mwr-d-13-00070.1

Wang, Qian, Xu, Yinglong, Wei, Na, Wang, Shuai, and Hu, Hao (2019). Forecast and service performance on rapidly intensification process of typhoons Rammasun (2014) and hato (2017). *Trop. Cyclone Res. Rev.* 8, 18–26. doi:10.1016/j.tcrr.2019.07.002

Yaroshevich, M. I., and Ingel, L. K. (2013). Diurnal variations in the intensity of tropical cyclones. *Izv. Atmos. Ocean. Phys.* 49, 375–379. doi:10.1134/s0001433813040117

Zhang, D. L., and Chen, H. (2012). Importance of the upper-level warm core in the rapid intensification of a tropical cyclone. *Geophys. Res. Lett.* 39. doi:10.1029/2011gl050578

Zhang, Xinghai, Duan, Yihong, Wang, Yuqing, Wei, Na, and Hu, Hao (2017). A high-resolution simulation of supertyphoon Rammasun (2014) — Part I: Model verification and surface energetics analysis. *Adv. Atmos. Sci.* 34 (6), 757–770. doi:10.1007/s00376-017-6255-7

Zhang, Xinyan, and Xu, Weixin (2022). Is there an outward propagating diurnal signal in the precipitation of tropical cyclones. *Geophys. Res. Lett.* 49 (4), 1944–8007. doi:10.1029/2021gl097166

frontiers | Frontiers in Earth Science

TYPE Original Research
PUBLISHED 12 August 2022
DOI 10.3389/feart.2022.942846

OPEN ACCESS

EDITED BY
Begoña Artiñano,
Medioambientales y Tecnológicas, Spain

REVIEWED BY
Kazuaki Nishii,
Mie University, Japan
Yanzhen Qian,
Ningbo Meteorological Bureau, China
Runling Yu,
China Meteorological Administration, China

*CORRESPONDENCE
Suping Zhang,
zsping@ouc.edu.cn

SPECIALTY SECTION
This article was submitted to Atmospheric Science, a section of the journal *Frontiers in Earth Science*.

RECEIVED 13 May 2022
ACCEPTED 14 July 2022
PUBLISHED 12 August 2022

CITATION
Li X, Zhang S, Koračin D, Yi L and Zhang X (2022), Atmospheric conditions conducive to marine fog over the northeast Pacific in winters of 1979–2019.
Front. Earth Sci. 10:942846.
doi: 10.3389/feart.2022.942846

Atmospheric conditions conducive to marine fog over the northeast Pacific in winters of 1979–2019

Xinbei Li[1], Suping Zhang[1]*, Darko Koračin[2,3], Li Yi[1] and Xin Zhang[1]

[1]Physical Oceanography Laboratory, Qingdao Collaborative Innovation Center of Marine Science and Technology, Ocean-Atmosphere Interaction and Climate Laboratory, Ocean University of China, Qingdao, China, [2]Physics Department, Faculty of Science, University of Split, Split, Croatia, [3]Division of Atmospheric Sciences, Desert Research Institute, Reno, NV, United States

Observations show that the northeast Pacific (NEP) is a fog-prone area in winter compared with the northwest and central Pacific where fog rarely occurs in winter. By synthesizing observations and reanalysis results from 1979 to 2019, this study investigates the atmospheric circulation and marine atmospheric boundary layer structure associated with marine fog over the NEP in winter. Composite analysis shows that the eastern flank of the Aleutian low and the northwestern flank of the Pacific subtropical high jointly contribute to a northward air flow over the NEP. Under such conditions, warm and moist air flows through a cooler sea surface and facilitates the formation of advection-cooling fog. The air near the sea surface in foggy areas is cooled by the downward sensible heat flux. The smaller upward latent heat flux (~10 W m^{-2}) compared to the surrounding area (> 60 W m^{-2}) demonstrates that the moisture originates from the advection instead of local evaporation. The lower (at 925 to 875 hPa) and stronger (up to 0.08 K hPa^{-1}) inversion layer, compared with cloudy cases and the turbulence in the lower atmosphere (below 975 hPa), also promotes fog formation and evolution. Approximately 68% of all fog cases (42242) show positive differences between surface air temperature (SAT) and sea surface temperature (SST), while 32% are negative, during southerly winds. Composite analysis of the latter shows lower specific humidity above the inversion bottom compared to the former. Dry air enhances longwave radiative cooling from the fog top, favoring cooling of the fog layer, gradually causing SAT to fall below SST.

KEYWORDS

northeast Pacific, marine fog, atmospheric circulation, marine atmospheric boundary layer, longwave radiative cooling, ICOADS, ERA5, surface turbulence fluxes

1 Introduction

Marine fog occurs over oceans and coastal regions when tiny water droplets sustain in the atmospheric boundary layer and cause the degradation of atmospheric horizontal visibility to less than 1 km (Wang, 1985). The low visibility in marine fog may cause ship damages, casualties, and economic losses (Gultepe et al., 2007).

The midlatitude region of the northwest Pacific (NWP) is the foggiest area worldwide. The annual marine fog frequency (MFF) is up to 23% (Fu and Song, 2014) and reaches 59.8% in summer (June–August) (Dorman et al., 2017). The large-scale circulation associated with marine fog in the NWP has been analyzed in previous literature. Sugimoto et al. (2013) indicate that the strengthened Okhotsk high and suppression of the northward extension of the northern Pacific surface high (NPSH) were responsible for the declining trend of MFF during 1931–2010 at Kushiro, Hokkaido, in July. Zhang et al. (2015) suggest that the position and orientation of the NPSH is the most important factor influencing the MFF in the NWP.

In a cold season (November–February), fog rarely occurs over the NWP, and the MFF is close to zero, under the influence of the cold winter monsoon from the Asian continent (Wang, 1985). However, the MFF over the northeast Pacific (NEP) is higher than the MFF over the NWP, with a maximum of 11% (Figure 1). It is unclear why marine fog often occurs in winter in the NEP. Some of the differences are because of specifics of atmospheric forcing that generates a separation of the North Pacific (NP) in winter into the eastern and western parts. By using the EOF computation of NCEP/NCAR reanalysis data (Kalnay et al., 1996) for 1948–2011, Xia et al. (2016) showed distinct synoptic-scale eddy regions at 850 hPa in winter in the eastern and western Pacific.

NEP should be also viewed in the context of long-term variability of main parameters. Based on an analysis of century-long observations, Johnstone and Mantua (2014) show that there is a warming trend over the NEP in the coastal sea surface temperature (SST) and sensible heat flux, while their negative trends are over the north-central Pacific (NCP). They attributed the warming trends to changes in atmospheric conditions and low interdecadal variability in surface-level pressure anomalies. This should also bear importance on understanding the climatology of marine fog, its frequency, and possible trends.

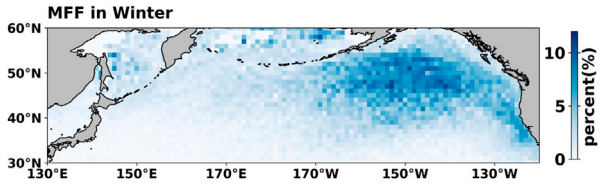

FIGURE 1
Spatial distribution of MFF (%) over the north Pacific in winter (derived from the ICOADS observations).

Previous studies indicate that marine fog can form over the cold sea surface under the conditions of abundant moisture supply and stable atmospheric stratification (Wang, 1985; Gao et al., 2007; Zhang et al., 2009). Marine stratus can convert to fog forced by synoptic-scale anticyclone in transient weather systems or the Pacific high (Koračin et al., 2001; Lewis et al., 2003). Studies such as those of Oliver et al. (1978), Koračin et al. (2005), and Yang et al. (2018) suggest that the longwave radiation cooling at the fog top plays an important role in advection fog. The physical processes for fog formation in the NEP in winter remain unclear so far.

In the present study, 40-year observations and reanalysis results were used to reveal the synoptic conditions and the marine atmospheric boundary layer (MABL) structure associated with marine fog over the NEP. The current study analyzes the main weather pattern affecting the formation of marine fog over the open water of the NEP in winter and how it controls the fog. Properties of the MABL structure are also investigated to reveal significant features of the fog compared to those of low clouds. These findings advance our knowledge of the physical mechanism of fog formation in the NEP in winter and help distinguish sea fog from low clouds since the influences of the two associated weather phenomena on human activities are different, which can be helpful for the improvement of boundary layer parameterization schemes and fog prediction in general.

The article is organized as follows: Following Section 1, Section 2 describes the data sets and the method. Section 3 analyzes the atmospheric circulation regarding the formation and evolution of fog. Section 4 examines the MABL structure during fog and low-cloud conditions to estimate the main determining essential features of fog. Section 5 discusses the cause of negative air–sea temperature differences. Section 6 provides a summary and discussion of the results.

2 Data and method

2.1 Data

To investigate the occurrence of sea fog, we used the present weather code from the International Comprehensive Ocean-Atmosphere Dataset (ICOADS) in IMMA (The International Maritime Meteorological Archive) format (Woodruff et al., 2011). The present weather code is an observer's subjective weather assessment with a two-digit code from 01 to 99 based on the rules of SYNOP (WMO, 2009) that characterizes the weather at the time of the observation. Code 40 to 49 indicates the

TABLE 1 The present weather code based on SYNOP rules.

Code	Weather	Comment
40	Fog or ice fog at a distance at the time of observation, but not at the station during the preceding hour, the fog or ice fog extending to a level above that of the observer	
41	Fog or ice fog in patches	
42	Fog or ice fog, sky visible	[42-43] has become thinner during the preceding hour
43	Fog or ice fog, sky invisible	
44	Fog or ice fog, sky visible	[44-45] no appreciable change during the preceding hour
45	Fog or ice fog, sky invisible	
46	Fog or ice fog, sky visible	[46-47] has begun or has become thicker during the preceding hour
47	Fog or ice fog, sky invisible	
48	Fog, depositing rime, sky visible	
49	Fog, depositing rime, sky invisible	

occurrence of fog. We used codes 46 and 47 to represent the existence of fog (Table 1). The dissipation stage of fog was excluded since the synoptic condition may be changed (Zhang et al., 2008; Guo et al., 2015). The study area covers 171°W-130°W, 39°N-55°N with a total of 42242 reported fog points (defined as fog cases). When referring to cases of low clouds, present weather code 03 was used with the cloud height indicator [1–8].

To investigate atmospheric circulations during marine fog, we used the fifth-generation reanalysis (ERA5) (Hersbach et al., 2020) provided by the European centre for medium-range weather forecasts (ECMWF). The ERA5 fields are on a 0.25° × 0.25° grid with 12 levels below 700 hPa. The spatial resolution is high enough to depict the large-scale atmospheric circulations and characterize their influence on the MABL (Yang et al., 2018). The time resolution is 1 h; therefore, the ERA5 can match ICOADS hour by hour.

2.2 Methods

Temperature inversions usually cap marine fog and exert a strong influence on the evolution of fog (Cao et al., 2007; Zhang et al., 2009; Yang et al., 2018). Following Cao et al. (2007), we identified the inversions between 1000 hPa and 800 hPa, corresponding approximately to the surface and 2000 m. All vertical profiles were divided into three layers: surface to inversion base, inversion base to inversion top, and inversion top to 800 hPa. We followed the scaling method of Norris (1998) to rescale the composite vertical profiles and capture the characteristics of the MABL.

Turbulence plays an important role in the formation of fog (Koračin et al., 2005; Guo et al., 2015; Huang et al., 2015). The bulk Richardson number (*Ri*) can be used as a measure of

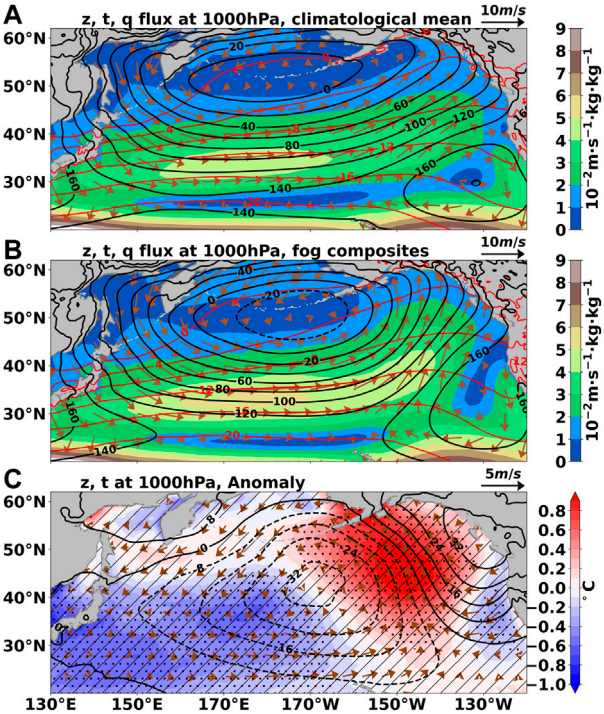

FIGURE 2
(A) Horizontal wind vectors (m·s^{-1}), geopotential height (black contour, gpm), temperature (red contour, °C), and water flux (shaded, in 10^{-2}m·s^{-1}·kg·kg^{-1}) at 1000 hPa in winter for the climate state. **(B)** Same as **(A)** but for NEP fog composite in winter **(C)** anomaly for the NEP fog composite: Geopotential height (black contour, in gpm), temperature (shaded, °C), and horizontal wind (vectors, m·s^{-1}). The black dots denote that the temperature anomaly is significant at the 95% confidence level based on the Student's *t*-test. The shade lines indicate the geopotential height anomaly significant at the 95% confidence level.

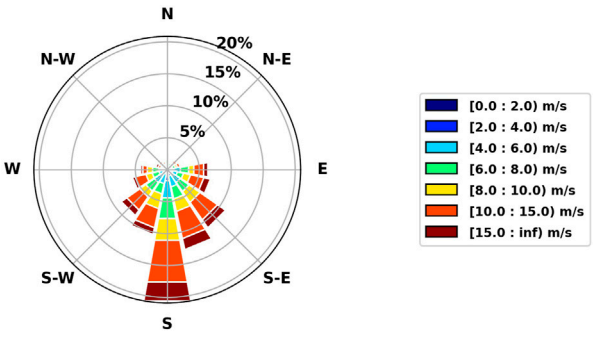

FIGURE 3
Surface wind rose diagrams (%) based on ICOADS observations during NEP fog in winter (1979–2019).

turbulence (Zhang et al., 2008; Huang et al., 2011; Kim and Yum, 2012):

$$Ri = \frac{g}{\theta} \frac{\Delta\theta/\Delta z}{(\Delta u/\Delta z)^2 + (\Delta v/\Delta z)^2}$$

where g is the gravitational constant, z is the reference level, θ is the potential temperature at the reference level, and u and v are the wind components at the reference level. The relative importance of static stability and dynamic instability is expressed by Ri. Arya (1972) proposed a value of 0.25 as the critical value for Ri, above which the air is no longer turbulent and mesoscale motions are important. Furthermore, if $Ri > 1$, then the air is statically and dynamically stable and no turbulence can occur. If $Ri < 0$, then the air is both statically unstable and dynamically unstable, and any disturbance can generate turbulence (Galperin et al., 2007).

The Student's t-test (Wilks, 1996) was applied to assess the statistical significance of the results in the composite analysis.

3 Synoptic background

3.1 Large-scale circulation

The NP weather is controlled by two semipermanent weather systems in winter climatology. One is the Aleutian Low, which brings persistent eastward winds to the midlatitude NCP at 1000 hPa (Figure 2A). Another is the NPSH, whose location shifts from the western to the eastern Pacific compared to summer (Zhang et al., 2015).

We calculated the composite large-scale circulation corresponding to the NEP fog based on the ERA5 reanalysis (Figure 2B). Results show that the circulation patterns of the fog composites differ from those of the climatological mean state. The area encircled by an isoline of 0 gpm extends southward, indicating a slight southward movement of the low-pressure center of the Aleutian Low. Meanwhile, the area encircled by an isoline of 160 gpm shrinks eastward. Such a circulation configuration contributes to abnormal southerly winds in fog areas. The southerly wind associated with the abnormal low pressure in the NCP carries more warm and moist air northward compared to conditions for the climatological mean state (Figures 2B,C).

Figure 3 shows surface wind rose diagrams based on the observations during NEP fog in winter. Almost all fog events are accompanied by southerly winds, consistent with the circulation pattern.

3.2 Air–sea interface

The difference between the surface air temperature (SAT) and the SST was used to represent the stability at the air–sea interface. The air and ocean properties of the narrow coastal region of North America differ from the open ocean westward in general (Figure 4). The SAT–SST anomaly in the offshore area is positive and greater than 0.8°C in most of the NEP fog region, indicating a stable air–sea interface, compared to the climatological mean state whose SAT–SST is negative in the NEP (Figure 4C). The SAT anomaly is positive with an abnormal southerly surface wind (Figure 4A), consistent with the circulation pattern (Figure 2C). The SST anomaly is less than 0.1°C and does not pass the significance test (Figure 4B). This condition indicates that the stable air–sea interface is dominated during these conditions.

The surface sensible heat flux (SHF) is dominantly downward and the surface latent heat flux (LHF) in the open ocean is upward in fog (Figures 4D,E). The sea surface continuously cools the marine fog as fog forms and develops (Figure 4D). The relatively low upward LHF (~10 W m^{-2}) in most of the fog areas indicates that local moisture supply from the sea surface is suppressed by the moist air from the south, compared to the surrounding area where LHF exceeds 60 W m^{-2} (Figure 4E).

The observations show that positive SAT–SST occurs in most fog cases (68%) (Figure 4F), which is consistent with the air–sea interface analysis above.

4 Marine atmospheric boundary layer structure

Both fog and clouds form when water vapor condenses or freezes in the air, forming tiny droplets or crystals. Sometimes they can convert to each other (Petterssen, 1936; Koračin et al., 2001; Kim and Yum, 2013). Figure 5 shows the distinct MABL structures between fog and low clouds over the NEP. For fog, the

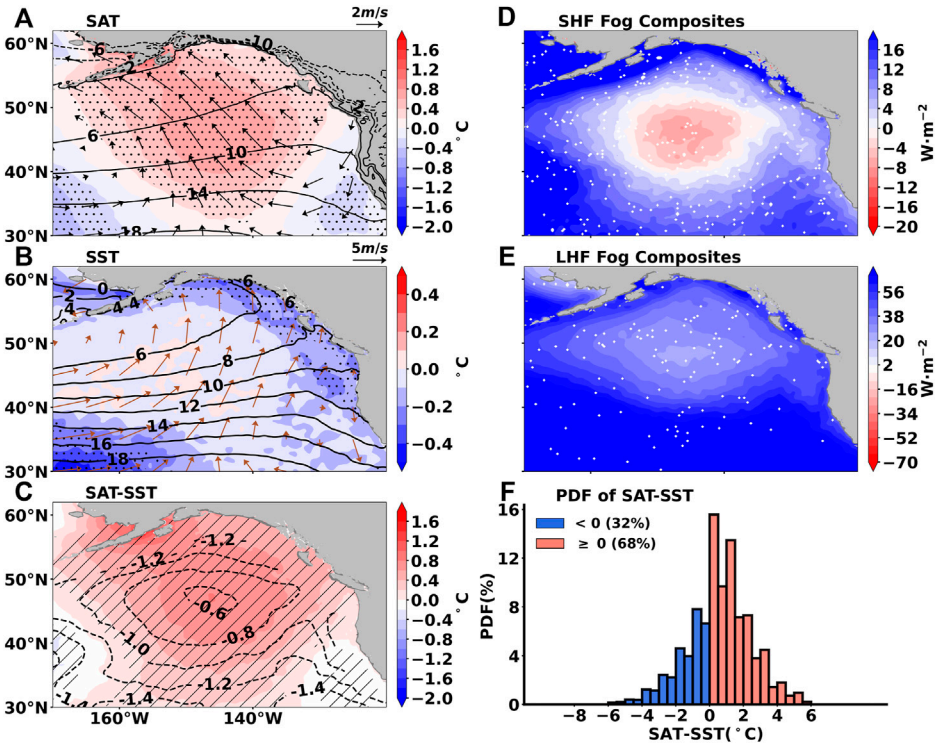

FIGURE 4
Air and ocean properties of the NEP fog. **(A)** Surface horizontal wind anomaly (vectors, m·s^{-1}), climatological mean SAT (black contour, °C), and SAT anomaly (shaded, °C); the black dots denote that the SAT anomaly is significant at the 95% confidence level. **(B)** Surface horizontal wind with fog (vectors, m·s^{-1}), climatological SST (black contour, °C), and SST anomaly (shaded, °C); the black dots indicate the SST anomaly significant at the 95% confidence level. **(C)** Climatological SAT–SST (black dashed contour, °C) and SAT–SST anomaly (shaded, °C); the shade lines indicate the SAT–SST anomaly significant at the 95% confidence level. **(D)** SHF with fog (shaded, W·m^{-2}). **(E)** LHF with fog (shaded, W·m^{-2}). **(F)** Probability density functions (%) of SAT–SST (°C).

inversion is found between 925 hPa and 875 hPa with a strength of 0.08 K hPa^{-1} (Figure 5A), while the inversion for low clouds is weaker (0.06 K hPa^{-1}) with a higher inversion base (900 hPa) (Figure 5C). The slope of the potential temperature (θ) as a function of height is positive for fog, indicating dry adiabatic stability. The θ below 950 hPa increases slightly, indicating a nearly mixing layer from 1000 hPa to 950 hPa in cases of low clouds. The slope of the saturated equivalent potential temperature (θ_{se}) is slightly negative for both fog and clouds below 975 hPa, indicating a wet adiabatic unstable stratification (Figures 5A,C).

Normalized frequency was used to highlight the differences between *Ri* ranges. The normalized frequency of an *Ri* range at a reference level x^* can be expressed as:

$$x^* = \frac{x - x_{min}}{x_{max} - x_{min}}$$

where x is the frequency of the *Ri* range, x_{max} is the maximum frequency in all of the *Ri* ranges, and x_{min} is the minimum frequency in all of the *Ri* ranges.

The *Ri* range of maximum frequency below 975 hPa is 0–0.25 for fog, whereas it is less than 0 for low clouds (Figures 5B,D). This indicates that the lower atmosphere is more unstable in cloudy cases compared to fog events, which is because of the unstable air–sea interface associated with the negative SAT–SST (Figure 6B).

The stability of the lower atmosphere is affected by the air–sea interaction (Cho et al., 2000; Heo and Ha, 2010; Huang et al., 2011; Koračin et al., 2014). We investigate the difference between the air–sea interface with low clouds and fog. The surface air in cases of low clouds is cooler compared to the cases of fog events (Figure 6A). It is the cooler surface air that leads to a negative SAT–SST (Figure 6B) because of the abnormal northwest wind, indicating weaker cooling or stronger warming of the air by the sea surface (Figure 6C). The upward LHF at the surface is greater because of less moist air, which is also related to the abnormal northwest wind (Figures 6D,E). There is a dipole morphology of the geopotential height anomaly with high west and low east, which causes the abnormal northwest wind (Figure 6E).

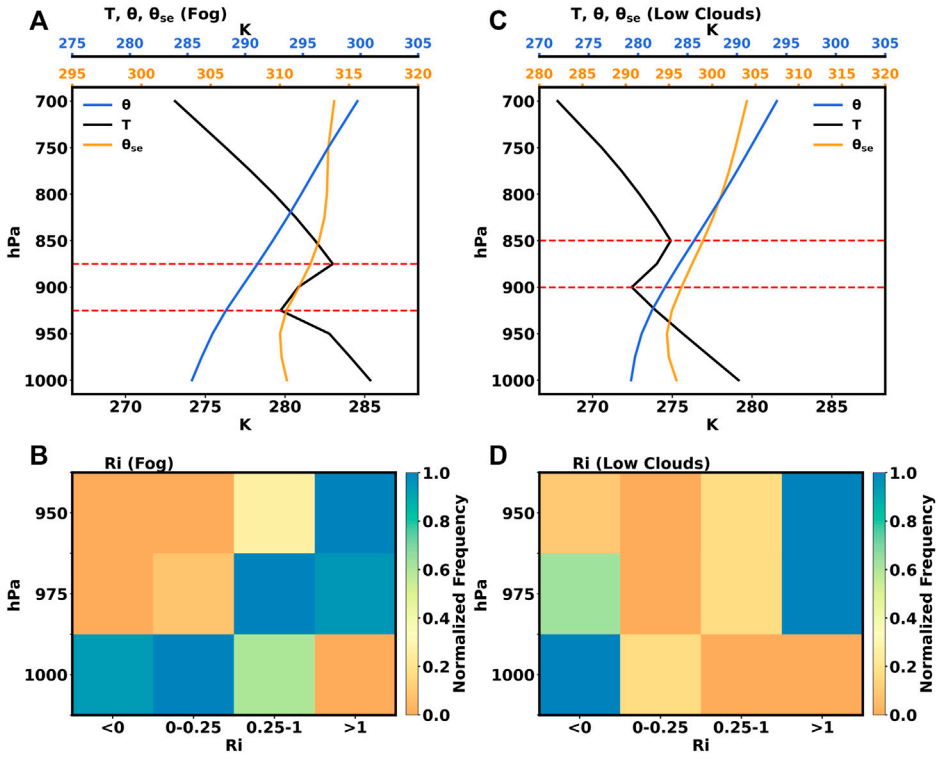

FIGURE 5
Composite profiles and the bulk Richardson number frequency distribution concurrent with fog **(A,B)** and low clouds **(C,D)**: temperature (*T*, black line, K), potential temperature θ(θ, blue line, K), saturated equivalent potential temperature θ_{se}(θ_{se}, orange line, K), and the bulk Richardson number (*Ri*, shaded). The red dashed lines denote the inversion layer.

5 The cause of the negative surface air temperature–sea surface temperature

It is notable that although most SAT–SST is positive during fog, there are approximately 32% of fog cases with a negative SAT–SST (Figure 4F). Fog resulting from the advection of colder air over the warm sea surface is called warm sea fog (Taylor, 1917). This type of fog formation stems from the advection of colder air over the warm sea where saturation occurs in response to the mixing of the cold and sufficiently moist air with warm/moist air (Koračin et al., 2014). Another type of fog associated with a warm sea surface is steam fog, which can occur when a stream of cold, dry air traverses a much warmer sea surface. Steam fog is always associated with extremely large (100s or more of W·m^{-2}) sensible and latent heat fluxes (Koračin et al., 2014).

To explore the causes of negative SAT–SST, we show in Figure 7 the differences between fog with negative and positive SAT–SST. The SST difference between the two kinds of fog is less than 0.1°C (Figure 7B). Moreover, both the specific humidity difference at 1000 hPa and the SAT difference between two kinds of fog are not significant in most areas (Figures 7A–C), suggesting that the lower atmosphere condition of fog with negative and positive SAT–SST is generally the same. Thus, these cases should not be considered warm sea fog. Both the SHF and LHF differences are less than 16 W m^{-2} (Figures 7D,E), which is not large enough to classify them as the steam fog mentioned above.

Yang et al. (2018) suggest that approximately 33% of the advection-cooling fog is with negative SAT–SST in the western Yellow Sea. As mentioned above, a similar phenomenon also occurs in the NEP. Under such circumstances, the sea surface can heat the air. Thus, the air–sea interface is divided into two states: air cooling by sea surface (ACSS) and air warming by sea surface (AWSS). The related expressions of "fog with ACSS" and "fog with AWSS" are used to name our fog cases. The different features between them are examined.

Figure 7F shows that for fog with AWSS, there is significantly abnormal high pressure at 850 hPa, suggesting abnormal sinking motion that can enhance thermal and moisture stratification between the MABL and the free atmosphere through adiabatic warming (Yang et al., 2018).

Figure 8 shows the surface wind rose diagrams based on the ICOADS observations during fog with ACSS and AWSS. The

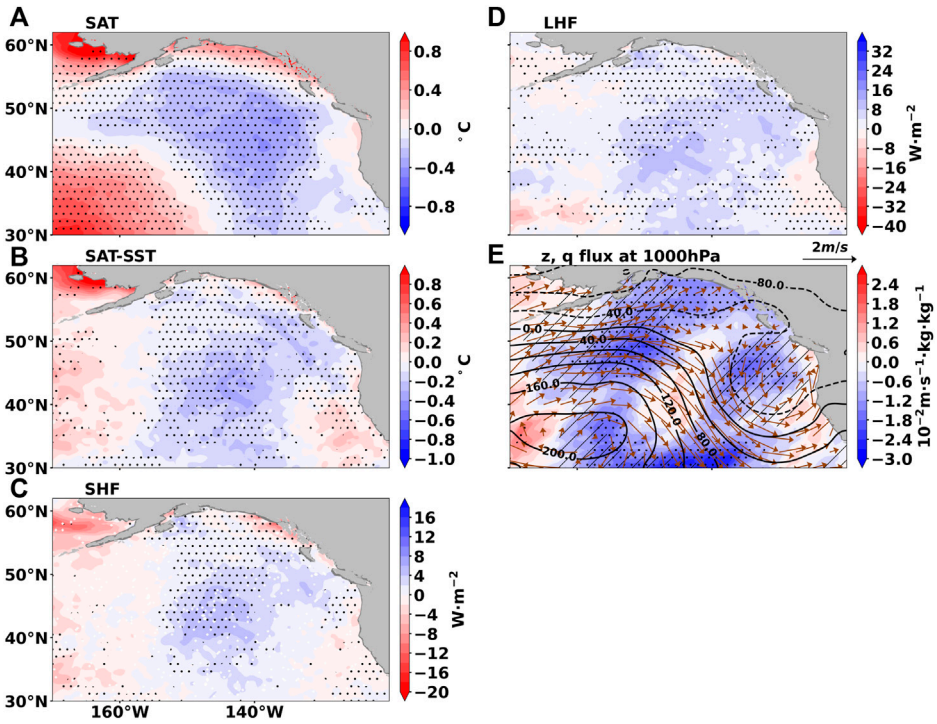

FIGURE 6
Difference between thermodynamic properties for cases of low clouds and fog. **(A)** SAT (shaded, °C), the black dots indicate the SAT difference significant at the 95% confidence level. **(B)** SAT−SST (shaded, °C); the black dots indicate the SAT−SST difference significant at the 95% confidence level. **(C)** SHF (shaded, W·m^{-2}); the black dots indicate the SHF difference significant at the 95% confidence level. **(D)** LHF (shaded, W·m^{-2}), the black dots indicate the LHF difference significant at the 95% confidence level. **(E)** Geopotential height (black contour, gpm), water flux (shaded, 10^{-2}m·s^{-1}·kg·kg^{-1}), and horizontal wind (vectors, m/s). The black dots indicate the water flux difference significant at the 95% confidence level. The shaded lines indicate the geopotential height difference significant at the 95% confidence level.

southerly wind dominates in both fog types. All the northerly winds occur in fog with AWSS. However, the frequencies and magnitudes are much smaller. The wind field is generally the same for fog with ACSS and fog with AWSS because the abnormal northerly wind is not significant in most areas (Figure 7C).

The MABL structures between fog with ACSS and that with AWSS are also compared (Figure 9). In general, results seem to be similar, but some differences exist. The inversion bottom of fog with AWSS is higher compared to fog with ACSS, indicating that the fog with AWSS may be thicker than fog with ACSS. The intensity of the inversion layer is the same. The slopes of θ as a function of height are both positive, indicating dry adiabatic stability. The θ_{se} profile shows that there are wet adiabatic unstable layers below 950 hPa in both types of fog. The top of the wet adiabatic mixing layer is at approximately 950 hPa for fog with ACSS, but at approximately 925 hPa for fog with AWSS (Figures 9B,D). The relative humidity for fog with AWSS decreases sharply upward beneath the inversion bottom. The relative humidity is approximately 0.7 for fog with AWSS but more than 0.8 for fog with ACSS at their inversion bottoms. It implies that the air is drier above the inversion bottom for fog with AWSS than for fog with ACSS (Figures 9C,F). This enhances longwave radiative cooling at the fog top. The difference between fog with ACSS and that with AWSS also shows that the specific humidity at 850 hPa is significantly low for fog with AWSS (Figure 7F), indicating a wide range of dry layers above the MABL that can enhance longwave radiative cooling.

Following the method proposed by Yang et al. (2018), the outgoing longwave radiation from the fog top was estimated by the upward longwave radiative flux at the top of atmosphere clouds and the Earth's radiant energy system. The average top of atmosphere upward longwave fluxes of fog with AWSS are 215 W m^{-2}, stronger than that of fog with ACSS (208 W m^{-2}).

Thus, fog with AWSS likely occurs during the developing and maintaining step of cold sea fog events because of longwave radiation from the fog top and turbulent mixing in the fog layer (Koračin and Dorman, 2017; Yang et al., 2018).

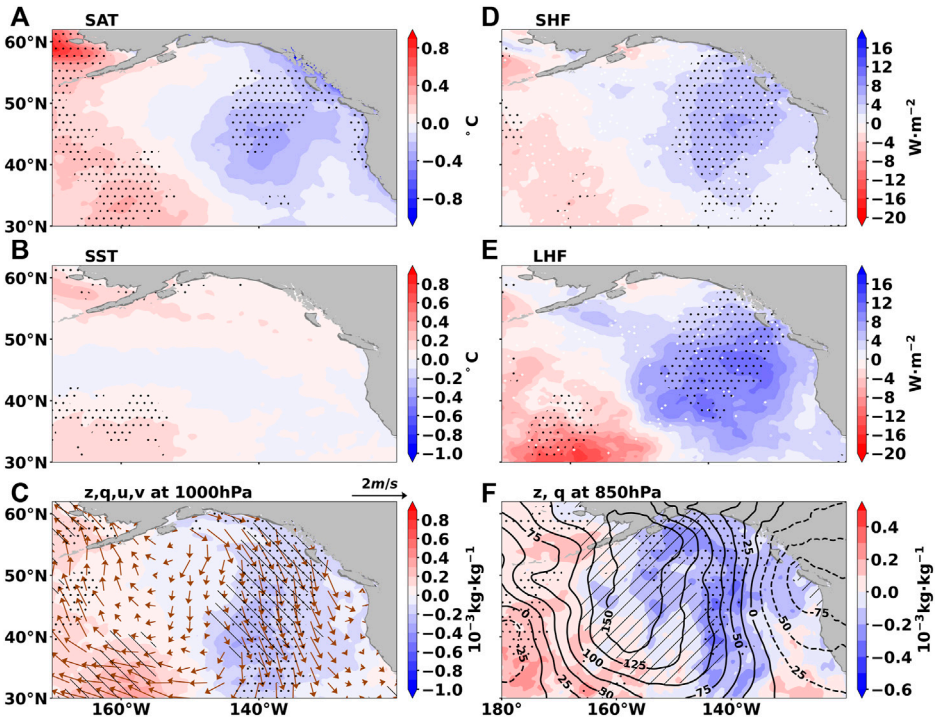

FIGURE 7
Difference between fog with AWSS and that with ACSS. **(A)** SAT (shaded, ˚C), the black dots indicate the SAT difference significant at the 95% confidence level. **(B)** SST (shaded, ˚C), the black dots indicate the SST difference significant at the 95% confidence level. **(C)** Horizontal wind (vectors, $m{\cdot}s^{-1}$) and specific humidity (shaded, 10^{-3}kg kg^{-1}) at 1000 hPa. The black dots indicate the temperature difference significant at the 95% confidence level. Slash lines indicate the geopotential height anomaly significant at the 95% confidence level. Backslashes indicate the meridional wind significant at the 95% confidence level. **(D)** SHF (shaded, $W{\cdot}m^{-2}$), and the black dots indicate the SHF difference significant at the 95% confidence level. **(E)** LHF (shaded, $W{\cdot}m^{-2}$); the black dots indicate the LHF difference significant at the 95% confidence level. **(F)** Geopotential height (black contour, gpm) and specific humidity (shaded, 10^{-3}kg kg^{-1}) at 850 hPa. The black dots indicate the specific humidity difference significant at the 95% confidence level. The slash lines indicate the geopotential height anomaly significant at the 95% confidence level.

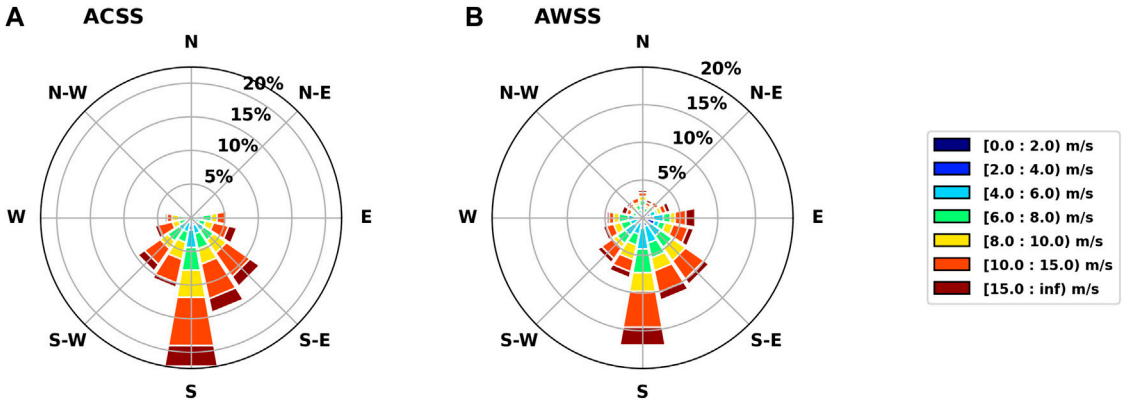

FIGURE 8
Surface wind rose diagrams (%) based on the ICOADS observations during NEP fog in winter (1979–2019). **(A)** Fog during ACSS. **(B)** Fog during AWSS.

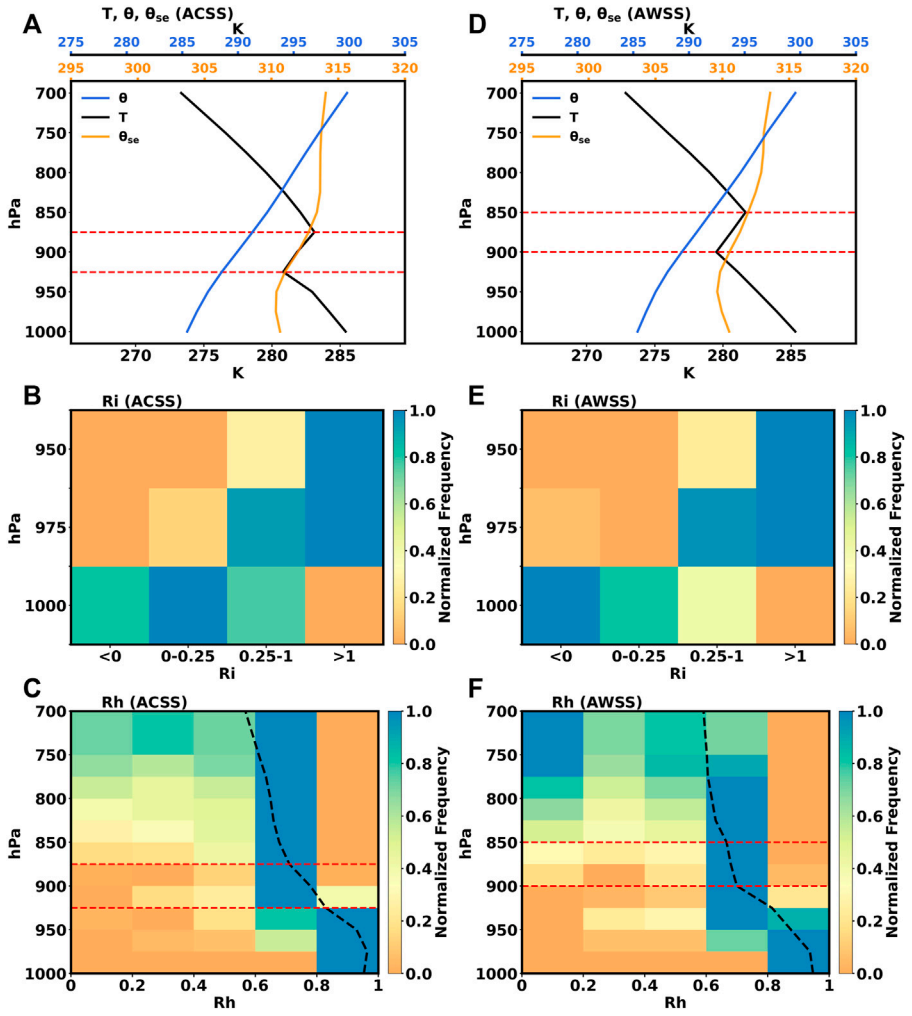

FIGURE 9
Composite profiles, the bulk Richardson number, and relative humidity frequency distribution concurrent with fog with ACSS **(A–C)** and fog with AWSS **(D–F)**: temperature (*T*, black line, in K), potential temperature (θ, blue line, in K), saturated equivalent potential temperature (θ_{se}, orange line, in K), the bulk Richardson number (*Ri*, shaded), and relative humidity (*Rh*, shaded). The red dashed lines denote the inversion layer.

6 Summary and discussions

The present study uses the 40-year ICOADS observations and ERA5 reanalysis results to reveal the synoptic conditions and the MABL structure of marine fog over the NEP in winter. By comparing the climatological mean state and fog composites, it was found that the fog-prone area is controlled by the eastern flank of the Aleutian Low and the northwestern flank of the Pacific subtropical high, which together contribute to a warm and moist northward airflow to form advection-cooling fog over the NEP.

The inversion structure, θ and θ_{se} profiles, and normalized frequency of the *Ri* were investigated to highlight the distinct MABL structures between fog and low clouds. During fog events, the inversion bottom is at lower elevations (at 925 to 875 hPa) compared to the cloudy cases (at 900 hPa). The inversion strength is greater for fog cases (0.08 K hPa^{-1}) compared to the low-cloud cases (0.06 K hPa^{-1}). The lower atmosphere is more stable during fog cases compared to low-cloud events.

Composite analysis of fog cases shows that atmospheric circulation has the characteristics of advection-cooling fog. It is notable that approximately 32% of fog cases have negative SAT–SST, which cannot be explained by warm advection fog and steam fog. To investigate this phenomenon, the difference between the fog with AWSS and that with ACSS was examined. The results show that for fog with AWSS, the air is drier above the inversion bottom than in cases of fog with ACSS. Dry air contributes to the cooling of the fog layer by enhancing the longwave radiative

cooling at the fog top and the vertical mixing beneath, which most probably lead to the negative SAT–SST.

This present study mainly focuses on fog formed over a cooler sea surface which appears most frequently in the NEP. Fog can also occur over warmer sea surfaces under the influence of cooler air advection, such as steam fog and fog associated with stratus lowering (thickening) (Oliver et al., 1978; Pilié et al., 1979; Koračin et al., 2001). These kinds of fog, though less frequent, are likely to appear in winter, which should be analyzed further. On the other hand, it is necessary to conduct numerical simulations and experiments to investigate quantitatively the physical processes in the marine boundary layer and the relationships between fog and low stratus. This will be a focus of a future study.

The longwave cooling at the top of the stratus or fog can create negative buoyancy, causing stratus thickening/lowering (Petterssen, 1936; Koračin et al., 2014). We note that this phenomenon is more closely associated with AWSS than with ACSS over the NEP. In fog with AWSS, the proportion of sinking motion near the LCL is greater than in fog with ACSS (not shown), implying a stronger longwave cooling and negative buoyancy. The sinking motion forced by synoptic-scale weather disturbances should also be considered. The stronger sinking motion indicates that the thickening and lowering of stratus also play a part in the fog with AWSS.

Further studies will also include an investigation of the impact of air–sea interaction, the evolution of the MABL structure, and radiation fluxes on the formation and dissipation of fog as well as on transitions between cloud and fog in the NEP region.

Data availability statement

The original contributions presented in the study are included in the article/Supplementary Material, further inquiries can be directed to the corresponding author.

Author contributions

XL: data analysis; methodology and software; and writing—original draft. SZ: supervision; providing research guidance for this article; and writing—review. DK: giving suggestions and corrections for the manuscript and writing—review. LY and XZ: data curation.

Funding

This work was supported by the National Key Research and Development Program of China (NKPs, 2019YFC1510102 and 2021YFC3101600) and the Natural Science Foundation of China (NSFC, 41876130 and 41975024). DK was supported under project STIM—REI, Contract Number: KK.01.1.1.01.0003, a project funded by European Union through the European Regional Development Fund—Operational Programme Competitiveness and Cohesion 2014-2020 (KK.01.1.1.01). DK was also partially funded by project CAAT (Coastal Auto-purification Assessment Technology) funded by European Union from European Structural and Investment Funds 2014—2020, Contract Number: KK.01.1.1.04.0064. DK also acknowledges significant support from the University of Notre Dame, USA (ONR Grant: N00014-21-1-2296).

Acknowledgments

We thank the management and publishing organizations responsible for the ECMWF ERA5 data and ICOADS data.

Conflict of interest

The authors declare that the research was conducted in the absence of any commercial or financial relationships that could be construed as a potential conflict of interest.

Publisher's note

All claims expressed in this article are solely those of the authors and do not necessarily represent those of their affiliated organizations, or those of the publisher, the editors, and the reviewers. Any product that may be evaluated in this article, or claim that may be made by its manufacturer, is not guaranteed or endorsed by the publisher.

References

Arya, S. (1972). The critical condition for the maintenance of turbulence in stratified flows. *Q. J. R. Meteorol. Soc.* 98 (416), 264–273. doi:10.1002/qj.49709841603

Cao, G., Giambelluca, T. W., Stevens, D. E., and Schroeder, T. A. (2007). Inversion variability in the Hawaiian trade wind regime. *J. Clim.* 20 (7), 1145–1160. doi:10.1175/jcli4033.1

Cho, Y.-K., Kim, M.-O., and Kim, B.-C. (2000). Sea fog around the Korean Peninsula. *J. Appl. Meteor.* 39 (12), 2473–2479. doi:10.1175/1520-0450(2000)039<2473:sfatkp>2.0.co;2

Dorman, C. E., Mejia, J., Koračin, D., and McEvoy, D. (2017). "Worldwide marine fog occurrence and climatology," in *Marine fog: Challenges and advancements in observations, modeling, and forecasting* (Springer), 7–152.

Fu, G., and Song, Y. J. (2014). Climatology characteristics of sea fog frequency over the Northern Pacific. *J. Ocean Univ. China.* 44 (10), 35–41.

Galperin, B., Sukoriansky, S., and Anderson, P. S. (2007). On the critical Richardson number in stably stratified turbulence. *Atmos. Sci. Lett.* 8 (3), 65–69. doi:10.1002/asl.153

Gao, S., Lin, H., Shen, B., and Fu, G. (2007). A heavy sea fog event over the Yellow Sea in March 2005: Analysis and numerical modeling. *Adv. Atmos. Sci.* 24 (1), 65–81. doi:10.1007/s00376-007-0065-2

Gultepe, I., Tardif, R., Michaelides, S., Cermak, J., Bott, A., Bendix, J., et al. (2007). Fog research: A review of past achievements and future perspectives. *Pure Appl. Geophys.* 164 (6), 1121–1159. doi:10.1007/s00024-007-0211-x

Guo, J., Li, P., Fu, G., Zhang, W., Gao, S., Zhang, S., et al. (2015). The structure and formation mechanism of a sea fog event over the Yellow Sea. *J. Ocean. Univ. China* 14 (1), 27–37. doi:10.1007/s11802-015-2466-7

Heo, K.-Y., and Ha, K.-J. (2010). A coupled model study on the formation and dissipation of sea fogs. *Mon. Weather Rev.* 138 (4), 1186–1205. doi:10.1175/2009mwr3100.1

Hersbach, H., Bell, B., Berrisford, P., Hirahara, S., Horányi, A., Muñoz-Sabater, J., et al. (2020). The ERA5 global reanalysis. *Q. J. R. Meteorol. Soc.* 146, 1999–2049. doi:10.1002/qj.3803

Huang, H., Liu, H., Jiang, W., Huang, J., and Mao, W. (2011). Characteristics of the boundary layer structure of sea fog on the coast of southern China. *Adv. Atmos. Sci.* 28 (6), 1377–1389. doi:10.1007/s00376-011-0191-8

Huang, H., Liu, H., Huang, J., Mao, W., and Bi, X. (2015). Atmospheric boundary layer structure and turbulence during sea fog on the southern China coast. *Mon. Weather Rev.* 143 (5), 1907–1923. doi:10.1175/mwr-d-14-00207.1

Johnstone, J. A., and Mantua, N. J. (2014). Atmospheric controls on northeast Pacific temperature variability and change, 1900–2012. *Proc. Natl. Acad. Sci. U. S. A.* 111 (40), 14360–14365. doi:10.1073/pnas.1318371111

Kalnay, E., Kanamitsu, M., Kistler, R., Collins, W., Deaven, D., Gandin, L., et al. (1996). *Bull. Am. Meteorol. Soc.* 77 (3), 437–471. doi:10.1175/1520-0477(1996)077<0437:tnyrp>2.0.co;2

Kim, C. K., and Yum, S. S. (2012). Marine boundary layer structure for the sea fog formation off the west coast of the Korean Peninsula. *Pure Appl. Geophys.* 169 (5), 1121–1135. doi:10.1007/s00024-011-0325-z

Kim, C. K., and Yum, S. S. (2013). A study on the transition mechanism of a stratus cloud into a warm sea fog using a single column model PAFOG coupled with WRF. *Asia. Pac. J. Atmos. Sci.* 49 (2), 245–257. doi:10.1007/s13143-013-0024-z

Koračin, D., Lewis, J., Thompson, W. T., Dorman, C. E., and Businger, J. A. (2001). Transition of stratus into fog along the California coast: Observations and modeling. *J. Atmos. Sci.* 58 (13), 1714–1731. doi:10.1175/1520-0469(2001)058<1714:tosifa>2.0.co;2

Koračin, D., Businger, J. A., Dorman, C. E., and Lewis, J. M. (2005). Formation, evolution, and dissipation of coastal sea fog. *Bound. Layer. Meteorol.* 117 (3), 447–478. doi:10.1007/s10546-005-2772-5

Koračin, D., Dorman, C. E., Lewis, J. M., Hudson, J. G., Wilcox, E. M., Torregrosa, A., et al. (2014). Marine fog: A review. *Atmos. Res.* 143, 142–175. doi:10.1016/j.atmosres.2013.12.012

Koračin, D., and Dorman, C. E. (2017). "Marine fog: Challenges and advancements in observations and forecasting," *Springer Atmospheric Sciences Series* (Cham, Switzerland: Springer International Publishing), 537. doi:10.1007/978-3-319-45229-6

Lewis, J., Koračin, D., Rabin, R., and Businger, J. (2003). Sea fog off the California coast: Viewed in the context of transient weather systems. *J. Geophys. Res.* 108 (D15), 4457. doi:10.1029/2002jd002833

Norris, J. R. (1998). Low cloud type over the ocean from surface observations. Part I: Relationship to surface meteorology and the vertical distribution of temperature and moisture. *J. Clim.* 11 (3), 369–382. doi:10.1175/1520-0442(1998)011<0369:lctoto>2.0.co;2

Oliver, D., Lewellen, W., and Williamson, G. (1978). The interaction between turbulent and radiative transport in the development of fog and low-level stratus. *J. Atmos. Sci.* 35 (2), 301–316.

Petterssen, S. (1936). On the causes and the forecasting of the California fog. *J. Aeronaut. Sci.* 3 (9), 305–309. doi:10.2514/8.246

Pilié, R. J., Mack, E. J., Rogers, C. W., Katz, U., and Kocmond, W. C. (1979). The Formation of marine fog and the development of fog-stratus systems along the California coast. *J. Appl. Meteor.* 18, 1275–1286. doi:10.1175/1520-0450(1979)018<1275:tfomfa>2.0.co;2

Sugimoto, S., Sato, T., and Nakamura, K. (2013). Effects of synoptic-scale control on long-term declining trends of summer fog frequency over the Pacific side of Hokkaido Island. *J. Appl. Meteorol. Climatol.* 52 (10), 2226–2242. doi:10.1175/jamc-d-12-0192.1

Taylor, G. (1917). The formation of fog and mist. *Q. J. R. Meteorol. Soc.* 43 (183), 241–268. doi:10.1002/qj.49704318302

Wang, B. (1985). *Sea fog.* Beijing: China Ocean Press.

Wilks, D. S. (1996). *Statistical methods in the atmospheric sciences*. San Diego, CA: Academic Press.

WMO (2009). *WMO-No. 306, manual on codes*.[Online]. International Codes, Vol. I.1. Available at: http://marswiki.jrc.ec.europa.eu/agri4castwiki/images/a/ad/WMO_306_VolI1_en.pdf (Accessed August 8, 2020).

Woodruff, S. D., Worley, S. J., Lubker, S. J., Ji, Z., Eric Freeman, J., Berry, D. I., et al. (2011). ICOADS release 2.5: extensions and enhancements to the surface marine meteorological archive. *Int. J. Climatol.* 31 (7), 951–967. doi:10.1002/joc.2103

Xia, L., Tan, Y., Li, C., and Cheng, C. (2016). The classification of synoptic-scale eddies at 850 hPa over the North Pacific in wintertime. *Adv. Meteorol.* 2016, 1–8. doi:10.1155/2016/4797103

Yang, L., Liu, J. W., Ren, Z. P., Xie, S. P., Zhang, S. P., Gao, S. H., et al. (2018). Atmospheric conditions for advection-radiation fog over the Western Yellow Sea. *J. Geophys. Res. Atmos.* 123 (10), 5455–5468. doi:10.1029/2017jd028088

Zhang, S., Ren, Z., Liu, J., Yang, Y., and Wang, X. (2008). Variations in the lower level of the PBL associated with the Yellow Sea fog-new observations by L-band radar. *J. Ocean. Univ. China* 7 (4), 353–361. doi:10.1007/s11802-008-0353-1

Zhang, S.-P., Xie, S.-P., Liu, Q.-Y., Yang, Y.-Q., Wang, X.-G., Ren, Z.-P., et al. (2009). Seasonal variations of Yellow sea fog: Observations and mechanisms. *J. Clim.* 22 (24), 6758–6772. doi:10.1175/2009jcli2806.1

Zhang, S., Chen, Y., Long, J., and Han, G. (2015). Interannual variability of sea fog frequency in the Northwestern Pacific in July. *Atmos. Res.* 151, 189–199. doi:10.1016/j.atmosres.2014.04.004

frontiers | Frontiers in Earth Science

TYPE Original Research
PUBLISHED 09 September 2022
DOI 10.3389/feart.2022.956977

OPEN ACCESS

EDITED BY
Darko Koracin,
University of Split, Croatia

REVIEWED BY
Boqi Liu,
Chinese Academy of Meteorological Sciences, China
Haikun Zhao,
Nanjing University of Information Science and Technology, China

*CORRESPONDENCE
Yinglong Xu,
xuyl@cma.gov.cn

SPECIALTY SECTION
This article was submitted to Atmospheric Science, a section of the journal Frontiers in Earth Science

RECEIVED 30 May 2022
ACCEPTED 26 July 2022
PUBLISHED 09 September 2022

CITATION
Xiang C, Xu Y, Lin J and Liu S (2022), Analysis of the inner rainbands of tropical cyclones over the South China Sea during the landfall process. *Front. Earth Sci.* 10:956977. doi: 10.3389/feart.2022.956977

Analysis of the inner rainbands of tropical cyclones over the South China Sea during the landfall process

Chunyi Xiang, Yinglong Xu*, Jian Lin and Shuang Liu

National Meteorological Centre, Beijing, China

Tropical cyclones (TCs) can undergo offshore rapid intensification (RI) shortly before making landfall over the South China Sea (SCS). In this study, the inner rainbands distribution of both RI and non-RI landfall TCs (LTCs) in the SCS during 2015–2020 is examined based on a multi-source merged precipitation dataset. It is found that those RI LTCs exhibit a relatively higher averaged rain rate in the inner core region than that of non-RI LTCs. Both offshore RI cases and non-RI LTCs appear to have an increasing tendency of averaged rain rate after landfall, with the rain rate peak of the RI cases a few hours earlier than that of non-RI cases. By defining an axisymmetric index, the inner rainband evolution of both offshore RI cases and non-RI ones are further discussed. For both categories, most of the axisymmetric rainfall is concentric around the center and over 70% axisymmetric rainfall dominates the inner core region within three times of radius of maximum wind speed (RMW). It is shown that there is an obvious inwards shrinkage of axisymmetric rainfall for both offshore RI and non-RI cases. Analysis of typical RI and non-RI LTCs (1713 Hato and 1714 Pakhar) also shows an increasing rain rate of the inner rainbands soon after landfall, with larger amplitude for RI example than non-RI case. The inner rainbands of 1713 Hato show that a clockwise propagation with maximum enhancement happened at the down-shear left-hand side a few hours after landfall.

KEYWORDS

landfall tropical cyclone, rapid intensification, inner rainbands, rain rate, landfalling process

Introduction

Accompanied by gale winds, torrential rains, inland floods and mudslides in mountainous terrain, tropical cyclones (TCs) are one of the most devastating natural disasters in the world (Chen et al., 2010). The South China Sea (SCS) is affected by summer Monsoon, Madden-Julian Oscillation, and Subtropical High, and therefore TCs in this area can have more unpredictable tracks and intensity change (Liang et al., 2011; Molinari and Vollaro, 2012; Wu et al., 2013; Chen et al., 2015). Recently, many studies have shown that the onset of rapid intensification (RI) in the SCS occurred under

favorable large-scale circulation, including weaker vertical wind shear (VWS), warmer ocean surface, and suitable low-level water vapor convergence (Leighton et al., 2018; Qiu et al., 2019; Cai et al., 2022; Zhao et al., 2022a). Both large-scale environment conditions and complex atmospheric interaction with land and ocean can induce asymmetric rainfall maximum distribution, especially during the landfall process. Forecasting and early warning of landfall TCs (LTCs) that undergo an offshore RI event before landfall is a considerable challenge. Recent LTCs such as Mujigae (1522), Mirinae (1603), Hato (1713), and Higos (2007) had all experienced RI shortly before landfall, which caused large forecasting errors and related disasters to the coastal area of the southern part of China. Consequently, offshore RI events and relevant heavy rainfall distribution are both crucial to disaster reduction.

Deep convection, in terms of rainbands within TCs, can be characterized by asymmetry affected by large-scale circulation (Corbosiero and Molinari, 2002; Chan et al., 2004; Lonfat et al., 2004; Chen et al., 2006; Cecil, 2007; Li and Dai, 2020). In addition to surface friction-induced low-level convergence caused by storm motion and uneven distribution of ocean thermal condition, environmental VWS in the surrounding areas of TC is a fundamental factor of asymmetric rainfall (Kaplan and Demaria, 2003; Kelvin and Johnny, 2011; Xu et al., 2014; Yu et al., 2015, 2017). The maximum convection in term of heavy rainfall occurs at the down-shear side and left-hand quadrant in the Northern Hemisphere, regardless of the storm's motion (Jiang et al., 2008a; Yu et al., 2015). Actually, not all observed rain rate distribution can be exactly explained by the shear induced asymmetries. Other influential factors include the ocean's thermal condition (Cecil, 2007, Jiang et al., 2008b), the surface land-sea contrast (Chen and Wu, 2016), and also interaction with other systems such as Monsoon Gyre (Qiu et al., 2020) or interaction between binary typhoon vortex (Xu et al., 2011) other large-scale atmospheric systems (Zhao et al., 2022b), and local topography (Liou et al., 2013).

During the landfall process, the rainfall distribution is very complicated when the development and collapse of the mesoscale circulation system of the inner TC circulation become dominant (Chen et al., 2004; Chen and Wu, 2016). Certain asymmetric rainfall or convective activities can be estimated through satellite image or radar rainfall estimation (Mueller et al., 2006; Reasor et al., 2013), or simulated by numerical models (Li and Wang, 2012). Recent studies have found that the size and structure change of TC inner rainbands is closely related to the rainfall distribution in landfall process (Dai et al., 2021; Yu et al., 2022). However, not enough observation analysis has been done, especially for the LTCs over the SCS. It is still unclear that whether the inner rainbands exhibit a similar structure change for both offshore RI LTCs and non-RI cases. Although the majority of previous studies have focused on the external factors caused by the large-scale environment, it is important to know the internal dynamical mechanism and mesoscale process to trigger the asymmetric distribution of rainfall during the landfall process. This study has used a newly developed multiple-source merged precipitation dataset to figure out the differences of inner rainbands between RI and non-RI LTCs during their landfall processes over the SCS.

Data and method

Data

The TC track that is used in this study is the best track dataset from the Shanghai Typhoon Institute (STI) of China Meteorological Administration (CMA). Using the maximum wind speed and minimum central sea level pressure to define the intensity, and the latitude and longitude to define the location, the STI best track provides TC information in the western North Pacific and SCS in 6h intervals (Ying et al., 2014). For offshore TCs (normally within 200 km from the coastal line), the STI best track dataset can additionally increase the time interval to 3 h because weather radar and coastal weather stations can capture their detailed structure. These multiple observations could be additionally beneficial to estimate the intensity and location of an offshore TC than other best track datasets in this region. To figure out the timely revolution of rainbands during the landfall process, linear interpolation was used to interpolate the every 6 h/3 h STI best track dataset to 1 h to specify the location migration during the landfall process. However, the size of TC cannot be directly obtained from STI best track dataset, and therefore we used the analysis from multi-platform tropical cyclone surface wind analysis (MTCSWA) from NOAA/NESDIS, in which the radius of maximum wind speed (RMW) is captured from satellite retrieved surface winds (Knaff et al., 2007). To specify the influence of VWS for the evolution of inner rain bands, ERA5 reanalysis from the European Centre for Medium-Range Weather Forecasts (ECMWF) is used to examining the large-scale conditions and circulation.

Given that satellite based rainfall estimation has a wide coverage and continuous monitoring, most previous research of TC rainfall characteristics have been based on satellite estimation datasets, such as the tropical rainfall measuring mission (TRMM; Chen and Wu et al., 2016; Yu et al., 2015; Yu et al., 2017), global precipitation measurement (GPM; Hou et al., 2014), or integrated multi-satellite retrievals of GPM (IMERG; Huffman et al., 2020; Guzman and Jiang, 2021). For TC overland, the precipitation retrieved from radar can also be used to estimate the TC rainfall in certain cases (Chan et al., 2004). Because few previous studies have used an *in-situ* rain gauge from an automatic weather station (AWS), we chose to use the CMA multi-source merged precipitation analysis system (CMPAS), which has includes more than 40,000 AWSs. Meanwhile, CMAPS has also included the satellite retrieved

rainfall from climate precipitation centre morphing (CMORH) and radar estimation. Other than a single source of observation, the CMPAS merged three sources of precipitation observation with different temporal and spatial resolutions using Bayesian multi-model averaging and optimal interpolation. Independent verification has confirmed that the estimation root square mean errors of CMPAS are lower than those of a single source of estimation, such as CMOPH and radar retrievals (Shen et al. 2014). By combining geostationary satellite, radar observations, and especially rain gauge observation (including inland, offshore, and on-islands), this multiple-source fusion data could give a full picture of rainfall structure during their landfall process considering equivalent merging technique over land and sea.

To discuss the inner rainbands distribution of LTCs during the landfall process, three preliminary conditions were defined according to the research purpose. First, only the first landfall event for each LTC is included. In this way, those LTCs that made landfall on Hainan Island and then followed the second or third landfall on the mainland after passing over the ocean's surface are excluded. Second, selected LTCs should maintain at least 12 h after making landfall on mainland and 6 h after making landfall over Hainan Island to ensure a sufficient analyzed period for the temporal and spatial evolution of the symmetric and asymmetric structure of rainfall. From the 24 h before landfall to the 12 h after landfall, all selected LTCs were captured in the same periods of time to examine the landfall process. Because the CMAPS dataset starts from 2015 with the domain of 5–60°N, 70–140°E, 10 LTCs from 2015 to 2020 over SCS were finally selected according to the previous two conditions. Detailed information of these LTCs will be given in third section.

Method

The asymmetric and symmetric components of precipitation are decomposed to study the relationship of asymmetric convection and other large-scale environmental factors (e.g., VWS) in previous studies (Lonfat et al., 2004; Uhlhorn et al., 2014; Yu et al., 2017). We used the same method to decompose precipitation distribution during a TC's landfall process into axisymmetric and asymmetric components, as follows:

$$\Phi(r,\lambda,t) = \bar{\Phi}(r,t) + \Phi'(r,\lambda,t) \quad (1)$$

in which $\bar{\Phi}$ and Φ' represent the axisymmetric and asymmetric components, respectively; and r,λ denote the radial and tangent direction, while t is the time variable.

Following the idea of defining the asymmetric convection in Miyamoto and Takemi (2003), we specified an axisymmetric index as a ratio of the axisymmetric precipitation to both axisymmetric and asymmetric components. Because the asymmetric component has both a positive and negative value, they were both squared, as follows:

$$\theta(r,t) = \frac{\bar{\Phi}(r,t)^2}{\bar{\Phi}(r,t)^2 + \int_0^{2\pi}\Phi'(r,\lambda,t)^2\frac{d\lambda}{2\pi}} \quad (2)$$

where r,λ, t have them same meaning as in Equation 1. The axisymmetric index θ denotes normalized axisymmetric degree of precipitation distribution regardless of the rain rate differences related to intensity of LTCs. If it is close to 1, then the precipitation is fully axisymmetric to the TC center. If it close to 0, then it equals extremely asymmetric rainfall distribution at a specified radium or time. To specify the inner rain rate, the radial distance from the center of TC is converted to multiples of RMW. The inner rainbands are defined as 3 times of RMW, where most of rainfall is induced by deep convection of the inner core region of the TC (Wang, 2009). Following previous research, the VWS is defined as the difference of averaged wind speed within a radius of 220–880 km to the center of TC (Kaplan and DeMaria 2003; Shu et al., 2012; Qiu et al., 2020).

Evolution of rain rate during the landfall process

Based on the criterion listed in the last section, 10 offshore LTCs in the SCS were selected during the period of 2015–2020 (see Table 1). Six of them made landfall on Guangdong Province and the other four made landfall on Hainan Island. The averaged landfall intensity is 36.9 m s^{-1}, with a maximum of 48 m s^{-1} (Mujigae, 1522) and a minimum of 23 m s^{-1} (Son-Tinh,1809). The earliest landfall time of those 10 LTCs is in June (Kujira, 1508) and the last one is in October (Sarika, 1621).

In previous studies, the 95th percentile of all the samples of 24h intensity change of maximum sustained wind speed for TCs was normally settled as the threshold to define RI (Kaplan and DeMaria, 2003). We used the threshold of 15 m s^{-1} in 24h to define a RI event in the Northwestern Pacific basin followed previous works (Kaplan et al., 2010; Knaff et al., 2018). Second, to investigate the offshore intensity change before landfall over SCS, only the RI events that happened within 200 km from coastal line were defined as offshore RIs (i.e., those LTCs that experienced RI and landfall process at the same time when they are approaching the coastal line). The track segments of these LTCs during the landfall process, from 24h before landfall to 12 h after landfall, are given in Figure 1. Among these, four LTCs—Mujigae (1522), Mirinae (1603), Hato (1713) and Higos (2007)—had experienced offshore RI before landfall. Among these four offshore RI cases, three had an increase of 20 m s^{-1} during 24 h and Mirinae (1603) had 15 m s^{-1}, respectively. The other six non-RI LTCs (presented in blue in Figure 1) had a more moderate intensity change during

TABLE.1 Information of 10 LTCs in SCS.

TC name (TC number)	Landfall time	Landfall intensity ($m \cdot s^{-1}$)
Kujira (1508)	20 UTC. 22 June2015	25
Mujigae (1522)	06 UTC. 4 October 2015	48
Mirinae (1603)	14 UTC. 26 July 2016	28
Nida (1604)	19 UTC. 1 August 2016	42
Sarika (1621)	02 UTC. 18 October 2016	45
Hato (1713)	06 UTC. 23 August 2017	45
Pakhar (1714)	01 UTC. 27 August2017	33
Son-Tinh (1809)	21 UTC. 17 July 2018	23
Mangkhut (1822)	09 UTC. 16 September 2018	45
Higos (2007)	22 UTC. 18 August 2020	35

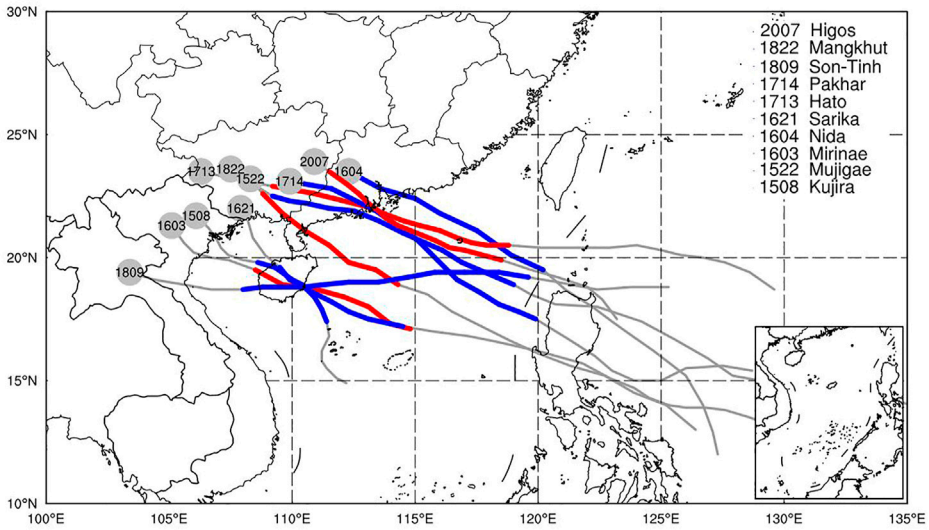

FIGURE 1
Track segments of 10 LTCs in SCS. The red (blue) lines represent RI (non-RI) in the period from 24 h before to 12 h after the landfall, respectively (the number and name of the LTCs are listed).

the landfall process. The landfall point spread from the east coast of Pearl River Estuary to the east of Hainan Island, covering the majority landfall places in this region. Further examination indicates that only Kujira (1508) was generated locally in the middle of SCS, while the others moved north-westward from the east of the Philippines.

With a fully developed structure, over 80% of deep convection in TC is enveloped inside the inner core regions (Miyamoto and Nolan, 2018), which is normally defined as three times of RMW (Wang, 2009). The spiral rainbands could be concentrated within inner core regions, where the inner rainbands and distant rainbands could overlap or coincide to intensify the rain rate within inner core regions. For RI TCs, the convective bursts (CBs) within the inner core region could trigger the rainfall increase (Chen et al., 2004; Reasor et al., 2013). To figure out the rain rate distribution within the inner core region for LTCs in the SCS during the landfall process, we first composited the radial rain rate of the RI and non-RI LTCs to present rainfall evolution. Recent studies have investigated the possible relationship between the TC size change and the radial distribution of rainfall, and found that a large amount of rainfall occurs in low inertial stability regions when intense convection happened (Tsuji and Nakajima, 2019). To avoid the possible influence of rainfall distribution from TC size, we normalized the rain rate from distance to TC center to multiples of RMW, which is closely related to the TC eyewall.

As shown in Figure 2, the inner core averaged rain rate of RI LTCs is obviously higher than that of non-RIs during the entire landfall process. In agreement with other observation analyzes, there

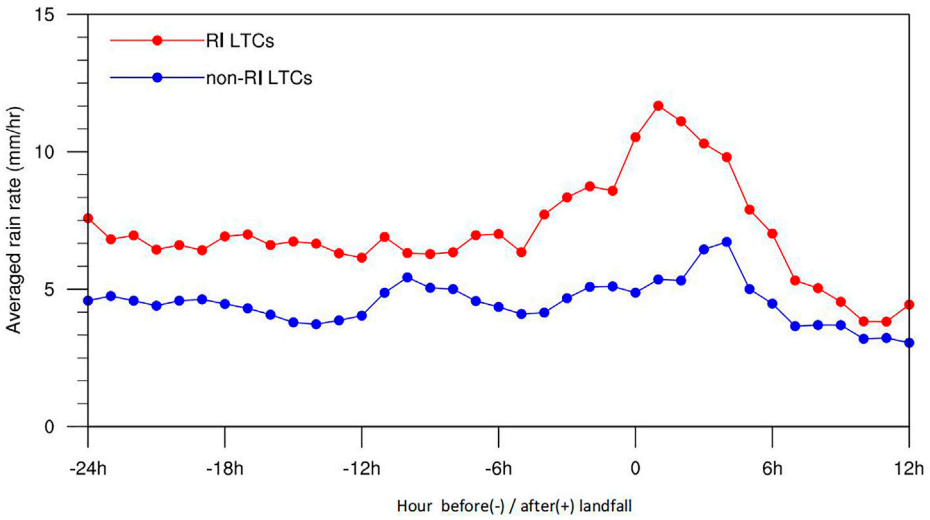

FIGURE 2
Comparison of averaged rain rate distribution within three RMW of four RI LTCs (indicated in red marked line) and six non-RI LTCs (indicated in blue) during the landfall process. The horizontal coordinate is the time before/after landfall.

is an obvious inner core CB in the RI cases (Reasor et al., 2013). Given that offshore RI LTCs actually have higher landfall intensity (39.0 m s^{-1} on average) compared to that of non-RIs (35.5 m s^{-1} on average), the averaged rain rate within inner core region indeed depends on the landfall intensity. It is also noticed that both RI LTCs and non-RI cases experienced an outbreak of rain rate during the first 6h after landfall, when the peak rain rate shows up at the 2h after landfall for RI cases and around 4h for non-RI cases. This obvious intensification of rain rate within inner core region nearly doubled the rain rate (with a maximum rain rate over 10 mm/h) just a few hours after landfall, which might be related to the outbreaks of deep convection in the inner core regions after the landfall for both RI and non-RI LTCs. In the following 6–12 h after landfall, the rain rate of both the RI and non-RI cases decreased sharply to less than 5 mm/h. During that period, the difference between the two categories narrowed because the LTCs' circulation were fully over land or island after the outbreak of rain rate within the first 6 h after landfall. The F-test is used to exam the statistical significance for the difference between RI and non-RI case during the landfall process. The yield results show that the difference of those two categories has passed 95% confidence level for the whole process.

Distribution of inner rainbands during the landfall process

We used an axisymmetric index defined in Section 2 to present the radial concentration of rainfall during the landfall process. The differences in axisymmetric evolution of rainfall between RI LTCs and non-RI LTCs are further examined as shown in Figure 3. The statistical significance of over 95% for the radial distribution is marked in shadows.

To avoid the possible influence of a TC's size on its radial structure, the radial distance to TC center is at first converted into its relevant multiples to RMW. For both RI and non-RI LTCs, the axisymmetric rainfall shows a tendency of inwards concentration during the landfall process, with over 70% axisymmetric rainfall dominating the inner core region (here referred to 3RMW) 1 day before landfall. However, as the TC's center approaches the coast line in the following hours, the inner core region is gradually dominated by asymmetric rainfall other than axisymmetric rainfall because only less than 50% total rainfall could be decomposed to azimuthal mean rainfall after landfall. This obvious inwards shrinkage of axisymmetric rainfall could also be found in the non-RI cases, while the differences appeared after the landfall. Compared to the steady asymmetric process, the non-RI LTCs show up the sharp collapse of axisymmetric rainfall soon after landfall, which means the asymmetric components of rainfall are eventually dominant outside the RMW for non-RI LTCs. It is found that the difference of axisymmetric rainfall after landfall for those two categories is of statistical significance when compared to the period before landfall.

To better distinguish the evolution of the inner rainbands' evolution between RI LTCs and non-RIs, two typical LTCs 1713 Hato and 1714 Pakhar were selected to represent RI and non-RI cases respectively. Generated in August 2017, Hato and Pakhar successively made landfall over the western part of Guangdong Province. Other than similar prevailing tracks before landfall, the tracks after landfall also bear little difference. Given that 1713 Hato experienced RI shortly

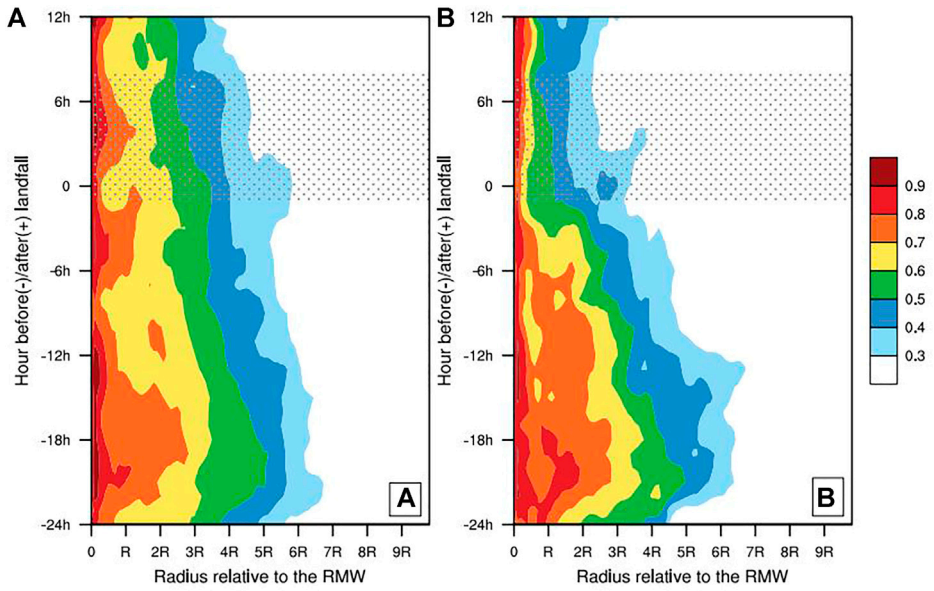

FIGURE 3
Composited radial-time distribution of asymmetric index of precipitation for **(A)** RI LTCs and **(B)** non-RI LTCs; the vertical coordinate is the hours before/after landfall and the horizontal coordinate is the multiple relative to RMW; area of significance over 95% is marked.

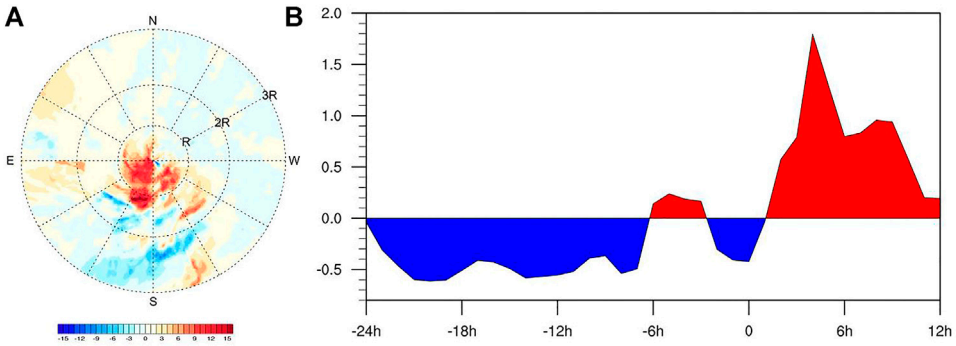

FIGURE 4
The first EOF pattern **(A)** (units: mm) and amplitude **(B)** of rainfall during the landfall process of 1713 Hato, R indicates the RMW. The horizontal coordinate is the time before/after landfall.

before landfall, the landfall intensity of 1713 Hato was higher than that of 1714 Pakhar. The Empirical Orthogonal Functions (EOF) analysis was used to simplify a spatial-temporal data set by transforming the rainfall to spatial patterns of variability and temporal projections of these patterns.

As in Figure 4A the radial coordinate is the radius relative to RMW, while only the inner rainbands distribution within 3R from the center was presented. From the typical EOF analysis, the first EOF pattern contributed over 40% variation of inner rainbands in the case of 1713 Hato. The majority of positive rainfall was concentric around the center within RMW, which means the inner rainbands were intensified during the landfall process, especially within the eyewall. The amplitude of EOF shows the time evolution of this pattern. As shown in Figure 4B, the inner core rainbands intensification exhibited an increase soon after its landfall, which means that the inner core rain rate actually double compared to the periods before landfall. The EOF analysis of a single example 1713 Hato has confirmed the previous composite analysis of inner core rainfall shown in Figure 2. We also examined the other three RI LTCs, 1522 Mujigae, 1603 Mirinae, and 2007 Higos using the same method. Although the first EOF pattern turned out to be

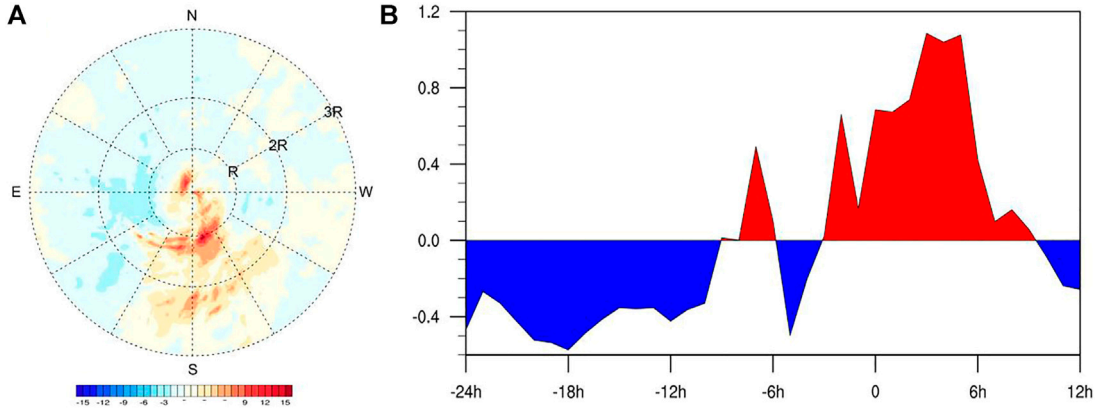

FIGURE 5
Same as in Figure 4, but for 1714 Pakhar.

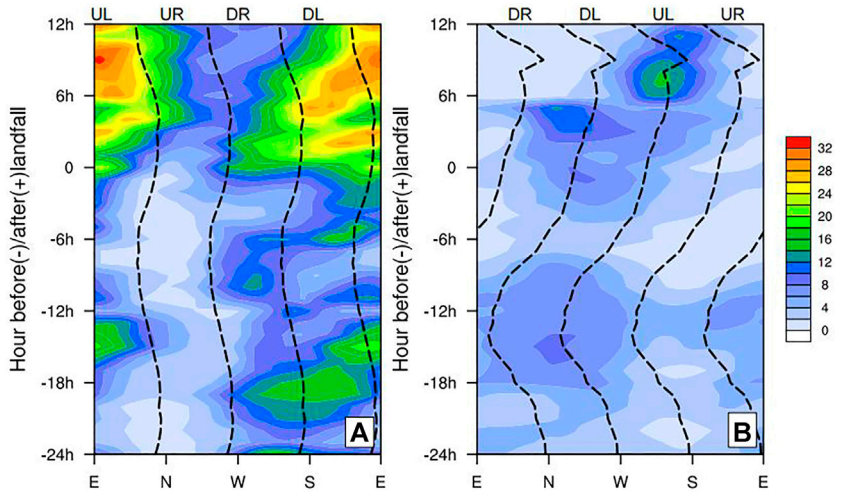

FIGURE 6
Azimuthal-time distribution of inner rain bands (units: mm) for **(A)** 1713 Hato and **(B)** 1714 Pakhar. The vertical coordinate is the hours before/after landfall and the horizontal coordinate is azimuth angle. Dashed lines indicate VWS; UL/UR represent up-shear left/right and DL/DR denote down-shear left/right.

distributed differently, the temporal series of amplitude for those patterns has all exhibited the same tendency of increasing after landfall.

The spatial and temporal distribution of inner rainbands of 1714 Pakhar, which made landfall to the west of the Pearl River Estuary around 4 days after 1713 Hato, are given in Figure 5. The first EOF pattern of 1714 Pakhar has shown as a pattern of spiral rainbands, which starts from the southeast quadrant outside RMW and rotates anticlockwise into the TC center. Although the maximum value in the first EOF pattern of 1714 Pakhar was lower than that of 1713 Hato, this enhancement of inner rainbands has also exhibited an increase after landfall. Compared to the RI cases, this increase of inner rainbands did not last as long as 1713 Hato, and another decreasing tendency of inner rainbands was dominant only 6 h after landfall. Even though the EOF analysis of other non-RI LTCs presented in different spatial patterns, a similar increasing tendency of rainfall could be shown.

As discussed in previous studies (Kaplan and Demaria, 2003; Kelvin and Johnny, 2011; Xu et al., 2014; Yu et al., 2015, 2017), environmental VWS is related to the asymmetric distribution of rainfall. The maximum rainfall often exhibit over the left-hand side

along the direction of shear (Chen et al., 2006; Shimada et al., 2017; Yu et al., 2017). To figure out the inner rainbands' evolution during the landfall process under different environmental VWS, the azimuthal-time distribution of inner rainbands of both 1713 Hato and 1714 Pakhar are given in Figure 6.

As shown in Figure 6A, the rain rate of inner rainbands was averaged within the domain of three RMW from the TC center. The inner rainbands of 1713 Hato have shown up an obvious clockwise propagation during the landfall process. Meanwhile, the averaged rain rate within 3R intensified after landfall, which confirmed the previous analysis (as shown in Figure 3). The maximum rain rate doubled during the post-landfall period compared to before landfall. It is also noticed that the inner rain bands presented an obvious clockwise propagation, during which the spiral rain bands started from the Down-shear Right (DR) side and intensified as the Down-shear Left (DL). This kind propagation of spiral rainbands has also been discussed in numerical simulation (Li and Wang, 2012; Li and Dai, 2020). In the case of 1713 Hato, the inner rain bands intensified at the southern part after landfall, which might be related to the rainfall enhancement over the coastal line. As the non-RI case, 1714 Pakhar presented a much moderate intensification of inner rainbands after landfall (shown in Figure 6B). The maximum rain rate of inner rainbands could be found at DL side of TC at nearly 6 h after landfall. Given that the direction of VWS experienced a much wider change compared to that of 1713 Hato, the phenomenon of clock-wised propagation of inner rainbands was less obvious in this case. The maximum rain rate can be found in the southern semicircle after landfall, which is also related to the topographic influence.

Conclusion and discussion

The northern part of the SCS is one of most prevalent areas for offshore RIs. Therefore, the inner rainband distribution of both offshore RIs and non-RI TCs was examined from 24 h before to 12 h after landfall during 2015–2020. The relationship between TC inner rainbands and previous intensity change before landfall was studied in this work based on a multiple merged dataset CMPAS. Finally, 10 LTCs were selected to be discussed. All LTC samples were classified into two groups according to the definition of offshore RI events. It is found that the offshore RI LTCs exhibit a relatively higher than average rain rate in the inner core region compared to the non-RI LTCs. Due to possible impact from land-sea contrast and topography, the averaged inner rain rates for both offshore RI and non-RI cases appear to have a tendency to increase after landfall. Even though both composited temporal evolution of inner core rain rates have a peak within 6 h of landfall, the composited RI LTCs have a peak value a few hours earlier than that of non-RI cases. Because most of the offshore RI LTCs have indeed higher landfall intensities than those non-RI counterparts, stronger LTCs might have higher rain rate during their landfall process than weaker ones. From previous studies, it is known that the large-scale VWS, which favors the enhancement of TC intensity, might also an important environmental factor for the development of deep convection (Yu et al., 2017; Tsuji and Nakajima, 2019). The offshore RI LTCs have more favorable background conditions for the growth of both intensity and axisymmetric rainfall.

By defining an axisymmetric index, the axisymmetric rain rate evolution of both offshore RI and non-RI cases are further discussed. RMW is an important parameter in determining the inner core region. Before compositing the RI LTCs and non-RI cases, the radius change throughout the landfall process was carefully analyzed to avoid mismatching the size difference and their rainfall distributions. For both of the two composited azimuthal axisymmetric indices, most of axisymmetric rainfall is concentric around the center, with over 70% of axisymmetric rainfalls dominating the inner core region within 3RMW. When the land-sea contrast and topography have a gradual impact on the vertical structure of the LTCs, the inner core region with higher percentage of axisymmetric rainfall before landfall has lower azimuthal mean rainfall after landfall. It is noted that there is an obvious inwards shrinkage of axisymmetric rainfall for both offshore RI and non-RI cases, while the differences only appeared after landfall. The non-RI LTCs have a sharper collapse of axisymmetric rainfall soon after landfall, which means that for non-RI LTCs the asymmetric components of rainfall eventually dominate the distribution outside the RMW. This could explain why weaker LTCs that have experienced weakening before landfall will have much more unpredictable rainfall distributions than RI cases. In 1508 Kujira and 1809 Son-Tinh, the inner rainbands hardly disappeared after landfall. However, the distance rainbands caused by the Monsoon surge might trigger robust heavy rainfall inland. It is therefore important to further research the structure evolution and rainfall distribution during the landfall process for weaker or already weakened LTCs.

Two typical LTCs (1713 Hato and 1714 Pakhar) were selected to study the primary patterns of inner rainbands and its related temporal evolution using EOF analysis. For the RI case, 1713 Hato, the inner core rainband intensification exhibited an increase soon after landfall, while the inner core rain rate was nearly double that of the periods before landfall. The weaker LTC 1714 Pakhar shows a pattern of spiral rainbands, but its increase of inner rainbands lasted only 6h after landfall. Similar to previous numerical studies, the inner rainbands presented a clockwise propagation, and maximum intensification happened at the DL side in 1713 Hato. The enhancement of inner rainbands was observed at the southern part of TC after landfall for both two typical LTCs. This could be closely related to convective convergence and lifting along coastal line, which triggered the enhancement of inner rainbands a few hours after landfall.

It is suggested that the obvious outbreaks of rain rate can be related to land-sea contrast in most LTCs. More precise studies of the inner core structure during the landfall process might explain the dynamic mechanism other than rainfall distribution. In this

article, we only discussed the relationship between previous intensity change and rainfall distribution of LTCs based on observations. The inner dynamic mechanism to explain the increase of inner rainbands within 6 h after landfall is hardly known. Numerical simulation or three-dimensional vertical structure analysis from other high-resolution observations (e.g., dual polarization radar) might help to answer the possible influence of topography and land-sea contrast, particularly during the landfall process.

Data availability statement

The datasets presented in this study can be found in online repositories. The names of the repository/repositories and accession number(s) can be found below: http://idata.cma/idata/web/data/index?dataCode=NAFP_NMIC_ART_CMPAS_0P05_CHN_DAY_PRE_RT

Author contributions

CX and YX contributed to main research part and design of the study. CX and SL organized the database. CX performed the statistical analysis and organization of manuscripts. LW provided suggestion and revision of this work.

Funding

This work is supported by The National Key Research and Development Program of China (2017YFC1501604).

Conflict of interest

The authors declare that the research was conducted in the absence of any commercial or financial relationships that could be construed as a potential conflict of interest.

Publisher's note

All claims expressed in this article are solely those of the authors and do not necessarily represent those of their affiliated organizations, or those of the publisher, the editors and the reviewers. Any product that may be evaluated in this article, or claim that may be made by its manufacturer, is not guaranteed or endorsed by the publisher.

References

Cai, Y., Han, X., Zhao, H., and Klotzbach, P. J. (2022). Enhanced predictability of rapidly intensifying tropical cyclones over the western North Pacific associated with snow depth changes over the Tibetan Plateau. *J. Clim.* 35, 2093–2110.

Cecil, D. J. (2007). Satellite-derived rain rates in vertically sheared tropical cyclones. *Geophys. Res. Lett.* 34 (2), L02811. doi:10.1029/2006gl027942

Chan, J. C.-L., Liu, K. S., Ching, S. E., and Lai, E. S. T. (2004). Asymmetric distribution of convection associated with tropical cyclones making landfall along the south China coast. *Mon. Weather Rev.* 132 (10), 2410–2420. doi:10.1175/1520-0493(2004)132<2410:adocaw>2.0.co;2

Chen, H. D.-L., Zhang, J. Carton, and Atlas, R. (2011). On the Rapid intensification of hurricane wilma (2005). Part I: Model prediction and structural changes. *Weather Forecast.* 26, 885–901. doi:10.1175/waf-d-11-00001.1

Chen, L., Li, Y., and Cheng, Z. (2010). An overview of research and forecasting on rainfall associated with landfalling tropical cyclones. *Adv. Atmos. Sci.* 27 (5), 967–976. doi:10.1007/s00376-010-8171-y

Chen, L., Luo, Z., and Li, Y. (2004). Research advances on tropical cyclone landfall process. *Acta. Meteor. Sin.* 62, 541–549.

Chen, S. S., Knaff, J. A., and Marks, F. D., 2006: Effects of vertical wind shear and storm motion on tropical cyclone rainfall asymmetries deduced from TRMM. Monthly weather review, 134, 3190–3208, doi:10.1175/1520-0469(2003)060<2294:asiasl>2.0.co;2

Chen, X., and Wu, L. (2016). Topographic influence on the motion of tropical cyclones landfalling on the coast of China. *Weather Forecast.* 31 (5), 1615–1623. doi:10.1175/waf-d-16-0053.1

Chen, X., Wang, Y., and Zhao, K. (2015). Synoptic flow patterns and large-scale characteristics associated with rapidly intensifying tropical cyclones in the south China sea. *Mon. Weather Rev.* 143, 64–87. doi:10.1175/mwr-d-13-00338.1

Chen, Y., and Yau, M. K. (2003). Asymmetric structures in a simulated landfalling hurricane. *J. Atmos. Sci.* 60 (18), 2294–2312.

Corbosiero, K. L., and Molinari, J. (2002). The effects of vertical wind shear on the distribution of convection in tropical cyclones. *Mon. Weather Rev.* 130 (8), 2110–2123. doi:10.1175/1520-0493(2002)130<2110:teovws>2.0.co;2

Dai, H., Zhao, K., Li, Q., Lee, W. C., Ming, J., Zhou, A., et al. (2021). Quasi-periodic intensification of convective asymmetries in the outer eyewall of typhoon lekima(2019). *Geophys. Res. Lett.* 48. doi:10.1029/2020gl091633

Frank, W. W., and Ritchie, E. A. (2001). Effects of vertical wind shear on the intensity and structure of numerically simulated hurricanes. *Mon. Weather Rev.* 129, 2249–2269. doi:10.1175/1520-0493(2001)129<2249:eovwso>2.0.co;2

Guzman, O., and Jiang, H. (2021). Global increase in tropical cyclone rain rate. *Nat. Commun.* 12, 5344. doi:10.1038/s41467-021-25685-2

Hou, A. Y., Kakar, R. K., Neeck, S., Azarbarzin, A. A., Kummerow, C. D., Kojima, M., et al. (2014). The global precipitation measurement mission. *Bull. Am. Meteorol. Soc.* 95, 701–722. doi:10.1175/bams-d-13-00164.1

Huffman, G. J., Adler, R. F., Rudolf, B., Schneider, U., Keehn, P. R., Gu, G., et al. (2007). The TRMM multisatellite precipitation analysis (TMPA): Quasi-global, multiyear, combined sensor precipitation estimates at fine scales. *J. Hydrometeorol.* 8, 38–55. doi:10.1175/jhm560.1

Huffman, G. J., Bolvin, D. T., Nelkin, E. J., and Tan, J. (2020). *Integrated multi-satellite retrievals for GPM (IMERG) technical documentation*, 83.

Jiang, H., Halverson, J. B., and Simpson, J. (2008a). 2008a: On the differences in storm rainfall from hurricanes isidore and lili. Part i: Satellite observations and rain potential. *Weather Forecast.* 23 (1), 29–43. doi:10.1175/2007waf2005096.1

Jiang, H., Halverson, J. B., and Zipser, E. J. (2008b). 2008b: Influence of environmental moisture on TRMM-derived tropical cyclone precipitation over land and ocean. *Geophys. Res. Lett.* 35 (17), L17806. doi:10.1029/2008gl034658

Kaplan, J., and DeMaria, M. (2003). Large-scale characteristics of rapidly intensifying tropical cyclones in the North Atlantic basin. *Weather Forecast.* 18, 1093–1108. doi:10.1175/1520-0434(2003)018<1093:lcorit>2.0.co;2

Kaplan, J., DeMaria, M., and Knaff, J. A. (2010). A revised tropical cyclone rapid intensification index for the Atlantic and eastern North Pacific basins. *Wea. Forecast.* 25, 220–241. doi:10.1175/2009WAF2222280.1

Kelvin, T. F. C., and Johnny, C. L. C. (2011). Size and strength of tropical cyclones as inferred from QuikSCAT data. *Mon. Weather Rev.* 140, 811–824. doi:10.1175/mwr-d-10-05062.1

Knaff, J., Sampson, C., DeMaria, M., Marchok, T., Gross, J., and Mcdie, C. (2007). Statistical tropical cyclone wind radii prediction using climatology and persistence. *Weather Forecast.* 22 (4), 781–791. doi:10.1175/waf1026.1

Knaff, J. A., Sampson, C. R., and Musgrave, K. D. (2018). An operational rapid intensification prediction aid for the western North Pacific. *Wea. Forecast.* 33, 799–811. doi:10.1175/WAF-D-18-0012.1

Leighton, H., Gopalakrishnan, S., Zhang, J. A., Rogers, R. F., Zhang, Z., and Tallapragada, V. (2018). Azimuthal distribution of deep convection, environmental factors, and tropical cyclone Rapid intensification: A perspective from HWRF ensemble forecasts of hurricane Edouard (2014). *J. Atmos. Sci.* 75, 275–295. doi:10.1175/jas-d-17-0171.1

Li, Q., and Dai, Y. (2020). Revisiting azimuthally asymmetric moist instability in the outer core of sheared tropical cyclones. *Mon. Weather Rev.* 148, 1297–1319. doi:10.1175/mwr-d-19-0004.1

Li, Q., and Wang, Y. (2012). A comparison of inner and outer spiral rainbands in a numerically simulated tropical cyclone. *Mon. Weather Rev.* 140 (9), 2782–2805. doi:10.1175/mwr-d-11-00237.1

Liang, J., Wu, L., Ge, X., and Wu, C.-C. (2011). Monsoonal influence on typhoon Morakot (2009). Part II: Numerical study. *J. Atmos. Sci.* 68, 2222–2235. doi:10.1175/2011jas3731.1

Liou, Y. C., Wang, T. C. C., Tsai, Y. C., Tang, Y. S., Lin, P. L., and Lee, Y. A. (2013). Structure of precipitating systems over Taiwan's complex terrain during Typhoon Morakot (2009) as revealed by weather radar and rain gauge observations. *J. Hydrol. Atmosphere* 506, 14–25.

Lonfat, M., Jr., Marks, F. D., and Chen, S. S. (2004). Precipitation distribution in tropical cyclones using the tropical rainfall measuring mission (TRMM) microwave imager: A global perspective. *Mon. Weather Rev.* 132, 1645–1660. doi:10.1175/1520-0493(2004)132<1645:pditcu>2.0.co;2

Miyamoto, Y., and Nolan, D. S. (2018). Structural changes preceding rapid intensification in tropical cyclones as shown in a large ensemble of idealized simulations. *J. Atmos. Sci.* 75, 555–569.

Miyamoto, Y., and Takemi, T. (2003). A transition mechanism for spontaneous axisymmetric intensification of tropical cyclone. *J. Atmos. Sci.* 70, 112–129.

Molinari, J., and Vollaro, D. (2012). A subtropical cyclonic gyre associated with interactions of the MJO and the midlatitude jet. *Mon. Weather Rev.* 140, 343–357. doi:10.1175/mwr-d-11-00049.1

Mueller, K. J. M. DeMaria, Knaff, J. A., Kossin, J. P., Vonder Haar, T. H., and Vonder Haar, T. H. (2006). Objective estimation of tropical cyclone wind structure from infrared satellite data. *Weather Forecast.* 21, 990–1005. doi:10.1175/waf955.1

Qiu, W., Ren, F., Wu, L., and Chen, L. (2019). Characteristics of tropical cyclone extreme precipitation and its preliminary causes in Southeast China. *Meteorol. Atmospheric Phys.* 131 (3), 613–626.

Qiu, W., Wu, L., and Ren, F. (2020). Monsoonal Influences on Offshore Rapid Intensification of Landfalling Typhoons in a Sheared Environment over the South China Sea. *Wea. Forecast.* 35 (2), 623–634.

Reasor, P. D., Rogers, R., and Lorsolo, S. (2013). Environmental flow impacts on tropical cyclone structure diagnosed from airborne Doppler radar composites. *Mon. Weather Rev.* 141 (9), 2949–2969. doi:10.1175/mwr-d-12-00334.1

Riemer, M., and Montgomery, M. T. (2001). Effects of vertical wind shear on the intensity and structure of numerically simulated hurricanes. *Mon. Weather Rev.* 129, 2249–2269. doi:10.1175/1520-0493(2001)129<2249:eovwso>2.0.co;2

Shen, Y. P., Zhao, Y., and Pan, (2014). A high spatiotemporal gauge-satellite merged precipitation analysis over China. *J. Geophys. Res.* 119, 3063–3075.

Shimada, U., Aonashi, K., and Miyamoto, Y. (2017). Tropical cyclone intensity change and axisymmetricity deduced from GSMaP. *Mon. Weather Rev.* 145, 1003–1017. doi:10.1175/mwr-d-16-0244.1

Shu, S., Ming, J., and Chi, P. (2012). Large-scale characteristics and probability of rapidly intensifying tropical cyclones in the Western North Pacific basin. *Weather Forecast.* 27, 411–423. doi:10.1175/waf-d-11-00042.1

Tsuji, H., and Nakajima, K. (2019). Relationship between the change in size of tropical cyclones and spatial patterns of precipitation. *JGR. Atmos.* 124, 9948–9962. doi:10.1029/2019jd030404

Uhlhorn, E. W. B. W., Klotz, T., Vukicevic, P. D., Rogers, R. F., and Vukicevic, T. (2014). Observed hurricane wind speed asymmetries and relationships to motion and environmental shear. *Mon. Weather Rev.* 142, 1290–1311. doi:10.1175/mwr-d-13-00249.1

Wang, Y. (2009). How do outer spiral rainbands affect tropical cyclone structure and intensity? *J. Atmos. Sci.* 66, 1250–1273. doi:10.1175/2008jas2737.1

Wu, L., Ni, Z., Duan, J., and Zong, H. (2013). Sudden tropical cyclone track changes over the western north pacific: A composite study. *Mon. Weather Rev.* 141, 2597–2610. doi:10.1175/mwr-d-12-00224.1

Xu, W., Jiang, H., and Kang, X. (2014). 2014: Rainfall asymmetries of tropical cyclones prior to, during, and after making landfall in south China and southeast United States. *Atmos. Res.* 139 (3), 18–26. doi:10.1016/j.atmosres.2013.12.015

Ying, M., Zhang, W., Yu, H., Lu, X., Feng, J., Fan, Y., et al. (2014). An overview of the China meteorological administration tropical cyclone database. *J. Atmos. Ocean. Technol.* 31, 287–301. doi:10.1175/jtech-d-12-00119.1

Yu, Z., Wang, Y., Xu, H., Davidson, N., Chen, Y., ChenY, Yu H., et al. (2017). On the relationship between intensity and rainfall distribution in tropical cyclones making landfall over China. *J. Appl. Meteorol. Climatol.* 56 (10), 2883–2901. doi:10.1175/jamc-d-16-0334.1

Yu, Z., Wang, Y., Xu, H., and Duan, Y. (2022). The relationship between the inner-core size and the rainfall distribution in landfalling tropical cyclones over China. *Geophys. Res. Lett.* 49, e32021GL097576. doi:10.1029/2021gl097576

Yu, Z., Wang, Y., and Xu, H. (2015). Observed rainfall asymmetry in tropical cyclones making landfall over China. *J. Appl. Meteorol. Climatol.* 54 (1), 117–136. doi:10.1175/jamc-d-13-0359.1

Zhao, H. K., Zhao, X., Jiang, P. J., Klotzbach, et al. (2022a). Interannual and interdecadal drivers of meridional migration of western north pacific tropical cyclone lifetime maximum intensity location. *J. Climate* 35, 2709–2722.

Zhao, H. K., Lu, Y., Jiang, X., Klotzbach, et al. (2022b). A statistical intra-seasonal prediction model of extended boreal summer western north pacific tropical cyclone genesis. *J. Climate* 35, 2459–2478.

frontiers | Frontiers in Earth Science

TYPE Review
PUBLISHED 12 September 2022
DOI 10.3389/feart.2022.961566

OPEN ACCESS

EDITED BY
Guihua Wang,
Fudan University, China

REVIEWED BY
Fanchao Lyu,
Chinese Academy of Meteorological Sciences, China
Yongbo Tan,
Nanjing University of Information Science and Technology, China

*CORRESPONDENCE
Gaopeng Lu,
gaopenglu@gmail.com

SPECIALTY SECTION
This article was submitted to Atmospheric Science, a section of the journal Frontiers in Earth Science

RECEIVED 04 June 2022
ACCEPTED 08 August 2022
PUBLISHED 12 September 2022

CITATION
Lu G, Peng K-M, Xian T, Wang Y, Ren H, Tian Y, Zhang M, Lucena F, Zhang X, Huang X and Cheng Z (2022), Contrast between continental and oceanic thunderstorms in producing red sprites and halos.
Front. Earth Sci. 10:961566.
doi: 10.3389/feart.2022.961566

Contrast between continental and oceanic thunderstorms in producing red sprites and halos

Gaopeng Lu[1,2,3]*, Kang-Ming Peng[1], Tao Xian[4], Yongping Wang[1], Huan Ren[1], Ye Tian[5], Mao Zhang[1], Frankie Lucena[6], Xiaoyang Zhang[7], Xin Huang[1] and Zhengwei Cheng[8]

[1]School of Earth and Space Sciences, University of Science and Technology of China, Hefei, Anhui, China, [2]Key Laboratory of Atmospheric Optics, Anhui Institute of Optics and Fine Mechanics, HFIPS, Chinese Academy of Sciences, Hefei, Anhui, China, [3]Collaborative Innovation Center on Forecast and Evaluation of Meteorological Disasters, Nanjing University of Information Science and Technology, Nanjing, Jiangsu, China, [4]Department of Mechanics and Aerospace Engineering, Southern University of Science and Technology, Shenzhen, Guangdong, China, [5]Beijing Meteorological Observation Center, Beijing, China, [6]Caribbean TLE Observatory, Cabo Rojo, PR, United States, [7]Guangzhou Power Supply Bureau, Guangzhou Power Grid Co, Ltd, China Southern Power Grid, Guangzhou, Guangdong, China, [8]State Key Laboratory of Space Weather, National Space Science Center, Chinese Academy of Sciences, Beijing, China

The observations of transient luminous events from space-borne platform extend our exploration on the mysteries of sprite phenomenology from continental thunderstorms to oceanic thunderstorms. By combining with ground-based measurements of causative strokes for hundreds of red sprites observed by the Imager of Sprites and Upper Atmospheric Lightnings (ISUAL) during 2004–2016, there is a consensus that negative cloud-to-ground (CG) strokes spawned by oceanic thunderstorms are more readily to produce sprites. The existing ground-based observations in both Caribbean Sea and near the coast of South China, mainly due to the contributions from numerous amateurs, are generally consistent with the implications of ISUAL observations. However, the physical mechanisms that might cause the enhancement of negative CG strength in the ocean remain not completely understood. There have been analyses on several cases of oceanic thunderstorms abundant in producing negative sprites. It seems that the production of negative sprites heavily depends on the size of parent thunderstorms, and they are often generated by thunderstorm conditions that are also favorable for gigantic jets.

KEYWORDS

red sprites and halos, oceanic thunderstorms, cloud-to-ground (CG) lightning strokes, impulse charge moment change (iCMC), charge structure of thunderstorm

Introduction

Red sprites are one primary category of transient luminous events (TLEs) appearing at altitudes of 50–90 km in the near space that are believed to be caused by intense tropospheric lightning (Pasko et al., 1997; Huang et al., 1999). In the past 3 decades, the efforts of many researchers all over the world, including numerous amateurs, have confirmed that red sprites are a fairly common phenomenon that could be produced by energetic cloud-to-ground (CG) lightning strokes spawned by various types of thunderstorms (Lyons, 1996; Huang et al., 2018a, Huang et al. 2018b; Wang et al., 2021b, Wang et al 2021c). Coordinated observations combining with the measurement of radio-frequency (RF) electromagnetic fields radiated by sprite-producing lightning strokes have revealed many details regarding the mechanism of sprite formation in the mesosphere (e.g., Li et al., 2012; Cummer et al., 2013; 2016; Ren et al., 2019; Kuo et al., 2021).

Lightning strokes of either polarity (i.e., positive or negative) could produce sprites. When the electric field (E-field) change caused by the charge transfer from thundercloud to ground exceeds the critical value of conventional breakdown (E_k) at certain altitude, the ionization will be initiated and became sustained only if the ambient E-field remains higher than E_k (Pasko et al., 1997; Qin et al., 2013). However, the ground-based observations over continental thunderstorms show that, despite of the well-known dominance of negative CG lightning on the land, the vast majority of sprites observed over continental thunderstorms are produced by positive CG strokes (e.g., Li et al., 2012). In particular, the documented fraction of sprites produced by negative CG strokes is substantially smaller than that inferred from the ground-based measurement of lightning strength on a global scale (e.g., Füllekrug et al., 2002; Sato and Fukunishi, 2003), constituting a sprite polarity paradox (Williams et al., 2007).

Halos, as relatively non-structured phenomena of diffusive emission that often accompany sprites (in the form of halo sprites), usually appear at relatively high altitudes (Frey et al., 2007). The formation of halos is suggested to follow a similar process to sprites, except for that the duration of lightning-induced E-field perturbation surpassing the critical E-field is relatively short (Li et al., 2012; Qin et al., 2013). Based on the space-borne observations from Imager of Sprites and Upper Atmospheric Lightnings (ISUAL) and ground-based observations of Photometric Imager of Precipitated Electron Radiation (PIPER) (Chen et al., 2008; Kuo et al., 2013; Newsome and Inan, 2010), Williams et al. (2012) proposed that the occurrence of halos might resolve the aforementioned sprite polarity paradox. That is, most halos are not registered by the conventional ground-based video observation due to the relatively short duration. Indeed, pure halos are rarely reported in ground-based observations by means of video cameras at regular frame rates (for example, 25 or 30 frames per second, depending on the encoding format).

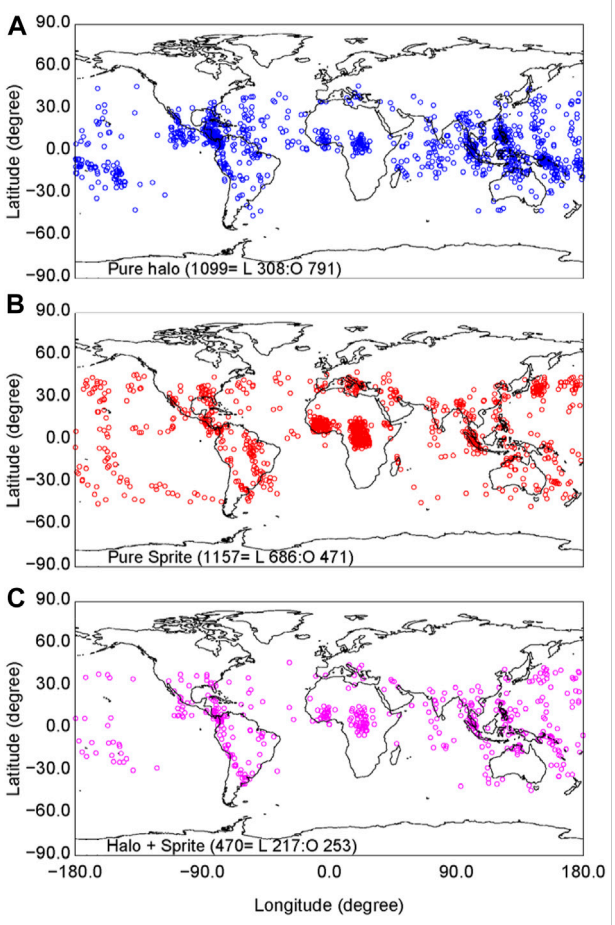

FIGURE 1
Geographic distribution of **(A)** pure halos, **(B)** pure sprites, and **(C)** halo-sprite events observed by ISUAL during 2004–2016.

In this paper, we mainly address the contrast between continental and oceanic thunderstorms as reflected by the observations of red sprites and halos from both space-borne and ground-based platforms. This contrast might be in line with the high incidence rate of high-peak current negative CG strokes in the ocean as found on the basis of ground-based lightning detections (Said et al., 2013). Therefore, the further efforts to characterize the oceanic sprite-producing thunderstorms might shed light on the meteorological conditions that favor the occurrence of intense negative CG strokes in the ocean (e.g., Chronis et al., 2016).

Implications from space-borne observations

The analysis of red sprites captured by the ISUAL payload on the FORMOSAT-2 satellite indicates that there is a much higher population of sprites produced by negative CG strokes over

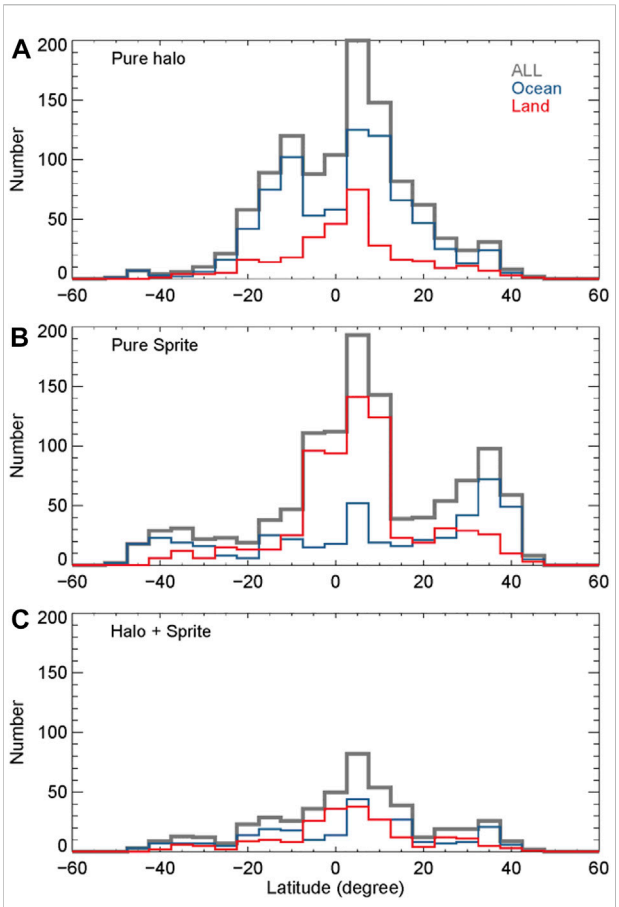

FIGURE 2
Distribution of ISUAL-observed TLEs along latitudes. The ISUAL TLEs are classified into three categories, i.e., **(A)** pure halo, **(B)** pure sprite, and **(C)** halo with sprite.

oceanic thunderstorms (Lu et al., 2017). As for halos, a similar category of TLEs that typically endure less than 1 ms (Frey et al., 2007; Newsome and Inan, 2010; Kuo et al., 2013), their causative strokes are predominantly of negative polarity and tend to crowd in the ocean (Lu et al., 2018).

Figure 1 shows the geographic distribution of halos, sprites, and halo/sprite events observed by ISUAL during 2004–2016. The sprite location is estimated by the ISUAL team according to the procedures described by Chen et al. (2008). By comparing with the location of causative CG stroke given by the National Lightning Location Network (NLDN), Liu et al. (2017) showed that the location of ISUAL-detected events has been determined with error typically less than 100 km. As shown in Figure 1A, there are totally 1,099 pure halo events that are mainly (791, or 72%) observed over oceanic regions. According to the results of Lu et al. (2018), intense negative CG strokes in the ocean might made a major contribution. For pure sprites (Figure 1B), however, most (686 out of 1,157, or 59.3%) were observed over land, which is primarily due to a remarkable high concentration in central Africa. It merits further investigation regarding the dominant polarity of sprites in this region. There were 470 sprites whose occurrence was accompanied by a preceding halo feature (Figure 1C), and these events were almost evenly distributed over land and ocean.

The analysis of Lu et al. (2017) with respect to sprites observed in the vicinity of North America shows that the continental thunderstorms primarily produce sprites through positive CG strokes, which is consistent with the ground-based observations in 2008–2013 (Huang et al., 2018a). The mesoscale convection systems (MCSs) prevailing in the Great Plain of North America are prolific sprite-producers, and many sprite-related studies at the early stage were conducted based on the observations of sprites over them (e.g., Lyons, 1996; Huang et al., 1999; Hu et al., 2002; Miyasato et al., 2002; Cummer and Lyons, 2005; Li and Cummer, 2011; Kuo et al., 2013, Kuo et al., 2016).

The distribution pattern of halos and sprites observed by ISUAL is substantially different from that of global lightning as indicated by both space observations (e.g., Christian et al., 2003) and ground-based lightning location results (Said et al., 2013), implying that lightning strokes in different places bear varying energies to impose electromagnetic stress on the lower ionosphere. Figure 2 shows the distribution of various TLE types with latitude. Both pure halos and sprites with halo feature were predominantly produced at low latitudes (Figures 2A,C). As shown in Figure 2B, the geographic distribution of pure sprite observations exhibits a secondary peak at middle latitudes especially in north hemisphere, which is mainly caused by the concentration of pure sprites in the Mediterranean.

Based on the identification of transient Schumann Resonances (SRs) in the extremely low-frequency (ELF) magnetic field waveform at two stations during a 1-year period, Sato and Fukunishi (2003) estimated the average global occurrence rate of sprites to be around 720 events/day. It is noticed that their results indicate a region with high occurrence rates of sprites beyond the east coast of southern Africa, which is however not clear in Figure 1. Instead, the ISUAL observations indicate the high occurrence rate of sprites in central Africa, which is also the capital of lightning in the world as seen from the space observation (Christian et al., 2003).

Ground-based observations of negative sprites

The first ground-based observation of sprite was probably serendipitously obtained by a research team who was testing their low-light-level TV camera designed for tracking rocket flight. This fortunate recording, along with existing reports from space-born observations, inspired more scientists from various continents to conduct the ground-based observations over thunderstorms. Sprites made by negative CG strokes were extremely rarely captured at the initial stage of sprite hunting

(Barrington-Leigh et al., 1999), and the dataset of negative sprites with coordinated lightning sferic measurements slowly accumulated (Taylor et al., 2008; Li et al., 2012; Lu et al., 2016).

However, although the space-borne observations indicate a population of negative sprites in the ocean, there is generally an absence of ground-based observations of red sprites over oceanic thunderstorms before 2016. While Huang et al. (2012), examined the occurrence of several gigantic jets over Typhoon Lionrock (2010), they also mentioned the observation of many sprites, while unfortunately, these events were not examined in details. Boggs et al. (2016) reported the observations of five sprites produced by negative CG strokes hosted in two coastal thunderstorms both associated with a tropical disturbance. All these sprite-producing negative CG strokes belonged to the categories recognized earlier by Lu et al. (2012). Huang et al. (2018b) reported the observations of tens of sprites over Hurricane Matthew (2016), whereas these events all turned out to be produced by positive CG strokes. However, in a further study on this particular thunderstorm case, Huang et al. (2021) showed that Hurricane Matthew (2016) could have produced hundreds of sprites during its lifetime, including quite many negative CG strokes with impulsive charge transfer in excess of the known threshold for sprite production.

Negative sprites produced by continental thunderstorms

Negative sprites were rarely produced by CG strokes hosted in continental thunderstorms. According to the survey of Williams et al. (2007), the percentage of confidential negative sprite observations is estimated to be about 0.1% before (Cummer et al., 2006b).

Barrington-Leigh et al. (1999) reported the first observation of negative sprites in North America, which was followed by Miyasato et al. (2002) who obtained the array photometric measurement of the sprite halo event produced by a negative CG stroke. Taylor et al. (2008) reported the observation of a negative halo-sprite event in South America. Li et al. (2012) also reported that during the 4-years observations (from 2008 to 2011) at several ground-based stations in the continental United States, among 1,651 sprites captured, only six events (and thus a ratio of 0.36%) were confirmed to be produced by negative CG strokes. The inclusion of ground-based sprite observations in the following 2 years (2012–2013) does not significantly change the percentage of negative sprites in the ground-based observations over continental thunderstorms. So far, there was no report of ground-based observations yet with respect to negative sprites over thunderstorms in Europe.

Almost all the sprite-producing negative CG strokes appear to bear several similar features: 1) the peak current usually reaches above -80 kA, and 2) the causative charge transfer is usually high (greater than −450 C km) and impulsive (with time scale <1 ms), and there is no evidence of long continuing current as often observed for intense positive CG strokes (Lu et al., 2009, 2013).

Li et al. (2012) examined six cases of sprites produced by negative CG strokes, and found that these negative sprites show similar features in their morphology: negative sprites are always accompanied by halos, and the downward streamers usually terminate at higher altitudes (approximately 55–60 km) than their positive counterparts. Li et al. (2012) also suggested that the timescale of causative CG strokes, primarily the impulse current, has a significant impact on the morphology of sprites (e.g., Qin et al., 2013). First of all, as shown in Figure 3 regarding one of the cases examined in details by Li et al. (2012), due to the relatively short duration and therefore a less influence by the relatively high conductivity at high altitudes, the lightning-induced *E*-field perturbation can penetrate into higher region; secondly, the short duration of charge transfer results in a greater induction component in the lightning-induced *E*-field perturbation (e.g., Contreras-vidal et al., 2021), and therefore the overall region of dielectric breakdown extends to a higher altitude.

Later on, Lu et al. (2016) reported an unusual case of negative sprite that was actually produced by the joint effect of a moderate negative CG stroke along with its ensuing current surge (likely associated with an *M*-component). This particular observation actually implies that the duration of causative stroke might be very critical for a particular CG stroke to produce sprites. To demonstrate this, we present the simulation results for three different waveforms of causative CG stroke (Figure 4A). The length of vertical lightning channel is assumed to be 5 km in all cases. All three current moments accumulate to the same total charge moment change of +500 C km (Figure 4B). As shown in Figure 4C, the computation results for current waveform of type 1 and type 2 shows the comparison between different durations (corresponding to different polarities). The implications of this comparison are generally consistent with Li et al. (2012).

Also, the third type of current moment exhibits an interesting non-linear effect that merits further discussions. As shown in Figure 4C, because the sub-critical *E*-field perturbation caused by the first current pulse actually reduces the conductivity in the region of interest, the *E*-field perturbation generated by the second current pulse will endure longer than usual. Indeed, the streamer feature of negative sprite examined by Lu et al. (2016) was more distinct than most cases previously reported (e.g., Taylor et al., 2008; Li et al., 2012). The discussions above also have some implications for the general scenario that the typical sprite-producing lightning flashes, either of positive polarity or negative polarity, usually develop an extensive intra-cloud channel system prior to the CG stroke (e.g., Lu et al., 2009, 2012).

Boggs et al. (2016) reported the observations of totally five negative sprites near the coast of Florida over two thunderstorms

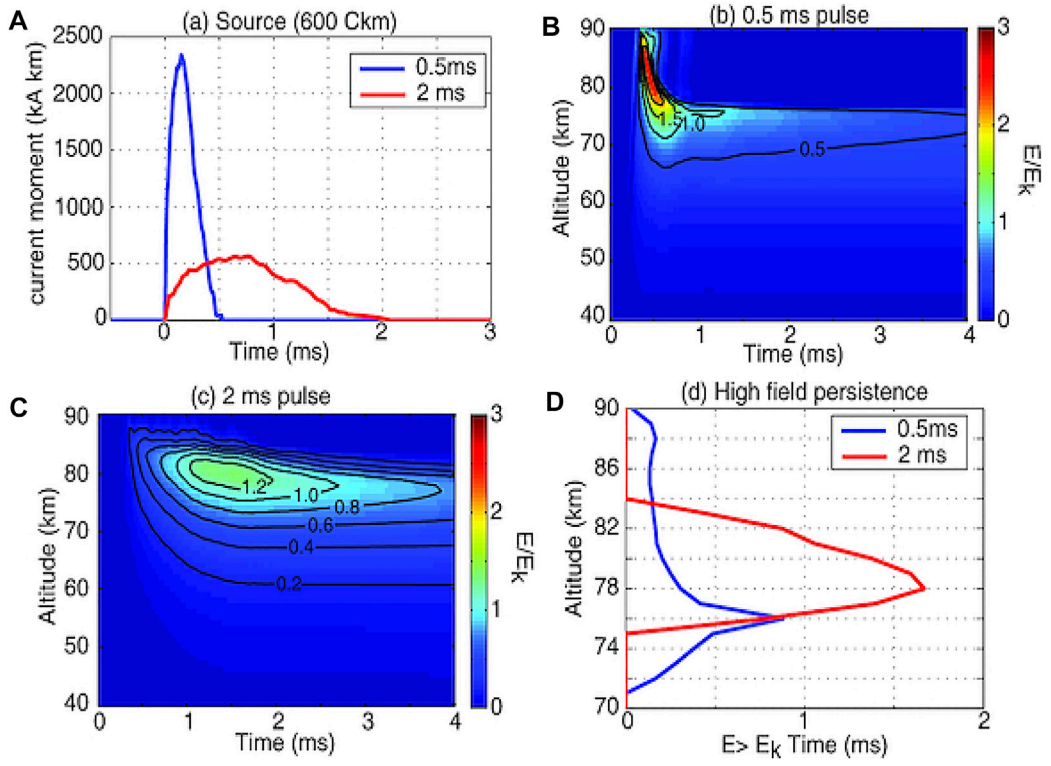

FIGURE 3
Comparison between two impulse charge transfer with different time scales to show the influence of charge transfer timescale on the lightning-induced E-field perturbation at the altitude of sprite initiation. The current moments with different time scales are shown in Panel **(A)**, and the lightning-induced E-field perturbation associated with each case is shown in panels **(B,C)**, respectively. Panel **(D)** shows the persistent time for the lightning-induced E-field to exceed the local E-field threshold of dielectric breakdown at different altitudes. Adopted from Li et al. (2012).

associated with a tropical disturbance. The parent lightning flashes of all these events were characterized by a high-level progression in the upper positive region. Their analyses indicate that an excess amount of midlevel negative charge in comparison with the upper positive charge is essential for the production of negative CG strokes with sprite-producible impulse charge transfer. This "charge imbalance" could be favored jointly by the high wind shear at the middle to upper regions and the low negative CG flash rate.

Ground-based observations from Puerto Rico

Huang et al. (2018b) examined the massive sprite production (about 40 events totally on two consecutive nights) over Hurricane Matthew (2016), as captured by an amateur photographer, Frankie Lucena, who began to capture TLEs from his places in Puerto Rico since May of 2016. After examining the broadband lightning sferics of these sprites recorded in Duke Forest, it was surprisingly found that all these events were produced by positive CG strokes. For approximately 86% of these sprites, the causative CG strokes were detected by the World-Wide Lightning Location Network (WWLLN) (e.g., Hutchins et al., 2012). As shown in Figure 5, these sprite-producing CG strokes were all located in the outer rainband region defined by relatively cold cloud-top brightness temperature (≤194 K).

The absence of negative sprite observation for this particular thunderstorm arose more curiosity, and therefore all the available observations from the very beginning were collected to make a long-term survey regarding the sprite phenomenology in the Caribbean area. After examining the sferic waveform recorded coordinately with these observations, as well as the characteristics of sprite morphology from existing studies, the polarity of causative lightning strokes is determined for the majority of sprites captured in the 5-years time period of 2016–2020. Nearly 100 red sprites produced by negative CG strokes were identified from this data set. Recently, with the data obtained by Frankie Lucena, (Wang et al., 2019), reported the observations of several negative sprites over a tropical depression that eventually developed into Hurricane Harvey (2017). It should also be

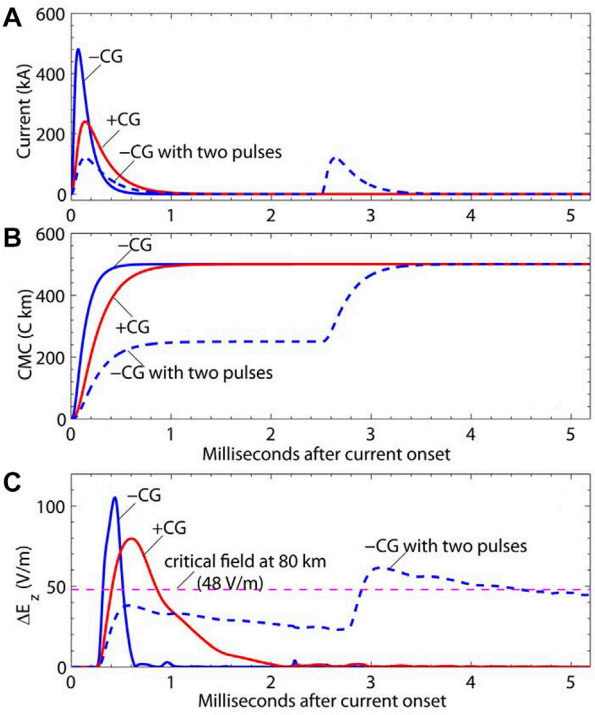

FIGURE 4
Vertical E-field perturbation caused by lightning current moment with different forms: type 1 for normal negative CG strokes, type 2 for normal positive CG strokes, and type 3 for a negative CG stroke with two consecutive current pulses as discussed by Lu et al. (2016). The current waveform of each type is shown in panel **(A)**, and the lightning channel is assumed to be vertical with a length of 5 km. The cumulated charge moment change (CMC) and resulted E-field perturbation at 80 km altitude are shown in panels **(B,C)**, respectively.

noted that, as indicated in Figure 6B, this particular thunderstorm also produced quite a few gigantic jets during the nighttime observation on August 19, similar to the case examined by Boggs et al. (2016), which provides further implications regarding the attributes of thunderstorm charge structure that might be favorable for producing negative sprites. One negative sprite and one gigantic jet were shown in the inset of Figure 6A, which shows the overall track of Hurricane Harvey (2017) since August 18, 2017.

In comparison with space-borne observations that cannot keep track of the sprite production over a specific thunderstorm, the ground-based observations remain more valuable in diagnosing the dynamics of a particular thunderstorm that could be essential for producing negative sprites. As more and more ground-based observations of negative sprites accumulate, more sophisticated measurements will be incorporated to diagnose the meteorological conditions and thunderstorm properties conducive to the generation of negative sprite-producible CG strokes.

Contributions from Chinese amateurs

The amateurs have made important contributions to the exploration of spatial and temporal connection between TLEs and their parent lightning (e.g., van der Velde et al., 2007; Lu et al., 2011; Lu et al., 2013). With critical observations of several amateurs residing in New Mexico, Texas, and Florida, respectively, a detailed understanding on the in-cloud lightning evolution associated with gigantic jets and red sprites has been achieved.

Since the summer season of (Chen et al., 2014), the amateurs in China, including some professional photographers, have been enthusiastically contributing to the research of TLEs, either by providing the critical observations (e.g., Chou et al., 2016; Yang et al., 2020), or arousing the attention from the publicity. Yang et al. (2020) reported the analysis of a gigantic jet event captured by two amateurs concurrently from different sites in southern part of China.

In 2021, there was a tremendous surge in the number of TLEs recorded by the amateurs. Although the timing is not perfectly in line with GPS, the uncertainty is relatively small so that the parent CG strokes can be readily identified in most cases. Figure 7 shows the distribution of identified causative CG strokes for the sprites captured by the amateurs in China. Note that the negative CG stroke received special attention by carefully inspecting the consistency between the location and direction of sprite observation. We can see a relatively clear abundance of negative sprite-producing CG strokes in the open sea near the coast of Guangdong Province. Exactly 20 years ago, Su et al. (2002) have reported the observations of red sprites in the similar region, while there was no confirmative report yet of sprites produced by negative CG strokes.

With the dramatic enhancement of captured events, some rare TLEs were also recorded, including quite a few gigantic jets and halos. In particular, on the night of three consecutive days in May of 2021, the massive sprite generation was recorded over a mesoscale convective system, which is the first observation of >100 sprites produced by one thunderstorm. This particular observation suggests that thunderstorms in East Asia could produce red sprites as actively as those in North America. Moreover, due to the influence of South Asian monsoon and East Asian monsoon, the unique three-step staircase topography in the mainland of China might exhibit some interesting patterns of sprite-producible CG strokes.

Implications on sprite phenomenology

The detailed development of sprite morphology can be resolved by means of high-speed video observations with enhanced sensitivity (e.g., Stanley et al., 1999; Stenbaek-Nielsen et al., 2000; Cummer et al., 2006a; Cummer et al., 2006b). Based on the high-

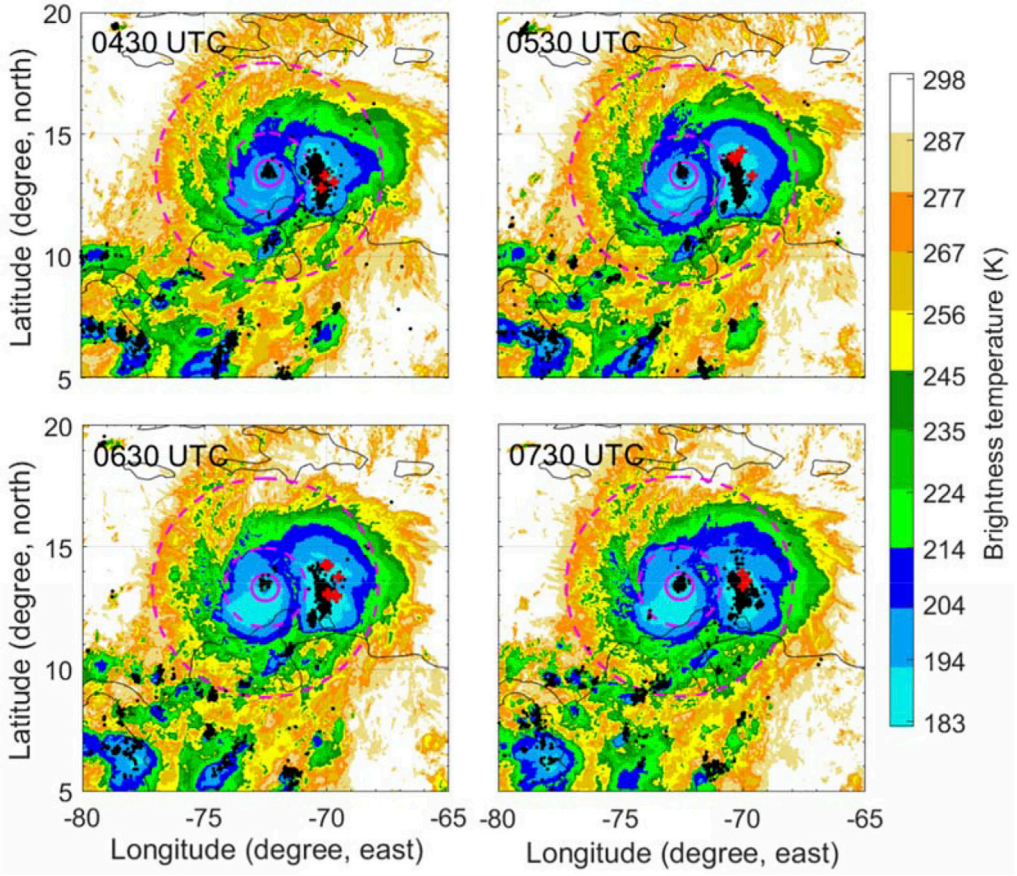

FIGURE 5
Distribution of parent strokes for the sprites observed during four consecutive 1-hour time windows (centered at the time specified in each panel) over Hurricane Matthew (2016). Adapted from Huang et al. (2018b).

speed video observations of sprites over a mesoscale convective system in the central United States, Ren et al. (2021) examined the time-resolved evolution of two sprite halo events in comparison with the charge moment change retrieved from the broadband sferic measurement. For the case shown in Figure 8, as an example, the halo feature appeared approximately at about 0.5 ms after the return stroke (see Figures 8A–C), and then the brightness remained growing until the sprite streamer became visible another 0.5 ms later (see Figures 8D–E). From this analysis, it can be seen that the transition from halo to sprite considerably depends on the duration of lightning-induced *E*-field perturbation exceeding the threshold of dielectric breakdown (e.g., Adachi et al., 2004; Hiraki, 2010). According to the analysis of Ren et al. (2021) based on the transmission line model of CG strokes, both induction and static component of lightning-induced *E*-field change contributed to the formation of halo; as time elapsed (about half millisecond after the return stroke), the electrostatic lightning *E*-field became dominant in supporting the streamer development.

Kuo et al. (2021) also examined the evolution of several TLE events (including two elves, one halo, and one halo sprite, and two sprites) captured with the high-speed video observations at speed of 10,000 fps from the Yushan weather station (at an altitude of 3,845 m) in Taiwan. The similar image sequences were obtained for two halo events produced by positive CG strokes with peak current of +118 kA and +172 kA, respectively. Their observations indicate that the elevation for the edge of halo emissions gradually declined over a time period of approximately 1.5 ms.

Critical electric field for sprite production

The analysis of Qin et al. (2012) with a two-dimensional (2D) plasma fluid model indicates that, under the same upper atmospheric ambient conditions, the sprite production requires a much larger charge moment change (CMC) for negative CG strokes than their positive counterpart (e.g., −300 C km vs. +200 C km).

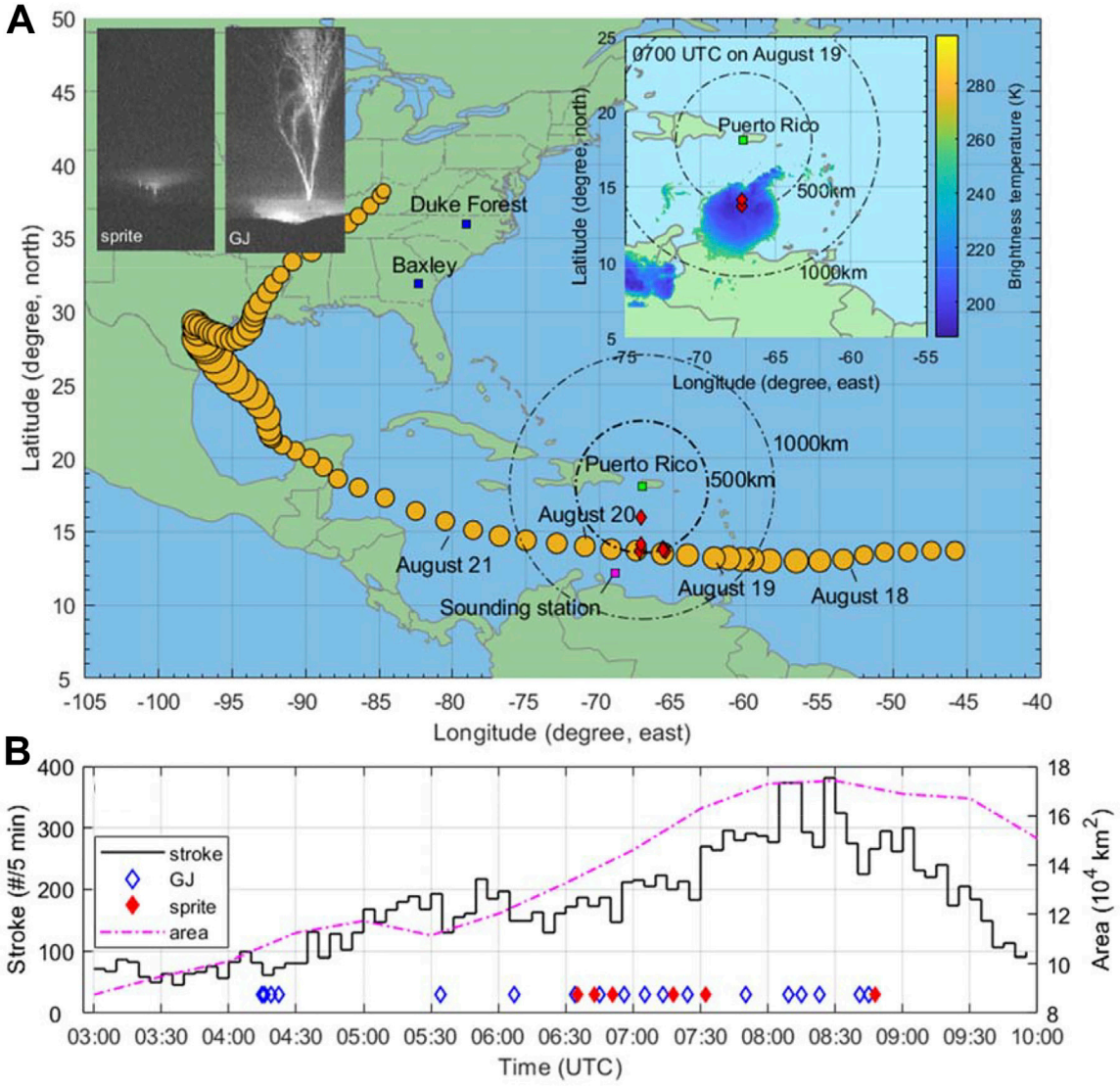

FIGURE 6
Observations of negative sprites over a tropical thunderstorm that eventually developed into Hurricane Harvey (2017). Panel **(A)** shows the overall track of the hurricane, and the parent lightning of TLE observations from Puerto Rico on the night of August 19. The inset images of panel **(A)** show the observations of one negative sprite and one gigantic jet, respectively. Panel **(B)** summarizes the observations in comparison with the lightning occurrence during the nighttime observation. Adapted from Wang et al. (2021b).

It has been suggested that the impulsive charge transfer within 2 ms after the return stroke can be used as a metric to evaluate the potential of a particular CG stroke in producing sprites (Hu et al., 2002). This is probably because the ensuing impulse current of CG strokes usually drive a major pulse of approximately 2 ms duration as measured by the very-low-frequency (VLF) or ultra-low-frequency (ULF) magnetic field sensor (e.g., Price et al., 2002; Hu et al., 2002; Li and Cummer, 2011; Lu et al., 2013), or E-field change measurement with slow antenna (e.g., Hager et al., 2012). In fact, as also pointed out by Li et al. (2012), such pulses detected for negative sprite-producing CG strokes usually appear to be more impulsive than those driven by positive CG strokes. Therefore, based on the analysis of Ren et al. (2021), the contribution of induction component to the lightning E-field perturbation at the formation height of halo will be more important for negative CG strokes.

It should be mentioned that due to the different duration of halos and sprites, it is not quite reasonable to determine the threshold for negative sprite production with a time interval of 2 ms to calculate the impulse charge moment change (iCMC). As we can see from Figure 8, the halo production usually reaches the greatest brightness within 1 ms after the causative return stroke. Therefore,

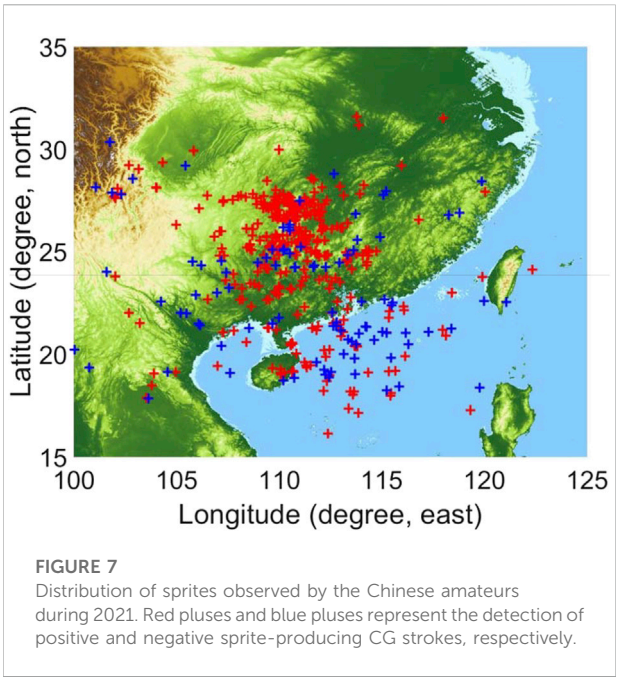

FIGURE 7
Distribution of sprites observed by the Chinese amateurs during 2021. Red pluses and blue pluses represent the detection of positive and negative sprite-producing CG strokes, respectively.

the iCMC over a time period of 2 ms might slightly overestimate the critical charge transfer for halo production, as well as negative sprites that are usually characterized by a halo feature (Li et al., 2012).

There are some other criteria that have been applied to evaluate the potential of individual lightning strokes in producing sprites or halos, such as peak current, which, however, has been shown not to be a good indicator for sprite production (Lu et al., 2013), especially for negative CG strokes (e.g., Lu et al., 2012). For the lightning detection of WWLLN, the energy of a specific lightning stroke was also estimated according to the received sferic waveform (e.g., Abarca et al., 2010; Hutchins et al., 2013), whereas it remains unknown whether this parameter can be used as an effective tool to evaluate the potential of a lightning stroke in producing sprite.

On the phenomenology of negative sprites

The morphology of negative sprites, since their first recording by Barrington-Leigh et al. (1999), has been fairly consistent by composing a pancake-shape diffusive region atop short vertical tendrils. The streamer region of negative sprites is usually very dim, and its termination altitude is also usually relatively high (e.g., Taylor et al., 2008; Li et al., 2012).

Wang et al. (2021a) reported the observation of an atypical negative sprite for which the broadband very low-frequency (VLF) magnetic sferics exhibit the signature of "sprite current," namely a secondary VLF pulse (see Figures 9B,D–H). This feature was typically observed for bright sprites produced by positive CG strokes (e.g., Cummer et al., 1998; Lu et al., 2013). The examination of optical signal radiated by the causative stroke indicates that its duration (5.25 ms, see Figure 9I) is significantly longer than that (about 2.5 ms, see Figure 9J) of regular negative parent strokes for sprites observed by ISUAL. Also, the streamer portion descended to an altitude of 50 km, which is the lowest ever recorded for negative sprites. Nevertheless, the analysis of this event indicates that provided a relatively long duration of intense charge transfer after the return stroke, the sprite produced by the negative CG could also be very bright, suggesting that the aforementioned dependence of sprite morphology on the duration of causative CG charge transfer is also present for negative sprites.

In the relatively large data set of negative sprites based on the observations of ISUAL, negative sprites could also bear a different morphology. It should be noted that despite of a quite standard morphology with a pancake-shaped cap atop vertical compact streamers, there are also some negative sprites taking on appearance that remain to be explained. Interestingly, these abnormal events were mostly produced by sub-critical impulse charge moment change (i.e., iCMC < -300 C km) (Lu et al., 2017), and the underlying physical mechanism remains unknown.

Thoughts for future studies

Apparently, more ground-based observations of sprites produced by vigorous negative CG strokes spawned by oceanic thunderstorms are desired to characterize the physical connection between impulse charge transfer of sprite-producing CG strokes and time-resolved evolution of sprites. There are no conclusive results yet regarding why the oceanic thunderstorms are so productive in spawning intense negative CG strokes. Chronis et al. (2016) discussed several factors that might contribute to making oceanic thunderstorm prolific in producing negative CG strokes with high peak current and probably also large impulse charge moment change. Their conclusion is that the enhancement of negative CG strength in the ocean is most likely caused by the modulation of thundercloud potential by sodium chloride (NaCl) and ice crystal size. The general connection between lightning strength and thunderstorm potential is consistent with that oceanic thunderstorms are prone to spawn intense negative CG strokes favorable for sprites (i.e., negative CG strokes with particularly large impulse charge transfer), as a greater difference between thunderstorm potential and ocean surface (with zero potential) is bound to cause a higher charge transfer. A better understanding on the lightning phenomenology related to oceanic thunderstorms is desired (e.g., Han et al., 2021).

Sufficient ground-based observations of red sprites, especially that with coordinated measurement of broadband lightning sferics to quantify the strength of parent lightning strokes, are still lacking in many places around the world. For negative CG flashes spawned by continental thunderstorms, they are known to usually deposit the in-cloud negative charge through several discrete strokes, and the

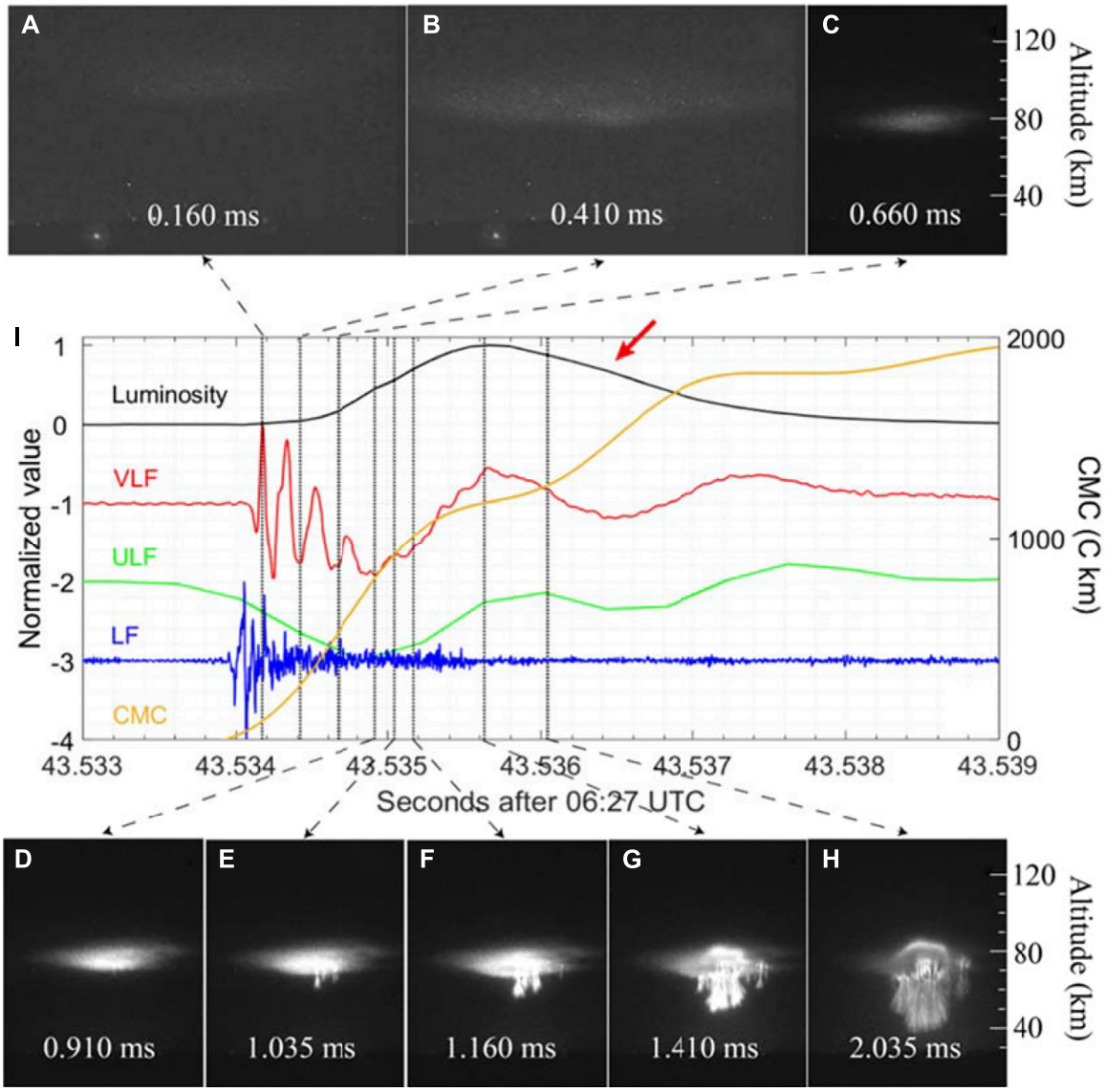

FIGURE 8
Examining the evolution of a halo-sprite event captured with the high-speed camera by comparing with the broadband lightning sferics [panel **(I)**]. The static images obtained by the high-speed observations were given in panels **(A–H)**. Adopted from Ren et al. (2021).

number of CG strokes contained in individual CG flashes is referred to as "multiplicity." Will the negative CG flashes generated by oceanic thunderstorms, on a statistical manner, exhibit a substantial difference from those produced by continental thunderstorms?

It also remains necessary to examine the characteristic time scale of impulse charge transfer for both negative and positive CG strokes. The existing work indicates that the charge transfer of negative sprite-producing CG stroke appears to be significantly more impulsive than their positive counterparts. Will the negative CG strokes produced by oceanic thunderstorms be less impulsive that produced by continental thunderstorms?

According to the ISUAL observations in 2004–2016, the maritime continent (MC) in South China Sea is a broad prolific region of red sprites and halos (as shown in Figure 1). However, the ground-based observations are relatively scarce in this region. Therefore, it is highly desired to conduct coordinated ground-based campaigns regarding discharge properties of lightning strokes around the maritime continent, including the coastal regions of South China. Wang et al. (2021c) reported some preliminary results of sprite observations over tropical thunderstorms from a station located in Malacca, Malaysia, and only a handful of

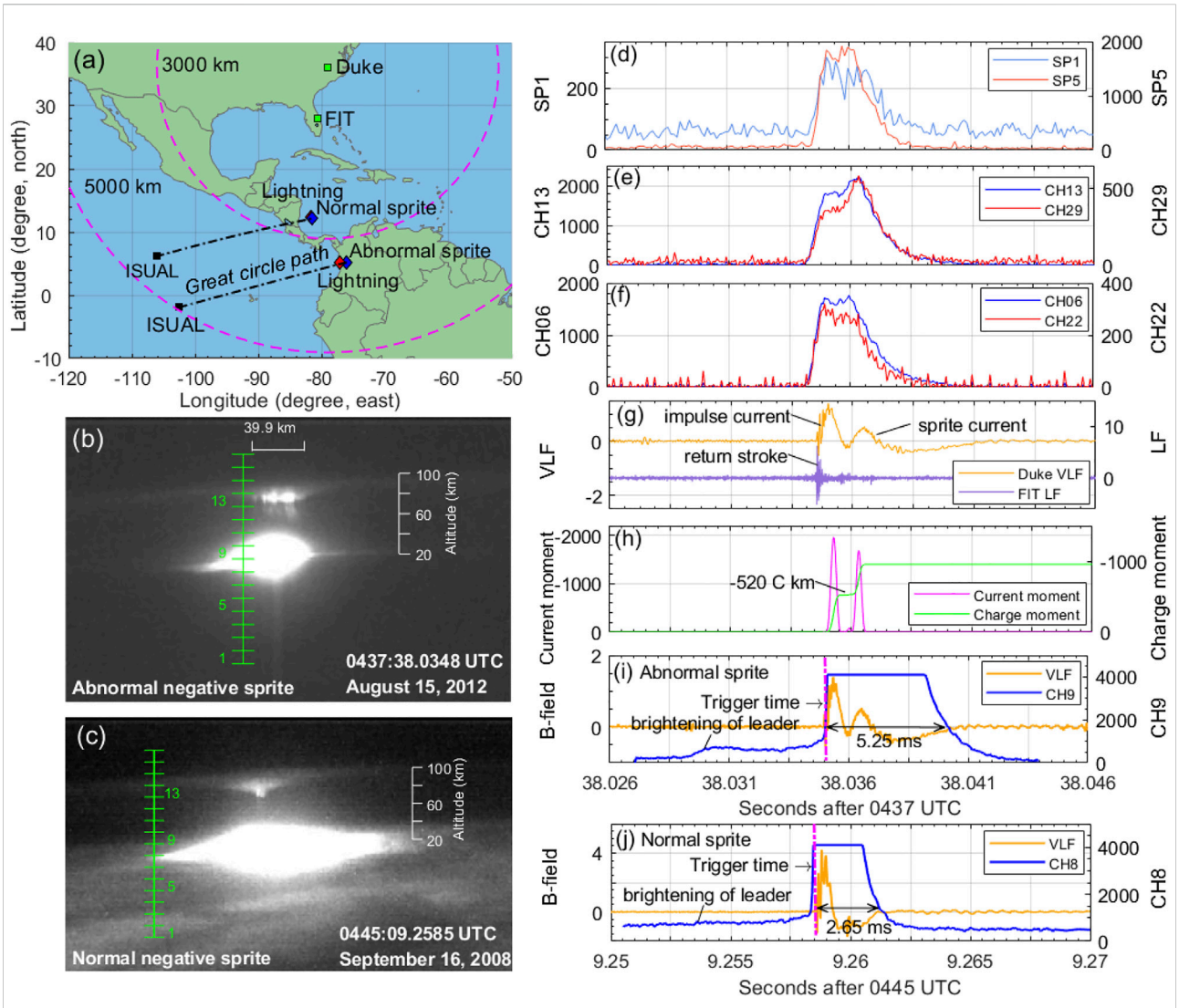

FIGURE 9
ISUAL observation of an unusual negative sprite for which the simultaneous measurement of VLF sferics also shows the signature of "sprite current.". Panel **(A)** shows the ISUAL observations of two negative sprites, including one abnormal event [panel **(B)**] demonstrating the sprite current feature shown in the very low-frequency (VLF) sferic signal recorded in Duke Forest [panel **(G)**] and one normal event [panel **(C)**]. The selected other ISUAL measurements for the abnormal event were plotted in panels **(D–F)**. The comparison between VLF signal and brightness curve is shown in panels **(I,J)**, respectively. Adapted from Wang et al. (2021a).

red sprites produced by positive CG strokes have been recorded from this station.

Concluding remarks

By combining the ISUAL observations and existing ground-based observations, there have been sufficient evidence to show that there is a considerable difference between continental and oceanic thunderstorms in posing electrical stress on the middle atmosphere. In particular, continental thunderstorms mainly impact on middle atmosphere with positive CG strokes, whereas oceanic thunderstorms are mainly through negative CG strokes. Primarily due to the lack of sufficient ground-based platforms, transient luminous events (TLEs) produced by oceanic thunderstorms are substantially less studied than their continental counterparts. However, there is increasing evidence, from both space-borne and ground-based observations, showing that red sprites and halos produced by negative CG strokes could be very popular in the ocean, where thunderstorms very likely bear some features that are favorable for spawning negative CG strokes with relatively large impulse charge transfer to the seawater. This is

partially in line with the abundance of high peak-current negative strokes indicated by various lightning detection networks, but it remains necessary to explore the exact cause of enhanced peak current for negative CG strokes in the ocean.

Both ground-based and space-borne observations of TLEs are important to further investigate the exact physical mechanism for the enhancement of negative CG strength in the ocean. Although the observations from space over years reveal some peculiarities of sprite genesis over oceanic thunderstorms, the underlying mechanism remains to be investigated through ground observations by combining with concurrent measurements regarding the lightning morphology and time-resolved charge transfer of causative CG strokes. In particular, it is desired to conduct more ground-based observations of TLEs over the maritime continent in South China Sea. Some general understandings on the difference in the typical charge structure between oceanic and continental thunderstorms could also be promoted by examining the remote sensing data of satellites.

Author contributions

Conceptualization and design of study, GL; Data Collection, GL, K-MP, FL, and XZ; Data analysis and interpretation, YW, MZ, K-MP, and HR; Writing and preparation of original draft, GL, YW, and HR; Funding acquisition, GL. All authors contributed to article revision, read and approved the submitted version.

Funding

This work was supported by National Key R&D Program of China (No. 2019YFC1510103), the CAS Project of Stable Support for Youth Team in Basic Research Field (No. YSBR-018), Natural Science Foundation of China (Nos. 41875006 and U1938115), the Chinese Meridian Project, and the International Partnership Program of Chinese Academy of Sciences (No. 183311KYSB20200003).

Acknowledgments

We truly appreciate the persistent efforts from many amateurs in China, whose contributions substantially boost the progress in the understanding on the difference between continental and oceanic thunderstorms in driving the transient luminous events. We acknowledge for the data resources from National Space Science Data Center, National Science and Technology Infrastructure of China (https://www.nssdc.ac.cn).

Conflict of interest

Author XZ was employed by Guangzhou Power Grid Co, Ltd.

The remaining authors declare that the research was conducted in the absence of any commercial or financial relationships that could be construed as a potential conflict of interest.

Publisher's note

References

Abarca, S. F., Corbosiero, K. L., and Galarneau, T. J., Jr. (2010). An evaluation of the worldwide lightning location network (WWLLN) using the national lightning detection network (NLDN) as ground truth. *J. Geophys. Res.* 115, D18206. doi:10.1029/2009JD013411

Adachi, T., Fukunishi, H., Takahashi, Y., and Sato, M. (2004). Roles of the EMP and QE field in the generation of columniform sprites. *Geophys. Res. Lett.* 31, L04107. doi:10.1029/2003GL019081

Barrington-Leigh, C. P., Inan, U. S., Stanley, M., and Cummer, S. A. (1999). Sprites triggered by negative lightning discharges. *Geophys. Res. Lett.* 26, 3605–3608. doi:10.1029/1999gl010692

Boeck, W. L., Vaughan, O. H., Jr., Blakeslee, R., Vonnegut, B., and Brook, M. (1992). Lightning induced brightening in the airglow layer. *Geophys. Res. Lett.* 19, 99–102. doi:10.1029/91gl03168

Boggs, L. D., Liu, N., Splitt, M., Lazarus, S., Glenn, C., Rassoul, H., et al. (2016). An analysis of five negative sprite-parent discharges and their associated thunderstorm charge structures. *J. Geophys. Res. Atmos.* 121, 759–784. doi:10.1002/2015JD024188

Chen, A. B.-C., Su, H.-T., and Hsu, R.-R. (2014). Energetics and geographic distribution of elve-producing discharges. *J. Geophys. Res. Space Phys.* 119, 1381–1391. doi:10.1002/2013JA019470

Chen, A. B., Kuo, C. L., Lee, Y. J., Su, H. T., Hsu, R. R., Chern, J. L., et al. (2008). Global distributions and occurrence rates of transient luminous events. *J. Geophys. Res.* 113, A08306. doi:10.1029/2008JA013101

Chern, R. J., Lin, S., and Wu, A. (2015). Ten-year transient luminous events and Earth observations of FORMOSAT-2. *Acta Astronaut.* 112, 37–47. doi:10.1016/j.actaastro.2015.02.030

Chou, C.-C., Dai, J., Kuo, C.-L., and Huang, T.-Y. (2016). Simultaneous observations of storm-generated sprite and gravity wave over Bangladesh. *J. Geophys. Res. Space Phys.* 121, 9222–9233. doi:10.1002/2016JA022554

Christian, H. J., Koshak, W. J., Hall, J. M., Driscoll, K. T., Boeck, W. L., Buechler, D., et al. (2003). Global frequency and distribution of lightning as observed from space by the Optical Transient Detector. *J. Geophys. Res.* 108 (D1), 4005. doi:10.1029/2002JD002347

Chronis, T., Koshak, W., and McCaul, E. (2016). Why do oceanic negative cloud-to-ground lightning exhibit larger peak current values? *J. Geophys. Res. Atmos.* 121, 4049–4068. doi:10.1002/2015JD024129

Contreras-Vidal, L., Sonnenfeld, R. G., da Silva, C. L., McHarg, M. G., Jensen, D., Harley, J., et al. (2021). Relationship between sprite current and morphology. *JGR. Space Phys.* 126, e2020JA028930. doi:10.1029/2020JA028930

Cummer, S. A., Frey, H. U., Mende, S. B., Hsu, R.-R., Su, H.-T., Chen, A. B., et al. (2006b). Simultaneous radio and satellite optical measurements of high-altitude sprite current and lightning continuing current. *J. Geophys. Res.* 111, A10315. doi:10.1029/2006JA011809

Cummer, S. A., Inan, U. S., Bell, T. F., and Barrington-Leigh, C. P. (1998). ELF radiation produced by electrical currents in sprites. *Geophys. Res. Lett.* 25 (8), 1281–1284. doi:10.1029/98GL50937

Cummer, S. A., Jaugey, N., Li, J., Lyons, W. A., Nelson, T. E., and Gerken, E. A. (2006a). Submillisecond imaging of sprite development and structure. *Geophys. Res. Lett.* 33, L04104. doi:10.1029/2005GL024969

Cummer, S. A., and Lyons, W. A. (2005). Implications of lightning charge moment changes for sprite initiation. *J. Geophys. Res.* 110, A04304. doi:10.1029/2004JA010812

Cummer, S. A., Lyons, W. A., and Stanley, M. A. (2013). Three years of lightning impulse charge moment change measurements in the United States. *J. Geophys. Res. Atmos.* 118, 5176–5189. doi:10.1002/jgrd.50442

Frey, H. U., Mende, S. B., Cummer, S. A., Li, J., Adachi, T., Fukunishi, H., et al. (2007). Halos generated by negative cloud-to-ground lightning. *Geophys. Res. Lett.* 34, L18801. doi:10.1029/2007GL030908

Füllekrug, M., and Constable, S. (2000). Global triangulation of intense lightning discharges. *Geophys. Res. Lett.* 27 (3), 333–336. doi:10.1029/1999gl003684

Füllekrug, M., Price, C., Yair, Y., and Williams, E. R. (2002). <i>Letter to the Editor</i> Intense oceanic lightning. *Ann. Geophys.* 20, 133–137. doi:10.5194/angeo-20-133-2002

Hager, W. W., Sonnenfeld, R. G., Feng, W., Kanmae, T., Stenbaek-Nielsen, H. C., McHarg, M. G., et al. (2012). Charge rearrangement by sprites over a north Texas mesoscale convective system. *J. Geophys. Res.* 117, D22101. doi:10.1029/2012JD018309

Han, Y., Luo, H., Wu, Y., Zhang, Y., and Dong, W. (2021). Cloud ice fraction governs lightning rate at a global scale. *Commun. Earth Environ.* 2, 157. doi:10.1038/s43247-021-00233-4

Hiraki, Y., and Fukunishi, H. (2006). Theoretical criterion of charge moment change by lightning for initiation of sprites. *J. Geophys. Res.* 111, A11305. doi:10.1029/2006JA011729

Hiraki, Y. (2010). Phase transition theory of sprite halo. *J. Geophys. Res.* 115, A00E20. doi:10.1029/2009JA014384

Hu, W., Cummer, S. A., Lyons, W. A., and Nelson, T. E. (2002). Lightning charge moment changes for the initiation of sprites. *Geophys. Res. Lett.* 29 (8), 120. doi:10.1029/2001GL014593

Huang, E. E., Williams, R., Boldi, S., Heckman, W., Lyons, M., Taylor, T., et al. (1999). Criteria for sprites and elves based on Schumann resonance observations. *J. Geophys. Res.* 104 (D14), 16943–16964. doi:10.1029/1999JD900139

Huang, S.-M., Hsu, R.-R., Lee, L.-J., Su, H.-T., Kuo, C.-L., Wu, C.-C., et al. (2012). Optical and radio signatures of negative gigantic jets: Cases from Typhoon Lionrock (2010). *J. Geophys. Res.* 117, A08307. doi:10.1029/2012JA017600

Huang, A., Lu, G., Yue, J., Lyons, W. A., Lucena, F., Lyu, F., et al. (2018b). Observations of red sprites above hurricane Matthew. *Geophys. Res. Lett.* 45, 13158–13165. doi:10.1029/2018GL079576

Huang, A., Lu, G., Zhang, H., Liu, F., Fan, Y., Zhu, B., et al. (2018a). Locating parent lightning strokes of sprites observed over a mesoscale convective system in Shandong Province, China. *Adv. Atmos. Sci.* 35, 1396–1414. doi:10.1007/s00376-018-7306-4

Huang, A., Yang, J., Cummer, S. A., Lyu, F., and Liu, N. (2021). Examining the capacity of hurricane Matthew (2016) in spawning halo/sprite-producible lightning strokes during its lifetime. *Geophys. Res. Atmos.* 126, e2021JD035097. doi:10.1029/2021JD035097

Hutchins, M. L., Holzworth, R. H., Rodger, C. J., and Brundell, J. B. (2012). Far-field power of lightning strokes as measured by the world wide lightning location network. *J. Atmos. Ocean. Technol.* 29, 1102–1110. doi:10.1175/jtech-d-11-00174.1

Hutchins, M. L., Holzworth, R. H., Virts, K. S., Wallace, J. M., and Heckman, S. (2013). Radiated VLF energy differences of land and oceanic lightning. *Geophys. Res. Lett.* 40, 2390–2394. doi:10.1002/grl.50406

Kuo, C.-L., Huang, T.-Y., Hsu, C.-M., Sato, M., Lee, L.-C., and Lin, N.-H. (2021). Resolving elve, halo and sprite halo images at 10, 000 fps in the taiwan 2020 campaign. *Atmosphere* 12, 1000. doi:10.3390/atmos12081000

Kuo, C. L., Williams, E., Bor, J., Lin, Y. H., Lee, L. J., Huang, S. M., et al. (2013). Ionization emissions associated with N_2^+ 1N band in halos without visible sprite streamers. *J. Geophys. Res. Space Phys.* 118, 5317–5326. doi:10.1002/jgra.50470

Li, J., and Cummer, S. (2011). Estimation of electric charge in sprites from optical and radio observations. *J. Geophys. Res.* 116, A01301. doi:10.1029/2010JA015391

Li, J., Cummer, S., Lu, G., and Zigoneanu, L. (2012). Charge moment change and lightning-driven electric fields associated with negative sprites and halos. *J. Geophys. Res.* 117, A09310. doi:10.1029/2012JA017731

Liu, N. Y., Dwyer, J. R., and Cummer, S. A. (2017). Elves accompanying terrestrial gamma ray flashes. *J. Geophys. Res. Space Phys.* 122 (10), 10563–10576. doi:10.1002/2017JA024344

Lu, G., Cummer, S. A., Blakeslee, R. J., Weiss, S., and Beasley, W. H. (2012). Lightning morphology and impulse charge moment change of high peak current negative strokes. *J. Geophys. Res.* 117, D04212. doi:10.1029/2011JD016890

Lu, G., Cummer, S. A., Chen, A. B., Lyu, F., Huang, S., Hsu, R. R., et al. (2017). Analysis of lightning strokes associated with sprites observed by ISUAL in the vicinity of North America. *Terr. Atmos. Ocean. Sci.* 28 (4), 583–595. doi:10.3319/TAO.2017.03.31.01

Lu, G., Cummer, S. A., Li, Jingbo, Han, Feng, Blakeslee, Richard J., and Christian, Hugh J. (2009). Charge transfer and in-cloud structure of large-charge-moment positive lightning strokes in a mesoscale convective system. *Geophys. Res. Lett.* 36, L15805. doi:10.1029/2009GL038880

Lu, G., Cummer, S. A., Lyons, W. A., and Krehbiel, P. R. (2011). Lightning development associated with two negative gigantic jets. *Geophys. Res. Lett.* 38, L12801. doi:10.1029/2011GL047662

Lu, G., Cummer, S. A., Li, J., Zigoneanu, L., and Lyons, W. A. (2013). Coordinated observations of sprites and in-cloud lightning flash structure. *J. Geophys. Res.* 118, 1–26. doi:10.1002/jgrd.50459

Lu, G., Cummer, S. A., Tian, Y., Zhang, H., Lyu, F., Wang, T., et al. (2016). Sprite produced by consecutive impulse charge transfers in a negative stroke: observation and simulation. *J. Geophys. Res. Atmos.*, 121. doi:10.1002/2015JD024644

Lu, G., Yu, B., Cummer, S. A., Chen, A. B., Lyu, F., Liu, F., et al. (2018). On the causative strokes of halos observed by ISUAL in the vicinity of North America. *Geophys. Res. Lett.* 45, 10781. doi:10.1029/2018GL079594

Lyons, W. A. (1996). Sprite observations above the U.S. High Plains in relation to their parent thunderstorm systems. *J. Geophys. Res.* 101 (23), 29641–29652. 641–29. doi:10.1029/96jd01866

Mende, S. B., Frey, H. U., Hsu, R. R., Su, H. T., Chen, A. B., Lee, L. C., et al. (2005). *D* region ionization by lightning-induced electromagnetic pulses. *J. Geophys. Res.* 110, A11312. doi:10.1029/2005JA011064

Miyasato, R., Taylor, M. J., Fukunishi, H., and Stenbaek-Nielsen, H. C. (2002). Statistical characteristics of sprite halo events using coincident photometric and imaging data. *Geophys. Res. Lett.* 29 (21), 2033. doi:10.1029/2001GL014480

Newsome, R. T., and Inan, U. S. (2010). Free-running ground-based photometric array imaging of transient luminous events. *J. Geophys. Res.* 115, A00E41. doi:10.1029/2009JA014834

Pasko, V. P., Inan, U. S., Bell, T. F., and Taranenko, Y. N. (1997). Sprites produced by quasi-electrostatic heating and ionization in the lower ionosphere. *J. Geophys. Res.* 102, 4529–4561. doi:10.1029/96ja03528

Price, C., Asfur, M., Lyons, W., and Nelson, T. (2002). An improved ELF/VLF method for globally geolocating sprite-producing lightning. *Geophys. Res. Lett.* 29 (3), 1031. doi:10.1029/2001GL013519

Qin, J., Celestin, S., and Pasko, V. P. (2013). Dependence of positive and negative sprite morphology on lightning characteristics and upper atmospheric ambient conditions. *J. Geophys. Res. Space Phys.* 118, 2623–2638. doi:10.1029/2012JA017908

Qin, J., Celestin, S., and Pasko, V. P. (2012). Minimum charge moment change in positive and negative cloud to ground lightning discharges producing sprites. *Geophys. Res. Lett.* 39, L22801. doi:10.1029/2012GL053951

Ren, H., Tian, Y., Lu, G., Zhang, Y., Fan, Y., Jiang, R., et al. (2019). Examining the influence of current waveform on the lightning electromagnetic field at the altitude of halo formation. *J. Atmos. Sol. Terr. Phys.* 189, 114–122. doi:10.1016/j.jastp.2019.04.010

Ren, H., Lu, G., Cummer, S. A., Peng, K.-M., Lyons, W. A., Liu, F., et al. (2021). Comparison between high-speed video observation of sprites and broadband sferic measurements. *Geophys. Res. Lett.* 48, e2021GL093094. doi:10.1029/2021GL093094

Said, R. K., Cohen, M. B., and Inan, U. S. (2013). Highly intense lightning over the oceans: Estimated peak currents from global GLD360 observations. *J. Geophys. Res. Atmos.* 118, 6905–6915. doi:10.1002/jgrd.50508

Sato, M., and Fukunishi, H. (2003). Global sprite occurrence locations and rates derived from triangulation of transient Schumann resonance events. *Geophys. Res. Lett.* 30 (16), 1859. doi:10.1029/2003GL017291

Sato, M., Ushio, T., Morimoto, T., Kikuchi, M., Kikuchi, H., Adachi, T., et al. (2015). Overview and early results of the global lightning and sprite measurements mission. *J. Geophys. Res. Atmos.* 120, 3822–3851. doi:10.1002/2014JD022428

Stanley, M., Krehbiel, P., Brook, M., Moore, C., Rison, W., and Abrahams, B. (1999). High speed video of initial sprite development. *Geophys. Res. Lett.* 26, 3201–3204. doi:10.1029/1999gl010673

Stenbaek-Nielsen, H. C., Moudry, D. R., Wescott, E. M., Sentman, D. D., and Sabbas, F. T. S. (2000). Sprites and possible mesospheric effects. *Geophys. Res. Lett.* 27, 3829–3832. doi:10.1029/2000gl003827

Su, H.-T., Hsu, R.-R., Chen, A. B., Lee, Y.-J., and Lee, L. C. (2002). Observation of sprites over the Asian continent and over oceans around Taiwan. *Geophys. Res. Lett.* 29 (4), 1044. doi:10.1029/2001gl013737

Surkov, V. V., and Hayakawa, M. (2020). Progress in the study of transient luminous and atmospheric events: A review. *Surv. Geophys.* 41, 1101–1142. doi:10.1007/s10712-020-09597-2

Taylor, M. J., Bailey, M. A., Pautet, P. D., Cummer, S. A., Jaugey, N., Thomas, J. N., et al. (2008). Rare measurements of a sprite with halo event driven by a negative lightning discharge over Argentina. *Geophys. Res. Lett.* 35, L14812. doi:10.1029/2008GL033984

University of Science and Technology of China *Transient luminous events over high-impact thunderstorms systems. V1.0*. Beijing: National Space Science Data Center. doi:10.12176/01.05.00070-V01.2021-09-25

van der Velde, O. A., Lyons, W. A., Nelson, T. E., Cummer, S. A., Li, J., and Bunnell, J. (2007). Analysis of the first gigantic jet recorded over continental North America. *J. Geophys. Res.* 112, D20104. doi:10.1029/2007JD008575

Wang, Y., Lu, G., Cummer, S. A., Lucena, F., Cohen, M., Ren, H., et al. (2021b). Ground observation of negative sprites over a tropical thunderstorm as the embryo of hurricane Harvey (2017). *Geophys. Res. Lett.* 48, e2021GL094032. doi:10.1029/2021GL094032

Wang, Y., Lu, G., Ma, M., Liu, F., Zhu, B., Zhou, R., et al. (2019). Triangulation of red sprites observed above a mesoscale convective system in North China. *Earth Planet. Phys.* 3, 111–125. doi:10.26464/epp2019015

Wang, Y., Lu, G., Peng, K.-M., Cheng, Z., Wang, R., Ahmad, M. R., et al. (2021c). Observations of red sprites in Melacca area in 2019 and analyses of parent thunderstorms [J]. *J. Trop. Meteorology* 37 (3), 370–380. doi:10.16032/j.issn.1004-4965.2021.036

Wang, Y., Lu, G., Peng, K.-M., Ma, M., Cummer, S. A., Chen, A. B., et al. (2021a). Space-based observation of a negative sprite with an unusual signature of associated sprite current. *JGR. Atmos.* 126, e2020JD033686. doi:10.1029/2020JD033686

Williams, E., Downes, E., Boldi, R., Lyons, W., and Heckman, S. (2007). Polarity asymmetry of sprite-producing lightning: A paradox? *Radio Sci.* 42, RS2S17. doi:10.1029/2006RS003488

Williams, E., Kuo, C. L., Bor, J., Satori, G., Newsome, R., Adachi, T., et al. (2012). Resolution of the sprite polarity paradox: The role of halos. *Radio Sci.* 47, RS2002. doi:10.1029/2011RS004794

Yang, J., Qie, X., Zhong, L., He, Q., Wang, Z., Liu, F., et al. (2020). Analysis of a gigantic jet in southern China: Morphology, meteorology, storm evolution, lightning and narrow bipolar events. *J. Geophys. Res. Atmos.* 125, e2019JD031538. doi:10.1029/2019JD031538

frontiers | Frontiers in Earth Science

TYPE Original Research
PUBLISHED 19 September 2022
DOI 10.3389/feart.2022.956836

OPEN ACCESS

EDITED BY
Guihua Wang,
Fudan University, China

REVIEWED BY
Jingchao Long,
Guangdong Ocean University, China
Huijun Huang,
China Meteorological Administration (CMA), China

*CORRESPONDENCE
Li Yi,
yili@ouc.edu.cn

SPECIALTY SECTION
This article was submitted to Atmospheric Science, a section of the journal Frontiers in Earth Science

RECEIVED 30 May 2022
ACCEPTED 16 August 2022
PUBLISHED 19 September 2022

CITATION
Song S-T, Shi X-M, Zhang S-P, Chen X-Y, Xue Y-C, Zhao W, Yang C, Huang B and Yi L (2022), Springtime sea fog penetration in Qingdao: Anomalous moistening and diurnal cooling. *Front. Earth Sci.* 10:956836. doi: 10.3389/feart.2022.956836

Springtime sea fog penetration in Qingdao: Anomalous moistening and diurnal cooling

Shu-Tong Song[1,2], Xiao-Meng Shi[3], Su-Ping Zhang[2,4], Xian-Yao Chen[1,2,5], Yun-Chuan Xue[3], Wei Zhao[6], Chao Yang[6], Bin Huang[6] and Li Yi[1,2]*

[1]Frontiers Science Center for Deep Ocean Multispheres and Earth System, Ocean University of China, Qingdao, China, [2]Physical Oceanography Laboratory, Ocean University of China, Qingdao, China, [3]Qingdao Meteorological Bureau, Qingdao, China, [4]Ocean-Atmosphere Interaction and Climate Laboratory, Ocean University of China, Qingdao, China, [5]Qingdao National Laboratory of Marine Science and Technology, Qingdao, China, [6]National Meteorological Centre, Beijing, China

Sea fog often penetrates adjacent coastal areas, a process called sea fog penetration (SFP). SFP can cause traffic accidents and other economic losses. Qingdao, an international port city with a dense population, suffers from SFP originating over the Yellow Sea in the boreal spring (March–May); the process, however, is not well-studied. Based on hourly observations from buoys and automatic weather stations distributed in Qingdao and its adjacent islands, we composite SFP events to reveal their spatiotemporal features and to investigate the mechanisms involved. Results show that these SFP events often penetrate inland areas from southeast to northwest and last 5–8 h at night. We further use reanalysis data to reveal that during the daytime before SFP, strong moisture advection at 925–975 hPa brings sufficient water vapor from the Yellow Sea to Qingdao; the water vapor then transfers downward to the surface via background descending motion and turbulent mixing. The daytime anomalous moistening, together with the following diurnal cooling at night, saturates the surface atmosphere and, hence, facilitates SFP. The strength of SFP depends on the strength of daytime anomalous moistening. Considering that moistening leads SFP by about a day, we use this relationship to predict the intensity of SFP. The accuracy of predicting SFP events could reach 50–80%, which highlights the predictability of intensity of SFP in Qingdao.

KEYWORDS

automatic weather station, coastal fog, inland penetration, moisture advection, boundary layer, prediction

Introduction

Sea fog, or marine fog, refers to the fog that occurs under ocean influence (Wang, 1985), with horizontal visibility of less than 1 km (World Meteorological Organization, 1966). It often occurs over coastal waters and penetrates inland to affect coastal cities (Figure 1B), a phenomenon termed sea fog penetration (SFP) (Lee and Chang, 2018). Some severe SFP events associated with low visibility can disrupt human activities,

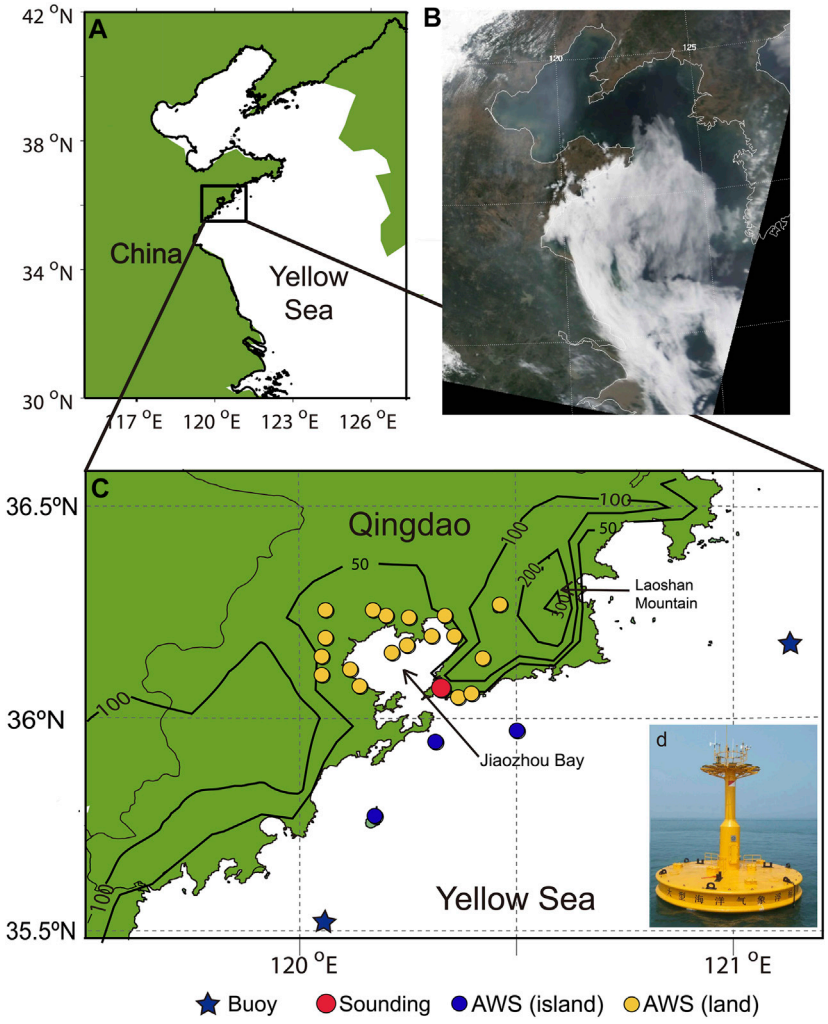

FIGURE 1
Locations of buoys, sounding stations, and automatic weather stations (AWSs) used in this study **(A,C)**. Black contour represents topography (m). There are three AWSs on the island (blue dots) and 19 AWSs on land (yellow dots). Only 21 AWSs are visible because one overlaps with the sounding station. Panel **(D)** shows the buoy near Qingdao. Panel **(B)** is a visible image of the MODIS swath scan at 0315 UTC 1 May 2015 during an SFP event.

causing flight delays or cancellations, and resulting in economic losses; they can also cause traffic accidents, threatening the safety of coastal residents (Leigh, 2007).

SFP occurs in coastal regions worldwide, though its causes may differ. In Scotland, the sea breeze determines SFP strength and dissipation (Findlater et al., 1989). Over the Korean Peninsula, when cold sea fog penetrates into warm land, a weak land–sea temperature contrast promotes SFP (Lee and Chang, 2018). Along the coasts of California and Chile, SFP is promoted by persistent onshore wind but blocked by mountain ranges further inland (Cereceda et al., 2002; Johnstone and Dawson, 2010). In addition to topography effects, SFP is affected by the land environment because a dry, warm, and unstable atmosphere over land tends to dissipate SFP (Koračin et al., 2014). Moreover, many works studied coastal fog and synoptic meteorological conditions and its life cycle, also improving the understanding of SFP (Dorman et al., 2021; Fernando et al., 2021; Gultepe et al., 2021).

Qingdao (Figure 1), a coastal city with a population of close to 10 million, experiences a high fog frequency in spring, for about 50 days every year (Zhang et al., 2009). The fog in Qingdao exhibits distinct seasonal variations that are highest during spring and summer. Considering different atmospheric circulations and features of fog from spring to summer, we only focus on spring in this study.

Previous studies show that springtime fog in Qingdao is often associated with sea fog over the Yellow Sea (Fu et al., 2008; Gao et al., 2007; Zhang et al., 2012). The Yellow sea fog is typical

TABLE 1 Information on the observations of this study.

	Visibility		RH		Temperature		Wind	
	Height (m)	Manufacturer	Height (m)	Manufacturer	Height (m)	Manufacturer	Height (m)	Manufacturer
Buoy	10	Vaisala (PWD20)	10	YOUNG (41382LC2)	10	YOUNG (41382LC2)	10	YOUNG (05106)
AWS	2.8	Huayun Sounding (DNQ1-V35)	1.5	Jiangsu Radio Scientific Institute (DHC2)	1.5	Jiangsu Radio Scientific Institute (WHSH-TW100)	10	Jiangsu Radio Scientific Institute (ZQZ-TF)

advection fog, occurring when prevailing southerlies transport moist and warm air from low latitude northward to the sea surface (Sugimoto et al., 2013; Gao et al., 2016). If the southerlies are persistent and strong enough, the fog or the moist air parcel may be advected northward to the Qingdao area, causing the occurrence of SFP. However, how the winds modulate the SFP processes in the Qingdao region remains unclear.

On the other hand, previous studies used sparse observations to explore SFP in Qingdao (e.g., Diao, 1992), such as data from a single sounding station (Fu et al., 2008) or satellite (Yi et al., 2015). However, the former cannot describe the spatial distribution of SFP and the latter can neither detect fog under higher cloud covers nor accurately separate fogs from low clouds (Zhang and Yi, 2013). Detailed processes associated with SFP need further studies, preferably using high-resolution observations.

Here, we use 22 automatic weather stations (AWSs) to obtain hourly SFP distribution in the Qingdao region for the first time. Such high-spatiotemporal-resolution measurements allow us to study spatiotemporal features, intensity, and mechanisms of SFP. The rest of the study is organized as follows. Data, methods, and definitions used in this study are discussed in *Material and methods*. Frequency and spatial distributions of SFP are shown in *Temporal and spatial distribution*. Mechanisms of SFP are presented in *Mechanisms of SFP*. What affects the intensity of SFP and how to predict it are studied in *Intensity of SFP*. Summary and discussion are given in *Summary and discussion*.

Material and methods

Observations

All the data used are from the boreal spring (March to May) each year from 2014–2018.

Two buoys, located at 119.9°E, 35.4°N and 121.2°E, 36.2°N, respectively, and three AWSs on nearby islands are chosen for sea fog detection (Figure 1B). Buoys (Figure 1C) provide hourly visibility, relative humidity (RH), temperature, and wind at 10 m above the sea level; details of the observations are given in Table 1. The three AWSs on islands provide the same measurements as the buoys.

In addition to the three AWSs on islands, there are also 19 AWSs on land in our study area. We use these hourly fog observations to detect inland fog associated with SFP and to obtain a high-spatiotemporal-resolution distribution of SFP.

Daily soundings are used to obtain the vertical structure of SFP. The soundings include the Global Telecommunication System1 (GTS1) digital radiosonde and the Government Furnished Equipment (GFE) L-band secondary wind radar, operated by the Chinese Meteorological Bureau (China Meteorological Administration, 2005). The sounding station (Figure 1B) is 75 m above sea level. These observations are operated at 20:00 local standard time (LST, which is UTC+8) each day. It provides the vertical profiles of temperature (error ±0.2°C), RH (error ±5%), and wind (error ± 1 m/s below 10 m/s) at 50 m vertical resolution (Li et al., 2009).

The ERA5 reanalysis from the European Centre for Medium-range Weather Forecasts is used to analyze the atmospheric circulation (Hersbach and Dee, 2016). The reanalysis data used in this study are on a 0.25° spatial grid at a 1 h interval.

SFP definition

SFP often occurs at midnight and dissipates the next morning (Tardif and Rasmussen, 2007). Hence, an SFP event is defined as a 24-h segment from 12 o'clock LST on day 0 to 12 o'clock LST next day (day+1), during which the following conditions are satisfied:

1) In an SFP event, land fog and sea fog need to exist at the same time. The land fog is detected when at least one inland AWS detects visibility of less than 1 km (World Meteorological Organization, 1966). The sea fog is detected when at least one buoy or one AWS on an island detects visibility of less than 1 km. Sometimes, the duration of low visibility (less than 1 km) for the station is too short to ensure that fog did occur, so the duration of the fog segment should be longer than 2 hours.

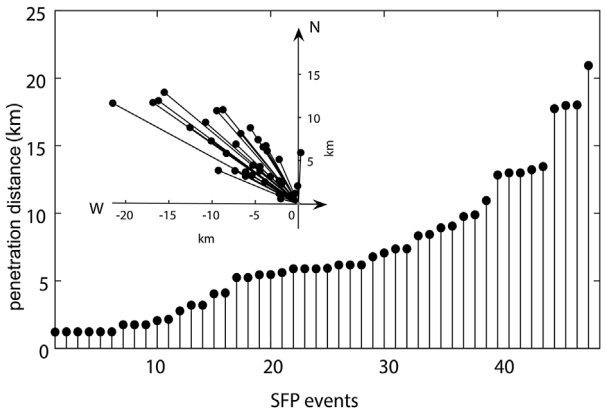

FIGURE 2
Penetration directions and distances (km) of 48 SFP events used in this study. The coordinator's origin in the inset indicates the SFP-center location when sea fog first appeared on land. The black dot indicates the SFP-center location when SFP covered most inland stations during an SFP event. The SFP-center location is defined as the mean location of fog-affected inland AWSs. The distance from the coordinator's origin to the dot indicates the penetration distance of the SFP event (main figure).

2) An SFP event is characterized by the movement of fog from the sea into land. Correspondingly, the fog should first appear at the station(s) near the sea and then be detected at the station(s) inland. To depict the movement of fog, we define an SFP-center location, the mean location of inland AWSs with fog in each hour. From the time when sea fog first penetrates the land area to the time when sea fog covers most inland AWSs, the SFP-center location must move onshore. As shown in Figure 2's inset, the movement direction of each SFP is marked by the vector from the coordinator's origin to each black dot. The SFP events mainly develop northwestward ranging from 233° clockwise to 53° (where 0° is to the north and the angle increases clockwise). The distance of each vector in Figure 2 is defined as the penetration distance. In addition, all fog-penetrated stations must detect onshore winds (wind direction in the range of 53°–233°, where 0° represents northerly wind).

Using the aforementioned definition, we identified 48 SFP events during the springs from 2014–2018. Their penetration directions were mainly from southeast to northwest (Figure 2), consistent with the direction from the sea to land. These directions are also consistent with one of the four airflow paths influencing spring sea fog in the Yellow Sea (Huang et al., 2018). The median direction was 310°, as shown by the arrow in Figure 4A. The distance from the origin to each black dot represents the penetration distance during an SFP event. The result shows that the penetration distance varied from 1 to 21 km, with a median of 5.9 km.

Temporal and spatial distribution

Frequency distribution

In a 24-h SFP event, sea fog penetrates into the land, lasts for hours or nearly a day, and then disappears. To analyze how long an SFP event can last, we obtain the number of SFP events of different durations (Figure 3A). Results show that the number of events generally decreases with duration. SFP events lasting 5–8 h are most common (15 events) and those lasting 14–17 h are least common (2 events). For SFP events of different durations, their penetration distances also differ. In general, the duration of SFP events increases the penetration distance. For example, the median distance increases from 3 to 14 km when the duration increases from 2 to 17 h. It is to be noted that for SFP events lasting more than 17 h, their median penetration distance decreases with the duration. This is because some SFP events that lasted nearly a day but did not penetrate far inland (just stayed near the coast).

To analyze how often SFP events occur, we obtain the number of SFP events in different months and years. The numbers of SFP events are similar in each month from March to May (Figure 3B), with a slight increase from 15 to 18. The increase may be related to the increase of the Yellow Sea fog, due to surface air temperature (SAT) increasing more quickly than sea-surface temperature (SST) and to the air-sea interface becoming increasingly stable from March to May (Leipper, 1994; Zhang et al., 2009). Figure 3C shows the annual numbers of SFP events from 2014–2018. The numbers increased rapidly from 3 to 16, with a drop in 2017. Although the number of SFP events increased rapidly, 5-year observations are not long enough to confirm an interannual variation of SFP. The variation of numbers of SFP events may be associated with interannual variations of SST and large-scale circulations (Norris and Leovy, 1994; Zhang et al., 2015).

Spatial distribution

Based on these high-resolution observations, we analyze the total numbers of SFP events detected by each AWS to obtain the spatial distribution of SFP events (Figure 4A). Over the sea, almost all SFP events were associated with the fogs detected by station S0 (Figure 4B). This suggests that most SFP events started from the southeastern corner of Qingdao. The sea fog first penetrated the east side of the southern mouth of Jiaozhou Bay (Figure 1B), where the stations (e.g., S1) detected more than 40 events. Then, following the median direction of the SFPs (arrow in Figure 4A), the fog penetrated Jiaozhou Bay, detected by two stations (e.g., S2) along a bridge over the bay; these

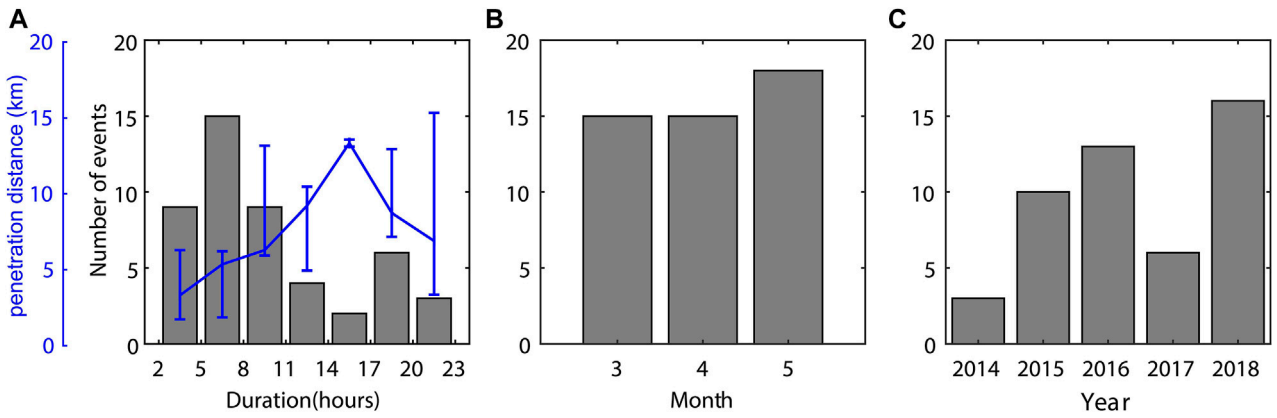

FIGURE 3
Numbers of SFP events (bars): different durations **(A)**, different months **(B)**, and different years **(C)**. The blue line in **(A)** represents the median penetration distance (km) of SFP events, and the error bars indicate 75 and 25% quantiles, respectively.

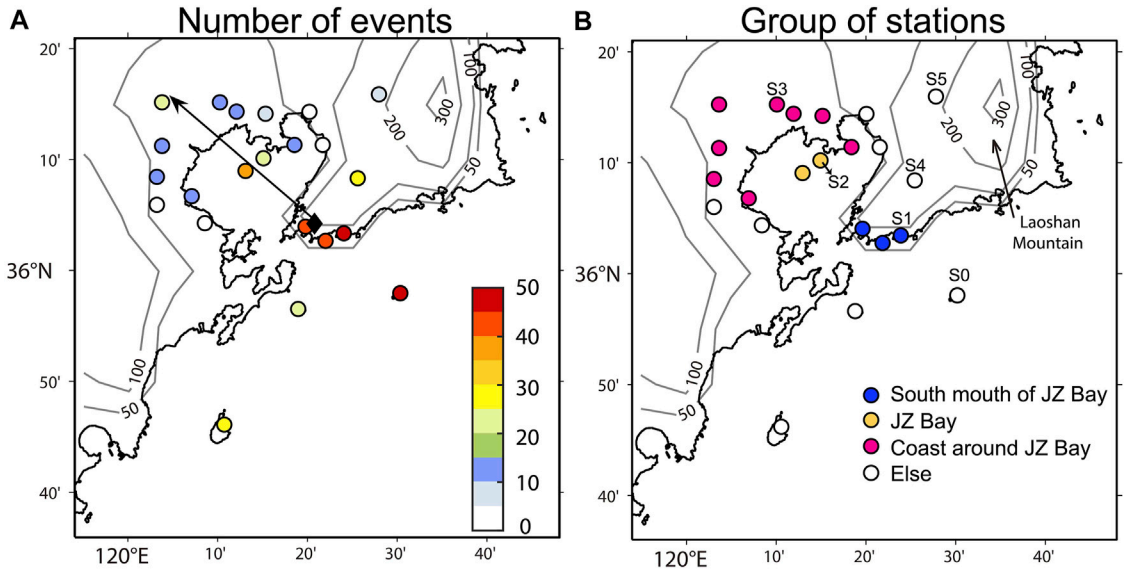

FIGURE 4
Numbers of SFP events at every AWS **(A)** and groups of AWSs based on locations **(B)**. The gray contours indicate topography (m). In **(A)**, the arrow expresses the median direction of the SFP events (shown in Figure 2's inset). The black diamond expresses the average location where SFP starts. In **(B)**, the names and groups of stations are given. S1, S2, and S3 are the typical stations for the three groups. S0 is a station on an island. S4 and S5 are located on Laoshan Mountain.

stations detected about half of the events. Finally, the fog reached the coastal stations around the bay (e.g., S3), most of which only detected less than 15 events. However, four stations along the coast of Jiaozhou Bay detected nearly zero events. It may be due to the fact that the stations are located on the leeward slope of the mountains, where the environment is relatively dry and warm induced by adiabatic subsidence. Apart from the main direction of SFP, there are two stations over Laoshan Mountain, S4 and S5. Previous studies found that sea fog can only reach locations lower than the inversion layer (Johnstone and Dawson 2010; Iacobellis and Cayan 2013). Because the altitudes of S4 and S5 are lower than ~250 m, a common height of inversion (Zhang et al., 2009), sea fog can reach these stations; as a result, 25 events (at S4) and seven events (at S5) were detected.

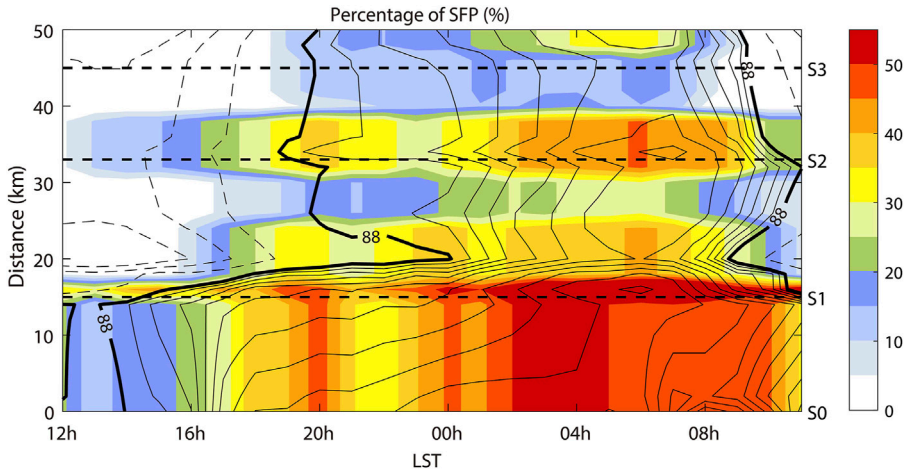

FIGURE 5
Composite results of development in SFP (%; shading) and RH (%; contouring) for all SFP events along the arrow in Figure 4A. The percentage of SFP is the mean value of fog conditions (fog is 100 and no fog is 0) among all SFP events. The interval of RH is 1% among solid lines and it is 5% among dashed lines. The *Y* axis is the distance from the S0 station along the arrow in Figure 4A. The distance from S0 to S1, S2, and S3 are indicated by dashed lines. The results along the arrow are interpolated by AWSs. LST is local standard time.

Mechanisms of SFP

Development of SFP

To examine the development of SFP events, we composite the hourly fog and RH along the median direction of SFP (Figure 5). The percentage of SFP at the S1 station always hovers at about 30 and 40%, and then it increases to more than 50% after midnight. At the S2 station, it starts at about 5%, and after 8 h it reaches 30%. In contrast, at the S3 station, the percentage of SFP remains only less than 20% during the night. The results depict the development of SFP from offshore to inland during the night.

The development of SFP can be described by a change of RH. First of all, the liquid water vapor in fog only appears after the air has saturated or the RH closed to 100%. Hence, the increase of RH is beneficial to forming fog droplets and develops SFP. Second, the percentage of SFP is highly correlated with composite RH at about 0.78 (Figure 5). At a given station, a larger composite RH means reaching saturation more frequently, that is, more SFP events occur (Isaac et al., 2020; Gultepe et al., 2021). Hence, it is available to use the change of RH to depict the development of SFP and to decompose RH to reveal the underlying mechanism.

Contributions of specific humidity (q) and temperature (T)

According to the Clausius–Clapeyron equation, the change in RH (∂RH/∂t) is mainly controlled by specific humidity (q) and temperature (T). Therefore, to understand what induces ∂RH/∂t variation, we quantitatively decompose ∂RH/∂t to the contributions of q and T as (Yang et al., 2021)

$$\frac{\partial \mathrm{RH}}{\partial \mathrm{t}} = \frac{\partial}{\partial \mathrm{t}}\left(\frac{\mathrm{q}}{q_s}\right) = \frac{1}{q_s}\frac{\partial \mathrm{q}}{\partial \mathrm{t}} - \frac{\mathrm{RH}}{q_s}\frac{\partial q_s}{\partial \mathrm{T}}\frac{\partial \mathrm{T}}{\partial \mathrm{t}}, \quad (1)$$

where q_s is the saturated specific humidity. The two terms on the right-hand side represent the contributions of q and T, respectively, to ∂RH/∂t, expressed as C_q and C_T for simplicity.

$$C_q = \frac{1}{q_s}\frac{\partial \mathrm{q}}{\partial \mathrm{t}}, \quad (2)$$

$$C_T = \frac{\mathrm{RH}}{q_s}\frac{\partial q_s}{\partial \mathrm{T}}\frac{\partial \mathrm{T}}{\partial \mathrm{t}}.$$

Notably, the diurnal cycle of T strongly affects ∂RH/∂t. This diurnal cycle and other processes that may promote SFP are all contained inC_T. Hence, C_T (and C_q) can be further decomposed into the monthly hourly mean value (shown by an overbar) and anomaly (shown by prime) as follows,

$$\frac{\partial \mathrm{RH}}{\partial \mathrm{t}} = C_q - C_T = \overline{C_q} + C_q' - \overline{C_T} - C_T'. \quad (3)$$

When temperature increases, C_T increases as well, leading to a negative contribution to RH change. We substitute hourly data from S1, S2, and S3 stations, as the example of three kinds of regions, under each SFP event into Formula 3 and calculate each decomposed terms. Figure 6 shows the composite results for all SFP events. We find that both C_q and C_T played important roles in increasing RH, but they were important at different times.

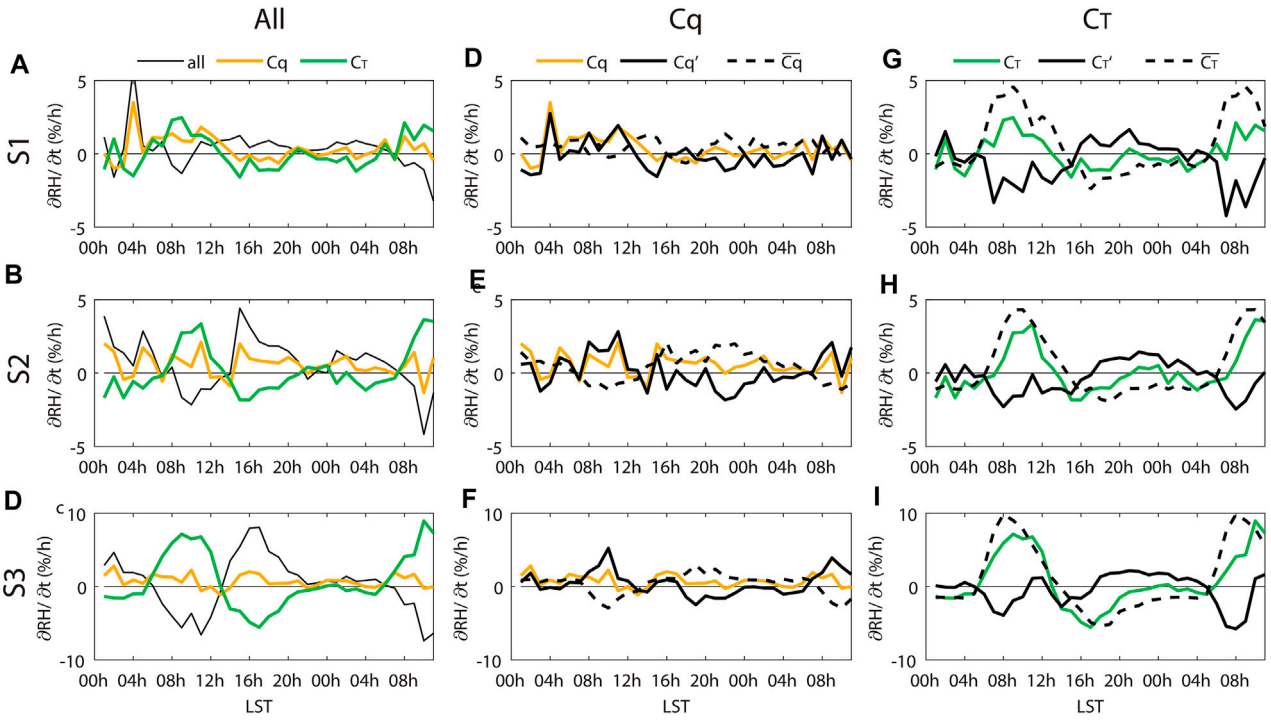

FIGURE 6
Composite ∂RH/∂t (black curve in the left column; %/h), contribution of q (C_q; yellow curve in the left and middle columns; %/h), and temperature (C_T; green curve in the left and right columns; %/h) at stations S1, S2, and S3 for all SFP events. The terms are calculated using hourly data at stations S1 (top row), S2 (middle row), and S3 (bottom row) based on Formula 3. In the middle column, C_q is decomposed to a mean diurnal cycle ($\overline{C_q}$; dashed curve) and anomaly (C_q'; solid curve). In the right column, C_T is decomposed to a mean diurnal cycle ($\overline{C_T}$; dashed curve) and anomaly (C_T'; solid curve). The time period starts from day 0 00 LST to day+1 12 LST.

C_T causes RH to increase from afternoon to midnight and dominates the variation of ∂RH/∂t, with correlation coefficients of -0.66, -0.87, and -0.96 at stations S1, S2, and S3, respectively (Figures 6A–C). The correlation is strongest at inland station S3. C_T exhibits a striking diurnal cycle with positive values during the day (00–14 LST day 0) and becomes negative from afternoon to night (14 LST day 0–04 LST day+1). The diurnal cycle of C_T is dominated by $\overline{C_T}$ with a correlation coefficient of ~0.85 (Figures 6G–I). $\overline{C_T}$ shows a similar diurnal cycle, which means climatological warming after sunrise and cooling after sunset. Cooling at night is the key process to increase RH and develop SFP. This cooling induces a less turbulent boundary layer and triggers or maintains the condensation during fog formation (Tardif and Rasmussen 2007; Lee and Chang 2018). In addition, C_T is also influenced by $C_T'$with a correlation coefficient of ~0.4. However, C_T' partly offsets the effect of $\overline{C_T}$as they show generally opposite signals during the SFP events (Figures 6G–I).

In addition to C_T, positive C_q during the morning is also necessary to increase RH for SFP (Figures 6A–C). C_q is positive during 00–14 LST day 0, which partly offsets the negative contribution of C_T to RH. Especially at the coastal station S1, C_q completely offsets and even exceeds C_T, leading to a rapid increase of RH. The variation of C_q is dominated by C_q' with a correlation coefficient of ~0.87, while $\overline{C_q}$ is near zero and hardly contributes to C_q (Figures 6D–F). It suggests that the anomalous moistening process during the morning before SFP is necessary to develop SFP.

Briefly, anomalous moistening and cooling during the day and climatological cooling at night are the main factors to increase RH and trigger SFP. It is to be noted that the aforementioned discussion concerns only surface variables, which may not represent the whole fog that extends to a few hundred meters vertically.

Physical mechanisms of anomalous moistening and cooling

During an SFP event, anomalous moistening and cooling are specific processes, which are important for understanding the development of these events. Here, we use ERA5 to explore the physical mechanisms and atmospheric circulation during the day before a developed SFP event. The surface results of ERA5 are validated by AWSs in the QD region (Table 2). The bias of

TABLE 2 Validation of AWS and ERA5 based on the region average of the Qingdao area from March to May 2014–2018. The data from AWS are at the surface and the data from ERA5 are at sea level pressure.

	Year	Mean of bias	Standard deviation of bias	Correlation
Temperature (°C)	2014–2018	0.15	3.43	0.81
	2014	0.14	3.36	0.81
	2015	-0.30	3.21	0.83
	2016	-0.25	3.42	0.79
	2017	-0.31	3.70	0.80
	2018	-0.10	3.45	0.80
Specific humidity (g/kg)	2014–2018	0.12	1.1	0.91
	2014	0.62	1.06	0.91
	2015	0.10	1.03	0.92
	2016	0.11	1.13	0.90
	2017	-0.05	1.30	0.89
	2018	-0.20	1.06	0.94

ERA5 may be due to the difference between sea level pressure and surface.

Figure 7 shows the composite moisture advections for all SFP events based on ERA5. The results suggest the importance of anomalous moisture advection (advq') to SFP formation. We composite moisture advection for all SFP events and find that advq' at 925 hPa is positive over the entire Qingdao region during day 0 due to anomalous southwesterlies (Figure 7C). This positive advq' at the upper boundary layer (from 975 to 925 hPa) transports excessive water vapor downward to the surface through descending motion and turbulent mixing (Figure 8). In contrast, at the surface, there is negative advq' at Jiaozhou Bay (Figure 7F) due to the weaker land–-sea difference in specific humidity. However, this negative advq' is overwhelmed by a downward moisture supply from the upper boundary layer, leading to the increase of anomalous specific humidity (q') in Figure 6.

As for temperature advection, negative anomalous temperature advection (advt') exists at the surface (Figure 9), cooling the surface and facilitating temperature inversion (details in *Intensity of SFP*). The temperature inversion favors moisture accumulation within the boundary layer instead of exchanging with a free atmosphere (Lewis, 2003). Hence, it provides a necessary background for downward moisture supply, which helps increase surface moisture to form an SFP event.

Intensity of SFP

Weak SFP events only reached the stations near the coast, and only severe SFP events could reach deep inland stations (Figure 4A). Therefore, based on the spatial distribution and penetration distance of fog, we separate the SFP events into three types using S1, S2, and S3 as the typical stations of the three regions of Qingdao. We define the following: type-1 SFP events are the events that fog only reached S1 (22 events); type-2 SFP events are those that only reached S1 and S2 (10 events); and type-3 SFP events are those that reached S1, S2, and S3 (11 events). As a result, only five events are left out.

We composite the time series of RH′ and q' at station S3 for the three types and compare their differences (Figure 10A). The results show that type-3 events had the most rapid increases of RH′ and q' during daytime. From 04 to 12 LST (day0), type-3, type-2, and type-1 RH′ increased by 18, 3, and 4%, respectively. Their q' increased by 1.7 g/kg, 0.5 g/kg, and 0.03 g/kg (Figure 10B). Moreover, q' at 925 hPa is also the greatest in type-3 (Figure 10C). Since type-3 events are the strongest, it suggests that the intensity of the SFP events may depend on the intensity of anomalous moistening in the middle boundary layer (925–975 hPa). It is to be noted that at day 0 00 LST, the q' in the middle boundary layer is already positive in all types (Figure 10C), suggesting that the moistening process occurs a day before SFP. We also composite the vertical structure based on the sounding data for the three types. The soundings were collected at 20 LST each day, but not every SFP event had already happened at that time. Therefore, the composite results only show the background environment of three types of SFP. Results show that type-1 and type-2 RH values decreased from ~90% at the surface to ~80% at 200 m, whereas type-3 RH remained above 90% from the surface to 300 m (Figure 11A). Similarly, type-1- and type-2-specific humidity values decreased with altitude, whereas type-3-specific humidity increased with an altitude below 300 m (Figure 11B). The RH and specific humidity of type-3 are significantly different from those of type-1 and type-2 (95% confidence level). As for temperature, there was no significant difference among the three types in terms of the vertical structure of temperature (Figure 11C). For example, their inversion layers had similar strengths and heights. These

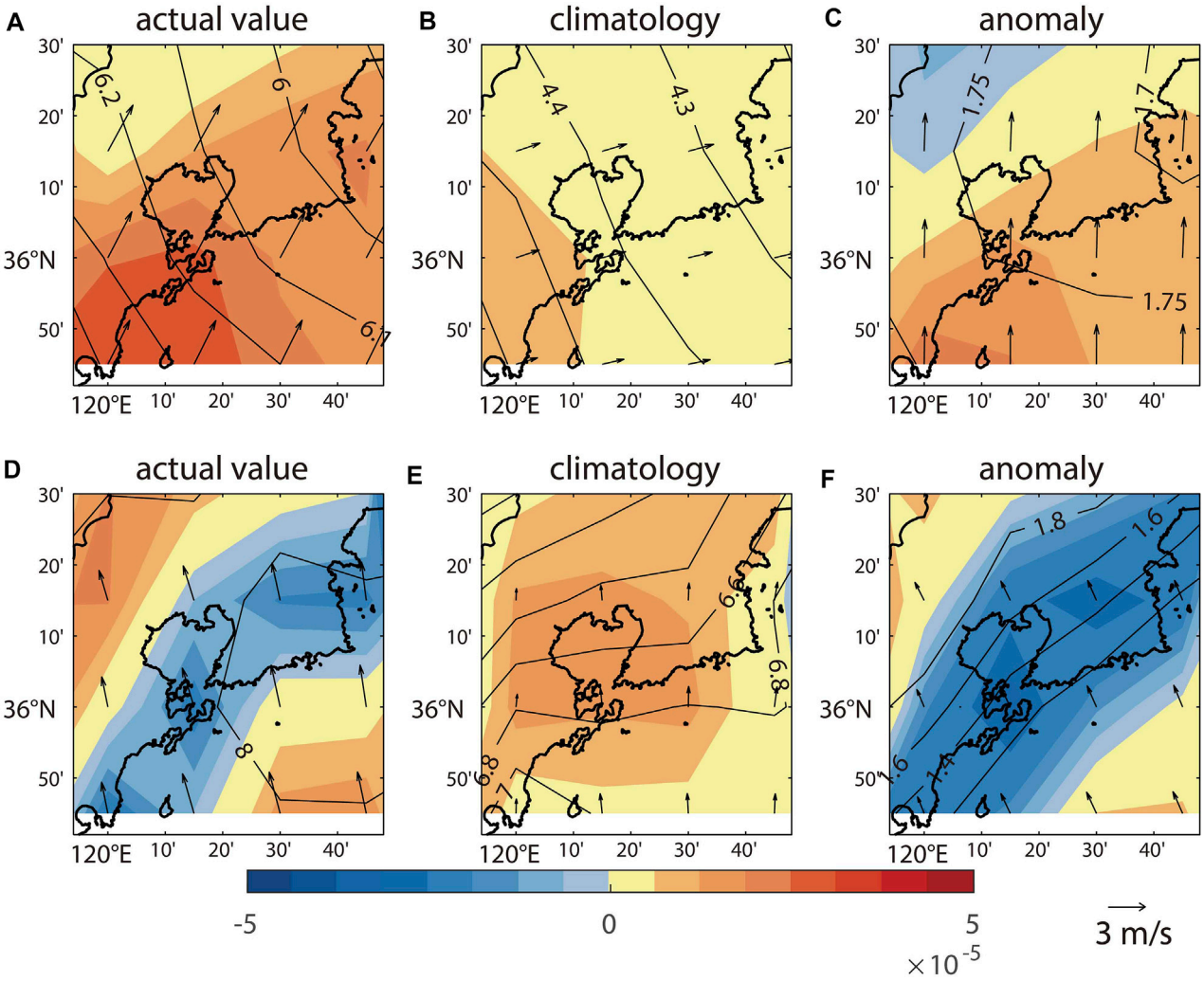

FIGURE 7
Composite results of time-averaged moisture advection (g/kg·s; shading) during day 0 00–23 LST at 925 hPa (top) and at the surface (bottom) for all SFP events based on ERA5. Left, middle, and right panels are actual, climatological, and anomalous values, respectively. The advection is given by shading, and specific humidity (g/kg) by contours. The arrows represent winds.

results support the relationship between moisture and SFP intensity, suggesting that a severe event was associated with a moister vertical environment below 300 m.

Anomalous moistening and cooling are two main factors leading to SFP events. Hence, we try to use these factors to predict the intensity of SFP. First, we define values X_1, X_2, and X

$$X_1 = \frac{q'_{12\,\mathrm{LST\,day0}} - q'_{00\,\mathrm{LST\,day0}}}{q_{00\,\mathrm{LST\,day0}}}, \quad (4)$$

$$X_2 = -1 * \frac{T'_{12\,\mathrm{LST\,day0}} - T'_{00\,\mathrm{LST\,day0}}}{T_{00\,\mathrm{LST\,day0}}}, \quad (5)$$

$$X = a * X_1 + b * X_2, \quad (6)$$

where the numerator of $X_1$is the change of q' from 00 LST to 12 LST day 0 at station 3 (Figure 9) and denominator of $X_1$is the q at 00 LST day 0 at station 3. X_2 is similar to X_1 but for temperature. X is the weighted sum of X_1 and X_2 where a and b are the weight coefficients. Here, the best ratio of a to b is 0.5 (Supplementary Table S1). We can obtain an X for each SFP event. Second, we find that the type-3 X is distinctly larger than the other two types' X (Supplementary Figure S1). Hence, it is possible to find thresholds of X to distinguish the three types' events. We take the average of the 75th of type-1 *X* and 25th of type-2 *X* (0.17, pink line in Supplementary Figure S1) and the average of 75th of type-2 *X* and 25th of type-3 (0.48, green line in Supplementary Figure S1) as two thresholds to distinguish three-types events. If *X* of an event

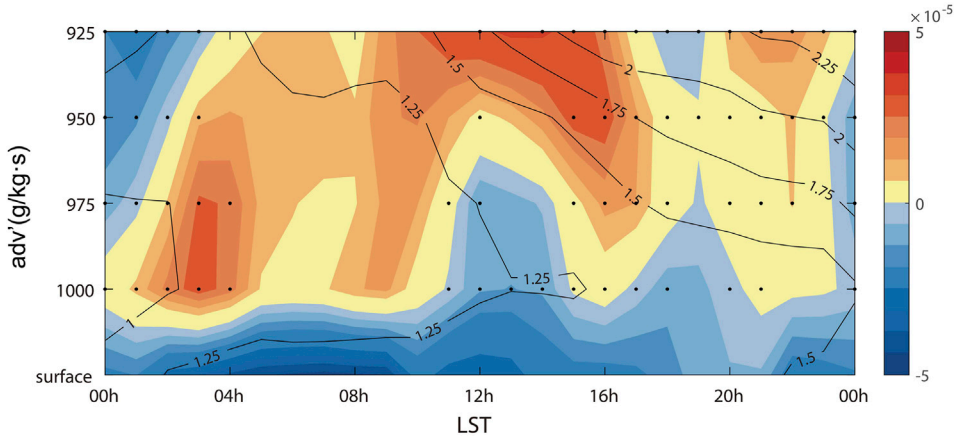

FIGURE 8
Composite results of anomalous moisture advection (g/kg·s; shading) at the Qingdao region from the surface to 925 hPa during day 0 based on ERA5. Anomalous specific humidity (g/kg) is contoured. Black dots represent anomalous descent movements. The results are based on the regional average of the Qingdao region (120.05°-120.5°W, 36°-36.25°N).

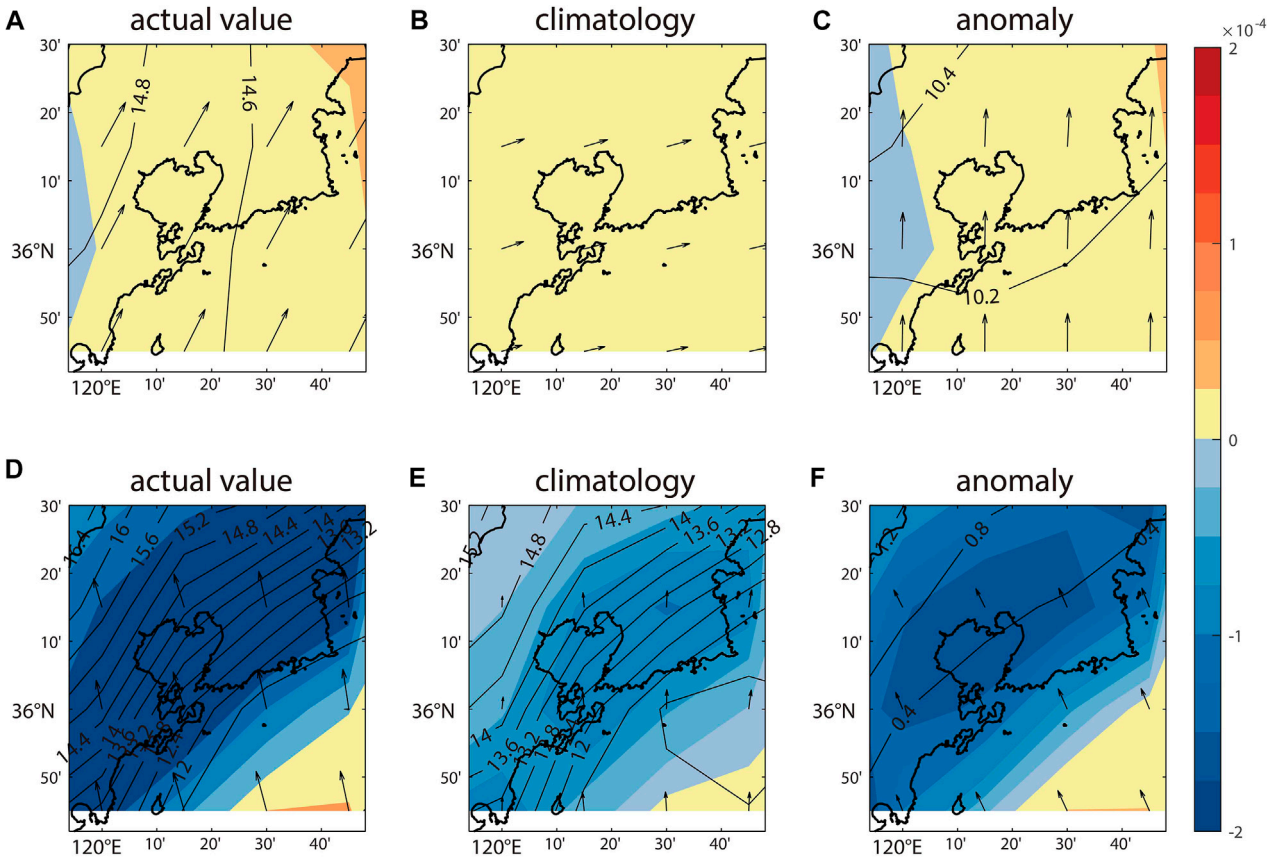

FIGURE 9
Composite results of time-averaged temperature advection (K/s; shading) during day 0 00–23 LST at 925 hPa (top) and at the surface (bottom) for all SFP events based on ERA5. Left, middle, and right panels are actual, climatological, and anomalous values, respectively. The advection is given by shading, and temperature (°C) is given by contour. The arrows represent winds.

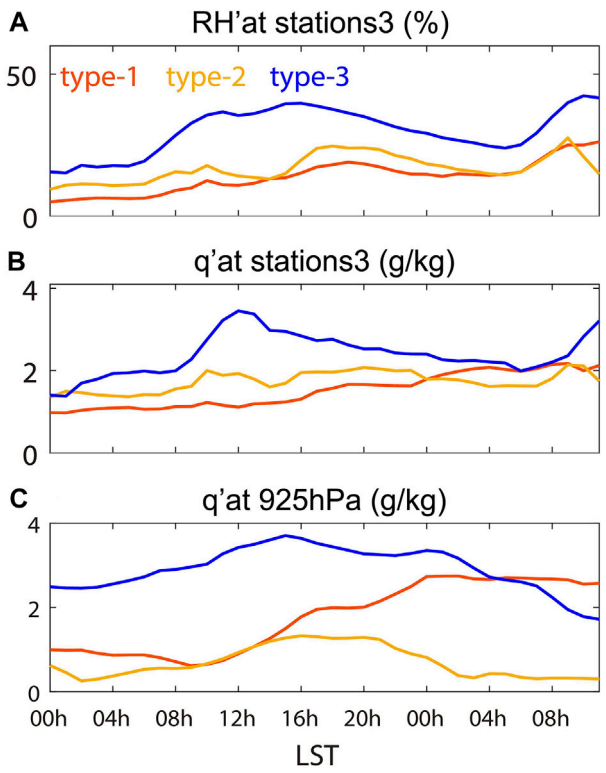

FIGURE 10
Composite results of anomalous RH (a; %), anomalous q (b; g/kg), and anomalous q at 925 hPa (c; g/kg). Red, yellow, and blue curves represent type-1, type-2, and type-3 SFP events, respectively. **(A)** and **(B)** are based on station S3. **(C)** is based on the regional average of the Qingdao area (120.05°-120.5°W, 36°-36.25°N) from ERA5. The time period starts from day 0 00 LST to day+1 12 LST.

is less than 0.17, the event is predicted as type-1. If X is between 0.04 and 0.48, the event is predicted as type-2. If X is larger than 0.48, the event is predicted as type-3. Third, the thresholds of X are used to hindcast all SFP events to test the predictive ability. As a result, the accuracy of predicting all events is 58% (Table 3). The accuracies of prediction for type-1, type-2, and type-3 events are 50, 50, and 82%, respectively. All types' accuracies are significant (p=0.1). In other words, anomalous moistening and cooling during 00–12 LST day 0 can help to forecast the strongest SFP events of type-3 which often occur in the early morning on day+1. Although less effective at distinguishing between type 1 and type 2 events than type 3, the result emphasizes the predictability of intensity of SFP.

Summary and discussion

SFP seriously impacts traffic safety and outdoor human activities in Qingdao. However, its spatial-temporal features and mechanisms are still unclear due to limited observations. In this study, we use the data from AWSs to show the high-spatiotemporal-resolution features of SFP in Qingdao. We also investigate the key processes behind these SFP events.

Using the definition of SFP events, we identify 48 SFP events during the spring of 2014–2018. We composite SFP events and draw the follwoing conclusions.

1) The SFP events often penetrate inland from southeast to northwest through Jiaozhou Bay. It tends to occur at night and most often lasts 5–8 h. The duration of SFP is generally proportional to the penetration distance.
2) The anomalous southwesterlies in the 975–925 hPa layer transport water vapor to the Qingdao region in the daytime before SFP. Then, the water vapor transfers downward by descending movement and turbulent mixing during the daytime, leading to anomalous moistening at the surface. At night, the surface temperature cools down and

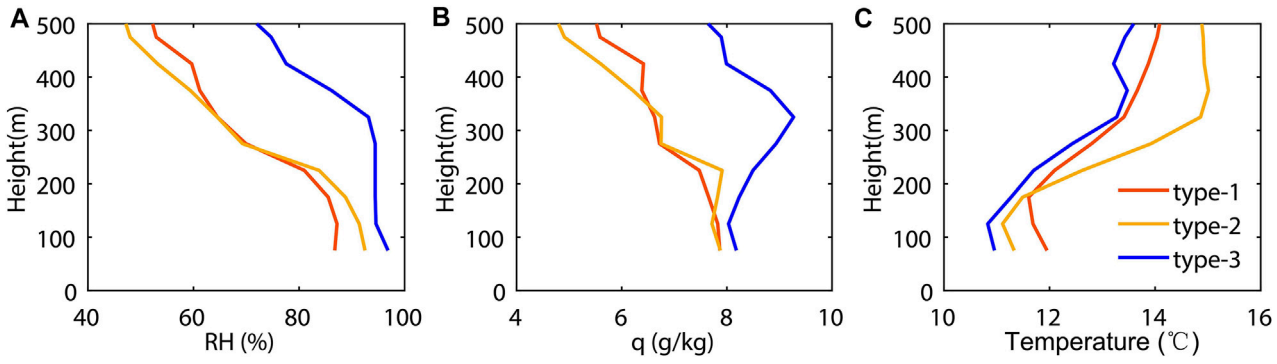

FIGURE 11
Composite results of vertical RH (**A**; %), q (**B**; g/kg), and temperature (**C**; °C) based on sounding data (75 m above the sea level). Red, yellow, and blue curves represent type-1, type-2, and type-3 SFP events, respectively.

TABLE 3 Accuracy of prediction. The bold font indicates successfully predicted events.

	Number of events	Accuracy (%)	Predict results		
			Type-1	Type-2	Type-3
Type-1	22	50	**11**	4	7
Type-2	10	50	3	**5**	2
Type-3	11	82	1	1	**9**
All types	43	58	-	-	-

triggers the condensation of water vapor and the formation of fog from offshore to the inland.

3) The stronger SFP event is associated with stronger anomalous moistening and cooling from the surface to 925 hPa which already begins 1 day before SFP. This feature provides the possibility to predict the intensity of SFP. The accuracy of predicting type-1, type-2, and type-3 events are 50, 50, and 82%, respectively, highlighting the predictability of the intensity of SFP in Qingdao.

Lee and Chang (2018) used the Weather Research and Forecasting (WRF) model and found that in cold sea fog (SST<SAT), decreasing inland temperature can help develop SFP events. We agree with the importance of cooling to develop SFP events, but we stress that the cooling is mainly due to the diurnal cycle rather than an anomalous process. Moreover, anomalous accumulating water vapor is also necessary for developing SFP. Previous studies (Zhang et al., 2009; Kim and Yum, 2012; Huang et al., 2018) suggested that the advection fog over the Yellow Sea is formed under the southerly wind, which is similar to the wind condition of SFP events. This is not surprising, because the SFP in Qingdao is originally from the Yellow Sea fog. However, we illustrate that SFP in Qingdao is closely related to humidity and temperature over land and even related to the local terrain, which is similar to the finding of Cereceda et al. (2002). Moreover, we highlight that moistening over land has already begun before SFP occurs and propose a simple method to predict the intensity of an SFP event. However, this method needs further improvement. More observation and research are needed, such as considering variables within the whole boundary layer instead of only at the surface.

This study only focuses on the meteorological conditions inland after the fog has already formed over the sea. We did not analyze which meteorological conditions above the sea favor SFP events, which need further study.

In summary, we find that anomalous moistening before SFP is primarily responsible for SFP development and further affects SFP intensity. The climatological cooling when SFP occurs is the secondary factor, which sustains SFP. We reveal the mechanisms of SFP, highlight the importance of moistening during the day and recommend that forecasters pay attention to meteorological changes before SFP appears.

Data availability statement

The original contributions presented in the study are included in the article/Supplementary Material; further inquiries can be directed to the corresponding author/s.

Author contributions

S-TS: investigation, software, visualization, validation, and original draft. X-MS: data curation, resources, review, and editing. S-PZ: funding acquisition, conceptualization, original draft, review, and editing. X-YC: review and editing. Y-CX: resources and project administration. WZ: data curation and resources. CY: data curation and resources. BH: data curation and resources. LY: conceptualization, methodology, supervision, original draft, review, and editing.

Funding

This work is supported by the National Key Research and Development Program of China (grant numbers 2019YFC1510102 and 2018YFA0605903), the National Natural Science Foundation of China [grant numbers 41975024 and 41876130] and the Marine Meteorology Research and Development Program of the Qingdao Meteorological Bureau (grant number 2019qdqxz02).

Acknowledgments

The authors wish to thank Jing-Wu Liu and Jun-Chao Yang for their valuable comments.

Conflict of interest

The authors declare that the research was conducted in the absence of any commercial or financial relationships that could be construed as a potential conflict of interest.

Publisher's note

All claims expressed in this article are solely those of the authors and do not necessarily represent those of their affiliated organizations, or those of the publisher, the editors, and the reviewers. Any product that may be evaluated in this article, or claim that may be made by its manufacturer, is not guaranteed or endorsed by the publisher.

Supplementary material

The Supplementary Material for this article can be found online at: https://www.frontiersin.org/articles/10.3389/feart.2022.956836/full#supplementary-material

References

Cereceda, P., Osses, P., Larrain, H., Farı´as, M., Lagos, M., Pinto, R., et al. (2002). Advective, orographic and radiation fog in the Tarapacá region, Chile. *Atmos. Res.* 64, 261–271. doi:10.1016/S0169-8095(02)00097-2

China Meteorological Administration (2005). *People's Republic of China meteorological industry standard:GTS1 digital radiosonde*. Beijing: Standards Press of China.

Diao, X. (1992). Statistical analysis of sea fog in Qingdao and offshore (in Chinese). *Mar. Forecast* 8, 45–55.

Dorman, C. E., Hoch, S. W., Gultepe, I., Wang, Q., Yamaguchi, R. T., Fernando, H. J. S., et al. (2021). *Large-scale synoptic systems and fog during the C-fog field experiment*. Netherlands: Springer. doi:10.1007/s10546-021-00641-1

Fernando, H. J. S., Gultepe, I., Dorman, C., Pardyjak, E., Wang, Q., Hoch, S. W., et al. (2021). C-FOG life of coastal fog. *Bull. Am. Meteorol. Soc.* 102, E244–E272. doi:10.1175/BAMS-D-19-0070.1

Findlater, J., Roach, W. T., and McHugh, B. C. (1989). The haar of north-east Scotland. *Q. J. R. Meteorol. Soc.* 115, 581–608. doi:10.1002/qj.49711548709

Fu, G., Guo, J., Pendergrass, A., and Li, P. (2008). An analysis and modeling study of a sea fog event over the Yellow and Bohai Seas. *J. Ocean. Univ. China* 7, 27–34. doi:10.1007/s11802-008-0027-z

Gao, S., Lin, H., Shen, B., and Fu, G. (2007). A heavy sea fog event over the Yellow Sea in March 2005: Analysis and numerical modeling. *Adv. Atmos. Sci.* 24, 65–81. doi:10.1007/s00376-007-0065-2

Gao, R., Li, X., Ren, Z., and Wang, J. (2016). Study of the sea fog prediction by classification and regression tree (CART) analyses in Qingdao coastal area. *Mar. Forecast.* 33, 80–87. doi:10.11737/j.issn.1003-0239.2016.04.010

Gultepe, I., Heymsfield, A. J., Fernando, H. J. S., Pardyjak, E., Dorman, C. E., Wang, Q., et al. (2021). A review of coastal fog microphysics during C-fog. *Bound. Layer. Meteorol.* 181, 227–265. doi:10.1007/s10546-021-00659-5

Hersbach, H., and Dee, D. (2016). ERA5 reanalysis is in production. *ECMWF Newsl.* 147, 5–6.

Huang, J., Wang, B., Wang, X., Huang, F., Lü, W., and Jing, T. (2018). The spring Yellow sea fog: Synoptic and air–sea characteristics associated with different airflow paths. *Acta Oceanol. Sin.* 37, 20–29. doi:10.1007/s13131-018-1155-y

Iacobellis, S. F., and Cayan, D. R. (2013). The variability of California summertime marine stratus: Impacts on surface air temperatures. *J. Geophys. Res. Atmos.* 118, 9105–9122. doi:10.1002/jgrd.50652

Isaac, G. A., Bullock, T., Beale, J., and Beale, S. (2020). Characterizing and predicting marine fog offshore newfoundland and labrador. *Weather Forecast.* 35, 347–365. doi:10.1175/WAF-D-19-0085.1

Johnstone, J. A., and Dawson, T. E. (2010). Climatic context and ecological implications of summer fog decline in the coast redwood region. *Proc. Natl. Acad. Sci. U. S. A.* 107, 4533–4538. doi:10.1073/pnas.0915062107

Kim, C. K., and Yum, S. S. (2012). A numerical study of sea-fog formation over cold sea surface using a one-dimensional turbulence model coupled with the weather research and forecasting model. *Bound. Layer. Meteorol.* 143, 481–505. doi:10.1007/s10546-012-9706-9

Koračin, D., Dorman, C. E., Lewis, J. M., Hudson, J. G., Wilcox, E. M., Torregrosa, A., et al. (2014). Marine fog: A review. *Atmos. Res.* 143, 142–175. doi:10.1016/j.atmosres.2013.12.012

Lee, H.-Y., and Chang, E.-C. (2018). Impact of land-sea thermal contrast on the inland penetration of sea fog over the coastal area around the Korean Peninsula. *J. Geophys. Res. Atmos.* 123, 6487–6504. doi:10.1029/2017JD027633

Leigh, R. J. (2007). Economic benefits of terminal aerodrome forecasts (TAFs) for sydney airport, Australia. *Met. Apps.* 2, 239–247. doi:10.1002/met.5060020307

Leipper, D. F. (1994). Fog on the U.S. West coast: A review. *Bull. Am. Meteorol. Soc.* 75, 229–240. doi:10.1175/1520-0477(1994)075<0229:FOTUWC>2.0.CO;2

Lewis, J. (2003). Sea fog off the California coast: Viewed in the context of transient weather systems. *J. Geophys. Res.* 108, 4457. doi:10.1029/2002JD002833

Li, W., Xing, Y., and Ma, S. (2009). The analysis and comparison between GTS1 radiosonde made in China and RS92 radiosonde of vaisala company (in Chinese). *Meteorol. Mon.* 35, 97–102.

Norris, J. R., and Leovy, C. B. (1994). Interannual variability in stratiform cloudiness and sea surface temperature. *J. Clim.* 7, 1915–1925. doi:10.1175/1520-0442(1994)007<1915:IVISCA>2.0.CO;2

Sugimoto, S., Sato, T., and Nakamura, K. (2013). Effects of synoptic-scale control on long-term declining trends of summer fog frequency over the pacific side of hokkaido island. *J. Appl. Meteorol. Climatol.* 52, 2226–2242. doi:10.1175/JAMC-D-12-0192.1

Tardif, R., and Rasmussen, R. M. (2007). Event-based climatology and typology of fog in the New York city region. *J. Appl. Meteorol. Climatol.* 46, 1141–1168. doi:10.1175/JAM2516.1

Wang, B. H. (1985). *Sea fog*. Beijing: China Ocean Press.

World Meteorological Organization (1966). *International meteorological vocabulary*.

Yang, L., Liu, J.-W., Xie, S.-P., and Shen, S. S. P. (2021). Transition from fog to stratus over the Northwest Pacific Ocean: large-eddy simulation. *Mon. Weather Rev.* 149, 1–45. doi:10.1175/MWR-D-20-0420.1

Yi, L., Zhang, S. P., Thies, B., Shi, X. M., Trachte, K., and Bendix, J. (2015). Spatio-temporal detection of fog and low stratus top heights over the Yellow sea with geostationary satellite data as a precondition for ground fog detection — a feasibility study. *Atmos. Res.* 151, 212–223. doi:10.1016/j.atmosres.2014.03.020

Zhang, S.-P., Xie, S.-P., Liu, Q.-Y., Yang, Y.-Q., Wang, X.-G., and Ren, Z.-P. (2009). Seasonal variations of Yellow sea fog: Observations and mechanisms. *J. Clim.* 22, 6758–6772. doi:10.1175/2009JCLI2806.1

Zhang, S.-P., and Yi, L. (2013). A comprehensive dynamic threshold algorithm for daytime sea fog retrieval over the Chinese adjacent seas. *Pure Appl. Geophys.* 170, 1931–1944. doi:10.1007/s00024-013-0641-6

Zhang, S., Chen, Y., Long, J., and Han, G. (2015). Interannual variability of sea fog frequency in the Northwestern Pacific in July. *Atmos. Res.* 151, 189–199. doi:10.1016/j.atmosres.2014.04.004

Zhang, S., Li, M., Meng, X., Fu, G., Ren, Z., and Gao, S. (2012). A comparison study between spring and summer fogs in the Yellow sea-observations and mechanisms. *Pure Appl. Geophys.* 169, 1001–1017. doi:10.1007/s00024-011-0358-3

frontiers | Frontiers in Earth Science

TYPE Original Research
PUBLISHED 23 September 2022
DOI 10.3389/feart.2022.968744

OPEN ACCESS

EDITED BY
Guihua Wang,
Fudan University, China

REVIEWED BY
Shanhong Gao,
Ocean University of China, China
Suping Zhang,
Ocean University of China, China

*CORRESPONDENCE
Mingsen Zhou,
zhoums@gd121.cn

SPECIALTY SECTION
This article was submitted to Atmospheric Science, a section of the journal Frontiers in Earth Science

RECEIVED 14 June 2022
ACCEPTED 16 August 2022
PUBLISHED 23 September 2022

CITATION
Zhou M, Huang H, Lao H, Cai J, Wu D and Zhang X (2022), Feasibility analysis of early warning of sea fog within six hours for two harbors in the South China Sea.
Front. Earth Sci. 10:968744.
doi: 10.3389/feart.2022.968744

Feasibility analysis of early warning of sea fog within six hours for two harbors in the South China Sea

Mingsen Zhou[1,2]*, Huijun Huang[1,2], Hanqiong Lao[3], Jingjiu Cai[4], Deping Wu[3] and Xinxin Zhang[3]

[1]Institute of Tropical and Marine Meteorology, China Meteorological Administration, Guangzhou, China, [2]Guangdong Provincial Key Laboratory of Regional Numerical Weather Prediction, China Meteorological Administration, Guangzhou, China, [3]Zhanjiang Meteorological Bureau, Zhanjiang, China, [4]Guangdong Meteorological Observatory, Guangzhou, China

Sea fog significantly impacts harbor operations, at times even causing navigation to cease. This study examines two harbors in the north of the South China Sea, analyzing the feasibility of increasing each harbor's sea fog early warning capability to 6 h in advance. Although the harbors are separated by only about 100 km, analysis of their backward trajectories reveals differences in the incoming flow and sea fog types. Concerning the types, at Xuwen harbor, warm advection fog represents 49.56% of the cases, cold advection representing 48.03%. At Zhanjiang harbor, 37.06% are warm advection fog, with 58.33% cold advection fog cases. We propose different monitoring and early warning schemes for the harbors. For Xuwen, we suggest eight visibility lidars located on the north and south sides of Qiongzhou Strait (two on the north, six on the south). Here, such a setup would give warning probabilities of sea fog of 87.50, 66.23, and 49.78% for advance times of 2, 3, and 4 h. For Zhanjiang, we suggest two visibility lidars and four buoys at the east side of the harbor. The corresponding warning probabilities are 83.77, 64.47, and 47.15% for the same advance times. For 5–6 h in advance, the early warning probabilities of both harbors drop quickly. We also suggest a flow chart for the early warning and monitoring scheme at each harbor.

KEYWORDS

sea fog, harbor, early warning, feasibility analysis, South China Sea

1 Introduction

Sea fog has various impacts on human activities, especially for harbor transportation. The fog makes marine transport, coastal traffic, as well as harbor operations much less safe (Wang, 1985; Leipper, 1994; Lewis et al., 2004; Gultepe et al., 2007; Zhang et al., 2009; Koračin et al., 2014; Koračin and Dorman, 2017; Dorman et al., 2019). According to Tremant (1987), 32% of all accidents at sea worldwide occur under a dense fog. Gultepe et al. (2007) pointed out that economic and human losses associated with fog and low visibilities are comparable to the losses from other weather disasters such as tornadoes and

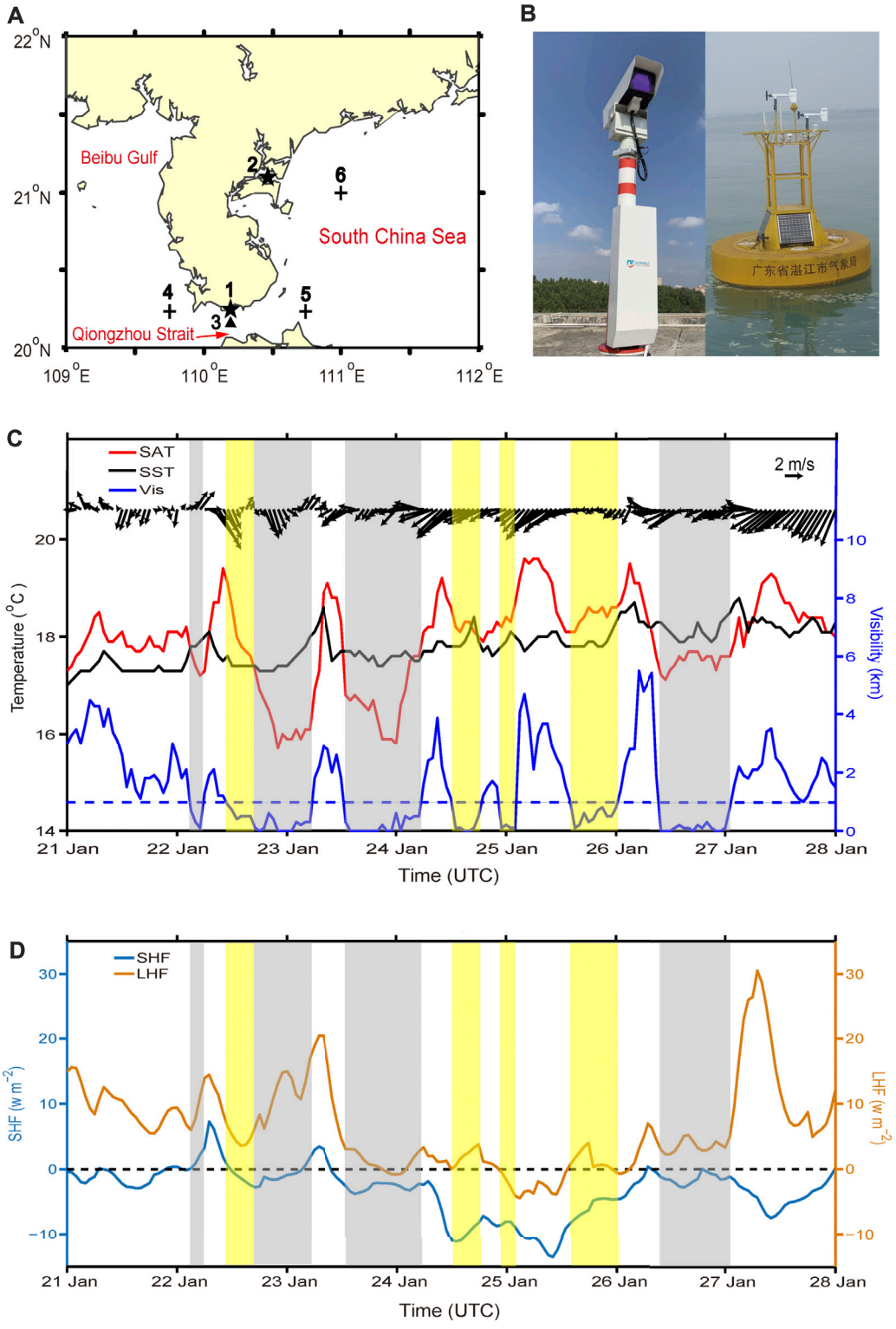

FIGURE 1
Overview of stations, instruments, and data. **(A)** Locations of 1) Xuwen harbor, 2) Zhanjiang harbor, 3) buoy, 4)—5) Selected points to calculate the average heat flux data for Xuwen. 6) Selected point to represent the heat flux data for Zhanjiang. **(B)** Monitoring instruments. Left: visibility lidar. Right: buoy. Photo courtesy of Xinxin Zhang. **(C)** Wind vector, surface air temperature (SAT), sea surface temperature (SST), and visibility at Xuwen harbor for the 202101 fog event. The wind vector, SAT and SST from 3 m buoy data and the visibility from Xuwen station. Yellow bands indicate warm advection fog, gray bands indicate cold. The adjacent yellow–gray band at 23 January is classified as abnormal "A" in Table 3. **(D)** Sensible heat flux (SHF) and latent heat flux (LHF) at Xuwen based on ERA5 data.

typhoons. For example, in China, there were 19 collision accidents caused by poor visibility in 2018, resulting in 30 missing and presumed dead (Maritime Safety Administration of the Ministry of transport of China, 2019).

Sea-fog forecasting remains full of challenges (Lewis et al., 2004; Gultepe et al., 2007; Koračin and Dorman, 2017). Mesoscale numerical modelling has been the primary method of such forecasting ever since Ballard et al. (1991) used a 3-dimensional mesoscale numerical model to forecast the sea fog of Northeast Scotland. Since then, many studies have aimed to improve the ability of sea-fog numerical simulation and prediction for various locations. Such studies include that for the US west coast (Koračin et al., 2001, 2005), the Yellow Sea and the East China Sea (Fu et al., 2006; Gao et al., 2007; Heo and Ha, 2010; Kim and Yum, 2012; Wang et al., 2014; Yang et al., 2019), the South China Sea (Yuan and Huang, 2011; Huang et al., 2016), and the sea fog off the east coast of Canada (Yang et al., 2010; Chen et al., 2020a). Concerning the ability of a long-term operational sea fog model, the model of Huang et al. (2019), with a horizontal resolution of 3 km, gave a 2-years-average equitable threat score (ETS) of 0.20 for 24 h forecasts in the South China Sea. Zhou and Du (2010) used a 10-member multimodel ensemble method, with a horizontal resolution is 15 km, and argued that the ETS score can be improved up to 0.334 for 12- and 36-h forecasts in eastern China and coastal areas.

The South China Sea (SCS) is one of the seven marginal seas with significant sea fog (Dorman et al., 2019). The coast region near Xuwen harbor and Zhanjiang harbor (Figure 1A) has the highest frequency of sea fog in the north part of the SCS (Wang, 1985; Huang et al., 2011, 2015; Zhang and Lewis, 2017; Han et al., 2022). Here, the fog season is usually from January to April. We focus on these two important harbors. Zhanjiang is a deep-water port designed and built by China. It has become one of the 25 major ports along the coast of China and, except for all the fog, has the best navigation conditions in the coastal areas of South China. Xuwen is an important transport port connecting Hainan Province and the Chinese mainland for passenger and freight transport.

Advection fog is the dominant type in SCS (Wang 1985). In general, two kinds of advection fog can occur over sea. One is warm advection fog in which the surface air temperature (SAT) exceeds the sea surface temperature (SST), the other is cold advection fog with SAT below SST (Taylor, 1917; Petterssen, 1938; Pilié et al., 1979; Findlater et al., 1989; Tachibana et al., 2008; Tanimoto et al., 2009; Huang et al., 2015). The warm advection fog and cold advection fog are the same as cold sea fog and warm sea fog in Koračin et al. (2014). Based on 60 fog cases observed at the Marine Meteorological Science Experiment Base (MMSEB) at Bohe, Maoming in 2007–12, Huang et al. (2015) found about 69% to be warm advection fog, 28% cold advection fog, and 3% being other types. The MMSEB is about 100 km from Zhanjiang harbor and about 180 km from Xuwen harbor, with different geographical and climatic characteristics (Compilation group of Guangdong Provincial Meteorological Bureau, 2006). Because different types of advection fog correspond to different synoptic situations, and the synoptic situation is a key factor to be considered in sea fog early warning, one goal of this study is to determine percentages of each fog type at the two harbors.

Both Xuwen and Zhanjiang harbors are seriously affected by sea fog weather during the fog season. For example, constant sea fog occurred from 15 to 25 February 2018 in Zhanjiang, with the minimum visibility less than 200 m, causing the suspension of shipping in Qiongzhou Strait. In this period, two ships collided here, resulting in two fatalities. Furthering the disruption, this period included China's spring Festival holiday with all of its increased travel and transport demand. For example, it resulted in a large number of passengers stranded. The queue for ferry service was as long as 20 km at the peak, with some people waiting in their car over day. Given such a major disruption, the Maritime Safety Administration later argued for an accurate early warning of sea fog within 6 h to help them to adjust the ferry operations. This urgent demand prompted this study.

What is the best method to predict sea fog within 6 h? Kamangir et al. (2021) predicted fog visibility for an airport by post-processing numerical weather prediction model output and satellite-based sea surface temperature using a 3D-Convolutional Neural Network (3D-CNN). Although they could give 6 h sea-fog forecast results, this method is based on model output, which is limited by the initial field preparation time and the running time of the model. Thus, it may be difficult to release the method's results 6 h ahead of the fog event. The most effective means for early warning of sea fog is by making direct observations. For example, Xian et al. (2020) suggest using visibility lidar systems.

Since 2019, Hainan Meteorological Bureau has built three visibility lidars to monitor the harbors and channels on both sides of the Qiongzhou Strait. The complementary observation of the lidar, together with satellite cloud images, works well to not only monitor the fog, but also improve the early warning ability (Chen et al., 2020b). However, for early warning of a harbor, further improvements are needed. For example, visibility lidar has a scanning radius of only 15 km. For advection fog, the early warning time is about 1–2 h (for a windspeed of 3 m s^{-1}). Also, satellites do a poor job distinguishing fog from low cloud (Bendix, 1995; Lee et al., 1997; Bendix et al., 2006; Zhang and Yi, 2013; Wilcox, 2017). The retrieval ability of satellite between sea fog and low cloud is particularly poor for warm advection fog as the two types often occur together (Huang et al., 2011, Huang et al., 2015). Hence, in addition to satellite monitoring, direct monitoring may be critical for early warning of sea fog. A feasibility analysis of early warning of sea fog would help determine the best method to reach the goal of a 6-h warning system.

This study focuses on the feasibility of advancing the early warning time of sea fog in Xuwen and Zhanjiang harbors to 6 h, and how to effectively arrange the monitoring instruments and

TABLE 1 The 13 sea fog events at both harbors in 2013–2021.

Year	S.N.[a]	Periods	Fog days	Suspension hours	Impact[b]
2013	201301	17–19 January	3	48	Strong
	201302	03–06 February	4	9.68	Medium
	201303	12–14 March	3	6.38	Light
2014	201401	30 January-02 February	4	44.25	Strong
2015	201501	24–26 Jan	3	15.58	Medium
	201502	15–17 February	3	9.83	Medium
2016	201601	04–07 March	4	36	Strong
	201602	18–20 March	3	33.58	Strong
	201603	26–29 April	4	7.5	Light
2017	201701	17–20 February	4	13.5	Medium
2018	201801	15–25 February	11	95.21	Strong
2019	201901	03–07 February	5	19.58	Medium
2021	202101	21–26 January	6	78	Strong

[a]S.N., means the serial number of the sea fog event.
[b]Impact means the degree of influence of the sea fog case. Strong: harbor suspension time due to sea fog exceeds 24 h; medium: suspension time is 8–24 h; light: suspension time less than 8 h.

equipment. The present paper is organized as follows: Section 2 describes the data and method used in this study. Section 3 analyses the backward trajectory frequency and the proportion of both types of advection fog for the harbors. Section 4 analyses the feasibility of sea fog early warning and provides early warning and monitoring schemes. Section 5 presents the main conclusions and discussion.

2 Data and method

2.1 Data

We use five sources of data: observations of meteorological stations, buoy data, climatological sea surface temperature (SST), analyzed products on gridpoints and heat flux data. The observations are operated by the China Meteorological Administration (CMA) and are from a weather station at Xuwen (110.16 °E, 20.24°N) and one at Zhanjiang (110.40°E, 21.20°N) (Figure 1). These two stations are within 3 km of their harbor. The stations provide data at intervals of 5 minutes, including wind direction, windspeed, temperature, air pressure, dew point temperature, precipitation, relative humidity, visibility, radiation, soil temperature, and cloud cover. In 2021, a buoy of diameter 3 m was placed in the middle of Qiongzhou Strait, mainly for sea fog monitoring. The main meteorological elements observed from buoy include wind direction, windspeed, temperature, humidity, air pressure, and sea surface temperature (Figure 1).

As the harbors are separated by only 100 km, fog generally occurs at both at the same time, especially for a continuous sea fog event. A fog event is defined as occurring when the visibility is less than 1 km at both stations with some port activities being suspended for three or more days. For 2013–2021 there were 13 such events with the total port-suspension duration of 57 days. In all events, the port suspension occurred at both harbors on the same days (Table 1).

The climatological SST data comes from the National Oceanic and Atmospheric Administration daily optimum interpolation sea surface temperature (DOISST) Version 2.1 (Huang et al., 2021). This dataset covers from September 1981 to December 2021 and is on a 1/4 degree global grid. The gridded, analyzed data is from the Global Forecast System (GFS), which is a global numerical weather prediction system containing a global computer model and variational analysis run by the U.S. National Weather Service (NWS). The GFS is run four times a day, and produces forecasts for up to 16 days in advance. The forecast component uses the FV3 (finite volume cubed) model with a resolution of ~13 km. The analyzed data is an archive of concatenated short-term GFS forecast model output having a 1/4 degree latitude–longitude grid on 55 hybrid levels. The data is hourly forecast data and can be downloaded at https://www.ready.noaa.gov/archives.php. Details about GFS are at https://www.emc.ncep.noaa.gov/emc/pages/numerical_forecast_systems/gfs.php.

We use the hourly surface sensible heat flux and surface latent heat flux from the European Centre for Medium-Range Weather Forecasts (ECMWF)'s ERA5 dataset. This dataset is the fifth generation ECMWF reanalysis of global climate and weather for the past 4–7 decades (currently, data is available from 1959). ERA5 combines model data with observations and has a horizontal resolution of 0.25 degree. (Reanalysis does not have the constraint of issuing timely forecasts and accommodates improved versions of the original observations to improve the

quality of the product (Hersbach et al., 2020). The download web site is https://cds.climate.copernicus.eu/cdsapp#!/dataset/reanalysis-era5-single-levels?tab=form.)

To evaluate the ERA5 heat fluxes, we selected a sea fog event in 2021 (the 202101 fog event), and compare it with the buoy data. Except for the cases of sea fog on January 22–23, the winds are mainly northeast and east (Figure 1C). Figure 1C also shows the changes of buoy SAT and SST data, indicating that this sea fog event includes both the cold advection fog (SAT ≤ SST) and the warm advection fog (SAT > SST). The overall trend starts from mainly cold advection fog, goes to warm advection fog, and then changes back to cold advection fog again. As pointed out in Huang et al. (2015), the direction of the heat flux of the cold advection fog is generally upward (from sea to air), whereas that of the warm advection fog is the opposite. The ERA5 data in Figure 1D show trends in sensible heat flux and latent heat flux that are consistent with the trends in buoy data. Given the 0.25 degree resolution of the ERA5 data, we use the average value of two over sea points on both sides of Xuwen harbor to represent the value of Xuwen harbor to reduce the influence of land on the over sea data. Similarly, we use the value of over sea on the east side of Zhanjiang harbor to represent the value of Zhanjiang harbor (Figure 1A).

2.2 Method

We use the NOAA hybrid single-particle Lagrangian integrated trajectory (HYSPLIT) model to calculate the backward tracking trajectory of the air mass and find the source of sea fog (Draxler and Hess 1998). This model was originally developed to calculate and analyze the transport and diffusion trajectory of air pollutants. It is often used to determine the origin of air masses and establish source–receptor relationships (Fleming et al., 2012). With continual improvement over 30 years (now latest version is HYSPLIT 5), it has been widely applied in the atmospheric sciences to track the source of air particles backward, determine the source of an air mass, and to help establish a relationship between the source and the affected place (Stein et al., 2015).

To analyze the source of sea fog, we run off-line HYSPLIT backwards for 72 h at the harbor location at six levels (10, 100, 300, 500, 800, and 1,500 m above sealevel). On a given sea-fog day, we ran the model every 3 h, making a total of 456 runs for each harbor. Similar to Dorman et al. (2019), we interpolate the backward trajectory data to a 0.05 degree grid over land and sea. Then we calculate the backward-trajectory frequency of each gridpoint, meaning the fraction (or number) of trajectories that passed over that point for the previous hours (for example, 1, 6, or 72 h). The early warning probability per hour is computed by the sum of gridpoints that can be detected with the sea fog monitoring instruments divided by the total runs (456) when fog approaches. Here, we define each run as one sea fog case. Hence, there are many sea fog cases in every fog event.

We consider here two instruments for monitoring and providing an early warning of sea fog: visibility lidar and offshore buoys. Examples are shown in Figure 1B. At present, the maximum range of visibility lidar is 15 km, though the actual effective detection range may be less. The buoy's effective observation range is 10 km if it has video monitoring equipment.

The initial cost of an over-sea buoy is about 3–5 times that of the visibility lidar, and due to its location, is difficult to operate and maintain. In comparison, although the monitoring effect of a visibility lidar may be better than that of a buoy, it is usually installed on shore because it requires a long-term stable power supply to achieve effective continuous monitoring.

Although we define warm advection fog and cold advection fog according to the air-sea temperature difference, we do not have buoy observation data for all sea fog events from 2013 to 2021. Also, we found that the air–sea temperature difference from the reanalysis data (such as ERA5 data) was not consistent with the actual observation value for 202101 sea fog event. Hence, we cannot distinguish warm advection fog and cold advection fog directly by the air–sea temperature difference, but through an indirect method, that is, by analyzing the backward trajectory of the air flow at a low altitude of 10 m, and checking the result against the heat flux from the ERA5 data. See Section 3.2 for more details.

3 Backward trajectory frequency and advection fog types

3.1 Features of the backward trajectory frequency

The occurrence and development of sea fog is very sensitive to SST. Here we calculate a 40-years (1982–2021) climatological mean of SST during the main fog season from January to March for the northern SCS and surrounding areas. Because of the East Asian monsoon (Tao and Chen, 1987), the prevailing surface wind during the fog season is from the northeast, cooling the sea surface off the southern China coast. The resulting cold water along the coast contributes to the formation of sea fog (Wang, 1985; Huang et al., 2015; Figure 2).

For all sea fog cases in 2013–2021, the 72-h backward trajectories from Xuwen at each level show different features. At the 10 m level (Figure 2A), the main direction of the backward trajectory is northeast along the coast. Along this direction, the gridpoint with the largest number has the value 48. East and south trajectories are also common. With the height rising from 100 to 500 m, the primary direction of the backward track flow changes from northeast to east (Figures 2B–D). At 800 m, although the easterly flow is still primary, the southerly and westerly flows become more common (Figure 2E). At 1,500 m, the main flow from the backward trajectory has turned to the west (Figure 2F). In general, with the height changing from low to

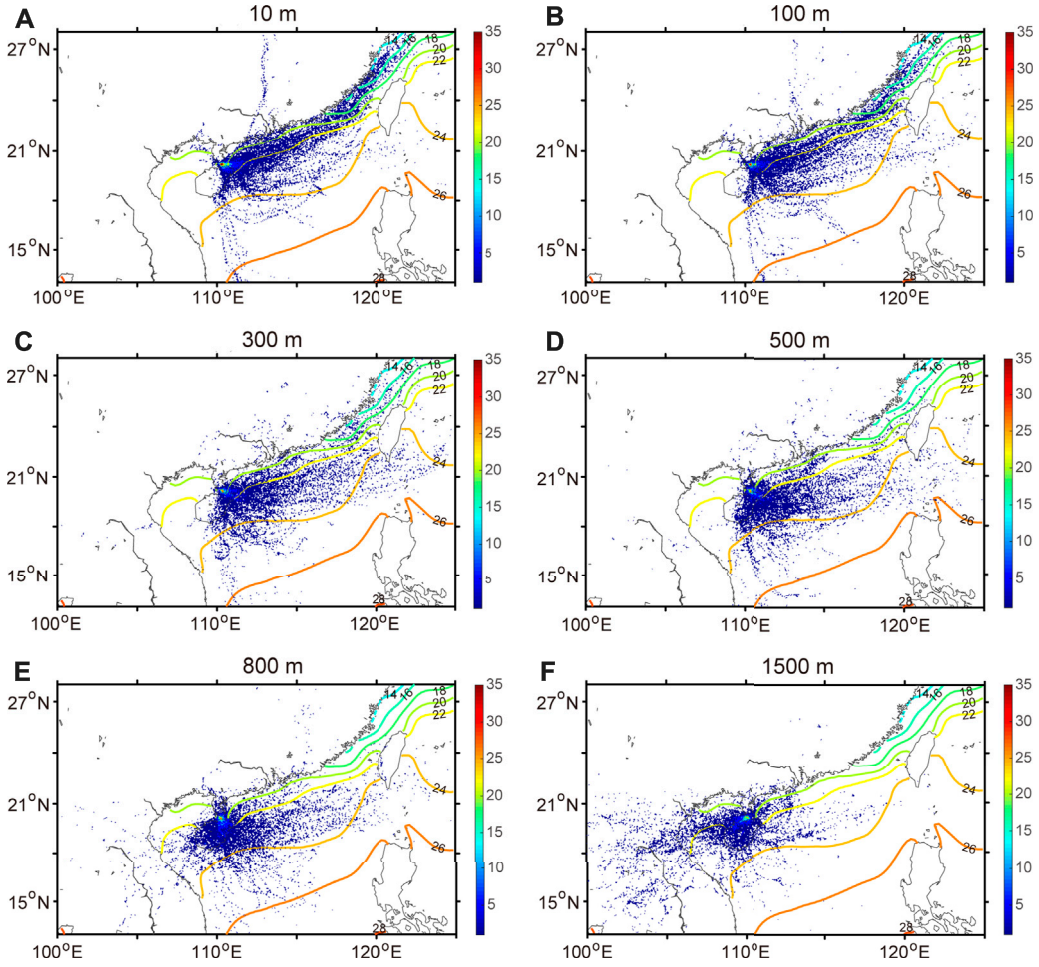

FIGURE 2
Number of 72 h backward trajectories for each level at Xuwen harbor during all sea fog events in 2013–2021. **(A–F)** represents 10, 100, 300, 500, 800, and 1500 m of the trajectory above sea level. Scale is number passing over a given gridpoint out of the 456 runs. Contours show the climatological mean of January–March SST for 1982–2021 (°C).

high, the inflow direction changes clockwise from northeast to west.

The analogous backward trajectories from Zhanjiang harbor are similar to those from Xuwen (Figure 3). However, at the 10 and 100 m levels, the main backward trajectory flow direction is more northerly than that from Xuwen and closer to the coastline (Figures 3A,B). At the 10 m level, the maximum number is approximately 35, smaller than that of Xuwen, a relation that holds at all levels, suggesting that the source direction of sea fog is more complex and elusive (Figures 3C–F).

To make a more detailed comparison between Xuwen and Zhanjiang harbor, we calculated the frequency difference between their backward trajectories. Results in Figure 4 show that at the 10 and 100 m levels, Zhanjiang harbor has more trajectories from the north (N), northeast (NE), and east–northeast (ENE). Conversely, Xuwen harbor has more incoming flow from the east (E), southeast (SE) and south (S). At the 300 and 500 m levels, both harbors show incoming flow from the SE and S. At 800 m, the flow is more southwest and west. Similarly, both harbors have more from the west at the 1,500 m level. The largest difference in the incoming flow is in the lower layer. The difference in the lower layer determines the difference in the underlying sea surface through which the air flows, which may affect the sea fog formation.

3.2 Proportion of advection fog types

In general, the cold advection fog type occurs when the low-level flow comes from a colder SST area (Huang et al., 2015). For these harbors, this direction is NE, ENE, and E. Conversely, the low-level flow for warm advection fog mainly comes from a warmer SST area. However, a change between the cold and the

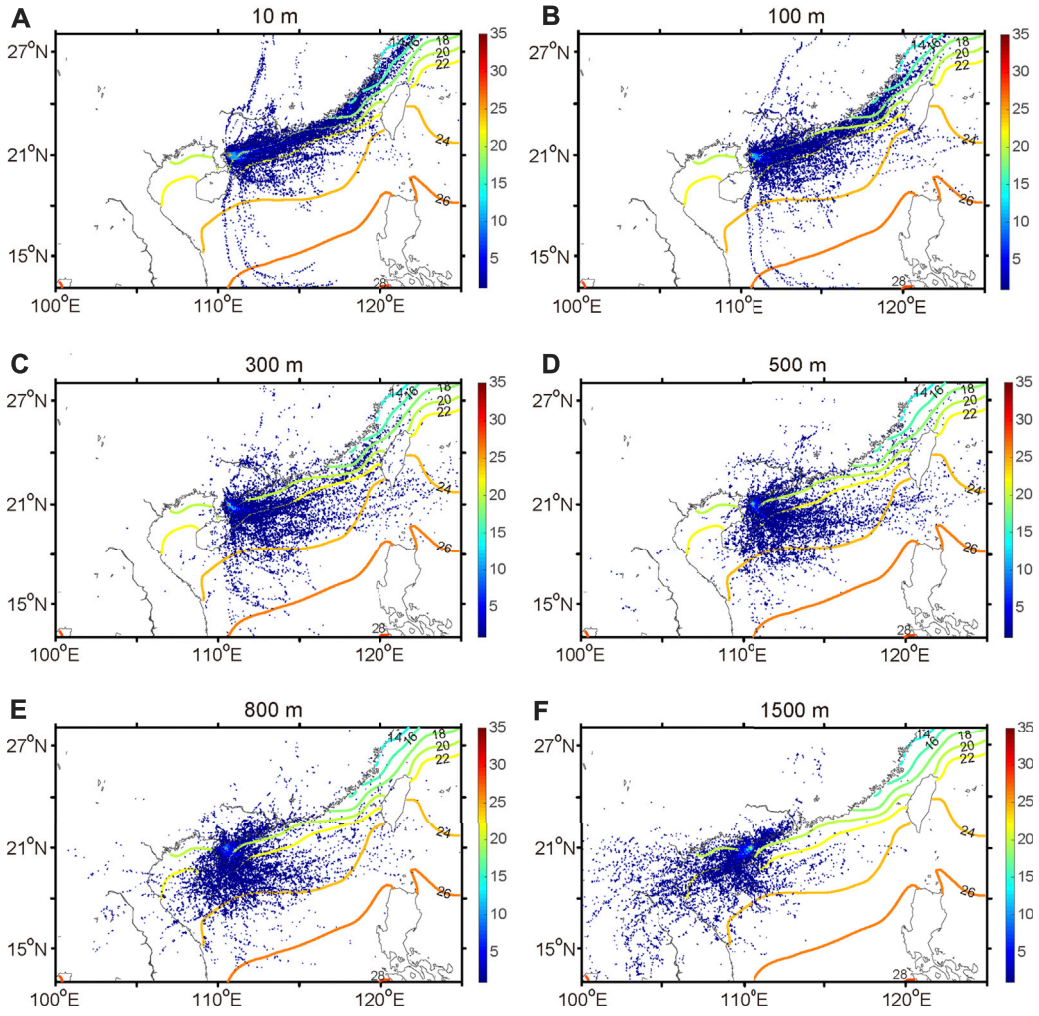

FIGURE 3
Same as Figure 2, but for Zhanjiang harbor.

warm advection fog types can occur during a single sea fog event in the North SCS.

For such changes between the two fog types, we recognize that two main types can occur. One type is that which occurs in the same sea fog process. For example, when a warm type fog forms, but then the air cools due to fog-top longwave cooling from the fog top, producing a cold type fog (Findlater et al., 1989; Yang et al., 2018). However, we did not have sufficient data to check for this possibility and instead relied upon the second type of change below.

This second type involves a change of near surface incoming flow caused by a change in the synoptic situation. For example, it can be seen in Figure 1C that the occurrence of an abnormal northwest wind is the reason that the cold advection fog changed from a warm type during January 22–23. Furthermore, compared with the cold advection fog on January 24, the warm advection fog on January 25–26 has little difference in the wind near the ground (Figure 1C). Therefore, it is necessary to distinguish whether warm advection fog or cold advection fog should occur based on the near surface backward incoming flow.

Here, we use a method similar to that in Huang et al. (2015) to distinguish cold-from warm-advection fog over the sea. In this method, the direction of the lowest backward trajectory is critical: if the 10 m flow comes from a cold SST area on the coast (e.g., NE, ENE, or E directions), we assume it will form cold advection fog. Otherwise, if the 10 m flow comes from the warm SST area (e.g., E, SE, and S directions), we assume it will form warm advection fog. There remain some complex paths that are hard to categorize that we label as abnormal paths (Figure 5). In addition, we use the ERA5 heat flux data to help distinguish the cold from the warm advection fog according to the direction of heat flux (i.e., upward indicating the cold type). After using the two methods at both

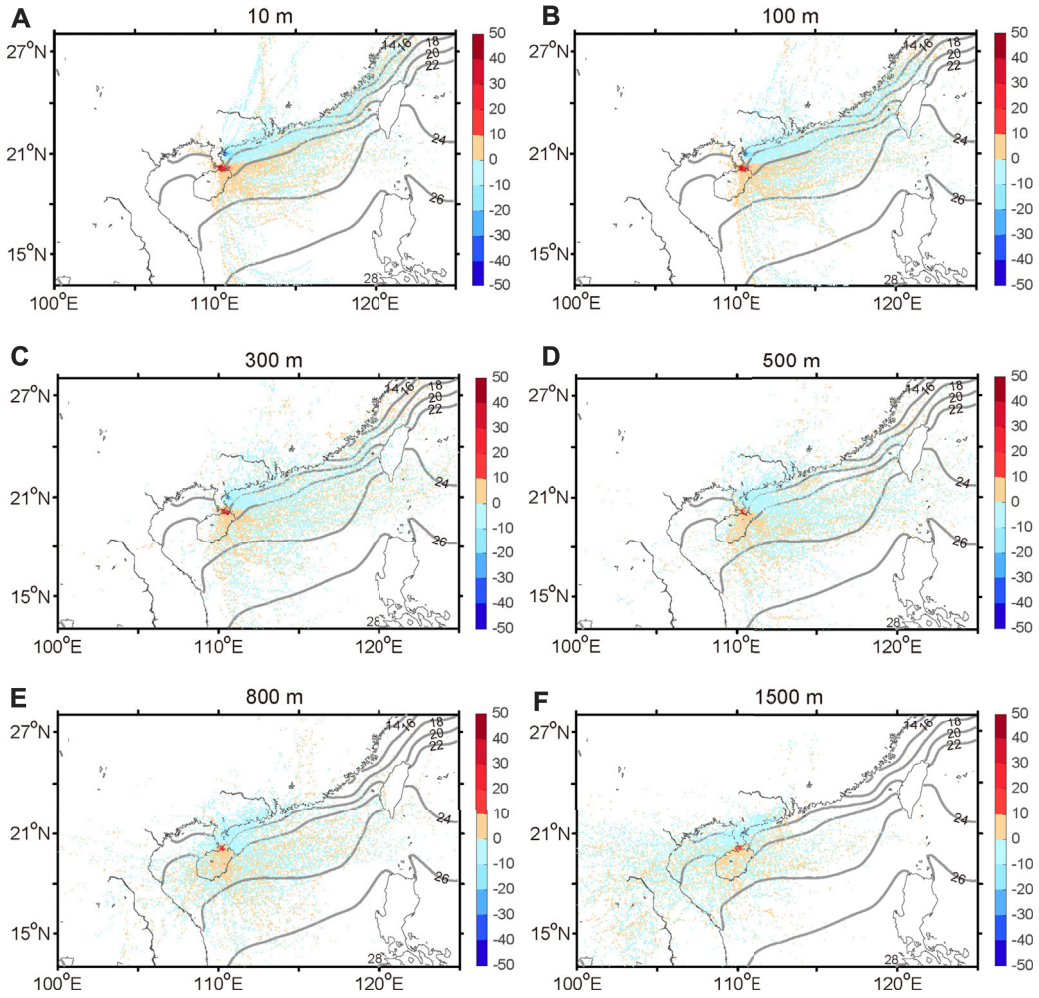

FIGURE 4
Difference in frequency of backward trajectories between Xuwen and Zhanjiang harbors. **(A–F)** represents 10, 100, 300, 500, 800 and 1500 m of the trajectory above sea level. Contours are the same as in Figure 2.

harbors, we found that about 70% of the sea fog cases have consistent evolution characteristics as described by the two methods. When there are inconsistencies, we take the 10 m flow method as the standard.

The case with easterly flow to Xuwen harbor sometimes is difficult to judge by the 10 m flow method. In this direction, although the nearby sea is relatively cool, distant sea has a warm SST (Figure 5). In this case, we argue that warm advection fog occurs when the easterly incoming flow exceeds 400 km (i.e., about 37 h for a 3 m s^{-1} windspeed). In such a case, sufficient heat- and water-vapor exchange between the sea and the air has occurred. Otherwise, we consider that cold advection fog forms.

Applying the above methods to the 456 backward trajectory runs, we find for Xuwen 49.56% warm advection fog cases and 48.03% cold advection fog cases. For Zhanjiang, the results are 37.06% warm advection fog cases and 58.33% cold advection fog cases (Table 2). Hence, Xuwen harbor has 12.5% more warm advection fog cases and 10.3% fewer cold advection fog cases than that in Zhanjiang harbor. The result arises from the difference of backward trajectories for the two harbors; specifically, the Xuwen harbor has more southeast and southward incoming flows in the low level, resulting more warm advection fog cases (Figure 4A).

In our analysis of the backward trajectories of these sea fog cases, we also find that the type of fog often changes during the fog event. That is, relatively few events include only one advection fog type, with most cases changing during the event (Table 3). The changes are assumed to arise from changes in the weather system and pressure field that leads to changes in near surface air flow. That is, the trajectories near the surface change frequently. Therefore, it is necessary to further analyze the incoming flow near the surface. We rely upon this analysis for the sea fog early warning.

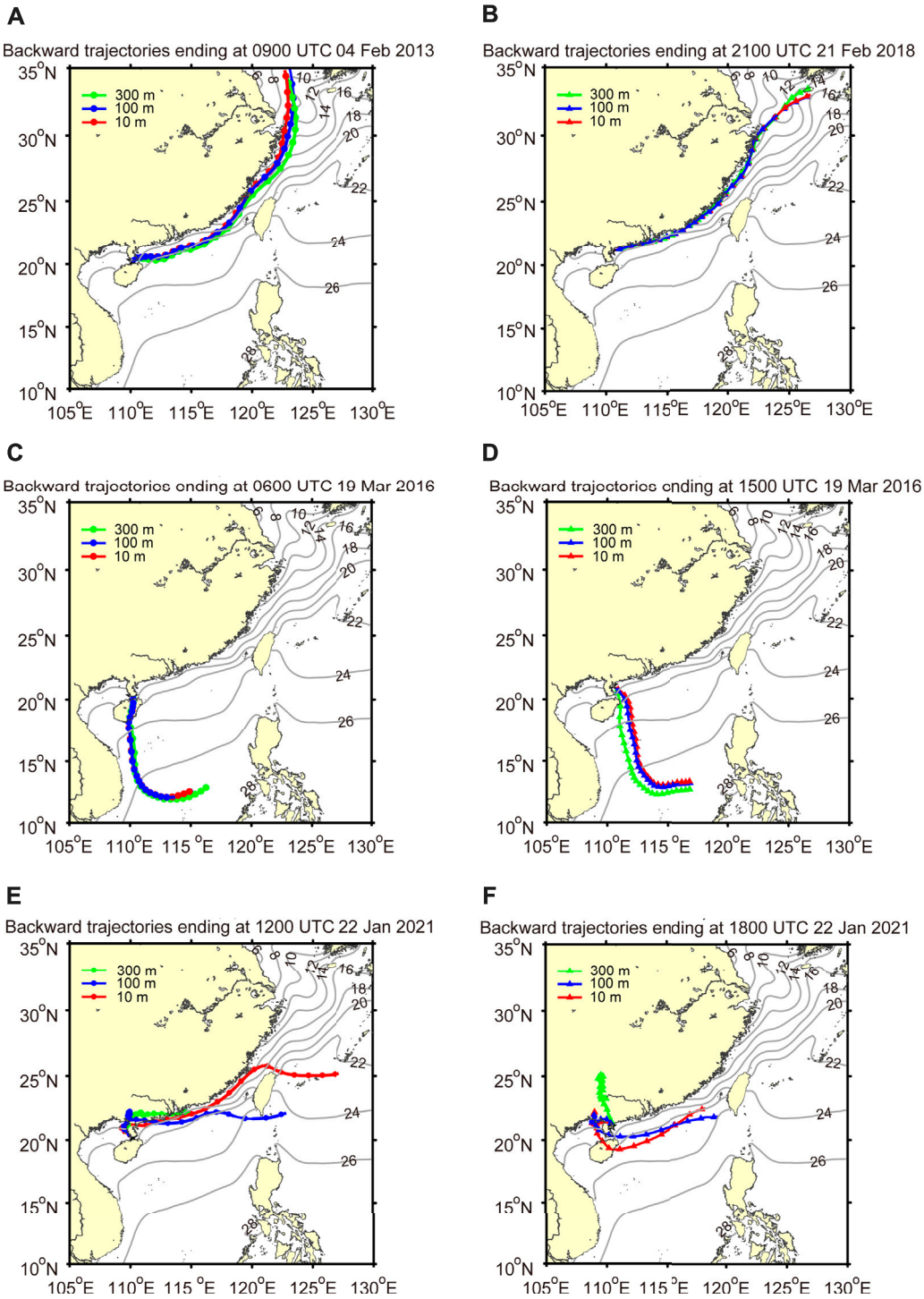

FIGURE 5
Trajectories for the fog types. Left side: Xuwen harbor. Right side: Zhanjiang harbor. Top row **(A,B)**: Typical trajectory for cold advection fog. Middle row **(C,D)**: warm advection fog. Bottom row **(E,F)**: abnormal paths.

TABLE 2 Main characteristics of advection fog cases for 2013–2021.

Harbor	Type[a]	Number of cases	Percent (%)	Main source direction at 10-m level
Xuwen	W	226	49.56	NE-SE[b], SE, E-SE, NE-E, E-S, S
	C	219	48.03	NE, ENE, NE-E
	A	11	2.41	
Zhanjiang	W	169	37.06	NE-SE, SE, E-SE, E-S, S
	C	266	58.33	NE, ENE, NE-E
	A	21	4.61	

[a]W is warm advection fog, C is cold advection fog, A is abnormal path that cannot classify as warm or cold advection fog.
[b]NE-SE, means the incoming flow direction changed from northeast to southeast.

TABLE 3 Characteristics of advection fog process at both harbors for 2013–2021.

Harbor	Advection characteristics	S.N.	Number	Percent (%)
Xuwen	W	201901, 201602	2	15.4
	C	201301	1	7.7
	W-C[a]	201303, 201501	2	15.4
	C-W	201302, 201401, 201701	3	23.1
	C-W-C-W	201601	1	7.7
	W-C-W-C	201502	1	7.7
	C-A-C-W-C	202101	1	7.7
	W-A-W-C-W	201603	1	7.7
	W-C-W-C-W-C-W-C-W-C	201801	1	7.7
Zhanjiang	W	201602, 201901	2	15.4
	C	201301	1	7.7
	C-W	201302, 201401, 201601, 201701	4	30.8
	W-C	201303, 201603	2	15.4
	C-W-C	201501, 201502	2	15.4
	C-A-C	202101	1	7.7
	W-C-W-C-A-C-A-C	201801	1	7.7

[a]W-C means the fog type changed from warm advection fog to cold advection fog. As in Table 2, A indicates an abnormal case.

4 Feasibility of sea fog monitoring and early warning

4.1 Hourly backward trajectory distribution

Here, we use the incoming flow near the surface (10 m level) to calculate the hourly backward-trajectory frequency distribution. For both harbors, as time goes back, the high-frequency region moves from the port to the east (Figures 6–8). However, 3 h before the sea fog formed (t = −3), a clear and complete high-frequency center affects Xuwen port, but the high-frequency centers affecting Zhanjiang port are dispersed (Figure 6).

In general, as time goes back, the high-frequency region of the backward trajectory becomes more and more scattered. Graphically, within 4 h of the fog event, the high-frequency regional center of the two ports is still relatively obvious, and thus the single point monitoring method may be used for effective early warning of sea fog (Figures 7, 8). However, the results indicate more difficulty in reaching an advance of 5–6 h. In particular, for 6 h prior to the fog (t = −6), the

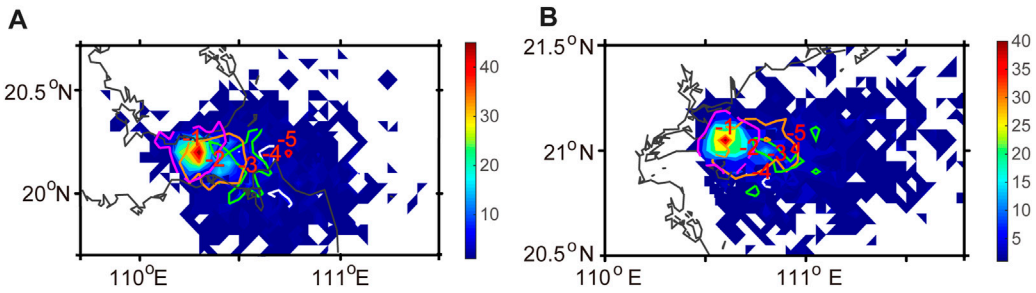

FIGURE 6
Superimposed hourly backward trajectory frequency distribution from 1 h before the onset of sea fog (t = −1) to 6 h before (t = −6). **(A)** Xuwen harbor. **(B)** Zhanjiang harbor. Shaded parts show the hourly frequency overlaid (but not accumulated) of each grid from t = −1 to t = −6. Contours are the isoline for frequency of at least five per hour at times t = −1 (pink), t = −2 (yellow), t = −3 (green), t = −4 (white), and t = −5 (red). For t = −6 the max frequency is less than 5. Numbers −1 to −5 are put at the geometric center of each isoline.

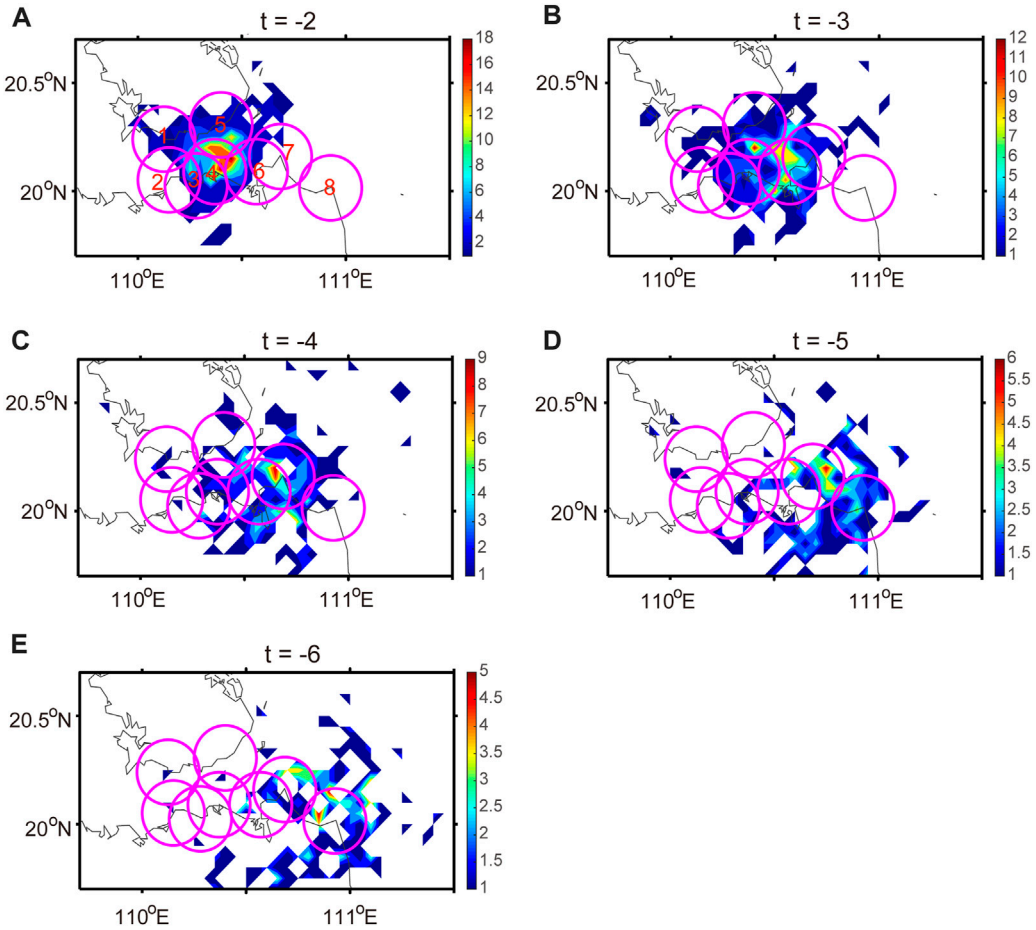

FIGURE 7
Proposed monitoring and early warning setup for Xuwen harbor. All eight visibility lidars, labeled and circled, are on the coast. Shading is the hourly backward-trajectory frequency distribution from **(A)** t = −2 h to **(E)** t = −6 h (indicate the advance time in hours) for Xuwen harbor. Pink circles are the effective radius of lidar (15 km). Positions 1–3 are built, positions 4-8 are proposed visibility lidars.

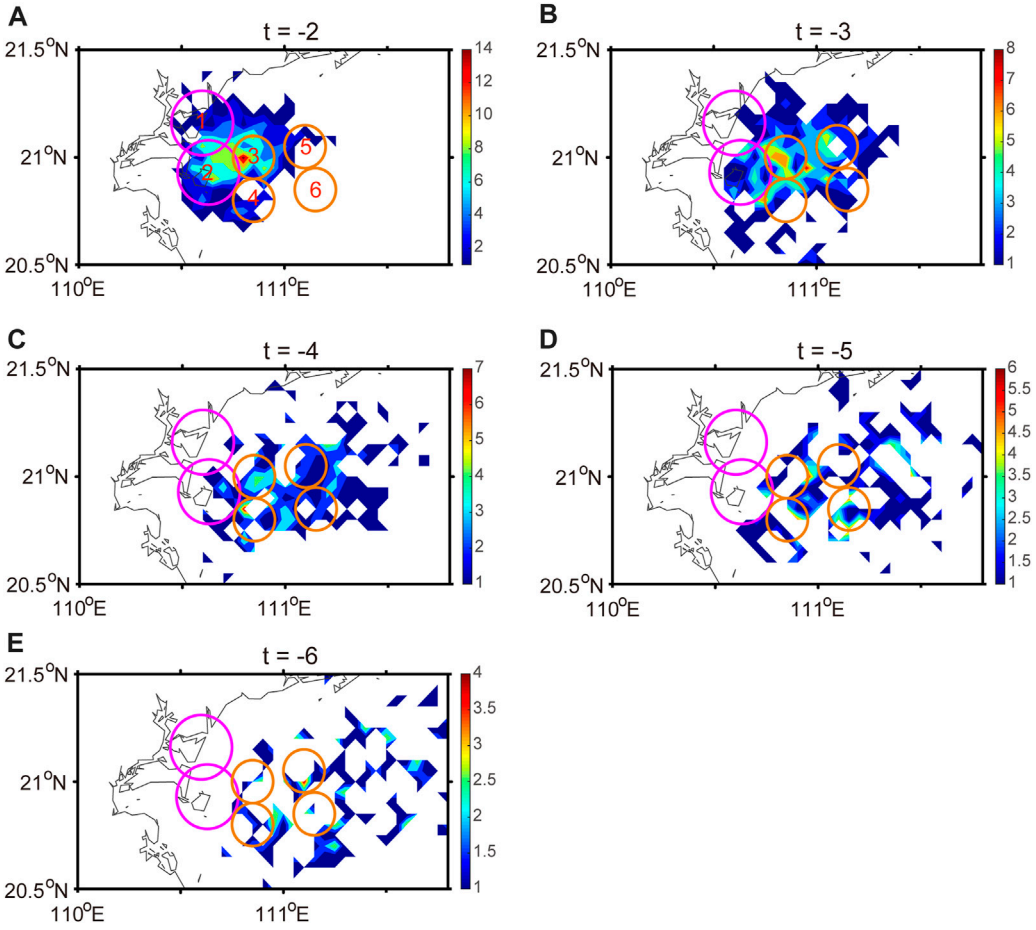

FIGURE 8
Same as Figure 7, but for Zhanjiang harbor. Numbers 1–6 are station locations: 1) and 2) are visibility lidars, 3) to 6) are buoys. Pink circles are the effective radius of the lidar (15 km), smaller brown circles are those for the buoys (10 km).

central area of the high-frequency area is less than 5. Such a low value reflects a largely decentralized state, indicating that at this time, the backward trajectory incoming flow is very dispersed, making it difficult to use the single point monitoring method to for sea fog early warning (Figures 7, 8).

4.2 Early warning and monitoring scheme

Before the harbor authorities install a monitoring operation for early warning of impending sea fog, they should know which arrangement of instruments has the more likely chance of success. Here we use the calculated backward trajectory frequency, combined with knowledge of the local geography and monitoring range of the instruments, to propose monitoring and early warning schemes for the two harbors.

TABLE 4 Sea-fog detection percentage.

Harbor	Prior warning (hr)	Number[a]	Percent (%)
Xuwen	2	399	87.50
	3	302	66.23
	4	227	49.78
	5	166	36.40
	6	115	25.22
Zhanjiang	2	382	83.77
	3	294	64.47
	4	215	47.15
	5	140	30.70
	6	94	20.61

[a]Number means the cumulative number of trajectories covered in the range of the monitoring and early warning scheme. The total frequency number of 1 h is 456.

10.3389/feart.2022.968744

TABLE 5 Sea fog detection percentage for Xuwen harbor.

Prior warning (hr)	Position[a]	Coast/Ocean	Lon	Lat	Number	Percent (%)
2	1	Coast	110.13	20.24	63	13.82
	2	Coast	110.15	20.05	38	8.33
	3	Coast	110.28	20.03	101	22.15
	4	Coast	110.37	20.09	215	47.15
	5	Coast	110.40	20.31	147	32.24
	6	Coast	110.57	20.09	111	24.34
	7	Coast	110.69	20.16	23	5.04
	8	Coast	110.93	20.02	0	0.00
3	1	Coast	110.13	20.24	25	5.48
	2	Coast	110.15	20.05	26	5.70
	3	Coast	110.28	20.03	58	12.72
	4	Coast	110.37	20.09	88	19.30
	5	Coast	110.40	20.31	73	16.01
	6	Coast	110.57	20.09	136	29.82
	7	Coast	110.69	20.16	69	15.13
	8	Coast	110.93	20.02	3	0.66
4	1	Coast	110.13	20.24	14	3.07
	2	Coast	110.15	20.05	13	2.85
	3	Coast	110.28	20.03	33	7.24
	4	Coast	110.37	20.09	40	8.77
	5	Coast	110.40	20.31	39	8.55
	6	Coast	110.57	20.09	84	18.42
	7	Coast	110.69	20.16	89	19.52
	8	Coast	110.93	20.02	15	3.29
5	1	Coast	110.13	20.24	7	1.54
	2	Coast	110.15	20.05	9	1.97
	3	Coast	110.28	20.03	25	5.48
	4	Coast	110.37	20.09	26	5.70
	5	Coast	110.40	20.31	11	2.41
	6	Coast	110.57	20.09	39	8.55
	7	Coast	110.69	20.16	60	13.16
	8	Coast	110.93	20.02	44	9.65
6	1	Coast	110.13	20.24	5	1.10
	2	Coast	110.15	20.05	4	0.88
	3	Coast	110.28	20.03	9	1.97
	4	Coast	110.37	20.09	13	2.85
	5	Coast	110.40	20.31	5	1.10
	6	Coast	110.57	20.09	24	5.26
	7	Coast	110.69	20.16	39	8.55
	8	Coast	110.93	20.02	44	9.65

[a]Locations shown in Figure 7.

TABLE 6 Same as Table 5, but for Zhanjiang harbor.

Prior warning (hr)	Position[a]	Coast/Ocean	Lon	Lat	Number	Percent (%)
2	1	Coast	110.60	21.16	76	16.67
	2	Coast	110.63	20.93	168	36.84
	3	Ocean	110.85	21.00	170	37.28
	4	Ocean	110.85	20.80	56	12.28
	5	Ocean	111.10	21.05	28	6.14
	6	Ocean	111.15	20.85	3	0.66
3	1	Coast	110.60	21.16	25	5.48
	2	Coast	110.63	20.93	65	14.25
	3	Ocean	110.85	21.00	99	21.71
	4	Ocean	110.85	20.80	66	14.47
	5	Ocean	111.10	21.05	73	16.01
	6	Ocean	111.15	20.85	41	8.99
4	1	Coast	110.60	21.16	8	1.75
	2	Coast	110.63	20.93	28	6.14
	3	Ocean	110.85	21.00	55	12.06
	4	Ocean	110.85	20.80	59	12.94
	5	Ocean	111.10	21.05	61	13.38
	6	Ocean	111.15	20.85	45	9.87
5	1	Coast	110.60	21.16	6	1.32
	2	Coast	110.63	20.93	15	3.29
	3	Ocean	110.85	21.00	40	8.77
	4	Ocean	110.85	20.80	37	8.11
	5	Ocean	111.10	21.05	31	6.80
	6	Ocean	111.15	20.85	44	9.65
6	1	Coast	110.60	21.16	2	0.44
	2	Coast	110.63	20.93	5	1.10
	3	Ocean	110.85	21.00	20	4.39
	4	Ocean	110.85	20.80	29	6.36
	5	Ocean	111.10	21.05	24	5.26
	6	Ocean	111.15	20.85	30	6.58

[a]Locations shown in Figure 8.

For Xuwen harbor, since the high-frequency area of sea fog is mainly in the south and the east side of Qiongzhou Strait, we suggest deploying more lidar along the south and east side of the strait. Here we assume that the effective range of the radar is 15 km. As there are presently three lidars (number 1–3) in this region, we propose adding five more (number 4–8) at the locations shown in Figure 7. Location selection is mainly based on backward trajectory, distance between locations and lidar coverage.

Because a 1 h warning may be too short, we mainly analyze the early warning ability of 2–6 h. According to this scheme, the early warning probabilities of sea fog in Xuwen harbor for 2, 3, and 4 h in advance are 87.50, 66.23, and 49.78% respectively. The probability then quickly drops to 36.40 and 25.22% for 5 and 6 h, respectively (Table 4). However, different locations have different sea fog warning probabilities. For example, for 2–3 h in advance, the probability at positions 4–6 (Figure 7) are the highest, whereas for 4 h in advance, the probability of positions 4, 6, and seven are the highest. As positions 1–3 are visibility lidars already built, it is necessary to build the position 4–8 visibility lidars for more effective early warning (Table 5).

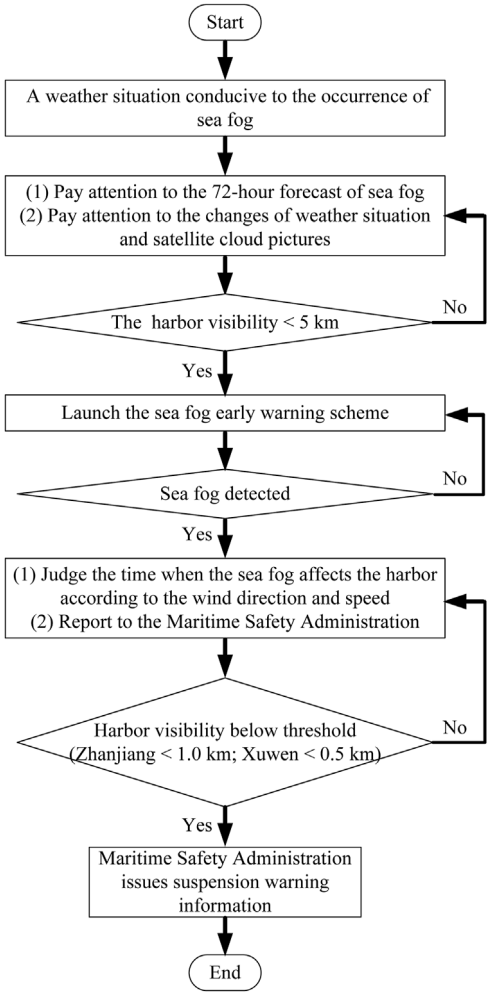

FIGURE 9
Flow chart of the early warning and monitoring scheme.

For Zhanjiang harbor, because the main incoming flow comes from the sea on the east side, we suggest a monitoring and early warning scheme with visibility lidars in positions 1-2 and four buoys in positions 3–6 (Figure 8). We assume that the radius represented by each buoy's observation is 10 km. To determine the lidar locations, we seek to have them spaced as far apart as possible, yet have each one in a region where the fog-producing trajectories pass. The selection of four buoy locations are a little more complicated. First, we select the initial locations by the same criteria as that for the lidar positions. This gives four initial locations. Second, a grid within a 20 km radius of each initial location is used for further statistical discrimination. Third, when several points have the same number of back trajectories, we choose the location with the highest probability at the first 4 hours.

With such an instrument setup, the early warning probabilities of sea fog in Zhanjiang harbor for 2, 3, and 4 h in advance are 83.77, 64.47, and 47.15% respectively. Similar to the Xuwen case, the probability quickly drops to 30.70 and 20.61% for 5 and 6 h, respectively (Table 4). As for the exact probability, for 2 h in advance, the probability of positions 1–3 are highest, whereas for 3–4 h in advance, positions 3–5 have the highest probability (Table 6).

Based on the above analysis and our review of previous daily sea fog early warning and prediction methods, we propose an operational sea fog early warning and monitoring scheme for the two harbors. We also argue that effective sea fog early warning and monitoring requires good cooperation between the Meteorological Bureau and the maritime safety administration (Figure 9).

5 Conclusion and discussion

In this study, we focused on the feasibility of a system for sea fog monitoring and early warning at Xuwen and Zhanjiang harbors on the South China Sea. We selected 13 sea fog events that occurred at both harbors that lasted for at least 3 days in the period 2013–2021. First, we ran a multi-layer 72 h backward trajectory analysis. Second, we analyzed the proportion of events that were either cold or warm advection fog cases. Finally, based on our analysis of the 10 m incoming flow, we proposed a measurement system for each harbor that would provide a sea fog early warning as well as a monitor for the sea fog. The main conclusions are as follows:

(1) For both harbors, the direction of incoming flow changed clockwise from northeast to west as the height increased from low to high. The main difference in incoming flow between the harbors was in the lower layer. In this layer, the primary directions to Zhanjiang harbor were from north, northeast and east-northeast, whereas for Xuwen, the directions were from east, southeast, and south.
(2) Based on low-level incoming flow and the heat flux analysis, the fog at Xuwen harbor was 49.56% warm advection fog and 48.03% cold advection fog cases. For Zhanjiang harbor, the cases were 37.06% warm advection fog and 58.33% cold advection fog. Xuwen harbor has 12.5% more warm advection fog cases and 10.3% fewer cold advection fog cases than that in Zhanjiang harbor.
(3) We proposed monitoring and early warning setups for each harbor. For Xuwen, we suggested eight visibility lidars located on the north and south sides of Qiongzhou Strait. This setup gave early warning probabilities of sea fog for 2, 3, and 4 h in advance of 87.50, 66.23, and 49.78% respectively. For Zhanjiang harbor, we suggested two visibility lidars and four buoys at the east side of the harbor. This setup gave early warning probabilities of sea fog for 2, 3, and 4 h in advance of 83.77, 64.47, and 47.15%. For 5–6 h in advance, the early warning probabilities of both harbors drop quickly.

Although the distance between the two harbors is only about 100 km, each has different near surface flow that results in different types of advection fog. We believe that these differences may come from local geographical and climatic characteristics, submarine topography, SST distribution characteristics, and local air–sea and land–air interactions (Koračin et al., 2014; Koračin and Dorman, 2017).

Methods of monitoring and early warning of sea fog need further improvement. First, we should use the direct, observed SAT and SST data (not the present indirect methods *via* low-level incoming flow and heat flux analysis) to reduce uncertainty in the classification of the two types of advection fog. Second, the selection of monitoring points may be improved, especially the locations at sea. Third, the flow chart of sea fog early warning and monitoring still needs to be improved in practice.

How to further strengthen the monitoring and early warning of sea fog in the future? We believe that the first is to build a unified sea fog monitoring and early warning center in each harbor. The second is to strengthen the complementarity of coastal monitoring, marine monitoring, and satellite monitoring, which will help to improve the accuracy and timeliness of sea fog early warning. In the future, we will strengthen our work in this area.

Data availability statement

The original contributions presented in the study are included in the article/supplementary material, further inquiries can be directed to the corresponding author.

Author contributions

MZ: Formal analysis; Methodology and software; Writing–original draft. HH: Conceptualization; Supervision; Writing–review and editing. HL: Data Curation; Resources. JC: Data Curation; Resources. DW: Data Curation; Resources. XZ: Data Curation; Resources.

Funding

This study was supported jointly by the National Natural Science Foundation of China (Grant Nos. 42275083 and 41675021), the Key Meteorological Sciences Research Project (Grant No. GRMC 2020Z01), and the Innovation team of severe weather mechanism and forecasting technology in the South China Sea of the Guangdong Provincial Meteorological Bureau.

Acknowledgments

Special thanks to the crew of the Xuwen County Meteorological Bureau, for their help in collecting the data.

Conflict of interest

The authors declare that the research was conducted in the absence of any commercial or financial relationships that could be construed as a potential conflict of interest.

Publisher's note

References

Ballard, S. P., Golding, B. W., and Smith, R. N. B. (1991). Mesoscale model experimental forecasts of the haar of northeast Scotland. *Mon. Wea. Rev.* 119, 2107–2123. doi:10.1175/1520-0493(1991)119<2107:MMEFOT>2.0.CO;2

Bendix, J. (1995). A case study on the determination of fog optical depth and liquid water path using AVHRR data and relations to fog liquid water content and horizontal visibility. *Int. J. Remote Sens.* 16, 515–530. doi:10.1080/01431169508954416

Bendix, J., Thies, B., Nauss, T., and Cermak, J. (2006). A feasibility study of daytime fog and low stratus detection with TERRA/AQUA-MODIS over land. *Meteorol. App.* 13, 111–125. doi:10.1017/s1350482706002180

Chen, C., Zhang, M., Perrie, W., Chang, R., Chen, X., Duplessis, P., et al. (2020a). Boundary layer parameterizations to simulate fog over Atlantic Canada waters. *Earth Space Sci.* 7, e2019EA000703. doi:10.1029/2019EA000703

Chen, Y., Cai, Q. B., Xu, W. J., Xian, J. H., Li, X., Zhang, C. H., et al. (2020b). Application of visibility lidar in a heavy fog in Qiongzhou Strait. *Adv. Meteorological Sci. Technol.* 10 (4), 128–132. doi:10.3969/j.issn.2095-1973.2020.04.023

Compilation group of Guangdong Meteorological Bureau (2006). *Technical guidance on weather forecasting in Guangdong.* Province, Beijing: China Meteorological Press, 526pp.

Dorman, C. E., Mejia, J., Koračin, D., and McEvoy, D. (2019). World marine fog analysis based on 58-years of ship observations. *Int. J. Climatol.* 40, 145–168. doi:10.1002/joc.6200

Draxler, R. R., and Hess, G. D. (1998). An overview of the HYSPLIT_4 modeling system for trajectories, dispersion, and deposition. *Aust. Meteor. Mag.* 47, 295–308.

Findlater, J., Roach, W. T., and Mchugh, B. C. (1989). The haar of north-east Scotland. *Q. J. R. Meteorol. Soc.* 115, 581–608. doi:10.1002/qj.49711548709

Fleming, Z. L., Monks, P. S., and Manning, A. J. (2012). Review: Untangling the influence of air-mass history in interpreting observed atmospheric composition. *Atmos. Res.* 104–105, 1–39. doi:10.1016/j.atmosres.2011.09.009

Fu, G., Guo, J., Xie, S., Duan, Y., Zhang, T., and Wang, J. (2006). Analysis and high-resolution modeling of a dense sea fog event over the Yellow Sea. *Atmos. Res.* 81, 293–303. doi:10.1016/j.atmosres.2006.01.005

Gao, S. H., Lin, H., Shen, B., and Fu, G. (2007). A heavy sea fog event over the Yellow Sea in March 2005: Analysis and numerical modeling. *Adv. Atmos. Sci.* 24 (1), 65–81. doi:10.1007/s00376-007-0065-2

Gultepe, I., Tardif, R., Michaelides, S. C., Cermak, J., Bott, A., Bendix, J., et al. (2007). Fog research: A review of past achievements and future perspectives. *Pure Appl. Geophys.* 164, 1121–1159. doi:10.1007/s00024-007-0211-x

Han, L. G., Long, J. C., Xu, F., and Xu, J. J. (2022). Decadal shift in sea fog frequency over the northern South China Sea in spring: Interdecadal variation and impact of the Pacific Decadal Oscillation. *Atmos. Res.* 265, 105905. doi:10.1016/j.atmosres.2021.105905

Heo, K. Y., and Ha, K. J. (2010). A coupled model study on the formation and dissipation of sea fogs. *Mon. Weather Rev.* 138 (4), 1186–1205. doi:10.1175/2009mwr3100.1

Hersbach, H., Bell, B., Berrisford, P., Hirahara, S., Horanyi, A., Munoz-Sabater, J., et al. (2020). The ERA5 global reanalysis. *Q. J. R. Meteorol. Soc.* 146, 1999–2049. doi:10.1002/qj.3803

Huang, B., Liu, C., Banzon, V., Freeman, E., Graham, G., Hankins, B., et al. (2021). Improvements of the daily optimum interpolation sea surface temperature (DOISST) version 2.1. *J. Clim.* 34, 2923–2939. doi:10.1175/jcli-d-20-0166.1

Huang, H. J., Huang, B., Yi, L., Liu, C. X., Tu, J., Wen, G. H., et al. (2019). Evaluation of the global and regional assimilation and prediction system for predicting sea fog over the South China Sea. *Adv. Atmos. Sci.* 36 (6), 623–642. doi:10.1007/s00376-019-8184-0

Huang, H. J., Liu, H. N., Huang, J., Mao, W. K., and Bi, X. Y. (2015). Atmospheric boundary layer structure and turbulence during sea fog on the southern China coast. *Mon. Weather Rev.* 143 (5), 1907–1923. doi:10.1175/mwr-d-14-00207.1

Huang, H. J., Liu, H. N., Jiang, W. M., Huang, J., and Mao, W. K. (2011). Characteristics of the boundary layer structure of sea fog on the coast of southern China. *Adv. Atmos. Sci.* 28 (6), 1377–1389. doi:10.1007/s00376-011-0191-8

Huang, H. J., Zhan, G. W., Liu, C. X., Tu, J., and Mao, W. K. (2016). A case study of numerical simulation of sea fog on the southern China coast. *J. Trop. Meteorology* 22 (4), 497–507. doi:10.16555/j.1006-8775.2016.04.005

Kamangir, H., Collins, W., Tissot, P., King, S. A., Dinh, H. T. H., Durham, N., et al. (2021). FogNet: A multiscale 3D CNN with double-branch dense block and attention mechanism for fog prediction. *Mach. Learn. Appl.* 5, 100038. doi:10.1016/j.mlwa.2021.100038

Kim, C. K., and Yum, S. S. (2012). A numerical study of sea fog formation over cold sea surface using a one-dimensional turbulence model coupled with the weather research and forecasting model. *Bound. Layer. Meteorol.* 143 (3), 481–505. doi:10.1007/s10546-012-9706-9

Koračin, D., Businger, J. A., Dorman, C. E., and Lewis, J. M. (2005). Formation, evolution, and dissipation of coastal sea fog. *Bound. Layer. Meteorol.* 117, 447–478. doi:10.1007/s10546-005-2772-5

Koračin, D., Dorman, C. E., Lewis, J. M., Hudson, J. G., Wilcox, E. M., and Torregrosa, A. (2014). Marine fog: A review. *Atmos. Res.* 143, 142–175. doi:10.1016/j.atmosres.2013.12.012

Koračin, D., and Dorman, C. (2017). "Marine fog: Challenges and advancements in observations, modeling, and forecasting," in *Springer atmospheric sciences* (Switzerland: Springer International Publishing), 537.

Koračin, D., Lewis, J., Thompson, W. T., Dorman, C. E., and Businger, J. A. (2001). Transition of stratus into fog along the California coast: Observations and modeling. *J. Atmos. Sci.* 58 (13), 1714–1731. doi:10.1175/1520-0469(2001)058<1714:tosifa>2.0.co;2

Lee, T. F., Turk, F. J., and Richardson, K. (1997). Stratus and fog products Using*GOES-8–93.9-μ*m data. *Wea. Forecast.* 12, 664–677. doi:10.1175/1520-0434(1997)012<0664:safpug>2.0.co;2

Leipper, D. F. (1994). Fog on the U. S. West coast: A review. *Bull. Amer. Meteor. Soc.* 75 (2), 229–240. doi:10.1175/1520-0477(1994)075<0229:fotuwc>2.0.co;2

Lewis, J. M., Koračin, D., and Redmond, K. T. (2004). sea fog research in the United Kingdom and United States: A historical essay including outlook. *Bull. Amer. Meteor. Soc.* 85, 395–408. doi:10.1175/bams-85-3-395

Maritime Safety Administration of the Ministry of transport of China (2019). Analysis of water traffic safety situation in 2018. *China Marit. Saf.* 5, 32–33. doi:10.16831/j.cnki.issn1673-2278.2019.05.015

Petterssen, S. (1938). On the causes and the forecasting of the California fog. *Bull. Am. Meteorol. Soc.* 19, 49–55. doi:10.1175/1520-0477-19.2.49

Pilié, R. J., Mack, E. J., Rogers, C. W., Katz, U., and Kocmond, W. C. (1979). The formation of marine fog and the development of fog-stratus systems along the California coast. *J. Appl. Meteor.* 18, 1275–1286. doi:10.1175/1520-0450(1979)018<1275:tfomfa>2.0.co;2

Stein, A. F., Draxler, R. R., Rolph, G. D., Stunder, B. J. B., Cohen, M. D., and Ngan, F. (2015). NOAA's HYSPLIT atmospheric transport and dispersion modeling system. *Bull. Am. Meteorol. Soc.* 96, 2059–2077. doi:10.1175/bams-d-14-00110.1

Tachibana, Y., Iwamoto, K., Ogawa, H., Shiohara, M., Takeuchi, K., and Wakatsuchi, M. (2008). Observational study on atmospheric and oceanic boundary-layer structures accompanying the Okhotsk anticyclone under fog and non-fog conditions. *J. Meteorological Soc. Jpn.* 86, 753–771. doi:10.2151/jmsj.86.753

Tanimoto, Y., Xie, S.-P., Kai, K., Okajima, H., Tokinaga, H., Murayama, T., et al. (2009). Observations of marine atmospheric boundary layer transitions across the summer Kuroshio Extension. *J. Clim.* 22, 1360–1374. doi:10.1175/2008jcli2420.1

Tao, S. Y., and Chen, L. X. (1987). "A review of recent research on the east asian summer monsoon in China," in *Monsoon meteorology*. Editors C. P. Chang and T. N. Krishnamurti (Oxford: Oxford University Press), 60–92.

Taylor, G. I. (1917). The formation of fog and mist. *Q. J. R. Meteorol. Soc.* 43, 241–268. doi:10.1002/qj.49704318302

Tremant, M. (1987). "La prévision du brouillard en mer," in *Météorologie Maritime et Activities Océanographique Connexes* (Geneva, Switzerland: World Meteorological Organization).

Wang, B. H. (1985). *sea fog*. Beijing: China Ocean Press, 358pp.

Wang, Y., Gao, S., Fu, G., Sun, J., and Zhang, S. (2014). Assimilating MTSAT-derived humidity in nowcasting sea fog over the Yellow Sea. *Weather Forecast.* 29, 205–225. doi:10.1175/WAF-D-12-00123.1

Wilcox, E. M. (2017). "Multi-spectral remote sensing of sea fog with simultaneous passive infrared and microwave sensors," in *Marine fog: Challenges and advancements in observations, modeling, and forecasting*. Editors D. Koračin and C. Dorman (Switzerland: Springer International Publishing), 511–526.

Xian, J. H., Sun, D. S., Amoruso, S., Xu, W. J., and Wang, X. (2020). Parameter optimization of a visibility LiDAR for sea-fog early warnings. *Opt. Express* 28, 23829–23845. doi:10.1364/oe.395179

Yang, D., Ritchie, H., Desjardins, S., Pearson, G., MacAfee, A., and Gultepe, I. (2010). High-resolution GEM-LAM application in marine fog prediction: Evaluation and diagnosis. *Weather Forecast.* 25, 727–748. doi:10.1175/2009waf2222337.1

Yang, L., Liu, J. W., Ren, Z. P., Xie, S. P., Zhang, S. P., and Gao, S. H. (2018). Atmospheric conditions for advection-radiation fog over the Western Yellow Sea. *J. Geophys. Res. Atmos.* 123, 5455–5468. doi:10.1029/2017JD028088

Yang, Y., Hu, X. M., Gao, S. H., and Wang, Y. M. (2019). Sensitivity of WRF simulations with the YSU PBL scheme to the lowest model level height for a sea fog event over the Yellow Sea. *Atmos. Res.* 215, 253–267. doi:10.1016/j.atmosres.2018.09.004

Yuan, J. N., and Huang, J. (2011). An observational analysis and 3-dimensional numerical simulation of a sea fog event near the Pearl River Mouth in boreal spring. *Acta Meteorol. Sin.* 69 (5), 847–859. doi:10.11676/qxxb2011.074

Zhang, S. P., and Lewis, J. M. (2017). in *Chapter 6, synoptic processes,* marine fog: Challenges and Advancements in observations, modeling, and forecasting. Editors D. Koračin and C. E. Dorman (Cham: Springer International Publishing AG), 537pp. doi:10.1007/978-3-319-45229-6_6

Zhang, S. P., Xie, S. P., Liu, Q. L., Yang, Y. Q., Wang, X. G., and Ren, Z. P. (2009). Seasonal variations of Yellow Sea fog: Observations and mechanisms. *J. Clim.* 22, 6758–6772. doi:10.1175/2009jcli2806.1

Zhang, S. P., and Yi, L. (2013). A comprehensive dynamic threshold algorithm for daytime sea fog retrieval over the Chinese adjacent seas. *Pure Appl. Geophys.* 170, 1931–1944. doi:10.1007/s00024-013-0641-6

Zhou, B. B., and Du, J. (2010). Fog prediction from a multimodel mesoscale ensemble prediction system. *Weather Forecast.* 25, 303–322. doi:10.1175/2009waf2222289.1

frontiers | Frontiers in Earth Science

TYPE Original Research
PUBLISHED 30 September 2022
DOI 10.3389/feart.2022.968736

OPEN ACCESS

EDITED BY
Guihua Wang,
Fudan University, China

REVIEWED BY
Chenghai Wang,
Lanzhou University, China
Michelle Simoes Reboita,
Federal University of Itajubá, Brazil

*CORRESPONDENCE
Ping Lu,
luping@mail.tsinghua.edu.cn
Shuqin Zhang,
zhangshuqin1234@126.com

SPECIALTY SECTION
This article was submitted to Atmospheric Science, a section of the journal Frontiers in Earth Science

RECEIVED 14 June 2022
ACCEPTED 09 September 2022
PUBLISHED 30 September 2022

CITATION
Gao X, Lu P, Zhang S, Hu Y, Fu G, Sun X and Zhang Q (2022), A comparative study on initial developments between explosive and nonexplosive cyclones off the East Asian coast in winter. *Front. Earth Sci.* 10:968736. doi: 10.3389/feart.2022.968736

A comparative study on initial developments between explosive and nonexplosive cyclones off the East Asian coast in winter

Xiaoyu Gao[1,2], Ping Lu[2]*, Shuqin Zhang[3]*, Yang Hu[2], Gang Fu[4], Xiaoyan Sun[5] and Qiuyang Zhang[6]

[1]State Key Laboratory of Severe Weather, Chinese Academy of Meteorological Sciences, Beijing, China, [2]Ministry of Education Key Laboratory for Earth System Modeling, Department of Earth System Science and Joint Center for Global Change Studies, Tsinghua University, Beijing, China, [3]College of Oceanography and Meteorology, South China Sea Institute of Marine Meteorology, Key Laboratory of Climate Resources and Environment in Continental Shelf Sea and Deep Sea of Department of Education of Guangdong Province, Guangdong Ocean University, Zhanjiang, China, [4]Department of Marine Meteorology, College of Oceanic and Atmospheric Sciences, Ocean University of China, Qingdao, China, [5]Collaborative Innovation Center on Forecast and Evaluation of Meteorological Disasters/Key Laboratory of Meteorological Disasters of Ministry of Education, Nanjing University of Information Science and Technology, Nanjing, China, [6]College of Atmospheric Sciences, Chengdu University of Information Technology, Chengdu, China

Explosive cyclones (ECs) pose serious challenges for weather forecasting and significant threats to human life and property. In searching for the key points that make a cyclone go through explosive deepening off the East Asian coast, we present a comparative analysis of ECs and nonexplosive cyclones (or ordinary cyclones; OCs) using 10 years of ERA5 reanalysis data with high temporal and spatial resolutions. Their differences in synoptic backgrounds are shown, and mechanisms of the initial developments are compared quantitatively from the perspective of potential vorticity (PV). Among the identified 135 cyclones, 72 went through explosive growth and 37.5/36.1/20.8/5.6% of these ECs are ranked as weak/medium/strong/super ECs. ECs feature stronger low-level baroclinicity and higher PV than OCs. The decomposition of the local PV tendency shows the dominant role of the PV advection (with a correlation coefficient of 0.8). During the initial development, ECs have an average meridional temperature contrast 4 K larger than OCs within 20 latitudes at the low troposphere in the upstream, due to a stronger cold advection. The upstream colder air increases the horizontal temperature gradient and thus produces steeper isentropic surfaces inclining to the west. Since the PV intrusion is mainly along the isentropic surfaces, the increase in their slope significantly enhances the downward transport of PV from upper air. The importance of the horizontal gradient of potential temperature is further proved by numerical experiments with the Weather Research and Forecast (WRF) model on typical winter ECs. In sensitivity experiments, the low troposphere meridional temperature contrast decreasing by the average difference between ECs and OCs significantly decreases PV and stops the cyclones from explosive deepening. Despite the importance of diabatic processes in the deepening of mid-latitude cyclones emphasized by many

studies, this study shows that the PV intrusion dominated by cold air mass is the key cause of winter explosive cyclogenesis in this region.

KEYWORDS

explosive cyclone, East Asian coast, potential vorticity, baroclinic instability, diabatic heating

1 Introduction

Explosive cyclones (ECs), also known as "meteorological bombs" (Rice 1979), are extratropical cyclonic systems that go through rapid development. They pose serious threats to maritime traffic safety (Sanders and Gyakum 1980; Lamb 1991; Liberato et al., 2011; Liberato et al., 2013) so they need to be paid much attention. The landmark study by Sanders and Gyakum (1980) defined EC as the extratropical cyclone with a central sea level pressure fall of at least 24 hPa within 24 h when adjusted geostrophically to 60°N. The latitude in this definition was adjusted to 42.5°N by Roebber (1984) and to 45°N by Gyakum et al. (1989) and Zhang et al. (2017), considering that ECs frequently occur at mid-latitude. Explosive cyclogeneses within shorter terms were also considered based on datasets with higher temporal resolution. Yoshida and Asuma (2004), Zhang et al. (2017), and Fu et al. (2020) used a 12-h pressure change to define ECs.

Despite the statistical differences, many studies marked offshore East Asia as one of the most frequent areas for explosive cyclogenesis. Sanders and Gyakum (1980), Roebber (1984), and Lim and Simmonds (2002) indicated that ECs often occur over the Northwestern Pacific in the cold season, especially in winter. The statistical analysis based on five cold seasons by Yoshida and Asuma (2004) showed that the rapid deepening of ECs over the Northwestern Pacific usually occurred within 30–60°N, 130–170°E. As shown in Figure 1A, the East Asian coast locates between the largest continent and ocean on the Earth, Eurasia, and Pacific. The Kuroshio Current transports warm seawater northeastward, which produces a large amount of heat flux into the atmosphere. In winter, the mean temperature trough is upstream of the mean geopotential height (GPH) trough within the troposphere (Figures 1B–D), and the geostrophic wind frequently brings cold air from higher latitudes to this area. The large thermal contrast cooperating with mid-latitude westerly produces strong baroclinic instability and many ECs (e.g., Yoshida and Asuma 2004). A statistical analysis based on 30 years of surface reanalysis (Chen et al., 1992) indicated that the eastern Sea of Japan and the Northwestern Pacific are two favorable areas for explosive cyclogenesis off the East Asian coast, the latter of which is located near the warm Kuroshio Current. A recent study (Zhang et al., 2022) showed that ECs over the Sea of Japan have stronger baroclinicity and cyclonic vorticity, but weaker water vapor convergence and upper-level jet stream than those over the Kuroshio/Kuroshio Extension. Although many studies have worked on the statistical characteristics of ECs off the East Asian coast, none of them discussed the cyclones that do not go through explosive cyclogenesis. This might be an important supplement to the climatology of ECs since the comparison between ECs and ordinary cyclones (OCs) can give the dominant factors for explosive cyclogenesis in a certain region, which helps to predict the deepening rate of a cyclone during its initial development.

Multiple dynamic and thermodynamic processes are related to the rapid deepening of cyclones. The upper-level jet stream provides dynamic forcing on the left side of its exit with strong divergence, cyclonic vorticity advection, and lifting (Uccellini and Kocin 1987; Wash et al., 1988; Cammas and Ramond 1989; Nakamura 1993). The cyclonic vorticity advection at the mid-troposphere enhances the simultaneous surface deepening of cyclones downstream (Sanders 1986). A large gradient of sea surface temperature (SST) is also favorable for ECs (Kuwano-Yoshida and Asuma 2008; Taguchi et al., 2009; Kuwano-Yoshida and Enomoto 2013) since it can produce a large horizontal thermal contrast and thus a strong baroclinicity at the low level. Baroclinicity is an important factor that drives explosive cyclogenesis (Sanders 1986; Manobianco 1989; Wash et al., 1992). Iwao et al. (2012) analyzed the changes of ECs over the Northwestern Pacific in the past 30 years and showed that enhancement of low-level baroclinicity leads to the increase of ECs.

To consider both dynamic and thermodynamic factors, many studies analyzed the distributions and changes of potential vorticity (PV). Some case studies showed that upper-tropospheric PV is associated with the development of low-level cyclogenesis. There are three distinct positive PV anomalies in an extratropical cyclone: surface, lower-tropospheric, and upper-tropospheric, which are produced by the surface warm anomaly, low-tropospheric diabatic processes, and upper-level stratospheric intrusion, respectively. Downward transport of high PV in the stratosphere effectively enhances downstream surface cyclones (Bosart and Lin 1984; Reader and Moore 1995; Zhang and Fu 2018). Low-level PV anomaly coupled with upper-level PV disturbance may induce the rapid deepening of cyclones (Cordeira and Bosart, 2011). The diabatic process (i.e., the local PV generation) is notable, which is usually attributed to the latent heat release (LHR). The LHR can increase the potential temperature, leading to larger static stability and thus higher PV at lower levels (e.g., Davis et al., 1993; Ahmadi-Givi et al., 2004). Using an idealized simulation, Schemn and Wernli (2014) proved that the LHR strengthened PV anomaly, leading to

speedup of both the surface wind and upper-level jet stream. Heo et al. (2015) showed that the LHR in the warm conveyor belt produces nearly half of the low-level PV generation during the initial development of a spring EC. A climatological analysis by Binder et al. (2016) indicated that the impact of the LHR depends on its location. The warm conveyor belts that ascend near the cyclone centers lead to more intensified cyclogenesis than those which ascend along the cold front since their PV generation by the LHR has greater impact on the cyclone centers. On the other hand, for cyclones with warm seclusion (also called the Shapiro–Keyser cyclones; Shapiro and Keyser, 1990), PV near the cyclone centers is strongly affected by the structure of the cold conveyor belt and bent-back front. Hirata et al. (2015) found that the cold conveyor belt-induced LHR plays a dominant role in the low-level PV generation for an EC with warm seclusion.

Despite multiple studies on the impacts of (1) PV transport from upper air and (2) low-level LHR on the PV generation and the intensity of cyclones, what makes the ECs develop faster than OCs in their early stage was rarely analyzed, which is discussed in this study. For instance, LHR mainly acts in the mature stage of cyclones, but its importance during the initial developments is still unknown. On the other hand, most discussions about mechanisms were based on case studies. To better understand the key physical processes of explosive cyclogenesis, we need a quantified comparison of ECs *versus* OCs by a statistical analysis. Following this motivation, this study presents the statistical analysis of both OCs and ECs which occurred off the East Asian coast in 10 winters, and compares the synoptic backgrounds for their initial developments in the perspective of PV. We also design a series of numerical experiments to further prove the conclusions. The study is organized as follows. Section 2 describes the data and methods. Section 3 shows the systematic comparison of ECs vs. OCs based on ERA5 reanalysis data, including cyclone intensity, low-level baroclinicity, and decomposition of local PV tendency. Section 4 discusses the design and results of modeling experiments. A summary is given in Section 5.

2 Data and methods

2.1 Data

This study uses the fifth generation of the European Centre for Medium-Range Weather Forecasts (ECMWF) Reanalysis (ERA5; available at https://cds.climate.copernicus.eu) to identify the cyclones and analyze their dynamic and thermal-dynamic structures. The dataset has 1-h temporal resolution, 0.25°×0.25° horizontal resolution, and 37 vertical levels. The high temporal and spatial resolutions help to analyze the changes in the fine structures of cyclones during their initial developments. The data cover 10 winters, including December, January, and February from 2010 to 2019. The ERA5 reanalysis data are also used to generate the initial and boundary conditions for the Weather Research and Forecast (WRF) model.

The satellite cloud images retrieved from visible channels of the satellite of Himawari-8 (available at https://himawari8.nict.go.jp/) are used to show the development of clouds around the ECs, as discussed in Section 4.

2.2 Algorithms for statistical analyses

Using the 0.25°×0.25° dataset, we attempted to identify all the winter cyclones that occurred over East Asia (20–50 °N, 105–155 °E, as shown in Figure 1A) during the 10 years from 2010 to 2019. The detection and tracking methods follow Hart (2003) and have been modified according to the temporal and spatial resolution of the ERA5 dataset.

To detect cyclones at each moment, the distribution of sea level pressure (SLP) is shown by contours starting at 900 hPa with an interval of 2.5 hPa. A cyclone is considered to exist when there is at least one close isobaric line within a circular area with a radius of 800 km and the local minimum of SLP is less than 1,020 hPa. The location of the minimum SLP is considered the cyclone center.

To track cyclones, the nearest two cyclones with a 1-h interval are considered the same cyclone when their distance is less than 500 km. Such a distance threshold ensures that a wide but shallow cyclone is not falsely identified as two or more cyclones when SLP around its center rapidly decreases. Finally, the cyclones whose appearances over East Asia lasted for less than 24 h are dismissed, which include those with a short lifetime as well as those that move away from this region.

The priority of this method is to find as many cyclones as possible with a low computational cost when dealing with such long-term data with high resolution. It gives reasonable results, and small changes in the thresholds do not affect the conclusions of this study.

The following definition of ECs is used to calculate the deepening rate (DR) of central SLP of the cyclone (e.g., Yoshida and Asuma 2004; Zhang et al., 2017; Fu et al., 2020):

$$\mathrm{DR}_{\delta t} = \frac{p_{t-\delta t/2} - p_{t+\delta t/2}}{\delta t} \cdot \frac{\sin \varphi_0}{\sin \frac{\varphi_{t-\delta t/2} + \varphi_{t+\delta t/2}}{2}}, \quad (1)$$

where δt is the time interval, p is the central SLP, φ is the latitude, and φ_0 is the standard latitude.

Following Zhang et al. (2017), φ_0 is set to be 45°. An EC is defined as a cyclone with a 12-h deepening rate (DR_{12}) ≥ 1 hPa/h. ECs can be classified into four categories according to DR_{12}: weak ($1.00 \le \mathrm{DR}_{12} \le 1.29$ hPa/h), moderate ($1.30 \le \mathrm{DR}_{12} \le 1.69$ hPa/h), strong ($1.70 \le \mathrm{DR}_{12} \le 2.29$ hPa/h), and super ($\mathrm{DR}_{12} \ge 2.30$ hPa/h) ECs.

We also calculate the 1-h deepening rate (DR_1) to analyze the short-term variation. Synthetic analysis is used to show the

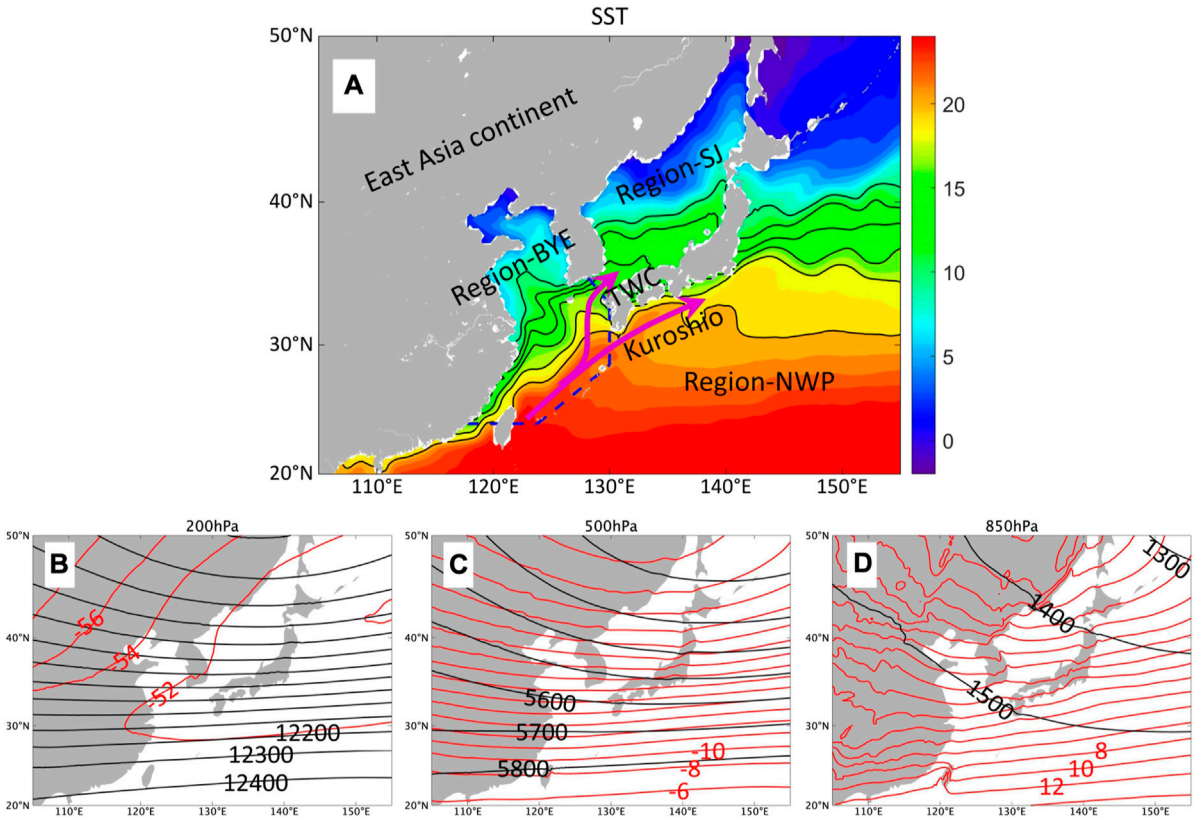

FIGURE 1
SST **(A)** and synoptic features at 200 hPa **(B)**, 500 hPa **(C)**, and 850 hPa **(D)** averaged in winters during 2010–2019. Contours in **(A)** show the SST within 10–20°C with an interval of 2°C. Blue dashed lines divide the ocean into three regions: Region-BYE (including the Bohai Sea, the Yellow Sea, and the East China Sea), Region-SJ (the Sea of Japan), and Region-NWP (the Northwestern Pacific). "TWC" denotes the Tsushima Warm Current. Black and red contours in **(B–D)** represent GPH (gpm) and air temperature (°C).

characteristics of ECs and OCs. For a category of cyclones, the distribution of each variable is averaged among all cases in relative geographic coordinates within a 20°×20° box around the centers. To eliminate the differences in cyclones due to their different latitudes, for each cyclone, we analyze the anomaly values of the potential temperature and GPH instead of their true values. An anomaly value is defined as the difference between the true value at any grid point and its mean value of the 20°×20° box at the same pressure level.

We measure the low-level baroclinic instability by using the Eady growth rate (EGR; Hoskins and Valdes, 1990), which is defined by

$$EGR = 0.31 f \left| \frac{\partial \vec{v}}{\partial z} \right| N^{-1}, \tag{2}$$

where f is the Coriolis parameter, $\vec{v}$ is the horizontal wind velocity, z is the GPH, g is the gravitational acceleration, and N is the Brunt–Väisälä frequency. The definition of the EGR is consistent with the concept that strong thermal contrast and static instability produce strong baroclinicity. Following Seiler and Zwiers (2016), the EGR is calculated by using daily values between 850 and 700 hPa.

The lapse rate of potential temperature (Γ) is used to analyze the static stability. It is calculated by

$$\Gamma = -\frac{\partial \theta}{\partial p}, \tag{3}$$

where θ is the potential temperature and p is the air pressure. The central difference method is used in computation. Γ at each level is determined by θ and p at the nearest upper and lower levels.

The Ertel PV (Ertel 1942) is calculated by

$$\mathrm{PV} = g\Gamma(\zeta_\theta + f), \tag{4}$$

where ζ_θ is the relative vorticity on the isentropic surface. PV is conserved following the adiabatic motion in the absence of friction and thus provides the balance among ζ_θ (i.e., the strength of the cyclone), f (i.e., the geostrophic vorticity), and static stability.

The local PV tendency ($\frac{\partial PV}{\partial t}$) can be decomposed into three terms by considering the diabatic PV generation while neglecting the surface friction effect:

$$\frac{\partial PV}{\partial t} = -\vec{v} \cdot \nabla PV - \omega \frac{\partial PV}{\partial p} + J_{PV}, \tag{5}$$

where ω is the vertical motion in the pressure coordinate and J_{pv} is the diabatic variation of PV. The three terms on the right-hand side are the horizontal advection of the PV term, the vertical transport of the PV term, and the diabatic term. Considering a volume around the cyclone center with x ranging from x_1 to x_2, y ranging from y_1 to y_2, and p ranging from p_1 to p_2 ($p_1<p_2$), the mean values of the PV tendency term, horizontal advection, and vertical transport term within this volume can be calculated as follows:

$$\frac{\partial PV}{\partial t} = \frac{1}{g\delta m}\int_{p_1}^{p_2}\int_{y_1}^{y_2}\int_{x_1}^{x_2}\frac{PV(x,y,p,t+\delta t) - PV(x,y,p,t-\delta t)}{2\delta t}dxdydp, \tag{6}$$

$$-\vec{v}\cdot\nabla PV = \frac{1}{g\delta m}\left\{\int_{p_1}^{p_2}\int_{y_1}^{y_2}[u(x_1,y,p,t)PV(x_1,y,p,t) - u(x_2,y,p,t)PV(x_2,y,p,t)]dydp + \int_{p_1}^{p_2}\int_{x_1}^{x_2}[v(x,y_1,p,t)PV(x,y_1,p,t) - v(x,y_2,p,t)PV(x,y_2,p,t)]dxdp\right\}, \tag{7}$$

$$-\omega\frac{\partial PV}{\partial p} = \frac{1}{g\delta m}\int_{y_1}^{y_2}\int_{x_1}^{x_2}[\omega(x,y,p_1,t)PV(x,y,p_1,t) - \omega(x,y,p_2,t)PV(x,y,p_2,t)]dxdy, \tag{8}$$

where δt is the time interval, and δm is the air mass within this volume, which is calculated by

$$\delta m = \frac{1}{g}\int_{p_1}^{p_2}\int_{y_1}^{y_2}\int_{x_1}^{x_2}dxdydp. \tag{9}$$

After the three terms are identified by Eqs 6–8, J_{pv} can be approximated by the residual of Eq. 5.

3 Statistical analysis

A total of 135 cyclones are found to stay over East Asia for at least 24 h, more than a half of which went through explosive cyclogenesis. Most of them were initiated over sea, and their frequency of occurrences is quite even among the 10 years. Their intensities, spatiotemporal distribution, synoptic background, and PV structures are compared, and the mechanisms for their differences are discussed.

3.1 Intensity

As shown in Figure 2A, 72 of the 135 cyclones are ECs, among which 37.5/36.1/20.8/5.6% are categorized as weak/medium/strong/super ECs. This suggests a higher proportion for stronger ECs than that proposed by Zhang et al. (2017) with the same methods, which gives a percentage of 65.1/29.1/3.9/1.9% over the Sea of Japan and 45.6/33.2/18.6/2.6% over the Northwestern Pacific. Zhang et al. (2017) analyzed ECs from October to April during 2000–2015 by using 1°×1° reanalysis data. Cooler months for the cyclones in this study are more beneficial to stronger cyclogenesis, and high-resolution reanalysis data could increase the climatological frequency of ECs.

Except for the super ECs, average central SLPs for other categories are quite similar at the initial moment (Figure 2B). Stronger ECs have a greater deepening rate for the whole time, and their explosive growths start earlier. It is notable that the maximum wind speed varies according to the central SLP (Figures 2B,C), but a greater deepening rate is not a guarantee for stronger wind. Before 20 h, the strong ECs have an average wind weaker than medium ECs (Figure 2C). In awareness of this fact, Fu et al. (2020) chose a wind speed of 17.2 m s^{-1} as the threshold value in the definition of ECs since the major threat of cyclones to shipping safety is due to strong winds.

3.2 Spatiotemporal distribution

The cyclone tracks are dense to the east of 120°E (Figure 3A). The mean 24-h tracks for OCs and different ECs distribute around Japan Island, and are quite close to the areas of the Kuroshio and Tsushima Warm Current (Figure 1A). Cyclones with greater deepening rates have a further south average initial location, indicating that explosive cyclogenesis might be related to deeper GPH trough in the mid-troposphere, higher SST, or more adequate water vapor.

As shown in Figures 3C,D, most ECs were initiated over sea, and the frequency of marine explosive cyclogeneses (i.e., the initial explosive deepening) is as high as 85%. More ECs started to explosively deepen in Region-SJ/NWP than in Region-BYE, which is probably related to the warm currents in these regions. A total of 19 ECs went through explosive deepening at their initial moments, 7/5/7 of which existed in Region-BYE/SJ/NWP.

Each year, 10 or more cyclones occurred in East Asia (Figure 3E). 2015 met both the most cyclones (16) and most ECs (10). It is to be noted that 2015 is the warmest year, and its highest frequency of ECs agrees with the conclusion drawn by Iwao et al. (2012) that global warming enhances extratropical cyclones with the increase in both low-level baroclinicity and humidity. As shown in Figure 3F, 46/37/52 cyclones occurred in December/January/February, 28/21/23 of which are ECs. Cyclones are more likely to go through explosive deepening in December and January than in February.

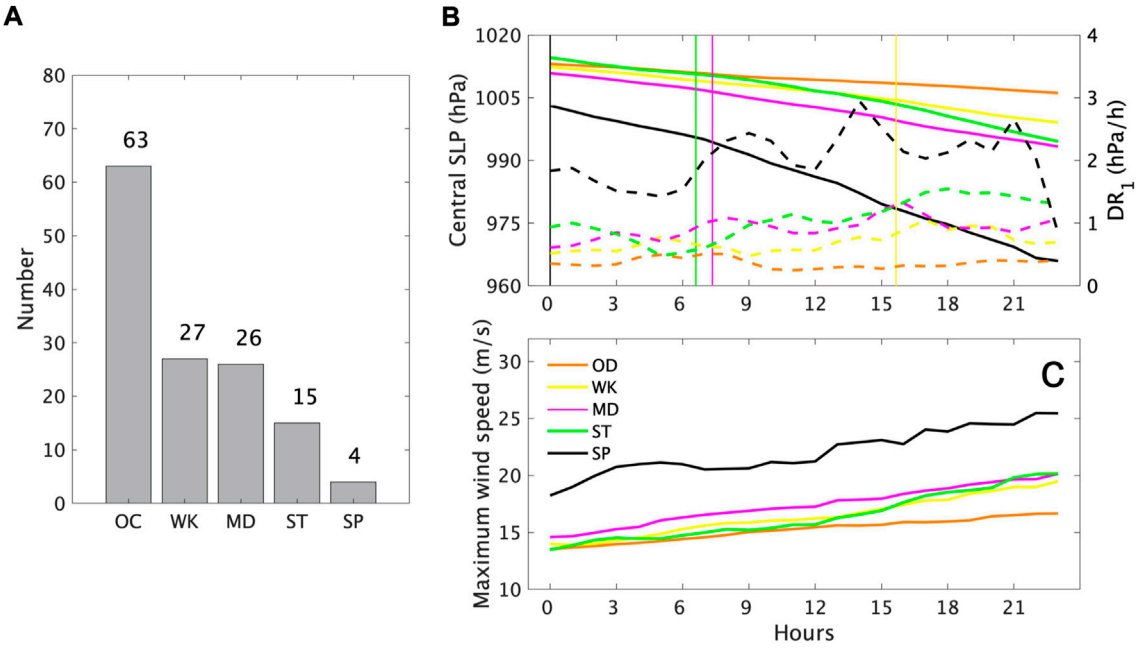

FIGURE 2
Numbers of different categories of cyclones **(A)**, 24-h variation of their central SLPs **(B)**, and maximum wind speed **(C)**. Solid and dashed curves in **(B)** represent the central SLPs and 1-h deepening rate, respectively, and vertical lines show the beginning of explosive growth. "WK," "MD," "ST," and "SP" denote weak, medium, strong, and super ECs, respectively.

3.3 Synoptic background

The synoptic background for ECs has stronger low-level baroclinicity than that for OCs. As shown in Figure 4, at the initial time, OCs usually have an upper-level GPH trough upstream, and the geostrophic wind is almost parallel to isotherms at 500 hPa. The thermodynamic structure (Figures 4A–C) shows that the strong cold/warm advections in the west/east of the cyclone centers mainly exist within the low troposphere. Horizontal thermal contrast is larger for ECs (Figures 4D–F), and the maximum difference is located about 6-degree north of the centers. GPH anomalies are lower around centers and higher in the east and west at 850 hPa and 925 hPa, respectively, indicating deeper troughs and stronger temperature advections within the low troposphere. The typical characteristics of cyclones also include upper-level jet streams with a maximum speed of about 50 m s^{-1} (Figure 4G) and abundant water vapor along the warm conveyor belt (Figure 4H). For ECs, the wind speed is larger in upper-level jet streams (Figure 4J), and precipitable water is more in the south (Figure 4K). Meanwhile, the SST for ECs in Region-BYE and Region-SJ is ~0.5°C higher than that for OCs (Figures 4I, L), which also helps to enhance the cyclones.

The stronger temperature advection and horizontal thermal contrast in the low troposphere for ECs lead to stronger low-level baroclinicity. As shown in Figure 5A, the low troposphere has much weaker static stability over sea than that over land. The average Γ decreases from southwest to northeast. It is above 7×10^{-4} K Pa^{-1} over the East China Sea and most of the Yellow Sea, but below 6×10^{-4} K Pa^{-1} over the Sea of Japan and the Northwestern Pacific Ocean where the average EGR is above 1 d^{-1}. The weak static stability can be attributed to the warm sea surface, which transports heat into the low troposphere and makes the potential temperature decrease slower according to the air pressure. Both the weak static stability and the strong baroclinicity are beneficial to cyclogenesis, which is an explanation for most winter cyclones going through these regions (Figure 3A). During the initial development of OCs, a large EGR exists within ±4 latitudes around centers (Figure 5B) and is more widely distributed in the east (since the warm front zone is usually wider than the cold front zone), while Γ is smaller around the center (since the warm tongue around the center enhances with pressure as shown in Figures 4A–C). Both variables are larger for ECs (Figure 5C). With stronger cold advection, the EGR increases by >0.2 d^{-1} in the southwest, and its maximum value near the cold front is pushed southward. Γ increases significantly in the same area, and the maximum increment exists in the south of the west boundary, leading to a larger difference in static stability between the center and the west for ECs. This is quite important for explosive cyclogenesis, which is discussed in Subsection 3.5.

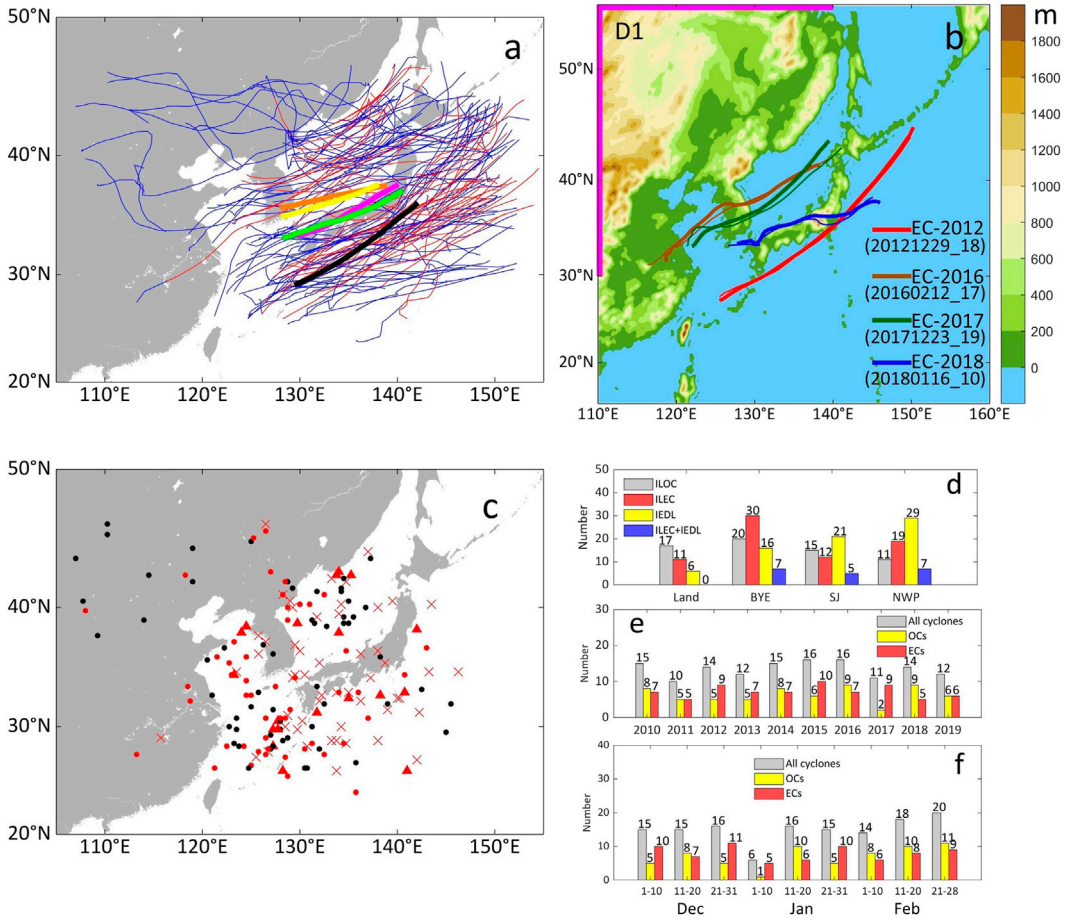

FIGURE 3
Distribution of cyclones over East Asia in 10 winters. Thin lines in **(A)** show the tracks for 135 cyclones, with red parts denoting where cyclones were explosively deepened. Thick orange, yellow, purple, green, and black lines denote the average 24-h tracks for OCs, weak, medium, strong, and super ECs, respectively. Black and red dots in **(C)** show the initial locations for OCs and ECs (denoted by ILOC and ILEC). Red crosses show the initial explosive deepening locations for ECs (denoted by IEDL), and red triangles show the initial locations for ECs which went through explosive deepening from the beginning (denoted by ILEC+IEDL). Bars in **(D)** denote the numbers of the four kinds of locations over land, Region-BYE, Region-SJ, and Region-NWP (located in Figure 1A). Bars in **(E)** and **(F)** denote the numbers of cyclones in different years and different dates, respectively. The model domain for WRF modeling discussed in Section 4 is shown in **(B)**. Shadings denote the terrain. Thick purple lines locate the boundaries where the temperature is modified for Exp-MT. Other thick lines show the tracks for the four ECs, thin lines show their tracks simulated by Exp-Ctrl, and the numbers show the initial moments of the four ECs in the form of yyyymmdd_hh in UTC.

3.4 PV budget

The enhancement of low-level PV plays an important role in cyclogenesis (Campa and Wernli, 2012). It usually comes from two mechanisms: PV intrusion from the upper air and PV production by diabatic heating. The former is done by a downdraft in the upstream of the westerly, and the latter involves the changes in the thermal structure by multiple processes. The warm sea surface heats the low troposphere and enhances the near-surface PV. The condensation within ascending motion releases latent heat and enhances the lower-level PV (while decreasing the upper-level PV). The evaporation of precipitation has the opposite effect. The diabatic term in the PV budget only focuses on their composite effects.

As shown in Figure 6, there is a PV intrusion in the west of cyclones, which is stronger for ECs than for OCs. For OCs, the initial PV is less than 1 PVU (1 PVU=1×10^{-6} m^2 s^{-1} K kg^{-1}) around the center and increases to over 1.2 PVU within 12 h (Figures 6A–C). A high PV tongue extends downward in the west, making the mid-troposphere have much higher PV in the west than in the east. When the cold air mass from the Eurasian continent meets the warm air mass above the ocean, a baroclinic atmospheric background is created. The isentropic surfaces incline to the west. Since adiabatic movements are parallel to the isentropic surfaces, the westerlies tend to transport high PV

10.3389/feart.2022.968736

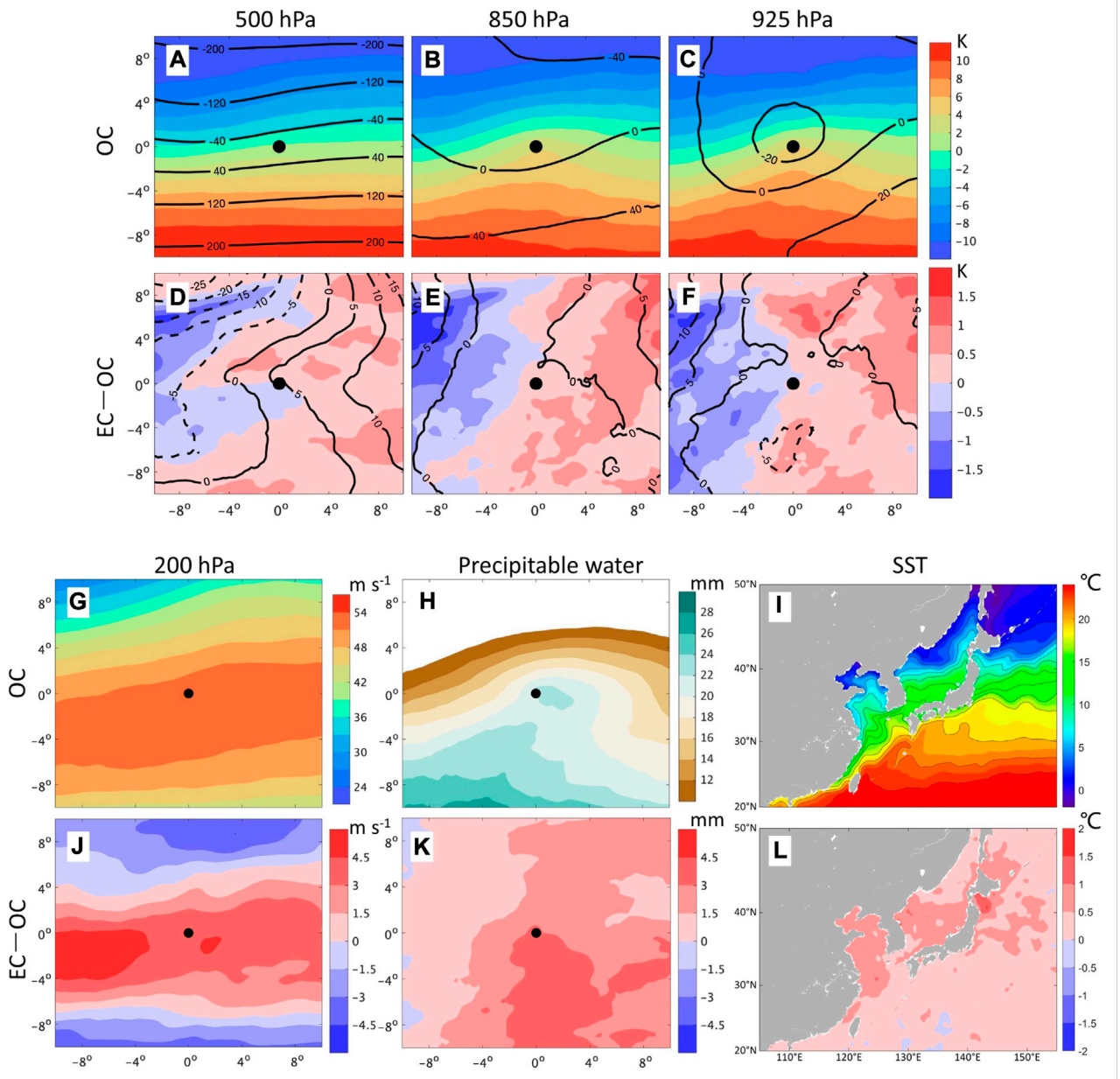

FIGURE 4
Comparison of initial conditions for OCs and ECs. The first row shows average potential temperature anomaly (shadings) and GPH anomaly (gpm; contours) for OCs at 500 **(A)**, 850 **(B)**, and 925 **(C)** hPa. The second row shows the difference in average potential temperature anomaly (shadings) and GPH anomaly (gpm; contours) between ECs and OCs at 500 **(D)**, 850 **(E)**, and 925 **(F)** hPa. The third row shows the average 200 hPa wind speed **(G)** and precipitable water **(H)** for OCs. The fourth row shows the difference in average 200 hPa wind speed **(I)** and precipitable water **(J)** between ECs and OCs. Black dots locate the cyclone centers.

from the upper air down to the low troposphere. The enhancement of local PV (i.e., horizontal advection and vertical transport of the PV term, diabatic PV production) and the weakening of static stability along the motion from upstream to the cyclone center (Figure 5B) can increase the local relative vorticity, which is increased by ~50% around the center within 12 h.

For ECs, the PV around centers is much higher (Figures 6D–F) and increases more rapidly. At the initial moment (0 h), a stripe where PV is over 10% higher for ECs starts over the center and inclines to the west (Figure 6D). Then the difference grows larger, and PV within 300–850 hPa is significantly higher for ECs in the west at 12 h. The relative vorticity difference has a pattern quite similar to the PV difference within the whole troposphere, indicating

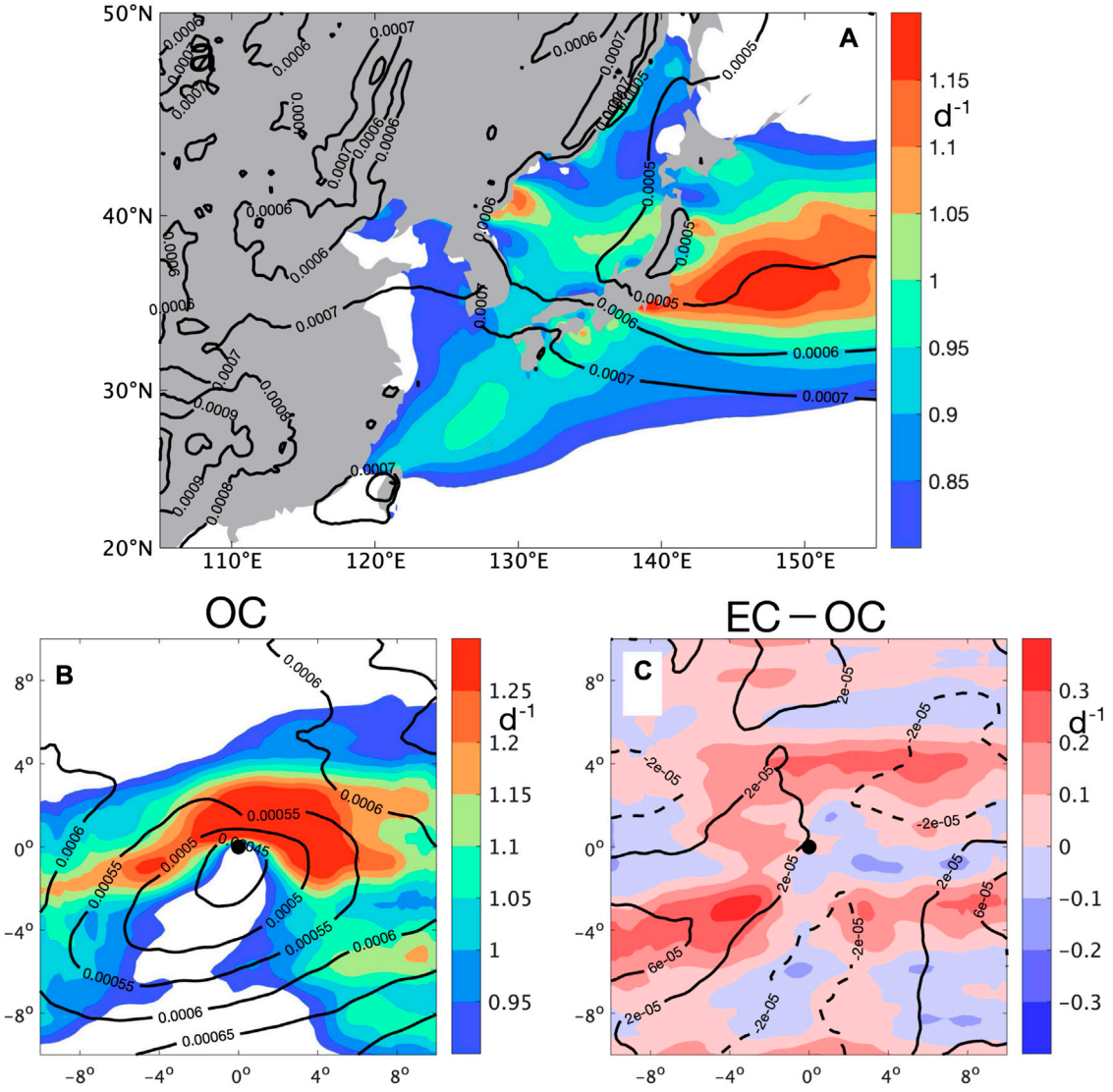

FIGURE 5
Low-level baroclinicity and static stability over East Asia **(A)** and around the OC center **(B)**, and the difference between ECs and OCs **(C)**. Shadings denote EGR, and contours denote Γ (unit: K Pa^{-1}). Solid/dashed lines in **(C)** denote average Γ for ECs larger/smaller than OCs. Both variables are retrieved from "daily values" between 850 and 700 hPa. For **(A)**, "daily values" are the potential temperatures and wind velocities averaged during 00–23 UTC of each day, and EGR and Γ are averaged within 10 winters. For **(B–C)**, "daily values" are averaged in relative geographic coordinates within the 20°×20° box around the center during the first 24 h for each cyclone, and EGR and Γ are averaged among all OCs or ECs.

the close relationship between PV and the dynamic strength of cyclones. It is to be noted that for both categories of cyclones, PV around the center is higher than low-troposphere PV in the west at the initial time, indicating that PV advection around the center is negative, and PV generation by a diabatic process is an important term in cyclogenesis, which is consistent with former studies (e.g., Schemn and Wernli, 2014; Heo et al., 2015).

The local PV tendency is analyzed to further discuss the origin of PV transport. The four terms in Eq. 5 are calculated in a quasi-cubic box within 500–950 hPa over the 20°×20° box around the center for each cyclone by Eqs 6–9. As shown in Figure 7, the PV advection dominates the enhancement of PV. During the first 3 h, PV tendencies are similar for both categories, but the adiabatic change (defined as the summation of advection and vertical transport) for ECs is larger than that for OCs (Figure 7A), with a larger positive advection term and a larger negative vertical transport term (Figure 7B). The advection term keeps increasing for ECs and

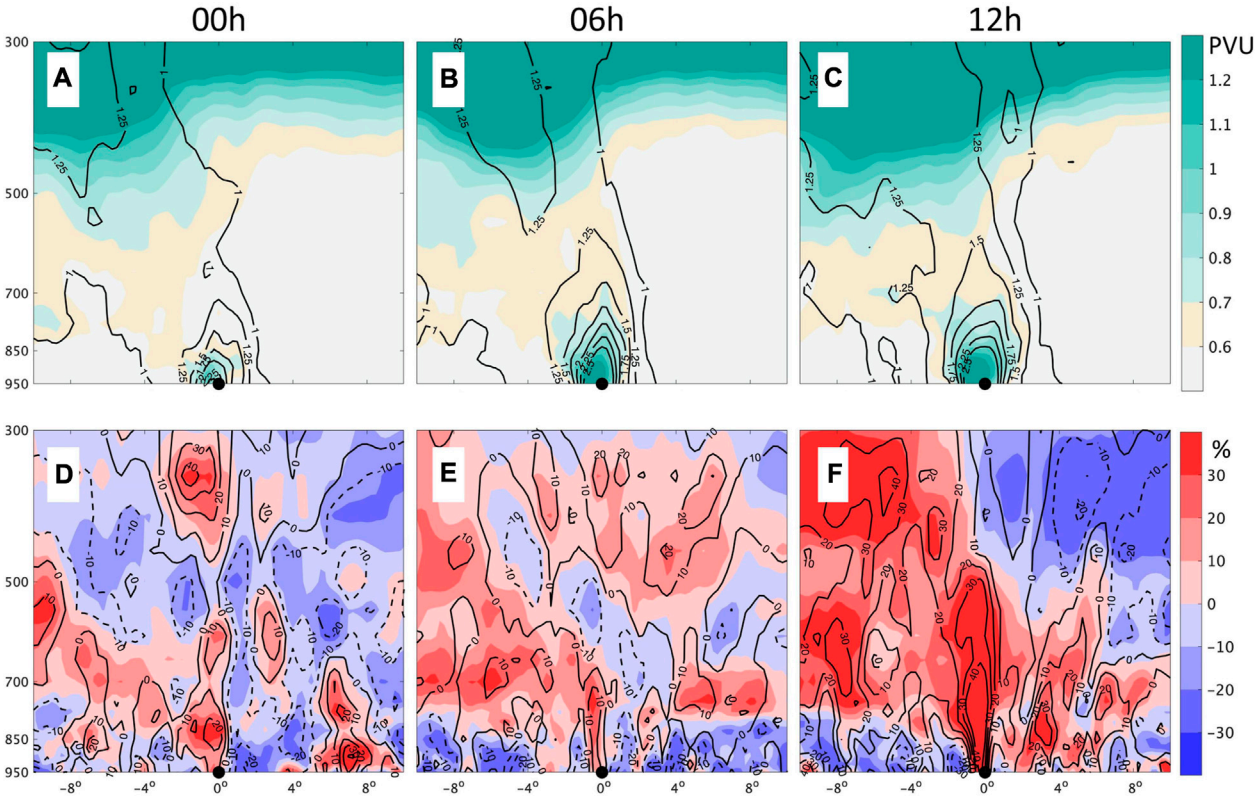

FIGURE 6
Zonal cross sections of the average PV and relative vorticity going through the cyclone center (denoted by the black dots) during initial development. The first row shows the average PV (shadings) and relative vorticity (contours; unit: 10^{-4} s^{-1}) for OCs. The second row shows the difference in PV (shadings) and relative vorticity (contours; unit: %) between ECs and OCs, with solid/dashed lines denoting relative vorticity for ECs larger/smaller than OCs. The left/middle/right column shows the situation 0/6/12-h after the cyclones are identified.

varies little for OCs in the next 18 h (Figure 7B), accompanied by the increasing difference in PV tendencies (Figure 7A). At 21 h, both the PV tendency and advection term for ECs are ~4 PVU/h larger than those for OCs. The vertical transport term varies with an opposite trend to the advection term, indicating that higher PV is converged into the box by horizontal airflow and is diverged by lifting. The net diabatic term over the column is negative for OCs as diabatic PV erosion above the maximum heating level may suppress the diabatic PV production below. The net diabatic PV is enhanced within ECs due to their stronger LHR. However, the difference is not significant before 10 h (Figure 7B) when the total PV tendency for ECs is already 1 PVU/h larger than that for OCs (Figure 7A), indicating that the enhancement of diabatic PV production is a result rather than the cause of the initial enhancement of PV. The correlation between PV advection and PV tendency is >0.8 (Figure 7C), which is much stronger than others (Figures 7D,E), further proving the crucial role of PV advection.

3.5 Structure of PV intrusion

What dominates the enhancement of the PV convergence for ECs? According to Eq. 7, within a quasi-cubic box, it can be decomposed into four terms, which denote the horizontal transport of PV across the box's four lateral boundaries. As shown in Figure 8, the most significant difference in PV transport exists at the west boundary, where northwesterly brings higher PV into the box for ECs. It is also evident at the north boundary (Figure 8D), which offsets part of the enhancement of PV input at the west boundary since a positive difference in vPV here means stronger PV output from the box. Thus, the stronger input of PV in the west of cyclones is the key cause for the higher PV for the ECs. At the north boundary, the vPV difference has a similar pattern to the v difference (Figure 8D), indicating that the stronger output of PV here is due to stronger wind. Meanwhile, the zonal and meridional winds at the west boundary for ECs are only 1–2 m s^{-1} stronger than those for OCs, and the difference in uPV is weakly related to wind speed (Figure 8A). It is because the ECs already have higher PV at the

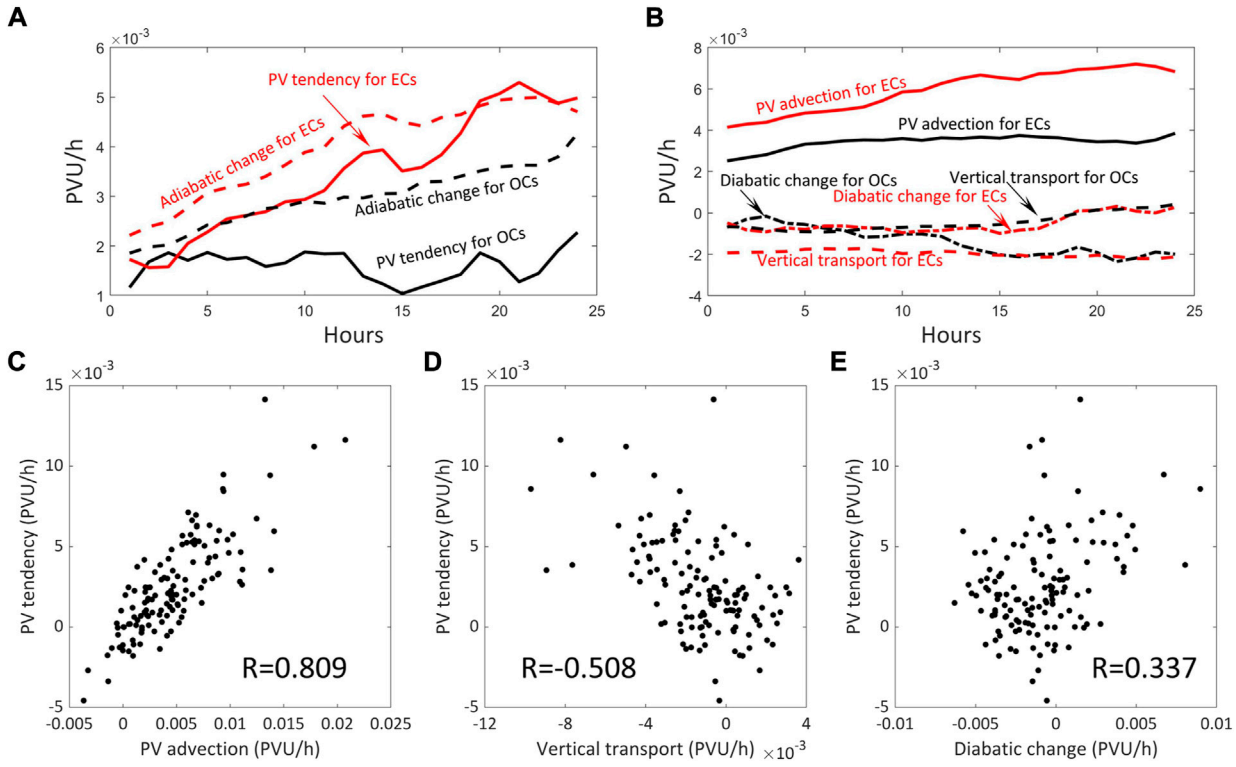

FIGURE 7
Contribution of PV advection, vertical transport, and diabatic change to PV tendency. The upper row shows the variation of each term during initial development averaged among OCs (black lines) and ECs (red lines). The lower row shows the distribution of PV tendency and PV advection **(C)**/vertical transport **(D)**/diabatic change **(E)** averaged during the initial 24 h for each cyclone, with R denoting the correlation coefficient.

west boundary during the initial development, which is produced by vertical PV intrusion rather than horizontal transport.

The difference in thermal structures gives an explanation for the stronger PV intrusion. As shown in Figures 8E,F, the horizontal gradient of potential temperature in the west of ECs is much stronger. At the initial moment, the meridional temperature contrast is ~3 K larger within 20 latitudes (Figure 8E), which is further enhanced later. During the next 24 h, colder air mass invades the lower levels while moving southward. The average temperature contrast for ECs is ~4 K larger than that for OCs (Figure 8F), and the difference of >1.5 K is significant in statistics (which can pass the *t*-test with confidence of 0.95). Figure 8F also shows a belt where the meridional gradient of the potential temperature (i.e., $\partial\theta/\partial y$) for ECs is much larger than that for OCs, and the largest *u*PV difference at each level just lies in the belt. PV transported eastwardly is probably related to the thermal contrast. Since a larger horizontal gradient of the potential temperature reflects a greater slope of the isentropic surface ($\nabla_H\theta \propto \nabla_\theta p$), adiabatic movement along the isentropic surface has a larger vertical component for ECs than for OCs. Higher PV is transported downward adiabatically along isentropic surfaces.

Figure 9 shows more details of the PV intrusion during initial development by comparing PV at zonal cross-sectors at 0°, −3°, and −6° (as shown in Figure 8E). As shown in Figures 9aA–aG, cA–cG, eA–eG, positive differences in both PV and the zonal gradient of the potential temperature (i.e., $\partial\theta/\partial x$) mainly exist in the west of cyclone centers. Again, there is a close relationship between PV and thermal contrast. The areas where $\partial\theta/\partial x$ for ECs is over 4×10–6 Km^{-1} larger than that for OCs exist higher/lower at the north/south section, and the stronger PV intrusion also exists higher/lower (as shown by the green vectors in Figures 9aA, cA, eA). At the initial moment, the difference in wind speed is quite small (Figures 9bA, dA, fA), especially in upper air, considering the typical wind speed here is over 20 m s^{-1}. It grows rapidly with the increase in PV (Figures 9bA, bG, dA–dG, fA–fG), which is a result of the enhancement of ECs. Moreover, during the first 24 h, the correlation coefficient between the zonal transport of PV (i.e., *u*PV) and the thermal contrast (i.e., $|\nabla_H\theta|$) at the west boundary is as high as 0.772, while that between *u*PV and zonal/meridional wind speed is only 0.434/0.112. This further proves the importance of the upstream thermal contrast.

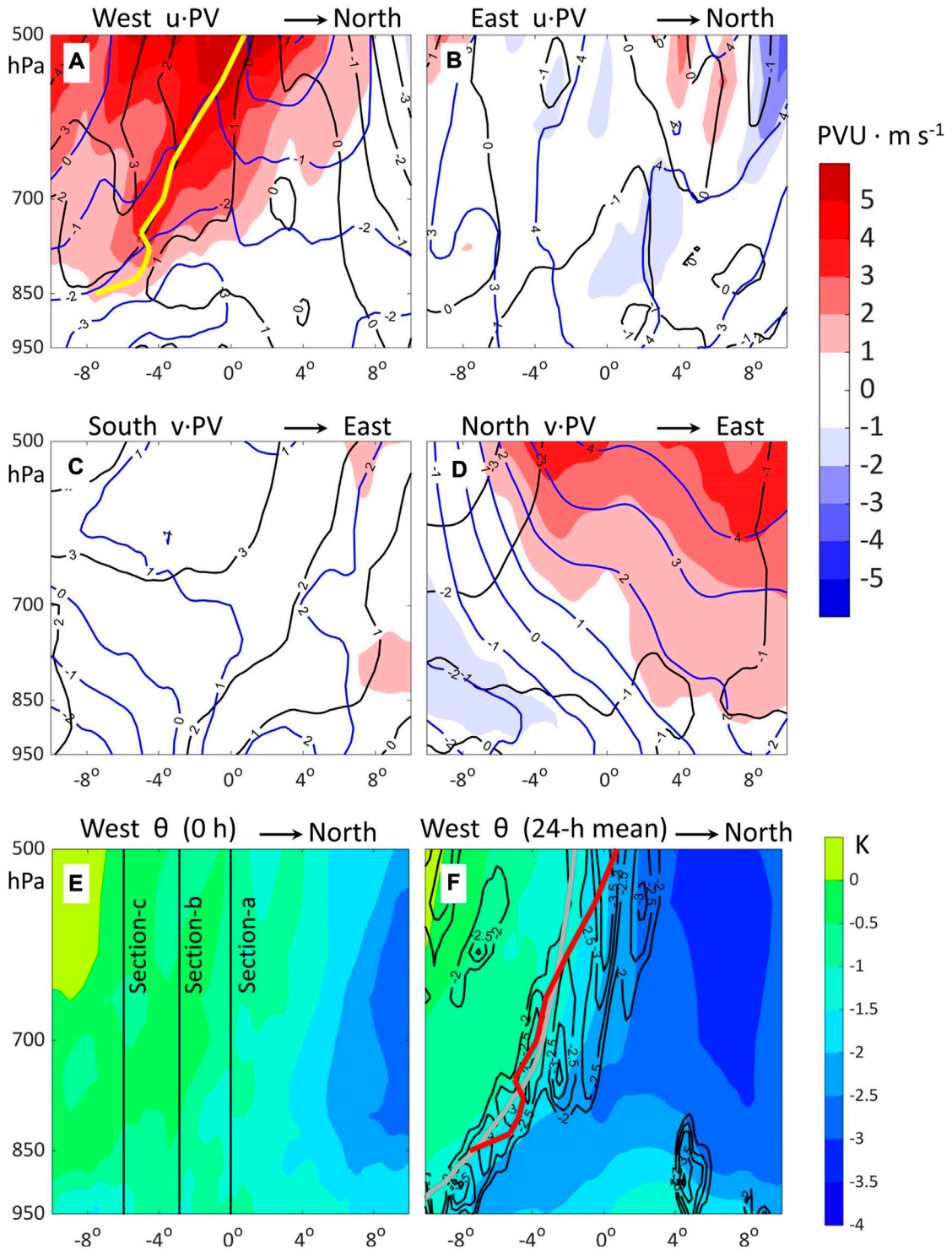

FIGURE 8
Difference in the 24-h averaged wind speed and PV transport between ECs and OCs at the west **(A)**, east **(B)**, south **(C)**, and north **(D)** boundary, as well as difference in thermal structures at the west boundary at initial time **(E)** and averaged during the first 24 h **(F)**. In **(A)** and **(B)**, shadings denote the difference in the product of the zonal wind speed and PV, while in **(C)** and **(D)**, shadings denote the difference in the product of the meridional wind speed and PV. Black/blue contours denote the difference in the zonal/meridional wind speed (unit: m s^{-1}). In **(E)** and **(F)**, shadings denote potential temperature, and contours in **(F)** denote its meridional gradient (i.e., $\frac{\partial \theta}{\partial y}$; unit: 10^{-6} K m^{-1}) with values >-2 not given; the difference to the north of the thick gray line in **(F)** has passed the significance test (*t*-test) with a confidence of 0.95. The thick yellow line in **(A)** and red line in **(F)** locate the maximum of uPV at each level. Black lines in **(E)** locate the three zonal cross-sections in Figure 9.

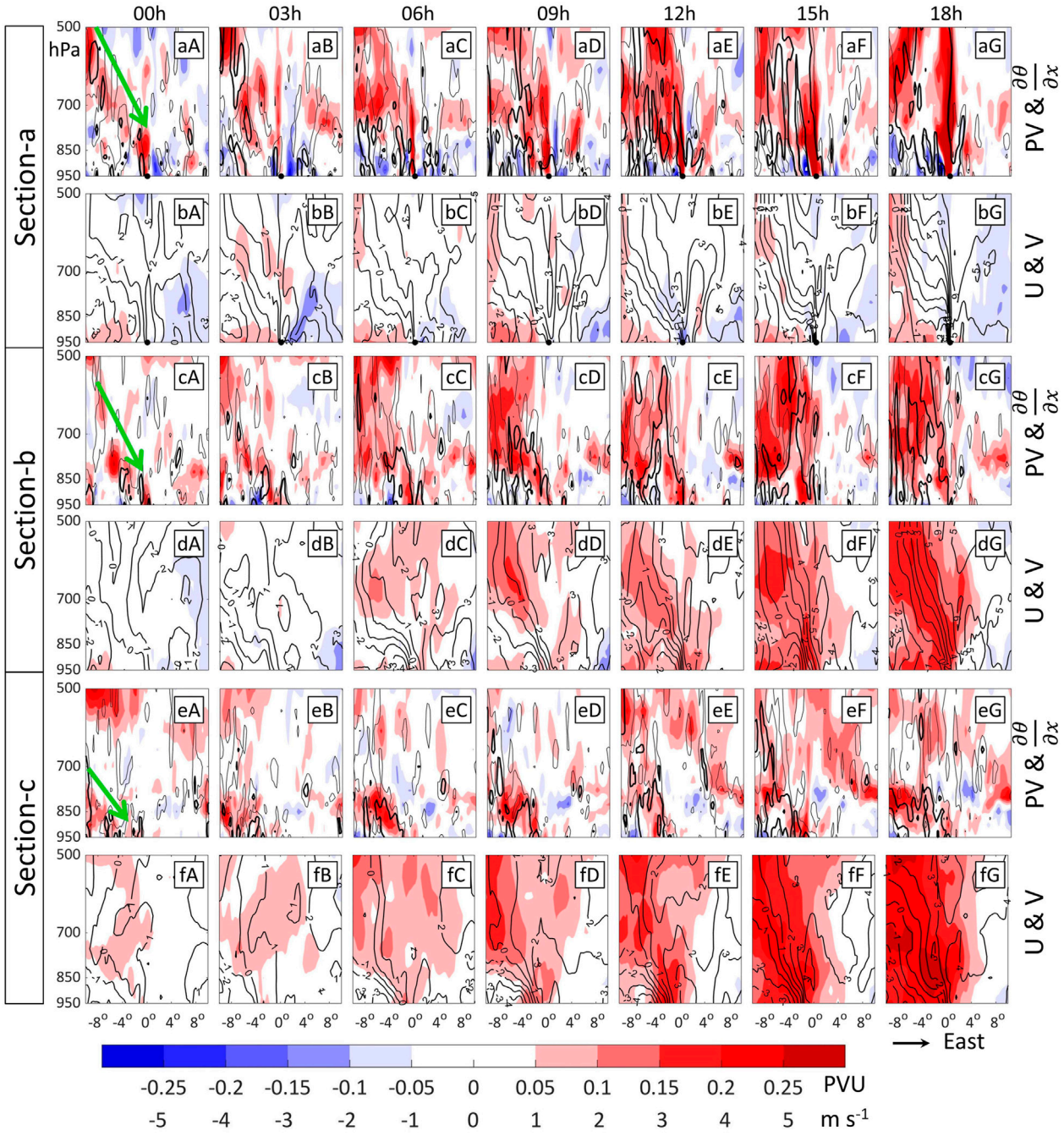

FIGURE 9
Difference in dynamic and thermal dynamic structures between ECs and OCs at the three zonal cross sections shown in Figure 8E during initial development. Each section connects the west and east boundaries of the 20°×20° box around cyclone centers. The first/third/fifth row shows differences in PV (shadings) and $\frac{\partial\theta}{\partial x}$ (contours) at section-a/b/c. Thick and thin contours denote $\frac{\partial\theta}{\partial x}$ for ECs 4×10^{-6} K m^{-1} and 2×10^{-6} K m^{-1} larger than OCs, respectively. The second/fourth/sixth row shows differences in the zonal wind speed (shadings) and meridional wind speed (contours; unit: m s^{-1}) at section-a/b/c. The time (after the cyclones are identified) for each column is marked at the top. Black dots locate the cyclone centers. Green vectors in **(aA)**, **(cA)**, and **(eA)** show the approximate directions of PV intrusion.

The perspective of PV well explains the EC development. The initiation and deepening of a cyclone can be attributed to the enhancement of PV around the cyclone center, which is impacted by both adiabatic and diabatic processes. The adiabatic process is the key cause for the initial development of a higher PV for ECs. Compared to OCs, there is a stronger

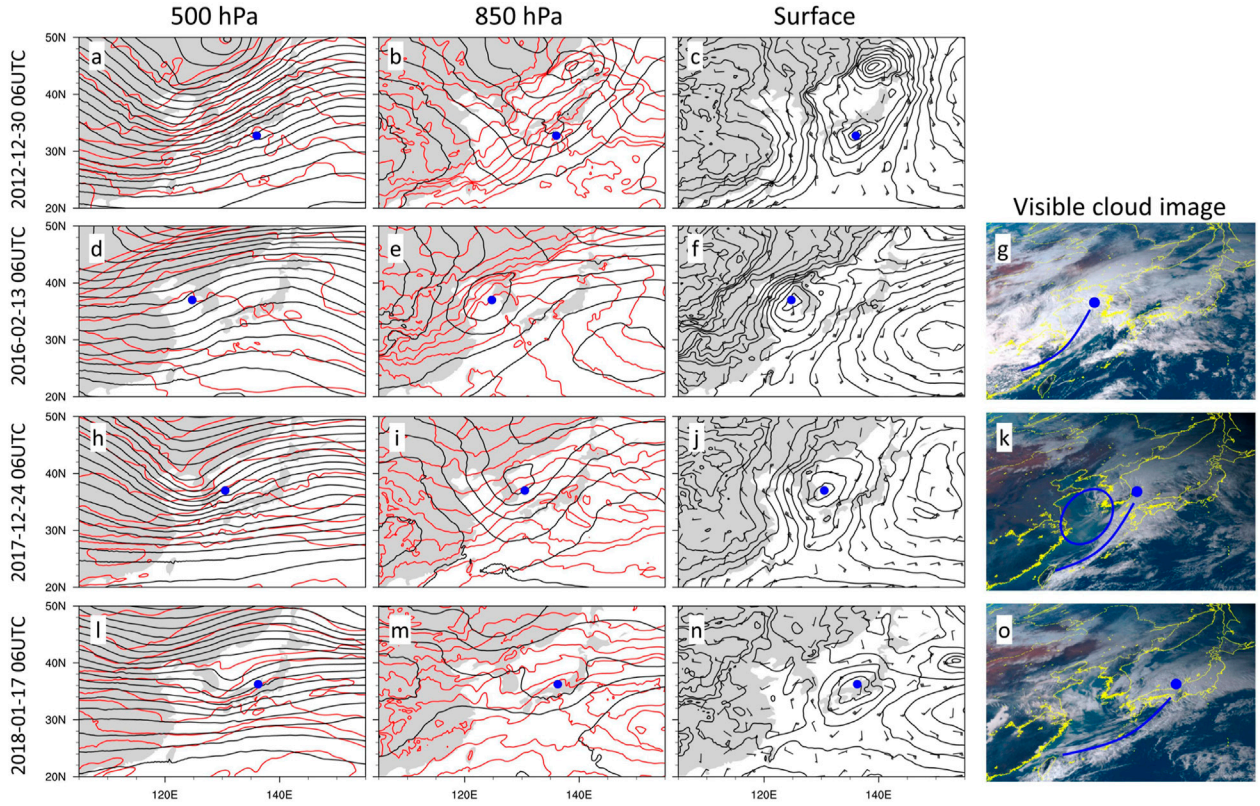

FIGURE 10
Synoptic backgrounds for the four ECs at their early stages. The first/second/third/fourth row shows the situation for EC-2012/2016/2017/2018. The time for each row is marked left. The first column shows GPH (black contours with interval of 40 gpm) and temperature (red contours with interval of 4°C) at 500 hPa. The second column is the same as the first column, except at 850 hPa. The third column shows the SLP (black contours with interval of 2.5 hPa) and surface wind (wind barbs). The fourth column shows the visible cloud images for the last 3 ECs. Blue dots locate the cyclone center, and blue lines in fourth column locate the cold fronts. The ellipse in (n) shows the clear sky area with sporadic low clouds left by cold advection.

upstream perturbation within the low troposphere for ECs, which brings colder air mass. The invasion of colder air increases upstream static stability so that PV from higher levels is transported downward along steeper isentropic surfaces, leading to a stronger southeastward PV advection. Meanwhile, stronger stability in the west makes the stretching of the air parcel more significant while moving eastward so that the relative vorticity is enhanced with a larger ratio than PV. The stronger relative vorticity provides dynamic forcing for cyclogenesis and further enhances the cold advection. The diabatic process includes the sensible heat flux from the underlying surface and LHR by moist processes. The latter is closely related to the dynamic strength since a stronger warm conveyor belt leads to thicker clouds and stronger precipitation. The net diabatic PV modification is stronger for ECs resulting from stronger LHR. Its correlation coefficient with PV tendency is only ~0.3, and the evident difference between ECs and OCs only starts after t=10 h, indicating that the diabatic effect is probably a by-product rather than the cause for the initial higher PV. The next section tries to prove the impact of the cold air mass based on numerical modeling, and compares it with other factors related to diabatic effects, such as background humidity and SST.

4 WRF numerical experiments

4.1 Case overview

A total of four EC cases (denoted by EC-2012, EC-2016, EC-2017, and EC-2018) were chosen to study with numerical modeling, whose initial moments and tracks are shown in Figure 3B. EC-2017 and EC-2016 are ranked as strong and weak ECs, respectively, and the others are medium ECs. All the cyclones were rapidly deepened while moving northeastward. They stayed over East Asia for less than 2 days, and their tracks are typical for winter cyclones in this region (Figure 3A). Figure 10 shows the synoptic backgrounds for all the cyclones during their explosive

deepening. The patterns are similar. A deep upper-air trough occurred upstream (the first column in Figure 10). Strong low-level cold advection was produced by the large temperature gradient along the geostrophic wind (the second column in Figure 10). Strong high-pressure systems were in the west of the cyclones (the third column in Figure 10), which are related to the cold air masses. There was a hook-shaped cloud system accompanied by EC-2017 (Figure 10K), which is a result of the cooperation of cold air and the warm conveyor belt. The low-level cold advection is quite strong, producing heavy precipitation along the cold front and pushing the clouds southeastward. It also produced some low clouds (in the ellipse in Figure 10K) by enhancing the static instability near the sea surface. This feature is not shared by EC-2016 and EC-2018. The cold advections for these two cyclones are weaker, and widespread clouds occurred on both sides of the fronts (Figures 10G, O).

Given the typicality of tracks and synoptic patterns of the four ECs, the modeling experiments for them can exhibit the common mechanisms for explosive cyclogenesis.

4.2 WRF modeling design

A series of numerical modeling experiments were conducted using the advanced research WRF model version 3.9.1. According to the cyclone tracks, the modeling domain occupies most of East Asia (Figure 3B) with 251×201 grid points and a horizontal grid of 0.2°. For each EC, the WRF modeling started at 0000 UTC on the same day it was initiated and lasted for 48 h. Other details of the model configuration are given in Table 1.

The initial and boundary conditions were derived from the ERA5 reanalysis. We conducted a group of control experiments (Exp-Ctrl) and five groups of sensitivity experiments (denoted by Exp-MT, Exp-MH, Exp-MH2, Exp-SST, and Exp-SST2). Other than Exp-Ctrl, each group weakened one process related to explosive cyclogenesis. Exp-MH (short for "modifying humidity") and Exp-MH2 cut the background relative humidity by 10% and half. Exp-SST and Exp-SST2 decreased the global SST by 0.7 and 4°C, respectively. In Exp-MT (short for "modifying temperature"), the background temperature was increased by $4\times(\varphi-30^{\circ})/20$ K (φ is the latitude) between 500 hPa and 850 hPa at the north and west boundaries (located by the thick purple lines in Figure 3B).

To discuss the mechanisms for explosive cyclogenesis, Exp-MH, Exp-SST, and Exp-MT eliminated the advantage of ECs over OCs in a way. The decrease of water vapor/SST in Exp-MH/Exp-SST is close to the difference between ECs and OCs (Figures 4K, L). Exp-MT heated the cold air mass and decreased the temperature gradient by 4 K per 20 latitudes at the west boundary, which also weakened the low-level thermal contrast down to the OC level (Figure 8F). The modification which can change the ECs to OCs indicates the key cause for their explosive development. On the other hand, both Exp-MH2 and Exp-SST2 gave ideal scenarios. Exp-MH2 can show cyclogenesis under extremely dry conditions. In Exp-SST2, the sea surface is almost as cold as the land surface, which can show whether the cyclones

TABLE 1 Configuration for WRF model.

Model setting and option		Specification
Domain	Map projection	Lat-lon
	Central point	35.0 °N, 135.0 °E
	Grid number	251×201
	Horizontal resolution	0.2°
	Vertical grid	51 η[a] with a pressure top at 50 hPa
Time step		120 s
Modeling duration		0000 UTC 29 December–0000 UTC 31 December 2012 for EC-2012
		0000 UTC 12 February–0000 UTC 14 February 2016 for EC-2016
		0000 UTC 23 December–0000 UTC 25 December 2017 for EC-2017
		0000 UTC 16 January–0000 UTC 18 January 2018 for EC-2018
PBL scheme		YSU scheme (Hong et al., 2006)
Cumulus parameterization		Kain–Fritsch scheme (Kain, 2004)
Microphysics		Thompson scheme (Thompson et al., 2008)
Long-shortwave radiation		RRTMG scheme (Iacono et al., 2008)
Land surface model		Noah land surface model (Tewari et al., 2004)

[a]η=1.00000, 0.99381, 0.98643, 0.97786, 0.96815, 0.95731, 0.94538, 0.93122, 0.91490, 0.89653, 0.87621, 0.85405, 0.82911, 0.80160, 0.77175, 0.73981, 0.70509, 0.66798, 0.62889, 0.58823, 0.54957, 0.51281, 0.47788, 0.44471, 0.41323, 0.38336, 0.35503, 0.32819, 0.30276, 0.27869, 0.25592, 0.23439, 0.21405, 0.19484, 0.17672, 0.15963, 0.14352, 0.12836, 0.11410, 0.10070, 0.08811, 0.07630, 0.06523, 0.05487, 0.04517, 0.03611, 0.02765, 0.01977, 0.01243, 0.00560, 0.00000.

could have gone through explosive deepening without sensible heating by the ocean.

4.3 Evaluation of the control run

Exp-Ctrl reasonably reproduces the development of the four ECs. As shown in Figure 3B, for each EC case, the cyclone track for Exp-Ctrl is similar to the reanalysis. The WRF model can capture the movement of EC-2018 along the west coast of Japan Island, and the model errors for EC-2012 are less than 50 km. Although the simulated cyclone center for EC-2017 is ~200 km away from reanalysis, it is still a small error considering the scale of subtropical cyclones. The model also well reproduces the decrease of their central SLP and the enhancement of maximum wind speed (Figure 11). The model slightly underestimates/overestimates the central SLP for EC-2012/EC-2017, which does not influence the following discussion since the simulated deepening rates are quite close to reanalysis. The maximum wind speed is larger for Exp-Ctrl than for reanalysis. It is to be noted that the model resolution is higher than ERA5, and stronger winds for Exp-Ctrl are probably more realistic. Furthermore, we interpolated the SLP and surface wind speed for Exp-Ctrl into the ERA5 grid within the 20°×20° boxes around the cyclone centers to compare with the reanalysis. The root-mean-square error (RMSE) of SLP/wind speed is 1.74 h Pa/2.7 m s^{-1} averaged among all the ECs during the last 36 forecast hours, and the average bias is only 0.31 h Pa/0.96 m s^{-1}. Given the good

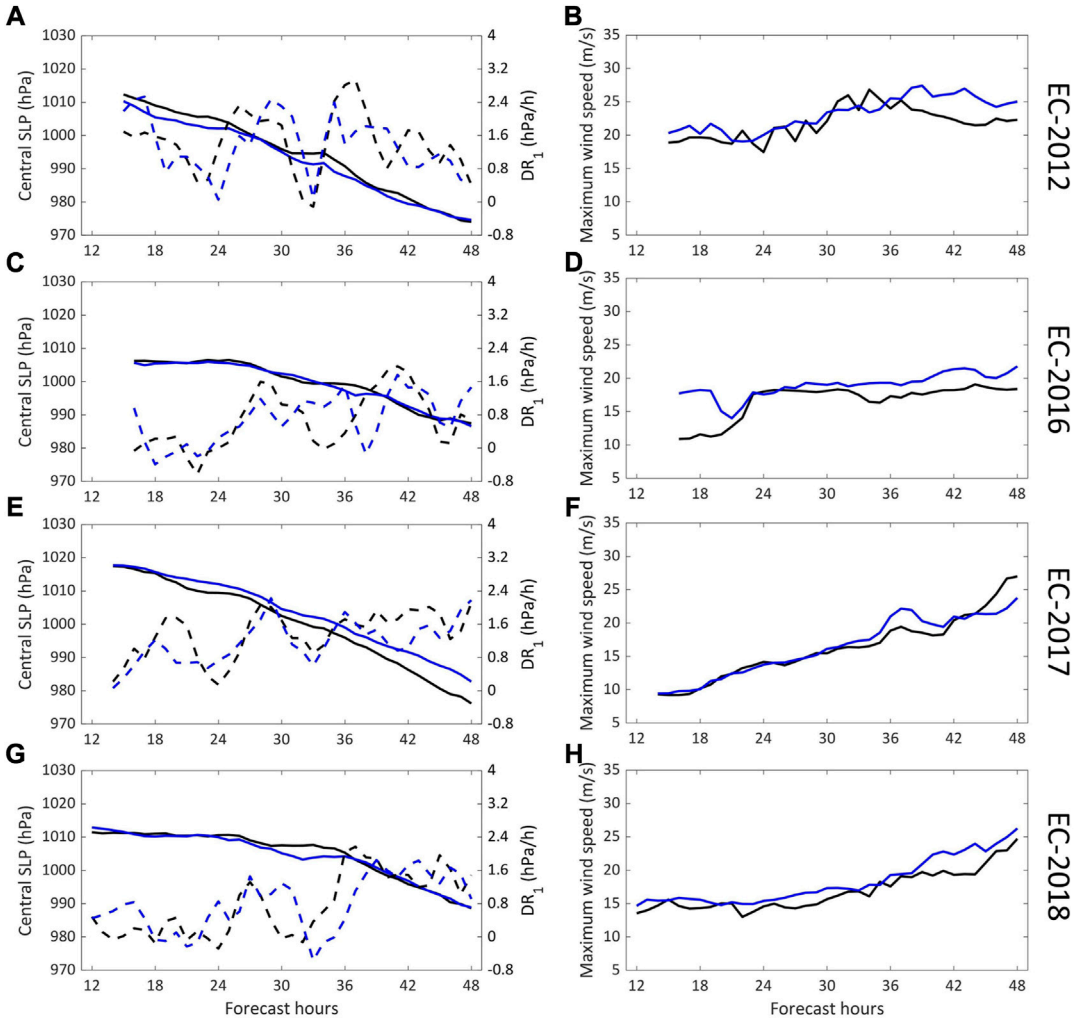

FIGURE 11
Comparison between the reanalysis and the model. The left column shows the time series of central SLP (solid lines) and hourly deepening rate (dashed lines) for the four ECs. The right column shows the time series of the maximum wind speed. Black and blue lines denote the ERA5 reanalysis and Exp-Ctrl, respectively. The EC number for each row is marked right.

agreement between the WRF model and reanalysis, we can treat Exp-Ctrl as the true atmosphere.

4.4 Sensitivity experiments

Exp-MT and Exp-SST2 can significantly weaken the cyclones and stop them from explosive cyclogenesis, while the other sensitivity experiments make minor differences. Note that in this subsection, all the variables mentioned are averaged among all the four EC cases. As shown in Figure 12A, the average 24-h deepening rate is 1.17 hPa h^{-1} for Exp-Ctrl. Exp-MT/Exp-SST2 decreases it to 0.89/0.91 hPa h^{-1}. The deepening rate for Exp-MH/Exp-MH2 is almost the same as that for Exp-Ctrl, while that for Exp-SST it is slightly lower. For Exp-Ctrl, the average central SLP is ~1010 hPa at 16 h and decreases to ~982 hPa at 48 h (Figure 12B). For Exp-MT/Exp-SST2, it is ~1013/1011 hPa at 16 h and ~994/990 hPa at 48 h, which is 12/8 hPa higher than that for Exp-Ctrl. Consistent with the strength of cyclones, the surface wind is also significantly weakened by these two groups (Figure 12C). Although the cyclones for Exp-SST2 are deeper than those for Exp-MT, its surface wind is weaker. It is because the modification in Exp-SST2 can directly change the near-surface convergence.

The strength of ECs is closely related to the PV structure. Figure 13 shows the difference in 24-h averaged PV and the potential temperature between Exp-Ctrl and Exp-MT. Along with the colder air mass, PV around cyclone centers for Exp-Ctrl is significantly larger than that for Exp-MT, and the positive difference mainly exists in the west. At 500 hPa, the west and north boundary meets the largest difference in >0.25 PVU. From 700 hPa down to 925 hPa, the area of the positive difference moves southward, which is close to the edge of the cold air mass. The difference in relative vorticity has a similar pattern to PV. At low levels, the relative vorticity around cyclone centers for Exp-Ctrl is ~2×10^{-5} s^{-1} larger than that for Exp-MT (Figures 13B–D). As shown in Figures 13E,F, the PV transport across the west boundary for Exp-Ctrl is much larger than that for Exp-MT, which is consistent with its larger meridional gradient of air temperature. The largest difference locates at a line tilting northward with height.

Comparing Figures 13E,F with Figures 8A,F, one can find that the differences in both the PV transport and temperature gradient between Exp-Ctrl and Exp-MT have similar patterns to those between ECs and OCs. By weakening the low-level meridional temperature gradient by 4 K per 20 latitudes, Exp-MT successfully weakens the upstream PV intrusion and changes the ECs to OCs. On the other hand, the warm sea surface is an important factor in the deepening of cyclones, which can be told from the performance of Exp-SST2. However, the difference in SST cannot distinguish ECs from OCs (cf., Exp-Ctrl and Exp-SST).

Many studies have proven that LHR is important for PV generation and explosive cyclogenesis. Heo et al. (2015) shut

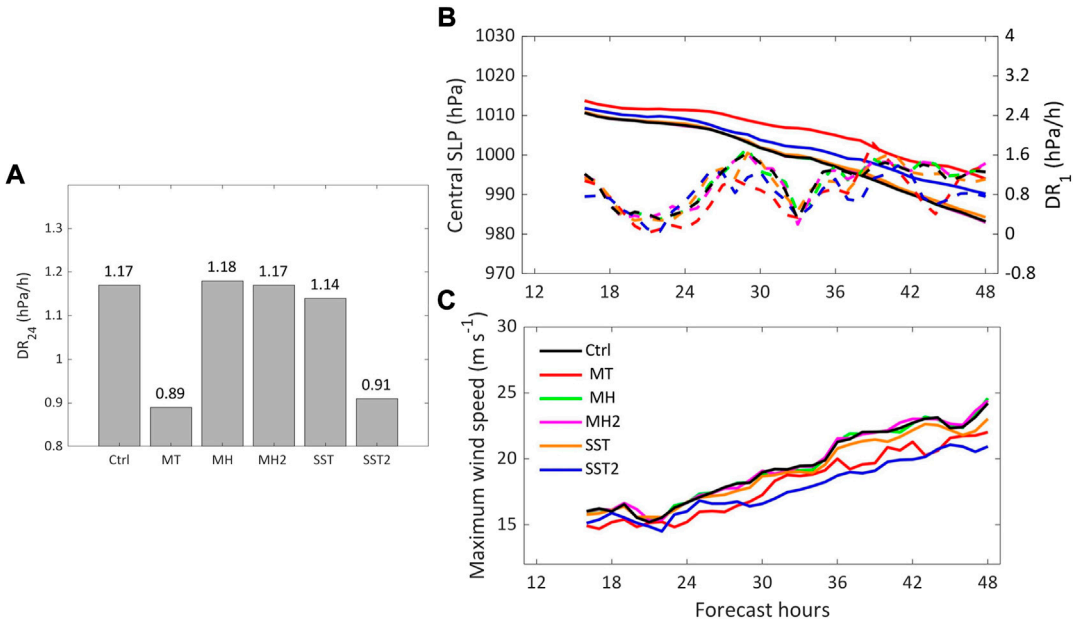

FIGURE 12
Simulated 24-h deepening rates (during the last 24 forecast hours) **(A)**, time series of cyclone central SLPs **(B)**, and maximum wind speeds **(C)** for six experiments. Solid and dashed curves in **(B)** represent the central SLPs and 1-h deepening rates, respectively. All variables are averaged among all the four ECs.

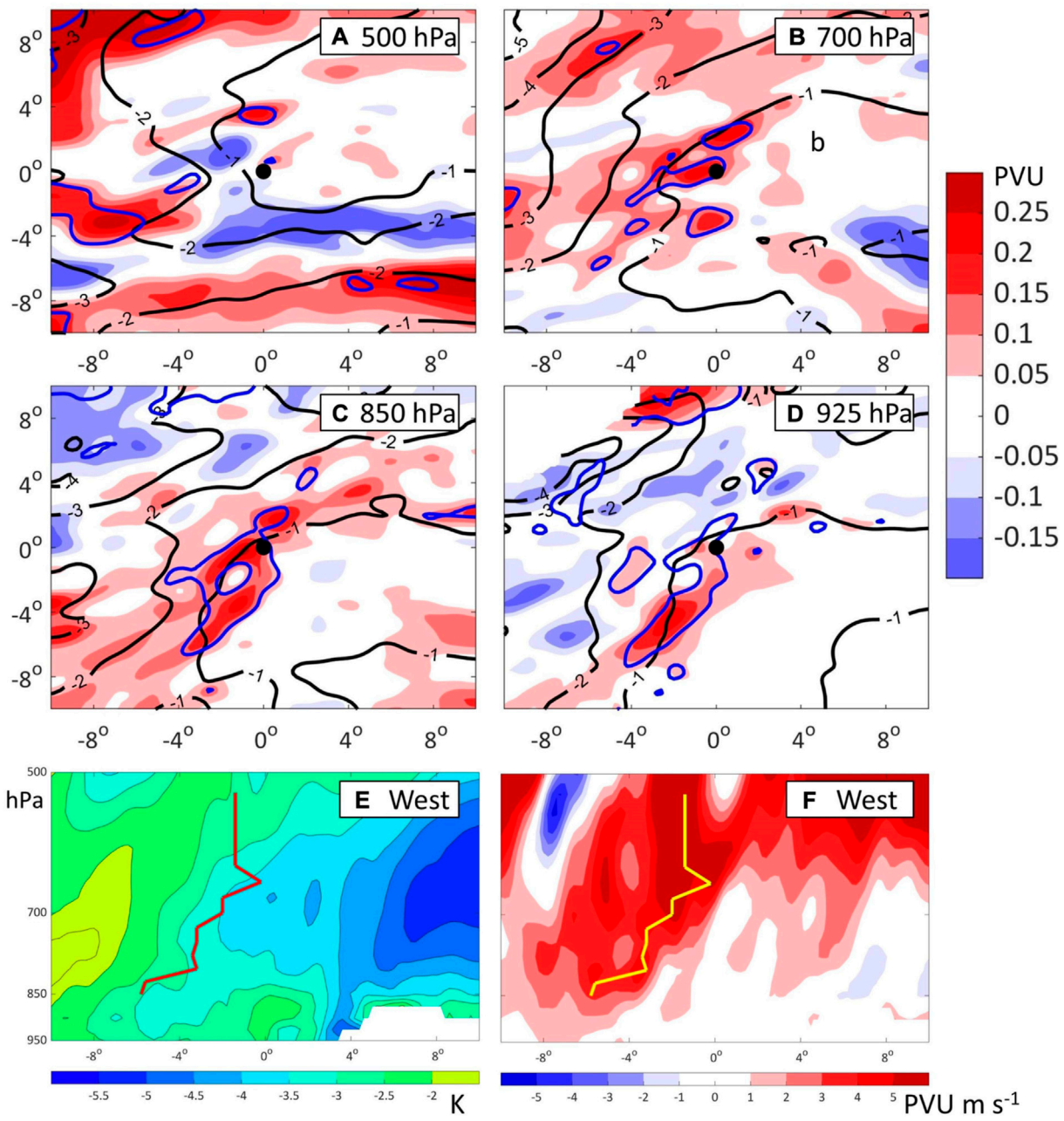

FIGURE 13
Differences in PV (shadings) and potential temperature (black contours; unit: K) between Exp-Ctrl and Exp-MT at different levels around the cyclone centers **(A–D)**, as well as differences in potential temperature **(E)** and uPV **(F)** at the west boundary. Blue lines in **(A–D)** show the relative vorticity for Exp-Ctrl 2×10^{-5} s^{-1} larger than Exp-MT. Black dots in **(A–D)** locate the cyclone centers. The thick red line in **(E)** and yellow line in **(F)** locate the maximum of uPV at each level. Each variable is averaged among the four ECs during their first 24-h.

down the cumulus parameterization and diabatic heating in a microphysics scheme in the sensitive experiment, and showed that ~50% of the low-level PV generation is contributed by LHR for an EC case. Interestingly, Exp-MH/Exp-MH2 cut the water vapor by 10/50% over the whole domain but can hardly decrease the deepening rate. As shown in Figure 14, the water vapor contents around cyclone centers for them are similar to those of Exp-Ctrl. The 24-h averaged precipitable water is abundant along the warm conveyor belt, and the gradient is large near the cold front. The decreases in Exp-MH and Exp-

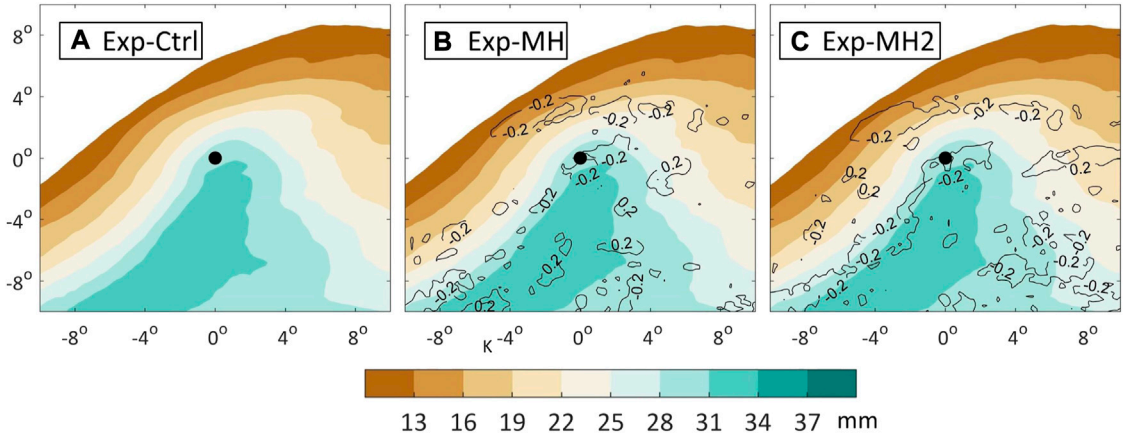

FIGURE 14
Precipitable water around cyclone centers for each modeling experiment. Contours in **(B)**/**(C)** denote the difference between Exp-MH/Exp-MH2 and Exp-Ctrl. Precipitable water is averaged among the four ECs during their first 24 h.

MH2 than in Exp-Ctrl are trivial, indicating a weak correlation between the background humidity and the humidity around cyclones. The transport of water vapor and thus the LHR are dominated by the dynamic strength of cyclones.

Results of the numerical experiments emphasize the important role of cold air mass on the intrusion of upper-level PV, which is fully consistent with statistical analysis. Background humidity has a weak impact. Although the warm sea surface is important in cyclogenesis, the difference in SST between ECs and OCs is too small to have significant impacts.

5 Conclusion

ECs frequently show up off the East Asian coast in winter and cause great casualties and property loss. To analyze the main reason for explosive cyclogenesis that makes ECs different from other cyclones, we compare the initial developments between ECs and OCs based on statistics.

Using the detection and tracking methods followed by Hart (2003), this study identifies 135 cyclones which form over East Asia for at least 24 h within 10 winters. More than half of them are ranked as ECs, and most of the initial explosive deepening occurs over sea. Detailed analyses are carried out to compare the synoptic backgrounds and changes in PV structures. The local PV tendency is decomposed to check the key factor in higher PV for ECs. The simulations of WRF numerical experiments on four typical winter ECs are quite consistent with the statistical analysis. The results show the following:

1) The PV intrusion plays a dominant role in changing the low-level PV for ECs. The correlation between PV tendency and the diabatic term is weak, indicating a similar impact of the diabatic process on both OCs and ECs. It is not the key cause of explosive cyclogenesis.
2) For ECs, the low-level cold advection is stronger. It increases upstream static stability so that stronger PV intrusion occurs along the steeper isentropic, which enhances the PV advection. Moreover, the stronger stability in the west makes the stretching of the air parcel more significant while moving eastward so that the relative vorticity is further enhanced.
3) Explosive cyclogenesis is not sensitive to the structure of water vapor content and LHR in the early stage. Conversely, the water vapor content and LHR are very dependent on the dynamic strength of the cyclone. Although LHR has an important impact on the mature stage of cyclones (e.g., Schemn and Wernli, 2014; Heo et al., 2015; Binder et al., 2016), it is a result rather than the cause of the initial development.

In addition to the consensus that diabatic processes play crucial roles in explosive cyclogenesis, we emphasize the importance of the cold advection (which is also associated with baroclinic instability) and quantitatively give the difference in the thermal structure that makes ECs different from OCs in this region. However, the relationship between diabatic processes and the thermal structure is complicated and still an open question, which will be discussed in our ongoing studies.

Data availability statement

The original contributions presented in the study are included in the article/Supplementary Material; further inquiries can be directed to the corresponding authors.

Author contributions

XG designed the research and performed the analysis. XG, PL, and SZ wrote the manuscript. GF revised the manuscript. All authors discussed the results and commented on the manuscript.

Funding

This research was jointly funded by the National Key Research and Development Program of China (Grant No. 2021YFC3101800) and the National Natural Science Foundation of China (41976200, 42005116 and 41905071).

Acknowledgments

We would like to thank the reviewers for their helpful comments and suggestions that improved the manuscript.

Conflict of interest

The authors declare that the research was conducted in the absence of any commercial or financial relationships that could be construed as a potential conflict of interest.

Publisher's note

References

Ahmadi-Givi, F., Graig, G. C., and Plant, R. S. (2004). The dynamics of a midlatitude cyclone with very strong latent-heat release. *Q. J. R. Meteorol. Soc.* 130 (596), 295–323. doi:10.1256/qj.02.226

Binder, H., Boettcher, M., Joos, H., and Wernli, H. (2016). The role of warm conveyor belts for the intensification of extratropical cyclones in northern hemisphere winter. *J. Atmos. Sci.* 73 (10), 3997–4020. doi:10.1175/JAS-D-15-0302.1

Bosart, L. F., and Lin, S. C. (1984). A diagnostic analysis of the Presidents' Day storm of February 1979. *Mon. Weather Rev.* 112 (11), 2148–2177. doi:10.1175/1520-0493(1984)112<2148:ADAOTP>2.0.CO;2

Cammas, J. P., and Ramond, D. (1989). Analysis and diagnosis of the composition of ageostrophic circulations in jet-front systems. *Mon. Weather Rev.* 117 (11), 2447–2462. doi:10.1175/1520-0493(1989)117<2447:aadotc>2.0.co;2

Chen, S. J., Kuo, Y. H., Zhang, P. Z., and Bai, Q. F. (1992). Climatology of explosive cyclones off the East Asian coast. *Mon. Weather Rev.* 120 (12), 3029–3035. doi:10.1175/1520-0493(1992)120<3029:coecot>2.0.co;2

Cordeira, J. M., and Bosart, L. F. (2011). Cyclone interactions and evolutions during the "perfect storms" of late october and early november 1991. *Mon. Weather Rev.* 139 (6), 1683–1707. doi:10.1175/2010MWR3537.1

Davis, C. A., Stoelinga, M. T., and Kuo, Y. H. (1993). The integrated effect of condensation in numerical simulations of extratropical cyclogenesis. *Mon. Weather Rev.* 121 (8), 2309–2330. doi:10.1175/1520-0493(1993)121<2309:TIEOCI>2.0.CO;2

Ertel, H. (1942). Ein neuer hydrodynamischer wirbelsatz. *Meteorol. Z* 59, 271–281.

Fu, G., Sun, Y., Sun, J., and Li, P. (2020). A 38-year climatology of explosive cyclones over the northern hemisphere. *Adv. Atmos. Sci.* 37 (2), 143–159. doi:10.1007/s00376-019-9106-x

Gyakum, J. R., Anderson, J. R., Grumm, R. H., and Gruner, E. L. (1989). North pacific cold-season surface cyclone activity: 1975–1983. *Mon. Weather Rev.* 117 (6), 1141–1155. doi:10.1175/1520-0493(1989)117<1141:npcssc>2.0.co;2

Hart, R. E. (2003). A cyclone phase space derived from thermal wind and thermal asymmetry. *Mon. Weather Rev.* 131 (4), 585–616. doi:10.1175/1520-0493(2003)131<0585:ACPSDF>2.0.CO;2

Heo, K. Y., Seo, Y. W., Ha, K. J., Park, K. S., Kim, J., Choi, J. W., et al. (2015). Development mechanisms of an explosive cyclone over East sea on 3–4 April 2012. *Dyn. Atmos. Oceans* 70, 30–46. doi:10.1016/j.dynatmoce.2015.03.001

Hirata, H., Kawamura, R., Kato, M., and Shinoda, T. (2015). Influential role of moisture supply from the kuroshio/kuroshio extension in the rapid development of an extratropical cyclone. *Mon. Weather Rev.* 143 (10), 4126–4144. doi:10.1175/mwr-d-15-0016.1

Hong, S. Y., Noh, Y., and Dudhia, J. (2006). A new vertical diffusion package with an explicit treatment of entrainment processes. *Mon. Weather Rev.* 134 (9), 2318–2341. doi:10.1175/mwr3199.1

Hoskins, B. J., and Valdes, P. J. (1990). On the existence of storm-tracks. *J. Atmos. Sci.* 47 (15), 1854–1864. doi:10.1175/1520-0469(1990)0472.0.CO;2

Iacono, M. J., Delamere, J. S., Mlawer, E. J., Shephard, M. W., Clough, S. A., and Collins, W. D. (2008). Radiative forcing by long-lived greenhouse gases: Calculations with the AER radiative transfer models. *J. Geophys. Res.* 113, D13103. doi:10.1029/2008JD009944

Iwao, K., Inatsu, M., and Kimoto, M. (2012). Recent changes in explosively developing extratropical cyclones over the winter Northwestern Pacific. *J. Clim.* 25 (20), 7282–7296. doi:10.1175/JCLI-D-11-00373.1

Kain, J. S. (2004). The kain–fritsch convective parameterization: An update. *J. Appl. Meteor.* 43 (1), 170–181. doi:10.1175/1520-0450(2004)043<0170:tkcpau>2.0.co;2

Kuwano-Yoshida, A., and Asuma, Y. (2008). Numerical study of explosively developing extratropical cyclones in the Northwestern Pacific region. *Mon. Weather Rev.* 132 (2), 712–740. doi:10.1175/2007mwr2111.1

Kuwano-Yoshida, A., and Enomoto, T. (2013). Predictability of explosive cyclogenesis over the Northwestern Pacific region using ensemble reanalysis. *Mon. Weather Rev.* 141 (11), 3769–3785. doi:10.1175/MWR-D-12-00161.1

Lamb, H. H. (1991). *Historic storms of the north sea, British isles and northwest europe*. Cambridge: Cambridge University Press, 204.

Liberato, M. L., Pinto, J. G., Trigo, I. F., and Trigo, R. M. (2011). Klaus–an exceptional winter storm over northern Iberia and southern France. *Weather* 66 (12), 330–334. doi:10.1002/wea.755

Liberato, M. L. R., Pinto, J. G., Trigo, R. M., Ludwig, P., Ordóñez, P., Yuen, D., et al. (2013). Explosive development of winter storm xynthia over the subtropical north atlantic ocean. *Nat. Hazards Earth Syst. Sci.* 13 (9), 2239–2251. doi:10.5194/nhess-13-2239-2013

Lim, E. P., and Simmonds, I. (2002). Explosive cyclone development in the southern hemisphere and a comparison with northern hemisphere events. *Mon. Weather Rev.* 130 (9), 2188–2209. doi:10.1175/1520-0493(2002)130<2188:ecdits>2.0.co;2

Manobianco, J. (1989). Explosive East Coast cyclogenesis over the west-central north atlantic ocean: A composite study derived from ECMWF operational

analyses. *Mon. Weather Rev.* 117 (11), 2365–2383. doi:10.1175/1520-0493(1989)117<2365:eeccot>2.0.co;2

Nakamura, H. (1993). Horizontal divergence associated with zonally isolated jet streams. *J. Atmos. Sci.* 50 (14), 2310–2313. doi:10.1175/1520-0469(1993)050<2310:hdawzi>2.0.co;2

Reader, M. C., and Moore, G. K. (1995). Stratosphere-troposphere interactions associated with a case of explosive cyclogenesis in the Labrador Sea. *Tellus A* 47 (5), 849–863. doi:10.1034/j.1600-0870.1995.00124.x

Rice, R. B. (1979). Tracking a killer storm. *Sail* 10, 106–107.

Roebber, P. J. (1984). Statistical analysis and updated climatology of explosive cyclones. *Mon. Weather Rev.* 112 (8), 1577–1589. doi:10.1175/1520-0493(1984)112<1577:saauco>2.0.co;2

Sanders, F., and Gyakum, J. R. (1980). Synoptic-dynamic climatology of the "bomb". *Mon. Weather Rev.* 108 (10), 1589–1606. doi:10.1175/1520-0493(1980)108<1589:sdcot>2.0.co;2

Sanders, F. (1986). Explosive cyclogenesis in the west-central North Atlantic Ocean, 1981-84. Part I: Composite structure and mean behavior. *Mon. Weather Rev.* 114 (10), 1781–1794. doi:10.1175/1520-0493(1986)114<1781:ecitwc>2.0.co;2

Schemm, S., and Wernli, H. (2014). The Linkage between the warm and the cold conveyor belts in an idealized extratropical cyclone. *J. Atmos. Sci.* 71 (4), 1443–1459. doi:10.1175/JAS-D-13-0177.1

Seiler, C., and Zwiers, F. W. (2016). How will climate change affect explosive cyclones in the extratropics of the Northern Hemisphere?. *Clim. Dyn.* 46, 3633–3644. doi:10.1007/s00382-015-2791-y

Shapiro, M. A., and Keyser, D. (1990). "Fronts, jet streams and the tropopause," *Extratropical cyclones*. Editors C. W. Newton and E. O. Holopainen (Boston, MA: American Meteorological Society), 167–191

Taguchi, B., Nakamura, H., Nonaka, M., and Xie, S. P. (2009). Influences of the Kuroshio/Oyashio extensions on air-sea heat exchanges and storm-track activity as revealed in regional atmospheric model simulations for the 2003/04 cold season. *J. Clim.* 22 (24), 6536–6560. doi:10.1175/2009JCLI2910.1

Tewari, M., Chen, F., Wang, W., Dudhia, J., LeMone, M. A., Mitchell, K., et al. (2004). "Implementation and verification of the unified NOAH land surface model in the WRF model," in 20th conference on weather analysis and forecasting/16th conference on numerical weather prediction, 11–15

Thompson, G., Field, P. R., Rasmussen, R. M., and Hall, W. D. (2008). Explicit forecasts of winter precipitation using an improved bulk microphysics scheme. Part II: Implementation of a new snow parameterization. *Mon. Wea. Rev.* 136, 5095–5115. doi:10.1175/2008MWR2387.1

Uccellini, L. W., and Kocin, P. J. (1987). The interaction of jet streak circulations during heavy snow events along the east coast of the United States. *Weather Forecast.* 2 (4), 289–308. doi:10.1175/1520-0434(1987)002<0289:tiojsc>2.0.co;2

Wash, C. H., Hale, R. A., Dobos, P. H., and Wright, E. J. (1992). Study of explosive and nonexplosive cyclogenesis during FGGE. *Mon. Weather Rev.* 120 (1), 40–51. doi:10.1175/1520-0493(1992)120<0040:soeanc>2.0.co;2

Wash, C. H., Peak, J. E., Calland, W. E., and Cook, W. A. (1988). Diagnostic study of explosive cyclogenesis during FGGE. *Mon. Weather Rev.* 116 (2), 431–451. doi:10.1175/1520-0493(1988)116<0431:dsoecd>2.0.co;2

Yoshida, A., and Asuma, Y. (2004). Structures and environment of explosively developing extratropical cyclones in the northwestern Pacific region. *Mon. Weather Rev.* 132 (5), 1121–1142. doi:10.1175/1520-0493(2004)132<1121:saeoed>2.0.co;2

Zhang, S., Fu, G., Lu, C., and Liu, J. W. (2017). Characteristics of explosive cyclones over the northern pacific. *J. Appl. Meteorol. Climatol.* 56 (12), 3187–3210. doi:10.1175/JAMC-D-16-0330.1

Zhang, S., and Fu, G. (2018). Structures and evolutions of explosive cyclones over the northwestern and northeastern pacific. *J. Ocean. Univ. China* 17, 581–593. doi:10.1007/s11802-018-3418-9

Zhang, S., Fu, G., Zhang, Y., Xu, J., Xue, Y., Tang, R., et al. (2022). Statistical characteristics and composite environmental conditions of explosive cyclones over the Japan Sea and kuroshio/kuroshio extension. *Atmosphere* 13, 17. doi:10.3390/atmos13010017

frontiers | Frontiers in Earth Science

TYPE Original Research
PUBLISHED 05 January 2023
DOI 10.3389/feart.2022.992246

OPEN ACCESS

EDITED BY
Darko Koracin,
University of Split, Croatia

REVIEWED BY
Zifeng Yu,
China Meteorological Administration, China
Runling Yu,
China Meteorological Administration, China

*CORRESPONDENCE
Shanhong Gao,
gaosh@ouc.edu.cn
Yongming Wang,
yongming.w@hotmail.com

SPECIALTY SECTION
This article was submitted to Atmospheric Science, a section of the journal Frontiers in Earth Science

RECEIVED 12 July 2022
ACCEPTED 13 September 2022
PUBLISHED 05 January 2023

CITATION
Gao X, Gao S, Li Z and Wang Y (2023), A revised method with a temperature constraint for assimilating satellite-derived humidity in forecasting sea fog over the Yellow Sea.
Front. Earth Sci. 10:992246.
doi: 10.3389/feart.2022.992246

A revised method with a temperature constraint for assimilating satellite-derived humidity in forecasting sea fog over the Yellow Sea

Xiaoyu Gao[1,2], Shanhong Gao[1]*, Ziru Li[1] and Yongming Wang[1,3]*

[1]Key Laboratory of Physical Oceanography, College of Oceanic and Atmospheric Sciences, Ocean University of China, Qingdao, China, [2]State Key Laboratory of Severe Weather, Chinese Academy of Meteorological Sciences, Beijing, China, [3]School of Meteorology, University of Oklahoma, Norman, OK, United States

Numerical forecast of sea fog is very challenging work because of its high sensitivity to model initial conditions. For better depicting the humidity structure of the marine atmospheric boundary layer (MABL), Wang et al. (2014) assimilated satellite-derived humidity from sea fog at its initial stage over the Yellow Sea (W14 method), using an extended three-dimensional variational data assimilation (3DVAR) with the Weather Research and Forecasting model (WRF). This article proposes a revised version of the W14 method. The major ingredient of the revision is the inclusion of a temperature constraint into the satellite-derived humidity, not only for the missed fog area that the W14 method primarily considers, but also for the false fog area that is not handled in the W14 method. The numerical experiment results of 10 sea fog cases over the Yellow Sea show that the revised method can effectively alleviate the wet bias occasionally occurring in the W14 method, resulting in an improvement by about 15% for an equitable threat score of the simulated fog area. In addition, a detailed case study is conducted to illustrate the working mechanism of the revised method, including sensitivity experiments focusing on the roles of two kinds of background error covariances (CV5 and CV6) in the assimilation by the

Abbreviations: CV5, a kind of background error covariance, in which moisture is an independent control variable and not correlated to other control variables; CV6, as CV5, but moisture is correlated to other control variables; MTSAT-RH, artificial humidity soundings within the fog area detected from MTSAT (see Figure 2A); MTSAT-T, artificial temperature soundings within the areas of hit, missed, and false sea fog (see Figure 3); obs, routine observations, including measurements from upper-air radiosondes, surface stations, and a small amount of satellite-retrieved temperature and humidity profiles; Exp-Ob5, the numerical experiment for Case 3 (the sea fog occurred in April 2008), in which only obs is assimilated with CV5. Ob5 denotes obs and CV5; Exp-Ob6, as Exp-Ob5, but CV6 is used instead of CV5; Exp-ObRH5, as Exp-Ob5, but MTSAT-RH is assimilated together with obs by using the W14 method. RH denotes MTSAT-RH; Exp-ObRH6, as Exp-ObRH5, but CV6 is used instead of CV5; Exp-ObRHT5, as Exp-ObRH5, but MTSAT-T is added into the assimilation of obs and MTSAT-RH by the revised method; Exp-ObRHT6, as Exp-ObRHT5, but CV6 is used instead of CV5; Group-A, the group of numerical experiments for 10 cases, assimilating obs only; Group-B, as Group-A, assimilating obs and MTSAT-RH by the W14 method; Group-C, as Group-A, assimilating obs, MTSAT-RH, and MTSAT-T by the revised method.

WRF-3DVAR. The results suggest that CV6 with multivariate cross-correlation is probably more beneficial to the revised method's performance.

KEYWORDS

sea fog, Yellow Sea, marine atmospheric boundary layer (MABL), WRF model, data assimilation, satellite-derived humidity, temperature constraint

1 Introduction

Sea fog refers to the fog that occurs over seas or coastal areas with the atmospheric horizontal visibility less than 1 km, threatening the safety of marine transportation and activities and causing heavy casualties and property losses (Wang, 1985; Gultepe et al., 2007). Most sea fogs belong to the advective cooling type, such as the sea fog over the Yellow Sea (Wang, 1985; Gao et al., 2007). Its formation mechanism is that warm-moist air mass flows over the cold sea surface and gradually cools down to the dew point, which usually occurs over the regions with a strong sea surface temperature (SST) gradient located north of a warm current (Lewis et al., 2003). The Yellow Sea is such a region, with the Kuroshio warm current in the south (Figure 1). It experiences frequent fog events with an average of ~50 fog days observed at its west coast, and its fog season starts in April and abruptly ends in August (Zhang et al., 2009; Fu et al., 2012). There are several major ports around the Yellow Sea, such as Qingdao, Dalian, Lianyungang, and Incheon. The busy international marine freight and traffic make it urgent to improve the forecasting skill of the sea fog over the Yellow Sea.

With the rapid improvement of numerical models and computing power, numerical modeling has already been an important approach for sea fog research and forecast (Koračin and Dorman 2017). However, there are still some challenges in the numerical simulation of sea fog, one of which is the initial condition problem. Many studies have indicated that a sea fog simulation is very sensitive to the initial condition (Lorenz, 1965; Nicholls, 1984; Findlater et al., 1989; Ballard et al., 1991; Koračin et al., 2001; Lewis et al., 2003; Koračin et al., 2005a; Koračin et al., 2005b; Gao et al., 2007; Gao et al., 2010). The dominant synoptic system responsible for sea fog over the Yellow Sea is usually an isolated anticyclone, a cyclone–anticyclone couplet system, or a high-pressure ridge (Wang 1985; Zhou et al., 2004), which generally drives warm-moist air mass to continuously flow northward from the warmer sea area at low latitudes to the colder Yellow Sea. Due to the cooling by the cold sea surface, the thermal structure of the marine atmospheric boundary layer (MABL) over the Yellow Sea changes, resulting in the formation of sea fog (Gao et al., 2007; Yang and Gao 2015, 2020; Kim et al., 2021). Therefore, the initial conditions for sea fog simulation focus on the temperature and humidity structure of MABL (Gao et al., 2010). However, it is difficult to depict the accurate temperature and humidity structure of MABL, particularly for humidity, due to the coarse resolution of the background from global analysis and the rarity of marine observations.

Aware of the importance of the initial MABL structure for sea fog simulation, many studies have been carried out on sea fog data assimilation, which can be roughly divided into two aspects: the assimilation of unconventional observation data (Liu et al., 2011; Li et al., 2012; Wang and Gao, 2016; Wu et al., 2017; Gao and Gao 2019) and the exploration of data assimilation methods (Gao et al., 2010; Wang et al., 2014; Gao et al., 2018; Yang et al., 2021). The initial MABL structure benefits little from the direct assimilation of satellite radiance data (Li et al., 2012) due to the coarse resolution in the lower troposphere of the radiance data. The assimilation of QuickSCAT sea surface wind and Doppler radar radial wind can make the sea fog simulation better because the wind component of the initial MABL structure is improved (Liu et al., 2011; Wang and Gao 2016). However, the precondition for this improvement is that the temperature and humidity structure of MABL is appropriate. Compared with 3DVAR (three-dimensional variational) assimilation with static background error covariance, EnKF (ensemble Kalman filter) can produce a higher quality initial condition for sea fog simulation when assimilating the same observations (Gao et al., 2018) because it uses a dynamic flow-dependent background error covariance that can improve

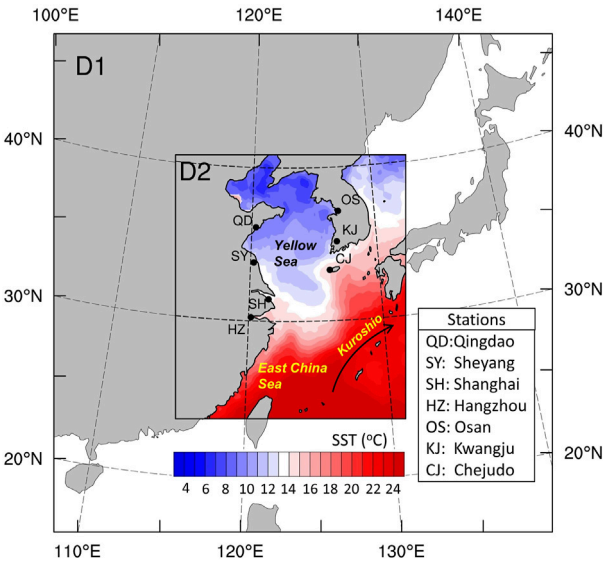

FIGURE 1
The Weather Research and Forecasting (WRF) model domain and the sites of radiosonde observations. Color shades denote the SST of the inner domain D2 on 28 April, 2008, and the thick line indicates the Kuroshio warm current.

humidity from assimilating temperature. These previous studies have noted that the failure of sea fog modeling is usually caused by the error of MABL humidity in the initial condition. There is usually a dry bias within the MABL, which is not conducive to the formation of sea fog.

In order to correct the dry bias of humidity, Wang et al. (2014) proposed a method for assimilating satellite-derived humidity (hereafter denoted by the W14 method; see Section 2.1 for a brief review). In the W14 method, the satellite-derived humidity (i.e., 100% relative humidity in the three-dimensional space of sea fog occurrence) is first retrieved from the multifunctional transport satellite (MTSAT) of Japan, and then assimilated by an extended cycling 3DVAR based on the Weather Research and Forecasting (WRF) model. Two sea fog cases, one which spreads widely over the Yellow Sea and the other which spreads narrowly along the coast, were studied in detail for analyzing the feasibility of the W14 method. Additionally, the W14 method was applied on extra 10 sea fog cases to evaluate the effect of the W14 method. The assimilation of satellite-derived humidity can improve the equitable threat score (ETS) of the forecasted sea fog area by about 15% for the widespread-fog case, while the WRF model completely fails to reproduce the sea fog event without the assimilation of satellite-derived humidity for the narrowly spread coastal case. Additionally, the W14 method was applied on extra 10 sea fog cases for evaluation, and the result showed that ETS was improved by nearly 72% on average.

However, Wang et al. (2014) pointed out that the dry bias was over-corrected in some sea fog cases, that is, humidity increased excessively in the assimilation of satellite-derived humidity by using the W14 method, resulting in a large wet bias and sequentially over-forecasting fog area. In the W14 method, the satellite-derived humidity is relative humidity (RH), and it has to be converted into specific humidity (Qv; an acceptable variable in the WRF-3DVAR). During the conversion, pressure and temperature are needed, and they are extracted from the background analysis in the 3DVAR where sea fog might not exist and the temperature is higher than the SST. For a typical advection sea fog over the Yellow Sea, the temperature profile is near neutral once the sea fog grows up to some extent (Gao et al., 2007), indicating that the temperature within the sea fog is near the SST. This means that the given temperature during the conversion of RH to Qv in the W14 method is overestimated, resulting in Qv being overestimated because warmer air is able to hold more water vapor. This is most likely the reason why a large wet bias is produced by the W14 method in some sea fog cases.

The purpose of this study is to propose a revised version based on the W14 method (called revised method) to improve the W14 method to correct its false wet bias by adding temperature constraints, which is based on the existing mechanism research on sea fog over the Yellow Sea (Wang, 1985; Gao et al., 2007; Yang and Gao, 2020). The remaining article is organized as follows. Section 2 introduces the W14 method briefly, and describes the proposal of improving the W14 method. In Section 3, numerical experiments on 10 sea fog cases over the Yellow Sea are conducted, including data, model configuration, and experimental design. The evaluation of the data assimilation effect by using the revised method is implemented in Section 4. In addition, Section 5 studies a case in detail to analyze the impact of the temperature constraint added in the W14 method. Finally, a summary is given in Section 6.

2 Assimilation method

2.1 Brief review of the W14 method

The W14 method aims at the operational forecast of the sea fog over the Yellow Sea (Wang et al., 2014). Its idea is that if part of the sea fog has been formed in the assimilation window of the forecast, its three-dimensional space (3D-Space) can be obtained by satellite inversion. Assuming that the RH of the fog patch is 100%, then 3DVAR assimilation of the RH is conducted to improve the initial condition of sea fog forecast.

Based on previous studies (Ellrod 1995; Heidinger and Stephens, 2000; Bendix et al., 2005; Liu and Hu, 2008; Gao et al., 2009; Fu et al., 2011), Wang et al. (2014) developed a detection algorithm for sea fog over the Yellow Sea to obtain its 3D space using geostationary satellite data, including horizontal area and thickness (see details in the Section 2 of their article). The 3D-space is discretized into numerous humidity profiles with given horizontal and vertical grid intervals (ΔX and ΔZ). Since the air in the fog is saturated or nearly saturated (Sorli et al., 2002; Kim and Yum, 2010), the RH within the fog layers is assumed to be 100%. In Figure 2A, the schematic diagram of this discretization is demonstrated, and the thick dashed line shows a humidity profile with the variables P (pressure), T (temperature), Z (height), and RH with a value of 100%. Thereafter, the humidity profile is denoted by the sea fog humidity sounding. The value of Z is determined from the retrieval algorithm for sea fog with ΔZ. However, P and T have to be extracted from the analysis in the WRF-3DVAR.

The extended cycling 3DVAR scheme used in the W14 method is based on the work by Gao et al. (2010). The entire 3DVAR assimilation process sequentially consists of several 3DVAR updates in the assimilation window, among which Wang et al. (2014) extend a 3DVAR update from one run to two runs. Figure 2B shows this extension marked by a dashed frame. In Figure 2B, OBS represents routine observations (surface measurements and radiosondes) and a few satellite-retrieved temperature and humidity profiles, while MTSAT-RH refers to sea fog humidity soundings in Figure 2A. It can be seen that the analysis from the first 3DVAR run produces a background field for the second 3DVAR run, especially the required P (pressure) and T (temperature) information for MTSAT-RH.

2.2 Proposal of the revised method

For a typical advection fog over the Yellow Sea, there is a version layer in the MABL prior to fog formation (i.e., warm fog

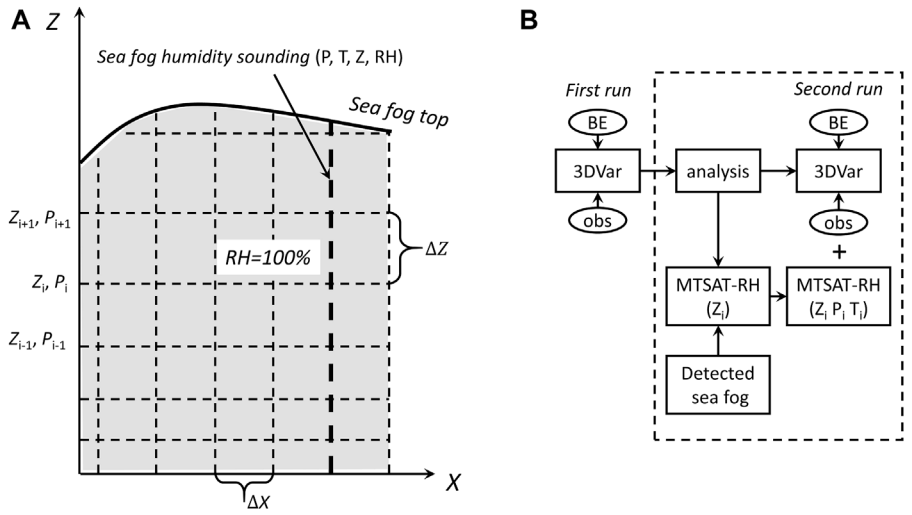

FIGURE 2
Schematic diagram for the two major ingredients of the W14 method: **(A)** sampling extraction of sea fog humidity sounding (i.e., MTSAT-RH) from the discretization of the observed fog area and **(B)** extension of one WRF-3DVAR update from running once to running twice for providing the MTSAT-RH with P (pressure) and T (temperature) from the analysis of the first run and then assimilating the MTSAT-RH. See the text for details.

phase), and the inversion layer gradually deforms into a neutral stratification due to the sea surface cooling (Lewis et al., 2003; Gao et al., 2007). With the increase of sea fog thickness, the long-wave radiation cooling at the fog top results in top-down turbulence mixing (Koračin et al., 2014; Yang and Gao, 2020), causing the temperature in the fog to fall lower than SST (i.e., cold fog phase). The warm and cold fog phases are often observed (Kim and Yum, 2012; Huang et al., 2015; Yang et al., 2018; Yang and Gao, 2020). The physics process of sea fog evolution shows that the temperature profiles inside and outside sea fog are obviously different.

As mentioned in the introduction, in some sea fog cases, the W14 method over-corrected the dry bias of the MABL moisture status and even caused a large wet bias, resulting in the forecast of a false sea fog. According to the assimilation scheme of MTSAT-RH in Figure 2B, we infer that this is due to the use of incorrect temperature information in the assimilation. In the W14 method, the temperature given to MTSAT-RH (humidity sounding in Figure 2A) is extracted from the analysis of the first 3DVAR run. If the analysis has no sea fog in the detected fog layers, the given temperature is not consistent with sea fog physics. This is a defect of the W14 method. In addition, there is another defect. The method only detects humidity according to the detected sea fog, regardless of the wrong humidity result from the false sea fog forecast in the DA window. Therefore, we improve the W14 method here, adding a reasonable temperature constraint to make the assimilation of MTSAT-RH physically coordinated. Furthermore, we also deal with the false fog area generated in assimilation process.

Figure 3A shows a comparison diagram of the observed sea fog and simulated sea fog in the analysis produced by the first 3DVAR run (Figure 2B). The observed sea fog is the sea fog detected by the detection algorithm in the W14 method, while the simulated sea fog is defined by the areas where the simulated cloud–water mixing ratio is ≥0.016 g kg^{-1} and the fog height is limited ≤400 m (Gao et al., 2010; Zhou and Du, 2010; Wang et al., 2014). In Figure 2B, "hit" denotes the area where both the observed sea fog and simulated sea fog exist, "false" denotes the area where the simulated sea fog exists but the observed sea fog does not, and "miss" denotes the area where the observed sea fog exists but the simulated sea fog does not (hereafter, these fog areas are called hit fog, false fog, and missed fog, respectively). The corresponding temperature profiles are also presented according to the previous research studies (Gao et al., 2007; Yang et al., 2018; Yang and Gao, 2020). The profiles T_c, T_f, T_h, and T_m indicate the temperature profiles within the areas of clear air, false fog, hit fog, and missed fog, respectively.

The focus to improve the W14 method is on the areas of missed fog and false fog, that is, adding a temperature constraint to these areas by the following operations:

$$T_m(i_m, j_m, k_m) = SST(i_m, j_m) + [SAT(i_h, j_h) - SST(i_h, j_h)], \quad (1)$$

$$T_f(i_f, j_f, k_f) = SST(i_f, j_f) + [T(i_c, j_c, k_f) - SST(i_c, j_c)] \quad (2)$$

where *SAT* is the simulated sea surface air temperature; i, j, and k represent model horizontal grid (i, j) and vertical grid (k), respectively; (i_m, j_m, k_m) denotes a point within the missed fog area; and (i_h, j_h) denotes the nearest point in the hit fog. (i_f, j_f, k_f) denotes a point within the false fog area, and (i_c, j_c) denotes the nearest point in the clear air area.

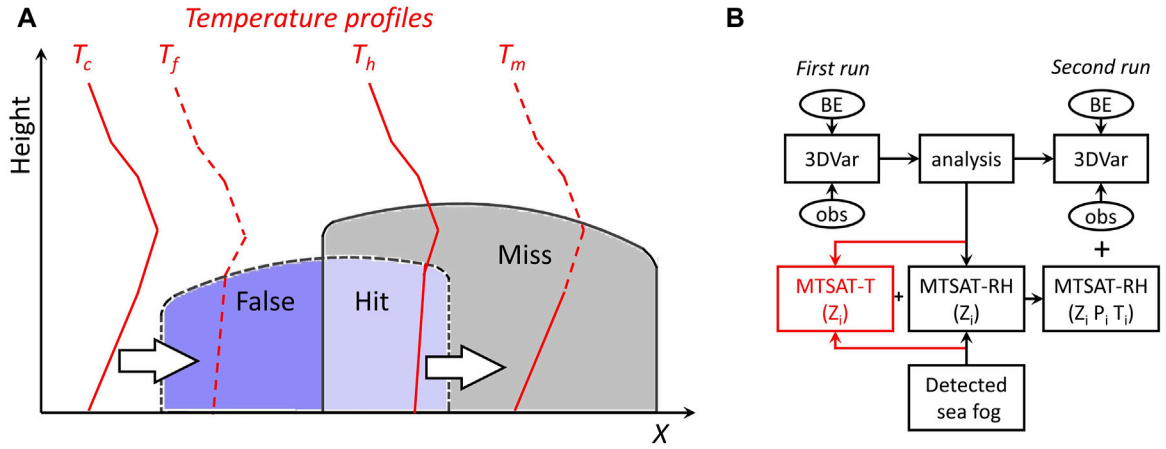

FIGURE 3
Schematic diagram of the revised method with the temperature constraint: **(A)** typical temperature profiles within the areas of clear air (T_c), false fog (T_f), hitting fog (T_h), and missed fog (T_m); **(B)** assimilation of sea fog humidity soundings in one 3DVAR update, including the temperature constraint (see the part marked in red color). See details in the text.

As seen from Eq. 1, within missed fog, T_m is re-assigned based on SST and the air–sea temperature contrast within the hit fog area, and the profile is vertically homogeneous (T_m does not vary with k_m; see Figure 3A). It can make the MABL of the missed fog area cooler and neutral, which is conducive to sea fog forming; whereas, within the false fog area, T_f is replaced by a temperature profile with the vertical structure within the nearest clear air area (Eq. 2), which helps the dissipation of false fog because this clear-air temperature profile is warmer than that of the false fog area.

The aforementioned improvement process is modularized and inserted into the codes of the W14 method (see the part marked by red color in Figure 3B). Theoretically, the new method should be better than the original version because it considers the improvements of both missed fog and false fog areas. In the following sections, we carefully evaluate the revised method by numerical experiments on 10 sea fog cases over the Yellow Sea.

3 Numerical experiments

3.1 Data

The National Centers for Environmental Prediction (NCEP) Final Analysis (FNL) (1° × 1°; six hourly) provided initial and lateral boundary conditions for the simulation, and the SST data as the model bottom condition were derived from datasets of the North-East Asian Regional Global Ocean Observing System (NEAR-GOOS) (0.25° × 0.25°; daily).

Observations (i.e., obs in Figure 2B) used for assimilation in this study were downloaded from NCEP, including routine observations (surface, buoy, island measurements, and radiosondes), and some temperature and humidity profiles were retrieved from the atmospheric infra-red sounder (AIRS). Additionally, the detection algorithm for sea fog over the Yellow Sea used hourly albedo, infrared and visible cloud images of the MTSAT satellite.

Surface synoptic charts from the Korea Meteorological Administration (KMA) were used to show the weather situation involved with sea fog. The evaluation of the forecast using the precipitable water (PW; also called the columnar atmospheric water vapor) dataset (0.25° × 0.25°) was derived from satellite-bone microwave images, including the special sensor microwave imager (SSM/I), the special sensor microwave imager sounder (SSMIS), the advanced microwave scanning radiometer-E (AMSR-E), and the tropical rainfall measuring mission (TRMM) microwave imager (TMI). These satellite datasets were provided with quality control by remote sensing systems (RSS).

3.2 Model configuration

The advanced research core of the WRF with its WRFDA module (version 3.5.1; Skamarock et al., 2008) was employed for numerical experiments in this study. Two-way nesting was designed with the outer domain (D1; 30 km × 30 km) covering the northwest Pacific and most regions of East Asia and the inner domain (D2; 10 km × 10 km) over the entire Yellow Sea (Figure 1). Previous studies (Lu et al., 2014) have shown that the optimum combination of parameterizations for modeling of the Yellow Sea fog is the YSU PBL (Hong et al., 2006; Hong 2010) scheme and the Purdue Lin microphysics scheme (Lin et al.,

TABLE 1 WRF configuration.

Model setting and option	Specification
Map projection	Lambert
Central point	(34.2 °N, 124.1 °E)
Domain Grid number	166 × 190 for D1, 120 × 120 for D2
Horizontal resolution	30 km for D1, 10 km for D2
Vertical grid	44 η^* with a pressure top at 50 hPa
Time step	Adaptive time step (60–90 s for D1)
PBL scheme	YSU scheme (Hong et al., 2006)
Cumulus parameterization	Kain–Fritsch scheme (Kain and Fritsch 1990)
Microphysics	Lin (Perdue) scheme (Lin et al., 1983)
Long/shortwave radiation	RRTMG scheme (Iacono et al., 2008)
Land surface model	Noah model (Chen and Dudhia 2001)

*η = 1.0000, 0.9975, 0.9925, 0.9850, 0.9775, 0.9700, 0.9540, 0.9340, 0.9090, 0.8800, 0.8506, 0.8212, 0.7918, 0.7625, 0.7084, 0.6573, 0.6090, 0.5634, 0.5204, 0.4798, 0.4415, 0.4055, 0.3716, 0.3397, 0.3097, 0.2815,0.2551, 0.2303, 0.2071, 0.1854, 0.1651, 0.1461, 0.1284, 0.1118, 0.0965, 0.0822, 0.0689, 0.0566, 0.0452,0.0346, 0.0249, 0.0159, 0.0076, and 0.0000.

1983);thus, YSU and Lin schemes were used in this study. The detailed model configurations were listed in Table 1.

The 3DVAR update used the default observation errors for assimilating different observations. The National Meteorology Center (NMC) method (Parrish and Derber, 1992) was adopted to generate a domain-dependent BE covariance for 3DVAR update. For each sea fog case, the WRF model was initialized every 12 h and ran 24 h for 15 days centered by the forecast initial time, and BE covariance was approximated by the average differences between 12-h and 24-h forecasts:

$$\mathrm{BE} \approx \overline{(\mathbf{x}^{12}-\mathbf{x}^{24})(\mathbf{x}^{12}-\mathbf{x}^{24})^{\mathrm{T}}}, \quad (3)$$

where $\mathbf{x}^{12}$ and $\mathbf{x}^{24}$ are 12-h and 24-h forecasts, respectively. The control variables in BE include stream function, velocity potential, temperature, surface pressure, and pseudo-RH. Since the cross-correlations among control variables is important to sea fog modeling (Gao and Gao 2020), in the case study of Section 5, we compared the impacts of two kinds of BE covariances (CV5 and CV6) defined by the WRFDA module. The correlations between moisture (i.e., pseudo-RH) and other control variables exist in CV6, but not in CV5. These correlations might amplify the impact of temperature correction in the revised W14 method.

3.3 Experimental design

Three groups of numerical forecast experiments (hereafter called Group-A, Group-B, and Group-C) were designed and conducted for 10 sea fog cases. All the groups share the same model configuration listed in Table 1. All forecast experiments ran 24-h forecasts with 12-h data assimilation (DA) windows before the initial time (LST, =UTC+8). In the 12-h DA window, the 3DVAR update cycled five times with a DA interval of 3 h.

In Group-A, only obs was assimilated. Both obs and MTSAT-RH were assimilated in the other two groups. The DA in Group-B was treated with the W14 method, whereas Group-C was treated with the revised method. All the groups employed CV5 BE covariance, which is widely applied in operational forecast. Note that the ten cases and experimental design for Group-A and Group-B are the same as those in the article of Wang et al. (2014), except that the ARW version was changed from 3.3 to 3.5.1.

The purpose of the experiments is to show whether the temperature constraint (Group-C) can further improve the results, given that forecast with the W14 method (Group-B) is already quite successful. We are also concerned about whether the W14 method is still effective when updating the model version.

4 Numerical experiments

4.1 Evaluation method

The most important aspect of sea fog forecast is the horizontal fog area (abbreviated as fog area). The fog area detected by the detection algorithm in the W14 method is called the observed fog area, while the fog area diagnosed from the WRF hourly output is called the simulated fog area (see Section 2.1 for its diagnostic method). The observed and simulated fog areas are produced hourly, and their spatial resolution are 4 and 10 km, respectively.

To quantitatively evaluate the effects of the revised method, a series of prediction statistics were calculated for each experiment based on the comparison between simulated and observed fog areas (Zhou and Du, 2010). The inner domain (i.e., D2 in Figure 1) was taken as the evaluation domain, and its grid

TABLE 2 Statistical scores for 10 cases. Bold numbers in parentheses for Group-B show the improvements (%) relative to Group-A, while those for Group-C show the improvements relative to Group-B.

Case	Group-A (only obs assimilated without the W14 method)				Group-B (obs and MTSAT-RH assimilated by the W14 method)				Group-C (obs and MTSAT-RH assimilated by the revised method)			
No. Initial time (yyyy-mm-dd_hh)	POD	FAR	BS	ETS	POD	FAR	BS	ETS	POD	FAR	BS	ETS
1.2012–05–09_20	0.392	0.358	0.610	0.191	0.859 (**119**)	0.515 (**−24.5**)	1.771 (**−97.7**)	0.216 (**13.1**)	0.738 (**−14.1**)	0.431 (**17.3**)	1.296 (**61.6**)	0.282 (**30.6**)
2.2009–04–09_20	0.055	0.608	0.141	0.028	0.677 (**1,131**)	0.321 (**73.2**)	0.996 (**99.5**)	0.434 (**145**)	0.732 (**8.1**)	0.272 (**−7.2**)	1.005 (**−25**)	0.502 (**15.7**)
3.2008–04–28_20	0.386	0.475	0.735	0.097	0.709 (**83.7**)	0.361 (**21.7**)	1.111 (**58.1**)	0.289 (**197.9**)	0.751 (**5.9**)	0.331 (**4.7**)	1.123 (**−10.8**)	0.338 (**17.0**)
4.2012–03–27_20	0.304	0.523	0.638	0.173	0.651 (**114**)	0.505 (**3.8**)	1.314 (**13.3**)	0.316 (**82.7**)	0.669 (**2.8**)	0.461 (**8.9**)	1.242 (**22.9**)	0.354 (**12.0**)
5.2010–02–22_20	0.675	0.340	1.123	0.279	0.955 (**41.5**)	0.385 (**−6.8**)	1.552 (**−349**)	0.335 (**20.1**)	0.939 (**−1.7**)	0.368 (**2.8**)	1.487 (**11.8**)	0.356 (**6.3**)
6.2007–02–05_20	0.493	0.506	0.989	0.250	0.582 (**18.1**)	0.474 (**6.5**)	1.106 (**−864**)	0.303 (**21.2**)	0.602 (**3.4**)	0.450 (**4.6**)	1.094 (**11.3**)	0.326 (**7.6**)
7.2010–04–04_20	0.489	0.219	0.626	0.157	0.756 (**54.6**)	0.310 (**−11.7**)	1.096 (**74.3**)	0.161 (**2.5**)	0.773 (**2.2**)	0.303 (**1.0**)	1.108 (**−12.5**)	0.177 (**9.9**)
8.2011–03–12_20	0.640	0.490	1.253	0.195	0.733 (**14.5**)	0.483 (**1.4**)	1.417 (**−64.8**)	0.225 (**15.4**)	0.849 (**15.8**)	0.487 (**−0.8**)	1.655 (**−57.1**)	0.248 (**10.2**)
9.2011–05–17_08	0.708	0.177	0.861	0.527	0.971 (**37.1**)	0.365 (**−22.8**)	1.687 (**−394**)	0.545 (**3.4**)	0.953 (**−1.9**)	0.323 (**6.6**)	1.555 (**19.2**)	0.597 (**9.5**)
10.2009–05–02_20	0.940	0.344	1.433	0.457	0.873 (**−7.1**)	0.360 (**−2.4**)	1.364 (**15.9**)	0.407 (**−10.9**)	0.937 (**7.3**)	0.292 (**10.6**)	1.324 (**11.0**)	0.527 (**29.5**)
Average	0.508	0.404	0.841	0.235	0.777 (**53.0**)	0.408 (**−0.7**)	1.341 (**−114**)	0.323 (**37.5**)	0.794 (**2.2**)	0.372 (**6.1**)	1.289 (**15.2**)	0.371 (**14.9**)

size was set to 0.1°. Both fog areas were meshed onto the grids of the evaluation domain, and point-to-point comparisons were conducted. Note that both the land and sea areas covered by high-altitude clouds were excluded from the evaluation domain. The statistical scores include probability of detection (POD), false alarm ratio (FAR), bias score (BS), and equitable threat score (ETS), which are defined as

$$\mathrm{POD} = \frac{H}{O}, \tag{4}$$

$$\mathrm{FAR} = \frac{F-H}{F}, \tag{5}$$

$$\mathrm{BS} = \frac{F}{O} \tag{6}$$

$$\mathrm{ETS} = \frac{H-R}{F+O-H-R} \tag{7}$$

where H, F, and O denote the numbers of hit points, forecasted fogy points, and observed foggy points, respectively. $R=F(O/N)$ is a random hit penalty, where N is the total number of grid points.

The radiosonde observations at seven coastal stations (shown in Figure 1) were used to evaluate the forecasted temperature and humidity profiles. Model results were interpolated to the pressure levels of the soundings, and the average bias and root-mean-square-error (RMSE) are calculated by

$$\mathrm{bias} = \frac{1}{n}\sum_{i=1}^{n}(x_i - y_i), \tag{8}$$

$$\mathrm{RMSE} = \sqrt{\frac{1}{n}\sum_{i=1}^{n}(x_i - y_i)^2}, \tag{9}$$

where n is the number of stations, and x_i/y_i is the forecasted/observed variable.

4.2 Effect analysis

The hourly simulated fog areas of the 10 sea fog cases were compared with the observed fog area. Table 2 shows the time averages of the statistical scores for all of the experiments.

It can be seen from Table 2 that the POD, FAR, BS, and ETS scores averaged over the 10 sea fog cases for Group-A which assimilate obs only are 0.508, 0.404, 0.841, and 0.235,

respectively; by further assimilating MTSAT-RH using the W14 method, Group-B gets the scores of 0.777, 0.408, 1.341, and 0.323, respectively. This shows that the W14 method is effective, which improves POD and ETS by 53.0% and 37.5%, respectively. However, the BS increases for all cases, ranging from 0.834 to 1.341, indicating that the W14 method enlarges the simulated fog area. This helps greatly improve the situation where the sea fog forecast has almost failed (e.g., Case 2 and Case 3), but may reduce the situation where it is somewhat overestimated (e.g., Case 10). Note that for the same 10 cases, Wang et al. (2014) reported that the improvements of POD and ETS by using the W14 method are 60% and 70%, respectively. This study used the same experimental designs as them except using a newer version of the WRF model with an updated YSU scheme. The lower improvements here (53.0% and 37.5% for POD and ETS) are probably attributable to the revision of the YSU scheme. The turbulent diffusion within stable PBL is weakened in the YSU scheme of the WRF version newer than 3.4.1 (Hu et al., 2013). It helps to reduce the vertical diffusion of moisture and is conducive to sea fog formation. As a result, Group-A has a much better performance in this study than that in Wang et al. (2014), making the improvement by the W14 method less significant.

Compared to Group-B using the W14 method, the average statistical scores of Group-C using the revised method are improved significantly. In particular, the BS is reduced from 1.341 to 1.289 with an improvement of 15.2%, resulting in an improvement of 14.9% for ETS. The BS of case 1 is 1.771 in Group-B, whereas it is 1.296 in Group-C. In Group-A, ETS of case 10 is 0.457, but it gets worse in Group-B with a value of 0.407, resulting from the increase of the false fog area and the decrease of the hit fog area (cf. Group-A and Group-B for POD and FAR, respectively). The temperature constraint in the revised method for both of the miss- and false-fog areas did work for case 10, resulting in lower FAR (0.292) and then higher ETS (0.527) in Group-C. Table 2 demonstrates that the relative improvement rates of ETS for all cases in Group-C are positive, which indicates that the introduction of a temperature constraint into the W14 method can alleviate the overestimation of sea fog forecast to some extent.

The 12-h forecast profiles of temperature and mixing ratio within the MABL were compared with the coastal radiosonde observations (see their sites in Figure 1). Figures 4A, B show the result of average mixing ratio and temperature at all sites of all cases, demonstrating that the biases of both temperature and mixing ratio for Group-C have the smallest values compared with Group-A and Group-B, as well as the RMSEs. It apparently shows that Group-A has a warm–dry bias within the MABL (red lines), and the warm–dry bias is reduced in Group-B (green lines) and further reduced in Group-C (blue lines). Compared with Group-B, for Group-C below 900 hPa, the RMSEs of temperature and mixing ratio decrease by about 0.4 K and 0.2 g kg^{-1}, respectively; and maximum biases of temperature and mixing ratio are improved by about 0.3 K and 0.05 g kg^{-1}. Figure 4C shows the bias of mixing ratio averaged from the surface to 850 hPa for each case. Among the 10 cases, there still exists dry bias for 7 cases after assimilation of obs (Group-A), except for cases 2, 8, and 10. This dry bias is alleviated to a certain extent by the W14 and revised methods. Especially, the revised method greatly inhibits the growth of wet bias by the W14 method in cases 8 and 10.

These aforementioned results are in line with our idea for the proposal of the revised method. Although it performs better than the W14 method, for some cases, the extent of its improvement is still not very satisfactory. For instance, the BS of cases 5, 8, and 9 are 1.487, 1.655, and 1.555, respectively (Table 2). Next, we take case 3 as an example to discuss the working mechanism of the revised method. Case 3 is chosen because it has the largest dry bias after assimilating obs only and the effect of the revised method relative to the W14 method is not obvious (Figure 4C).

5 Case study

5.1 Sensitivity experiments

Sea fog of case 3 is a typical advection fog that began to occur over the junction of the Yellow Sea and East China Sea under the control of high pressure in the evening of 28 April, 2008 (Figure 5A). The Yellow Sea was dominated by weak southerly winds, and high pressure changed little until the next morning (figure not shown), transporting the warm moist air mass northward to promote sea fog developing northward (Figure 5B; nighttime fog was detected by the algorithm in the W14 method). Till 2000, LST 29 April, the high pressure strengthened and moved eastward slightly, and the sea fog almost occupied the entire Yellow Sea and bordered on the west bank of the Korean Peninsula. (Figures 5C,D). The detailed evolution of the sea fog is shown in Figure 6 (see the first row; daytime fog is directly denoted by visible images). Forced by the intensified pressure gradient, the southerly wind became stronger, and then dissipated the south part of the fog patch.

As mentioned in Section 3.2 about BE (CV5 and CV6), the multivariate cross-correlations among control variables in BE are important to sea fog modeling (Gao and Gao 2020). The aforementioned experiments employed CV5, which has no cross-correlation between moisture and other control variables, such as temperature. In the revised method, the added temperature constraint is mainly used for better conversion of RH to Qv. If CV5 is used, assimilations of moisture (QV) and temperature are completed independently. On the contrary, if CV6 is used, assimilation of temperature can directly affect humidity. Therefore, we further conducted three sensitivity experiments: Exp-Ob6, Exp-ObRH6, and Exp-ObRHT6. Note that the letters Ob and RH and the number six in these experimental names denote the assimilation of obs,

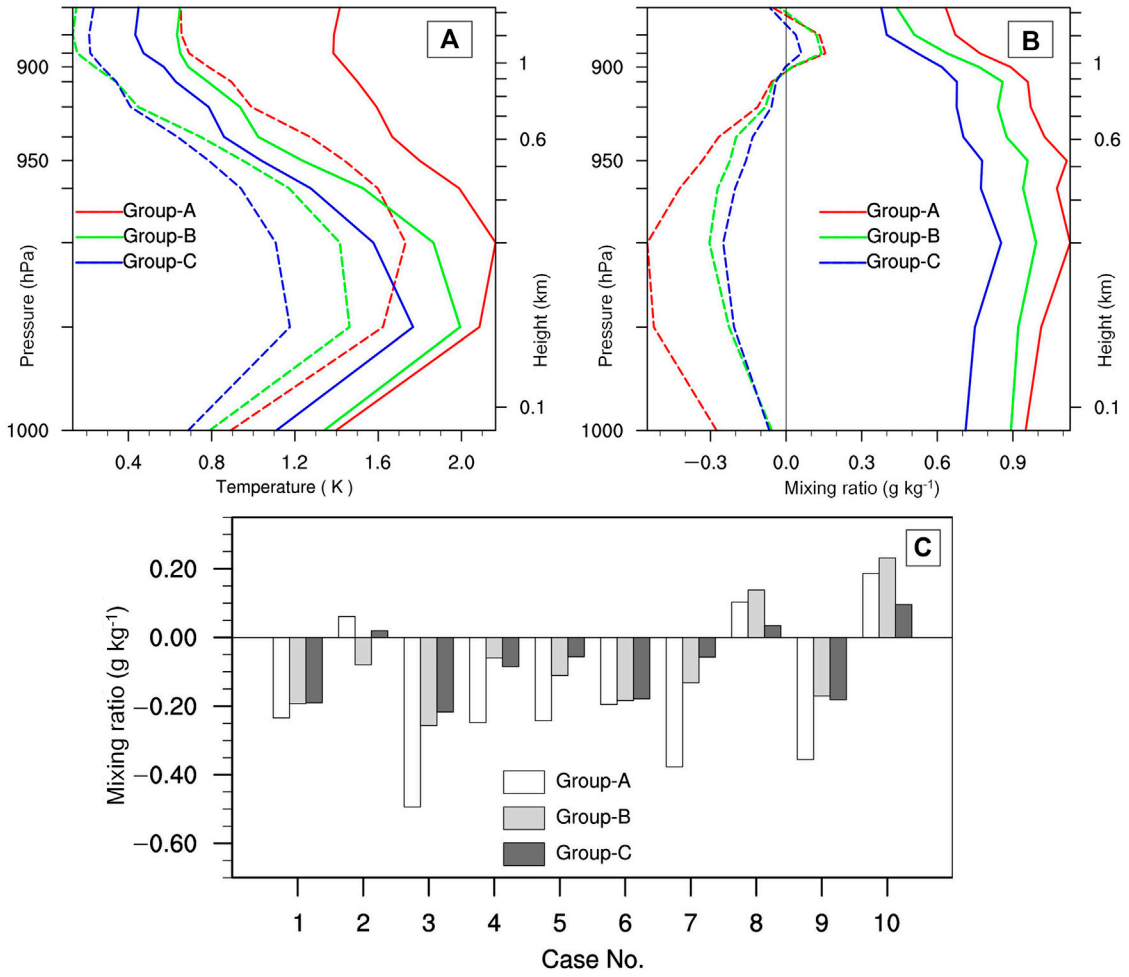

FIGURE 4
Average vertical profiles of the RMSE (solid lines) and biases (dash lines) between the 12-h forecast and the radiosonde observations in Figure 1 for **(A)** temperature, **(B)** mixing ratio, and **(C)** the bias of the mixing ratio profiles averaged from the surface to 850 hPa for the 10 cases.

assimilation of MTSAT-RH, and employment of CV6 in the experiments, respectively. Similarly, the experiments for case 3 in Group-A, Group-B, and Group-C are named as Exp-Ob5, Exp-ObRH5, and Exp-ObRHT5, respectively.

5.2 Results analysis

5.2.1 Simulated fog area

The simulated fog areas of the sensitivity experiments were evaluated. Table 3 shows the statistical scores of POD, FAR, BS, and ETS. For comparison, the results of Exp-Ob5, Exp-ObRH5, and Exp-ObRHT5 are also shown in Table 3.

As shown in Table 3, POD for Exp-Ob5 is only 0.386 and its BS is 0.735, indicating that the simulated fog area is about 25% smaller than the observed one. Because of the assimilation of MTSAT-RH, all the four scores improved in Exp-ObRH5, for example, POD increased up to 0.709 and BS changed to 1.111, meaning that the simulated fog area was about 11% larger than the observed one. ETS of Exp-ObRHT5 improved by 17% relative to Exp-ObRH5, resulting from the temperature constraint. However, BS of Exp-ObRHT5 got worse relative to Exp-ObRH5. For those experiments with CV6, all scores of Exp-ObRH6 were significantly better than those of Exp-Ob6, and so is Exp-ObRHT6 relative to Exp-ObRH6. ETS of Exp-Ob5 is dramatically raised from 0.097 to 0.445 in Exp-ObRHT6, owing to benefits from the assimilation of MTSAT-RH using CV6 with the temperature constraint. The BS deterioration of Exp-ObRHT5 relative to Exp-ObRH5 does not occur in the similar experiments with CV6. Results of Table 3 indicate that the revised method with CV6 performs much better than with CV5, and the relative improvement rate reaches 45%.

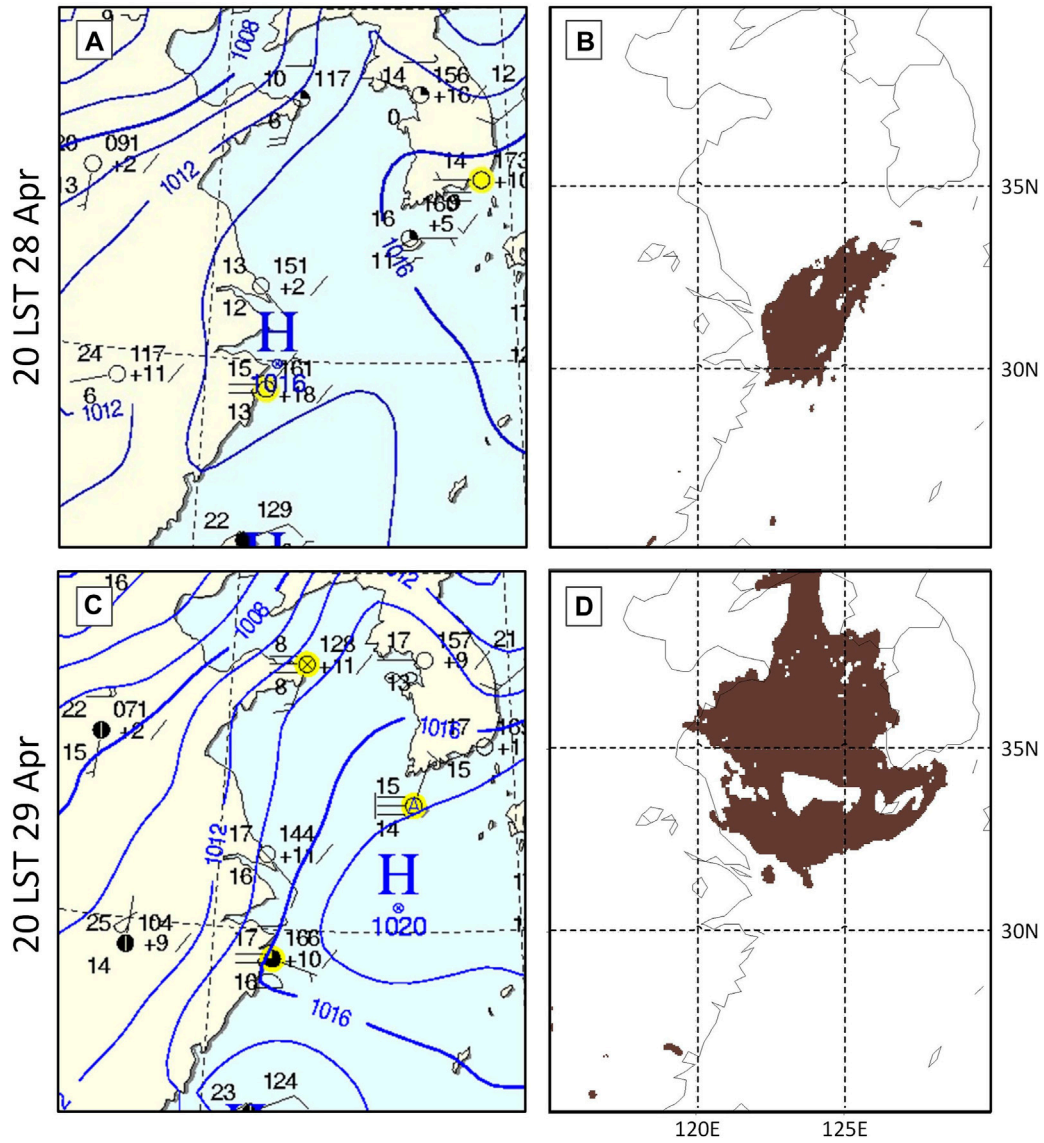

FIGURE 5
Surface synoptic chart (left; **(A,C)** and MTSAT-detected fog patch (right; **(B,D)** at 20 LST 28 April 2008 (upper; **(A,B)** and 20 LST 29 April 2008 later (bottom; **(C,D)**.

Figure 6 presents the comparison between the observed fog area and simulated fog area. The observed fact (the first row in Figure 6) shows that the sea fog formed over the southern Yellow Sea with a small patch (Figure 6A), slowly extending northward and then almost covering the entire Yellow Sea (Figures 6aB–aE). At the same time, the southern part of the sea fog retreated slightly northward (Figure 6aF). This evolution process is basically captured by all experiments (cf. the first row and the other rows in Figure 6). The simulation effect of Exp-ObRHT6 is the best because both the northward expansion of the fog area and the contraction of its southern part are the closest to the observed facts (cf. the panels of the rightmost column in Figure 6).

Compared with the observed fog area at 2000 LST 28 April (Figure 6A), there was a large proportion of spurious fog in the simulated fog area of the experiments with CV5. The spurious fog did not disappear in the next 3 h (e.g., Figure 6dB). By comparison, the experiments with CV6 had obviously different simulated fog areas at 2000 LST 28 April (e.g., Figure 6eA). In Exp-Ob6 and Exp-ObRH6, the fog area included two patches, among which the patch marked with B was literally spurious (Figures 6eA, fA). However, this spurious

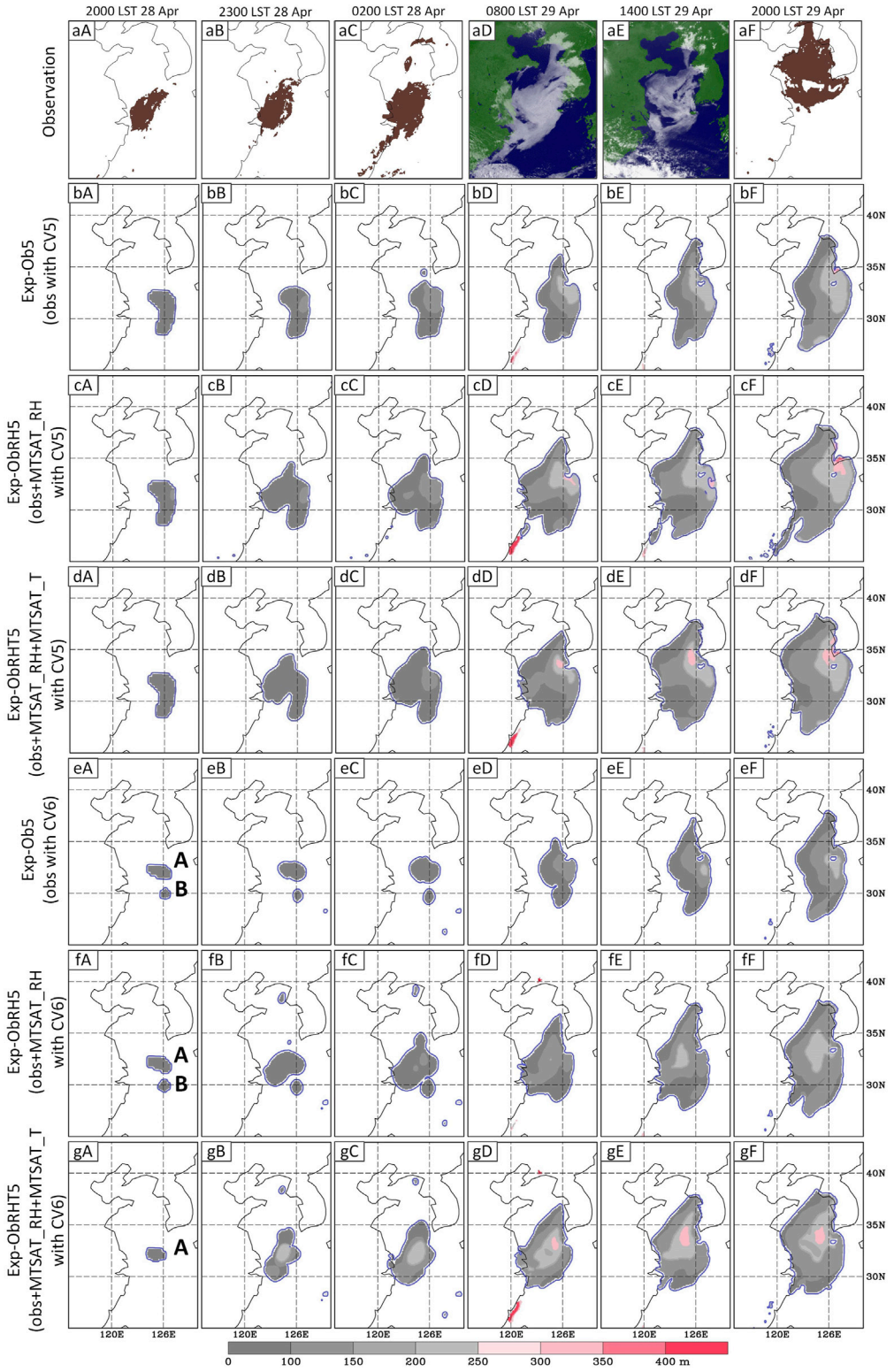

FIGURE 6
Comparison between the observed and simulated fog areas. Time for each column is placed on the top. The first row is the satellite-observed sea fog, among which MTSAT-visible cloud images are used for daytime fog and the MTSAT-derived fog area with thickness height denotes nighttime fog. The second to seventh rows show the simulated fog area with thickness for the experiments where names are given on the left marginal side. The fog patches marked with A in (eA), (fA), and (gA) are related to the hit fog area, while the patches marked with B in (eA) and (fA) are literally spurious. These patches are referred in detail in Section 5.2.1.

TABLE 3 Statistical scores for each experiment in the case study. Numbers in parentheses for Exp-ObRH5/6 show the improvements (%) relative to Exp-Ob5/6, while those for Exp-ObRHT5/6 show the improvements relative to Exp-ObRH5/6.

Scores	Experiments with CV5			Experiments with CV6		
	Ob5	ObRH5	ObRHT5	Ob6	ObRH6	ObRHT6
POD	0.386	0.709 (**83.7**)	0.751 (**5.9**)	0.303	0.609 (**101.0**)	0.710 (**16.6**)
FAR	0.475	0.361 (**21.7**)	0.331 (**4.7**)	0.387	0.285 (**16.6**)	0.195 (**12.6**)
BS	0.735	1.111 (**58.1**)	1.123 (**−10.8**)	0.495	0.851 (**70.5**)	0.882 (**20.8**)
ETS	0.097	0.289 (**197.9**)	0.338 (**17.0**)	0.113	0.307 (**171.7**)	0.445 (**45.0**)

patch did not exist in Exp-ObRHT6 (Figure 6gA). Within the next 3 h, the patch marked with A of Exp-ObRHT6 gradually grew, and its shape was very close to that of the observed fog area (cf. Figures 6gB and 6aB), and the subsequent sea fog was also closer to the observed fact than all the other experiments (e.g., the third column in Figure 6). It indicates that the revised method needs to cooperate with CV6 to have better effect.

5.2.2 Structure of the marine atmospheric boundary layer

Similar to the analysis in Section 4.2, the 00-h and 12-h forecast bias profiles of temperature and mixing ratio within the MABL were compared with the coastal radiosonde observations (see their sites in Figure 1). Similar to the profiles in Figure 4, the comparison results demonstrated that the RMSEs of both temperature and mixing ratio for Exp-ObRH5/6 were smaller than those of Exp-Ob5/6, respectively (Figure 7), and it is the same for Exp-ObRHT5/6 relative to Exp-ObRH5/6, respectively. For intuitively and quantitatively evaluating the temperature and humidity structure of MABL simulated by the six experiments, the profiles of biases and RMSEs are averaged from 1,000 hPa to 950 hPa, and the results are listed in Table 4.

As can be seen from Table 4, compared with Exp-Ob5/6 without assimilation of MTSAT-RH, the large dry biases at 00-h forecast (i.e., initial time) in Exp-ObH5/6 are reduced by nearly 50% (from −1.01 g kg^{-1} to −0.58 g kg^{-1} for Exp-ObH5, and from −1.45 g kg^{-1}to −0.79 g kg^{-1}for Exp-ObH6), resulting in the moisture status of the MABL at 12-h forecast getting improved (e.g., −0.58 g kg^{-1} at 00-h forecast becomes 0.05 g kg^{-1} at 12-h forecast for Exp-ObRH5). The dry bias of Exp-ObHT6 is basically equivalently to that of Exp-ObHT5 at both 00-h and 12-h forecasts. Whether CV5 or CV6 is used, the RMSE of the mixing ratio of the experiment with temperature constraint is the smallest. As for the profile of temperature, at the 00-h forecast, Exp-ObRHT6 has the smallest bias and RMSE in all experiments (1.35 and 1.79 K, respectively), and the bias at the 12-h forecast is also the smallest (1.47 K). It suggests that the temperature constraint can improve the temperature and humidity structure of MABL; particularly, the usage of CV6 can further help significantly improve the temperature structure of MABL.

In addition, in order to evaluate the forecasted humidity structure over sea, we compared the PW of model results (simulated PW) with that of satellite–bone microwave image observation (observed PW). The simulated PW was interpolated onto the horizontal grids of the observed PW to facilitate point-to-point statistics. Considering the system bias of the observed PW and its retrieval algorithm, the correlation between the simulated PW and the observed PW is as important as their mean difference (i.e., bias) because it shows the model's ability to predict the pattern of water vapor. The correlation coefficient was calculated within the forecasted fog areas:

$$\rho = \frac{\frac{1}{n}\sum\left[pw_f(i,j) - \overline{pw_f}\right]\left[pw_o(i,j) - \overline{pw_o}\right]}{\sqrt{\frac{1}{n}\sum\left[pw_f(i,j) - \overline{pw_f}\right]^2}\sqrt{\frac{1}{n}\sum\left[pw_o(i,j) - \overline{pw_o}\right]^2}}, \quad (10)$$

where pw_f and pw_o are simulated and observed PW, respectively; and the sum was done at all the grid points within the simulated fog whose total number was n (missing values for observation were excluded). Figure 8 presents the mean bias (color shades) and correlation coefficient (number in bottom-left corner of each panel) of PW for all experiments. At approximately 6-h, 9-h, 10-h, and 11-h forecasts, the corresponding observed PW was provided by AMSR-E, SSM/I, SSMIS, and WindSAT, respectively.

Looking through the correlation coefficients given in Figure 8, it is found that only half of the coefficients improved in Exp-ObRH5/6 after assimilating MTSAT-RH together with obs, while all coefficients greatly increased in Exp-ObRHT5/6 with the temperature constraint (cf. the numbers in the third/sixth column and those in the first/fourth column, respectively). Through contrasting the biases (color shades), it can be seen that Exp-Ob5 and Exp-Ob6 have dry biases (see blue colors) in most of the observed fog areas (outlined by coarse lines), while small wet biases only partially existed (see red colors). At the 06-h forecast, the bias in the fog area was between −10.33 and 3.93 mm for Exp-Ob5 (Figure 8A) and between −12.33 and −0.68 mm for Exp-Ob6 (Figure 8D), and the mean value for Exp-Ob5/6 was −5.11/−7.13 mm. At the 09-h forecast, the mean bias for Exp-Ob5/

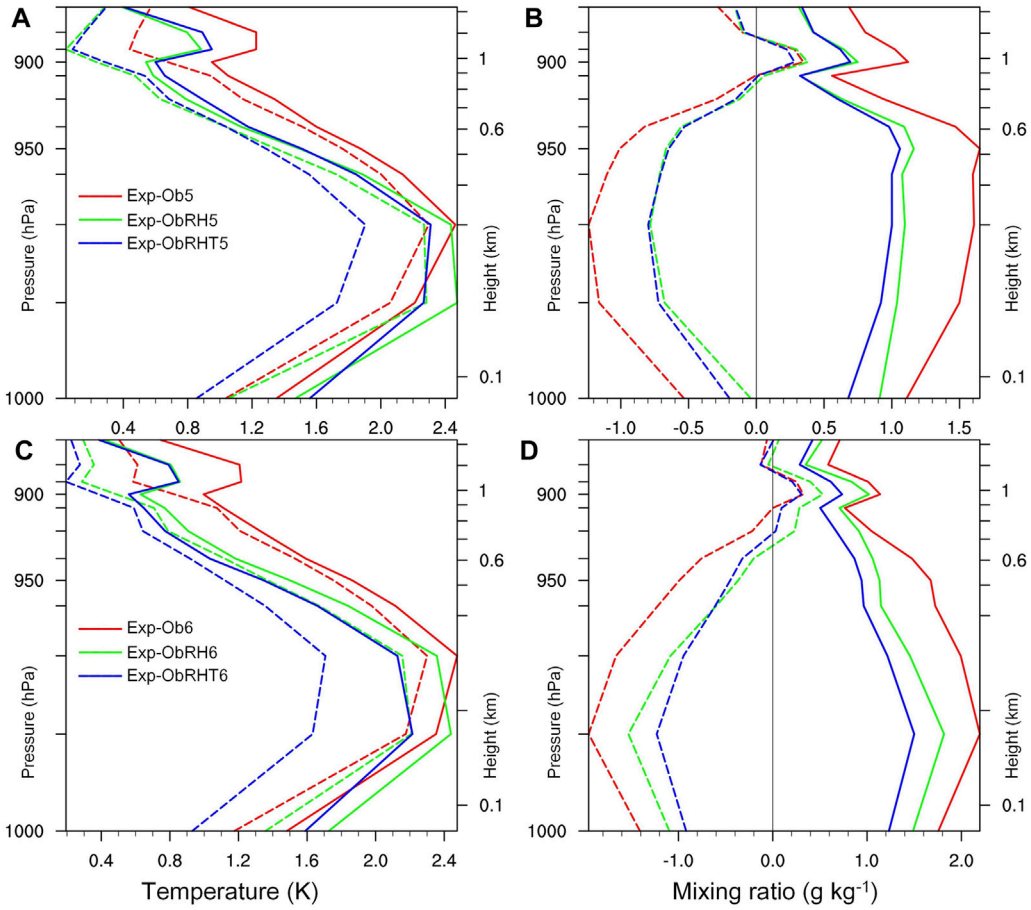

FIGURE 7
As in Figures 4A, B, the time of 2000 LST 28 April 2008 and **(A)** and **(B)** are for Exp-Ob5, Exp-ObRH5, and Exp-ObRHT5, and **(C)** and**(D)** are for Exp-Ob6, Exp-ObRH6, and Exp-ObRHT6.

TABLE 4 Average biases and RMSEs of the temperature and mixing ratio from 1,000 hPa to 950 hPa at the 00-h and 12-h forecasts for verifying against the seven radiosonde observations around the Yellow Sea (see Figure 1).

Forecast time (h)	Variables		Sensitivity experiments (Exp-*)					
			Ob5	ObRH5	ObRHT5	Ob6	ObRH6	ObRHT6
00	Temperature (K)	bias	1.83	1.74	1.47	1.88	1.75	1.35
		RMSE	2.01	1.95	1.90	2.06	1.97	1.79
	Mixing ratio (g kg^{-1})	bias	−1.01	−0.58	−0.61	−1.45	−0.79	−0.83
		RMSE	1.49	1.06	0.93	1.87	1.41	1.17
12	Temperature (K)	bias	1.96	1.78	1.60	2.17	2.01	1.47
		RMSE	2.41	2.42	2.21	2.68	2.59	2.32
	Mixing ratio (g kg^{-1})	bias	−0.42	0.05	−0.08	−0.82	−0.24	−0.33
		RMSE	1.42	1.47	1.00	1.40	1.22	1.00

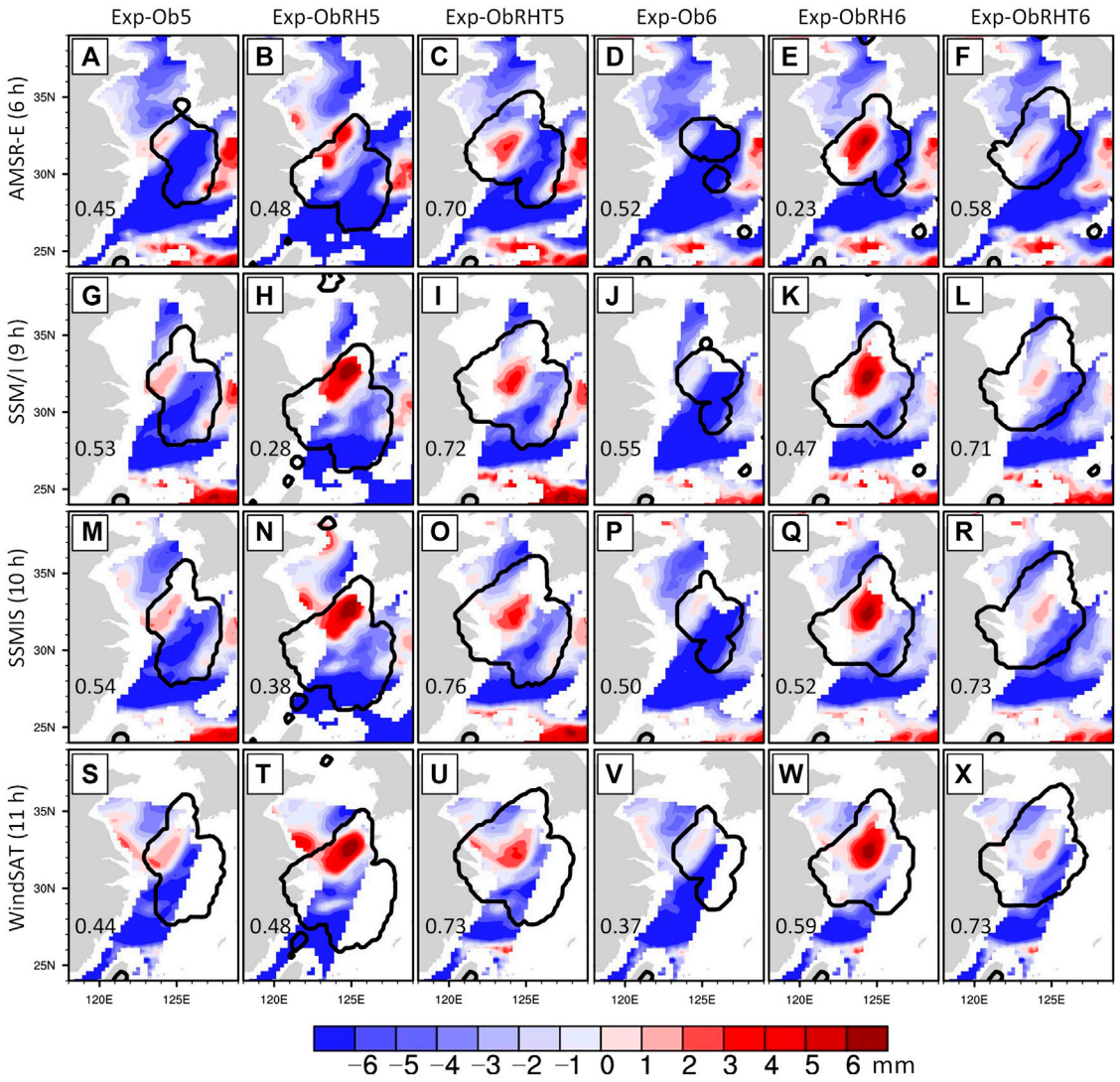

FIGURE 8
Bias (color shades) and correlation coefficient (number on the bottom-left corner of each panel) between the simulated and satellite-observed precipitable waters within the simulated fog area that is outlined by a thick black line. Experiment names are shown on the top, and forecast hours related with the satellite sensor are given on the left marginal side. Panels **(A–F)** show the comparison between Exp-Ob5, Exp-ObRH5, Exp-ObRHT5, Exp-Ob6, Exp-ObRH6, Exp-ObRHT6, and AMSR-E observation at the 6-h forecast (1400 LST 29 April), respectively. Similarly, panels **(G–L)** are for SSM/I observation at the 9-h forecast, panels **(M–R)** are for SSMIS observation at the 10-h forecast, and panels **(S–X)** are for WindSAT observation at the 11-h forecast.

6 was −3.43/−5.21 mm (Figures 8G, I). After assimilation of MTSAT-RH in Exp-ObRH5/6, these dry biases were overcorrected and significant large wet biases resided in most of the observed fog areas (e.g., see the red shadings in Figures 8N, Q, T, W). The temperature constraint with CV5 slightly alleviated the large wet biases (e.g., cf. Figures 8H, I), whereas the wet biases greatly decreased under the temperature constraint with CV6 (e.g., cf. Figures 8K, L). In Exp-ObRHT6, there are slight wet biases (~1 mm) in most of the observed fog areas, and the correlation coefficients vary from 0.58 to 0.73, which indicates that the moisture status is successfully simulated during the fog evolution.

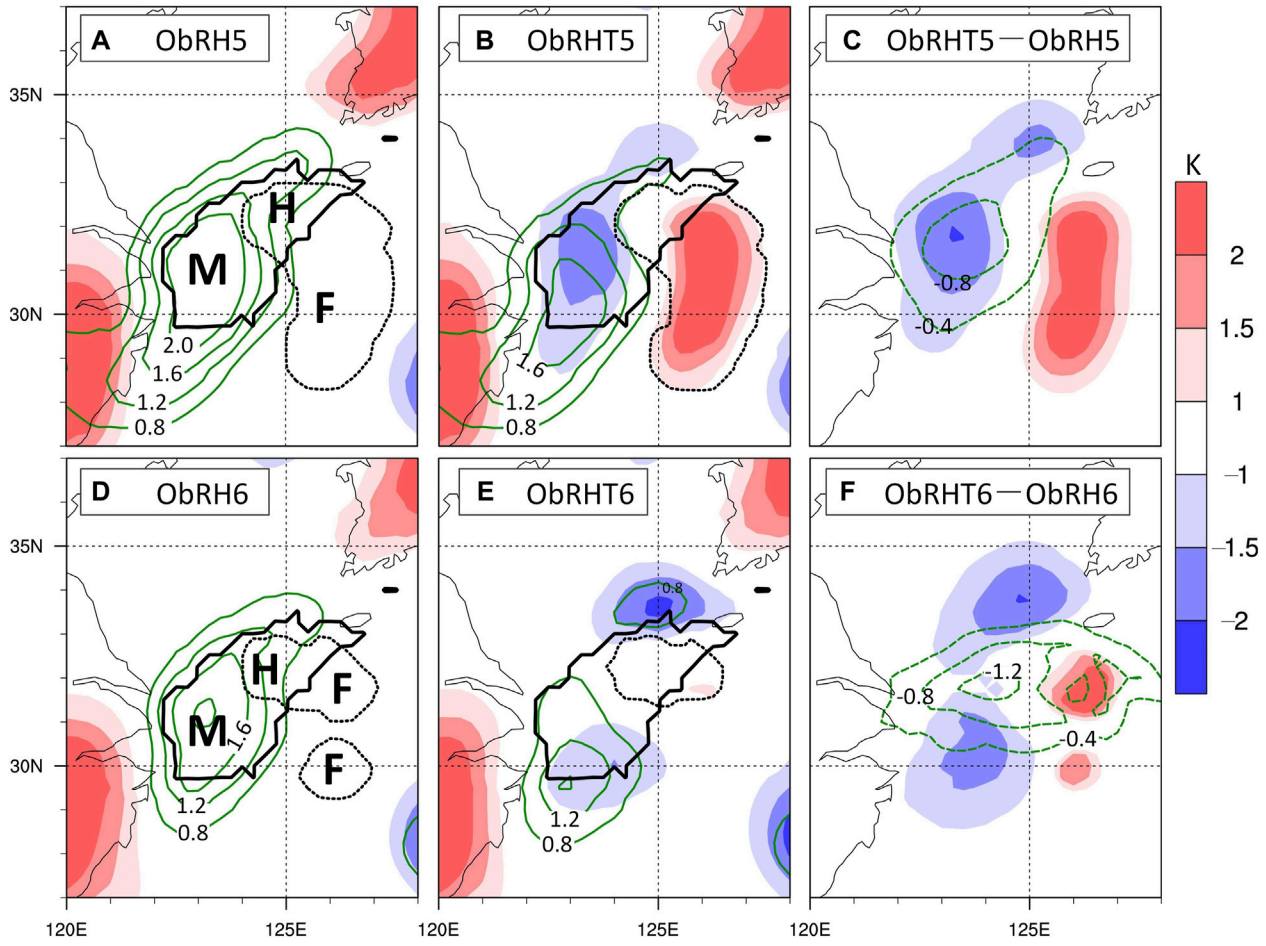

FIGURE 9
Analysis increments at the initial time for Exp-ObRH5 **(A)**, Exp-ObRHT5 **(B)**, Exp-ObRH5 **(D)**, and Exp-ObRHT5 **(E)** at the model bottom level. **(C,D)** are Exp-ObRHT5 minus Exp-ObRH5 and Exp-ObRHT6 minus Exp-ObRH6 **(F)**, respectively. Shadings, green contours denote the temperature (K), mixing ratio (g kg^{-1}), respectively. Black solid and dashed lines outline the observed and forecasted fog areas, respectively. M, H, and F denote the missed fog, hitting fog and false fog, respectively.

The aforementioned results show the importance of the temperature constraint with CV6 in the assimilation of MTSAT-RH in the revised method. The next subsection explains how the improvements in Exp-ObRHT6 are achieved.

5.3 Role of CV6 for the revised method

To investigate the reason why Exp-ObRHT6 has a better performance than Exp-ObRHT5, we looked at the insight into the analysis increments at the model bottom level of the 3DVAR update (see Figure 3B). Figure 9 shows the analytic increments of temperature and moisture at the final 3DVAR update for Exp-ObRH5/6 (Figures 9A, D), Exp-ObRHT5/6 (Figures 9B, E), and the differences between Exp-ObRHT5/6 and Exp-ObRH5/6 (Figures 9C, F). In Figure 9, the observed fog area is outlined by the thick black line, and the thick dash line is for the simulated fog area. The areas of hit fog, missed fog, and false fog are denoted by H, M, and F, respectively. The missed fog and hit fog areas of Exp-ObRH5 and Exp-ObRH6 are almost the same; however, their false fog areas differ greatly (see H, M, and F in Figures 9A, D). The false fog area still appears in Exp-ObRHT5 after assimilating MTSAT-RH with the temperature constraint (cf. Figures 9A, B), but almost disappears in Exp-ObRHT6 (cf. Figures 9D, E).

Overviewing the increment distribution in Figure 9, it is found that 1) Exp-ObRH5/6 only has analytic increments of the mixing ratio related to the observed fog area (Figures 9A, D) because the temperature in humidity sounding (Figure 2A) is extracted from the analysis, leading to no observable increment of temperature in the 3DVAR update; 2) Exp-ObRHT5/6 has analysis increments of both mixing ratio and temperature (Figures 9B, E, C, F), owing to the temperature constraint in the revised method; 3) compared with Exp-ObRH5/6, Exp-

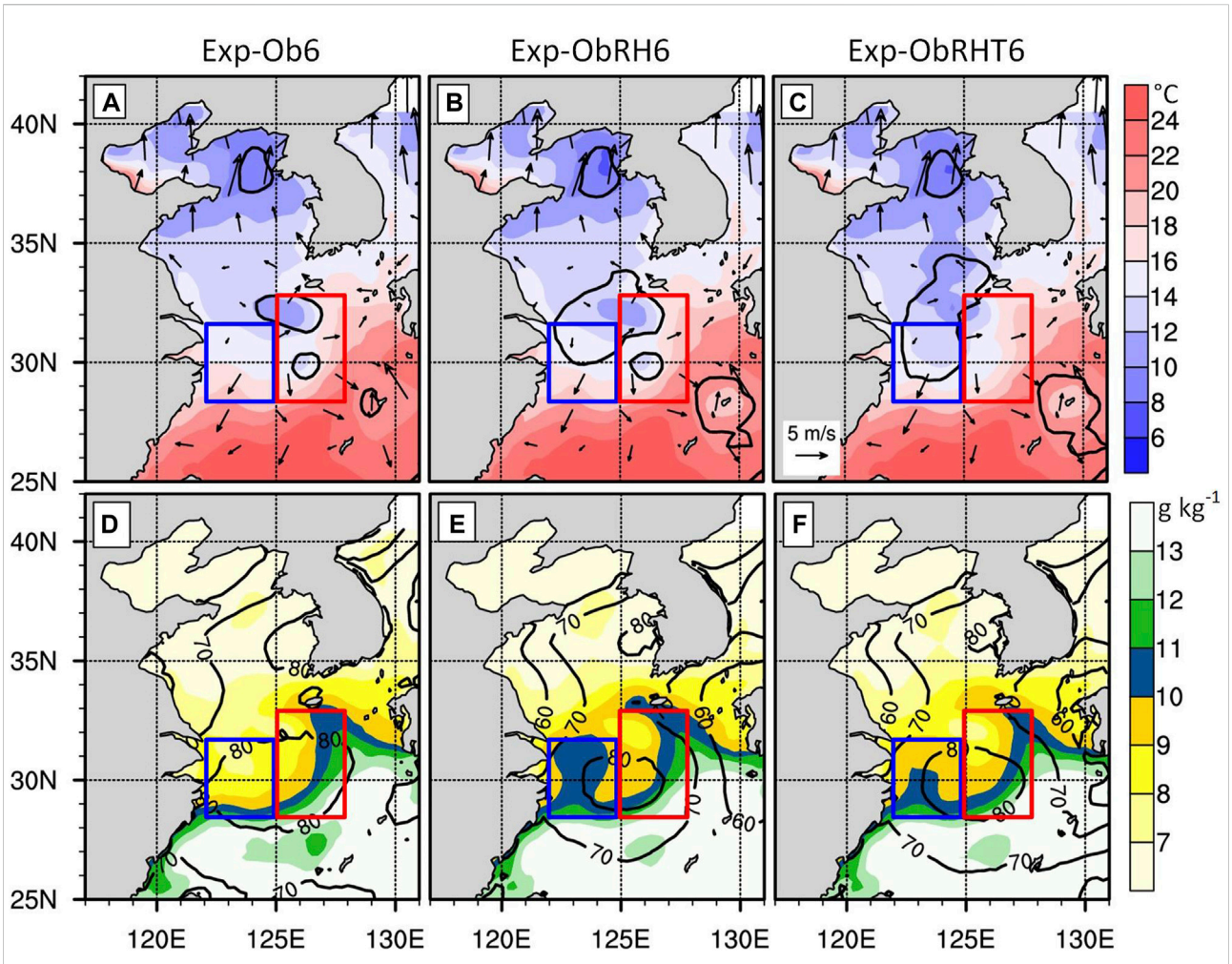

FIGURE 10
Distributions of 2-m temperature and 10-m wind [shades and vectors in **(A–C)**], and 2-m mixing ratio and geopotential height at 1,000 hPa level [shades and contours in **(D–F)**]. In **(A–C)**, the contour of 2-m RH with a value of 95% roughly outlines the simulated fog area. See the text for details of the blue and red boxes in each panel.

ObRHT5/6 has a more accurate coverage over the observed fog area and its maximum is about 0.4 g kg^{-1} smaller (cf. the green contours of Figures 9A, D, B, E, respectively), which is contributed from the cross-correlation between moisture and temperature in CV6.

Because of the positive increments of mixing ratio over the missed fog area (M in Figures 9A, D), 3 h later, sea fog occurred over the missed fog area (e.g., cf. Figures 6cA and cB, fA and fB, etc.). It means that both the W14 method and revised method do work on compensating the missed fog area. However, the revised method only using CV6 is effective for eliminating the false fog area. For instance, the southern patch of the missed fog area denoted by F in Figure 9D does not appear in Figure 9E. Benefitting from the correction of the temperature profile in the nearest clear air area replacing that in the false fog area (see Figure 3A), there are positive temperature increments over the false fog area (e.g., see the red shadings in Figures 9C, F), which is beneficial to dissipate the false fog area. However, positive temperature increment is not enough to eliminate the false fog area. It seems that the reason that the false fog area only dissipates in Exp-ObRHT6 is that, relative to Exp-ObRH6, there are extra negative increments of the mixing ratio over its false fog area, which does not exist in Exp-ObRHT5 relative to Exp-ObRH5 (see the green contours in Figures 9C, F).

Figure 10 presents the distributions of 2-m temperature, 10-m wind, and 2-m RH with a value of 95% for roughly denoting the simulated fog area, 2-m mixing ratio, and geopotential height at 1,000 hPa level. According to the observed fog area (Figure 3B) and the simulated fog area of Exp-Ob6 (Figure 6eA), two areas designated by blue and red boxes are used to determine the missed fog area and false fog area, respectively. The missed fog in Exp-Ob6 appears in both Exp-ObRH6 and Exp-ObRHT6, resulting from the existence of the wet tongue of the mixing ratio (Figures 10B, E). Although the wet tongue of Exp-ObRHT6

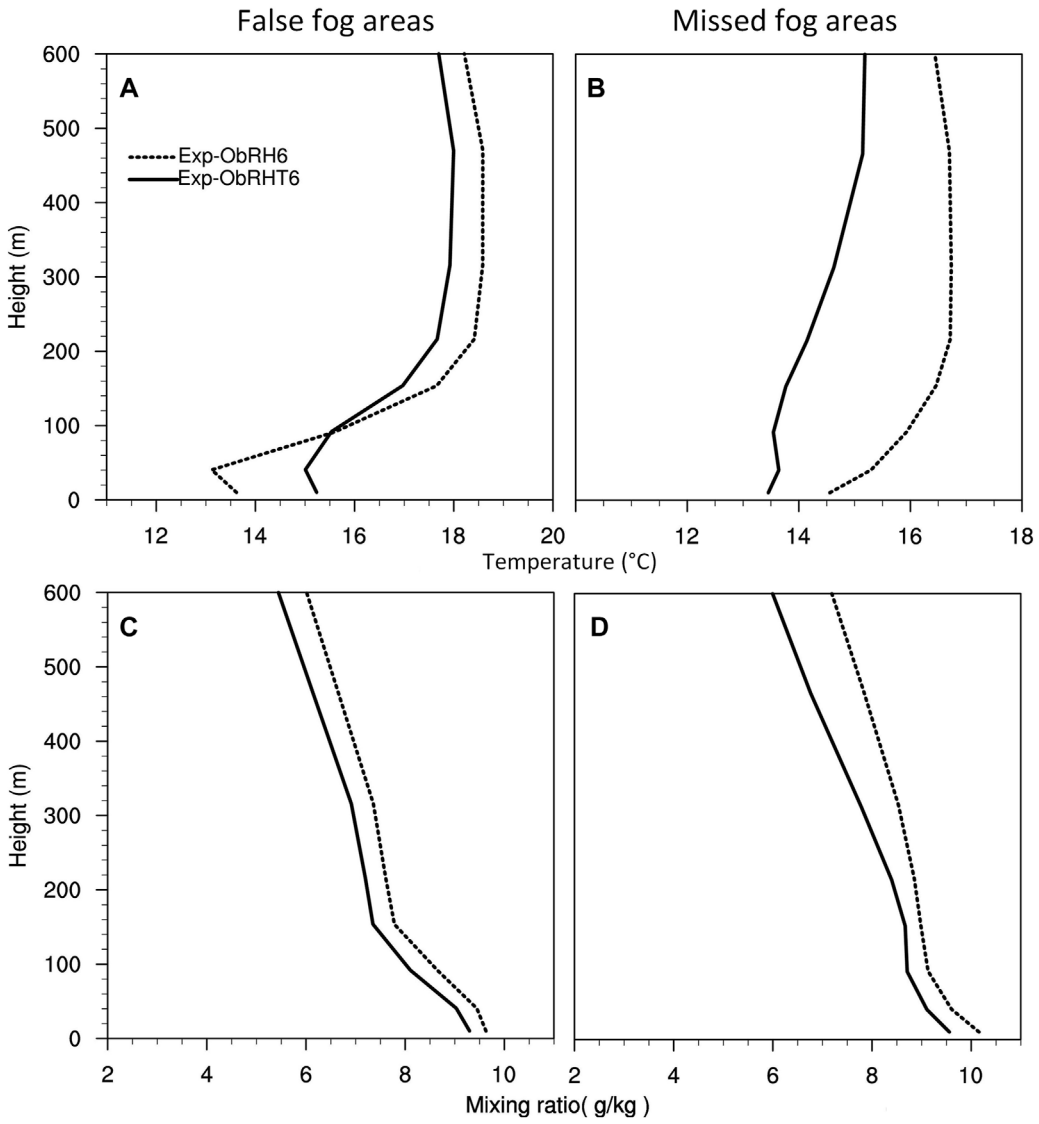

FIGURE 11
Average profiles of the 00-h forecasted air temperature within the areas of false fog **(A)** and missed fog **(B)**, as well as the average profiles of the mixing ratio within the areas of false fog **(C)** and missed fog **(D)**. Solid and dash lines denote Exp-ObRHT6 and Exp-ObRH6, respectively. Note that the missed fog and false fog areas are determined by the comparison of the observed fog and the simulated fog from Exp-ObRH6 (see Figure 9D).

is weaker than that of Exp-ObRH6 (cf., Figures 10E, F), its simulated fog expands more northward and is closer to the observation, which results from a stronger sea surface wind (1–2 m s^{-1} larger) by the enhanced high-pressure system. This is obviously seen from the comparison of the geopotential heights between Figures 10B, C, E, F, respectively. This shows that in addition to the aforementioned advantages, the temperature constraint with CV6 can also provide a more accurate low-level pressure system. As a result of the enhanced high-pressure system in Exp-ObRHT6, a drier area of the mixing ratio exists over the false fog area than Exp-ObRH6, which leads to the elimination of its false fog.

To check the impact of the temperature constraint with CV6 on the vertical structure of MABL, the profiles of temperature and mixing ratio of 00-h forecast (i.e., the initial condition) within the false and missed fog areas were collected and averaged. For unifying the number and locations of the profile samples, the false and missed fog areas were determined according to the comparison of the observed fog area and the simulated fog area by Exp-ObRH6 (see the areas denoted by M and F in Figure 9D). Figure 11 gives the averaged profiles of Exp-ObRH6 and Exp-ObRHT6 within MABL, showing that the difference of temperature profiles (Figures 11A, B) between Exp-ObRH6 and Exp-ObRHT6 is apparently larger than that of the mixing ratio profiles (Figures 11C, D) for both the false area and the missed fog

area. In the false fog area, the temperature profile of Exp-ObRHT6 is about 1.5 K warmer than that of Exp-ObRH6 within 100 m (Figure 11A), and the overall mixing ratio profile of Exp-ObRHT6 is about 0.5 g kg^{-1} drier than that of Exp-ObRH6, contributing to the elimination of the false fog area. In spite of the fact that the overall mixing ratio profile of Exp-ObRHT6 is 0.5–1.0 g kg^{-1} drier than that of Exp-ObRH6, the mixing ratio is still 8.5–9.5 g kg^{-1}. In addition, the temperature profile of Exp-ObRHT6 is nearly 2.5 K colder than that of Exp-ObRH6, and the stability becomes nearly neutral from the strong inversion within 200 m, which is beneficial to the subsequent fog formation over the missed fog area.

6 Summary

Sea fog forecast is sensitive to initial conditions because the formation and evolution of sea fog over the Yellow Sea are strongly affected by the thermal structure of MABL. To solve the deficiency of MABL moisture for the Yellow Sea forecast, Wang et al. (2014) developed the W14 method to assimilate satellite-derived humidity. This method can significantly improve the sea fog forecast. However, it causes much moisture into initial conditions and ignores dealing with spurious fog area, which produces wet bias and increases false alarms. For alleviating this problem, we proposed a revised method with the temperature constraint based on the W14 method. In the new method, the temperature given for a humidity sounding is not directly extracted from the 3DVAR analysis, but from the nearest fog area. In addition, the revised method also intends to eliminate spurious fog by adding the temperature provided from the nearest clear air area.

A series of numerical forecast experiments were conducted for 10 sea fog cases that occurred over the Yellow Sea to evaluate the revised method's effect, and one of the cases was selected for a case study to explore the impact of temperature constraint in the revised method. In the case study, we especially compared the assimilation effect of using CV5 and CV6, while in the aforementioned experiments for 10 cases, CV5 was used to be consistent with the W14 method. The main conclusions are as follows:

1) The revised method outperforms the W14 method. The moisture and temperature structure in the MABL is more realistic, and the large wet bias in the W14 method can be greatly alleviated. The comprehensive score ETS is increased by about 15% on average, which is due to the significant improvement brought by the reduction of the false fog area.
2) The benefits of the revised method are mainly reflected in two aspects: one is to make up for the missed fog area and the other is to eliminate the false fog area. The temperature constraint cools MABL in the missed fog area and warms that in the false one, which helps sea fog develop as accurately as possible.
3) The effect of the revised method depends largely on the BE type used in the 3DVAR, and its performance using CV6 is much better than that using CV5. In the experiment with CV5, the false fog area is hardly eliminated, while it is eliminated well in the experiment with CV6 due to the contributions by the cross-correlations between temperature and humidity in CV6. It indicates that the revised method jointly with CV6 is probably a better solution for sea fog forecast.

Although this study has achieved encouraging results, it should be emphasized that the retrieval of sea fog needs to be improved, and the current treatment process of temperature constraints is somewhat rough. More work needs to be done to improve the revised method. On the other hand, multivariate BE covariance is seldom used in the sea fog forecast. Performance of the revised method with CV6 is to be evaluated in more cases which occur not only over the Yellow Sea, but also over other Chinese seas. We hope that the revised method in this study can be applied into the operational forecast of sea fog in the future.

Data Availability Statement

The original contributions presented in the study are included in the article/Supplementary Material; further inquiries can be directed to the corresponding authors.

Author contributions

XG: Formal analysis; methodology and software; and writing—original draft. SG and YW: Conceptualization; supervision; and writing—review and editing. ZL: Data curation and resources. All authors discussed the results and commented on the manuscript.

Funding

This research was financially supported by the National Natural Science Foundation of China (42075069).

Acknowledgments

We would like to thank the reviewers for their helpful comments and suggestions that improved the manuscript.

Conflict of interest

The authors declare that the research was conducted in the absence of any commercial or financial relationships that could be construed as a potential conflict of interest.

Publisher's note

References

Ballard, S. P., Golding, B. W., and Smith, R. N. B. (1991). Mesoscale model experimental forecasts of the haar of northeast Scotland. *Mon. Wea. Rev.* 119, 2107–2123. doi:10.1175/1520-0493(1991)119<2107:mmefot>2.0.co;2

Bendix, J., Thies, B., Cermak, J., and Nauß, T. (2005). Ground fog detection from space based on MODIS daytime data—a feasibility study. *Weather Forecast.* 20, 989–1005. doi:10.1175/waf886.1

Chen, F., and Dudhia, J. (2001). Coupling an advanced land surface–hydrology model with the penn state–NCAR MM5 modeling system. Part I: Model implementation and sensitivity. *Mon. Wea. Rev.* 129, 569–585. doi:10.1175/1520-0493(2001)129<0569:caalsh>2.0.co;2

Ellrod, G. P. (1995). Advances in the detection and analysis of fog at night using GOES multispectral infrared imagery. *Wea. Forecast.* 10, 606–619. doi:10.1175/1520-0434(1995)010<0606:aitdaa>2.0.co;2

Findlater, J., Roach, W. T., and McHugh, B. C. (1989). The haar of north-east Scotland. *Q. J. R. Meteorol. Soc.* 115, 581–608. doi:10.1002/qj.49711548709

Fu, G., Xu, J., and Zhang, S. Q. (2011). Comparison of modeling atmospheric visibility with visible satellite imagery. *J. Ocean. Univ. China* 41, 001–010. (in Chinese). doi:10.16441/j.cnki.hdxb.2011.04.002

Fu, G., Zhang, S. P., Gao, S. H., and Li, P. Y. (2012). *Understanding of sea fog over the China seas*. Beijing: China Meteorological Press, 220.

Gao, X., and Gao, S. (2019). EnKF assimilation of cloud water path in nowcasting sea fog over the Yellow Sea (in Chinese). *Oceanol. Limnol. Sin.* 50 (2), 248–260.

Gao, X., and Gao, S. (2020). Impact of multivariate background error covariance on the WRF-3DVAR assimilation for the Yellow Sea fog modeling. *Adv. Meteorol.* 2020, 1–19. doi:10.1155/2020/8816185

Gao, S. H., Lin, H., Shen, B., and Fu, G. (2007). A heavy sea fog event over the Yellow Sea in March 2005: Analysis and numerical modeling. *Adv. Atmos. Sci.* 24, 65–81. doi:10.1007/s00376-007-0065-2

Gao, S. H., Wu, W., Zhu, L. L., Fu, G., and Huang, B. (2009). Detection of nighttime sea fog/stratus over the Huanghai Sea using MTSAT-1R IR data. *Acta Oceanol. Sin.* 28, 23–35. doi:10.3969/j.issn.0253-505X.2009.02.003

Gao, S. H., Qi, Y. L., Zhang, S. B., and Fu, G. (2010). Initial conditions improvement of sea fog numerical modeling over the Yellow Sea by using cycling 3DVAR. Part I: WRF numerical experiments (in Chinese). *J. Ocean. Univ. China* 40, 001–009. doi:10.16441/j.cnki.hdxb.2010.10.001

Gao, X., Gao, S., and Yang, Y. (2018). A comparison between 3DVAR and EnKF for data assimilation effects on the Yellow Sea fog forecast. *Atmosphere* 9, 346. doi:10.3390/atmos9090346

Gultepe, I., Tardif, R., Michaelides, S. C., Cermak, J., Bott, A., Bendix, J., et al. (2007). Fog research: A review of past achievements and future perspectives. *Pure Appl. Geophys.* 164, 1121–1159. doi:10.1007/s00024-007-0211-x

Heidinger, A. K., and Stephens, G. L. (2000). Molecular line absorption in a scattering atmosphere. Part II: Application to remote sensing in the O_2 A band. *J. Atmos. Sci.* 57, 1615–1634. doi:10.1175/1520-0469(2000)057<1615:mlaias>2.0.co;2

Hong, S. Y., Noh, Y., and Dudhia, J. (2006). A new vertical diffusion package with an explicit treatment of entrainment processes. *Mon. Weather Rev.* 134, 2318–2341. doi:10.1175/mwr3199.1

Hong, S. Y. (2010). A new stable boundary-layer mixing scheme and its impact on the simulated East Asian summer monsoon. *Q. J. R. Meteorol. Soc.* 136, 1481–1496. doi:10.1002/qj.665

Hu, X. M., Klein, P. M., and Xue, M. (2013). Evaluation of the updated YSU planetary boundary layer scheme within WRF for wind resource and air quality assessments. *J. Geophys. Res. Atmos.* 118 (18), 10490–10505. doi:10.1002/jgrd.50823

Huang, H., Liu, H., Huang, J., Mao, W., and Bi, X. (2015). Atmospheric boundary layer structure and turbulence during sea fog on the southern China coast. *Mon. Weather Rev.* 143, 1907–1923. doi:10.1175/mwr-d-14-00207.1

Iacono, M. J., Delamere, J. S., Mlawer, E. J., Shephard, M. W., Clough, S. A., and Collins, W. D. (2008). Radiative forcing by long-lived greenhouse gases: Calculations with the AER radiative transfer models. *J. Geophys. Res.* 113, D13103. doi:10.1029/2008jd009944

Kain, J. S., and Fritsch, J. M. (1990). A one-dimensional entraining/detraining plume model and its application in convective parameterization. *J. Atmos. Sci.* 47, 2784–2802. doi:10.1175/1520-0469(1990)047<2784:aodepm>2.0.co;2

Kim, C. K., and Yum, S. S. (2010). Local meteorological and synoptic characteristics of fogs formed over Incheon international airport in the west coast of Korea. *Adv. Atmos. Sci.* 27 (4), 761–776. doi:10.1007/s00376-009-9090-7

Kim, C. K., and Yum, S. S. (2012). A numerical study of sea-fog formation over cold sea surface using a one-dimensional turbulence model coupled with the weather research and forecasting model. *Bound. Layer. Meteorol.* 143 (3), 481–505. doi:10.1007/s10546-012-9706-9

Kim, S., Moon, J. H., and Kim, T. (2021). A coupled numerical modeling study of a sea fog case after the passage of Typhoon Muifa over the Yellow Sea in 2011. *Geophys. Res. Atmos.* 126, e2020JD033875. doi:10.1029/2020jd033875

Koračin, D., and Dorman, C. E. (2017). *Marine fog: challenges and advancements in observations, modeling, and Forecasting*. New York: Springer International Publishing, 537.

Koračin, D., Lewis, J., Thompson, W. T., Dorman, C. E., and Businger, J. A. (2001). Transition of stratus into fog along the California coast: Observations and modeling. *J. Atmos. Sci.* 58, 1714–1731. doi:10.1175/1520-0469(2001)058<1714:tosifa>2.0.co;2

Koračin, D., Businger, J. A., Dorman, C. E., and Lewis, J. M. (2005a). Formation, evolution, and dissipation of coastal sea fog. *Bound. Layer. Meteorol.* 117, 447–478. doi:10.1007/s10546-005-2772-5

Koračin, D., Leipper, D. F., and Lewis, J. M. (2005b). Modeling sea fog on the U.S. California coast during a hot spell event. *Geofizika* 22, 59–82.

Koračin, D., Dorman, C. E., Lewis, J. M., Hudson, J. G., Wilcox, E. M., and Torregrosa, A. (2014). Marine fog: A review. *Atmos. Res.* 143, 142–175. doi:10.1016/j.atmosres.2013.12.012

Lewis, J. M., Koračin, D., Rabin, R., and Businger, J. (2003). sea fog off the California coast: Viewed in the context of transient weather systems. *J. Geophys. Res.* 108, 4457. doi:10.1029/2002jd002833

Li, R., Gao, S. H., and Wang, Y. M. (2012). Numerical study on direct assimilation of satellite radiances for sea fog over the Yellow Sea (in Chinese). *J. Ocean. Univ. China* 42, 10–20. doi:10.16441/j.cnki.hdxb.2012.03.002

Lin, Y. L., Farley, R. D., and Oriville, H. D. (1983). Bulk parameterization of the snow field in a cloud model. *J. Clim. Appl. Meteor.* 22, 1065–1092. doi:10.1175/1520-0450(1983)022<1065:bpotsf>2.0.co;2

Liu, X., and Hu, X. Q. (2008). Sea fog automatic detection over the East China Sea using MTSAT data (in Chinese). *J. Oceanogr. Taiwan* 27, 112–117.

Liu, Y. D., Ren, J. P., and Zhou, X. (2011). The impact of assimilating sea surface wind aboard QuickSCAT on sea fog simulation (in Chinese). *J. Appl. Meteor. Sci.* 22 (04), 472–481.

Lorenz, E. N. (1965). A study of the predictability of a 28-variable atmospheric model. *Tellus* 17, 321–333. doi:10.1111/j.2153-3490.1965.tb01424.x

Lu, X., Gao, S. H., Rao, L. J., and Wang, Y. M. (2014). Sensitivity study of WRF parameterization schemes for the spring sea fog in the Yellow Sea (in Chinease). *J. Appl. Meteor. Sci.* 25, 312–320.

Nicholls, S. (1984). The dynamics of stratocumulus: Aircraft observations and comparisons with a mixed layer model. *Quart. J. Roy. Meteor. Soc.* 110, 783–820. doi:10.1002/qj.49711046603

Parrish, D. F., and Derber, J. C. (1992). The National Meteorological Center's spectral statistical-interpolation analysis system. *Mon. Wea. Rev.* 120, 1747–1763. doi:10.1175/1520-0493(1992)120<1747:tnmcss>2.0.co;2

Skamarock, W. C., Klemp, J. B., Dudhia, J., Gill, D. O., Barker, D., Duda, M. G., et al. (2008). A description of the Advanced Research WRF version 3. Note NCAR/TN–4751STR. NCAR Tech. 113.

Sorli, B., Pascal-Delannoy, F., Giani, A., Foucaran, A., and Boyer, A. (2002). Fast humidity sensor for high range 80%– 95% RH. *Sens. Actuators* 100, 24–31. doi:10.1016/S0924-4247(02)00063-8

Wang, Y., and Gao, S. (2016). Assimilation of Doppler Radar radial velocity in Yellow Sea fog numerical modeling (in Chinese). *J. Ocean. Univ. China* 46, 1–12. doi:10.16441/j.cnki.hdxb.20150361

Wang, Y., Gao, S., Fu, G., Sun, J., and Zhang, S. (2014). Assimilating MTSAT-derived humidity in nowcasting sea fog over the Yellow Sea. *Weather Forecast.* 29, 205–225. doi:10.1175/waf-d-12-00123.1

Wang, B. H. (1985). *Sea fog*. Beijing: China Ocean Press, 330.

Wu, X. J., Zhu, J., Wang, X., and Yang, B. (2017). Sea fog simulation with assimilation of FY-3A microwave data (in Chinese). *Chin. J. Atmos. Sci.* 41 (3), 421–436. doi:10.3878/j.issn.1006-9895.1610.16105

Yang, Y., and Gao, S. H. (2015). Analysis on the synoptic characteristics and inversion layer formation of the Yellow Sea fogs (in Chinese). *J. Ocean. Univ. China* 45 (06), 19–30. doi:10.16441/j.cnki.hdxb.20140059

Yang, Y., and Gao, S. H. (2020). The Impact of turbulent diffusion driven by fog-top cooling on sea fog development. *J. Geophys. Res. Atmos.* 125, e2019JD031562. doi:10.1029/2019jd031562

Yang, Y., Hu, X., Gao, S., and Wang, Y. (2018). Sensitivity of WRF simulations with the YSU PBL scheme to the lowest model level height for a sea fog event over the Yellow Sea. *Atmos. Res.* 215, 253–267. doi:10.1016/j.atmosres.2018.09.004

Yang, Y., Wang, Y., Gao, S., and Yuan, X. (2021). A new observation operator for the assimilation of satellite-derived relative humidity: Methodology and experiments with three sea fog cases over the Yellow Sea. *J. Meteorol. Res.* 35 (6), 1104–1124. doi:10.1007/s13351-021-1084-0

Zhang, S. P., Xie, S. P., Liu, Q. Y., Yang, Y. Q., Wang, X. G., and Ren, Z. P. (2009). Seasonal variations of Yellow Sea fog: Observations and mechanisms. *J. Clim.* 22 (24), 6758–6772. doi:10.1175/2009jcli2806.1

Zhou, B., and Du, J. (2010). Fog prediction from a multimodel mesoscale ensemble prediction system. *Weather Forecast.* 25, 303–322. doi:10.1175/2009waf2222289.1

Zhou, F. X., Wang, X., and Bao, X. W. (2004). Climatic characteristics of sea fog formation of the Huanghai Sea in spring (in Chinese). *Acta Oceanol. Sin.* 26, 28–37.

frontiers | Frontiers in Earth Science

TYPE Original Research
PUBLISHED 12 January 2023
DOI 10.3389/feart.2022.1004350

OPEN ACCESS

EDITED BY
Kevin Cheung,
Independent Researcher, Sydney, Australia

REVIEWED BY
Fan Ping,
Institute of Atmospheric Physics (CAS), China
Shouting Gao,
Institute of Atmospheric Physics (CAS), China

*CORRESPONDENCE
Jie Cao,
003542@nuist.edu.cn

SPECIALTY SECTION
This article was submitted to Atmospheric Science, a section of the journal Frontiers in Earth Science

RECEIVED 27 July 2022
ACCEPTED 31 October 2022
PUBLISHED 12 January 2023

CITATION
Zhou G, Du J, Cao J, Liu L and Li X (2023), Comparative analyses of the effects of divergent winds on the kinetic energy budget with the adoptions of two methods during the extratropical transition of Typhoon Rumbia (1818). *Front. Earth Sci.* 10:1004350. doi: 10.3389/feart.2022.1004350

Comparative analyses of the effects of divergent winds on the kinetic energy budget with the adoptions of two methods during the extratropical transition of Typhoon Rumbia (1818)

Guanbo Zhou[1,2,3], Jia Du[4], Jie Cao[1,2]*, Lu Liu[3] and Xingyu Li[5]

[1]National Meteorological Centre, Beijing, China, [2]Key Laboratory of Meteorological Disaster (KLME), Ministry of Education and Collaborative Innovation Center on Forecast and Evaluation of Meteorological Disasters (CIC-FEMD), Nanjing University of Information Science and Technology, Nanjing, China, [3]State Key Laboratory of Severe Weather (LASW), Chinese Academy of Meteorological Sciences, Beijing, China, [4]Institute of Atmospheric Physics, Chinese Academy of Sciences, Beijing, China, [5]Institute of Atmospheric Physics, Chinese Academy of Sciences, Beijing, China

Modification of the divergent wind components and domain of interests can result in obvious changes in the kinetic energy (KE) budget of typhoons and other synoptic systems. Before analyzing the effects of divergent winds on the KE budget of Typhoon Rumbia (2018) during its entire life cycle, especially in its extratropical transition (ET) process, a hybrid integral method to partition the horizontal wind fields in a limited domain with high accuracy is adopted, in comparison with the commonly used iterative method under two sets of domains, that is, the typhoon following domain and the outermost domain that covers the entire typhoon track. The relative importance of the divergent and non-divergent winds in the KE budget is investigated in the three stages of the ET process, namely, the pre-development, re-intensification, and dissipation stages. It is found that the divergent winds computed by the iterative method with a lower accuracy result in sizable errors in spatiotemporal variations of the KE of the typhoon during its ET process, which thus leads to obvious forecasting errors.

KEYWORDS

typhoon, kinetic energy, extratropical transition, divergent winds, typhoon-following domain

Highlights

1) The significant modification of divergent winds could change the kinetic energy variations.
2) Kinetic energy budgets by the divergent winds during the entire extratropical transition of the typhoon are important.

Introduction

Extratropical transition (ET) is a special process by which a tropical cyclone (TC), upon encountering the mid-latitude circulation systems, transforms into an extratropical cyclone. The ET process often makes the meso- and small-scale systems in typhoons develop and dissipate frequently (Meng et al., 2002), resulting in severe weather. When the TC changes into an extratropical cyclone, obvious changes in the wind field structure, moving speed and direction, and precipitation distribution are observed (Knox 1955; Sekioka 1956; Harr et al., 2000; Klein et al., 2000 and 2002; Niu et al., 2005; Chen et al., 2001). Therefore, the accuracy and timeliness of relevant forecasting are required, which thus brings great difficulty to forecasting. Severe weather such as heavy precipitation, strong wind, and storm surge formed during the ET often poses a great threat to life safety and causes great economic losses to coastal areas of mid-latitudes because of low forecasting accuracy and short warning time. Therefore, the ET of TCs has been widely concerned and has become the research focus of meteorologists (Zhong et al., 2009; Li et al., 2008; Klein et al., 2000; Harr et al., 2000a, b; Evans et al., 2004; Han et al., 2005).

The kinetic energy (KE) budget analysis is a powerful tool for studying severe storms in synoptic-scale systems, such as extratropical cyclogenesis, severe wind, southwest vortex, and the associated torrential rainfall (Chen and Wiin-Nielsen 1976; Chen et al., 1978; Fu et al., 2016; Smith et al., 2018; Zhong et al., 2021). In addition, the impacts of divergent winds on the KE budget are mostly used when examining the TC movement, particularly during the period of TC generation or intensification (Dimego and Bosart 1982a, b; Ding and Liu 1985a, b; Sun et al., 2012; Peng et al., 2014a, b). According to Roberson and Smith (1980), the horizontal flux convergence serves as the major source of the upper-level jet and a determinant of its strength, while its rotating component dominates when the upper-level trough increases rapidly (Dimego and Bosart 1982a, b). The asymmetric structure of the TC was poorly reflected in earlier KE budget analyses, which mostly took the targeting systems as a whole. By further dividing the rotational and divergent KE budgets into the axisymmetric and asymmetric components, Wang et al. (2016) took into consideration the asymmetry during TC generation.

The horizontal velocity field can be partitioned into rotational and divergent components represented by the stream function and velocity potential, respectively. This flow decomposition approach has been widely used in studying atmospheric and oceanic circulations, weather analyses, and data assimilations (Haltiner and Williams 1980; Dimego and Bosart 1982; Hollingsworth and LÄonnberg 1986; Allen et al., 1990; Daley 1991; Vallis et al., 1997; Xu and Wei 2001 and 2001; Mewes and Shapiro 2002; Jung and Arakawa 2008; Zhao and Cook 2021). Cao et al. (2022a) reviewed three previous methods, namely, the classical successive over-relaxation (SOR) scheme, which is a commonly used iterative method, the spectral method by Chen and Kuo (1992a), and the integral method by Xu et al. (2011). Although they have been applied to various velocity fields in diagnostic studies of weather systems, they all tend to lose accuracy considerably when used in mesoscale studies of strong and complex flow fields. In order to get a better understanding of the KE budgets and their evolutions during the complicated ET, the newly developed hybrid method (Cao et al., 2022a), which optimally combines the SOR method and the integral approach with high accuracy, is adopted in this study. A comparative analysis is also performed with results obtained from the traditionally used SOR method (Cao et al., 2019; Chen and Kuo, 1992b; Dimego and Bosart, 1982b; Ullah et al., 2020; Ullah et al., 2021; You and Fung, 2019).

With the aim to investigate the characteristics of KE in the ET and the effects of an accurate wind-partitioning solver on the KE budget during the ET under different domains of interests, Typhoon Rumbia (2018) is taken as an example for its record-breaking long durations after landing. Theoretical considerations of the KE equation and wind partitioning methods are reviewed in *Methodology and case overview*. The synoptic analysis of Typhoon Rumbia and domains of interests are described in *Kinetic energy analyses*, followed by comparative studies of KE during the three periods of the ET in *Kinetic energy analyses*. Finally, the conclusions are in the last section.

Methodology and case overview

Kinetic energy budget equations

The kinetic energy K is thus expressed as follows (Chen et al., 1978):

$$\mathrm{K} = \frac{1}{2}V.V = K_R + K_D + V_R.V_D. \tag{1}$$

Here, the kinetic energy per unit mass (k) is given as $k = \boldsymbol{v}.\boldsymbol{v}/2$. According to Helmholtz's theorem, the horizontal wind ($\boldsymbol{v}$) is the summation of the rotational component ($\boldsymbol{v_r}$) and the divergent component ($\boldsymbol{v_d}$). The subscripts R and D represent the rotational and divergent components, respectively.

The KE budget equation together with its two components over a limited domain is as follows (Buechler and Fuelberg, 1986; Abdeldym et al., 2019; Cao et al., 2022b):

$$\frac{\partial \mathrm{K}}{\partial t} = \frac{1}{sg}\int_0^{p_0}\int_S \frac{\partial k}{\partial t}dsdp,$$
$$= -\frac{1}{sg}\int_0^{p_0}\int_S \nabla\cdot(\boldsymbol{v}k)dsdp - \frac{1}{sg}\int_0^{p_0}\int_S \frac{\partial(\omega k)}{\partial t}dsdp - \iint \boldsymbol{v}\cdot\nabla\Phi - D(\mathrm{K}). \tag{2}$$

Among them, $\mathrm{T1} = -\frac{1}{sg}\int_0^{p_0}\int_S \nabla\cdot(\boldsymbol{v}k)dsdp$, $\mathrm{T2} = -\frac{1}{sg}\int_0^{p_0}\int_S \frac{\partial(\omega k)}{\partial t}dsdp$, $\mathrm{T3} = -\int\int \boldsymbol{v}\cdot\nabla\Phi$

$$\frac{\partial K_d}{\partial t} = -C(Kd, Kr) + \frac{1}{sg}\iint\left[- v_d\cdot\frac{\partial \boldsymbol{v_r}}{\partial t} - v_d\cdot\nabla\Phi - \nabla\cdot(\boldsymbol{v_d}k) - \frac{\partial(\omega k)}{\partial p}\right]dsdp + D(k_d) \tag{3}$$

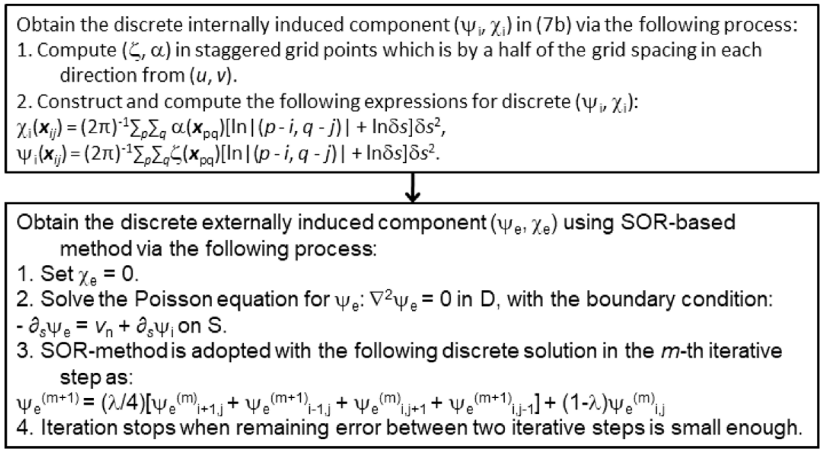

FIGURE 1
Computational procedure of the hybrid integral–SOR method (Modified from Figure 1 in Cao et al., 2022a).

Among them, $\mathrm{T0d} = \frac{\partial \mathrm{K_d}}{\partial t}$, $\mathrm{INTD} = \frac{1}{sg}\iint(-v_\mathrm{d}\cdot\frac{\partial \mathrm{vr}}{\partial t})dsdp$,

$$\mathrm{T3d} = \frac{1}{sg}\iint(-v_\mathrm{d}\cdot\nabla\Phi)dsdp,\ \mathrm{T1d} = \frac{1}{sg}\iint(-\nabla\cdot(v_\mathrm{d}\mathrm{k}))dsdp,$$

$$\mathrm{T2} = \frac{1}{sg}\iint(-\frac{\partial(\omega\mathrm{k})}{\partial \mathrm{p}})dsdp.$$

$$\frac{\partial \mathrm{K_r}}{\partial t} = \mathrm{C(Kd, Kr)} + \frac{1}{sg}\iint\Big[-\boldsymbol{v_r}\cdot\frac{\partial \boldsymbol{v_d}}{\partial t} - \boldsymbol{v_r}\cdot\nabla\Phi - \nabla\cdot(\boldsymbol{v_r}k)\Big]dsdp + D(k_r) \tag{4}$$

Among them, $\mathrm{T0r} = \frac{\partial \mathrm{Kr}}{\partial t}$, $\mathrm{INTR} = \frac{1}{sg}\iint(-v_\mathrm{r}\cdot\frac{\partial v_\mathrm{d}}{\partial t})dsdp$,

$$\mathrm{T3r} = \frac{1}{sg}\iint(-v_\mathrm{r}\cdot\nabla\Phi)dsdp,$$

$$\mathrm{T1r} = \frac{1}{sg}\iint(-\nabla\cdot(v_\mathrm{r}k))dsdp.$$

$$\mathrm{C(Kd, Kr)} = \iint\Big[-f(v_ru_d - u_rv_d) - \zeta(v_ru_d - u_rv_d) - \omega\frac{\partial k_r}{\partial p} - \omega\boldsymbol{v_r}\frac{\partial \boldsymbol{v_d}}{\partial p}\Big]dsdp \tag{5}$$

Among them, $\mathrm{Af} = \iint[-f(v_ru_d - u_rv_\mathrm{d})]dsdp$,

$$\mathrm{Az} = \iint[-\zeta(v_ru_d - u_rv_\mathrm{d})]$$

$$dsdp,\ \mathrm{B} = \iint(-\omega\frac{\partial k_r}{\partial p})dsdp,\ \mathrm{C} = \iint(-\omega vr\frac{\partial vd}{\partial p})dsdp.$$

Here, s is the area of the limited domain. T0, T0r, and T0d represent the temporal variations of KE, Kr, and Kd, respectively. T1r and T1d represent the horizontal flux divergence of total K by $\boldsymbol{v_r}$ and $\boldsymbol{v_d}$, respectively. T2 is the vertical divergence of K. T3r and T3d represent conversions between the available potential energy and Kr and Kd through baroclinic processes, respectively. INTR is the interactions between Kd and Kr due to the presence of Kd, and INTD is similar. Af and Az are to satisfy the conservation of angular momentum on the tangential and rotational motions, respectively. Terms B and C are vertical exchanges of rotational and divergent momentums, respectively.

The hybrid method for computing the stream function and velocity potential

The detailed computational procedures of the hybrid integral-SOR method (Cao et al., 2022a) are shown in Figure 1. To be specific, (ψ, χ) is divided into (ψ_i, χ_i) and (ψ_e, χ_e) for the internally and externally induced components, respectively, in the same way as in the integral method. To retain the strength and related advantages for the integral method, the internally induced component, (ψ_i, χ_i), should be calculated in the first step in the same way as that in the integral method. The SOR-based method can be used adaptively for computing the externally induced ψ_e (with χ_e = 0) in the second step. This can improve the accuracy of (ψ_e, χ_e) computed in the second step. This hybrid method is less sensitive than the integral method to increased variations of original $\boldsymbol{v}$ across or along the domain boundary and their caused errors in solvability conditions and related boundary condition errors. The test results from the hybrid method in computing (ψ, χ) from original $\boldsymbol{v}$ fields with complex flow patterns in mesoscale domains will be shown in the following section in comparison with the results from the SOR method.

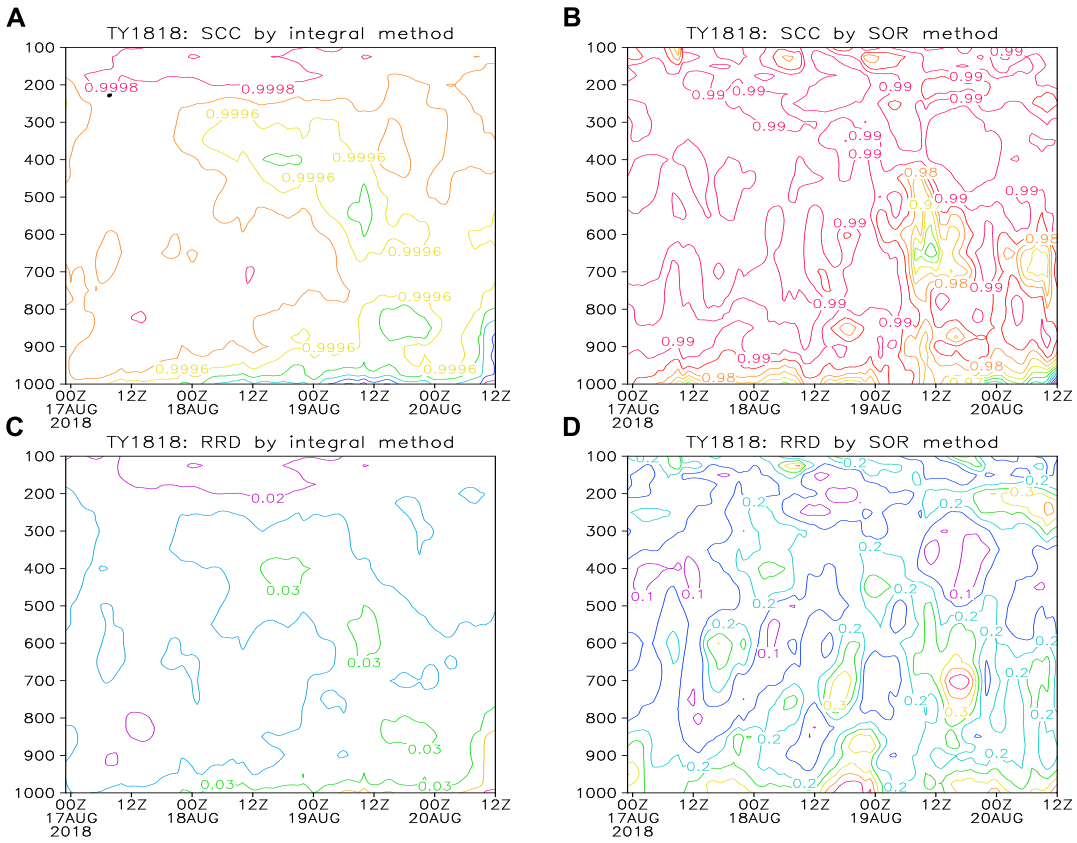

FIGURE 2
SCC (a, interval = 0.0001) and RRD (c, interval = 0.005) by the integral method in all vertical levels from 00 UTC 17 August to 12 UTC 20 August 2018. The lower panels are SCC (interval = 0.005) and RRD (interval = 0.05) by the SOR method, respectively.

Modifications of divergent winds obtained from two methods

Evaluations and verifications can be performed only by comparing the reconstructed horizontal velocity [denoted by $v_c \equiv (u_c, v_c)$] with the original velocity [still denoted by $v \equiv (u, v)$] for the closeness of v_c to v. Quantitatively, the closeness of v_c to v can be measured in terms of the spatial correlation coefficient (SCC) and relative root mean square difference (RRD) defined by

$$\mathrm{SCC} = \sum_{i,j}\left\{\left[u_c(i,j) - U_c\right]\left[u(i,j) - U\right] + \left[v_c(i,j) - V_c\right]\left[v(i,j) - V\right]\right\} \Big/ (mn\sigma_c\sigma), \tag{6a}$$

$$\mathrm{RDD} = \left\{\sum_{i,j}\left[\left(u_c(i,j) - u(i,j)\right)^2 + \left(v_c(i,j) - v(i,j)\right)^2\right] \Big/ \sum_{i,j}\left[u(i,j)^2 + v(i,j)^2\right]\right\}^{1/2}. \tag{6b}$$

Here, m and n are the numbers of grid points in x and y directions, respectively, inside of the concerned domain; $\sum_{i,j}$ denotes the summation over i from 1 to m and j from 1 to n; U_c, V_c, U, and V are the mean values of u_c, v_c, u, and v, respectively, over the concerned domain, and

$$\sigma_c^2 = \sum_{i,j}\left\{\left[u_c(i,j) - U_c\right]^2 + \left[v_c(i,j) - V_c\right]^2\right\} \Big/ mn, \tag{7c}$$

$$\sigma^2 = \sum_{i,j}\left\{\left[u(i,j) - U\right]^2 + \left[v(i,j) - V\right]^2\right\} \Big/ mn, \tag{7d}$$

A high SCC and small RRD indicate a high accuracy of $\mathbf{v}_c$ and vice versa.

For the TY1818 case (Figure 2), SCC by the hybrid method >0.999 in all levels at all times, while SCC by the relaxation method <0.99. RRD by the hybrid method <0.03 in all levels at all times, while RRD by the relaxation method >0.1. Accuracy of the relaxation method is 1/30 of the hybrid method in most levels at most times. Larger deviations between the original **v** and reconstructed $\mathbf{v}_c$ can be seen at lower levels beneath 700 hPa than the results at other vertical levels and during ET in both methods, due to the complexity of the flow patterns. However, the accuracy loss at lower levels by the hybrid method is less than 1%, while that by the relaxation method is more than 10%, which may result in misrepresenting the real features of the partitioned $\mathbf{v}_d$ during ET. The comparative analysis of the KE budgets computed by partitioned $\mathbf{v}_r$ and $\mathbf{v}_d$ from the hybrid and SOR methods will be performed in the following section.

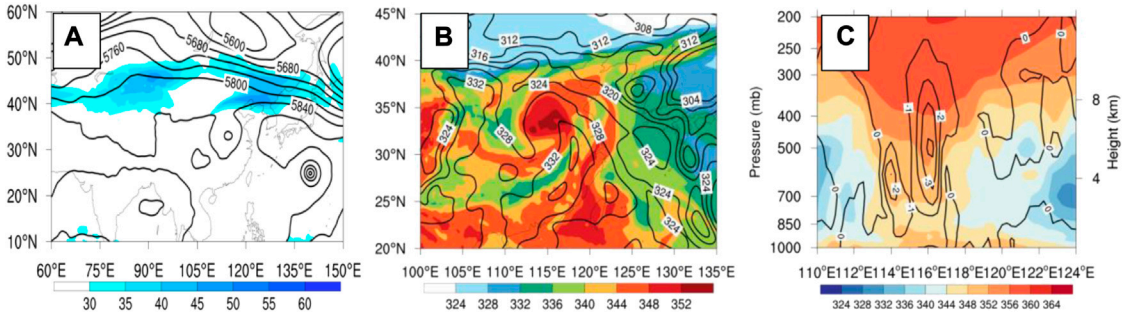

FIGURE 3
(A) 500-hPa height field (contours) with 200-hPa high-altitude rapids (>30 m/s, filled area), **(B)** 500-hPa pseudo-equivalent potential temperature (filled area, in K) and 500-hPa 336-K contours (solid black line), and **(C)** vertical distribution of the pseudo-equivalent potential temperature at 1200 UTC on 18 August 2018.

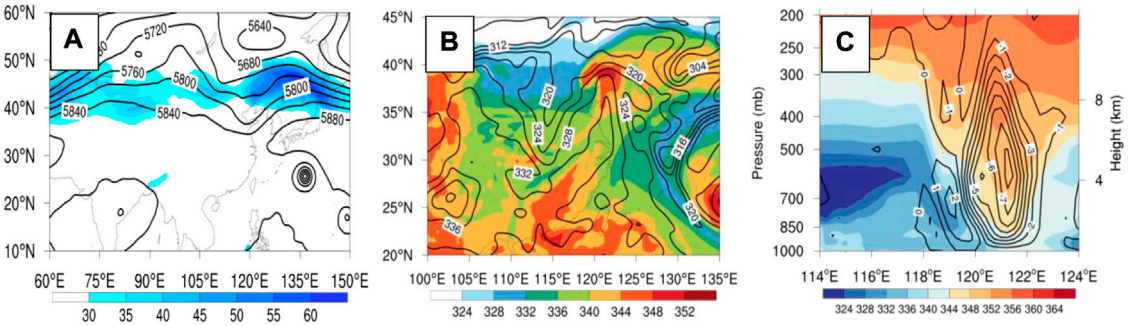

FIGURE 4
(A) 500-hPa height field (contours) with 200-hPa high-altitude rapids (>30 m/s, filled area), **(B)** 500-hPa pseudo-equivalent potential temperature (filled area, in K) and 500-hPa 336-K contours (solid black line), and **(C)** vertical distribution of the pseudo-equivalent potential temperature at 0000 UTC on 20 August 2018.

Kinetic energy analyses

Case overview

A tropical depression formed over the northwestern Pacific Ocean at 0000 UTC on 15 August 2018, which developed into the tropical storm Rumbia (No. 1818) at 0600 UTC on the same day. At 2000 UTC on August 16, it caused a landfall (force 9 on the Beaufort scale, 23 m s^{-1}, 985 hPa) over the coast of the southern Pudong New District in Shanghai before weakening into a tropical depression within the Henan province in the afternoon of August 18, transforming into an extratropical cyclone in the northern Shandong province and further weakening over the northern Yellow Sea on the night of August 20. On August 21, the National Meteorological Center stopped its numbering.

On the night of August 18 (Figure 3), Rumbia moved slowly in the saddle field at 500 hPa geopotential height, blocked by the weak high-pressure barrier on the north side. Meanwhile, the warm core structure in the upper level was still intact, and the cold air effect was not obvious.

From the night of August 19 to the early morning of August 20 (Figure 4), Rumbia began to merge into the westerly trough. The cold air behind the trough gradually moved from the low level to the left side of Rumbia, and the warm core structures in the middle and upper levels were gradually destroyed.

During the daytime on August 20, Rumbia over the Bohai Sea and Yellow Sea was in the process of extratropical transition. On the night of the 20th (Figure 5), the process of transitioning to an extratropical cyclone was basically completed over the northern Yellow Sea. In this process, Rumbia in the low level was quickly surrounded by the cold air from the northwest side, and the warm core structure in the upper level completely disappeared, presenting an obvious frontal structure.

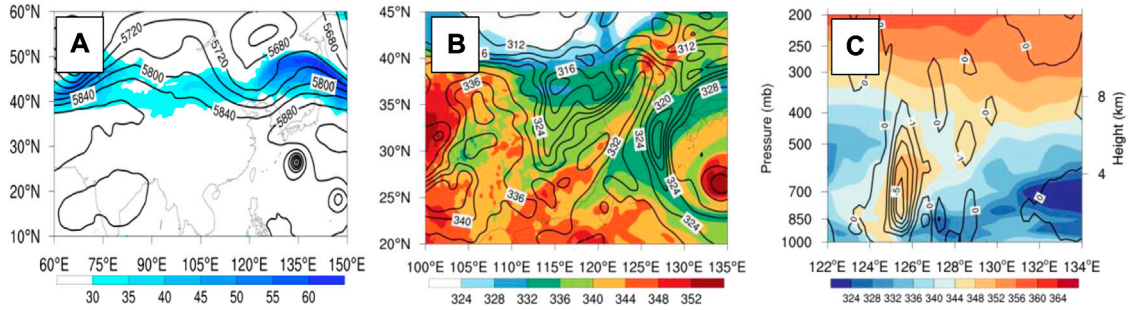

FIGURE 5
(A) 500-hPa height field (contours) with 200-hPa high-altitude rapids (>30 m/s, filled area), **(B)** 500-hPa pseudo-equivalent potential temperature (filled area, in K) and 500-hPa 336-K contours (solid black line), and **(C)** vertical distribution of the pseudo-equivalent potential temperature at 1200 UTC on 20 August 2018.

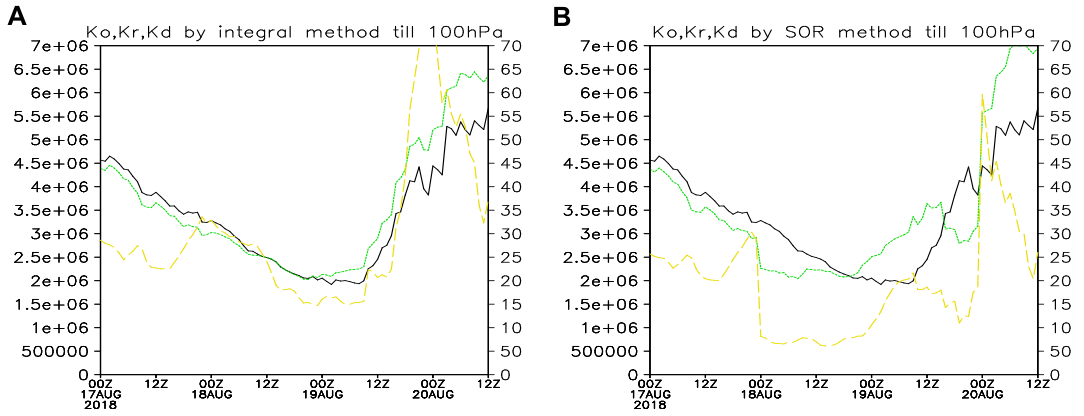

FIGURE 6
K0 (black), Kr (green), and Kd (yellow) by **(A)** the hybrid method, and **(B)** the SOR method.

Applications in diagnosing ET

The rotational component of kinetic energy (Kr) of TC following domain vertically integrated by the integral method decreases at the same rate as K0 before the ET and starts to increase ahead of K0 (Figure 6A) at 0000 UTC on August 18. The divergent component of the kinetic energy (Kd) varies less abruptly before the ET and doubles its magnitude suddenly within 12 h, which then decreases since 0000 UTC on August 20. Before the ET, the evolution of Kr by the SOR method (Figure 6B) deviates from that of K0 since 0000 UTC on August 18, while Kd decreases sharply. Their temporal evolutions after the ET are similar to the aforementioned results by the integral method but of different magnitudes. This discrepancy is consistent with the locations of the low accuracy shown in Figures 2B,D. The large error from the SOR method causes the fluctuation of Kd before the ET, but the increasing range of Kd decreases, and the time of increase shortens after the ET. Compared with the divergent wind component (V_d) obtained by the integral method, the SOR method will lose the signal of Kd, indicating the beginning of ET. Therefore, we should use the integral method which can accurately calculate the rotational wind component V_r and V_d.

Kinetic energy analyses

Vertical distributions of the temporal mean kinetic energy in different periods of ET

The conversions from PE to Kd and from Kd to Kr are known to be the main source of Kr (Figure 7). The time-averaged KE budgets for TC in its following domain and all domains at each pressure level are depicted in Figure 7. The intense low-level structure of typhoon circulation manifests as the maxima below 800 hPa in the Kr and Kd

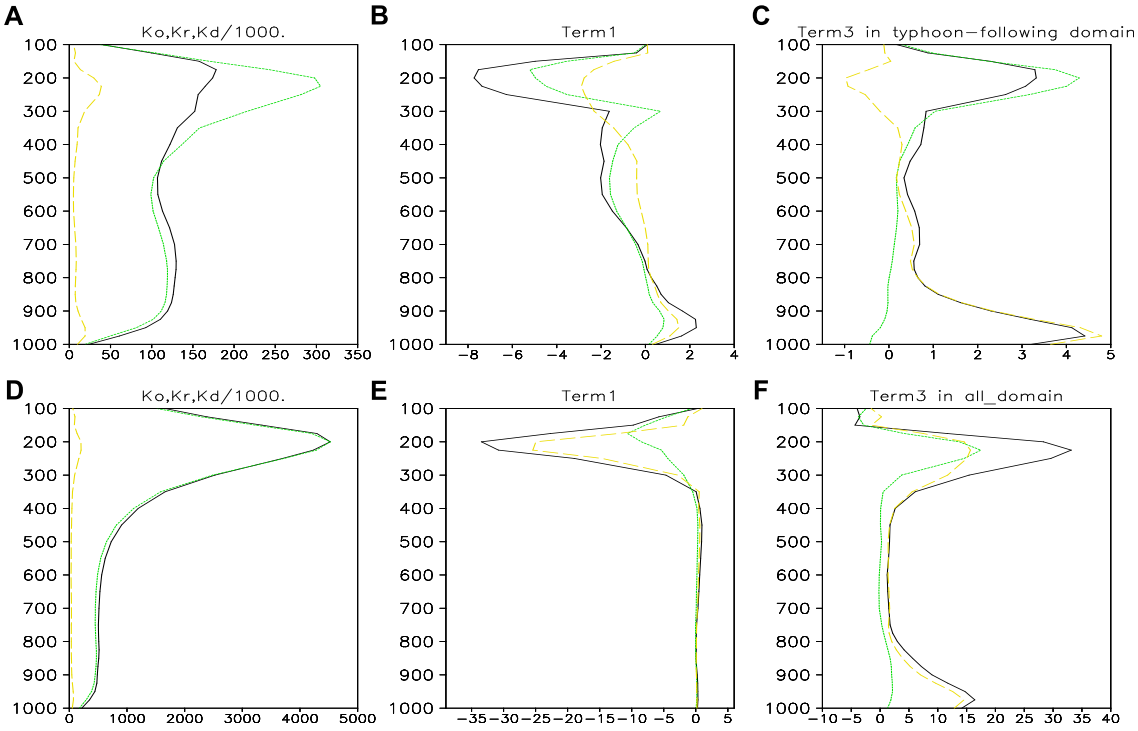

FIGURE 7
(A) K0 (black), Kr (green), and Kd (yellow); **(B)** T1 (black), T1r (green), and T1d (yellow), and **(C)** T3 (black),T3r (green), and T3d (yellow) by hybrid method averaged over the entire ET process in the TC following domain. **(D–F)** are corresponding all domain.

curves (Figure 7A), while in contrast, only the maxima of Kr and K0 around 200 hPa associated with the subtropical strong jet are retained (Figure 7D). T1 in the typhoon following domain (Figure 7B) plays the role of either a source or sink at different levels, while the corresponding values in the outermost domain (Figure 7E) present identical sink characteristics. The increase in T3r in the upper level and the decrease in T3d in the whole layer (Figure 7C) are not detected in the outermost domain (Figure 7F) due to the influence of the strong upper-level jet.

In the outermost domain, only the influence of the upper-level jet at 200 hpa can be found (Figures 8D–F). The large-value center of Kr appears one after another, which represents the southward extension of the 200 hPa jet, while Kd reflects that the divergence center of the 200-hPa jet is close. Figures 8A–C display that K0 in the upper level decreases first, then increases, and gradually transfers to the lower level, while K0 in the lower level decreases first, varies little from 0000 UTC to 1800 UTC on August 19, and then increases. The Kr in the upper level increases in advance, and its intensity is greater than that of K0, but it is transferred to the lower level later than K0, and the change of Kr in the lower level is consistent with that of K0. The time for Kd to weaken and start to increase in the upper level is consistent with that of K0. Kd rapidly weakens after 1800 UTC on August 19 (when the divergence accompanying the typhoon circulation in the upper level disappeared and transitioned into an extratropical cyclone), and the transfer to the lower level stops, after which a large-value center appears in the lower level. Therefore, the results in the TC-following domain are adopted to further analyze the ability to represent the vertical variation of the KE budget. Based on the K0 evolution, the ET process is divided into three stages, namely, the pre-development stage (from 0600 UTC to 2200 UTC on August 18), re-intensification stage (from 2300 UTC on August 18 to 1700 UTC on August 19), and ET stage (from 2000 UTC on August 19 to 1200 UTC on August 20).

In terms of the average over the entire TC life cycle, the KE generated by the cross-contour flow (T3 in Figure 7C) is a persistent source with two maxima at 950 hPa and 200 hPa, while T1 acts as the main sink in the middle and upper levels. Known as the major source or sink terms of different levels at different stages of the TC life cycle, T1 and T3 are analyzed in three stages during the ET (Figure 9). As the TC loses its tropical characteristics, V_r-related terms become dominant in T1 and T3. T3r is the main source as the upper-level trough rapidly intensifies. In response to the developing cyclonic vortex in the upper level, the cross-contour flow toward lower height is generated. From stages 1 to 3, K0 reduces in the lower level (as indicated by the vorticity changes at

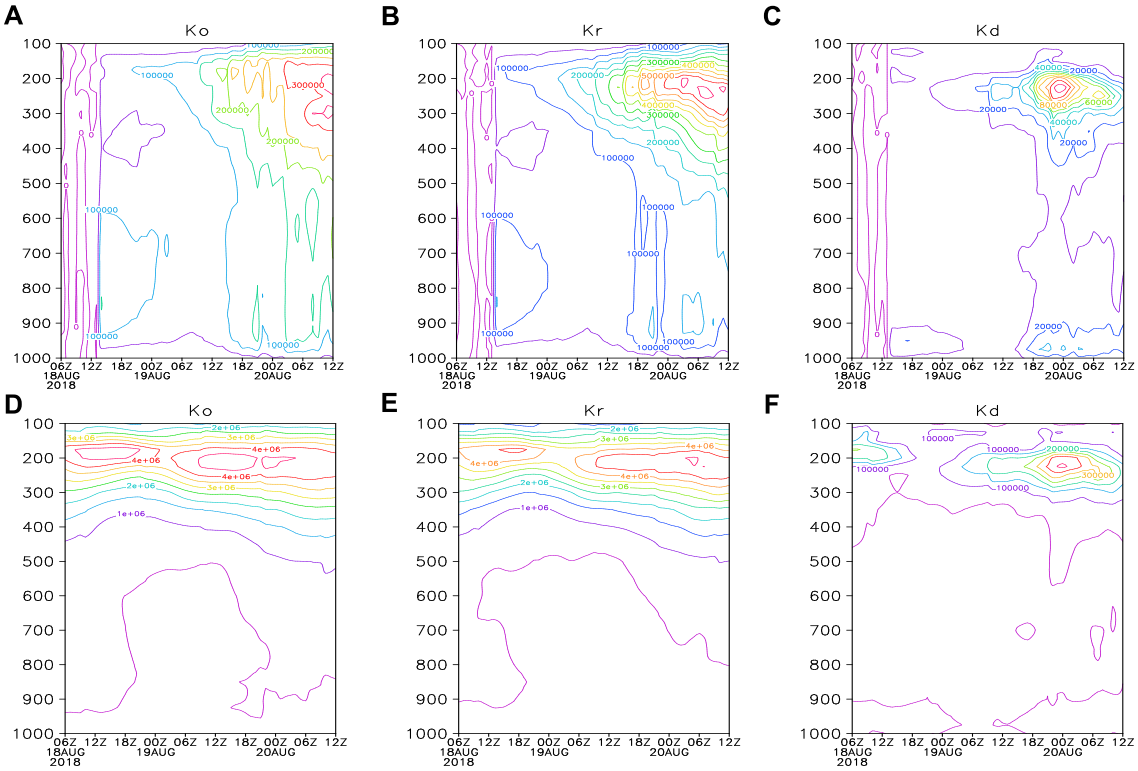

FIGURE 8
K0, Kr, and Kd in the typhoon-following domain **(A–C)** and outermost domain **(D–F)**.

200 hPa and 850 hPa, figures omitted) and increases in the upper level. However, Kr increases more and more in the upper level (corresponding to the enhancement of the westerly center in the vertical profile), and Kd increases in the upper level (corresponding to the divergence area on the right side of the jet). Kd increases in the lower level, corresponding to the convergence of extratropical cyclones, which is half the magnitude of Kr. T1 is a source in the lower level (decreasing first and then increasing), while a sink in the middle and upper levels (becoming bigger and bigger). T1r in the lower level is a source, with little change in its intensity, while it acts as sinks in the middle and upper levels, with increasing values. The T1d in the lower level acts as a source, which increases slightly in its intensity, while a sink in the middle level, and the large value is gradually transferred to the upper level. T3 is a source in the lower level (decreasing first and then increasing), which is always determined by T3d, while a sink in the middle level, determined by T3d first and then a source determined by T3r. T3r acts as a sink only below the height of 900 hPa; it plays the role of sources at other heights, which is increasingly being transferred to the higher layers over time. T3d is a sink above 200 hPa, which is increasingly being transferred downward over time, that is, the degree of response to T3r in the upper level is increasing.

Time–height variations of kinetic budget quantities

Figure 10 distinctly displays the KE budget calculated by the integral method in the TC-following domain during the three stages of ET. Before the occurrence of ET, T1 in the upper and lower layers changes little but decreases in the lower layer (determined by T3d) and gradually increases in the upper layer (determined by T3r). Since the start of the ET, T1 changes little in the lower layer, while T1r in the upper layer presents a strong sub-center and is transferred downward. T1r varies little in the lower layer, which manifests as a sub-center but is not transferred downward obviously in the upper layer. T1d presents a maximum in the lower layer and a sub-center in the upper layer, which is transferred downward obviously. T3 in the lower layer increases first and then decreases, which has a change trend consistent with that of T3d, while its intensity is weaker than that of T3d. Meanwhile, T3 in the upper layer increases first and then decreases. This increase appears later than that in the lower layer, and then, the positive value is transferred downward. However, there is no signal in the lower layer, and the T3 in the upper layer increases first and then decreases without obvious

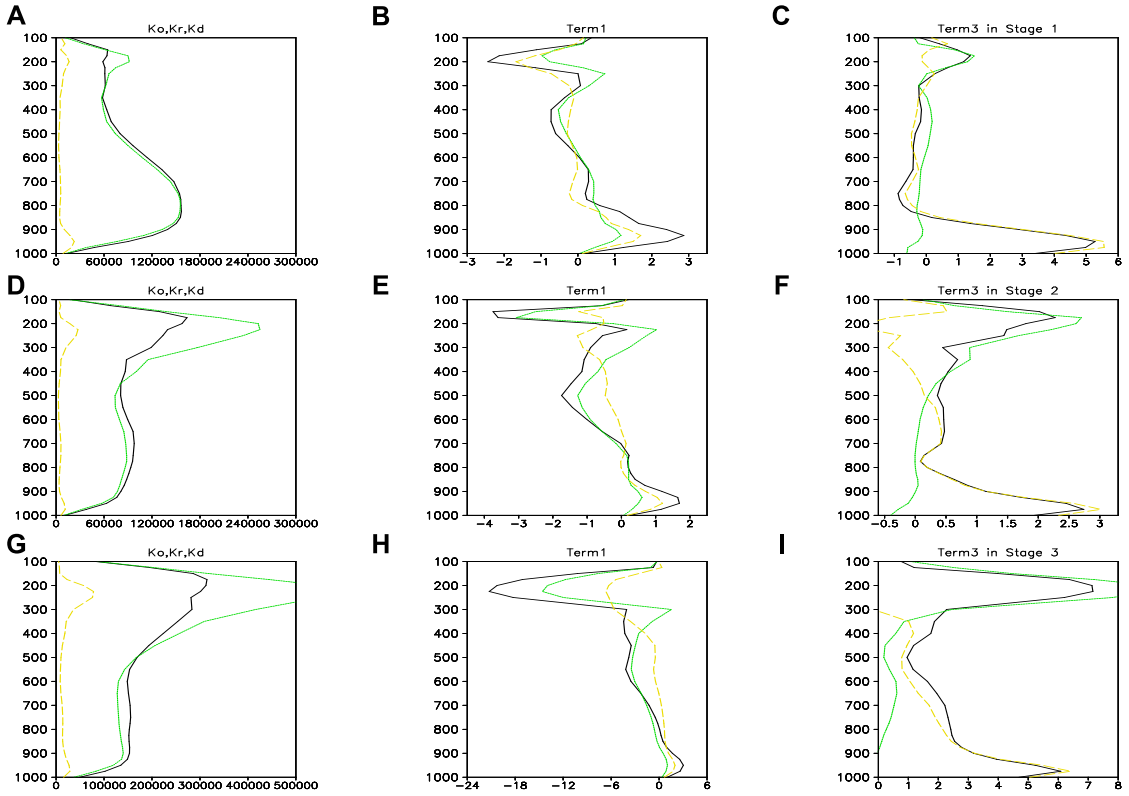

FIGURE 9
Same as Figures 7A–C but averaged over the pre-development stage **(A–C)**, the reintensification stages **(D–F)** and the ET stage **(G–I)**.

downward transfer. T3d in the lower layer first increases and then decreases, the positive value is transferred to the upper layer, and thus, a sub-center appears in the upper layer. After the ET process, T1 and T3 present opposite changes at the top level, especially because T1 reflects the trend that K0 weakens first and then strengthens in the upper level, as shown in Figure 9A. The ET needs V_d to provide start-up energy, which is transferred to the upper layer through T1d and T3d in the lower layers to realize the conversion from Kd to Kr, and then, V_r is enhanced, and the baroclinity is weakened, resulting in the ET.

Figure 11 reveals that T3 calculated by the SOR method shows obvious differences before and after the ET. However, T3d does not reflect the process of storing kinetic energy to stimulate the ET before its occurrence in the lower layer but presents false signals of evolution (first increase and then decrease) in the upper layer, which reflects the delay of ET occurrence time. After the ET, T3d shows a downward transfer of the positive value center, which is contrary to the upward transfer of the positive value center shown in Figure 10F. The results indicate that the SOR method in the TC-following domain performs poorly in T3, T3r, and T3d.

Quantitative analysis of the interaction term between Kd and Kr

Quantitative values for Af, Az, B and C at upper and lower levels are recorded in Table 1. In order to present the specific comparisons during ET of Typhoon Rumbia (2018), the ET from 15 UTC on the 19th to 03 UTC on the 20th is divided into three stages, that is, before the ET(the first 3 hours), at ET time (21 UTC on the 19th), and after the ET (the last 3 hours). Af is to satisfy the conservation of angular momentum on the tangential motion, Az is to satisfy the conservation of angular momentum on the rotational motion, B represents the vertical exchange of rotational momentum, and C represents the vertical exchange of divergent momentum.

It can be seen from Table 1 that in the ET stage, B in the upper layer is the maximum value and B in the lower layer is the minimum value. After the ET, B in the upper layer decreases significantly and B in the lower layer increases significantly. The value of C is just the opposite. In the ET stage, C in the upper layer is the minimum value and C in the lower layer is the maximum value. After the ET, B in the upper layer obviously increases, while C in the lower layer

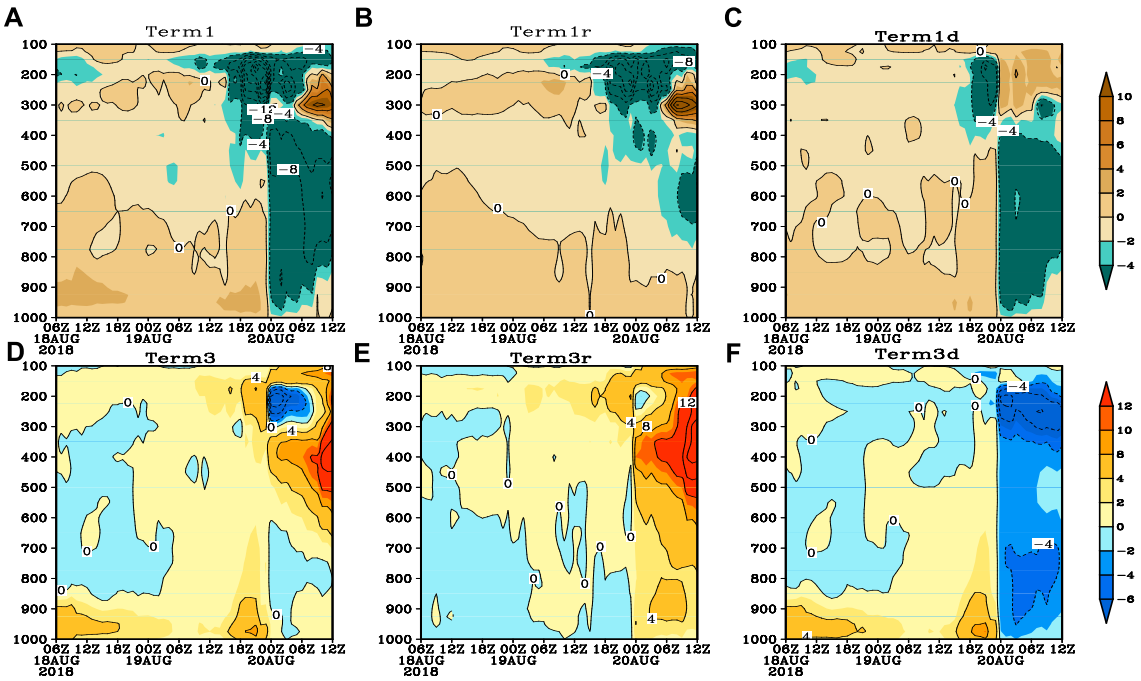

FIGURE 10
(A) T1, **(B)** T1r, **(C)** T1d, **(D)** T3, **(E)** T3r, and **(F)** T3d by the hybrid method in the typhoon-following domain.

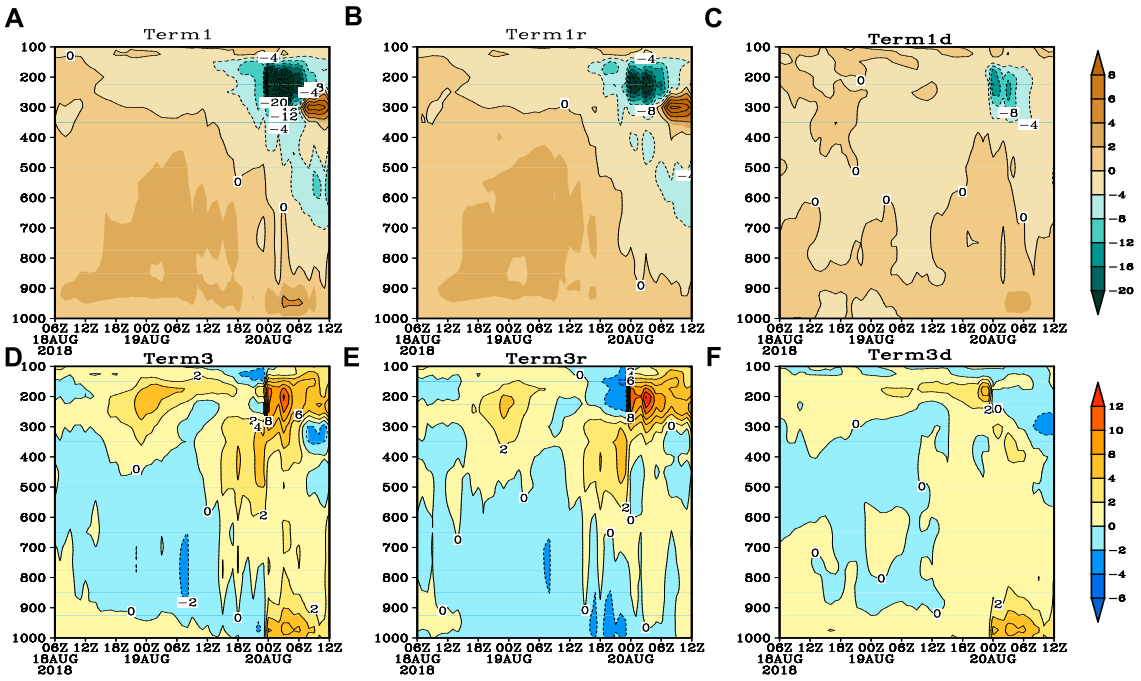

FIGURE 11
(A) T1, **(B)** T1r, **(C)** T1d, **(D)** T3, **(E)** T3r, and **(F)** T3d by the SOR method in the typhoon-following domain.

TABLE 1 Af, Az, B, and C at 200 hPa and 950 hPa (unit: Wm^{-2}).

	200 hPa				950 hPa			
	Af	Az	B	C	Af	Az	B	C
3 h before the ET	0.00362	−0.000979	0.0124	−0.021	0.0114	0.0110	−0.0075	−0.0019
ET process	0.000081	−0.00051	0.0210	−0.0134	0.0130	0.0109	−0.0120	0.00093
3 h after the ET	−0.00593	−0.00360	0.00993	−0.0046	0.00674	0.00853	−0.0024	−0.00205

obviously decreases. Before and after the ET stage, the magnitude of AF and AZ was similar, and AF and AZ decreased significantly after the ET.

It shows that the change trend of the rotational wind energy in the vertical direction before and after the ET stage is opposite to that of the divergent wind energy. After the ET stage, the rotational wind energy in the vertical direction increases significantly, while the divergent wind energy in the vertical direction decreases significantly. In particular, the divergent wind energy in the lower layer shows a positive value in the ET stage, and it is negative before and after the ET stage. This shows that the obvious change of the divergent wind energy has a certain indicative significance for the ET.

Conclusion and discussions

By using a hybrid method to partition the horizontal wind field in a limited domain, this study analyzes the effects of divergent winds on the KE budget of Typhoon Rumbia (1818) during its entire life cycle, especially during the ET in the TC-following domain and the outermost domain that covers the entire typhoon track. Comparisons with the results from the commonly used SOR method have proved the high accuracy of the hybrid method. The roles of Kd in the ET during the life cycle of Typhoon Rumbia are analyzed with the following preliminary results:

1) The KE budget analysis is useful for studying ET. It is found that the KE budgets by the divergent winds are of vital importance during the entire ET of the typhoon.
2) The adoption of the accurate mathematical approach is more appropriate for complex flow patterns such as the one during the ET is proved in this study. It is found that modification of the divergent wind components leads to obvious changes in the spatiotemporal variations of the KE budget. The divergent winds computed by the SOR method with a lower accuracy result in sizable errors in spatiotemporal variations of the KE during the ET, which thus leads to significant forecasting errors. Although the three complicated stages with distinct characteristic flow patterns in the ET period of Rumbia (1818) are investigated with the same conclusions, more cases will be checked to amend limitations to this study in the future.
3) The distribution of the divergent winds in the KE budget is found to be asymmetric after Typhoon Rumbia's landfall. In our subsequent research, the relationship between the KE budgets in different quadrants and the tremendous precipitation will be explored by using the integral method in the TC-following domain.

Data availability statement

The raw data supporting the conclusions of this article will be made available by the authors, without undue reservation.

Author contributions

Conceptualization, GZ and JC; methodology, JD and JC; analyze data and software, LL and XL; validation, GZ and JC; formal analysis, JD and XL; writing—original draft preparation, GZ; writing—review and editing, JC; funding acquisition, LL.

Funding

This work was supported by the National Key R&D Program of China (2022YFC3004200), the National Natural Science Foundation of China (42175011), the Open Grants of the State Key Laboratory of Severe Weather (2022LASW-B09), and the Key Laboratory of South China Sea Meteorological Disaster Prevention and Mitigation of Hainan Province (SCSF202101).

Acknowledgments

The authors are thankful to the reviewers for their comments and suggestions on the original manuscript that improved the structures and presentations of the results. The computing for

this project was performed at the Supercomputing Center for Education and Research at the University of Oklahoma (OU), USA.

Conflict of interest

The authors declare that the research was conducted in the absence of any commercial or financial relationships that could be construed as a potential conflict of interest.

Publisher's note

All claims expressed in this article are solely those of the authors and do not necessarily represent those of their affiliated organizations, or those of the publisher, the editors, and the reviewers. Any product that may be evaluated in this article, or claim that may be made by its manufacturer, is not guaranteed or endorsed by the publisher.

References

Cao, J., Xu, Q., Chen, H., and Ma, S. (2022a). Hybrid methods for computing the streamfunction and velocity potential for complex flow fields over mesoscale domains. *Adv. Atmos. Sci.* 39 (9), 1417–1431. doi:10.1007/s00376-021-1280-y

Cao, J., Zhou, G., Zhao, L. Liu W., and Yan, Y. (2022b). Kinetic energy budget analyses among different quadrants during typhoon recurvature: A case study of typhoon Rumbia (2018). *Atmos. Res.*, 106319. doi:10.1016/j.atmosres.2022.106319

Cao, Z., Xu, Q., and Zhang, D. (2019). A new method to diagnose cyclone-cyclone interaction and its influences on precipitation. *J. Appl. Meteorol. Climatol.* 58, 1821–1851. doi:10.1175/jamc-d-18-0344.1

Chen, Q. S., and Kuo, Y. H. (1992b). A consistency condition for wind-field reconstruction in a limited area and a harmonic-cosine series expansion. *Mon. Wea. Rev.* 120, 2653–2670. doi:10.1175/1520-0493(1992)120<2653:accfwf>2.0.co;2

Chen, T. C., Alpert, J. C., and Schlatter, T. W. (1978)., 106. TEODAN>2.0.CO, 458–468. doi:10.1175/1520-0493The effects of divergent and nondivergent winds on the kinetic energy budget of amid latitude cyclone: A case study*Mon. Wea. Rev.*

Chen, T. C., and Wiin-Nielsen, A. (1976). On the kinetic energy of the divergent and nondivergent flow in the atmosphere. *Tullus* 28, 486–498. doi:10.3402/tellusa.v28i6.11317

Dimego, G. J., and Bosart, L. F. (1982a). The transformation of tropical storm agnes into an extratropical cyclone. Part I: The observed fields and vertical motion computations. *Mon. Wea. Rev.* 385–411. doi:10.1175/1520-0493(1982)110<0385:TTOTSA>2.0.CO;2

Dimego, G. J., and Bosart, L. F. (1982b). The transformation of tropical storm agnes into an extratropical cyclone. Part II: Moisture, vorticity and kinetic energy budgets. *Mon. Wea. Rev.* 110 (5), 412–433. doi:10.1175/1520-0493(1982)110<0142:TTOTSA>2.0.CO;2

Ding, Y. H., and Liu, Y. Z. (1985a). On the analysis of typhoon kinetic energy, PartI Budget of total kinetic energy and eddy kinetic energy. *Sci. China B* 10, 956–966. (in Chinese).

Ding, Y. H., and Liu, Y. Z. (1985b). On the analysis of typhoon kinetic energy, PartII Conversion between divergent and nondivergent wind. *Sci. China B* 11, 1045–1054. (in Chinese).

Fu, S. M., Wang, H. J., Sun, J. H., and Zhang, Y. (2016). Energy budgets on the interactions between the mean and eddy flows during a persistent heavy rainfall event over the Yangtze River valley in summer 2010. *J. Meteorol. Res.* 30 (4), 513–527. doi:10.1007/s13351-016-5121-3

Peng, J., Peng, M. S., Li, T., and Hendricks, E. (2014b). Effect of baroclinicity on vortex axisymmetrization. PartII: Baroclinic basic vortex. *Adv. Atmos. Sci.* 31, 1267–1278. doi:10.1007/s00376-014-3238-9

Peng, M. S., Peng, J., Li, T., and Hendricks, E. (2014a). Effect of baroclinicity on vortex axisymmetrization. Part I: Barotropic basic vortex. *Adv. Atmos. Sci.* 31, 1256–1266. doi:10.1007/s00376-014-3237-x

Sun, Y., Zhong, Z., and Wang, Y. (2012). Kinetic energy budget of Typhoon Yagi (2006) during its extratropical transition. *Meteorol. Atmos. Phys.* 118, 65–78. doi:10.1007/s00703-012-0200-1

Ullah, W., Wang, G., Gao, Z., Tawia Hagan, D. F., Bhatti, A. S., and Zhua, C. (2020). Observed linkage between Tibetan plateau soil moisture and South asian summer precipitation and the possible mechanism. *J. Clim.* 34, 361–377. doi:10.1175/jcli-d-20-0347.1

Ullah, W., Wang, G., Lou, D., Ullah, S., Bhatti, A. S., Ullah, S., et al. (2021). Large-scale atmospheric circulation patterns associated with extreme monsoon precipitation in Pakistan during 1981–2018. *Atmos. Res.* 232, 105489. doi:10.1016/j.atmosres.2021.105489

Vallis, G. K., Shutts, G. J., and Gray, M. E. B. (1997). Balanced mesoscale motion and stratified turbulence forced by convection. *Q. J. R. Meteorol. Soc.* 123, 1621–1652. doi:10.1002/qj.49712354209

Wang, Y., Cui, X., Li, X., Zhang, W., and Huang, Y. (2016). Kinetic energy budget during the Genesis period of tropical cyclone durian (2001) in the South China Sea. *Mon. Weather Rev.* 144, 2831–2854. doi:10.1175/MWR-D-15-0042.1

Xu, Q., Cao, J., and Gao, S. (2011). Computing streamfunction and velocity potential in a limited domain of arbitrary shape. Part I: Theory and integral formulae. *Adv. Atmos. Sci.* 28, 1433–1444. doi:10.1007/s00376-011-0185-6

You, C., and Fung, J. (2019). Characteristics of the sea-breeze circulation in the pearl river delta region and its dynamical diagnosis. *J. Appl. Meteorol. Climatol.* 58, 741–755. doi:10.1175/jamc-d-18-0153.1

Zhao, S., and Cook, K. (2021). Influence of walker circulations on east african rainfall. *Clim. Dyn.* 7, 2127–2147. doi:10.1007/s00382-020-05579-7

Zhong, S. X., Meng, W. G., and Tian, F. Y. (2021). Budgets of rotational and divergent kinetic energy in the warm-sector torrential rains over South China: A case study. *Meteorol. Atmos. Phys.* 133, 759–769. doi:10.1007/s00703-021-00778-1

Frontiers in Earth Science

Investigates the processes operating within the major spheres of our planet

Advances our understanding across the earth sciences, providing a theoretical background for better use of our planet's resources and equipping us to face major environmental challenges.

Discover the latest Research Topics

See more →

Frontiers

Avenue du Tribunal-Fédéral 34
1005 Lausanne, Switzerland
frontiersin.org

Contact us

+41 (0)21 510 17 00
frontiersin.org/about/contact